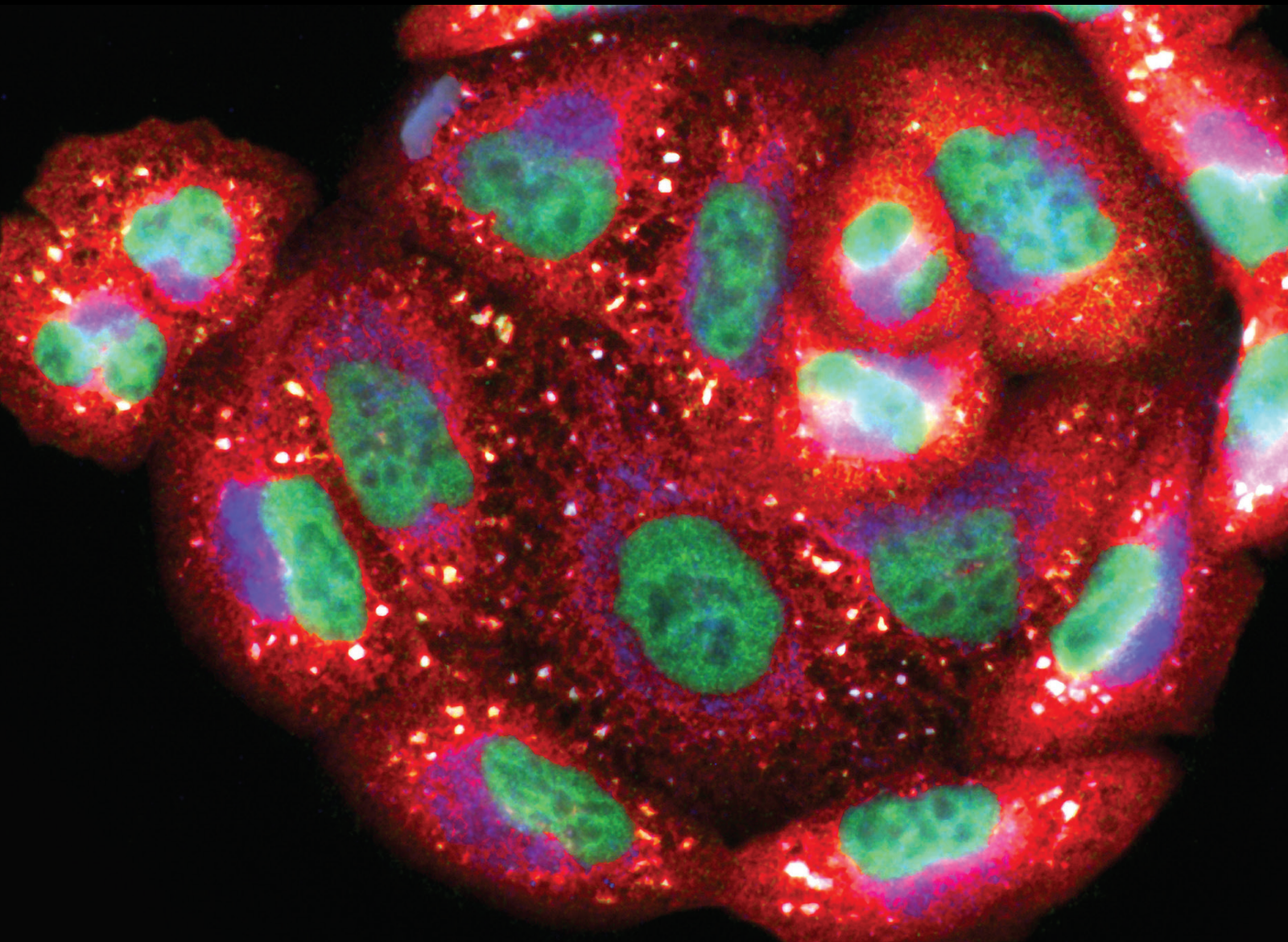


# Lipid Metabolism and Oxidative Stress: Crosstalk Between the Intestine and Other Metabolic Organs

Lead Guest Editor: Tongxing Song

Guest Editors: Demin Cai, Hao Wu, Yingping Xiao, and Zhihao Jia





---

**Lipid Metabolism and Oxidative Stress:  
Crosstalk Between the Intestine and Other  
Metabolic Organs**

Oxidative Medicine and Cellular Longevity

---

**Lipid Metabolism and Oxidative Stress:  
Crosstalk Between the Intestine and  
Other Metabolic Organs**

Lead Guest Editor: Tongxing Song

Guest Editors: Demin Cai, Hao Wu, Yingping Xiao,  
and Zhihao Jia



---

Copyright © 2024 Hindawi Limited. All rights reserved.

This is a special issue published in "Oxidative Medicine and Cellular Longevity" All articles are open access articles distributed under the Creative Commons Attribution License, which permits unrestricted use, distribution, and reproduction in any medium, provided the original work is properly cited.

# Chief Editor

Jeannette Vasquez-Vivar, USA

## Associate Editors

Amjad Islam Aqib, Pakistan  
Angel Catalá , Argentina  
Cinzia Domenicotti , Italy  
Janusz Gebicki , Australia  
Aldrin V. Gomes , USA  
Vladimir Jakovljevic , Serbia  
Thomas Kietzmann , Finland  
Juan C. Mayo , Spain  
Ryuichi Morishita , Japan  
Claudia Penna , Italy  
Sachchida Nand Rai , India  
Paola Rizzo , Italy  
Mithun Sinha , USA  
Daniele Vergara , Italy  
Victor M. Victor , Spain

## Academic Editors

Ammar AL-Farga , Saudi Arabia  
Mohd Adnan , Saudi Arabia  
Ivanov Alexander , Russia  
Fabio Altieri , Italy  
Daniel Dias Rufino Arcanjo , Brazil  
Peter Backx, Canada  
Amira Badr , Egypt  
Damian Bailey, United Kingdom  
Rengasamy Balakrishnan , Republic of Korea  
Jiaolin Bao, China  
Ji C. Bihl , USA  
Hareram Birla, India  
Abdelhakim Bouyahya, Morocco  
Ralf Braun , Austria  
Laura Bravo , Spain  
Matt Brody , USA  
Amadou Camara , USA  
Marcio Carcho , Portugal  
Peter Celec , Slovakia  
Giselle Cerchiaro , Brazil  
Arpita Chatterjee , USA  
Shao-Yu Chen , USA  
Yujie Chen, China  
Deepak Chhangani , USA  
Ferdinando Chiaradonna , Italy

Zhao Zhong Chong, USA  
Fabio Ciccarone, Italy  
Alin Ciobica , Romania  
Ana Cipak Gasparovic , Croatia  
Giuseppe Cirillo , Italy  
Maria R. Ciriolo , Italy  
Massimo Collino , Italy  
Manuela Corte-Real , Portugal  
Manuela Curcio, Italy  
Domenico D'Arca , Italy  
Francesca Danesi , Italy  
Claudio De Lucia , USA  
Damião De Sousa , Brazil  
Enrico Desideri, Italy  
Francesca Diomede , Italy  
Raul Dominguez-Perles, Spain  
Joël R. Drevet , France  
Grégory Durand , France  
Alessandra Durazzo , Italy  
Javier Egea , Spain  
Pablo A. Evelson , Argentina  
Mohd Farhan, USA  
Ioannis G. Fatouros , Greece  
Gianna Ferretti , Italy  
Swaran J. S. Flora , India  
Maurizio Forte , Italy  
Teresa I. Fortoul, Mexico  
Anna Fracassi , USA  
Rodrigo Franco , USA  
Juan Gambini , Spain  
Gerardo García-Rivas , Mexico  
Husam Ghanim, USA  
Jayeeta Ghose , USA  
Rajeshwary Ghosh , USA  
Lucia Gimeno-Mallench, Spain  
Anna M. Giudetti , Italy  
Daniela Giustarini , Italy  
José Rodrigo Godoy, USA  
Saeid Golbidi , Canada  
Guohua Gong , China  
Tilman Grune, Germany  
Solomon Habtemariam , United Kingdom  
Eva-Maria Hanschmann , Germany  
Md Saquib Hasnain , India  
Md Hassan , India

Tim Hofer , Norway  
John D. Horowitz, Australia  
Silvana Hrelia , Italy  
Dragan Hrnčić, Serbia  
Zebo Huang , China  
Zhao Huang , China  
Tariq Hussain , Pakistan  
Stephan Immenschuh , Germany  
Norsharina Ismail, Malaysia  
Franco J. L. , Brazil  
Sedat Kacar , USA  
Andleeb Khan , Saudi Arabia  
Kum Kum Khanna, Australia  
Neelam Khaper , Canada  
Ramoji Kosuru , USA  
Demetrios Kouretas , Greece  
Andrey V. Kozlov , Austria  
Chan-Yen Kuo, Taiwan  
Gaocai Li , China  
Guoping Li , USA  
Jin-Long Li , China  
Qiangqiang Li , China  
Xin-Feng Li , China  
Jialiang Liang , China  
Adam Lightfoot, United Kingdom  
Christopher Horst Lillig , Germany  
Paloma B. Liton , USA  
Ana Lloret , Spain  
Lorenzo Loffredo , Italy  
Camilo López-Alarcón , Chile  
Daniel Lopez-Malo , Spain  
Massimo Lucarini , Italy  
Hai-Chun Ma, China  
Nageswara Madamanchi , USA  
Kenneth Maiese , USA  
Marco Malaguti , Italy  
Steven McAnulty, USA  
Antonio Desmond McCarthy , Argentina  
Sonia Medina-Escudero , Spain  
Pedro Mena , Italy  
V́ctor M. Mendoza-Núñez , Mexico  
Lidija Milkovic , Croatia  
Alexandra Miller, USA  
Sara Missaglia , Italy

Premysl Mladenka , Czech Republic  
Sandra Moreno , Italy  
Trevor A. Mori , Australia  
Fabiana Morroni , Italy  
Ange Mouithys-Mickalad, Belgium  
Iordanis Mourouzis , Greece  
Ryoji Nagai , Japan  
Amit Kumar Nayak , India  
Abderrahim Nemmar , United Arab Emirates  
Xing Niu , China  
Cristina Nocella, Italy  
Susana Novella , Spain  
Hassan Obied , Australia  
Pál Pacher, USA  
Pasquale Pagliaro , Italy  
Dilipkumar Pal , India  
Valentina Pallottini , Italy  
Swapnil Pandey , USA  
Mayur Parmar , USA  
Vassilis Paschalis , Greece  
Keshav Raj Paudel, Australia  
Ilaria Peluso , Italy  
Tiziana Persichini , Italy  
Shazib Pervaiz , Singapore  
Abdul Rehman Phull, Republic of Korea  
Vincent Pialoux , France  
Alessandro Poggi , Italy  
Zsolt Radak , Hungary  
Dario C. Ramirez , Argentina  
Erika Ramos-Tovar , Mexico  
Sid D. Ray , USA  
Muneeb Rehman , Saudi Arabia  
Hamid Reza Rezvani , France  
Alessandra Ricelli, Italy  
Francisco J. Romero , Spain  
Joan Roselló-Catafau, Spain  
Subhadeep Roy , India  
Josep V. Rubert , The Netherlands  
Sumbal Saba , Brazil  
Kunihiro Sakuma, Japan  
Gabriele Saretzki , United Kingdom  
Luciano Saso , Italy  
Nadja Schroder , Brazil

Anwen Shao , China  
Iman Sherif, Egypt  
Salah A Sheweita, Saudi Arabia  
Xiaolei Shi, China  
Manjari Singh, India  
Giulia Sita , Italy  
Ramachandran Srinivasan , India  
Adrian Sturza , Romania  
Kuo-hui Su , United Kingdom  
Eisa Tahmasbpour Marzouni , Iran  
Hailiang Tang, China  
Carla Tatone , Italy  
Shane Thomas , Australia  
Carlo Gabriele Tocchetti , Italy  
Angela Trovato Salinaro, Italy  
Rosa Tundis , Italy  
Kai Wang , China  
Min-qi Wang , China  
Natalie Ward , Australia  
Grzegorz Wegrzyn, Poland  
Philip Wenzel , Germany  
Guangzhen Wu , China  
Jianbo Xiao , Spain  
Qiongming Xu , China  
Liang-Jun Yan , USA  
Guillermo Zalba , Spain  
Jia Zhang , China  
Junmin Zhang , China  
Junli Zhao , USA  
Chen-he Zhou , China  
Yong Zhou , China  
Mario Zoratti , Italy

## Contents

**Retracted: Dietary Quercetin Supplementation Attenuates Diarrhea and Intestinal Damage by Regulating Gut Microbiota in Weanling Piglets**

Oxidative Medicine and Cellular Longevity

Retraction (1 page), Article ID 9869280, Volume 2024 (2024)

**Retracted: Rocaglamide Prolonged Allograft Survival by Inhibiting Differentiation of Th1/Th17 Cells in Cardiac Transplantation**

Oxidative Medicine and Cellular Longevity

Retraction (1 page), Article ID 9810207, Volume 2024 (2024)

**Retracted: Taurine Ameliorates Iron Overload-Induced Hepatocyte Injury via the Bcl-2/VDAC1-Mediated Mitochondrial Apoptosis Pathway**

Oxidative Medicine and Cellular Longevity


Retraction (1 page), Article ID 9804902, Volume 2024 (2024)

**Retracted: Novel lncRNA AL033381.2 Promotes Hepatocellular Carcinoma Progression by Upregulating PRKRA Expression**

Oxidative Medicine and Cellular Longevity

Retraction (1 page), Article ID 9894384, Volume 2023 (2023)

**[Retracted] Taurine Ameliorates Iron Overload-Induced Hepatocyte Injury via the Bcl-2/VDAC1-Mediated Mitochondrial Apoptosis Pathway**

Xiaoyu Feng, Wenfeng Hu, Yujiao Hong, Linlin Ruan, Yueben Hu, and Dan Liu 




Research Article (14 pages), Article ID 4135752, Volume 2022 (2022)

**In Silico Establishment and Validation of Novel Lipid Metabolism-Related Gene Signature in Bladder Cancer**

Xianchao Sun , Ying Zhang , Yilai Chen , Shiyong Xin , Liang Jin , Xiang Liu , Zhen Zhou , Jiabin Zhang , Wangli Mei , Bihui Zhang , Xudong Yao , Guosheng Yang , and Lin Ye 

Research Article (20 pages), Article ID 3170950, Volume 2022 (2022)

**Identification of Resolvin D1 and Protectin D1 as Potential Therapeutic Agents for Treating Kidney Stones**

Bohan Wang, Jingchao Wei , Qi Huangfu, Fei Gao, Lanxin Qin, Jiao Zhong, Jiaming Wen, Zhangqun Ye, Xiaoqi Yang , and Haoran Liu 

Research Article (12 pages), Article ID 4345037, Volume 2022 (2022)



**N<sup>6</sup>-Methyladenosine Modification Profile in Bovine Mammary Epithelial Cells Treated with Heat-Inactivated *Staphylococcus aureus***

Ting Li , Yifan Zhu , Changjie Lin , Jie Chen , Yiya Yin , Xin Tang , Yingyu Chen , Aizhen Guo , and Changmin Hu 


Research Article (15 pages), Article ID 1704172, Volume 2022 (2022)





**Sodium Butyrate Ameliorates Oxidative Stress-Induced Intestinal Epithelium Barrier Injury and Mitochondrial Damage through AMPK-Mitophagy Pathway**

Xin Li , Chunchun Wang, Jiang Zhu, Qian Lin, Minjie Yu, Jiashu Wen, Jie Feng, and Caihong Hu   
Research Article (23 pages), Article ID 3745135, Volume 2022 (2022)



**Differentially Expressed Hepatic Genes Revealed by Transcriptomics in Pigs with Different Liver Lipid Contents**

Wentao Lyu , Yun Xiang, Xingxin Wang, Jingshang Li, Caimei Yang, Hua Yang , and Yingping Xiao   
Research Article (16 pages), Article ID 2315575, Volume 2022 (2022)

**Exploring the Possible Link between the Gut Microbiome and Fat Deposition in Pigs**

Guangmin Zhao , Yun Xiang, Xiaoli Wang, Bing Dai, Xiaojun Zhang, Lingyan Ma, Hua Yang , and Wentao Lyu   
Research Article (13 pages), Article ID 1098892, Volume 2022 (2022)


**[Retracted] Rocaglamide Prolonged Allograft Survival by Inhibiting Differentiation of Th1/Th17 Cells in Cardiac Transplantation**

Chen Dai , Xi Zhou, Lu Wang, Rumeng Tan, Wei Wang, Bo Yang, Yucong Zhang, Huibo Shi, Dong Chen, Lai Wei, and Zhishui Chen   
Research Article (15 pages), Article ID 2048095, Volume 2022 (2022)


**[Retracted] Novel lncRNA AL033381.2 Promotes Hepatocellular Carcinoma Progression by Upregulating PRKRA Expression**

Feiran Wang , Lirong Zhu , Qiang Xue , Chong Tang , Weidong Tang , Nannan Zhang , Chen Dai , and Zhong Chen   
Research Article (24 pages), Article ID 1125932, Volume 2022 (2022)



**[Retracted] Dietary Quercetin Supplementation Attenuates Diarrhea and Intestinal Damage by Regulating Gut Microbiota in Weanling Piglets**

Baoyang Xu, Wenxia Qin, Yunzheng Xu, Wenbo Yang, Yuwen Chen, Juncheng Huang, Jianan Zhao, and Libao Ma   
Research Article (19 pages), Article ID 6221012, Volume 2021 (2021)


**Emerging Pathological Engagement of Ferroptosis in Gut Diseases**

Weihua Gao , Ting Zhang , and Hao Wu   
Review Article (16 pages), Article ID 4246255, Volume 2021 (2021)

**Exogenous and Endogenous Serine Deficiency Exacerbates Hepatic Lipid Accumulation**

Liuqin He, Yonghui Liu, Di Liu, Yanzhong Feng, Jie Yin , and Xihong Zhou   
Research Article (10 pages), Article ID 4232704, Volume 2021 (2021)

***Lactobacillus plantarum* Exhibits Antioxidant and Cytoprotective Activities in Porcine Intestinal Epithelial Cells Exposed to Hydrogen Peroxide**

Jing Wang , Wei Zhang, Sixin Wang, Yamin Wang, Xu Chu, and Haifeng Ji  
Research Article (13 pages), Article ID 8936907, Volume 2021 (2021)

## *Retraction*

# **Retracted: Dietary Quercetin Supplementation Attenuates Diarrhea and Intestinal Damage by Regulating Gut Microbiota in Weanling Piglets**

### **Oxidative Medicine and Cellular Longevity**

Received 8 January 2024; Accepted 8 January 2024; Published 9 January 2024

Copyright © 2024 Oxidative Medicine and Cellular Longevity. This is an open access article distributed under the Creative Commons Attribution License, which permits unrestricted use, distribution, and reproduction in any medium, provided the original work is properly cited.

This article has been retracted by Hindawi following an investigation undertaken by the publisher [1]. This investigation has uncovered evidence of one or more of the following indicators of systematic manipulation of the publication process:

- (1) Discrepancies in scope
- (2) Discrepancies in the description of the research reported
- (3) Discrepancies between the availability of data and the research described
- (4) Inappropriate citations
- (5) Incoherent, meaningless and/or irrelevant content included in the article
- (6) Manipulated or compromised peer review

The presence of these indicators undermines our confidence in the integrity of the article's content and we cannot, therefore, vouch for its reliability. Please note that this notice is intended solely to alert readers that the content of this article is unreliable. We have not investigated whether authors were aware of or involved in the systematic manipulation of the publication process.

Wiley and Hindawi regrets that the usual quality checks did not identify these issues before publication and have since put additional measures in place to safeguard research integrity.

We wish to credit our own Research Integrity and Research Publishing teams and anonymous and named external researchers and research integrity experts for contributing to this investigation.

The corresponding author, as the representative of all authors, has been given the opportunity to register their agreement or disagreement to this retraction. We have kept a record of any response received.

### **References**

- [1] B. Xu, W. Qin, Y. Xu et al., "Dietary Quercetin Supplementation Attenuates Diarrhea and Intestinal Damage by Regulating Gut Microbiota in Weanling Piglets," *Oxidative Medicine and Cellular Longevity*, vol. 2021, Article ID 6221012, 19 pages, 2021.

## Retraction

# Retracted: Rocaglamide Prolonged Allograft Survival by Inhibiting Differentiation of Th1/Th17 Cells in Cardiac Transplantation

### Oxidative Medicine and Cellular Longevity

Received 8 January 2024; Accepted 8 January 2024; Published 9 January 2024

Copyright © 2024 Oxidative Medicine and Cellular Longevity. This is an open access article distributed under the Creative Commons Attribution License, which permits unrestricted use, distribution, and reproduction in any medium, provided the original work is properly cited.

This article has been retracted by Hindawi following an investigation undertaken by the publisher [1]. This investigation has uncovered evidence of one or more of the following indicators of systematic manipulation of the publication process:

- (1) Discrepancies in scope
- (2) Discrepancies in the description of the research reported
- (3) Discrepancies between the availability of data and the research described
- (4) Inappropriate citations
- (5) Incoherent, meaningless and/or irrelevant content included in the article
- (6) Manipulated or compromised peer review

The presence of these indicators undermines our confidence in the integrity of the article's content and we cannot, therefore, vouch for its reliability. Please note that this notice is intended solely to alert readers that the content of this article is unreliable. We have not investigated whether authors were aware of or involved in the systematic manipulation of the publication process.

Wiley and Hindawi regrets that the usual quality checks did not identify these issues before publication and have since put additional measures in place to safeguard research integrity.

We wish to credit our own Research Integrity and Research Publishing teams and anonymous and named external researchers and research integrity experts for contributing to this investigation.

The corresponding author, as the representative of all authors, has been given the opportunity to register their agreement or disagreement to this retraction. We have kept a record of any response received.

### References

- [1] C. Dai, X. Zhou, L. Wang et al., "Rocaglamide Prolonged Allograft Survival by Inhibiting Differentiation of Th1/Th17 Cells in Cardiac Transplantation," *Oxidative Medicine and Cellular Longevity*, vol. 2022, Article ID 2048095, 15 pages, 2022.

## *Retraction*

# **Retracted: Taurine Ameliorates Iron Overload-Induced Hepatocyte Injury via the Bcl-2/VDAC1-Mediated Mitochondrial Apoptosis Pathway**

### **Oxidative Medicine and Cellular Longevity**

Received 8 January 2024; Accepted 8 January 2024; Published 9 January 2024

Copyright © 2024 Oxidative Medicine and Cellular Longevity. This is an open access article distributed under the Creative Commons Attribution License, which permits unrestricted use, distribution, and reproduction in any medium, provided the original work is properly cited.

This article has been retracted by Hindawi following an investigation undertaken by the publisher [1]. This investigation has uncovered evidence of one or more of the following indicators of systematic manipulation of the publication process:

- (1) Discrepancies in scope
- (2) Discrepancies in the description of the research reported
- (3) Discrepancies between the availability of data and the research described
- (4) Inappropriate citations
- (5) Incoherent, meaningless and/or irrelevant content included in the article
- (6) Manipulated or compromised peer review

The presence of these indicators undermines our confidence in the integrity of the article's content and we cannot, therefore, vouch for its reliability. Please note that this notice is intended solely to alert readers that the content of this article is unreliable. We have not investigated whether authors were aware of or involved in the systematic manipulation of the publication process.

Wiley and Hindawi regrets that the usual quality checks did not identify these issues before publication and have since put additional measures in place to safeguard research integrity.

We wish to credit our own Research Integrity and Research Publishing teams and anonymous and named external researchers and research integrity experts for contributing to this investigation.

The corresponding author, as the representative of all authors, has been given the opportunity to register their agreement or disagreement to this retraction. We have kept a record of any response received.

### **References**

- [1] X. Feng, W. Hu, Y. Hong, L. Ruan, Y. Hu, and D. Liu, "Taurine Ameliorates Iron Overload-Induced Hepatocyte Injury via the Bcl-2/VDAC1-Mediated Mitochondrial Apoptosis Pathway," *Oxidative Medicine and Cellular Longevity*, vol. 2022, Article ID 4135752, 14 pages, 2022.

## *Retraction*

# **Retracted: Novel lncRNA AL033381.2 Promotes Hepatocellular Carcinoma Progression by Upregulating PRKRA Expression**

### **Oxidative Medicine and Cellular Longevity**

Received 26 September 2023; Accepted 26 September 2023; Published 27 September 2023

Copyright © 2023 Oxidative Medicine and Cellular Longevity. This is an open access article distributed under the Creative Commons Attribution License, which permits unrestricted use, distribution, and reproduction in any medium, provided the original work is properly cited.

This article has been retracted by Hindawi following an investigation undertaken by the publisher [1]. This investigation has uncovered evidence of one or more of the following indicators of systematic manipulation of the publication process:

- (1) Discrepancies in scope
- (2) Discrepancies in the description of the research reported
- (3) Discrepancies between the availability of data and the research described
- (4) Inappropriate citations
- (5) Incoherent, meaningless and/or irrelevant content included in the article
- (6) Peer-review manipulation

The presence of these indicators undermines our confidence in the integrity of the article's content and we cannot, therefore, vouch for its reliability. Please note that this notice is intended solely to alert readers that the content of this article is unreliable. We have not investigated whether authors were aware of or involved in the systematic manipulation of the publication process.

Wiley and Hindawi regrets that the usual quality checks did not identify these issues before publication and have since put additional measures in place to safeguard research integrity.

We wish to credit our own Research Integrity and Research Publishing teams and anonymous and named external researchers and research integrity experts for contributing to this investigation.

The corresponding author, as the representative of all authors, has been given the opportunity to register their agreement or disagreement to this retraction. We have kept a record of any response received.

### **References**

- [1] F. Wang, L. Zhu, Q. Xue et al., "Novel lncRNA AL033381.2 Promotes Hepatocellular Carcinoma Progression by Upregulating PRKRA Expression," *Oxidative Medicine and Cellular Longevity*, vol. 2022, Article ID 1125932, 24 pages, 2022.

## *Retraction*

# **Retracted: Taurine Ameliorates Iron Overload-Induced Hepatocyte Injury via the Bcl-2/VDAC1-Mediated Mitochondrial Apoptosis Pathway**

### **Oxidative Medicine and Cellular Longevity**

Received 8 January 2024; Accepted 8 January 2024; Published 9 January 2024

Copyright © 2024 Oxidative Medicine and Cellular Longevity. This is an open access article distributed under the Creative Commons Attribution License, which permits unrestricted use, distribution, and reproduction in any medium, provided the original work is properly cited.

This article has been retracted by Hindawi following an investigation undertaken by the publisher [1]. This investigation has uncovered evidence of one or more of the following indicators of systematic manipulation of the publication process:

- (1) Discrepancies in scope
- (2) Discrepancies in the description of the research reported
- (3) Discrepancies between the availability of data and the research described
- (4) Inappropriate citations
- (5) Incoherent, meaningless and/or irrelevant content included in the article
- (6) Manipulated or compromised peer review

The presence of these indicators undermines our confidence in the integrity of the article's content and we cannot, therefore, vouch for its reliability. Please note that this notice is intended solely to alert readers that the content of this article is unreliable. We have not investigated whether authors were aware of or involved in the systematic manipulation of the publication process.

Wiley and Hindawi regrets that the usual quality checks did not identify these issues before publication and have since put additional measures in place to safeguard research integrity.

We wish to credit our own Research Integrity and Research Publishing teams and anonymous and named external researchers and research integrity experts for contributing to this investigation.


The corresponding author, as the representative of all authors, has been given the opportunity to register their agreement or disagreement to this retraction. We have kept a record of any response received.

### **References**

- [1] X. Feng, W. Hu, Y. Hong, L. Ruan, Y. Hu, and D. Liu, "Taurine Ameliorates Iron Overload-Induced Hepatocyte Injury via the Bcl-2/VDAC1-Mediated Mitochondrial Apoptosis Pathway," *Oxidative Medicine and Cellular Longevity*, vol. 2022, Article ID 4135752, 14 pages, 2022.

## Research Article

# Taurine Ameliorates Iron Overload-Induced Hepatocyte Injury via the Bcl-2/VDAC1-Mediated Mitochondrial Apoptosis Pathway

Xiaoyu Feng,<sup>1</sup> Wenfeng Hu,<sup>1,2</sup> Yujiao Hong,<sup>1</sup> Linlin Ruan,<sup>1</sup> Yueben Hu,<sup>1</sup> and Dan Liu<sup>1</sup> 

<sup>1</sup>Jiangxi Provincial Key Laboratory of Basic Pharmacology, Nanchang University School of Pharmaceutical Science, Nanchang 330006, China

<sup>2</sup>Department of Pharmacy, Jiujiang Traditional Chinese Medicine Hospital, Jiujiang 332900, China

Correspondence should be addressed to Dan Liu; [liudan1201jx@163.com](mailto:liudan1201jx@163.com)

Received 6 December 2021; Revised 20 May 2022; Accepted 31 May 2022; Published 16 July 2022

Academic Editor: Zhihao Jia

Copyright © 2022 Xiaoyu Feng et al. This is an open access article distributed under the Creative Commons Attribution License, which permits unrestricted use, distribution, and reproduction in any medium, provided the original work is properly cited.

Iron overload can induce reactive oxygen species (ROS) burst and liver damage. Taurine can reduce ROS production and ameliorate liver injury caused by iron overload; however, the underlying molecular mechanism remains elusive. Herein, L02 cells treated with 120  $\mu$ M iron dextran for 48 h showed marked oxidative stress damage and significantly increased apoptosis. Taurine protected hepatocytes by stabilizing mitochondrial membranes and resisting oxidative stress damage caused by iron overload. However, transfection with siRNA Bcl-2 virus abrogated the observed protective effects. Following treatment with taurine, B cell lymphoma-2 (Bcl-2) could inhibit the opening of the mitochondrial permeability transition pore (mPTP), subsequently stabilizing the mitochondrial membrane potential by interacting with voltage-dependent anion channel 1 (VDAC1) of mPTP. The present study is the first to clarify the mechanism underlying taurine-afforded hepatocyte protection against iron overload-induced oxidative stress via Bcl-2-mediated inhibition of mPTP opening and the antiapoptotic pathway.

## 1. Introduction

Given changing eating habits and dietary structure, iron cooking utensils are widely employed, and large amounts of red meat (including heme iron), iron-fortified foods, and iron supplements are often abused [1]. Both researchers and clinical investigators have reported that excess or misplaced iron in specific tissues and cells can promote a vast array of acute and chronic illnesses [2]. The liver is the most likely organ to accumulate iron [3], and long-term liver iron overload is highly correlated with the occurrence, development, and prognosis of hepatitis, liver fibrosis, cirrhosis, and tumors. The ability of iron to exchange single electrons with several substrates can induce reactive oxygen species (ROS) generation [4–6], which, in turn, can lead to oxidative stress, lipid peroxidation, and DNA damage, inducing genomic instability and DNA repair defects [7, 8], ultimately impairing cell viability and promoting programmed cell death (PCD) [9]. Mitochondria, one of the sources of signals that initiate apoptosis, play a key role in apoptotic cell death [10]. It is well-known that mitochondrial permeability tran-

sition pore (mPTP) opening plays an important role in mitochondria-mediated apoptosis [11]. The opening of mPTP can also result in mitochondrial swelling, mitochondrial membrane damage, and subsequent release of cytochrome c which are hallmarks of mitochondria-mediated apoptosis [12].

Taurine is a sulfur-containing amino acid. Studies have shown that taurine is involved in the maintenance and regulation of nearly all normal physiological activities in the body, as well as mediates important inhibitory and protective effects against several pathological conditions [13–15]. Altered taurine expression can reportedly impact physiological processes such as development, lung function, mitochondrial and cartilage function, antioxidation, and apoptosis [16]. Studies have found that taurine can reduce heavy metal-induced toxic liver damage and highlighted that taurine is a good dietary antioxidant [17]. Previously, we have reported that taurine supplementation can reduce liver oxidative stress and damage, protecting liver function and improving survival in an iron-overloaded murine model [18]. Therefore, we aimed to verify the underlying

mechanism through which iron overload causes oxidative stress and excessive apoptosis in liver cells. Using taurine as a therapeutic agent, we examined the mechanism underlying its protective effect against iron overload-induced liver injury, especially oxidative stress and mitochondrial pathway-mediated apoptosis.

## 2. Method

**2.1. Materials.** Taurine (purity  $\geq 99.0\%$ ) was purchased from Beijing Solarbio Science & Technology Co. (Beijing, China), Ltd., and iron dextran was purchased from Sigma-Aldrich (St. Louis, Missouri, USA). Lentivirus siRNA Bcl-2 and a negative control virus were constructed by GeneChem Co. (Shanghai, China). Protein G Plus/Protein A Agarose was purchased from Merck Millipore (USA). Antibodies against Bcl-2, COX-4, and cytochrome c (Cyt c) were purchased from Cell Signaling Technology (Beverly, MA, USA), while the antibody against voltage-dependent anion channel 1 (VDAC1) was purchased from Santa Cruz Biotechnology (USA). Antibodies against  $\beta$ -actin and horseradish peroxidase-conjugated IgG secondary antibodies were obtained from ZsBio (Beijing, China). L02 cells were derived from normal human hepatocytes and provided by Prof. Zhinjun Luo (Nanchang University). L02 cells were cultured in DMEM/F12 (Gibco, USA) supplemented with 10% fetal bovine serum (Gibco, South America) and antibiotics (100 U/mL penicillin and 100  $\mu$ g/mL streptomycin; Solarbio, Beijing, China) at 37°C in a 5% CO<sub>2</sub> incubator (Forma™310, Thermo Fisher, USA).

**2.2. Experimental Groups.** Herein, we constructed an iron overload injury model by treating cells with 120  $\mu$ M iron dextran for 48 h. Five cell groups were established: control group, L02 cells cultured under normal conditions; iron overload group, cells cultured with 120  $\mu$ M iron dextran for 48 h; iron+taurine group, cells treated with 120  $\mu$ M iron dextran and 40 mM taurine for 48 h; iron+taurine+negative control virus group, cells infected with Bcl-2 unloaded lentivirus negative control for 10 h before the iron overload injury model was constructed; iron+taurine+siRNA Bcl-2 group, infected with Bcl-2 knockdown virus for 10 h before the iron overload injury model was constructed. All experiments were performed in triplicate.

**2.3. Cell Viability.** Cell viability was detected using the CCK-8 kit (Apexbio, USA). Briefly, cells were seeded in 96-well plates. After treatment, cells were washed with phosphate-buffered saline (PBS; Solarbio, Beijing, China), and 90  $\mu$ L serum-free medium and 10  $\mu$ L CCK-8 reagent were added to each well and mixed evenly. Cells were then incubated at 37°C in a 5% CO<sub>2</sub> incubator for 2 h in the dark. Absorbance was measured at 450 nm using an enzyme labeling instrument (Bio-Rad 680, USA). The optical density (OD) was directly proportional to the cell survival rate, and the cell survival rate was calculated according to the formula.

**2.4. Apoptosis.** Annexin V-FITC and propidium iodide (PI) (BestBio, Shanghai, China) double staining were used to examine apoptosis. After treatment, cells were digested with

trypsin without EDTA (Solarbio, Beijing, China), and the supernatant was subsequently removed. Then, cells were resuspended in 500  $\mu$ L annexin binding solution, and 5  $\mu$ L of annexin V-FITC dye was added to cells in the dark. After incubation at 4°C in the dark for 15 min, 10  $\mu$ L PI dye was added and mixed well, followed by incubation at 4°C in the dark for another 5 min. Flow cytometry detection was performed at an excitation wavelength of 488 nm and emission wavelength of 525 nm (Cytomics FC 500, Beckman Kurt, Brea, CA, USA).

**2.5. ROS.** A reactive oxygen kit was used to detect ROS levels in cells. 2',7'-Dichlorodihydrofluorescein diacetate (DCFH-DA) (Beyotime Biotechnology, Shanghai, China) was used as the probe. Cells from each experimental group were collected in Eppendorf tubes. The probes were prepared in serum-free medium with DCFH-DA at a ratio of 1000:1. Then, 500  $\mu$ L of the prepared solution was added to each tube, incubated at 37°C in a 5% CO<sub>2</sub> incubator for 20 min in the dark, washed twice with PBS, and analyzed by flow cytometry.

**2.6. Degree of mPTP Opening.** Mitochondrial swelling fluid and CaCl<sub>2</sub> solution were prepared, and the intracellular mitochondria in each group were separated using a mitochondrial extraction kit (Keygenbio, Nanjing, China). Briefly, 160  $\mu$ L of mitochondrial swelling fluid was added, and the mixture was resuspended in a microplate reader at 520 nm to detect the absorbance value of each group OD<sub>1</sub>. Then, 40  $\mu$ L CaCl<sub>2</sub> solution was added to each experimental group and detected every minute, calculated as  $\Delta OD/\text{min} = (OD_1 - OD_2) \times 1000$  to indicate the degree of mPTP opening.

**2.7. Western Blot Analysis.** Cells from each experimental group were collected, and lysates were prepared using RIPA:PMSF (100:1; Beyotime Biotechnology, Shanghai, China, and Solarbio, Beijing, China, respectively); cells were lysed at 4°C for 20 min. Next, cells were centrifuged at 4°C for 15 min at 12000 rpm/min. Subsequently, cells were separated from the supernatant and used to determine the protein concentration with the BCA kit (Tiangen Biology, Beijing, China). Protein (30  $\mu$ g) was loaded on 10% sodium dodecyl sulfate-polyacrylamide gel electrophoresis (SDS-PAGE) using a gel apparatus (Bio-Rad, USA) and separated, followed by transfer to polyvinylidene fluoride (PVDF) membranes (Millipore Corp., Bedford, MA, USA) at 90 mA, 0°C wet for 1.5 h. The membrane was blocked for 2 h with 5% skim milk at room temperature. Bcl-2, VDAC1, the membrane of  $\beta$ -actin protein, and its primary antibody (1:1000 dilution) were incubated overnight at 4°C. After 24 h, the membrane was washed with 1× TBST (Tris-Buffer Saline, 0.25% Tween-20) for 10 min ( $\times 5$  times), incubated with the horseradish peroxidase-conjugated secondary antibody (1:2000 dilution) for 1.5 h at room temperature, and washed with TBST for 10 min ( $\times 4$  times). After coating the wetting film with an enhanced chemiluminescence reagent (ECL kit,



Thermo Fisher Scientific, USA), the protein was developed using the Image Laboratory System (Bio-Rad, USA).

Mitochondrial and cytoplasmic proteins were extracted using the mitochondrial extraction kit for each experimental group, and the protein concentration was determined using the BCA method. After separation by SDS-PAGE, proteins were transferred to a PVDF membrane and blocked for 2 h. The primary antibody was combined with COX-4 and Cyt c proteins and incubated overnight at 4°C. After 24 h, cells were washed five times and incubated with a secondary antibody at room temperature for 2 h. The membrane was then moistened with the chemiluminescence solution.

**2.8. Coimmunoprecipitation.** Briefly, a measured concentration of the protein extracted was combined with the indicated primary antibodies and incubated overnight at 4°C. After 24 h, the Protein G Plus/Protein A Agarose was washed twice, and agarose was mixed and incubated with the protein and its primary antibody overnight. After 24 h, cells were thrice washed with PBS. The supernatant was removed, and protein loading buffer was added to the precipitate and heated for 10 min at 100°C. The samples were analyzed by SDS-PAGE.

**2.9. Oxidative Stress and Lipid Peroxidation.** It is well known that ROS generation can cause oxidative stress, and the formation of lipid peroxides can induce cell damage. Superoxide dismutase (SOD) is the most commonly used indicator of oxidative stress, and malondialdehyde (MDA) is an indicator of the degree of lipid peroxidation. Briefly, the cell protein supernatant was extracted from each experimental group, and indices were measured according to the SOD and MDA kit instructions (Jiancheng Bioengineering Institute, Nanjing, China).

**2.10. Intracellular Iron Ion.** Intracellular iron ions combine with protein to form a complex, which is dissociated in acidic medium and reduced to divalent iron by a reducing agent, forming a purple-red compound with ferrozine. The cells of the experimental group were lysed to obtain the supernatant, and the iron ion concentration of each group was detected according to the instructions of the iron ion detection kit (APPLYGEN, Beijing, China).

**2.11. Statistical Analysis.** For each experimental group, data values are expressed as mean  $\pm$  standard error of the mean (SEM), and the homogeneity of variance test and one-way variance (one-way ANOVA) were performed using GraphPad Prism 6.0 (GraphPad Software, Inc., San Diego, CA, USA). A *P* value < 0.05 indicated statistical significance.

### 3. Results

**3.1. Effect of Taurine Treatment on Iron Overload Damage.** First, L02 cells were treated with media containing different concentrations of iron dextran for 48 h. L02 cells were treated with 0, 10, 20, 40, 80, 120, 160, 200, and 240  $\mu$ M iron dextran for 48 h. The half-maximal inhibitory concentration of dextran was 128.4  $\mu$ M (Figure 1(a)). Iron dextran (120  $\mu$ M)-treated L02 cells were then treated with taurine

at concentrations of 10, 20, 40, 50, 60, 80, and 100 mM, and 40 mM was found to be an optimal concentration to afford protection (Figure 1(b)).

We observed that treatment with 120  $\mu$ M iron dextran decreased cell viability. Taurine could reverse this effect, and we observed that L02 cell viability was significantly restored by 40 mM taurine (Figure 1(c)). As determined by flow cytometry, the apoptosis results further confirmed that taurine inhibited iron dextran-induced apoptosis (Figure 1(d)). Based on these findings, L02 cells incubated with 120  $\mu$ M iron dextran and 40 mM taurine were used in subsequent experiments.

**3.2. Role of Bcl-2 in Taurine-Mediated Protective Effects against Iron Overload Injury.** The protective effect of taurine against iron overload could be associated with Bcl-2 expression level. Taurine exhibited a protective effect against iron overload-induced cell damage (Figure 2). Western blotting revealed that taurine increased the Bcl-2 protein level (Figure 2(a)). Accordingly, we constructed a Bcl-2 knockdown virus (Figure 2(b)). CCK-8 results showed that taurine improved cell viability (Figure 2(c)). Bcl-2 gene knockdown using a Bcl-2 knockdown virus abrogated the protective effects of taurine.

Furthermore, we observed that taurine could reduce the apoptosis rate. Flow cytometry was used to determine the rate of apoptosis (Figure 2(e)). Apoptosis was significantly increased in the iron overload group when compared with the control group. Treatment with 40 mM taurine significantly decreased apoptosis. The optimal concentration of taurine was determined to be 40 mM. In addition, apoptosis was significantly reduced in the iron+taurine and iron+taurine+NC groups but was significantly elevated in siRNA Bcl-2 cells, suggesting that the protective effect of taurine was abolished. These results indicated that taurine could exert antiapoptotic effects through Bcl-2.

Moreover, taurine did not significantly impact the cellular concentration of iron ions. The concentration of iron ions in each group was determined by measuring the absorbance value using the specific kit. Compared with the control group, the concentration of iron ions was significantly elevated in the other groups (Figure 2(d)). The results revealed that taurine did not significantly alter the intracellular iron ion concentration.

**3.3. Impact of Bcl-2 and VDAC1 Interaction on the Anti-Iron Overload Injury Mediated by Taurine.** The effect of taurine on Bcl-2 and VDAC1 protein level was examined using western blotting. Bcl-2 protein level was significantly higher in the iron+taurine and iron+taurine+NC groups than in the control group (Figure 3(a)). Taurine treatment decreased the expression level of VDAC1 when compared with that in the control group. Following Bcl-2 gene knockdown, the level of Bcl-2 protein decreased, and VDAC1 level was also significantly reduced, suggesting that the level of VDAC1 may be related to Bcl-2.

Previous studies have shown that Bcl-2 interacts with VDAC1, and taurine can increase Bcl-2 protein level. We postulated that the protective effect of taurine might be

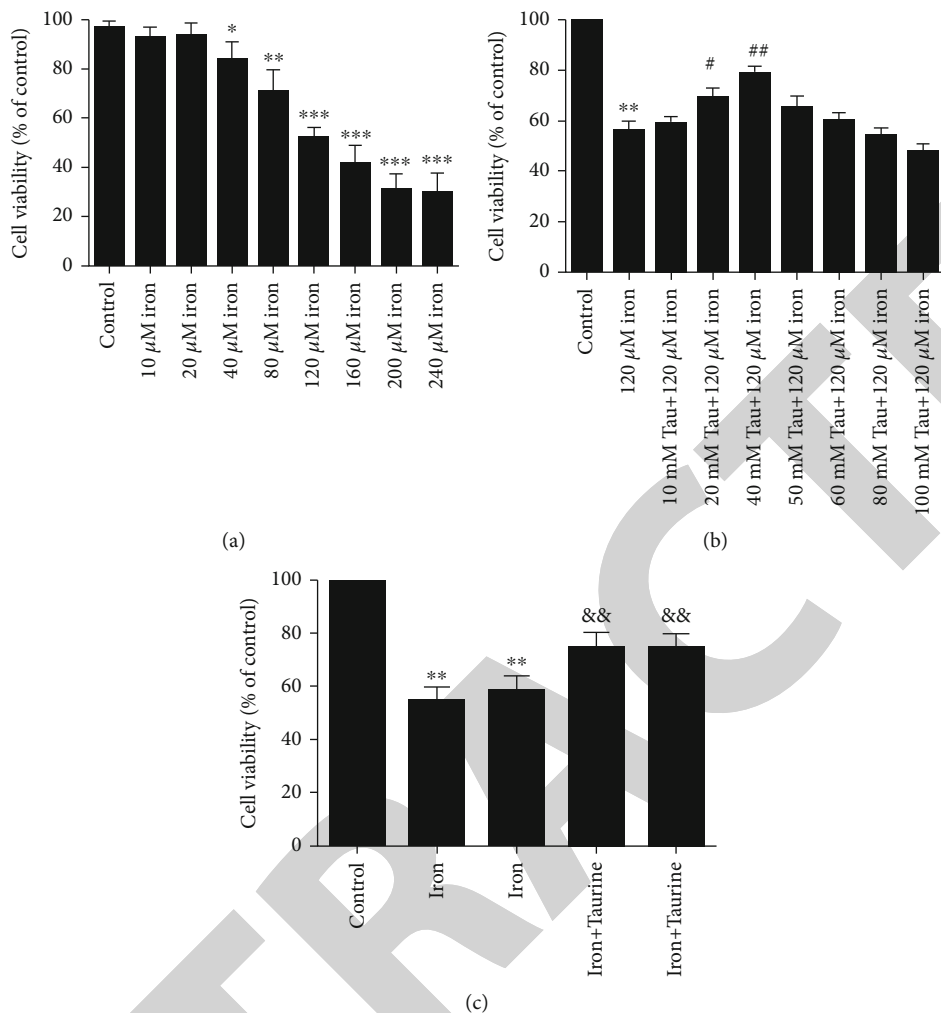


FIGURE 1: Continued.

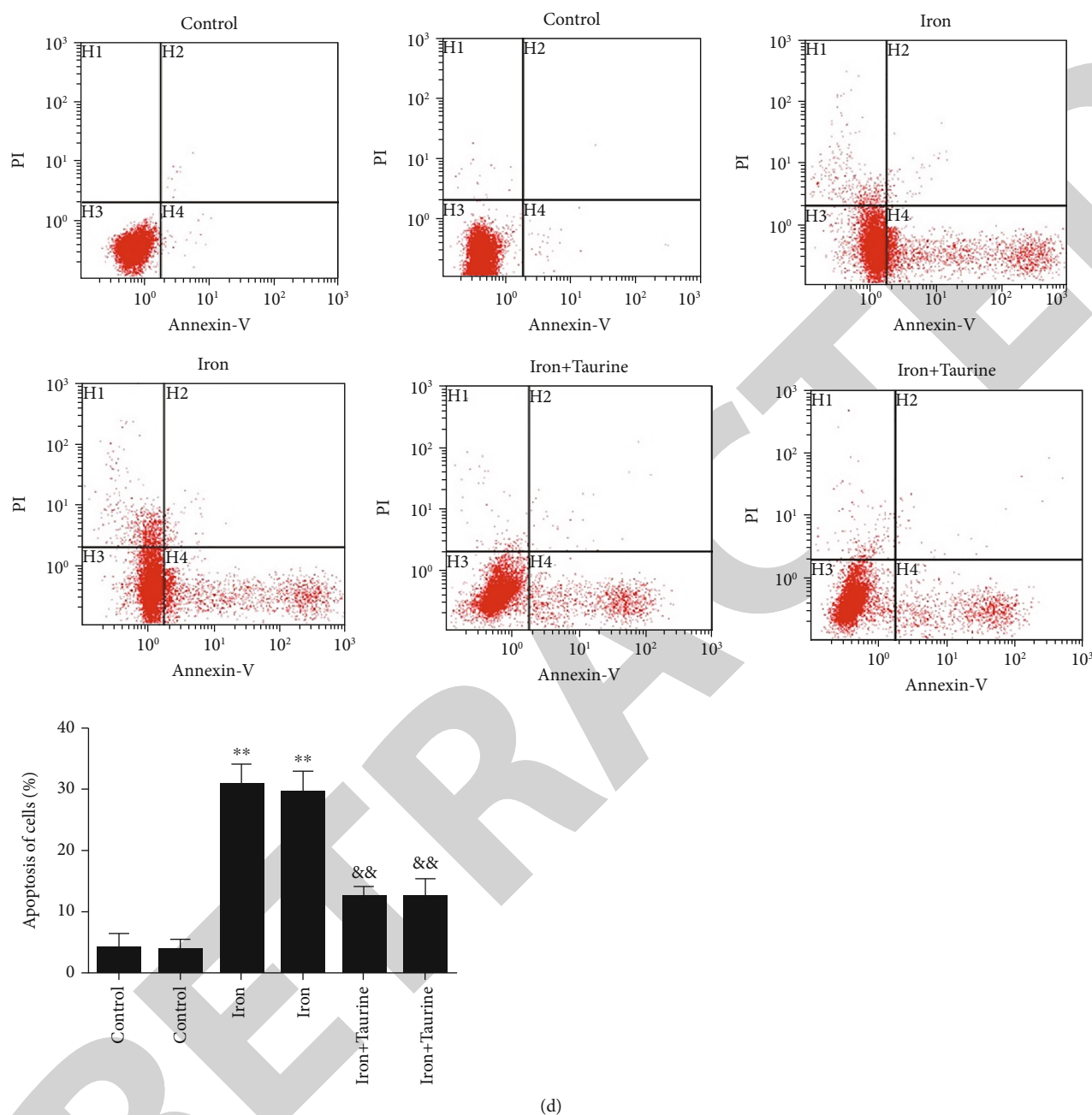


FIGURE 1: The effect of taurine treatment on iron overload damage. (a) L02 cells were individually treated with different concentrations of iron dextran. (b) The effect of taurine on cell viability. (c) Taurine treatment significantly increases the cell survival rate. (d) Taurine decreases the rate of apoptosis. Data values are expressed as mean  $\pm$  standard error of the mean (SEM) of 3 individual experiments. \*\*\* $P < 0.001$ , \*\* $P < 0.01$ , and \* $P < 0.05$  vs. the control group. # $P < 0.05$  and ## $P < 0.01$  vs. the iron group. \*\* $P < 0.01$  vs. the control group. && $P < 0.01$  vs. the iron group.

related to the interaction between Bcl-2 and VDAC1. To further confirm this hypothesis, the interaction between Bcl-2 and VDAC1 was examined using coimmunoprecipitation (Co-IP) after taurine treatment. The results revealed that under normal conditions (control group), Bcl-2 interacted with VDAC1 (Figure 3(d)). After taurine treatment, the interaction between Bcl-2 and VDAC1 was enhanced. On infecting L02 cells with siRNA Bcl-2 lentivirus, Bcl-2 was knocked out, the observed effects were reversed, and the interaction between Bcl-2 and VDAC1 decreased. As shown

in Figure 3, taurine pretreatment could promote the interaction between Bcl-2 and VDAC1. Additionally, the above findings revealed that VDAC1 activation might be associated with Bcl-2 upregulation, suggesting that taurine combats iron overload damage and that this effect could be related to the interaction between Bcl-2 and VDAC1.

**3.4. Effect of Taurine on Cell Lipid Peroxidation.** Taurine can reduce ROS levels in iron overload-damaged cells. The cellular ROS levels were measured by flow cytometry

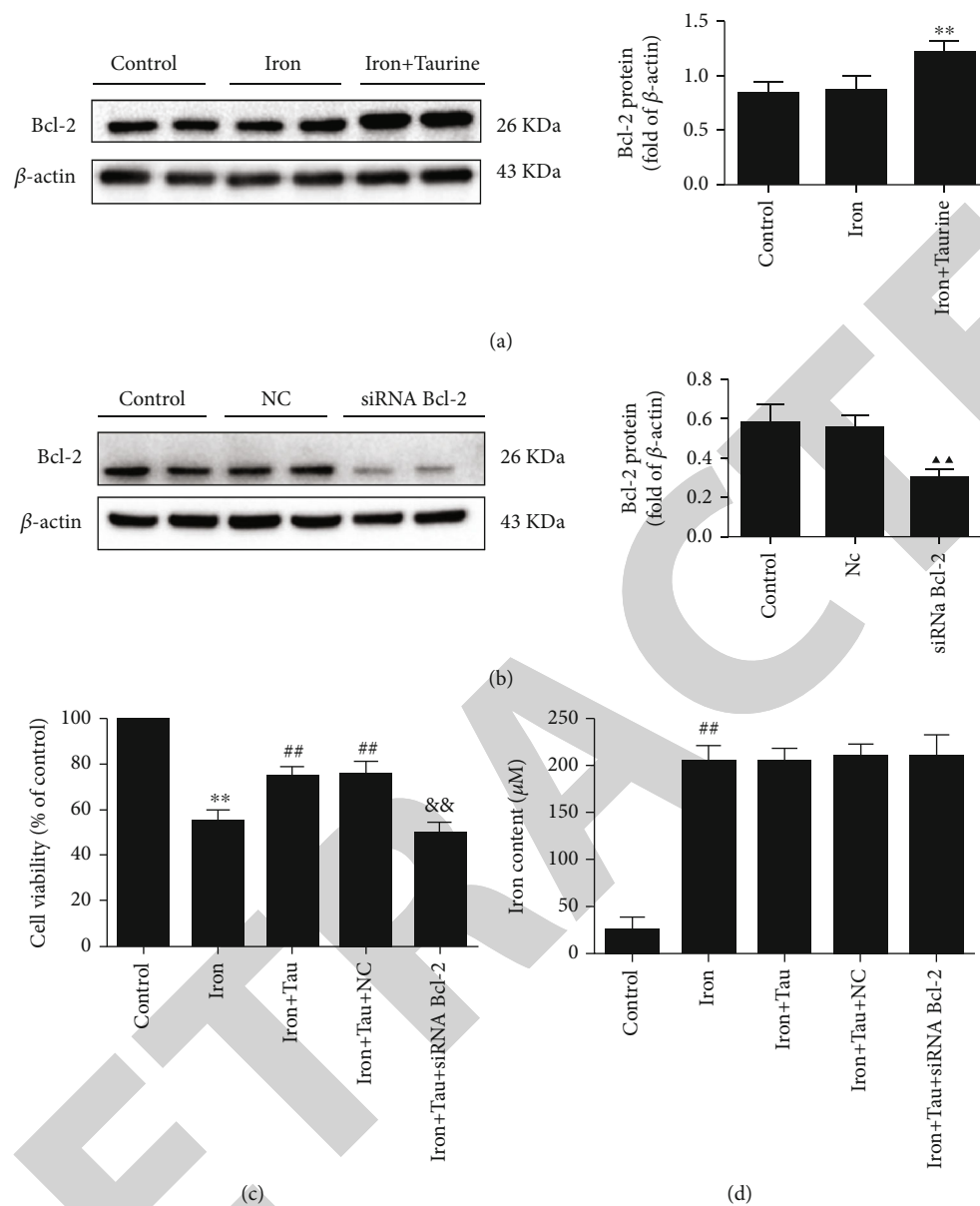
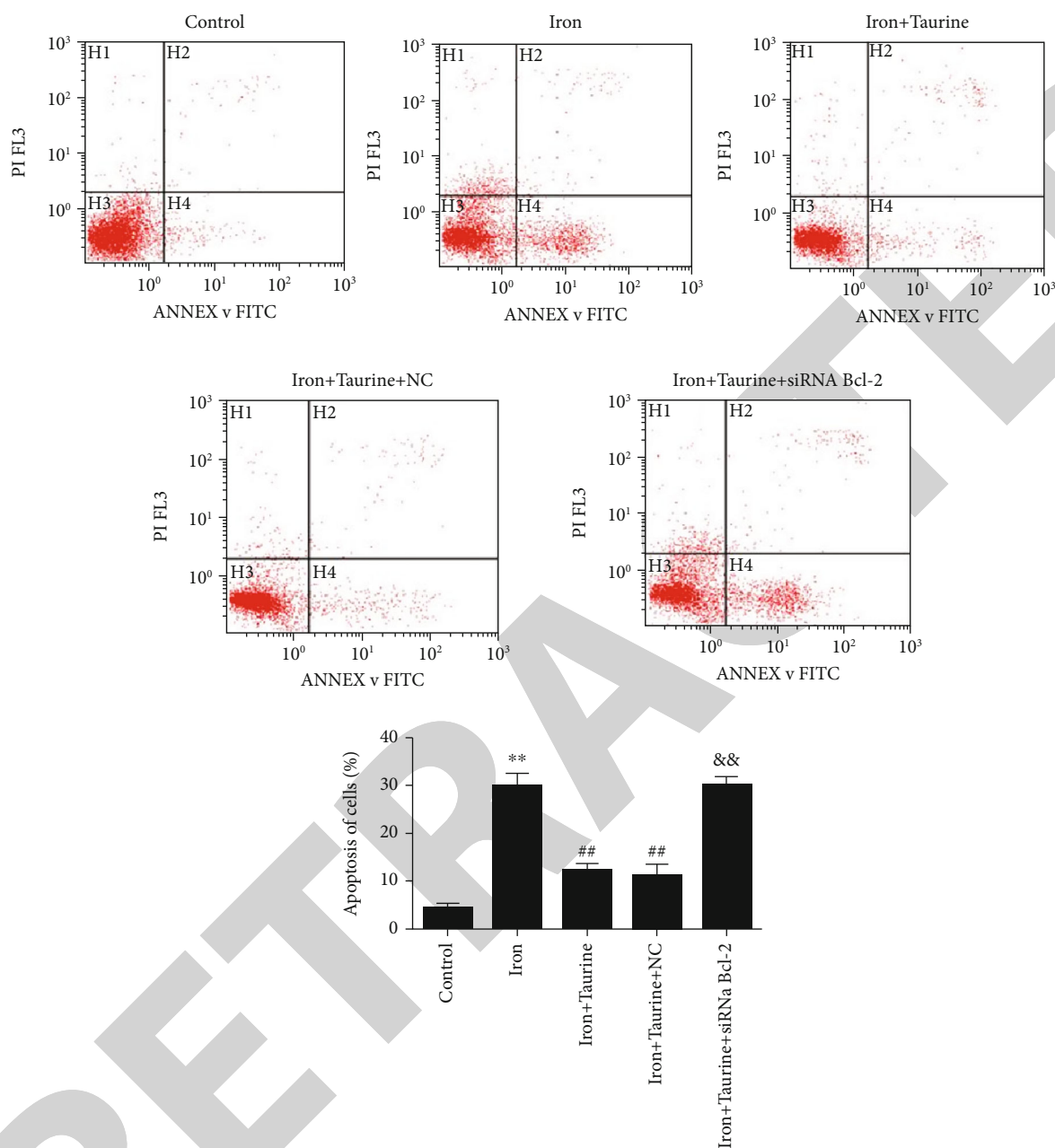


FIGURE 2: Continued.



(e)

FIGURE 2: The role of Bcl-2 in taurine-mediated effects against iron overload injury. (a) Bcl-2 protein level in different groups. (b) Western blot analysis of Bcl-2 knockdown virus-transfected cells. (c) CCK-8 detected cell survival rates in different groups. (d) The effect of taurine on the concentration of iron ions in cells. (e) The effect of taurine on cell apoptosis. Data values are expressed as mean  $\pm$  standard error of the mean (SEM),  $n = 3$ . ## $P < 0.01$  vs. the control group.  $\blacktriangle P < 0.01$  vs. the NC group.  $^{##}P < 0.01$  vs. the iron group.  $^{\&\&}P < 0.01$  vs. the iron+taurine group.

(Figure 4(a)). Compared with the control group, the ROS level was significantly increased in the iron overload group, while those in the iron+taurine and iron+taurine+NC groups were significantly decreased. Accordingly, it can be suggested that taurine reduces intracellular ROS levels. Bcl-2 gene knockdown abolished the taurine-mediated effects.

SOD indicates the ability of cells to scavenge oxygen free radicals, whereas MDA indicates the severity of cells being

attacked by free radicals; both these indicators can indirectly reflect the degree of cell damage. Iron overload decreased the SOD activity and increased the MDA content in cells. Taurine treatment significantly enhanced SOD activity and reduced MDA content (Figures 4(c) and 4(d)). However, following Bcl-2 knockdown, these taurine-mediated effects were reversed, suggesting that taurine treatment could reduce the degree of lipid peroxidation in cells via Bcl-2, thereby reducing damage.

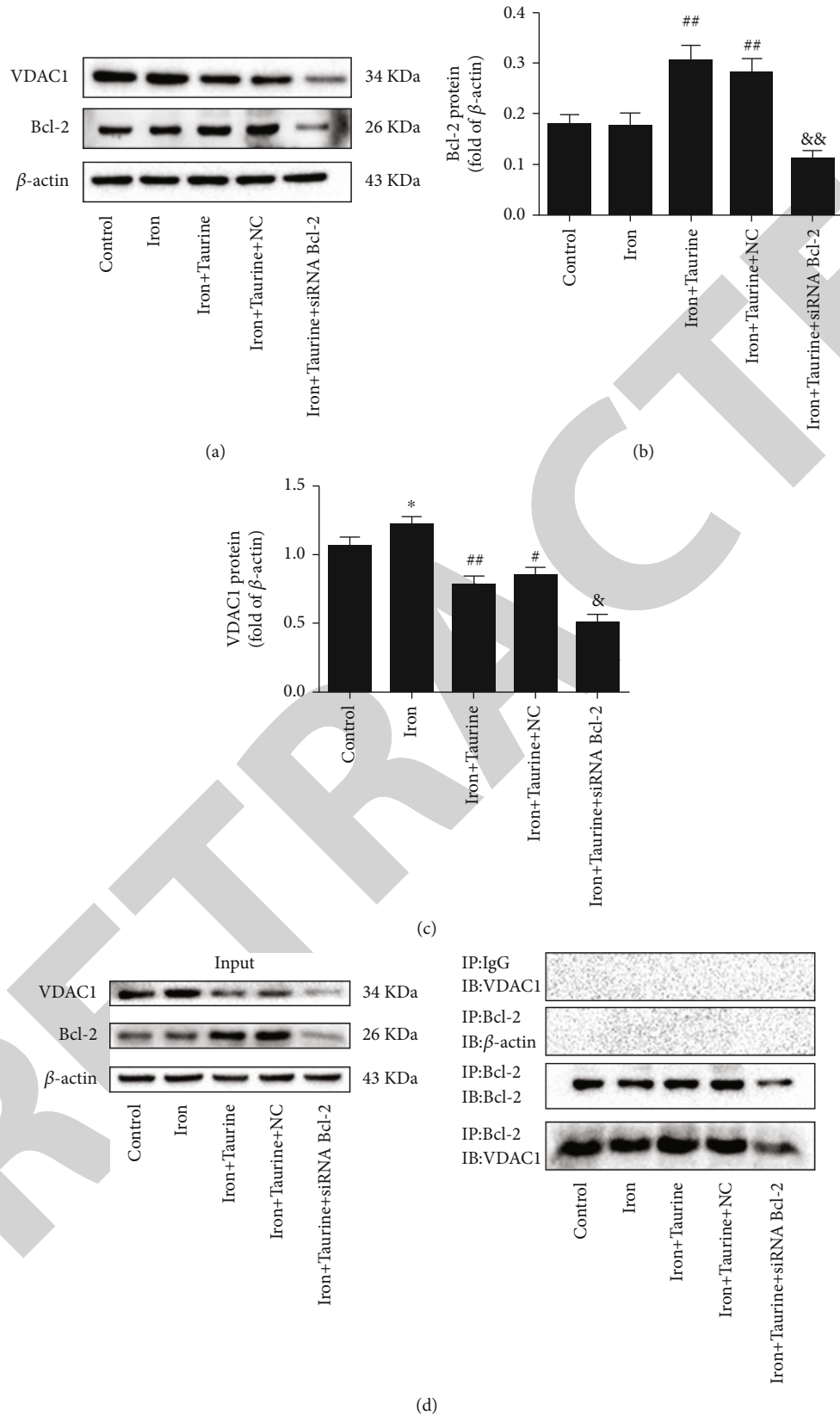


FIGURE 3: (a) Western blot analysis was performed to examine the expression level of Bcl-2 and VDAC1 in L02 cells. (b) Bcl-2 protein level in L02 cells. (c) VDAC1 protein level in L02 cells. (d) Coimmunoprecipitation was used to study the interaction between Bcl-2 and VDAC1 in different experimental groups. Data values are expressed as mean  $\pm$  standard error of the mean (SEM),  $n = 3$ . <sup>##</sup> $P < 0.01$  vs. the control group. <sup>&&</sup> $P < 0.01$  vs. the iron+taurine group. <sup>\*</sup> $P < 0.05$  vs. the control group. <sup>#</sup> $P < 0.05$  and <sup>##</sup> $P < 0.01$  vs. the iron group. <sup>&</sup> $P < 0.05$  vs. the iron+taurine group.

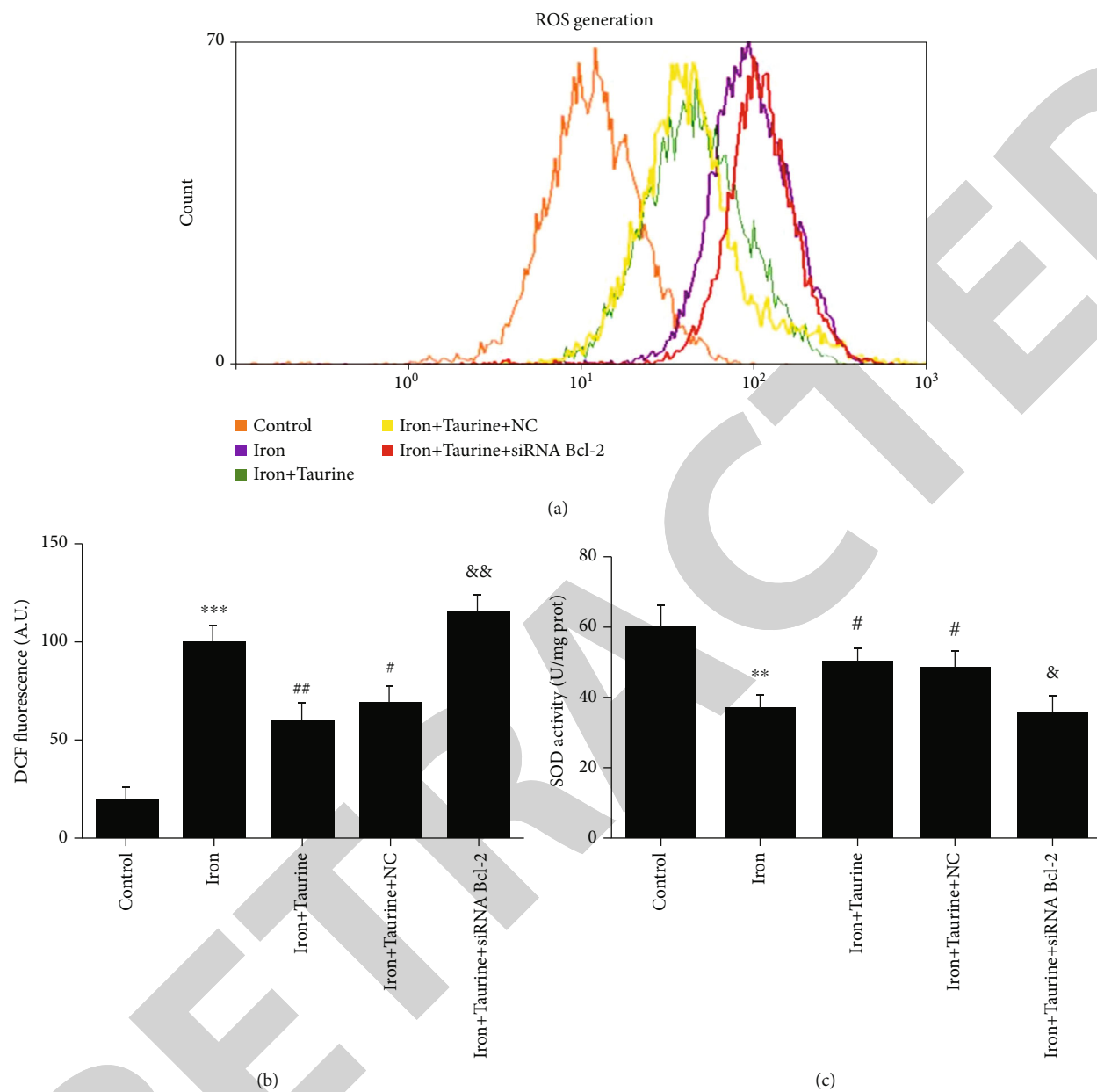
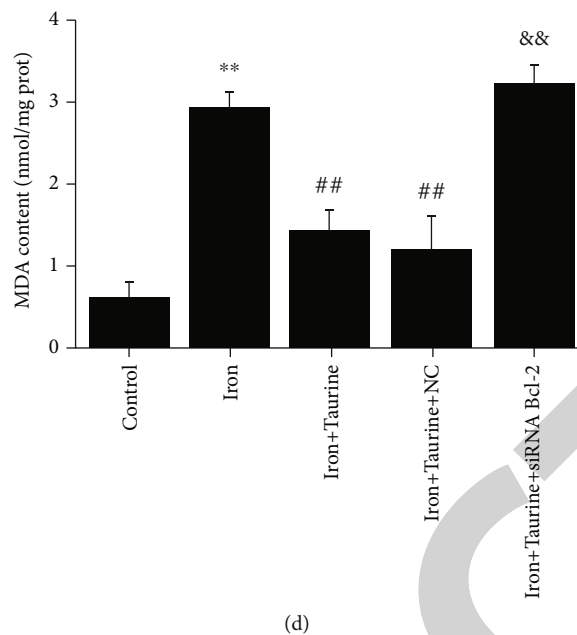


FIGURE 4: Continued.



(d)

FIGURE 4: The effect of taurine treatment on oxidative stress and lipid peroxidation caused by iron overload injury. (a) DCF fluorescence analysis by flow cytometry. (b) Histogram of ROS content, measured as DCF fluorescence. Taurine treatment increases (c) SOD activity and decreases (d) MDA content. Data values are expressed as the mean  $\pm$  standard error of the mean (SEM) ( $n = 3$ ). \*\*\* $P < 0.01$  vs. the control group. ## $P < 0.01$  vs. the iron group. && $P < 0.01$  vs. the iron+taurine group. \*\* $P < 0.01$  vs. the control group. ## $P < 0.01$  vs. the iron group. && $P < 0.01$  vs. the iron+taurine group. # $P < 0.05$  vs. the iron group.

### 3.5. Taurine Protected Mitochondrial Membrane Integrity.

We observed that taurine treatment could reduce the degree of mPTP opening (Figures 5(a) and 5(b)). A microplate reader was used to measure the absorbance of each group to determine the degree of mPTP opening, calculated as  $\Delta \text{OD}/\text{min} \times 1000$ . Compared with the control group, the degree of mPTP opening increased in iron-treated cells. The degree of mPTP opening decreased in the iron+taurine and iron+taurine+NC groups. In cells infected with siRNA Bcl-2 lentivirus for Bcl-2 knockdown, the degree of mPTP opening continued increasing despite taurine treatment, suggesting that the protective effect of taurine was abolished.

Treatment with taurine blocked Cyt c transfer from the mitochondria to the cytoplasm. Western blotting was used to detect the protein level of Cyt c, an indicator of cell apoptosis, in the mitochondria and cytoplasm. Compared with the control group, iron overload induced Cyt c accumulation in the cytoplasm, with minimal accumulation observed in the mitochondria (Figures 5(c) and 5(d)). In the taurine treatment group, Cyt c accumulated in the mitochondria and decreased in the cytoplasm. The taurine-mediated effect was abolished in the iron+taurine+siRNA Bcl-2 group, suggesting that taurine could protect L02 cells from iron overload damage via Bcl-2, inhibit the transfer of Cyt c from the mitochondria to the cytoplasm, and maintain mitochondrial membrane integrity.

## 4. Discussion

Iron is an essential micronutrient for most organisms, well known to be involved in growth and metabolism, erythrocyte production, oxygen transport, DNA synthesis, and cel-

lular immune response [19, 20]. However, excessive iron poses a substantial health risk during several diseases. Iron is stored and accumulates in the liver. It is most likely to cause iron damage to the liver, eventually resulting in liver fibrosis, cirrhosis, and even liver cancer. Iron can participate in redox reactions, causing oxidative stress and generating substantial ROS generation. Mitochondria are not only a source but also a target of ROS [21]. Disruption of mitochondrial dynamics produce increased levels of ROS [22]. Using the oxidant-sensing probe DCFH-DA to measure ROS levels, we found that hepatocytes treated by iron overload accumulated more ROS than hepatocytes without iron treatment. The high levels of ROS contribute directly to oxidative stress. SOD and MDA are commonly used biomarkers for oxidative stress [23]. By measuring SOD activity and MDA content, it was revealed that iron overload led to significantly increased MDA levels and decreased SOD levels, suggesting increased oxidative stress in hepatocytes.

Taurine is an endogenously synthesized sulfur-containing  $\beta$ -amino acid found in mammals and is derived from methionine and cysteine. It participates in diverse physiological functions. For example, it is involved in modulating osmotic pressure and calcium regulation and plays a major role in maintaining membrane stability and immune regulation [24–26]. Taurine also exhibits a variety of physiological activities, including anti-inflammatory, antioxidant, and antiapoptotic activities. In the present study, CCK-8 and apoptosis tests showed that the application of 120  $\mu\text{M}$  iron dextran for 48 h damaged hepatocytes. Treatment with an effective dose of taurine restored liver cell viability and alleviated apoptosis.

Bcl-2 family proteins include Bcl-2, B cell lymphoma-extra large (Bcl-xL), and Bcl-2-associated X (Bax). Bcl-2



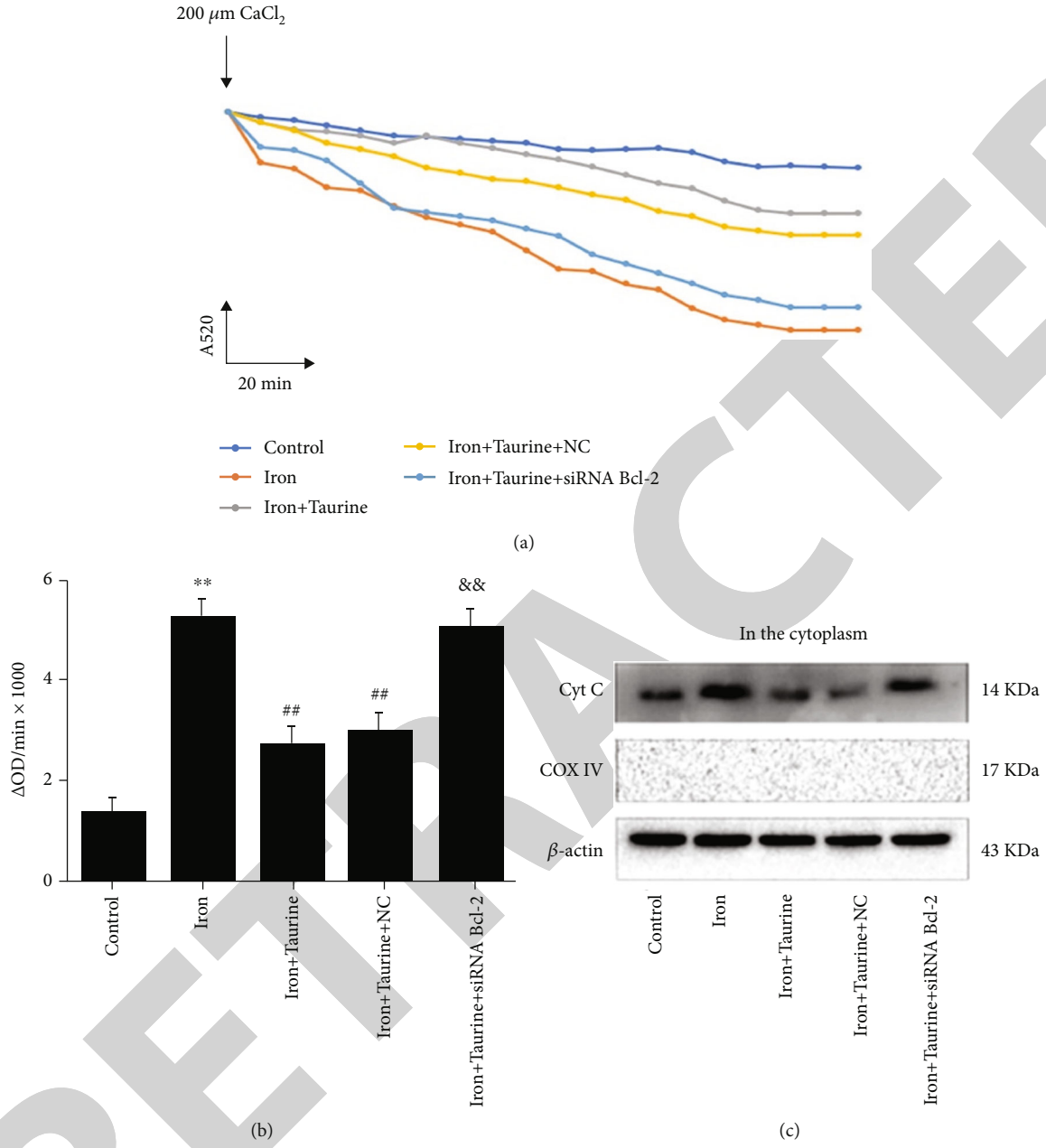


FIGURE 5: Continued.

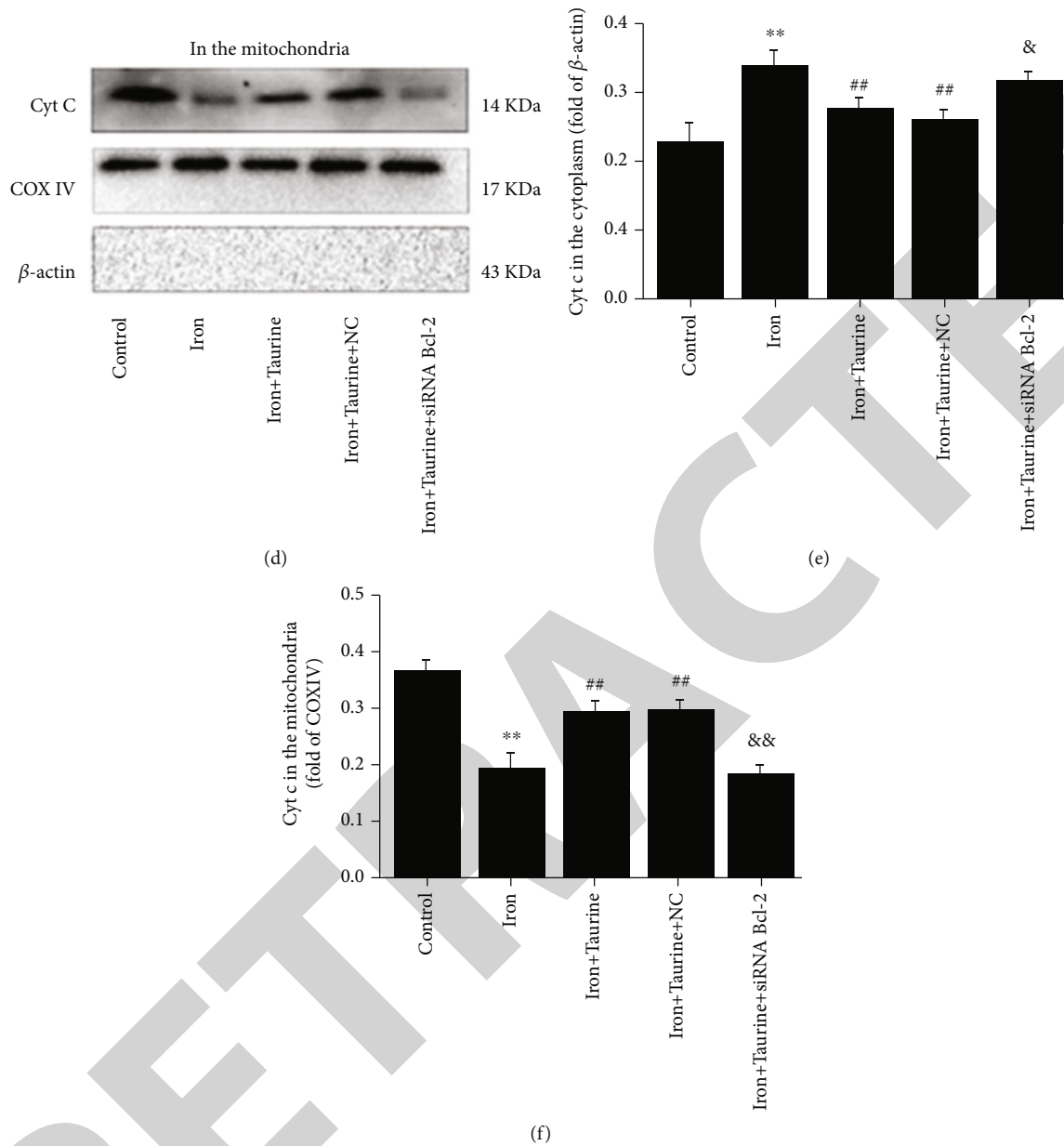


FIGURE 5: Taurine protects mitochondrial membrane integrity. Taurine treatment blocks the opening of mPTP in L02 cells caused by iron overload injury. (a)  $\text{CaCl}_2$  ( $200 \mu\text{M}$ ) was added for 20 min, and absorbance was measured at a wavelength of  $A = 520 \text{ nm}$  to indicate the opening of mPTP. (b) Calculating the opening of mPTP as  $\text{OD} = A_{520_{0 \text{ min}}} - A_{520_{20 \text{ min}}}$ . Taurine treatment blocks the transfer of Cyt c from mitochondria to the cytoplasm. (c, d) Cyt c protein level in the cytoplasm and mitochondria. (e) Histogram of Cyt c expression level in the cytoplasm. (f) Histogram of Cyt c expression level in the mitochondria. Data values are expressed as the mean  $\pm$  standard error of the mean (SEM),  $n = 3$ . \*\* $P < 0.01$  vs. the control group. \*\* $P < 0.01$  vs. the iron group. && $P < 0.01$  vs. the iron+taurine group. & $P < 0.05$  vs. the iron+taurine group.

family proteins are considered one of the main regulators of apoptosis [27]. Studies have also shown that members of the Bcl-2 family are new types of intracellular calcium ( $\text{Ca}^{2+}$ ) regulators. Most apoptotic pathways occur in the cell mitochondria, and the permeability changes in the mitochondrial membrane are closely related to the Bcl-2 protein [28–30]. Therefore, we speculated that taurine could suppress iron overload-induced cell damage, reduce cell apoptosis, and improve cell survival, potentially via the Bcl-2 protein. Western blotting revealed that taurine upregulated Bcl-2 protein

level. We used siRNA Bcl-2 lentiviral to knock out the Bcl-2 protein and observed that the protective effect of taurine was abolished. These results indicated that the protective effect of taurine could be related to Bcl-2. Several studies have shown that the Bcl-2 family can participate in the formation of lipid membrane ion channels [31, 32], and alterations in cell membrane permeability play a key role in apoptosis [33, 34]. And mPTP is a multiprotein complex pore composed of mitochondrial voltage-dependent anion channel 1 (VDAC1), adenylate transferase (ANT) in the

inner membrane, and cyclophilin (CyP-D) in the substrate [35, 36]. Recent studies have shown that outer membrane channels, such as the mitochondrial apoptosis-inducing channel and VDAC, are directly or indirectly involved in regulating mitochondrial permeability during apoptosis and necrosis [37–39]. Therefore, we postulated that the change in the mPTP might be related to VDAC1 [40]. In addition, Bcl-2 regulates the permeability of mitochondria from many aspects and plays an important role in mitochondrial-mediated apoptosis. Bcl-2 directly modulates cellular energy metabolism by regulating the respiratory chain [41]. Bcl-2 can bind to ion channels to regulate the release of Cyt c [42]. Bcl-2 can bind to VDAC1 to interact, shut down mPTP, and maintain the integrity of mitochondrial membranes [43]. In the present study, following the knockdown of Bcl-2, the level of VDAC1 was also significantly downregulated. It has been speculated that Bcl-2 may be related to VDAC1. Therefore, we speculated that Bcl-2 acts on VDAC1 to exert antiapoptotic effects. Co-IP experiments were used to detect the interaction between Bcl-2 and VDAC1 in liver cells. We observed that the interaction between Bcl-2 and VDAC1 was more potent in the taurine-administered group than in the control group. These results suggest that the protective effect of taurine may be mediated via the interaction between Bcl-2 and VDAC1.

In the present study, taurine did not impact the iron concentration in hepatocytes damaged by excessive iron overload. Interestingly, taurine exhibited a significant protective effect on hepatocytes damaged by iron overload. Our results showed that taurine induced the protein level of Bcl-2 and turned off mPTP, thereby inhibiting the ROS burst and maintaining mitochondrial membrane integrity by preventing the release of Cyt c from the mitochondria to the cytoplasm. Therefore, it is essential to detect the degree of mPTP opening. The prolonged opening of the mPTP causes swelling of organelles and mitochondrial depolarization, eventually leading to the rupture of the outer mitochondrial membrane, and the material in the interstitial space is released into the cytoplasm. Studies have found that mPTP is not only related to the rupture of the outer mitochondrial membrane during apoptosis but is also associated with a variety of pathologies [44, 45]. If mPTP is opened for a prolonged period, mitochondria release a considerable amount of Cyt c and apoptosis-inducing factors into the cytoplasm after rupture of the outer membrane. Compared with the iron overload group, taurine reduced the opening of the mPTP, decreased ROS burst, and inhibited Cyt c from the mitochondria to the cytoplasm. Following the knockdown of Bcl-2 protein, the protective effect of taurine was abolished, along with an increased degree of mPTP opening, elevated ROS burst, and enhanced Cyt c accumulated in the cytoplasm.

## 5. Conclusion

In summary, taurine inhibited hepatocyte apoptosis primarily via regulation of the mitochondrial-dependent pathway. Taurine was found to upregulate Bcl-2 protein level, enhance the interaction between Bcl-2 and VDAC1, reduce the opening of the mPTP, inhibit ROS burst, and inhibit the transfer of Cyt c from the mitochondria to the cytoplasm

to maintain mitochondrial membrane integrity, thereby inhibiting hepatocyte apoptosis.

## Data Availability

The data used to support the findings of this study are included within the article.

## Conflicts of Interest

The authors report no conflicts of interests.

## Authors' Contributions

Xiaoyu Feng and Wenfeng Hu contributed equally to this work.

## Acknowledgments












This work was supported by the Natural Science Foundation of China (Nos. 81460551, 81760587, 81460371, and 81760731), the Graduate Student Innovation Special Foundation of Nanchang University (No. cx2016299), and the Jiangxi Province Technology Support and Social Development Projects (No. 2010BSA13900).

## References

- [1] C. Geissler and M. Singh, "Iron, meat and health," *Nutrients*, vol. 3, no. 3, pp. 283–316, 2011.
- [2] E. D. Weinberg, "The hazards of iron loading," *Metallomics*, vol. 2, no. 11, pp. 732–740, 2010.
- [3] E. R. Anderson and Y. M. Shah, "Iron homeostasis in the liver," *Comprehensive Physiology*, vol. 3, no. 1, pp. 315–330, 2013.
- [4] H. M. Moukhadder, R. Halawi, M. D. Cappellini, and A. T. Taher, "Hepatocellular carcinoma as an emerging morbidity in the thalassemia syndromes: a comprehensive review," *Cancer*, vol. 123, no. 5, pp. 751–758, 2017.
- [5] L. J. Britton, V. N. Subramaniam, and D. H. Crawford, "Iron and non-alcoholic fatty liver disease," *World Journal of Gastroenterology*, vol. 22, no. 36, pp. 8112–8122, 2016.
- [6] A. Fonseca-Nunes, P. Jakszyn, and A. Agudo, "Iron and cancer risk—a systematic review and meta-analysis of the epidemiological evidence," *Cancer Epidemiology, Biomarkers & Prevention*, vol. 23, no. 1, pp. 12–31, 2014.
- [7] C. Zhang, "Essential functions of iron-requiring proteins in DNA replication, repair and cell cycle control," *Protein & Cell*, vol. 5, no. 10, pp. 750–760, 2014.
- [8] V. D. Paul and R. Lill, "Biogenesis of cytosolic and nuclear iron-sulfur proteins and their role in genome stability," *Biochimica et Biophysica Acta*, vol. 1853, no. 6, pp. 1528–1539, 2015.
- [9] R. Gozzelino and P. Arosio, "The importance of iron in pathophysiological conditions," *Frontiers in Pharmacology*, vol. 6, p. 26, 2015.
- [10] W. Zeng, X. Wang, P. Xu, G. Liu, H. S. Eden, and X. Chen, "Molecular imaging of apoptosis: from micro to macro," *Theoretical and Applied Biophysics*, vol. 5, no. 6, pp. 559–582, 2015.
- [11] M. P. Mattson and T. V. Arumugam, "Hallmarks of brain aging: adaptive and pathological modification by metabolic states," *Cell Metabolism*, vol. 27, no. 6, pp. 1176–1199, 2018.

## Research Article

# In Silico Establishment and Validation of Novel Lipid Metabolism-Related Gene Signature in Bladder Cancer

Xianchao Sun <sup>1</sup>, Ying Zhang <sup>2</sup>, Yilai Chen <sup>3</sup>, Shiyong Xin <sup>1</sup>, Liang Jin <sup>4</sup>,  
Xiang Liu <sup>1</sup>, Zhen Zhou <sup>1</sup>, Jiaxin Zhang <sup>4</sup>, Wangli Mei <sup>4</sup>, Bihui Zhang <sup>4</sup>,  
Xudong Yao <sup>4</sup>, Guosheng Yang <sup>1</sup>, and Lin Ye <sup>1</sup>

<sup>1</sup>Department of Urology, Shanghai East Hospital, School of Medicine, Tongji University, Shanghai 200120, China

<sup>2</sup>Department of Urology, The Second Affiliated Hospital of Anhui Medical University, Hefei 230032, China

<sup>3</sup>Department of Urology, Karamay People's Hospital, Xinjiang 834000, China

<sup>4</sup>Department of Urology, Shanghai Tenth People's Hospital, School of Medicine, Tongji University, Shanghai 200072, China

Correspondence should be addressed to Xudong Yao; yaoxudong67@sina.com, Guosheng Yang; ygs\_uro@163.com, and Lin Ye; ericyelin@tongji.edu.cn

Received 10 December 2021; Revised 19 March 2022; Accepted 30 March 2022; Published 18 April 2022

Academic Editor: Demin Cai

Copyright © 2022 Xianchao Sun et al. This is an open access article distributed under the Creative Commons Attribution License, which permits unrestricted use, distribution, and reproduction in any medium, provided the original work is properly cited.

**Background.** Aberrant lipid metabolism is an alteration common to many types of cancer. Dysregulation of lipid metabolism is considered a major risk factor for bladder cancer. Accordingly, we focused on genes related to lipid metabolism and screened novel markers for predicting the prognosis of bladder cancer. **Methods.** RNA-seq data for bladder cancer were obtained from The Cancer Genome Atlas (TCGA) and Gene Expression Omnibus (GEO) databases. The nonnegative matrix factorization (NMF) algorithm was used to classify the molecular subtypes. Weighted correlation network analysis (WGCNA) was applied to identify coexpressed genes, and least absolute shrinkage and selection operator (LASSO) multivariate Cox analysis was used to construct a prognostic risk model. External validation data and *in vitro* experiments were used to verify the results from *in silico* analysis. **Results.** Bladder cancer samples were grouped into two clusters based on the NMF algorithm. A total of 1467 genes involved in coexpression modules were identified in WGCNA. We finally established a 5-gene signature (TM4SF1, KCNK5, FASN, IMPDH1, and KCN15) that exhibited good stability across different datasets and was also an independent risk factor for prognosis. Furthermore, the predictive efficacy of our model was generally higher than the predictive efficacy of other published models. Distinct risk groups of patients also showed significantly different immune infiltration cell patterns and associations with clinical variables. Moreover, the 5 signature genes were verified in clinical samples by quantitative real-time polymerase chain reaction (qRT-PCR) and immunohistochemistry, which were in agreement with the *in silico* analysis. For *in vitro* experiments, knockdown of IMPDH1 markedly inhibited cell proliferation in bladder cancer. **Conclusion.** We established a 5-gene prognosis signature based on lipid metabolism in bladder cancer, which could be an effective prognostic indicator.

## 1. Introduction

As one of the most common genitourinary malignancies, bladder cancer (BC) has become a global health problem. The development and progression of BC are a multistage sophisticated process that includes genetic characteristics and environmental factors [1]. Epidemiological studies have demonstrated that modification in dietary intake is associ-

ated with the risk of BC [2, 3]. A positive association between red and processed meat and the risk of BC has been reported [4]. Lipids are a ubiquitous class of structurally complex molecules composed of different fatty acids involved in various biological processes. Lipids play an integral role in homeostasis, cell membrane structure, and cell signaling [5]. Abnormal synthesis, degradation, digestion, and absorption of lipid substances in lipid metabolism

contribute to excessive lipids in various tissues as well as tumorigenesis [6, 7].

Metabolic reprogramming is an important hallmark of cancer cells. Increased nutrient requirements are necessary to achieve rapid tumor growth and satisfy the metabolic needs of a tumor, and tumor cells have been observed to undergo metabolic reprogramming [8]. Tumor cells will choose the appropriate metabolic reprogramming method for metabolism so that they can better adapt to changing conditions. In tumorigenesis, fat is an important source of energy. In particular, researchers have found that lipid metabolic reprogramming exists in a variety of tumors, providing energy storage and intermediates of various metabolic activities for tumor proliferation, metastasis, and progression and even serving as a major intracellular metabolic type for cellular energy supply [9].

Recently, alterations in lipid metabolism have been recognized as a sign of many malignancies. Cheng et al. investigated whether fatty acid metabolism was activated in BC tissues, and inhibition of fatty acid oxidation showed a great impact on BC [10]. Previous studies have shown that general patterns and mechanisms of lipid metabolism participate in the development of BC, particularly blocking fatty acid synthesis to suppress the malignant phenotype of BC [11]. Furthermore, lipids mediate intercellular communication in the tumor-immune microenvironment. Lipid metabolism promotes the generation of M2-like tumor-associated macrophages (TAMs) and is crucial for TAM activity [12]. In tumor progression, cancer-stroma interactions are exacerbated, and fatty acids secreted in the microenvironment can influence the function and phenotype of infiltrating immune cells [13].

In this study, the expression of genes related to lipid metabolism in BC was investigated to screen hub genes that could predict patient prognosis. We developed and verified a 5-gene prognostic signature to effectively predict BC patient prognosis, as well as the relationship with immune infiltration cell patterns. This prognostic signature has the potential for clinical application in BC.

## 2. Methods

**2.1. Data Preparation.** Human lipid metabolism pathways were obtained from the Molecular Signature Database (MSigDB) [14], and 776 genes involved in lipid metabolism (Supplementary Table S1) were collated from 6 lipid metabolism pathways (Table 1). RNA-seq data were obtained from TCGA database for 433 BC samples, including 414 cancer samples and 19 normal samples, and corresponding clinicopathological information. RNA-seq data of 165 BC samples (GSE13507) and corresponding clinical information were downloaded from the GEO database.

**2.2. Identification of Molecular Subtypes.** First, we extracted 776 genes related to lipid metabolism from TCGA dataset; 24 genes were not identified, and 752 genes were included in subsequent analyses. Then, genes with significant differential expression were selected, and BC samples were clus-

tered using a nonnegative matrix factorization (NMF) clustering algorithm with 50 iterations of the standard “brunet” [15]. The number of clusters  $k$  was set from 2 to 10, and the average contour width of the common member matrix was determined through the R package “NMF.” The optimal number of clusters was determined according to cophenetic, dispersion, and silhouette index.

**2.3. Weighted Correlation Network Analysis (WGCNA).** The WGCNA algorithm was applied to screen coexpressed coding genes and modules according to the expression profile of protein-coding genes [16]. The soft threshold for network construction was determined by the criterion of approximate scale-free topology. After transformation of an adjacency matrix into a topological overlap matrix (TOM), genes were clustered with average linkage hierarchical clustering.

**2.4. Gene Set Enrichment Analysis (GSEA).** To investigate the molecular mechanism, GSEA was applied [17]. The gene sets “c5.go.v7.4.symbols” and “c2.cp.kegg.v7.4.symbols” were obtained from the MSigDB database. An adjusted  $p$  value less than 0.05 was considered statistically significant. The R package “clusterProfiler” was used to carry out enrichment analyses.

**2.5. Comprehensive Analysis of Immune Characteristics and Gene Mutations in Different Risk Groups.** Kaplan-Meier survival curves were applied to compare prognoses between the two risk subgroups. To further investigate the gene mutations between different risk subgroups, we obtained information on genetic alterations from the cBioPortal database, and different gene mutations in the two risk subgroups were analyzed using the “Maftools” R package. To determine the immune profile of BC samples, their expression data were imported into CIBERSORT and iterated 1000 times to estimate the relative proportions of 22 types of immune cells. We then compared the relative proportions of immune cells and clinicopathological factors between different risk subgroups, and the results are presented as a landscape map.

**2.6. Construction of the Nomogram.** A nomogram is a visual model used to evaluate the prognosis of cancer. We therefore constructed a nomogram to predict the prognosis of patients with BC. Moreover, a calibration plot was constructed to estimate the accuracy and consistency of the prognostic model.

**2.7. Analysis of DCA.** Decision curve analysis (DCA) represents a novel method for evaluating clinical usefulness. DCA can determine the clinical utility based on the predictive nomogram, and the best model has a higher net benefit than the others.

**2.8. Clinical Patients and Bladder Specimens.** Fifty paired normal and tumor tissues were collected from BC patients who underwent radical cystectomy at Shanghai Tenth People’s Hospital (Shanghai, China). Patients had diagnostic criteria in accordance with the World Health Organization (WHO) classification and did not receive any preoperative

TABLE 1: Six pathways involved in lipid metabolism.

Pathway	Database	Gene count
Peroxisome proliferator-activated receptor alpha	Reactome	119
Metabolism of lipids	Reactome	738
Transcriptional regulation of white adipocyte differentiation	Reactome	84
Sphingolipid metabolism	Reactome	89
Glycerophospholipid metabolism	KEGG	77
Fatty acid metabolism	Reactome	177
	Total: 1284	
	Unique: 776	

treatment. All patients provided informed consent prior to inclusion in the study, and ethical approval was obtained from the Ethics Committee of Shanghai Tenth People's Hospital. Detailed information is shown in Supplementary Table S2.

**2.9. Cell Culture and Transfection.** The immortalized human normal bladder epithelial cell line (SV-HUC-1) and bladder cancer T24, 5637, and UMUC3 cell lines were obtained from the Chinese Academy of Sciences (Shanghai, China). The UMUC3, T24, and 5637 cell lines were cultured in Roswell Park Memorial Institute- (RPMI-) 1640 medium (Gibco, USA), and the SV-HUC-1 cell line was maintained in F12K medium (Gibco). All cells were grown at 37°C in 5% CO<sub>2</sub>. The IMPDH1 siRNA (ATGGCTCTGATGGGAGGTATT), FASN siRNA (TGGCAAATTCGACCTTTCTCAGA), and TM4SF1siRNA (CGGCTAATATTTTGTCTTACTTT) were synthesized by Sangon Biotech (Shanghai, China). Lipofectamine 3000 (Invitrogen, USA) was used as a transfection reagent. T24 and UMUC3 cell lines were transfected with siRNA based on the protocol.

**2.10. RNA Extraction and Quantitative Real-Time Polymerase Chain Reaction (qRT-PCR).** For the qRT-PCR assay, TRIzol (Invitrogen, USA) was used to extract the total RNA. Next, SYBR-Green Mix (Vazyme, Nanjing, China) with different primers (Sangon Biotech, China) was used according to the manufacturer's protocol. GAPDH was used as an internal control. Fold changes were calculated by the 2<sup>-ΔΔCt</sup> method. Primer information is shown in Supplementary Table S3.

**2.11. Cell Proliferation Assay.** A total of 1 × 10<sup>3</sup> cells were grown in each well of a 96-well plate. Cell viability was calculated with the cell counting kit-8 (CCK-8) system. The optical density (OD) value per well was measured at 450 nm (BioTek, USA).

**2.12. Cell Colony Formation Assay.** A total of 500 cells were grown in each well of 6-well plates for approximately 2 weeks until colony formation was evident. Then, the cells were fixed, stained, and photographed.

**2.13. Western Blot.** Western blot was carried out based on standard protocol. Briefly, cells were washed with chilled PBS and lysed with lysis solution. Total protein extracts were

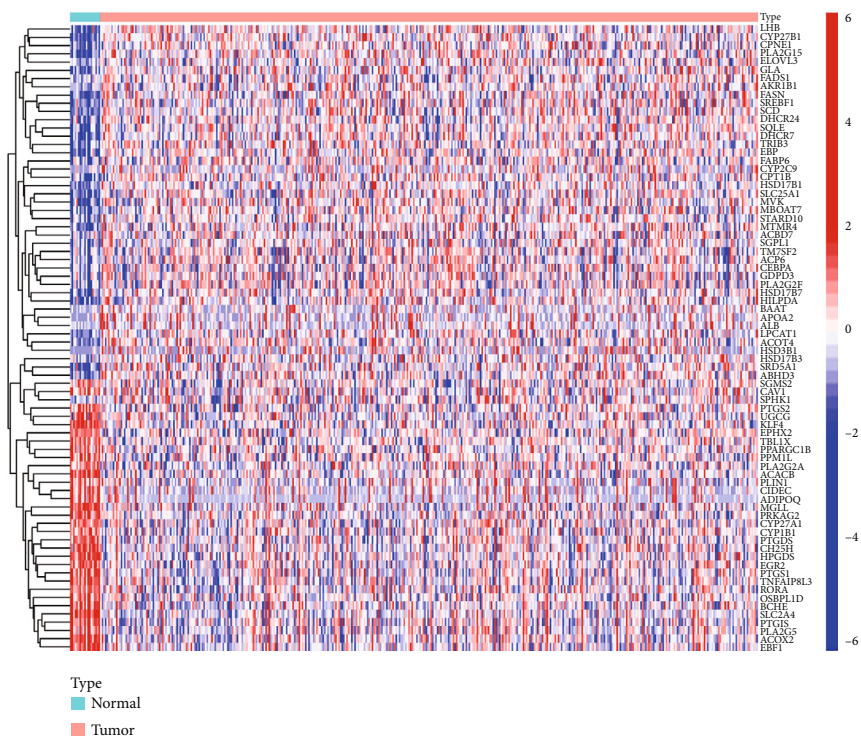
separated on a 10% SDS-PAGE gel and transferred onto PVDF membrane. After blocking with 5% nonfat dry milk, the PVDF membrane was incubated with primary antibody overnight at 4°C.

**2.14. Immunohistochemistry (IHC).** Tissue samples were fixed and cut into 4 μm slices. During dewaxing, rehydration, and antigen retrieval, sections were incubated with primary antibodies against TM4SF1, KCNK5, FASN, IMPDH1, and KCN15 (Thermo Fisher Scientific). Images were obtained with a microscope.

**2.15. Statistical Analysis.** Bioinformatics analyses were conducted using R version 4.1.1. GraphPad Prism 8 (GraphPad Software, Inc.) was used for statistical analysis. Student's *t* test or the Wilcoxon test was used to compare continuous data. The chi-square test and Fisher test were used to compare clinical and pathological parameters. Survival rates were assessed using Kaplan-Meier (K-M) curves and the log-rank test, and univariate and multivariate Cox regression was used to analyze the independent parameters associated with the overall survival. Pearson coefficient of correlation was calculated to measure the correlation between two variables. LASSO regression was carried out by using the "glmnet" R package to build a prognostic model. R software package "WGCNA" was used to construct a weighted co-expressed network. The correlation between the risk signature and immune cells was analyzed by Spearman correlation analysis. The results of multivariate Cox regression analysis were visualized by the nomogram. C-index, time-dependent ROC curves, and calibration curves were used to evaluate the nomogram. All statistical *p* values were two-sided, and *p* < 0.05 was considered statistically significant.

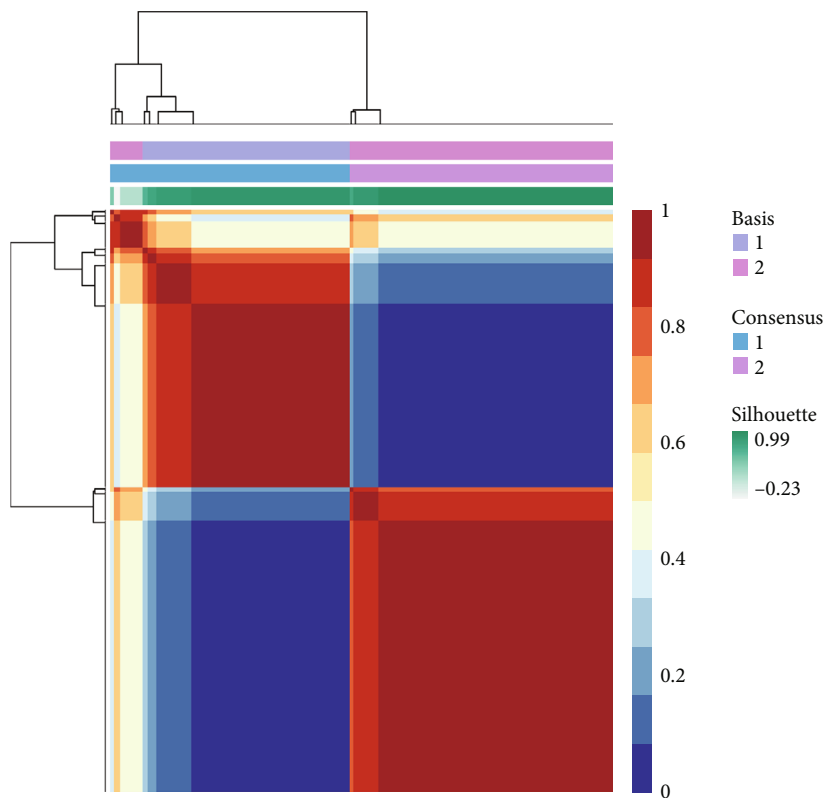
### 3. Results

**3.1. Molecular Subtypes Were Classified by the NMF Algorithm.** Figure S1 presents the flow diagram of the current study. First, we selected six gene sets associated with lipid metabolism from MSigDB. To investigate gene expression in BC, RNA-seq data from TCGA bladder cancer cohort (TCGA-BLCA) were downloaded. The "limma" R package was used to screen the genes with differential expression. A total of 76 differentially expressed



(a)

Consensus matrix



(b)

FIGURE 1: Continued.

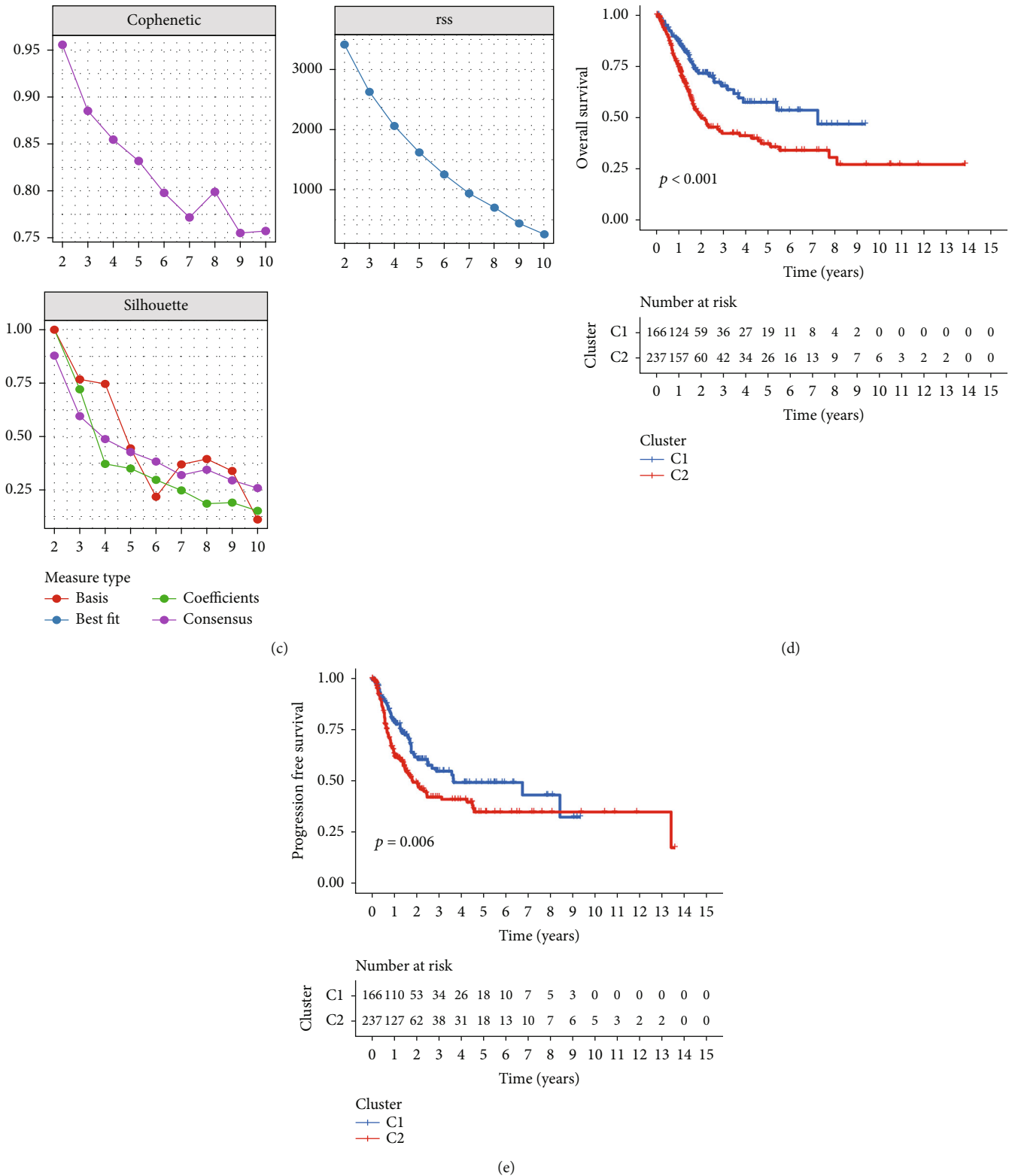


FIGURE 1: Cluster subtypes classified by the NMF algorithm. (a) Heatmap showing the differentially expressed lipid metabolism-related genes in TCGA. Red: upregulation; blue: downregulation. (b) NMF clustering consensus map. (c) NMF distributions when rank = 2-10. (d) Overall survival analysis of the two molecular subtypes. (e) Progression-free survival analysis of the two molecular subtypes.



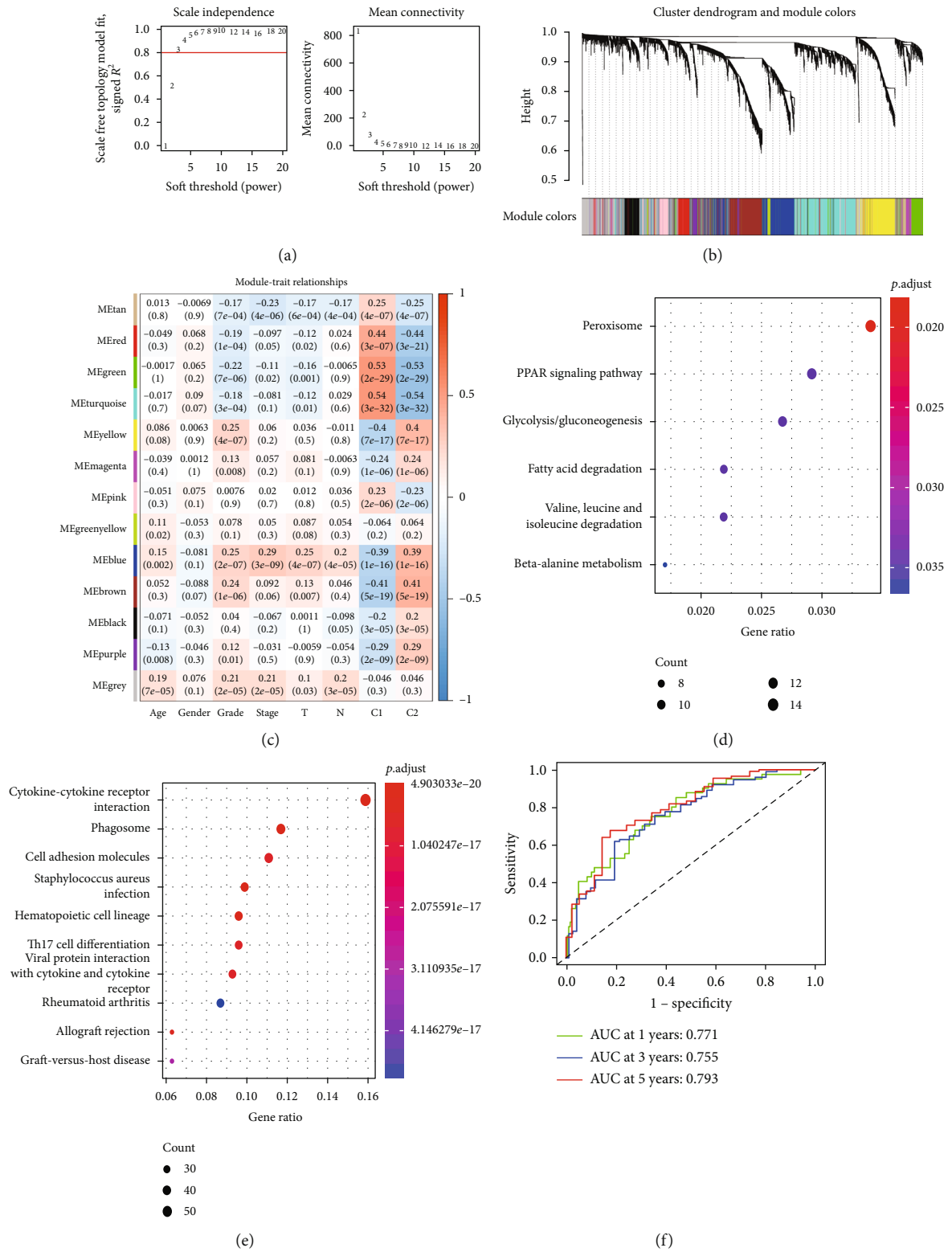


FIGURE 2: Continued.

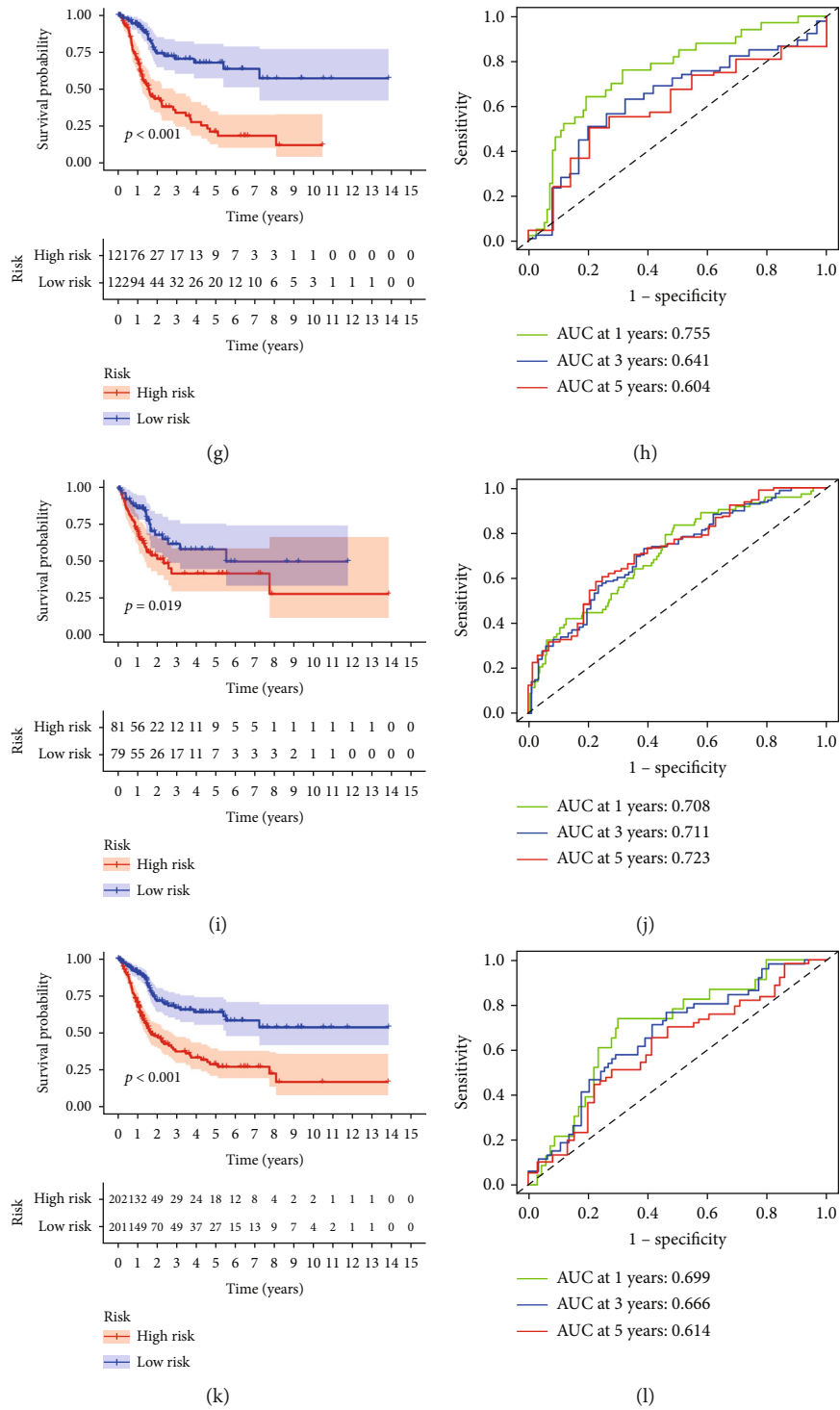


FIGURE 2: Continued.

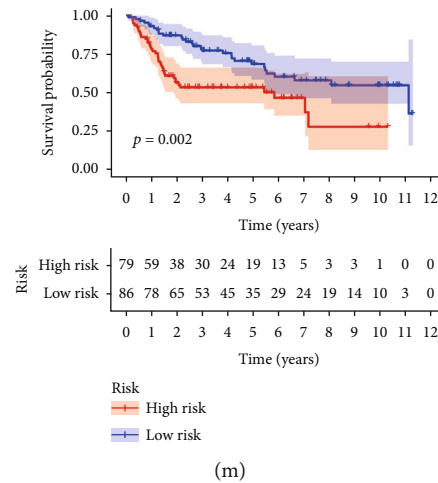


FIGURE 2: Identification of modules and construction of the model. (a) Cluster analysis and soft-thresholding powers. (b) WGCNA module colors. (c) Correlations of thirteen modules with clinical variables and clusters. (d, e) KEGG enrichment in the turquoise and brown modules. (f) ROC curve of the model in TCGA training cohort. (g) Survival curves of the groups in TCGA training cohort. (h) ROC curve of the model in TCGA testing cohort. (i) Survival curves of the groups in TCGA testing cohort. (j) ROC curve of the model in the entire TCGA cohort. (k) Survival curves of the groups in the entire TCGA cohort. (l) ROC curve of the model in the GSE13507 cohort. (m) Survival curves of the groups in the GSE13507 cohort.

TABLE 2: Clinical characteristics of bladder cancer patients from TCGA and GSE13507 datasets.

Clinical characteristics	TCGA cohort ( <i>n</i> = 412)	TCGA train ( <i>n</i> = 243)	TCGA test ( <i>n</i> = 160)	GSE13507 cohort ( <i>n</i> = 165)
Age at diagnosis (year)				
≤65	162	95	65	74
>65	250	148	95	91
Gender				
Male	304	177	121	135
Female	108	66	39	30
Grade				
Low grade	21	10	10	105
High grade	388	233	147	60
Stage				
I/II	133	77	53	135
III/IV	277	166	105	30

lipid metabolism-related genes on BC were obtained ( $p < 0.05$ , Figure 1(a)). Next, BC samples were clustered using the NMF method with 50 iterations by the “brunet” selection criterion. The optimal number of clusters chosen based on cophenetic, dispersion, and silhouette is  $k = 2$ . (Figures 1(b) and 1(c)). The prognostic relationship between Cluster 1 (C1) and Cluster 2 (C2) with overall survival (OS) (Figure 1(d), log rank  $p < 0.001$ ) and progression-free survival (Figure 1(e), log rank  $p = 0.006$ ) showed that subgroup C1 exhibited better prognosis than subgroup C2.

**3.2. Identification of Functional Modules by WGCNA.** The WGCNA algorithm was used to identify coexpressed coding genes and modules according to the expression profile of protein-coding genes. Hierarchical clustering analysis showed no outlier samples, and a soft threshold of 3 was chosen (Figure 2(a)). Genes were clustered using average linkage hierarchy clustering to obtain 13 modules with height = 0.25, deepSplit = 2, and minModuleSize = 30 (Figures 2(b) and 2(c)). Correlations of the modules with gender, age, clinical stage, N stage, T stage, C1, and C2 were further analyzed, in which modules significantly correlated with C1 and C2 were turquoise and brown modules. The turquoise module contained 907 genes, and the brown module contained 560 genes (Supplementary Table S4). These 1467 genes were used to establish the prognostic risk model. Analysis of Gene Ontology (GO) and Kyoto Encyclopedia of Genes and Genomes (KEGG) pathway enrichment in the two module genes was performed using the R package “cluster profiler.” The top 10 GO terms (Figures S2A and S2B) and KEGG pathways (Figures 2(d) and 2(e)) in the turquoise and brown modules were obtained.

**3.3. Establishment of the Prognostic Risk Model.** BC samples were divided randomly into a training cohort and testing cohort in a 6:4 ratio. The detailed information of the patient cohorts is summarized in Table 2. Univariate Cox proportional hazard analysis was performed to screen prognosis-related significant genes in the training set. Based on a threshold  $p$  value less than 0.01, 46 genes were identified with significant prognostic differences (Supplementary Table S5). To further narrow the range of genes and construct a highly accurate prognostic model, LASSO Cox regression and multivariate Cox analysis were used to select the hub genes (Figures S3A and S3B). Combining

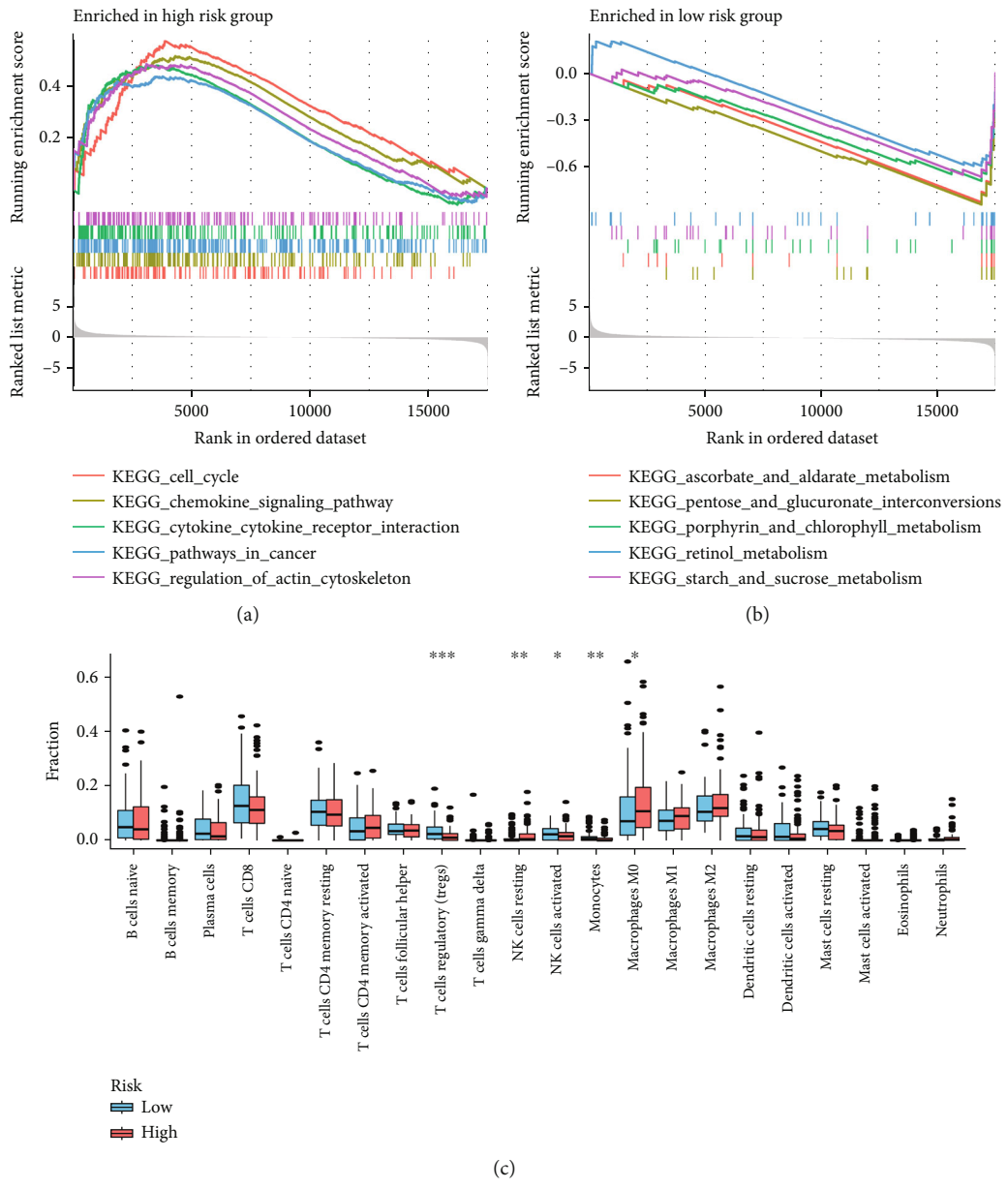


FIGURE 3: Continued.

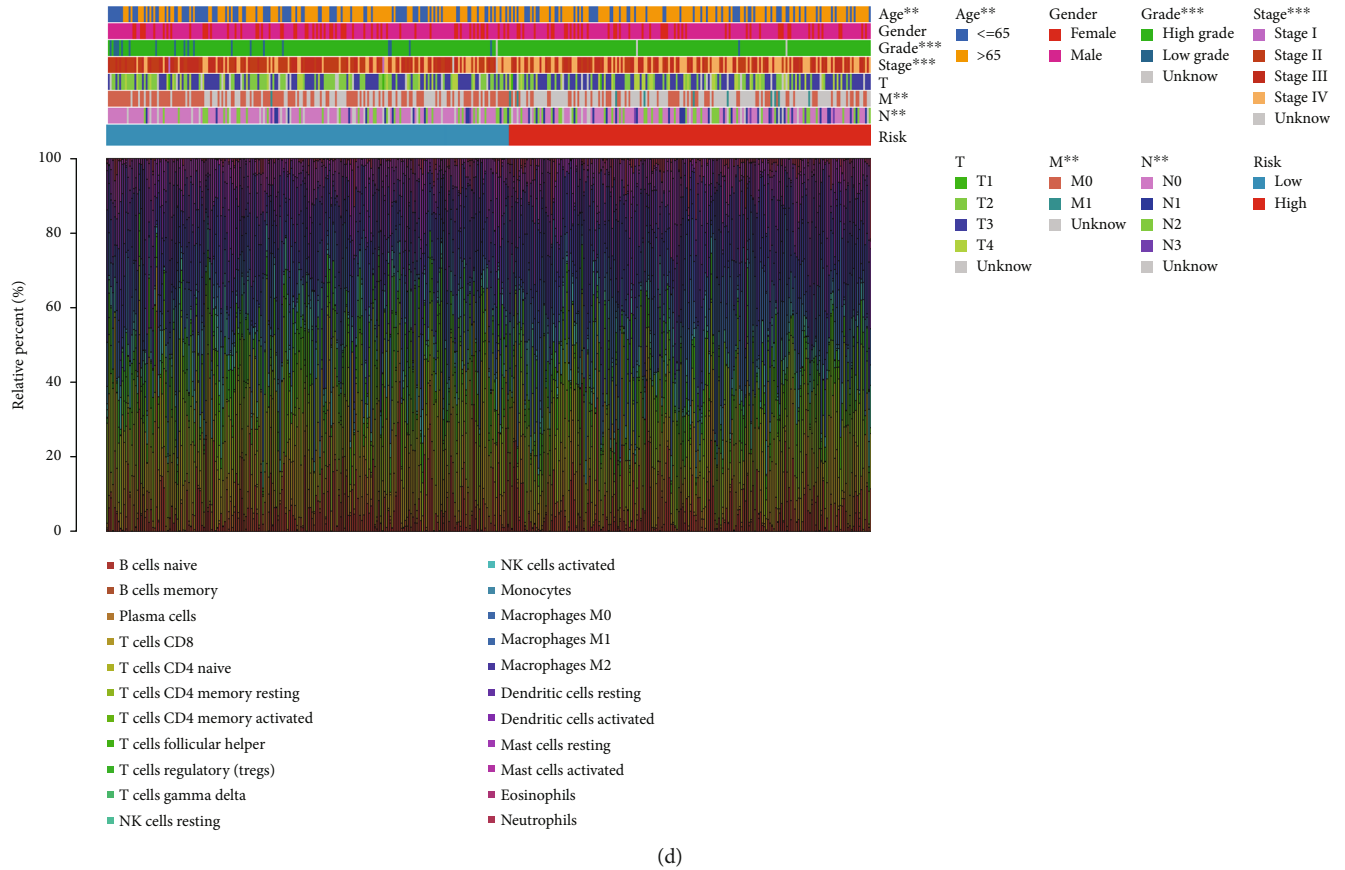


FIGURE 3: Molecular characteristics of the two risk subgroups and correlation between the risk model and immunity. GSEA for high-risk patients (a) and low-risk patients (b). (c) The relative proportions of 22 kinds of immune cells in the two risk subgroups. (d) Clinicopathological characteristics of two risk subgroups with the immune landscape.

TABLE 3: Univariate and multivariate cox analysis.

Clinical variables	HR	Univariable analysis		HR	Multivariable analysis	
		95% CI	<i>p</i> value		95% CI	<i>p</i> value
Age	1.040	1.021-1.059	2.75E-05	1.042	1.023-1.062	1.48E-05
Gender	1.110	0.761-1.620	0.5860	1.192	0.812-1.750	0.3679
Stage	1.951	1.524-2.497	1.10E-07	1.279	0.827-1.978	0.2669
T	1.658	1.275-2.154	0.0001	1.395	1.021-1.908	0.0365
N	1.592	1.334-1.901	2.58E-07	1.214	0.893-1.650	0.2154
Risk score	1.371	1.238-1.517	1.24E-09	1.337	1.195-1.496	3.66E-07

the analysis, 5 target genes were selected. The 5-gene signature formula was as follows: risk score = expression level of TM4SF1 \* (0.197) + expression level of KCNK5 \* (-0.373) + expression level of FASN \* (0.408) + expression level of IMPDH1 \* (0.342) + expression level of KCNJ15 \* (-0.171). Then, we analyzed the predictive classification efficiencies of the model, and the area under the curve (AUC) values for 1, 3, and 5 years were 0.771, 0.755, and 0.793, respectively, indicating good predictive performance (Figure 2(f)). Moreover, we divided the risk score into two risk subgroups, plotted the K-M curve as shown in Figure 2(g), and found a significant difference between them ( $p < 0.001$ ). To further determine the robustness of

this model, we used the same coefficients in the internal testing cohort, all TCGA cohorts, and the independent validation cohort GSE13507. In the testing cohort, the AUC values for 1, 3, and 5 years were 0.755, 0.641, and 0.604, respectively (Figure 2(h)); in all TCGA cohorts, the AUC values for 1, 3, and 5 years were 0.708, 0.711, and 0.723, respectively (Figure 2(i)). In the GSE13507 cohort, the AUC values for 1, 3, and 5 years were 0.699, 0.666, and 0.614, respectively (Figure 2(l)). Similar results were obtained in these cohorts, and significant differences were observed between the two risk subgroups (Figures 2(i), 2(k), and 2(m)). These results showed that the constructed risk signature has good robustness and could be used to

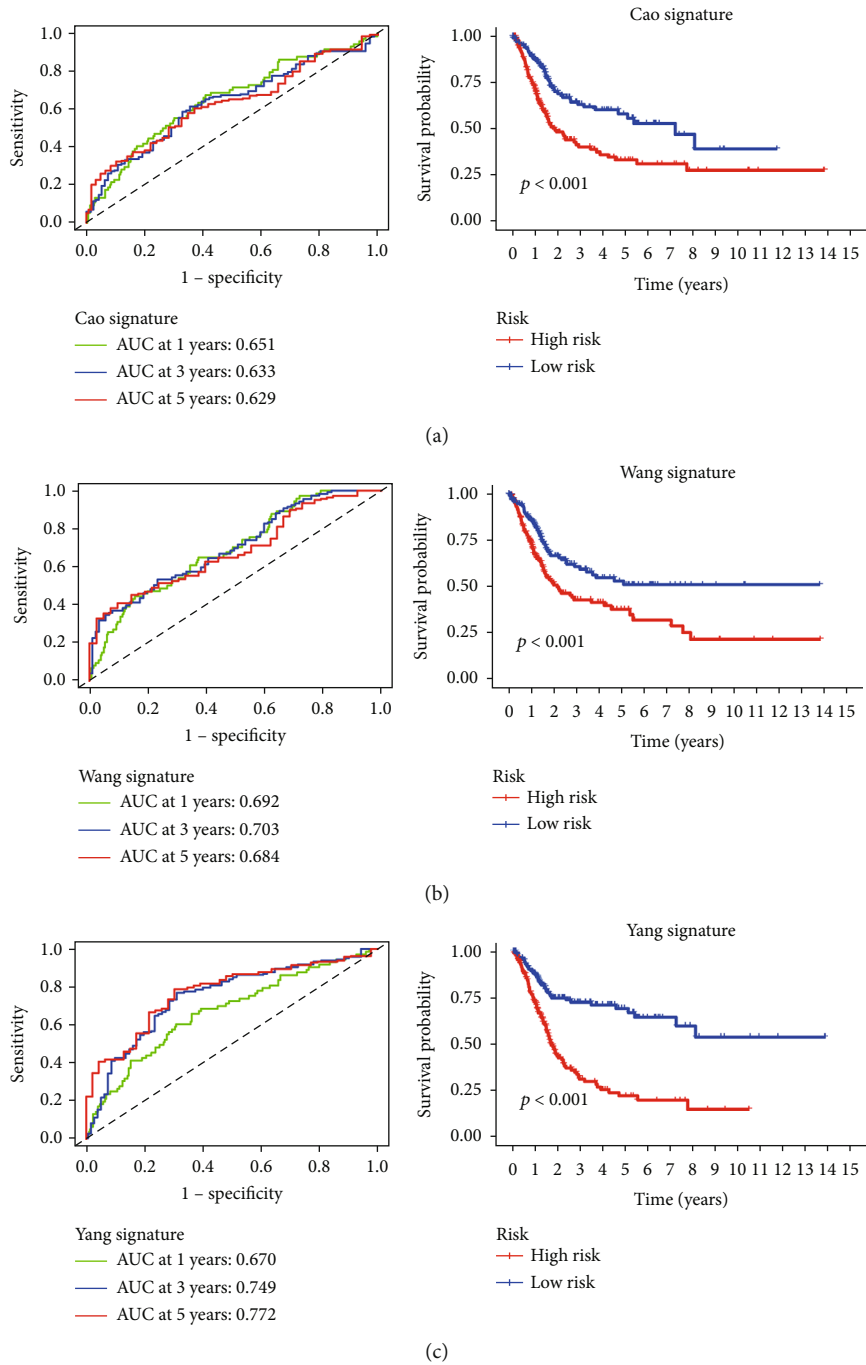


FIGURE 4: Continued.

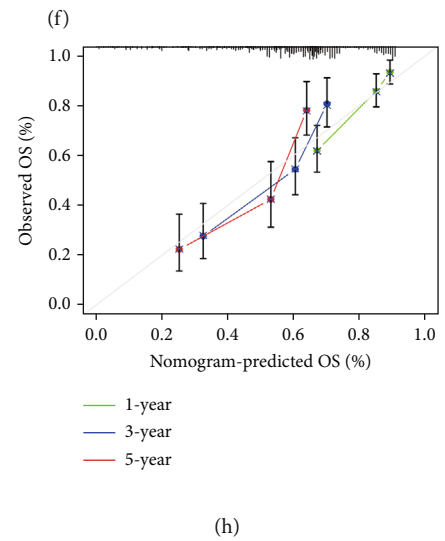
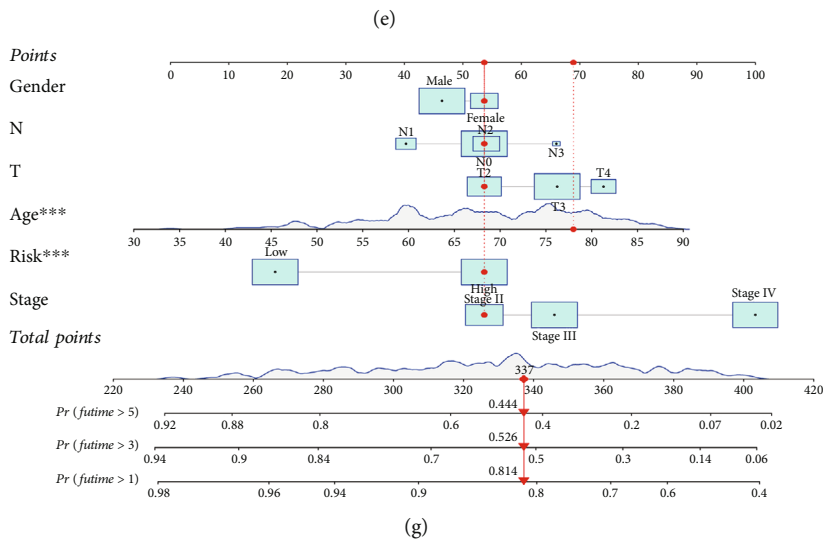
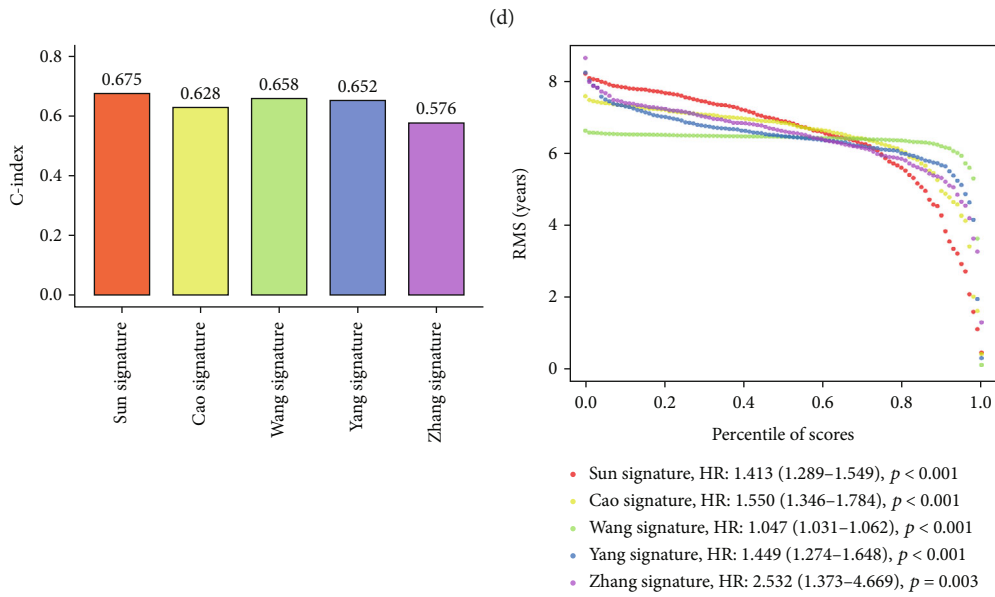
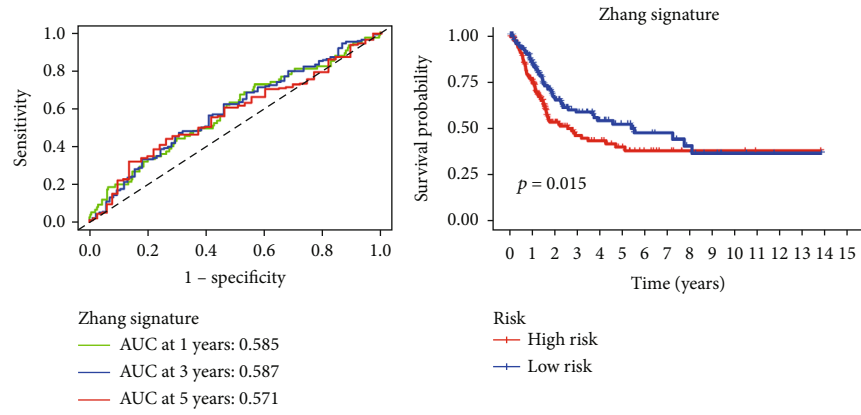


FIGURE 4: Continued.

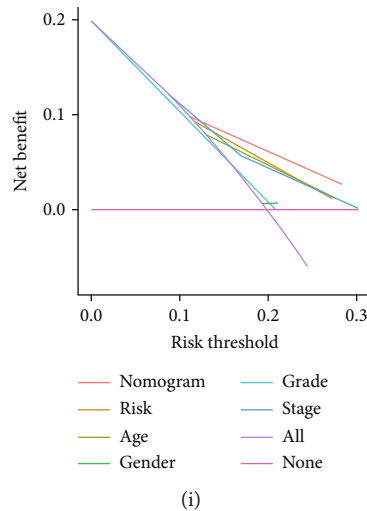


FIGURE 4: Comparison with other signatures and construction of the nomogram. (a) ROC and survival curves of the Cao signature. (b) ROC and survival curves of the Wang signature. (c) ROC and survival curves of the Yang signature. (d) ROC and survival curves of the Zhang signature. (e) C-index between the five signatures. (f) RMS result of the five signatures. (g) A nomogram to predict overall survival. (h) Calibration plots for prediction. (i) DCA for the nomogram, risk, and clinical variables.

predict the prognostic risk of BC patients in different cohorts.

**3.4. Molecular Characteristics between Different Risk Subgroups.** Mutation analysis in TCGA-BLCA samples revealed that 3%, 2.4%, 6%, 3%, and 2.2% of patients had mutations in TM4SF1, KCNK5, FASN, KCNJ15, and IMPDH1, respectively (Figure S4A). Missense variations, nonsense variations, and frameshift deletions were the common mutation types between the subgroups. The mutation rates of TTN, TP53, ARID1A, MUC16, KDM6A, and KMT2D were more than 20% in the two subgroups (Figures S4B and S4C). GSEA was used to identify the gene sets enriched in different risk subgroups. Gene sets from samples with high-risk score samples were enriched in pathways related to the cell cycle, chemokine signaling pathway, cytokine-cytokine receptor, pathways in cancer, and regulation of actin cytoskeleton, while the gene sets of low-risk score samples were enriched in metabolism pathways (Figures 3(a) and 3(b)).

**3.5. Prognostic Analysis of Risk and Clinical Characteristics.** We further compared the risk score between patients with different clinical characteristics. Correlation analysis of the risk score and clinical characteristics such as age, pathological grade, clinical stage, N stage, T stage, and M stage revealed a statistically significant association (Figure S5). We further performed survival analysis of the clinical subgroup with the risk score. As shown in Figure S6, the 5-gene signature can clearly distinguish patients by age, gender, T stage, and N stage. These results suggested that our risk model retained strong power in predicting different clinical variables. Furthermore, univariate and multivariate Cox regression analyses were used to investigate the independence of the risk (Table 3). The proportional hazards assumption was tested using the

Schoenfeld residual test (Figure S7). Univariate Cox regression analysis showed that age, stage, T stage, N stage, and risk were closely related to survival. Based on multivariate analysis, only age (HR = 1.042, 95%CI = [1.023 – 1.062],  $p = 1.48E - 05$ ), T stage (HR = 1.395, 95%CI = [1.021 – 1.908],  $p = 0.0365$ ), and risk score (HR = 1.337, 95%CI = [1.195 – 1.496],  $p = 3.66E - 07$ ) were significantly associated with survival. This finding indicated that this 5-gene signature was an independent risk factor for predicting prognosis.

**3.6. Correlation between the Risk Model and Immunity.** To explore the indicative roles of this risk model on the tumor microenvironment (TME), CIBERSORT was adopted to evaluate the relative proportion of 22 kinds of immune cells [18]. The results showed that the high-risk subgroup was significantly associated with natural killer (NK) resting cells and M0 macrophages, while the low-risk subgroup was significantly associated with regulatory T cells (Tregs), NK activated cell, and monocytes (Figure 3(c)). The correlations between the clinicopathological characteristics of different risk subgroups and the immune landscape are displayed in Figure 3(d). The results showed that our risk model could potentially reflect the status of the TME.

Furthermore, we explored whether the risk model had the potential to predict treatment response to immune checkpoint inhibitors (ICIs). We found that the expression of PD-1, PD-L1, LAG3, and CTLA4 was markedly higher in the high-risk subgroup, indicating a positive correlation with risk (Figures S8B–S8E). Moreover, the enrichment scores of immune-related pathways were quantified. Interestingly, most of the functions associated with antigen presentation, such as T cell costimulation and MHC and APC coinhibition, showed a bias toward the high-risk group (Figure S8A).



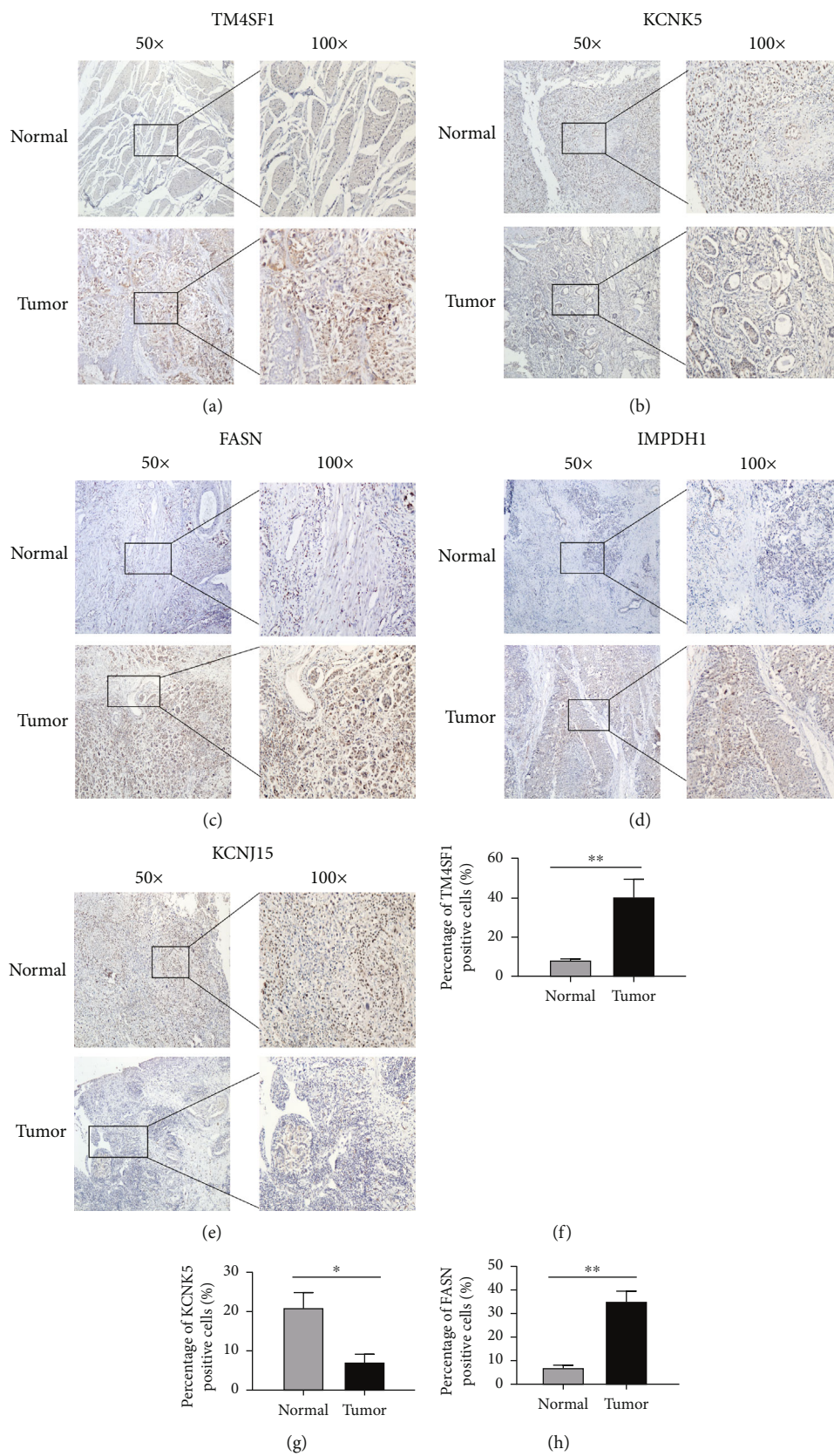


FIGURE 5: Continued.

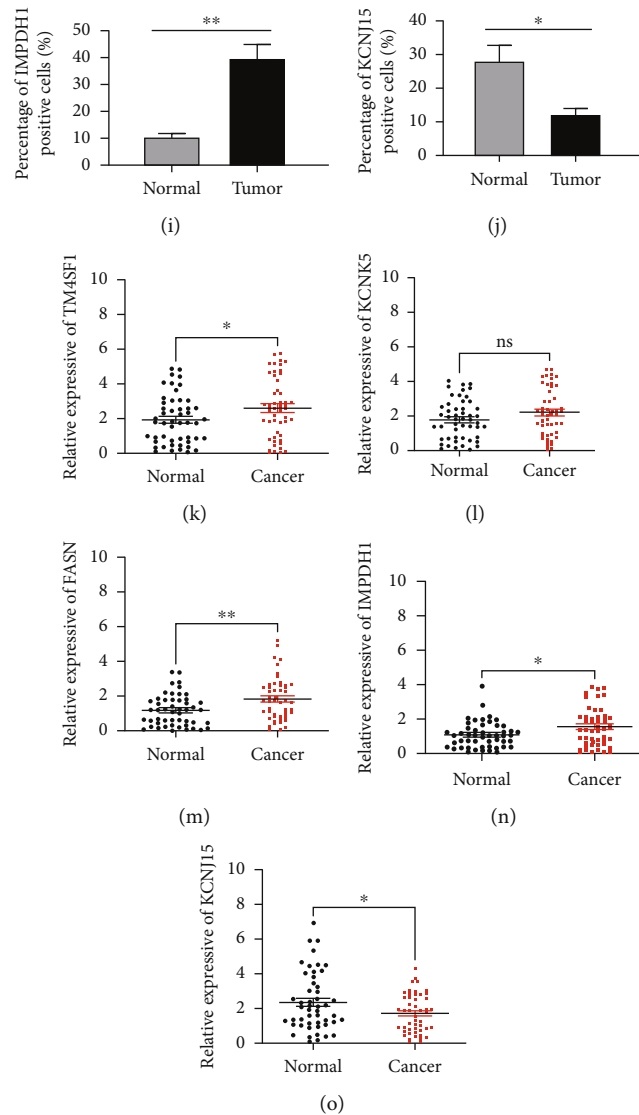


FIGURE 5: Immunohistochemistry and qRT-PCR results of the 5 genes in tissue samples. The protein expression of TM4SF1 (a), KCNK5 (b), FASN (c), IMPDH1 (d), and KCNJ15 (e) in clinical samples. (f–j) Percentage of positive cells of the 5 genes. (k–o) qRT-PCR analysis of TM4SF1, FASN, IMPDH1, KCNJ15, and KCNK5 mRNA levels in tissue samples. \* $p < 0.05$ , \*\* $p < 0.01$ , \*\*\* $p < 0.001$ , and ns  $p > 0.05$ .

### 3.7. Comparison of the Risk Model with Other Signatures.

Four prognostic risk signatures, the 4-gene, 5-gene, 7-gene, and 9-gene signatures, were chosen for comparison with this risk signature. We also used the same method to calculate every risk score in TCGA dataset according to the corresponding genes in the four risk signatures. Survival differences in the low- and high-risk subgroups were also detected with these risk signatures (Figures 4(a)–4(d), log rank  $p < 0.05$ ). To further validate prognostic prediction performance among them, the R package “rms” was used to calculate the concordance index (C-index). The results showed that our model had the highest C-index, highlighting a better performance (Figures 4(e) and 4(f)).

**3.8. Construction of the Nomogram with Risk Score.** To evaluate the potential clinical practicality of the prognostic model, we combined the clinicopathological features and

risk to construct a nomogram. As shown in Figure 4(g), a prognostic nomogram with risk score and clinical variables was constructed. The 1-, 3-, and 5-year calibration plots demonstrated the performance of the nomogram (Figure 4(h)). Finally, DCA indicated that the nomogram had a higher overall net benefit for clinical utility (Figure 4(i)).

### 3.9. Clinical and In Vitro Validation of 5 Gene Expressions.

To further confirm the above results, 50 cases of BC tissue specimens were included. Immunohistochemistry results showed that TM4SF1, FASN, and IMPDH1 were significantly highly expressed in cancer tissues, and KCNK5 and KCNJ15 were highly expressed in normal tissues (Figures 5(a)–5(j)). The results were basically consistent with the in silico analysis. The findings also showed that the mRNA expression levels of TM4SF1, FASN, and IMPDH1

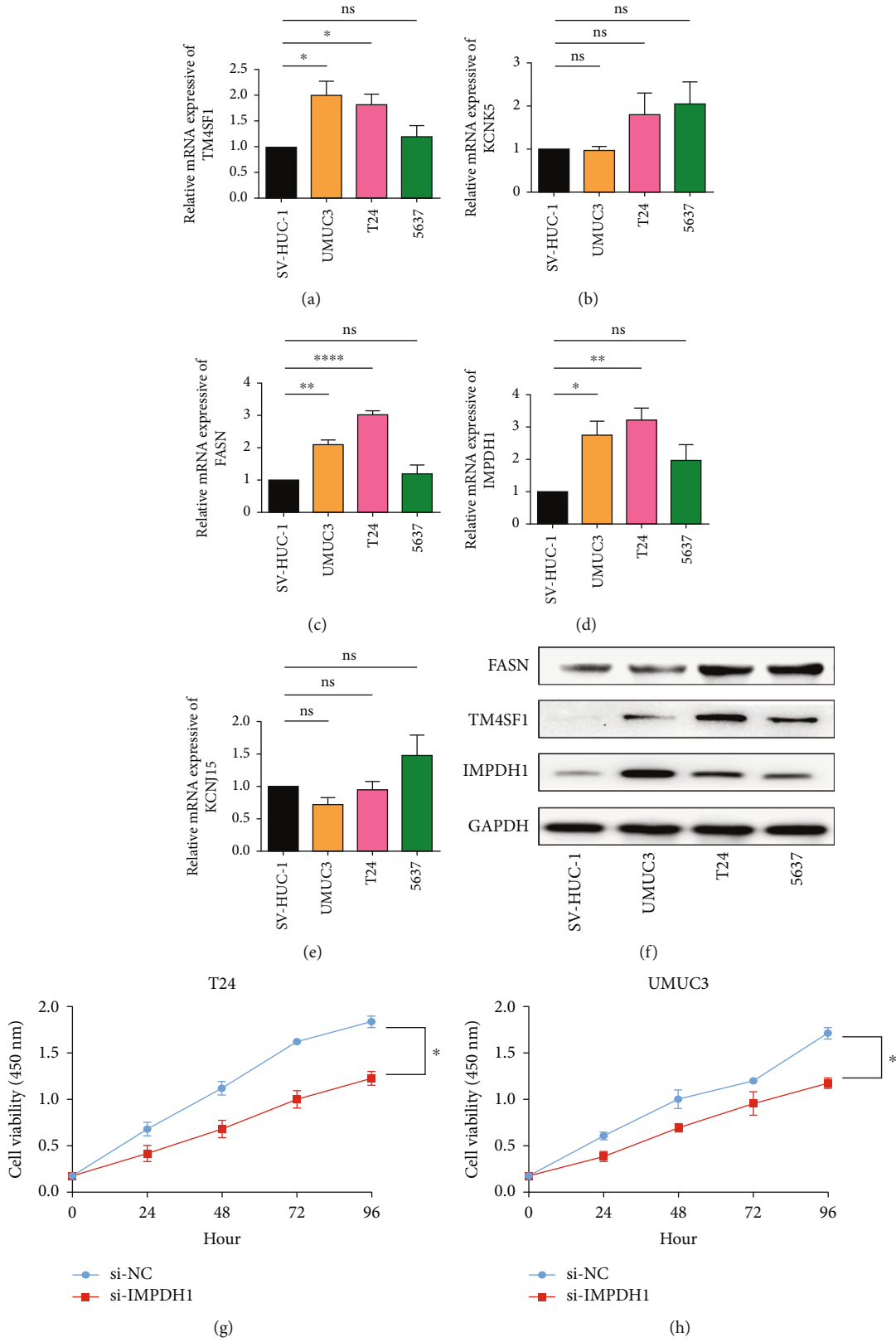


FIGURE 6: Continued.

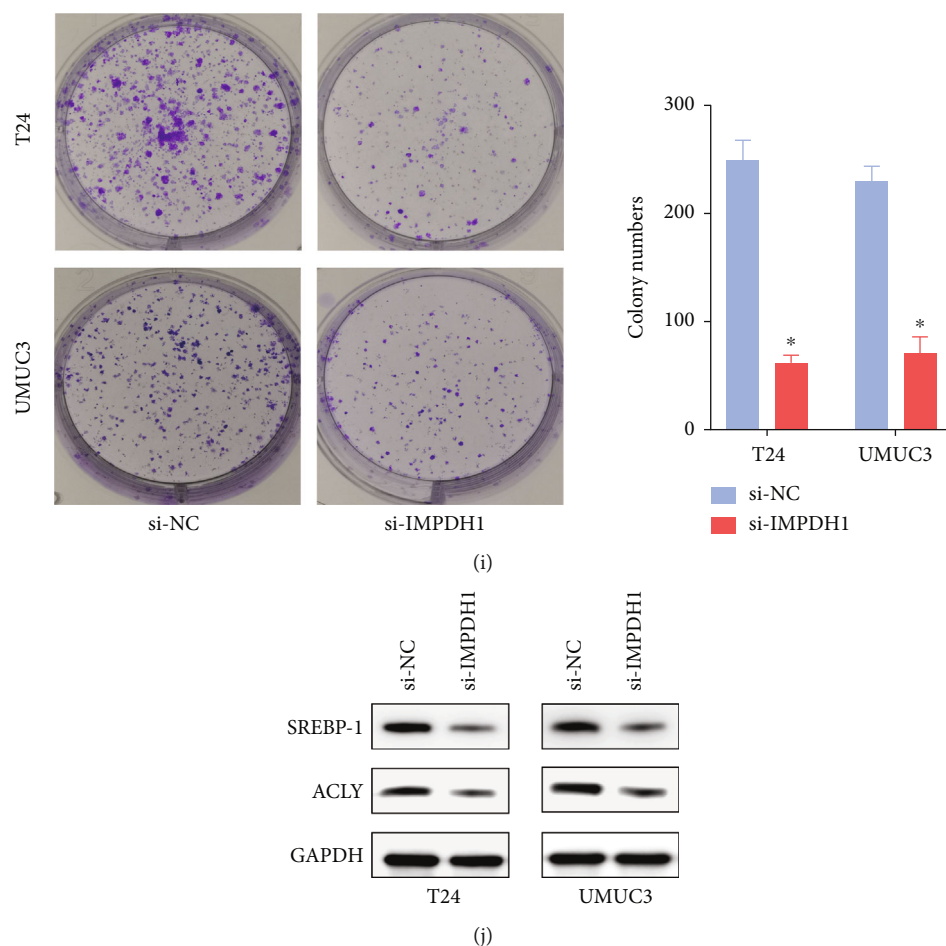


FIGURE 6: *In vitro* validation of the expression of 5 genes. (a–e) qRT-PCR analysis of TM4SF1, FASN, IMPDH1, KCN15, and KCN5 mRNA levels in cell lines. (f) The protein expression levels of the identified genes (TM4SF1, FASN, and IMPDH1) in cell lines by western blot. (g–i) CCK-8 and colony formation assays showed that silencing IMPDH1 suppressed cell proliferation. (j) Downregulation of IMPDH1 decreased the protein levels of SREBP-1 and ACLY in T24 and UMUC3 cells. \* $p < 0.05$ , \*\* $p < 0.01$ , \*\*\* $p < 0.001$ , and ns  $p > 0.05$ .

were higher in cancer tissues (Figures 5(k), 5(m), and 5(n)), whereas the mRNA expression of KCN15 was higher in normal tissues (Figure 5(o)). Moreover, the current study findings showed that the levels of TM4SF1, FASN, and IMPDH1 were significantly increased in BC cell lines (UMUC-3 and T24) compared with SV-HUC-1 (Figures 6(a)–6(f)). The qRT-PCR and western blotting validation findings confirmed the important roles of the signature genes in BC. Next, we analyzed the potential function of IMPDH1 in BC. Silencing IMPDH1 inhibited the proliferation and colony formation of bladder cancer cells *in vitro* (Figures 6(g)–6(i)). The results indicated that IMPDH1 may act as an oncogene in BC. Similar results were also observed after silencing FASN or TM4SF1 in bladder cancer cells (Figure S9). We further investigated the influence of IMPDH1 on lipid metabolism-related pathways; the expressions of two key enzymes in the fatty acid synthesis pathway were measured in IMPDH1 knockdown and control bladder cancer cells. As shown in Figure 6(j), downregulation of IMPDH1 decreased the protein levels of SREBP-1 and ACLY in T24 and UMUC3 cells. Thus, we

suggest that IMPDH1 plays an important role in regulating lipid metabolism on BC.

#### 4. Discussion

BC is a common malignant tumor worldwide and has high rates of progression and recurrence. Despite advances in surgery and comprehensive treatment regimens, effective targeted therapies and prognostic markers are still lacking in patients with BC [19]. In the process of transforming normal cells into malignant cells, one of the key steps is metabolic reprogramming, including glycolysis and glutamine and fatty acid metabolism [20]. There is growing evidence that certain specific changes in lipid metabolism have an impact on the synthesis and degradation of tumor cell membranes, thus maintaining the energy balance in the body [21, 22].

In the present study, we identified two subtypes of BC by using the NMF algorithm based on genes related to lipid metabolism. Next, WGCNA was applied to screen modules of coexpressed genes, and 1467 genes were obtained. Then, LASSO and multivariate Cox analyses were performed to

construct a 5-gene prognostic risk model. Our findings showed that this risk model had stable performance in the prognosis of BC patients and was implicated in clinical characteristics and immune infiltration cells.

This risk signature was constructed with TM4SF1, KCNK5, FASN, IMPDH1, and KCNJ15. According to our study results, TM4SF1, FASN, and IMPDH1 were significantly and highly expressed in BC tissues, while KCNK5 and KCNJ15 were poorly expressed. In accordance with the corresponding coefficients of these five genes, the risk score was calculated, and samples were grouped with different risks. Survival analysis exhibited significant discrepancies between different risk subgroups. We also confirmed that the risk score was an independent prognostic factor for survival. Stratified survival analysis also indicated the good feasibility of this model. Furthermore, CIBERSORT showed that patients in the high-risk subgroup had higher proportions of M0 macrophages and NK resting cells, while Tregs and NK-activated cells were upregulated in the low-risk group, indicating a differential infiltration pattern between the subgroups [23]. GSEA indicated that the cell cycle, regulation of actin cytoskeleton, pathways in cancer, cytokine-cytokine receptor interaction, and chemokine signaling pathway increased with risk score, suggesting that risk was closely related to tumor development and immune activity [24, 25]. Immune checkpoints could be regarded as potential therapeutic targets of tumor treatment, and the inhibitors have exhibited superior anticancer efficacy [26]. We found that the high-risk subgroup was associated with immune checkpoints such as PD-1, PD-L1, LAG3, and CTLA-4, implying that patients with different risks respond differently to immunotherapy.

TM4SF1 acts as an integral membrane glycoprotein that transmits signals from the extracellular space to the cytoplasm. Previous studies have shown that TM4SF1 is overexpressed in various cancers and is strongly upregulated in BC tissues [27]. FASN is a key enzyme in fatty acid synthesis. FASN levels have been reported to be closely associated with cell proliferation and apoptosis. Research on the relationship between FASN and BC has proven that FASN is associated with the progression of BC [28]. IMPDH1 is a key regulator of GTP synthesis and is required for signal transduction. IMPDH1 has been indicated to be positively associated with renal cancer metastasis [29]. KCNK5 is a member of the KCNK family, which can regulate membrane potential and excitability. The expression of KCNK5 is associated with the maintenance of hearing [30]. KCNJ15 is a member of the inwardly rectifying potassium channel family. Liu et al. demonstrated that KCNJ15 inhibits renal cell proliferation [31].

Next, we further validated the expression of these five genes in tissue specimens and cell lines. The immunohistochemistry results suggested that the expression of TM4SF1, FASN, and IMPDH1 was significantly elevated in tumor tissue specimens, while the expression of KCNK5 and KCNJ15 was downregulated. The mRNA expression levels detected in the tissue specimens were also generally consistent with the above results. In an *in vitro* experiment, we demonstrated that TM4SF1, FASN, and IMPDH1 were elevated in some

bladder cancer cell lines. These results are in accordance with the bioinformatics analysis. Finally, we focused on the function of IMPDH1 in BC and found that cell proliferation and colony formation were significantly inhibited after knocking down IMPDH1, implying that IMPDH1 has a tumor-promoting effect.

Previous studies have also developed cancer biomarkers associated with BC prognosis. Cao et al. constructed a 7-gene signature related to EMT for predicting the outcome of BC patients [32], while a 9-gene signature related to ferroptosis was established by Yang et al. [33]. Zhang et al. identified a glycolysis-based 4-mRNA signature to promote therapeutic options in BC [34]. Wang et al. used univariate and robust methods to establish a 5-gene risk model in BC [35]. To further examine the advantages of our signature, we compared these risk models simultaneously. The results demonstrated that our model had the highest C-index, exhibiting good application value compared with the others. Our risk signature obtained a more stable and effective prediction with fewer genes, which is better suited for clinical applications. Although the results were derived from multiomics data with a large sample, some limitations also need to be improved. Despite the rigorous bioinformatics analysis in the current study, further verification is still needed.

Aberrant activities of lipid metabolism have unique functional roles in cancer progression, and their imbalanced status has been a topic for screening therapeutic targets. Therefore, we attempted to fill the knowledge gap between lipid gene status and prognosis prediction in BC. Based on this study, we think these five genes may be implicated in lipid metabolism processes, and this risk signature may serve as a prognostic biomarker for BC treatment.

In conclusion, we established and validated a 5-gene signature associated with lipid metabolism, which was an independent prognostic factor in different datasets. The risk signature exhibited superior predictive performance compared to other published models. This 5-gene signature could be recognized as a prognostic marker to reflect the survival of BC.

## Abbreviations

NMF:	Nonnegative matrix factorization
WGCNA:	Weighted correlation network analysis
BC:	Bladder cancer
TCGA:	The Cancer Genome Atlas
GEO:	Gene Expression Omnibus
ROC:	Receiver-operating characteristic
OS:	Overall survival
LASSO:	Least absolute shrinkage and selection operator
AUC:	Areas under the curve
TME:	Tumor microenvironment
DCA:	Decision curve analysis
GSEA:	Gene set enrichment analysis
GO:	Gene Ontology
KEGG:	Kyoto Encyclopedia of Genes and Genomes
ICIs:	Immune checkpoint inhibitors
C-index:	Concordance index
NC:	Negative control.

## Data Availability

The authors declare that the data supporting the findings of the current study are provided in the article. Datasets analyzed for this work can be obtained from TCGA (<https://portal.gdc.cancer.gov/>), GEO (<https://www.ncbi.nlm.nih.gov/geo/>), MSigDB (<https://www.gsea-msigdb.org/gsea/msigdb>), cBioPortal (<https://www.cbioportal.org/>), and CIBERSORT (<https://cibersort.stanford.edu/>).

## Ethical Approval

This study was approved by the Ethics Committee of Shanghai Tenth People's Hospital.

## Conflicts of Interest

The authors declare that they have no competing interests.

## Authors' Contributions

XS, YZ, YC, and LY designed the experiments. SX, LJ, XL, ZZ, JZ, WM, GY, and BZ performed the statistical analyses. XS, YZ, YC, GY, and XY participated in the coordination of the study. XS, GY, and LY wrote the manuscript. All authors read and approved the final manuscript. Xianchao Sun, Ying Zhang, and Yilai Chen have contributed equally to this work.

## Acknowledgments

This work was supported by the National Natural Science Foundation of China (No. 81972409 and No. 81672549).

## Supplementary Materials

Figure S1: flow diagram of the current study. Figure S2: GO analysis of coexpressed genes. GO enrichment of genes in the turquoise (A) and brown (B) modules. Figure S3: construction of the model. (A) LASSO coefficient profile plot. (B) The values of lambda in the model. Figure S4: gene mutations between the two risk subgroups. (A) Mutation analysis of the five genes. Gene mutation distributions in high-risk (B) and low-risk subgroups (C). Figure S5: correlation analysis of risk score with clinical characteristics in age (A), grade (B), clinical stage (C), M stage (D), N stage (E), and T stage (F). Figure S6: stratified survival analysis. (A) Survival analysis of two risk subgroups in age  $\leq 65$  years. (B) Survival analysis of two risk subgroups in age  $> 65$ . (C) Survival analysis of two risk subgroups in females. (D) Survival analysis of two risk subgroups in males. (E) Survival analysis of two risk subgroups in stages I + II. (F) Survival analysis of two risk subgroups in stages III + IV. (G) Survival analysis of two risk subgroups in T1 + T2. (H) Survival analysis of two risk subgroups in T3 + T4. (I) Survival analysis of two risk subgroups in N0. (J) Survival analysis of two risk subgroups in N1 + N2 + N3. Figure S7. The proportional hazards assumption was tested using the Schoenfeld residual test. Figure S8: correlation between the risk model and immune checkpoint inhibitors. (A) Immune-related path-

ways were quantified between the two risk subgroups. The relationship between risk score and PD-1 (B), PD-L1 (C), CTLA4 (D), and LAG3 (E). Figure S9: CCK-8 assay showed that silencing FASN (A, B) or TM4SF1 (C, D) suppressed cell proliferation in T24 and UMUC3 cell lines. Table S1: lipid metabolism-related genes. Table S2: clinical characteristics of 50 bladder cancer patients. Table S3: primer information. Table S4: 907 genes in turquoise module and 560 genes in brown module. Table S5: 46 genes with significant prognostic differences. (*Supplementary Materials*)

## References

- [1] J. A. Witjes, H. M. Bruins, R. Cathomas et al., "European Association of Urology guidelines on muscle-invasive and metastatic bladder cancer: summary of the 2020 guidelines," *European Urology*, vol. 79, no. 1, pp. 82–104, 2021.
- [2] A. M. Mondul, S. J. Weinstein, S. Mannisto et al., "Serum vitamin D and risk of bladder cancer," *Cancer Research*, vol. 70, no. 22, pp. 9218–9223, 2010.
- [3] V. Edefonti, C. La Vecchia, M. Di Maso et al., "Association between nutrient-based dietary patterns and bladder cancer in Italy," *Nutrients*, vol. 12, no. 6, p. 1584, 2020.
- [4] A. Crippa, S. C. Larsson, A. Discacciati, A. Wolk, and N. Orsini, "Red and processed meat consumption and risk of bladder cancer: a dose-response meta-analysis of epidemiological studies," *European Journal of Nutrition*, vol. 57, no. 2, pp. 689–701, 2018.
- [5] L. A. Broadfield, A. A. Pane, A. Talebi, J. V. Swinnen, and S. M. Fendt, "Lipid metabolism in cancer: new perspectives and emerging mechanisms," *Developmental Cell*, vol. 56, no. 10, pp. 1363–1393, 2021.
- [6] X. Bian, R. Liu, Y. Meng, D. Xing, D. Xu, and Z. Lu, "Lipid metabolism and cancer," *The Journal of Experimental Medicine*, vol. 218, no. 1, 2021.
- [7] P. Morigny, J. Boucher, P. Arner, and D. Langin, "Lipid and glucose metabolism in white adipocytes: pathways, dysfunction and therapeutics," *Nature Reviews. Endocrinology*, vol. 17, no. 5, pp. 276–295, 2021.
- [8] L. K. Borouh and R. J. DeBerardinis, "Metabolic pathways promoting cancer cell survival and growth," *Nature Cell Biology*, vol. 17, no. 4, pp. 351–359, 2015.
- [9] H. Iwamoto, M. Abe, Y. Yang et al., "Cancer lipid metabolism confers antiangiogenic drug resistance," *Cell Metabolism*, vol. 28, no. 1, pp. 104–117.e5, 2018.
- [10] S. Cheng, G. Wang, Y. Wang et al., "Fatty acid oxidation inhibitor etomoxir suppresses tumor progression and induces cell cycle arrest via PPAR $\gamma$ -mediated pathway in bladder cancer," *Clinical Science (London, England)*, vol. 133, no. 15, pp. 1745–1758, 2019.
- [11] A. Li, L. Yao, Y. Fang et al., "Specifically blocking the fatty acid synthesis to inhibit the malignant phenotype of bladder cancer," *International Journal of Biological Sciences*, vol. 15, no. 8, pp. 1610–1617, 2019.
- [12] P. Su, Q. Wang, E. Bi et al., "Enhanced lipid accumulation and metabolism are required for the differentiation and activation of tumor-associated macrophages," *Cancer Research*, vol. 80, no. 7, pp. 1438–1450, 2020.
- [13] K. C. Corn, M. A. Windham, and M. Rafat, "Lipids in the tumor microenvironment: from cancer progression to treatment," *Progress in Lipid Research*, vol. 80, article 101055, 2020.

- [14] A. Liberzon, A. Subramanian, R. Pinchback, H. Thorvaldsdottir, P. Tamayo, and J. P. Mesirov, "Molecular signatures database (MSigDB) 3.0," *Bioinformatics*, vol. 27, no. 12, pp. 1739–1740, 2011.
- [15] Y. Gao and G. Church, "Improving molecular cancer class discovery through sparse non-negative matrix factorization," *Bioinformatics*, vol. 21, no. 21, pp. 3970–3975, 2005.
- [16] P. Langfelder and S. Horvath, "WGCNA: an R package for weighted correlation network analysis," *BMC Bioinformatics*, vol. 9, no. 1, p. 559, 2008.
- [17] R. K. Powers, A. Goodspeed, H. Pielke-Lombardo, A. C. Tan, and J. C. Costello, "GSEA-InContext: identifying novel and common patterns in expression experiments," *Bioinformatics*, vol. 34, no. 13, pp. i555–i564, 2018.
- [18] S. Sui, X. An, C. Xu et al., "An immune cell infiltration-based immune score model predicts prognosis and chemotherapy effects in breast cancer," *Theranostics*, vol. 10, no. 26, pp. 11938–11949, 2020.
- [19] V. G. Patel, W. K. Oh, and M. D. Galsky, "Treatment of muscle-invasive and advanced bladder cancer in 2020," *CA: a Cancer Journal for Clinicians*, vol. 70, no. 5, pp. 404–423, 2020.
- [20] X. Li, M. Wenes, P. Romero, S. C. Huang, S. M. Fendt, and P. C. Ho, "Navigating metabolic pathways to enhance antitumour immunity and immunotherapy," *Nature Reviews. Clinical Oncology*, vol. 16, no. 7, pp. 425–441, 2019.
- [21] C. W. Fhu and A. Ali, "Fatty acid synthase: an emerging target in cancer," *Molecules*, vol. 25, no. 17, p. 3935, 2020.
- [22] H. Li, Z. Feng, and M. L. He, "Lipid metabolism alteration contributes to and maintains the properties of cancer stem cells," *Theranostics*, vol. 10, no. 16, pp. 7053–7069, 2020.
- [23] T. Z. Tan, M. Rouanne, K. T. Tan, R. Y. Huang, and J. P. Thiery, "Molecular subtypes of urothelial bladder cancer: results from a meta-cohort analysis of 2411 tumors," *European Urology*, vol. 75, no. 3, pp. 423–432, 2019.
- [24] Y. Zhang, X. Y. Guan, and P. Jiang, "Cytokine and chemokine signals of T-cell exclusion in tumors," *Frontiers in Immunology*, vol. 11, article 594609, 2020.
- [25] L. Rosano and A. Bagnato, "New insights into the regulation of the actin cytoskeleton dynamics by GPCR/ $\beta$ -arrestin in cancer invasion and metastasis," *International Review of Cell and Molecular Biology*, vol. 346, pp. 129–155, 2019.
- [26] L. Galluzzi, J. Humeau, A. Buque, L. Zitvogel, and G. Kroemer, "Immunostimulation with chemotherapy in the era of immune checkpoint inhibitors," *Nature Reviews. Clinical Oncology*, vol. 17, no. 12, pp. 725–741, 2020.
- [27] R. Cao, G. Wang, K. Qian et al., "TM4SF1 regulates apoptosis, cell cycle and ROS metabolism via the PPAR  $\gamma$ -SIRT1 feedback loop in human bladder cancer cells," *Cancer Letters*, vol. 414, pp. 278–293, 2018.
- [28] T. Tao, Q. Su, S. Xu et al., "Down-regulation of PKM2 decreases FASN expression in bladder cancer cells through AKT/mTOR/SREBP-1c axis," *Journal of Cellular Physiology*, vol. 234, no. 3, pp. 3088–3104, 2019.
- [29] H. Ruan, Z. Song, Q. Cao et al., "IMP1D1/YB-1 positive feedback loop assembles cytoophidia and represents a therapeutic target in metastatic tumors," *Molecular Therapy*, vol. 28, no. 5, pp. 1299–1313, 2020.
- [30] Y. Cazals, M. Bevingut, S. Zanella, F. Brocard, J. Barhanin, and C. Gestreau, "KCNK5 channels mostly expressed in cochlear outer sulcus cells are indispensable for hearing," *Nature Communications*, vol. 6, no. 1, p. 8780, 2015.
- [31] Y. Liu, H. Wang, B. Ni et al., "Loss of *KCNJ15* expression promotes malignant phenotypes and correlates with poor prognosis in renal carcinoma," *Cancer Management and Research*, vol. Volume 11, pp. 1211–1220, 2019.
- [32] R. Cao, L. Yuan, B. Ma, G. Wang, W. Qiu, and Y. Tian, "An EMT-related gene signature for the prognosis of human bladder cancer," *Journal of Cellular and Molecular Medicine*, vol. 24, no. 1, pp. 605–617, 2020.
- [33] L. Yang, C. Li, Y. Qin et al., "A novel prognostic model based on ferroptosis-related gene signature for bladder cancer," *Frontiers in Oncology*, vol. 11, article 686044, 2021.
- [34] C. Zhang, X. Gou, W. He, H. Yang, and H. Yin, "A glycolysis-based 4-mRNA signature correlates with the prognosis and cell cycle process in patients with bladder cancer," *Cancer Cell International*, vol. 20, no. 1, p. 177, 2020.
- [35] L. Wang, Y. Wang, J. Wang, L. Li, and J. Bi, "Identification of a prognosis-related risk signature for bladder cancer to predict survival and immune landscapes," *Journal of Immunology Research*, vol. 2021, Article ID 3236384, 26 pages, 2021.

## Research Article

# Identification of Resolvin D1 and Protectin D1 as Potential Therapeutic Agents for Treating Kidney Stones

Bohan Wang,<sup>1</sup> Jingchao Wei ,<sup>1</sup> Qi Huangfu,<sup>1</sup> Fei Gao,<sup>2</sup> Lanxin Qin,<sup>2</sup> Jiao Zhong,<sup>3</sup> Jiaming Wen,<sup>1</sup> Zhangqun Ye,<sup>4</sup> Xiaoqi Yang ,<sup>4</sup> and Haoran Liu <sup>5,6</sup>

<sup>1</sup>Department of Urology, The Second Affiliated Hospital, School of Medicine, Zhejiang University, Hangzhou 310000, China

<sup>2</sup>Durbrain Medical Laboratory, Hangzhou 310000, China

<sup>3</sup>Department of Urology, The Second Affiliated Hospital of Kunming Medical University, Kunming 650000, China

<sup>4</sup>Department of Urology, Tongji Hospital, Tongji Medical College, Huazhong University of Science and Technology, Wuhan 430000, China

<sup>5</sup>Department of Urology, The First Affiliated Hospital of Anhui Medical University, Hefei 230000, China

<sup>6</sup>Department of Urology, Stanford University School of Medicine, Stanford, 94305 California, USA

Correspondence should be addressed to Xiaoqi Yang; xiaoqi\_yang66@126.com and Haoran Liu; hrliu66@stanford.edu

Received 21 December 2021; Accepted 26 January 2022; Published 24 February 2022

Academic Editor: Yingping Xiao

Copyright © 2022 Bohan Wang et al. This is an open access article distributed under the Creative Commons Attribution License, which permits unrestricted use, distribution, and reproduction in any medium, provided the original work is properly cited.

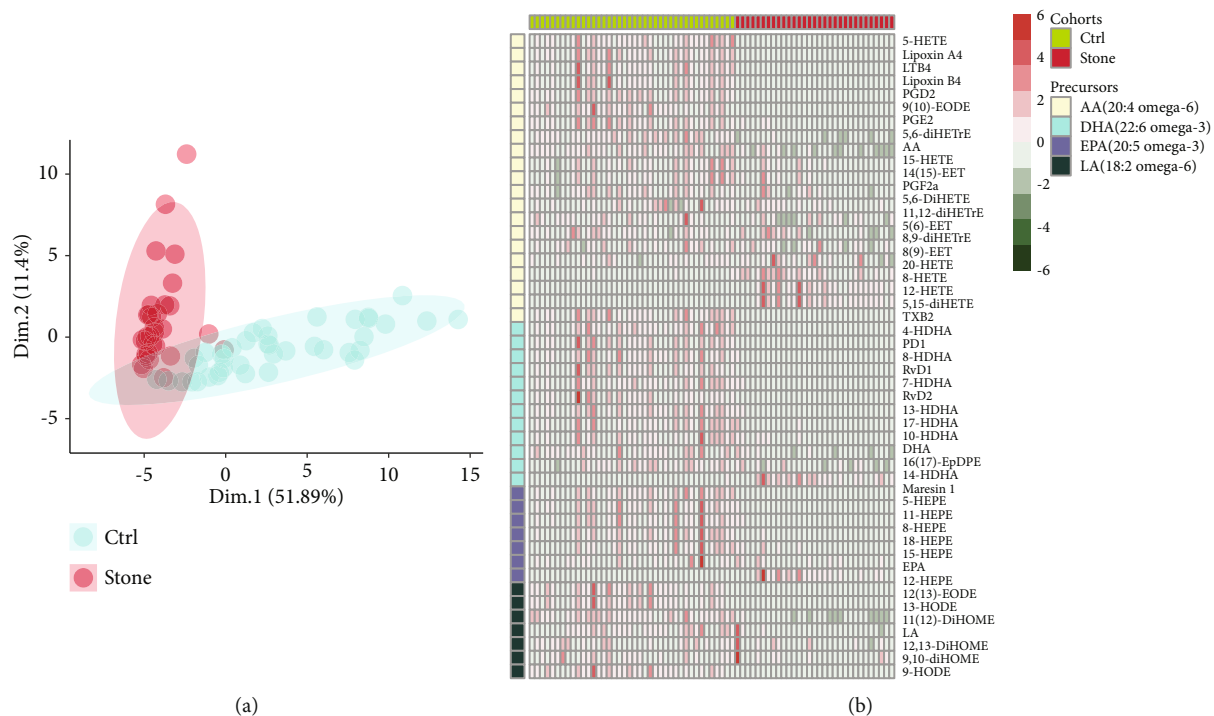
Intrarenal calcium oxalate (CaOx) crystals induce renal tubular epithelial cell (TEC) inflammatory and oxidative injury. This study is aimed at exploring potential therapeutic lipid components in kidney stones because lipids are involved in the development of several diseases and indicate the risk of kidney stones. Serum specimens were collected from 35 kidney stone patients and 35 normal controls. The lipid components in serum were measured, and differences were analyzed. The documented biological importance was comprehensively reviewed to identify lipids that differed significantly between the two groups to find potential agents associated with kidney stones. CaOx nephrocalcinosis mouse model was established to examine the therapeutic effects of specific lipids on CaOx deposition and CaOx-induced oxidative renal injury. Several lipids with significantly different levels were present in the serum of patients with stones and normal controls. Resolvin D1 (RvD1) (4.93-fold change,  $P < 0.001$ ) and protectin D1 (PD1) (5.06-fold change,  $P < 0.001$ ) were significantly decreased in the serum of patients with kidney stones, and an integrative review suggested that these factors might be associated with inflammatory responses, which is a crucial mechanism associated with stone damage. The administration of RvD1 and PD1 significantly inhibited kidney CaOx deposition and suppressed CaOx-induced renal tubular cell inflammatory injury and necrosis in a CaOx nephrocalcinosis mouse model. Furthermore, RvD1 and PD1 facilitated the expression of the oxidative indicator superoxide dismutase 2 (SOD2), inhibited NADPH oxidase 2 (NOX2) expression, and diminished intracellular reactive oxygen species (ROS) levels. This study preliminarily elucidated the role of lipids in kidney stones. The inhibitory effects of RvD1 and PD1 on oxidative damage induced by CaOx deposition provide a promising perspective for kidney stone treatment strategies.

## 1. Introduction

The prevalence of kidney stones, which is a disorder that affects the urinary system, has increased in various regions worldwide in the past decade [1]. According to their composition, kidney stones are mainly categorized as oxalate, phosphate, or uric acid stones. Uric acid and cystine stones are

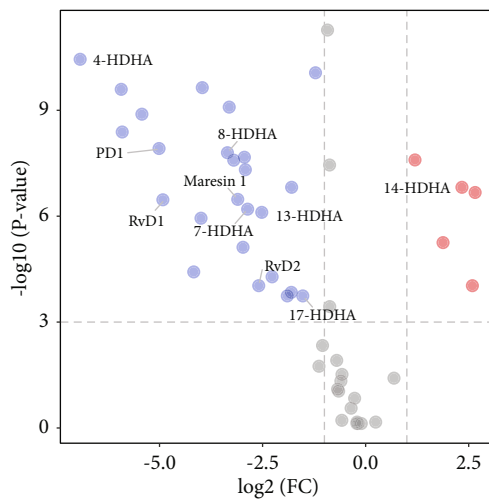
also common. Some insoluble or poorly soluble medications in the urine may also develop into stones [2]. Most kidney stones are formed of calcium oxalate (CaOx) and calcium phosphate (CaP). Kidney stones are free or attached to the kidney pelvis or calyces in the form of mineral clots. Specifically, specific minerals in the urine filtered by the kidneys become supersaturated, and then, the crystals continue to lin-





(a)

(b)



(c)

FIGURE 1: Continued.

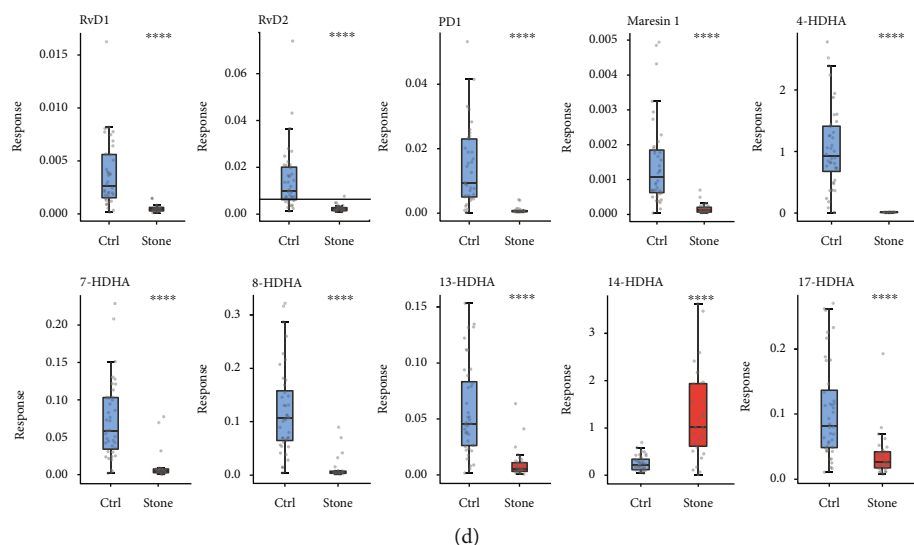


FIGURE 1: Identification of significantly reduced DHA-derived lipid mediators of serum in urolithiasis samples. (a) Principal component analysis of lipid mediators using expression data. (b) Lipid mediators are shown in a heat map. Lipid mediators are colour-coded based on the different polyunsaturated fatty acid (PUFA) precursors. (c) Volcano plots showing lipids that were differentially expressed in serum from stone patients and healthy controls. Red/blue dots represent up- or downregulated proteins, respectively, with a FC cut-off of 2 and a  $P$  value  $< 0.005$ . (d) Relative quantitation of DHA and DHA-derived lipid mediators in human serum. AA: arachidonic acid; DHA: docosahexaenoic acid; EPA: eicosapentaenoic acid; LA: linoleic acid.

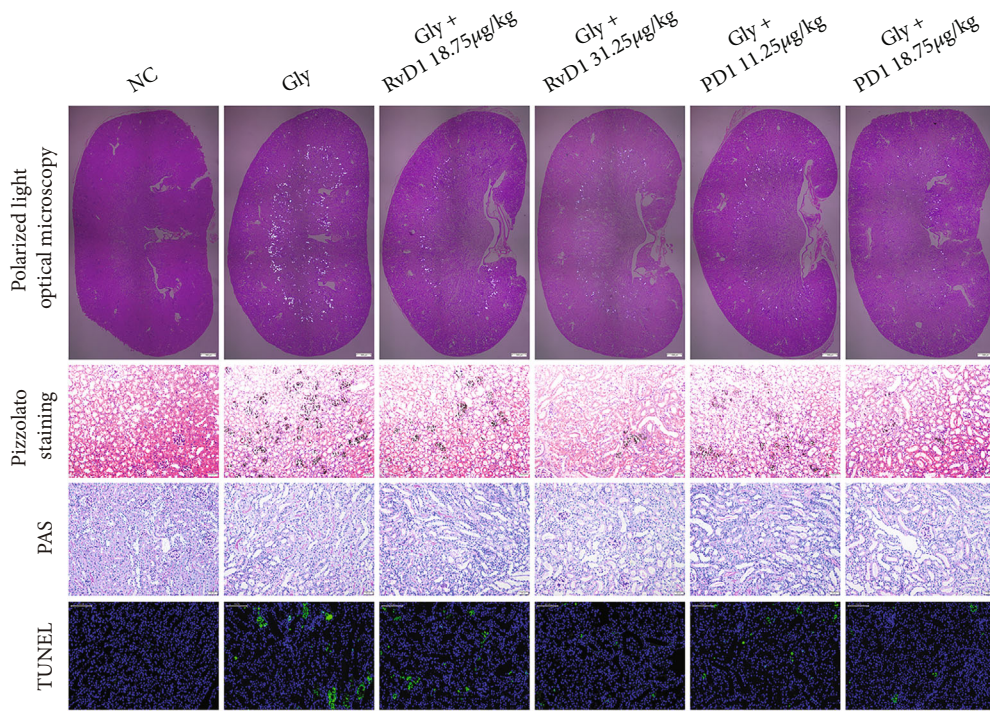
ger, grow, and eventually form stones. Proteins, chemical polymers, and other mineral crystals present in urine might also serve as nuclei for the formation of stones [3].

The recurrence risk of kidney stones can be as high as 50% following the first kidney colic within five years [4]. Such a high recurrence rate underscores the fact that the mechanism of kidney stone formation is not simple. Kidney stones are now increasingly recognized as a systemic disease. Risk factors associated with stone formation include diabetes, hypertension, and metabolic syndrome [5]. Particular focus is being given to the involvement of metabolic factors in the development of kidney stones [6]. Along with crystals, stones frequently contain a significant amount of organic matrix. These organic matrices are present within and around the crystals. A few studies have shown a relationship between crystals and the organic matrix in stone formation. It is worth mentioning that the matrix incorporates a variety of lipids [7]. Another noteworthy fact is that children have a considerably lower incidence of urolithiasis than adults. Several studies have revealed an association between abnormal lipid metabolism and the development of urolithiasis in children. Additionally, epidemiological studies have revealed an increased risk of developing kidney stones in individuals with dyslipidaemia [8]. These findings indicate that lipids may be involved in the formation of stones. However, the association between lipids and kidney stones, as well as the underlying mechanisms, remains elusive.

Lipids are engaged in various cellular metabolic processes as essential bioactive components, including the maintenance of normal cellular morphology, cellular energy metabolism, signal transduction, and substance transport. Mounting evidence shows that dyslipidaemia is associated with various diseases. For instance, dyslipidaemia is significantly associated with diabetes and hyperten-

sion, while diabetes and hypertension are well-established risk factors for kidney stones [9]. Given the relationship between these diseases and kidney stones, it would be intriguing to investigate the involvement of lipids in stone formation.

Lipidomics refers to the extensive investigation and integrated characterization of lipid structure and function on a spatial and temporal scale. The field of lipidomics research has grown rapidly since the advent of mass spectrometry, providing solid evidence for the function of lipids in various diseases. To date, there have been few lipidomics studies of kidney stones. Based on the practical needs and existing theoretical achievements, the present study used mass spectrometry to examine the potential lipid molecules associated with the formation of kidney stones, which may assist in elucidating the mechanism by which lipid metabolic components contribute to stone formation. We found that serum levels of resolvin D1 (RvD1) and protectin D1 (PD1) were significantly lower in patients with kidney stones than in normal controls, indicating their possible protective role in kidney stones. As anti-inflammatory and antioxidant agents, RvD1 and PD1 were reported to exert protective effects in many diseases. Bathina and Das found that RvD1 can prevent streptozotocin-induced type 1 diabetes by reducing oxidative stress and suppressing inflammation [10]. In mouse model of lipopolysaccharide-induced keratitis, RvD1 was reported to ameliorate the inflammatory process [11]. In addition, PD1 was also found to enhance resolution of inflammation in lipopolysaccharide-induced acute lung injury [12]. Duffield et al. demonstrated that resolvin D series and PD1 may play an important role in protecting against acute kidney injury [13]. The protective role of RvD1 and PD1 in kidney stones and the underlying mechanisms are worth further investigation. Attempts to



(a)

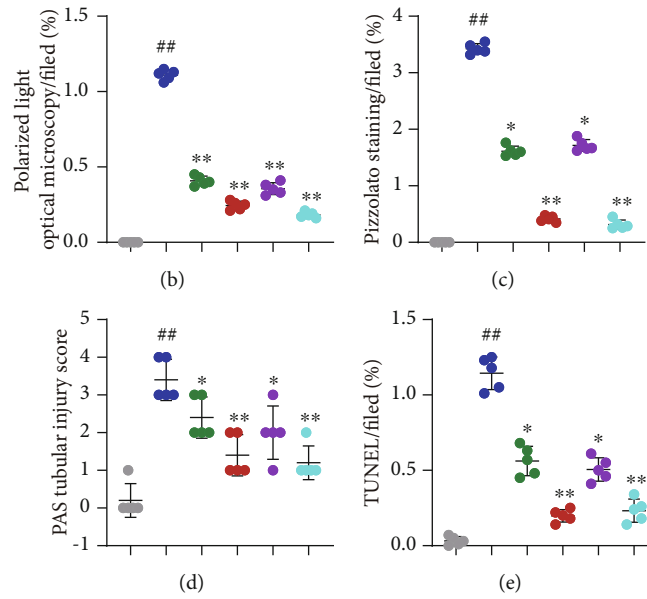


FIGURE 2: Continued.

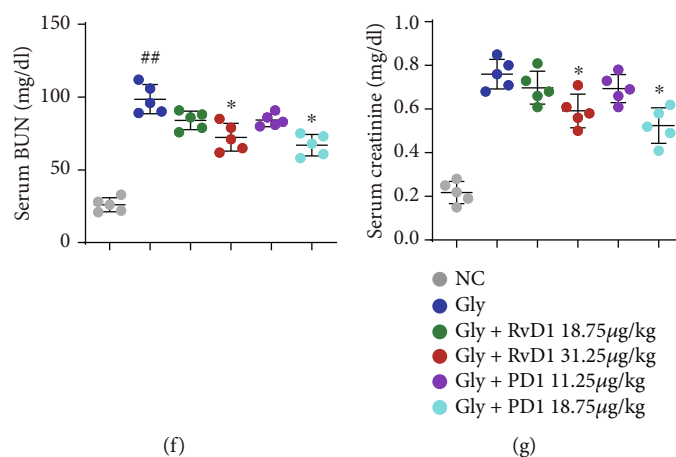


FIGURE 2: RvD1 and PD1 inhibited CaOx deposition-induced cell damage. A mouse model of CaOx deposition was constructed, and the effects of RvD1 and PD1 on CaOx deposition were observed after the administration of different concentrations of RvD1 (18.75 and 31.25 μg/kg) and PD1 (11.25 and 18.75 μg/kg). (a) Representative map of CaOx deposition in the whole kidney as observed by polarized light optical microscopy (×20, scale bar: 500 μm). Pizzolato staining was performed to examine CaOx deposition in local tissues (×200; scale bar: 20 μm). PAS staining was performed to examine cell damage (×200; scale bar: 20 μm). A TUNEL assay was performed to examine apoptosis (×200; scale bar: 100 μm). (b) The ratio of the areas of kidneys with crystal deposition, as determined by polarized light optical microscopy. (c) The ratio of the areas of kidneys with corticomedullary junction area crystal deposition. (d) The tubular injury score was determined by PAS staining. (e) The average number of TUNEL-positive cells per high-power field. (f, g) BUN and serum creatinine were used to assess renal function ( $n = 5$ ). The data are the means ± SEM of three independent experiments. One representative plot of  $n = 5$  mice is shown. # $P < 0.05$ ; ## $P < 0.01$  compared with NC, \* $P < 0.05$ ; \*\* $P < 0.01$  compared with Gly, one-way ANOVA (b–g).

identify therapeutic lipid molecules for kidney stones are aimed at bringing genuine insight and a basis for novel therapeutic approaches.

## 2. Materials and Methods

**2.1. Ethics Statements.** The study was conducted according to the guidelines of the Declaration of Helsinki and approved by The Institutional Research Ethics Committee of The Second Affiliated Hospital, School of Medicine, Zhejiang University, Hangzhou, China (#IR2021001315).

**2.2. Patients.** Sera were collected from 35 patients with kidney stones and 35 normal controls from December 01, 2020, to February 01, 2021, at The Second Affiliated Hospital, School of Medicine, Zhejiang University. Written informed forms were obtained from all participants. Patients who had a history of renal stones and underwent ureteral flexible lithotripsy at our institution were included in the stone group. Exclusion criteria included hypertension, diabetes mellitus, history of gallstones, urinary tract abnormalities, and hyperparathyroidism. The inclusion criteria for the normal group were good health as confirmed by physical examination. There were no exclusion criteria for the normal group.

**2.3. Lipid Mediator Extraction.** All lipid mediator standards were purchased from the Cayman Chemical Company (Ann Arbor, MI, USA). HLB SPE cartridges were purchased from Anbocis Technology (Beijing, China). All HPLC grade solvents were acquired from Sigma–Aldrich (St. Louis, MO, USA) or Merck & Co., Inc. (Kenilworth, NJ, USA). Aliquots

of 100 μL of thawed human serum were used. A mixture of deuterium-labelled internal standards was added to each sample, followed by 1.5 mL of cold methanol (MeOH). The samples were vortexed for 5 min and stored at -20°C overnight. Cold samples were centrifuged at 14,000 rpm for 5 min, and the supernatant was then transferred to a new tube. Samples were evaporated under nitrogen to volumes less than 50 μL, after which 1 mL of acidified H<sub>2</sub>O (pH 3.5) was added to each sample before HLB SPE extraction as previously described [14]. In brief, the acidified samples were loaded onto an HLB SPE column, washed with water and hexane, and eluted with methyl formate. The methyl formate fractions were collected, dried under nitrogen, and reconstituted in 100 μL of MeOH:H<sub>2</sub>O (2:3, v/v). Samples were centrifuged at 20,000 rpm, and 80 μL of the supernatants was subjected to LC–MS/MS lipid mediator metabolomics analysis.

**2.4. LC–MS/MS Lipid Mediator Metabolomics Platform.** Determination of lipid mediators was achieved by LC–MS/MS using a Shimadzu LC-20ACXR (Shimadzu, Kyoto, Japan) and Sciex 5500 triple quadrupole mass spectrometer (Sciex, MA, USA) with heated electrospray ionization (ESI). A Phenomenex Kinetex C18 column (100 × 2.1 mm, 2.6 μm) was maintained at 40°C. Solvent A was composed of 100% H<sub>2</sub>O with 0.1% formic acid, and solvent B was 100% acetonitrile (ACN) with 0.1% formic acid. The flow rate was 0.3 mL/min, and the gradient was 35% B at 0 min, increased to 50% B until 4.0 min, increased to 95% B at 9.0 min, maintained at 95% B until 11.5 min, returned to 35% B at 12.0 min, and maintained at 35% B until 14.0 min. ESI–MS was operated in negative mode with a

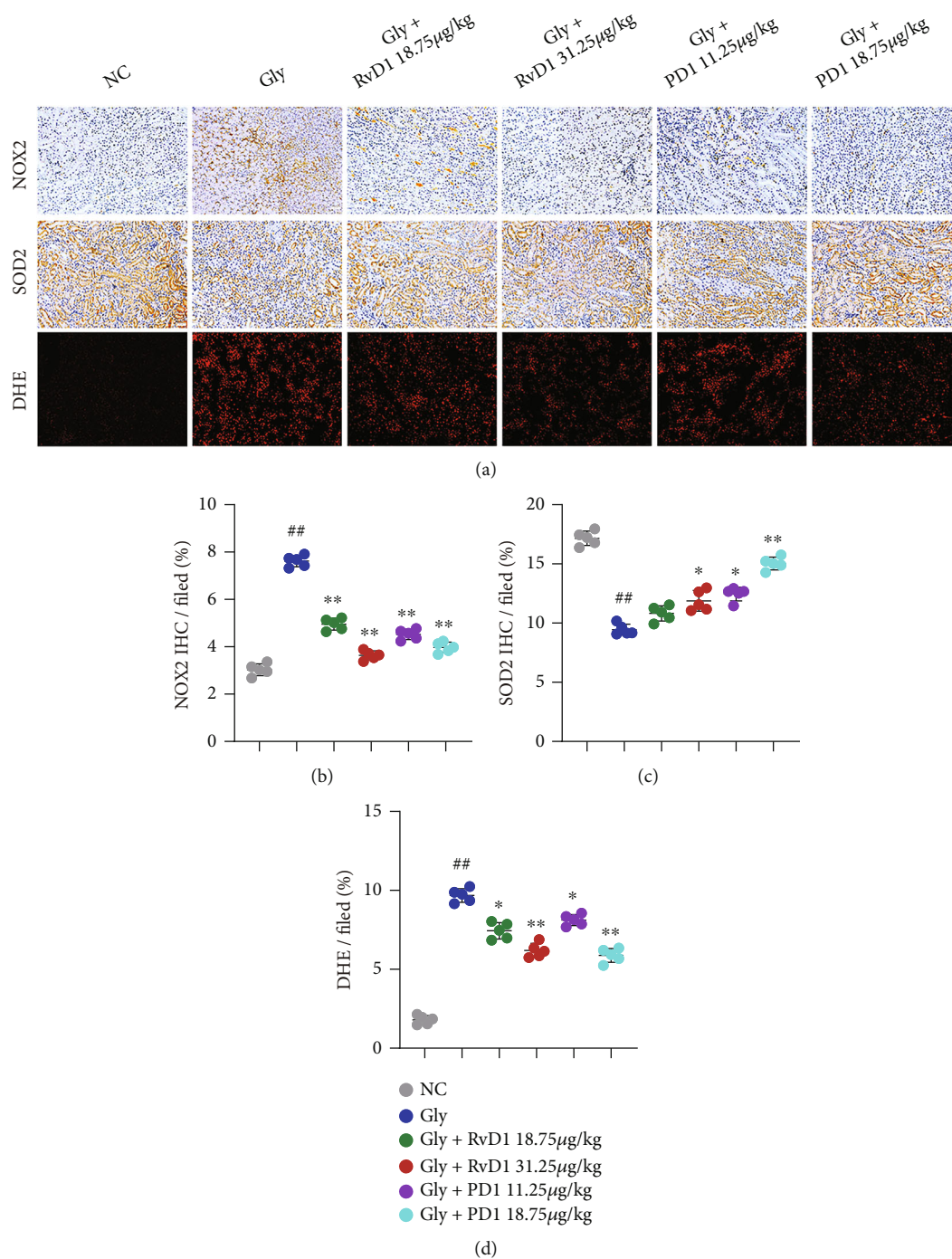


FIGURE 3: RvD1 and PD1 reduced kidney injury by inhibiting oxidative damage. (a) Treatment with different concentrations of RvD1 (18.75 and 31.25  $\mu\text{g}/\text{kg}$ ) and PD1 (11.25 and 18.75  $\mu\text{g}/\text{kg}$ ) in the CaOx deposition mouse model. Representative plots showing NOX2 and SOD2 are presented ( $\times 200$ ; scale bar: 20  $\mu\text{m}$ ). Intracellular ROS levels were measured by the DHE method ( $\times 200$ ; scale bar: 20  $\mu\text{m}$ ). (b–d) The ratio of the areas with positive expression of NOX2, SOD2, and DHE, as determined by IHC. One representative plot of  $n = 5$  mice is shown. # $P < 0.05$ ; ## $P < 0.01$  compared with NC, \* $P < 0.05$ ; \*\* $P < 0.01$  compared with Gly, as determined by one-way ANOVA (b–d).

voltage of  $-4500\text{ V}$ , a temperature of  $500^{\circ}\text{C}$ , curtain gas at 30 psi, GS1 at 40 psi, and GS 2 at 40 psi. The mass spectrometry parameters for each compound were optimized, and a scheduled multiple reaction monitoring (MRM) strategy was applied. Retention time and specific MRM transitions were used to identify each lipid mediator. Relative quantita-

tion with an appropriate internal standard was performed using the MutliQuant software (Sciex, MA, USA).

**2.5. Establishment of the CaOx Deposition Mouse Model.** All experimental procedures followed the rules of the National Institutes of Health Guide for the Care and Use of

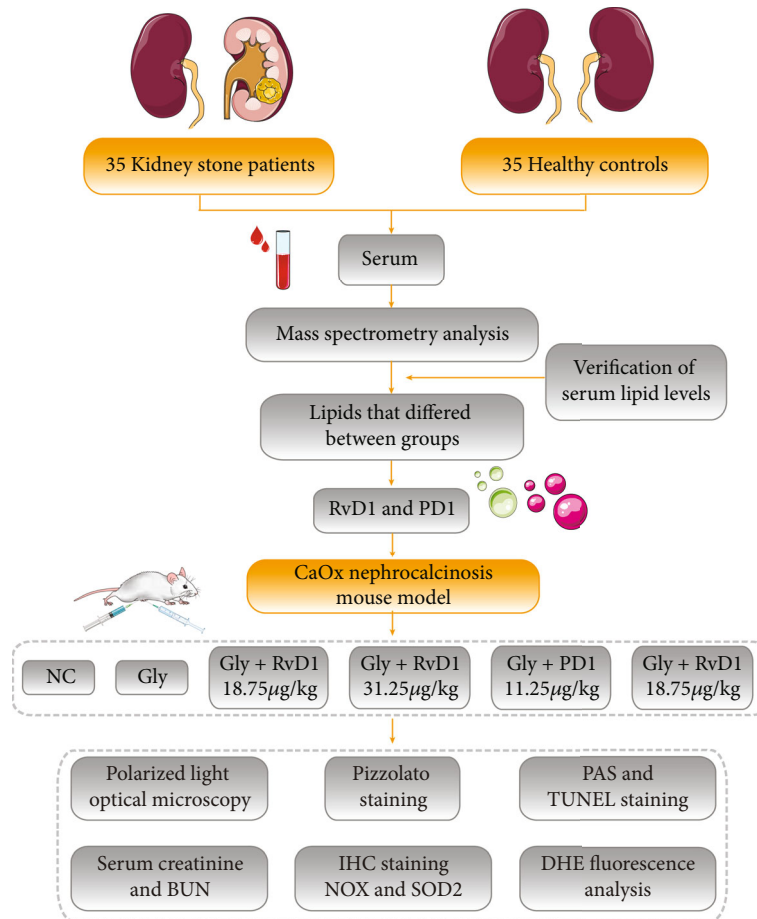


FIGURE 4: A flow chart of study design in human samples and mouse model.

**Laboratory Animals.** Male C57BL/6J mice (6–8 weeks) were obtained from the Experimental Animal Research Centre of Hubei and were used for the animal experiment. The mice were randomly allocated to different experimental and control groups. To establish the CaOx deposition model, each mouse was intraperitoneally injected with glyoxylate (Gly) (75 mg/kg/d) or saline from day 4 to day 10 as previously described [15]. RvD1 and PD1 were obtained from Cayman Chemical (Ann Arbor, Michigan, USA). Mice in the intervention group were intraperitoneally injected with different concentrations (18.75, 31.25 µg/kg/d; 75, 125 µL) of RvD1 or (11.25, 18.75 µg/kg/d; 75, 125 µL) of PD1 from day 1 to day 10. Ten days later, all mice were sacrificed and underwent further laparotomy and assessment.

**2.6. Detection of CaOx Crystal Deposition.** Mouse kidney tissues were fixed with formalin, paraffin-embedded for routine sectioning, and then stained with haematoxylin-eosin (HE). Then, CaOx crystal deposition in the kidneys was determined using a polarized light optical microscope (Zeiss, Oberkochen, Germany). In addition, the kidney sections were stained using Pizzolato's method to further examine crystal deposition [16]. The percent area of crystal deposition per kidney section was quantified with the ImageJ software (National Institutes of Health, USA).

**2.7. Periodic Acid-Schiff (PAS) Staining.** Kidney tissue sections were stained with PAS to assess tubular injury, including tubular dilation, tubular atrophy, tubular cast formation, sloughing of tubular epithelial cells (TECs), or thickening of the tubular basement membrane. Ten nonoverlapping microscopic fields (×200) were randomly selected, and the percentage of cells with tubular injury among total TECs was calculated (scoring: none, 0; <25%, 1; 25–50%, 2; 51–75%, 3; and >75%, 4). The average score was calculated to represent the average injury level of the 10 fields examined.

**2.8. Terminal Deoxynucleotidyl Transferase dUTP Nick-End Labelling (TUNEL) Fluorescence Staining.** TUNEL fluorescence staining was conducted to assess kidney cell death using an In Situ Cell Death Detection Kit (Roche, Rotkreuz, Switzerland) according to the manufacturer's instructions [17]. The number of TUNEL-positive cells was counted in ten randomly chosen magnification fields for each slice.

**2.9. Immunohistochemistry (IHC).** Mouse kidneys were fixed with formalin and embedded in paraffin for routine sectioning, followed by HE staining. For immunohistochemical staining, the slices were incubated with primary antibodies against superoxide dismutase 2 (SOD2) (1:800, Boster, BM4813) and NADPH oxidase 2 (NOX2) (1:200, Boster, BA2811) overnight at 4°C and then visualized by an

Envision HRP Polymer system (Boster, Wuhan, China). Image capture ( $\times 200$  magnification) was performed with an Olympus BX51 microscope (Olympus, Japan). Relative expression levels were analyzed using the ImageJ software.

**2.10. Dihydroethidium (DHE) Fluorescence Analysis.** Mouse kidneys were washed with phosphate-buffered saline and then frozen immediately. Subsequently, the frozen tissues were cut into sections ( $5\ \mu\text{m}$ ) using a freezing microtome and incubated with a  $5\ \mu\text{M}$  DHE solution at  $37^\circ\text{C}$  for 30 min. The slides were rinsed with phosphate-buffered saline and sealed with an antifluorescence quenching agent. They were then observed and imaged under a fluorescence microscope (Nikon, Japan). Fluorescence intensity was quantified with the ImageJ software (National Institutes of Health, USA).

**2.11. Measurement of Blood Urea Nitrogen (BUN) and Serum Creatinine.** Blood samples were collected from the mice on day 10. Serum levels of BUN and creatinine were determined using commercial kits (Stanbio Laboratory, Boerne, TX, USA).

**2.12. Statistical Analysis.** The Shapiro–Wilk test was used to determine the normality of continuous variables. The  $P$  value was calculated by Student's  $t$  test and adjusted by Bonferroni correction, and values larger than 0.05 were considered to represent statistically significant differences. Measurement results from human serum are expressed as the mean  $\pm$  standard deviation (SD). To identify differential lipid mediators, a  $P$  value of 0.001 and a fold change (FC) greater than 1.5 were used as cut-off values. Heat maps and principal component analysis were used to visualize the characteristics of all differential lipid mediators based on the quantile-normalized values. Data analysis and plots were generated using R version 4.0.4 [18] and GraphPad Prism version 8.0.1 (GraphPad Software, CA, USA).

### 3. Results

**3.1. Identification of Differential Lipids in Serum between Kidney Stone Patients and Healthy Controls.** To examine potential lipid components that may be associated with stone formation, serum specimens were collected from 35 stone patients and 35 healthy controls at The Second Affiliated Hospital, School of Medicine, Zhejiang University. There were no differences between the two groups in terms of sex ratio, age, height, or weight (Table S1). Mass spectrometry analysis of the lipid components in these blood specimens was performed. Principal component analysis based on the levels of all lipid components showed that samples from stone patients and healthy controls were clustered and were significantly different between the two groups. These findings established the reliability of the mass spectrometry results and demonstrated that the sera of stone patients and healthy controls contained distinct lipids (Figure 1(a)). Hierarchical clustering with heat map classification based on lipid precursors and serum lipid levels directly revealed the lipids that differed between the serum of kidney stone patients and healthy controls.

Notably, multiple products of docosahexaenoic acid (DHA) consistently showed “elimination” in the serum of patients with kidney stones (Figure 1(b)). These results revealed some serum lipids that may be associated with kidney stone formation.

**3.2. Verification of Serum Lipid Levels in Patients with Kidney Stones.** A “volcano plot” was drawn according to the differences ( $|\text{Log}_2\text{FC}| \geq 1$ ;  $P < 0.05$ ) in DHA products between the two groups to visualize the lipids that may be associated with kidney stones (Figure 1(c)). To further confirm the levels of these lipids in kidney stone patients, serum was collected again from the aforementioned 35 kidney stone patients and 35 healthy controls. DHA products in the serum were measured. The results were consistent with the mass spectrometry results. Specifically, 14-HDHA was significantly higher in patients with kidney stones than in healthy controls, whereas 17-HDHA, 13-HDHA, RvD2, RvD1, 4-HDHA, 8-HDHA, PD1, Maresin 1, and 7-HDHA were significantly lower in the serum of patients with kidney stones than in healthy controls (Figure 1(d)). These results suggest an association between DHA products and kidney stone formation.

**3.3. RvD1 and PD1 Attenuated CaOx Deposition and Cellular Damage in the Kidneys.** RvD1 and PD1 are known to have stronger biological functional activity than other members of the DHA family and can block proinflammatory neutrophil and macrophage migration, which plays a key role in inflammatory renal injury. To investigate the therapeutic effects of RvD1 and PD1 on CaOx nephrocalcinosis, we pretreated mice with RvD1 and PD1 for 3 days and developed a CaOx nephrocalcinosis mouse model by intraperitoneal injection of Gly. Polarized light optical microscopy and Pizzolato staining showed that Gly significantly induced CaOx crystal deposition in the kidneys of mice, while RvD1 and PD1 reversed this effect in a dose-dependent manner. PAS and TUNEL staining further confirmed that RvD1 and PD1 reduced CaOx crystal-induced kidney damage (Figures 2(a)–2(e)). In addition, we measured the levels of serum creatinine and BUN to evaluate kidney function and tubular injury. We observed gradual recovery of kidney function during the treatment with RvD1 and PD1 in a dose-dependent manner (Figures 2(f) and 2(g)).

**3.4. RvD1 and PD1 Protected against CaOx Deposition by Inhibiting Oxidative Damage in the Kidneys.** To further explore the mechanism by which RvD1 and PD1 inhibit CaOx-induced kidney inflammation and oxidative damage and thereby reduce CaOx crystal deposition, we examined reactive oxygen species- (ROS-) related indicators. NOX2 is a superoxide-generating enzyme that forms ROS [19]. SOD2 degrades superoxide, a toxic byproduct of the mitochondrial electron transport chain, to form hydrogen peroxide and diatomic oxygen. This function enables SOD2 to eliminate mitochondrial ROS and thereby protect cells from death [20]. Immunohistochemical staining of NOX2 and SOD2 showed that RvD1 and PD1 reversed the effects of

Gly-induced oxidative damage (Figures 3(a)–3(c)). Furthermore, we measured intracellular ROS using the DHE approach. Both RvD1 and PD1 significantly reduced ROS levels (Figures 3(a) and 3(d)). Collectively, these data suggested that RvD1 and PD1 inhibited CaOx deposition and antagonized the risk of kidney stones by inhibiting ROS (Figure 4).

#### 4. Discussion

Kidney stones pose a significant risk to human health and impose a substantial economic burden on society. Urinary stone formation is a complex process involving multiple factors. The mechanisms of stone formation involve CaOx crystallization, crystal growth, aggregation, and adhesion to renal tubular epithelial cells have been extensively studied during the last few decades [21]. Although numerous investigations on the formation of kidney stones have been conducted and several theories have been established, the mechanisms of kidney stone formation are not yet unequivocally understood. A few pieces of evidence have shown that lipid components might play a role in the formation of kidney stones [22]. For instance, oxidized low-density lipoprotein (LDL) is abundant in patients with kidney stones. In addition, glycolipids and cholesterol are involved in the formation of kidney stones [23]. However, a limited number of papers are available about kidney stones and lipids. In this study, serum lipids were measured, and patients with kidney stones had considerably lower DHA metabolites than healthy individuals. Further exploration revealed that the DHA products RvD1 and PD1 reduced CaOx deposition in the kidneys. In addition, RvD1 and PD1 alleviated kidney inflammation and oxidative damage, which might be the mechanism by which RvD1 and PD1 reduced CaOx deposition. As CaOx deposition is a critical process in the formation of CaOx stones, RvD1 and PD1 might protect against the development of kidney stones.

Both RvD1 and PD1 are produced from DHA, a long-chain, highly unsaturated omega-3 (n-3) fatty acid that is one of the main components of fish oils. DHA is involved in the regulation of various cellular activities and functions, including altering membrane structure, membrane protein function, cell signalling, and lipid mediator production [24]. Endogenous conversion of DHA into resolvins, protectins, and maresins has been demonstrated. DHA is currently broadly used as a dietary supplement, and a considerable body of evidence indicates that DHA has numerous health benefits. DHA significantly improved oxidative stress in kidneys of LPS-challenged mice by restoring oxidation and antioxidant balance [25]. EPA and DHA seem to help lag the progression of chronic kidney disease by decreasing the production of ROS and lipid peroxidation, promoting mitochondrial damage and tissue inflammation, which result in glomerular and tubular lesions [26]. However, the molecular mechanisms remain unclear [27].

Resolvins and protectins dominate the resolution phase of inflammation. Protectins are inflammatory mediators that inhibit leukocyte activation [28]. These factors foster the natural resolution of acute inflammation by diminishing

proinflammatory mediators and clearing inflammatory cells. PD1 belongs to the resolvins family. PD1 is present in various tissues, including the retina, lung, and nervous system. PD1 has anti-inflammatory, antiapoptotic, and neuroprotective effects [29]. PD1 protects cells by reducing oxidative stress-induced inflammation and inhibiting apoptotic signalling pathways. Resolvins are lipid mediators derived from eicosapentaenoic acid (EPA) and DHA. RvD1 is physiologically produced by the sequential oxygenation of DHA by 15- and 5-lipoxygenases. RvD1 inhibits polymorphonuclear leukocyte transendothelial migration, which is an early event in acute inflammation. In addition to being anti-inflammatory, RvD1 promotes the resolution of inflammation [30]. This study provides new evidence that RvD1 and PD1 are anti-inflammatory and antioxidant agents.

Inflammation, oxidant-antioxidant imbalance, and urea cycle disruption have been established as plausible mechanisms underlying stone formation [31]. Different metabolic lipids are involved in inflammatory and oxidative stress responses, which is consistent with the kidney stone hypothesis, such as the calcium plaque theory and the supersaturated crystalline theory. Inflammation is a multifaceted and dynamic process and is mainly mediated by inflammatory factors. The inflammatory response is pivotal in homeostasis and disease development in the body. Numerous hard-to-treat disorders, including cardiovascular disease, diabetes, and neurological issues, have been intimately connected with uncontrolled inflammation [32]. Emerging evidence suggests the pivotal role of specific lipid mediators in modulating inflammation resolution [33]. The present study showed that the DHA products RvD1 and PD1 reduce CaOx deposition by alleviating the ROS-induced inflammatory response, providing strong evidence for the inhibitory effect of active lipid components on inflammation and expanding our understanding of the role of lipid components in inflammation regulation.

ROS are critical regulators of cell signalling. Low concentrations of ROS facilitate cellular adaptability to changing microenvironments through a variety of approaches. Consequently, ROS promote apoptosis and thus assist in eliminating severely damaged cells. However, high concentrations of ROS contribute to the development of various diseases, including kidney stones. Increased prooxidant damage indicators have been observed in the urine of patients with kidney stones [34]. There are multiple associations between ROS and kidney stone formation, and an imbalance between prooxidants and antioxidants drives kidney stone formation [35]. Lipids such as polyunsaturated fatty acids, which are peroxidized, can cause damage to cells, affecting protein activity and the physical properties of cell membranes. There is evidence that these oxidized lipids damage the kidney tubules and significantly contribute to the generation of kidney stones. Interestingly, it has been found that the deposition of CaOx crystals causes the activation of NOX through a complex mechanism, which in turn exacerbates the production of ROS [36]. The current study revealed that various lipid components might harm or protect the kidney. RvD1 and PD1 inhibited the deposition of CaOx through a mechanism that inhibited oxidative damage and thus suppressed the formation of kidney stones.



The regulatory mechanisms of SOD2 and NOX2 by RvD1 and PD1 remain unclear. There is evidence showing that RvD1 inhibits NOX activity by reducing the release of IL-1 $\beta$  and dephosphorylating specific proteins [37, 38]. Furthermore, RvD1-mediated inhibition of NOX was dependent on cAMP-activated protein kinase (PKA) signaling [38]. The inhibition of ROS-mediated damage by PD1 is mediated by dephosphorylation of B-cell lymphoma-extra large and is dependent on activation of phosphoinositide 3-kinase/protein kinase B signaling [39–41]. Nevertheless, the regulatory mechanisms of RvD1 and PD1 on SOD2 and NOX2 still need more exploration.

There are some limitations in this study. The specific mechanisms underlying the reduced levels of RvD1 and PD1 in patients with kidney stones were not investigated in depth, and further elucidation of this issue will be necessary. In addition, we bear in mind the difference between animal experiments and humans, so whether the conclusions drawn from the animal experiments in this study are applicable to humans is also subject to further study.

## 5. Conclusions

Although investigations targeting kidney stones are still in their early stages, there is a lack of significant, evidence-based insight into the role of lipids. Our findings shed light on the lipid changes associated with kidney stone formation. The inhibitory effect of RvD1 and PD1 on CaOx deposition suggests therapeutic strategies for kidney stones. These findings establish a preliminary theoretical basis for the development of innovative kidney stone therapeutic strategies.

## Abbreviations

CaOx:	Calcium oxalate
RvD1:	Resolvin D1
PD1:	Protectin D1
SOD2:	Superoxide dismutase 2
NOX2:	NADPH oxidase 2
ROS:	Reactive oxygen species
CaP:	Calcium phosphate
MeOH:	Methanol
ESI:	Electrospray ionization
ACN:	Acetonitrile
MRM:	Multiple reaction monitoring
Gly:	Glyoxylate
HE:	Haematoxylin-eosin
PAS:	Periodic acid-Schiff
TECs:	Tubular epithelial cells
TUNEL:	Terminal deoxynucleotidyl transferase dUTP nick-end labelling
IHC:	Immunohistochemistry
DHE:	Dihydroethidium
BUN:	Blood urea nitrogen
SD:	Standard deviation
FC:	Fold change
DHA:	Docosahexaenoic acid
LDL:	Low-density lipoprotein
EPA:	Eicosapentaenoic acid.

## Data Availability

Data are included within the article or can be obtained from the authors upon request. The supplementary material and raw data for this article can be found online at <https://www.jianguoyun.com/p/DbDYz71QIM6BChj17J8E>.

## Consent

Informed consent was obtained from each patient.

## Conflicts of Interest

The authors have declared that no conflicts of interest exist.

## Authors' Contributions

Bohan Wang was responsible for the conceptualization and funding acquisition. Jingchao Wei wrote the original draft and reviewed and edited the manuscript. Qi Huangfu, Fei Gao, Xin Lan, Jiao Zhong, and Jiaming Wen were responsible for the resources, data curation, and formal analysis. Zhangqun Ye, Xiaoqi Yang, and Haoran Liu were responsible for the investigation, visualization, methodology, and project administration. All authors read and approved the final manuscript. Bohan Wang and Jingchao Wei contributed equally to this work and shared the first authorship. Xiaoqi Yang and Haoran Liu contributed equally to this work and shared the last authorship.

## Acknowledgments

The authors acknowledge that this work was supported by the National Natural Science Foundation of China (Nos. 81970601 to Bohan Wang and 82100808 to Haoran Liu) and the Postdoctoral researchers in Anhui Province (2021A482).

## Supplementary Materials

Supplementary 1. Supplementary Table S1: baseline characteristics. (*Supplementary Materials*)

## References

- [1] V. Romero, H. Akpınar, and D. G. Assimos, "Kidney stones: a global picture of prevalence, incidence, and associated risk factors," *Revista de Urologia*, vol. 12, pp. e86–e96, 2010.
- [2] S. A. Howles and R. V. Thakker, "Genetics of kidney stone disease," *Nature Reviews Urology*, vol. 17, no. 7, pp. 407–421, 2020.
- [3] S. R. Khan, M. S. Pearle, W. G. Robertson et al., "Kidney stones," *Nature Reviews Disease Primers*, vol. 2, no. 1, article 16008, 2016.
- [4] S. Ebihara, F. Gotoh, T. Kanda, F. Yamaguchi, and K. Nakahara, "Cerebral blood flow and metabolism in moyamoya disease (occlusion of the circle of Willis)," *Acta Neurologica Scandinavica Supplementum*, vol. 64, pp. 404–405, 1977.
- [5] E. N. Taylor, M. J. Stampfer, and G. C. Curhan, "Obesity, weight gain, and the risk of kidney stones," *JAMA*, vol. 293, no. 4, pp. 455–462, 2005.

- [6] C. N. Serhan, "Resolution phase of inflammation: novel endogenous anti-inflammatory and proresolving lipid mediators and pathways," *Annual Review of Immunology*, vol. 25, no. 1, pp. 101–137, 2007.
- [7] S. R. Khan and P. A. Glenton, "Increased urinary excretion of lipids by patients with kidney stones," *British Journal of Urology*, vol. 77, no. 4, pp. 506–511, 1996.
- [8] J. K. Kirejczyk, A. Korzeniecka-Kozerska, M. Baran, H. Porowska, T. Porowski, and A. Wasilewska, "Dyslipidaemia in overweight children and adolescents is associated with an increased risk of kidney stones," *Acta Paediatrica*, vol. 104, no. 9, pp. e407–e413, 2015.
- [9] J. Lu, S. M. Lam, Q. Wan et al., "High-coverage targeted lipidomics reveals novel serum lipid predictors and lipid pathway dysregulation antecedent to type 2 diabetes onset in normoglycemic Chinese adults," *Diabetes Care*, vol. 42, no. 11, pp. 2117–2126, 2019.
- [10] S. Bathina and U. N. Das, "Resolvin D1 decreases severity of streptozotocin-induced type 1 diabetes mellitus by enhancing BDNF levels, reducing oxidative stress, and suppressing inflammation," *International Journal of Molecular Sciences*, vol. 22, no. 4, p. 1516, 2021.
- [11] F. Petrillo, M. C. Trotta, C. Bucolo et al., "Resolvin D1 attenuates the inflammatory process in mouse model of LPS-induced keratitis," *Journal of Cellular and Molecular Medicine*, vol. 24, no. 21, pp. 12298–12307, 2020.
- [12] X. Li, C. Li, W. Liang, Y. Bi, M. Chen, and S. Dong, "Protectin D1 promotes resolution of inflammation in a murine model of lipopolysaccharide-induced acute lung injury via enhancing neutrophil apoptosis," *Chinese Medical Journal*, vol. 127, no. 5, pp. 810–814, 2014.
- [13] J. S. Duffield, S. Hong, V. S. Vaidya et al., "Resolvin D series and protectin D1 mitigate acute kidney injury," *Journal of Immunology*, vol. 177, no. 9, pp. 5902–5911, 2006.
- [14] M. D. Lynes, L. O. Leiria, M. Lundh et al., "The cold-induced lipokine 12,13-diHOME promotes fatty acid transport into brown adipose tissue," *Nature Medicine*, vol. 23, no. 5, pp. 631–637, 2017.
- [15] H. Liu, X. Yang, K. Tang et al., "Sulforaphane elicits dual therapeutic effects on renal inflammatory injury and crystal deposition in calcium oxalate nephrocalcinosis," *Theranostics*, vol. 10, no. 16, pp. 7319–7334, 2020.
- [16] P. Pizzolato, "Histochemical recognition of calcium oxalate," *The Journal of Histochemistry and Cytochemistry*, vol. 12, no. 5, pp. 333–336, 1964.
- [17] S. R. Mulay, J. Desai, S. V. Kumar et al., "Cytotoxicity of crystals involves RIPK3-MLKL-mediated necroptosis," *Nature Communications*, vol. 7, no. 1, p. 10274, 2016.
- [18] R. C. Team, *R: A Language and Environment for Statistical Computing*, R Core Team, 2013.
- [19] F. Violi, A. Oliva, R. Cangemi et al., "Nox2 activation in COVID-19," *Redox Biology*, vol. 36, article 101655, 2020.
- [20] S. Sharma, S. Bhattarai, H. Ara et al., "SOD2 deficiency in cardiomyocytes defines defective mitochondrial bioenergetics as a cause of lethal dilated cardiomyopathy," *Redox Biology*, vol. 37, article 101740, 2020.
- [21] S. R. Mulay, A. Evan, and H. J. Anders, "Molecular mechanisms of crystal-related kidney inflammation and injury. Implications for cholesterol embolism, crystalline nephropathies and kidney stone disease," *Nephrology, Dialysis, Transplantation*, vol. 29, no. 3, pp. 507–514, 2014.
- [22] Y. Liu, X. Jin, H. G. Hong et al., "The relationship between gut microbiota and short chain fatty acids in the renal calcium oxalate stones disease," *The FASEB Journal*, vol. 34, no. 8, pp. 11200–11214, 2020.
- [23] A. C. P. de Freitas, L. C. Torres, M. C. M. B. Duarte, M. C. da Matta, D. E. Casarini, and N. Schor, "Is oxidized low-density lipoprotein the connection between atherosclerosis, cardiovascular risk and nephrolithiasis?," *Urolithiasis*, vol. 47, no. 4, pp. 347–356, 2019.
- [24] C. Cardoso, C. Afonso, and N. M. Bandarra, "Dietary DHA, bioaccessibility, and neurobehavioral development in children," *Critical Reviews in Food Science and Nutrition*, vol. 58, no. 15, pp. 2617–2631, 2018.
- [25] X. Liu, J. Lu, Y. Liao et al., "Dihydroartemisinin attenuates lipopolysaccharide-induced acute kidney injury by inhibiting inflammation and oxidative stress," *Biomedicine & Pharmacotherapy*, vol. 117, article 109070, 2019.
- [26] Z. Gai, T. Wang, M. Visentin, G. Kullak-Ublick, X. Fu, and Z. Wang, "Lipid accumulation and chronic kidney disease," *Nutrients*, vol. 11, no. 4, p. 722, 2019.
- [27] C. N. Serhan, C. B. Clish, J. Brannon, S. P. Colgan, N. Chiang, and K. Gronert, "Novel functional sets of lipid-derived mediators with antiinflammatory actions generated from omega-3 fatty acids via cyclooxygenase 2-nonsteroidal antiinflammatory drugs and transcellular processing," *The Journal of Experimental Medicine*, vol. 192, no. 8, pp. 1197–1204, 2000.
- [28] B. D. Levy, P. Kohli, K. Gotlinger et al., "Protectin D1 is generated in asthma and dampens airway inflammation and hyper-responsiveness," *Journal of Immunology*, vol. 178, no. 1, pp. 496–502, 2007.
- [29] A. Ariel, P.-L. Li, W. Wang et al., "The docosatriene protectin D1 is produced by TH2 skewing and promotes human T cell apoptosis via lipid raft clustering," *The Journal of Biological Chemistry*, vol. 280, no. 52, pp. 43079–43086, 2005.
- [30] A. Ariel and C. N. Serhan, "Resolvins and protectins in the termination program of acute inflammation," *Trends in Immunology*, vol. 28, no. 4, pp. 176–183, 2007.
- [31] P. Wigner, R. Grębowski, M. Bijak, J. Szmraj, and J. Saluk-Bijak, "The molecular aspect of nephrolithiasis development," *Cell*, vol. 10, no. 8, p. 1926, 2021.
- [32] J. K. Innes and P. C. Calder, "Omega-6 fatty acids and inflammation," *Prostaglandins, Leukotrienes, and Essential Fatty Acids*, vol. 132, pp. 41–48, 2018.
- [33] E. Brennan, P. Kantharidis, M. E. Cooper, and C. Godson, "Pro-resolving lipid mediators: regulators of inflammation, metabolism and kidney function," *Nature Reviews. Nephrology*, vol. 17, no. 11, pp. 725–739, 2021.
- [34] V. V. Bet, K. H. Deshpande, A. N. Suryakar, R. D. Ankush, and R. V. Katkam, "Depleted nitrite and enhanced oxidative stress in urolithiasis," *Indian Journal of Clinical Biochemistry*, vol. 21, no. 2, pp. 177–180, 2006.
- [35] A. Abhishek, S. Benita, M. Kumari et al., "Molecular analysis of oxalate-induced endoplasmic reticulum stress mediated apoptosis in the pathogenesis of kidney stone disease," *Journal of Physiology and Biochemistry*, vol. 73, no. 4, pp. 561–573, 2017.
- [36] B. Qin, Q. Wang, Y. Lu et al., "Losartan ameliorates calcium oxalate-induced elevation of stone-related proteins in renal tubular cells by inhibiting NADPH oxidase and oxidative stress," *Oxidative Medicine and Cellular Longevity*, vol. 2018, Article ID 1271864, 2018.

- [37] R. Cox Jr., O. Phillips, J. Fukumoto et al., "Resolvins decrease oxidative stress mediated macrophage and epithelial cell interaction through decreased cytokine secretion," *PLoS One*, vol. 10, no. 8, article e0136755, 2015.
- [38] H. N. Lee and Y. J. Surh, "Resolvin D1-mediated NOX2 inactivation rescues macrophages undertaking efferocytosis from oxidative stress-induced apoptosis," *Biochemical Pharmacology*, vol. 86, no. 6, pp. 759–769, 2013.
- [39] R. Antony, W. J. Lukiw, and N. G. Bazan, "Neuroprotectin D1 induces dephosphorylation of Bcl-xL in a PP2A-dependent manner during oxidative stress and promotes retinal pigment epithelial cell survival," *The Journal of Biological Chemistry*, vol. 285, no. 24, pp. 18301–18308, 2010.
- [40] N. A. Halapin and N. G. Bazan, "NPD1 induction of retinal pigment epithelial cell survival involves PI3K/Akt phosphorylation signaling," *Neurochemical Research*, vol. 35, no. 12, pp. 1944–1947, 2010.
- [41] Z. Faghiri and N. G. Bazan, "PI3K/Akt and mTOR/p70S6K pathways mediate neuroprotectin D1-induced retinal pigment epithelial cell survival during oxidative stress-induced apoptosis," *Experimental Eye Research*, vol. 90, no. 6, pp. 718–725, 2010.

## Research Article

# N<sup>6</sup>-Methyladenosine Modification Profile in Bovine Mammary Epithelial Cells Treated with Heat-Inactivated *Staphylococcus aureus*

Ting Li <sup>1</sup>, Yifan Zhu <sup>2,3</sup>, Changjie Lin <sup>1</sup>, Jie Chen <sup>4</sup>, Yiya Yin <sup>1</sup>, Xin Tang <sup>1</sup>,  
Yingyu Chen <sup>2,3</sup>, Aizhen Guo <sup>2,3</sup>, and Changmin Hu <sup>1</sup>

<sup>1</sup>Department of Clinical Veterinary Medicine, Faculty of Veterinary Medicine, Huazhong Agricultural University, Wuhan, 430070 Hubei Province, China

<sup>2</sup>Department of Preventive Veterinary Medicine, Faculty of Veterinary Medicine, Huazhong Agricultural University, Wuhan, 430070 Hubei Province, China

<sup>3</sup>State Key Laboratory of Agricultural Microbiology, Huazhong Agricultural University, Wuhan, 430070 Hubei Province, China

<sup>4</sup>Institute of Animal Husbandry and Veterinary Medicine, Wuhan Academy of Agricultural Sciences, Wuhan, 430023 Hubei Province, China

Correspondence should be addressed to Changmin Hu; [hcm@mail.hzau.edu.cn](mailto:hcm@mail.hzau.edu.cn)

Received 8 November 2021; Revised 4 January 2022; Accepted 1 February 2022; Published 23 February 2022

Academic Editor: Zhihao Jia

Copyright © 2022 Ting Li et al. This is an open access article distributed under the Creative Commons Attribution License, which permits unrestricted use, distribution, and reproduction in any medium, provided the original work is properly cited.

The symptoms of mastitis caused by *Staphylococcus aureus* (*S. aureus*) in dairy cows are not obvious and difficult to identify, resulting in major economic losses. N<sup>6</sup>-Methyladenosine (m<sup>6</sup>A) modification has been reported to be closely associated with the occurrence of many diseases. However, only a few reports have described the role of m<sup>6</sup>A modification in *S. aureus*-induced mastitis. In this study, after 24 h of treatment with inactivated *S. aureus*, MAC-T cells (an immortalized bovine mammary epithelial cell line) showed increased expression levels of the inflammatory factors IL-1 $\beta$ , IL-6, TNF- $\alpha$ , and reactive oxygen species. We found that the mRNA levels of METLL3, METLL14, WTAP, and ALKBH5 were also upregulated. Methylated RNA immunoprecipitation sequencing analysis revealed that 133 genes were m<sup>6</sup>A hypermethylated, and 711 genes were m<sup>6</sup>A hypomethylated. Biological functional analysis revealed that the differential m<sup>6</sup>A methylated genes were mainly related to oxidative stress, lipid metabolism, inflammatory response, and so on. In the present study, we also identified 62 genes with significant changes in m<sup>6</sup>A modification and mRNA expression levels. These findings elucidated the m<sup>6</sup>A modification spectrum induced by *S. aureus* in MAC-T cells and provide the basis for subsequent m<sup>6</sup>A research on mastitis.

## 1. Introduction

Mastitis is one of the most common diseases in dairy cows, with a high incidence rate, and its treatment remains a challenge. Most cases of mastitis are caused by pathogenic microorganisms that invade the mammary gland tissues [1]. To date, more than a hundred pathogenic microorganisms have been isolated from bovine mammary gland tissues [2]. When the gland is stimulated by pathogenic microorganisms, bovine mammary epithelial cells activate the innate immune response to resist invasion. Innate immunity plays a major role in the early stages of infection. Pathogen-

associated molecular patterns are recognized by receptors on the surface of bovine mammary epithelial cells, causing an immune response that wipes out pathogenic microorganisms [3]. Among the many pathogenic microorganisms that cause mastitis, *Staphylococcus aureus* is one of the most common gram-positive bacteria [1, 4]. Previous studies have shown that *S. aureus* is involved in many pathological processes, including breast tissue destruction and chronic inflammation [5, 6]. The main toxins produced by *S. aureus*, such as endotoxins, and modifications to their peptidoglycan layer and lipoteichoic acid moieties, can cause mastitis [7]. Exotoxins secreted by *S. aureus* can destroy the basic

structure of the mammary gland, leading to the degeneration and necrosis of mammary epithelial cells. After *S. aureus* infection, bovine mammary epithelial cells release inflammatory factors through the toll-like receptors (TLRs) and nuclear factor-kappa B (NF- $\kappa$ B) signaling pathway and activate innate immunity [8–10]. In addition, *S. aureus* has been reported to induce fibrosis [11]. Mastitis caused by *S. aureus* infection is usually recessive or subacute; thus, it is not easily detected in clinical settings. Owing to the high infection rate and drug resistance of *S. aureus*, *S. aureus*-induced mastitis is difficult to cure [7, 12]. Therefore, further studies on the mechanism of *S. aureus*-induced mastitis are of great significance for clinical diagnosis, treatment, and prevention.

N<sup>6</sup>-Methyladenosine (m<sup>6</sup>A) modification is a type of RNA modification during which the N<sup>6</sup> position of adenine in RNA is methylated. As a reversible dynamic modification [13, 14], its biological function is mainly determined by the methylase system [15]. The system includes “Writer,” methyltransferases, including methyltransferase-like 3 (METTL3) and 14 (METTL14), and Wilms tumor 1-associated protein (WTAP) [16, 17]; “Eraser,” demethylase such as fat mass and obesity-associated gene (FTO) and alkB homolog 5 (ALKBH5) [17]; and “Reader,” m<sup>6</sup>A methylated reading proteins [18, 19], such as the YTH family of proteins, IGF2BP protein, and eukaryotic initiation factor (eIF3 protein) [20]. Studies have shown that most diseases are accompanied by changes in the levels of methylating enzymes; methylation enzymes are often involved in the regulation of diseases [21–23]. Changes in m<sup>6</sup>A modifications are closely related to immune regulation [24]. Feng et al. found that m<sup>6</sup>A levels are responsible for lipopolysaccharide-induced inflammatory reactions in human dental pulp cells [25]. In addition, m<sup>6</sup>A can also regulate T-cell homeostasis, resistance to viruses and bacteria, and antitumor immunity [26–28]. Furthermore, Jiaying et al. summarized the role of m<sup>6</sup>A modification in stem cell death and survival and further explained the role of m<sup>6</sup>A modification in immune response, cell apoptosis, autophagy, and senescence [29]. Moreover, m<sup>6</sup>A modification has been confirmed to play an important role in the development of many diseases. However, whether m<sup>6</sup>A affects *S. aureus*-induced mastitis in bovines has not been reported.

In this study, we detected changes in the expression levels of methyltransferase and demethylase in bovine mammary epithelial cells induced by *S. aureus* and analyzed the detected differential m<sup>6</sup>A modified transcripts by using methylated RNA immunoprecipitation sequencing (MeRIP-seq). These findings shed light on the role of m<sup>6</sup>A modification in *S. aureus*-induced mastitis.

## 2. Materials and Methods

**2.1. Bacterial Strains and Cell Line.** MAC-T cells (an immortalized bovine mammary epithelial cell line) were kindly donated by Professor Mark Hanigan of Virginia Tech University. We used DME/F12 medium (Hyclone, Tauranga, New Zealand) supplemented with 10% fetal bovine serum (FBS) (Gibco, New York, NY, United States) to culture the

cells, with incubation at 37°C in a 5% CO<sub>2</sub> incubator. We used 0.25% trypsin and 0.02% EDTA to digest and passage the cells.

*Staphylococcus aureus* (ATCC 29213) was donated by Professor Zhou Rui of Huazhong Agricultural University. A 100  $\mu$ L *S. aureus* suspension was inoculated into 10 mL Luria-Bertani (LB) liquid medium at a ratio of 1:100 and grown in a shaker incubator at 220 rpm/min and 37°C. Then, 100  $\mu$ L of the bacterial culture was serially diluted from 10<sup>-1</sup> to 10<sup>-8</sup>, spread plated onto LB solid medium, and incubated overnight in a bacterial incubator at 37°C. The number of bacteria was counted, and the remaining bacteria in the broth culture were inactivated in a water bath at 63°C for 30 min.

**2.2. Sample Collection and RNA Extraction.** The MAC-T cells were seeded at a density of 10<sup>6</sup> cells per well in a cell culture dish (Corning, New York, NY, USA). The cells were set up in triplicate per group. After 12 h, the DMEM was replaced with 2% FBS in the cell culture dish. Then, the inactive bacterial cells were added to the dish at a 10:1 ratio (bacteria: cells) [30]. In the control group, an equal volume of LB medium was added, and the cells were incubated for 24 h. After incubation, we discarded the medium and then used cold phosphate-buffered saline (PBS) to wash the cells three times.

Total RNA was extracted from the MAC-T cells using TRIzol Reagent (Invitrogen, Carlsbad, CA, USA) in accordance with the manufacturer’s instructions. The RNA concentrations were measured using a NanoDrop 2000 instrument (Thermo, Waltham, MA, USA). Ribonucleic acid integrity and gDNA contamination were assessed using agarose gel electrophoresis.

**2.3. Real-Time Quantitative Polymerase Chain Reaction (RT-qPCR).** The RNA samples were reverse transcribed using HiScript III Reverse Transcriptase (Vazyme, Nanjing, Jiangsu, China). Then, we used AceQ qPCR SYBR Green Master Mix (Vazyme) to configure the sample to be tested by RT-qPCR. The samples were placed in a ViiA™ 7 Real-Time PCR System instrument (Applied Biosystems Inc., Foster, CA, USA), and the qPCR program was run. Data were analyzed using the 2<sup>- $\Delta\Delta$ Ct</sup> method. The relevant primer information is summarized in Table 1.

**2.4. Enzyme-Linked Immunosorbent Assay (ELISA).** The supernatants of the MAC-T cells exposed to the bacteria for 24 h and of the control group were collected. The concentrations of the inflammatory factors (IL-1 $\beta$ , IL-6, and TNF- $\alpha$ ) in the supernatant were then measured using an ELISA kit (Cusabio, Wuhan, Hubei, China) following the manufacturer’s instructions.

**2.5. Cellular Reactive Oxygen Species Detection.** Cellular reactive oxygen species (ROS) were detected using a commercially available kit (Beyotime, Shanghai, China) according to the manufacturer’s instructions. Specifically, the supernatant of the MAC-T cells was discarded, and the cells were washed three times with cold PBS. Next, trypsin without EDTA was used to collect the cells. The cells were then

TABLE 1: Primer sequence of mRNA in RT-qPCR.

Gene name	Forward primer	Reverse primer
$\beta$ -Actin	AGATCAAGATCATCGCGCCC	TAACGCAGCTAACAGTCCGC
IL-1 $\beta$	TTCCATATTCCTCTGGGGTAGA	AAATGAACCGAGAAGTGGTGT
IL-6	AGCAGGTCAGTGTGGTGG	CTGGGTTCAATCAGGCGAT
TNF- $\alpha$	TCTTCTCAAGCCTCAAGTAACAAGC	CCATGAGGGCATTGGCATAAC
METTL3	GGAACACTGCTTGGTTGGTG	GGTTGCACATTGTGTGGTTCG
METTL14	TTGGAGCAAGGGTTCATCCG	CACCTTCAGCTCCCAACTGC
FTO	CTCCGTCTGGAGAGGATTCA	TGCTCCTTGGTTGCTAGTCG
WTAP	CTCCGTCTGGAGAGGATTCA	CTGCGTGCAGATTCTTGCTG
ALKBH5	CCCATCCACATCTTCGAGCG	AGCAGCGTATCCACTGAGCAC

TABLE 2: Primer sequence of m<sup>6</sup>A modified part in mRNA in RT-qPCR.

Gene name	Forward primer	Reverse primer
TNF- $\alpha$	AATTATGGGCTCAGGGCTGG	TCCTTGATGGTGGTTGGTGG
PDGFRA	GACCAGCAGGTTCTAGTCTAAT	GCAGGAGGCCAAAAAGGAAAC
TRAF1	ATGAAGGCGGAAGGTCCAGA	CAGAGTCCACCTCCACGTTC
TLR4	CCGGCTGGTTTGGGAGAAT	ATGGTCAGGTTGCACAGTCC

resuspended in PBS. Finally, flow cytometry (Beckman Coulter, Indianapolis, IN, USA) was used to detect the fluorescence intensity at 488 nm and 525 nm, respectively.

**2.6. Methylated RNA Immunoprecipitation Quantitative Polymerase Chain Reaction (MeRIP-qPCR).** The following experiments were performed in accordance with the manufacturer's instructions (Millipore, Bedford, MA, USA): (1) total RNA was fragmented by Zn<sup>2+</sup> at 94°C; (2) magnetic beads (Thermo Fisher Scientific, Waltham, MA, USA) and m<sup>6</sup>A antibody (Abcam, Cambridge, UK) were incubated for 1 h at room temperature; (3) the system was incubated with the fragmented RNA at 4°C for 2 h; (4) elution buffer was used to elute the mixture twice at 4°C for 1 h; and (5) the collected eluate was subjected to RNA extraction and reverse transcription (Vazyme). In accordance with manufacturer's the instructions, cDNA was detected by RT-qPCR using the AceQ SYBR qPCR Master Mix (Vazyme). The data were analyzed by % input; that is, %input =  $2^{-(\text{Average CT}_{\text{RIP}} - \text{Average CT}_{\text{input}} - \log_2(\text{input dilution factor}))}$ . CT<sub>RIP</sub> means the CT value of the RNA immunoprecipitation (IP RNA) samples, and CT<sub>input</sub> means the CT value of the input RNA samples. The primers for the relevant methylated RNA were as follows (Table 2).

**2.7. MeRIP-seq and mRNA-seq.** The collected RNA was sent for MeRIP-seq and ribonucleic acid sequencing (RNA-seq) at Cloud-Seq Biotech (Shanghai, China) (GSE161050). In this study, the m<sup>6</sup>A-MeRIP kit (Millipore, Burlington, MA, USA) was used to perform the m<sup>6</sup>A RNA immunoprecipitation reaction. RNA sequencing libraries were constructed from the input RNA samples and IP RNA samples after immunoprecipitation with the NEBNext Ultra II Directional RNA Library Prep Kit (New England Biolabs, Ipswich, MA, USA). After library quality control, high throughput

sequencing was performed with Illumina HiSeq (Illumina, San Diego, CA, USA).

**2.8. Bioinformatic Analysis.** Clean reads of high quality were obtained after Q30 quality control and removal of the connector using the Cutadapt (v1.9.3 software). Then, HISAT2 (v2.0.4 software) was used to match the clean reads of the samples to the reference genome (bosTau9), and the MACS (v1.4.2 software) was used to identify RNA m<sup>6</sup>A methylation. Enrichment analyses were performed using Gene Ontology (GO, <http://www.geneontology.org>) and the Kyoto Encyclopedia of Genes and Genomes (KEGG, <http://www.genome.jp/kegg>) for the differentially methylated genes.

**2.9. Statistical Analysis.** In this study, Prism v7.0 (GraphPad software) was mainly performed using for data analyses. The results are presented as the mean values ( $\pm$ SD) of three independent experiments, and *p* values <0.05 were considered statistically significant.

### 3. Results

**3.1. Heat-Inactivated *S. aureus* Induced Inflammation and Oxidative Stress in the MAC-T Cells.** After the MAC-T cells were stimulated with heat inactivated *S. aureus* at an MOI ratio of 10 : 1 for 24 h, the expression of inflammatory factors was detected using RT-qPCR and ELISA. Compared with the control group, the *S. aureus* group showed significantly increased mRNA and protein levels of IL-1 $\beta$ , IL-6, and TNF- $\alpha$  (Figures 1(a) and 1(b)). In previous studies, mastitis was also accompanied by oxidative stress [31]. As shown in Figure 1(c), compared with the control group, the expression level of ROS in the *S. aureus* group was significantly increased. These data thus indicated that heat-inactivated

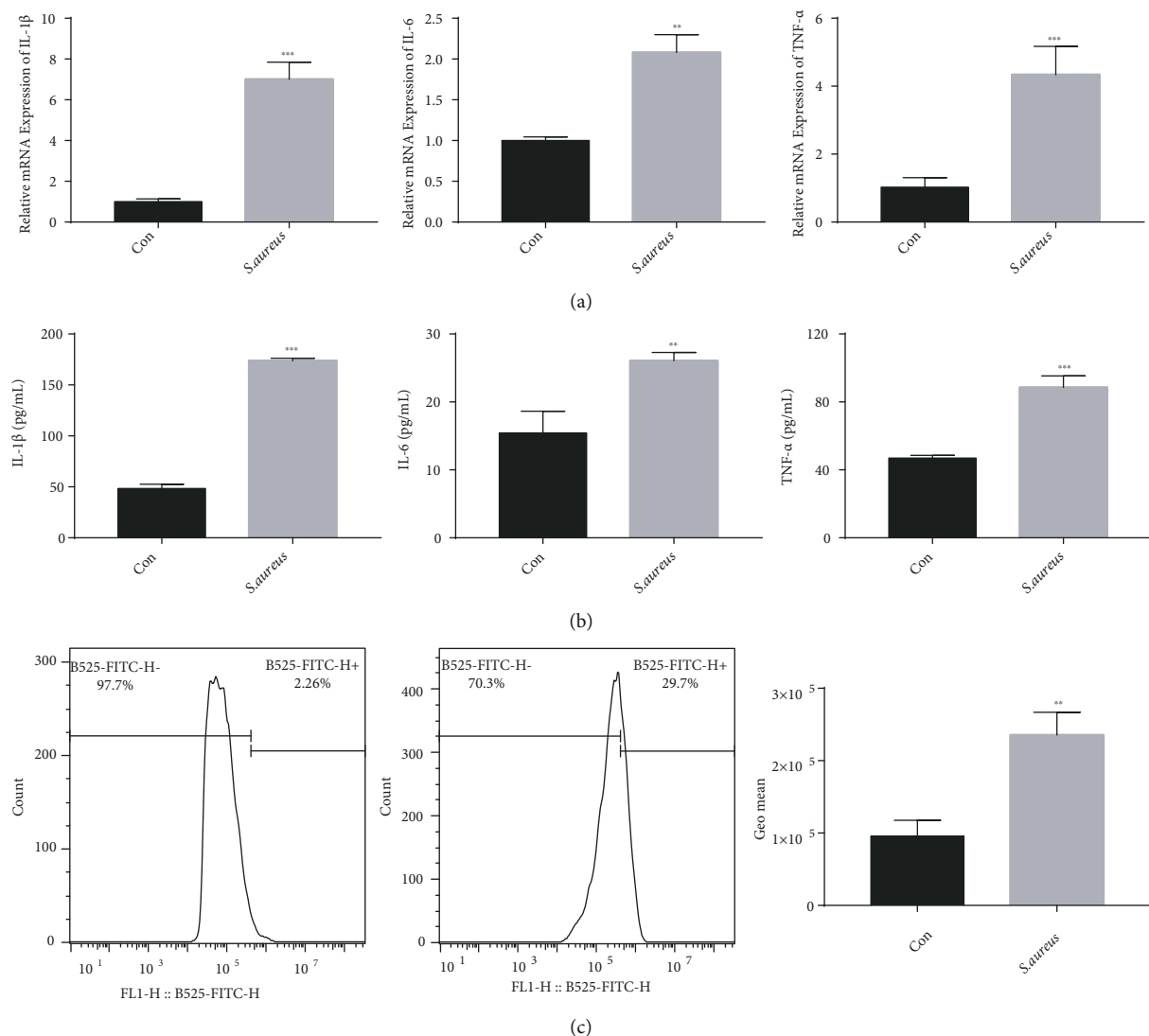


FIGURE 1: Detection of inflammatory factors and reactive oxygen species in MAC-T cells treated with *S. aureus*. (a) mRNA expressions of the inflammatory factors IL-1 $\beta$ , IL-6, and TNF- $\alpha$  detected by RT-qPCR. (b) Protein expressions of the inflammatory factors IL-1 $\beta$ , IL-6, and TNF- $\alpha$  detected by ELISA. (c) Changes in the expression levels of reactive oxygen species in the control and *S. aureus* groups, detected by flow cytometry. \* $p < 0.05$ , \*\* $p < 0.01$ , and \*\*\* $p < 0.001$ .

*S. aureus* induces inflammation and oxidative stress in MAC-T cells.

**3.2. Abnormal Expression Levels of  $m^6A$  Transferase/Demethylase Were Induced by *S. aureus* in the MAC-T Cells.** The  $m^6A$  enzyme system plays an important role in RNA  $m^6A$  modification [18, 19]. Some studies have indicated that the occurrence of disease is related to the abnormal expression of the  $m^6A$  enzymes [32]. In this study, the expression levels of methyltransferases METTL3, METTL14, and WTAP and demethylases ALKBH5 and FTO were detected using RT-qPCR. The results showed that compared with the control group, the *S. aureus* group had significantly increased mRNA expression levels of METTL3, METTL14, WTAP, and ALKBH5 (Figures 2(a)–2(d)), but no significant difference in the expression level of FTO was observed (Figure 2(e)). This suggests that  $m^6A$  modification may be

related to the inflammatory response and oxidative stress induced by *S. aureus* in the MAC-T cells.

**3.3. Overview of the  $m^6A$  Methylation Map in the Control and *S. aureus* Groups.** Based on the expression levels of the  $m^6A$  enzymes, we speculated that  $m^6A$  methylation differed between the control and the *S. aureus* groups, which was further detected using MeRIP-seq. Compared with the control group, the *S. aureus* group obtained 1,006 significantly distinct  $m^6A$  peaks in 844 mRNAs ( $p < 0.00001$ , fold change  $> 2$ , Table S1), among which 133 mRNAs had 135 hypermethylated sites such as PDGFRA and 711 mRNAs had 871 hypomethylated sites such as TNF and TRAF1 (Figures 3(a) and 3(b)). In addition, by MeRIP-qPCR, this study confirmed the hypermethylation of PDGFRA and hypomethylation of TNF and TRAF1 in *S. aureus*-induced MAC-T cells by MeRIP-qPCR (Figure 3(c)). Table 3 lists the top 20 differential  $m^6A$  peaks.

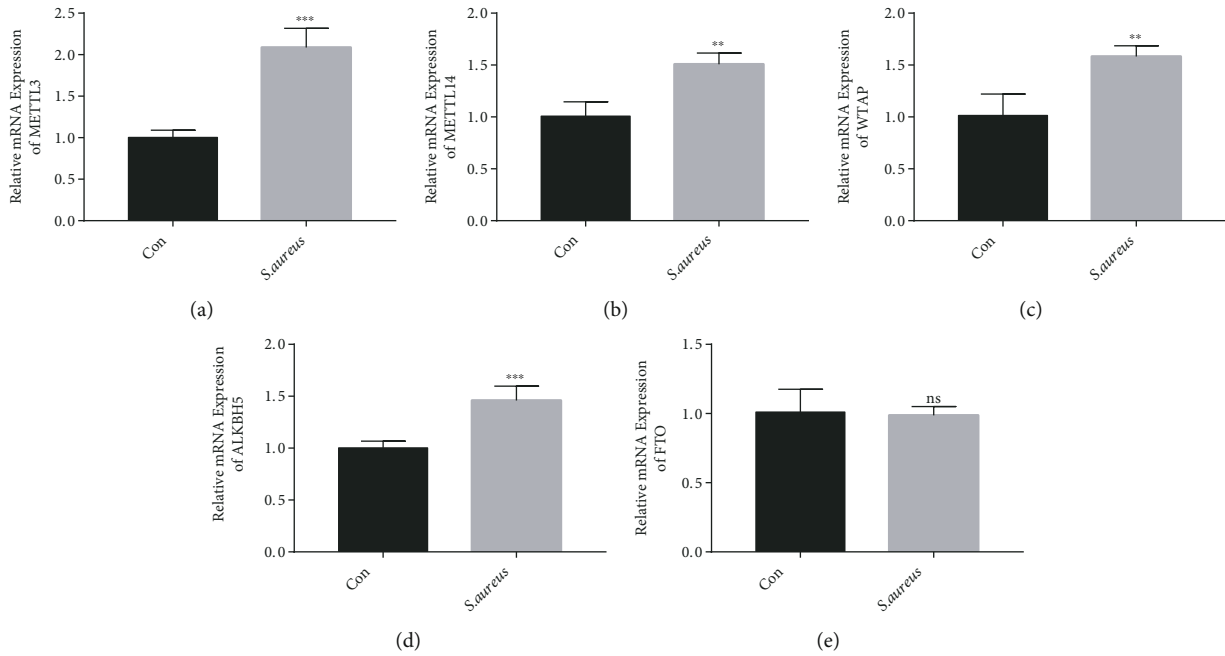


FIGURE 2: Variation in the mRNA expression levels of the m<sup>6</sup>A enzymes in *S. aureus*-induced mastitis. The mRNA expressions of the methyltransferases METTL3 (a), METTL14 (b), and WTAP (c) and the demethylases ALKBH5 (d) and FTO (e) were detected by RT-qPCR. ns: not significant, \* $p < 0.01$  and \*\* $p < 0.001$ .

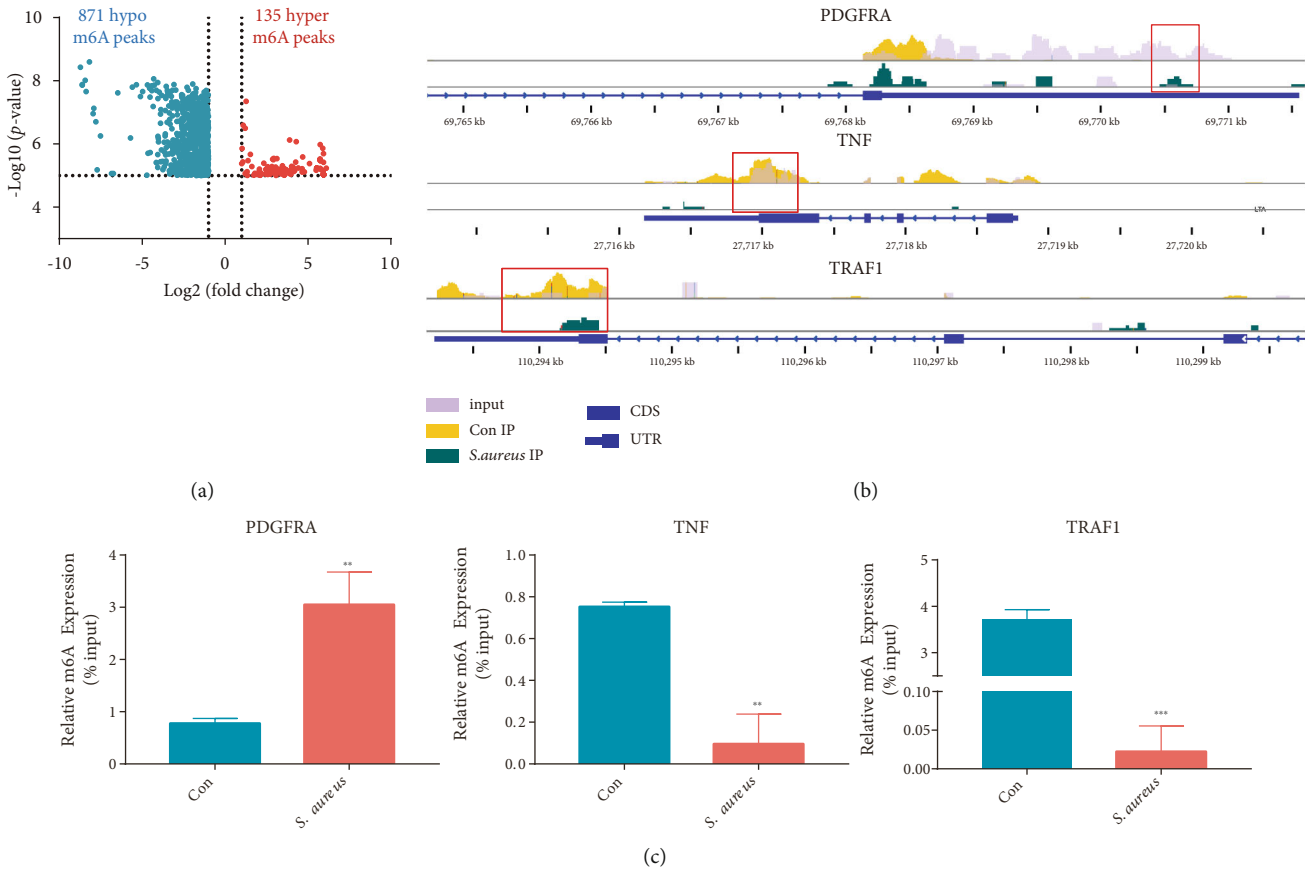


FIGURE 3: Analysis of differential m<sup>6</sup>A-modified genes between the control and *S. aureus* groups. (a) Volcano plot analysis of differential m<sup>6</sup>A methylation genes ( $p < 0.00001$ , fold change  $> 2$ ). (b) Visualization of PDGFRA, TNF, and TRAF1 using the IGV software. (c) Verification of PDGFRA, TNF, and TRAF1 by MeRIP-seq.



TABLE 3: The top 20 differential m<sup>6</sup>A-modified peaks between *S. aureus* and con based on *p* value.

Gene name	Peak region	Peak start	Peak end	Chromosome	Log10 ( <i>p</i> value)	Log2 (fold change)	Hyper/hypo
KDM3A	CDS	48394594	48394800	NC_037338.1	-7.35	1.27	Hyper
C18H19orf81	StopC	56747061	56748820	NC_037345.1	-6.59	1.09	Hyper
LZTS1	CDS	67371075	67371555	NC_037335.1	-6.49	1.21	Hyper
USP26	CDS	16901441	16901740	NC_037357.1	-6.12	3.89	Hyper
CDH4	CDS	55180735	55180969	NC_037340.1	-6.07	4.30	Hyper
CRCT1	StopC	18184161	18184773	NC_037330.1	-5.98	5.74	Hyper
KLHL6	CDS	83597549	83597780	NC_037328.1	-5.86	5.90	Hyper
SPECC1	5'UTR	33638477	33638721	NC_037346.1	-5.86	1.03	Hyper
LOC781261	5'UTR	74730061	74730340	NC_037335.1	-5.69	5.94	Hyper
GAB2	3'UTR	17794541	17795150	NC_037356.1	-5.67	1.52	Hyper
LOC101903326	StopC	1089721	1090900	NC_037341.1	-8.60	8.19	Hypo
LOC616254	StopC	48235186	48235992	NC_037346.1	-8.43	8.73	Hypo
LOC100848799	CDS	52319261	52319860	NC_037334.1	-8.06	4.30	Hypo
FAM198B	StartC	40796022	40797166	NC_037344.1	-8.01	8.43	Hypo
TACR2	StopC	25769941	25770440	NC_037355.1	-7.94	4.06	Hypo
GPR132	StopC	69438921	69439920	NC_037348.1	-7.90	1.95	Hypo
FRMPD1	CDS	61863921	61865028	NC_037335.1	-7.88	3.09	Hypo
ANGPT4	StopC	60234003	60234780	NC_037340.1	-7.88	8.61	Hypo
OR9Q2	CDS	81371461	81372540	NC_037342.1	-7.87	5.35	Hypo
SAA3	CDS	26414395	26414676	NC_037356.1	-7.87	4.68	Hypo

Further analysis revealed the differential methylation sites on all chromosomes, especially chromosomes 3, 4, and 5 (Figure 4(a)). To obtain the preferred location distribution of the m<sup>6</sup>A methylation peaks in the genes, this study performed a statistical analysis of the transcriptome. We found that the m<sup>6</sup>A peak was mainly enriched in the coding sequence, stop codon, and 3'-untranslated regions in the two groups (Figures 4(b) and 4(c)). The most enriched motif sequence of the m<sup>6</sup>A peaks was GGACU in the control group and UGGAC in the *S. aureus* group (Figure 4(d)). These data are similar to those obtained in previous studies, further enhancing the reliability and authenticity of the available data [33].

**3.4. Differentially m<sup>6</sup>A Methylated RNAs Were Involved in Mastitis-Related Processes.** To further explore the biological function of m<sup>6</sup>A methylation in bovine mammary epithelial cells stimulated by *S. aureus*, gene with different m<sup>6</sup>A peaks was analyzed by GO and KEGG analyzed. The GO analysis showed that the m<sup>6</sup>A hypermethylated genes in the *S. aureus* group were more closely associated with the regulation of vascular-associated smooth muscle cell migration and phosphatidylethanolamine metabolic process (biological process, [BP]), COP9 signalosome (cellular component, [CC]), and phospholipase activity (molecular function, [MF]) (Figure 5(a)). The hypomethylated genes were significantly involved in transcription regulation, DNA-templated synthesis (BP), nucleoplasm (CC), and transcription regulator activity (MF, Figure 5(b)).

Remarkably, according to the KEGG analysis, we identified that the m<sup>6</sup>A hypermethylation genes were significantly

associated with fatty acid degradation and adipocytokine signaling pathway, amongst others (Figure 5(c)), whereas the hypomethylated genes were mainly enriched in the TGF- $\beta$ , NF- $\kappa$ B, and Hippo signaling pathways (Figure 5(d)), which are associated with the progression of mastitis.

**3.5. Conjoint Analysis of Differential m<sup>6</sup>A Modification and mRNA.** RNA-seq was used to detect the mRNA expressions in the control and *S. aureus* groups (Figures 6(a) and 6(b)). Compared with the control group, 848 differentially expressed genes (DEGs) were found in *S. aureus* groups (fold change > 2 and *p* < 0.05, Table S2); among those genes, there are 249 upregulated genes and 599 downregulated genes. Table 4 shows the top 20 DEGs in the control and *S. aureus* groups. Meanwhile, we verified that the mRNA expression of the genes PHOAPHO2 and MAPKBPI was upregulated, and that of CHRN1 and MYH11 was downregulated by RT-qPCR (Figures 6(c)–6(f)).

By crossanalysis of the MeRIP-seq and RNA-seq data, we discovered that in 135 hypermethylated sites (fold change > 2 and *p* < 0.05), four genes were upregulated (called “hyper-up”), and one gene was downregulated (called “hyper-down,” fold change > 2 and *p* < 0.05). In the 871 hypomethylated sites (fold change > 2 and *p* < 0.05), six genes were upregulated (called “hypo-up”), and 50 genes were downregulated (called “hypo-down,” fold change > 2 and *p* < 0.05, Figure 6(g)). We presented 15 differentially methylated and expressed genes (Table 5). The KEGG analysis of the 62 genes revealed that these genes were mainly enriched in pyruvate metabolism, the TGF- $\beta$ , and Hippo signaling pathway (Figure 6(h)).

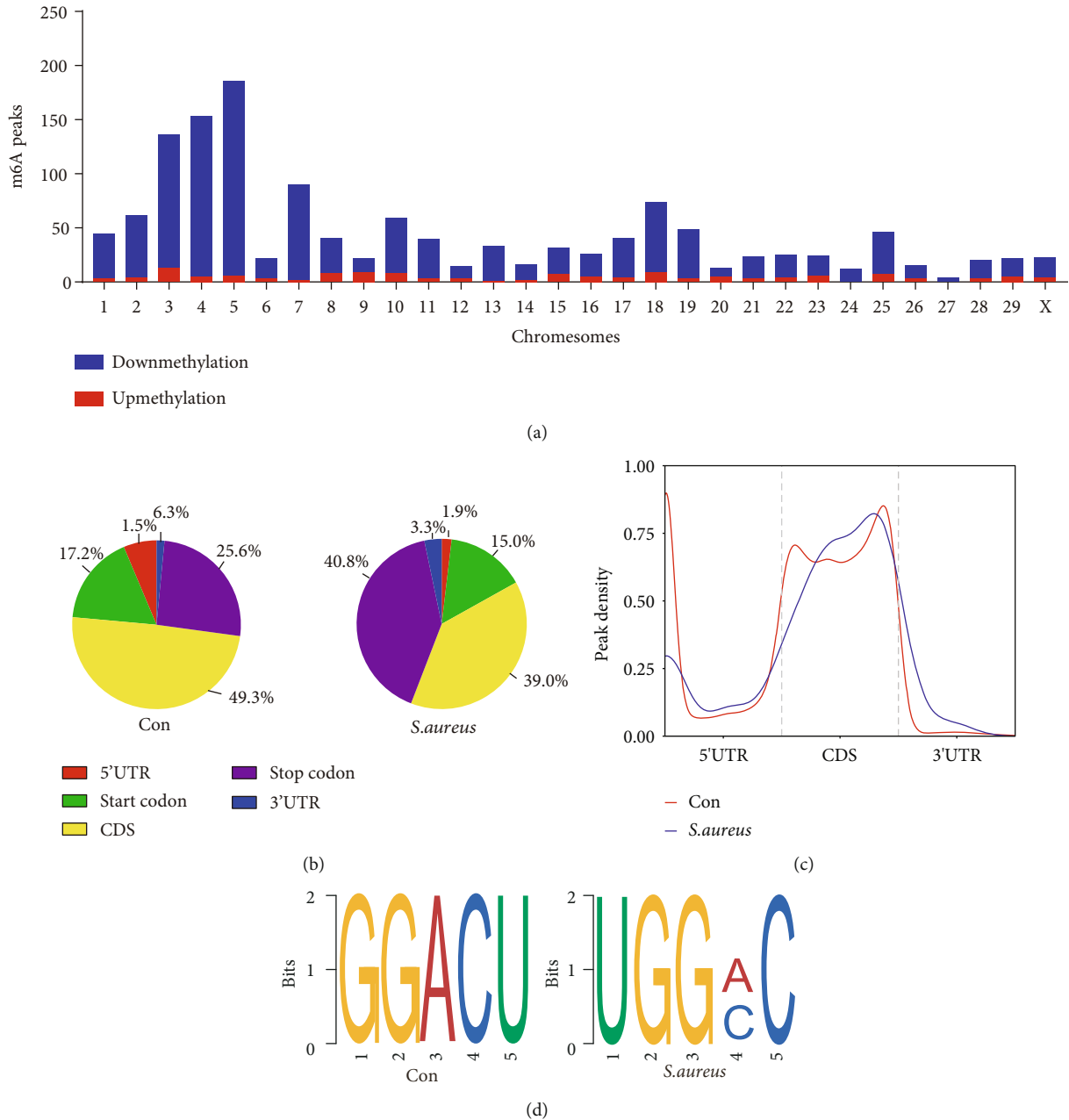


FIGURE 4: m<sup>6</sup>A modification map of *S. aureus*-induced mastitis. (a) The distribution of the differential m<sup>6</sup>A-modified genes on bovine chromosomes. (b) Gene position distribution of the differential m<sup>6</sup>A modification sites in the control and *S. aureus* groups. (c) Peak density distribution of the differential m<sup>6</sup>A modification sites in the control and *S. aureus* groups. (d) Motif sequence analysis of m<sup>6</sup>A-modified genes in the control and *S. aureus* groups.

#### 4. Discussion

In mastitis in dairy cows, pathogenic microorganisms usually induce breast inflammation. *Staphylococcus aureus* is one of the most common pathogens that often causes subclinical mastitis [34]. Previous studies have shown that bovine mammary epithelial cells are the first line of defense against the invasion of mammary glands by microorganisms such as *S. aureus* [1, 35], which leads to the release of various chemokines and cytokines [36]. Although there is currently much research into mastitis, the molecular mechanism of mastitis

caused by *S. aureus* is still unclear. There are many challenges in improving mastitis diagnosis, treatment, and prevention. m<sup>6</sup>A methylation modification can affect RNA splicing, transcription, and translation [37–39] and thereby participating in the initiation and progression of many diseases such as cancer and cardiovascular diseases [26, 40, 41]. However, only a few studies have reported m<sup>6</sup>A methylation modification in mastitis. To our knowledge, this is the first study to report the m<sup>6</sup>A map of *S. aureus*-induced mastitis, which provides a clue for further study of m<sup>6</sup>A modification in mastitis.

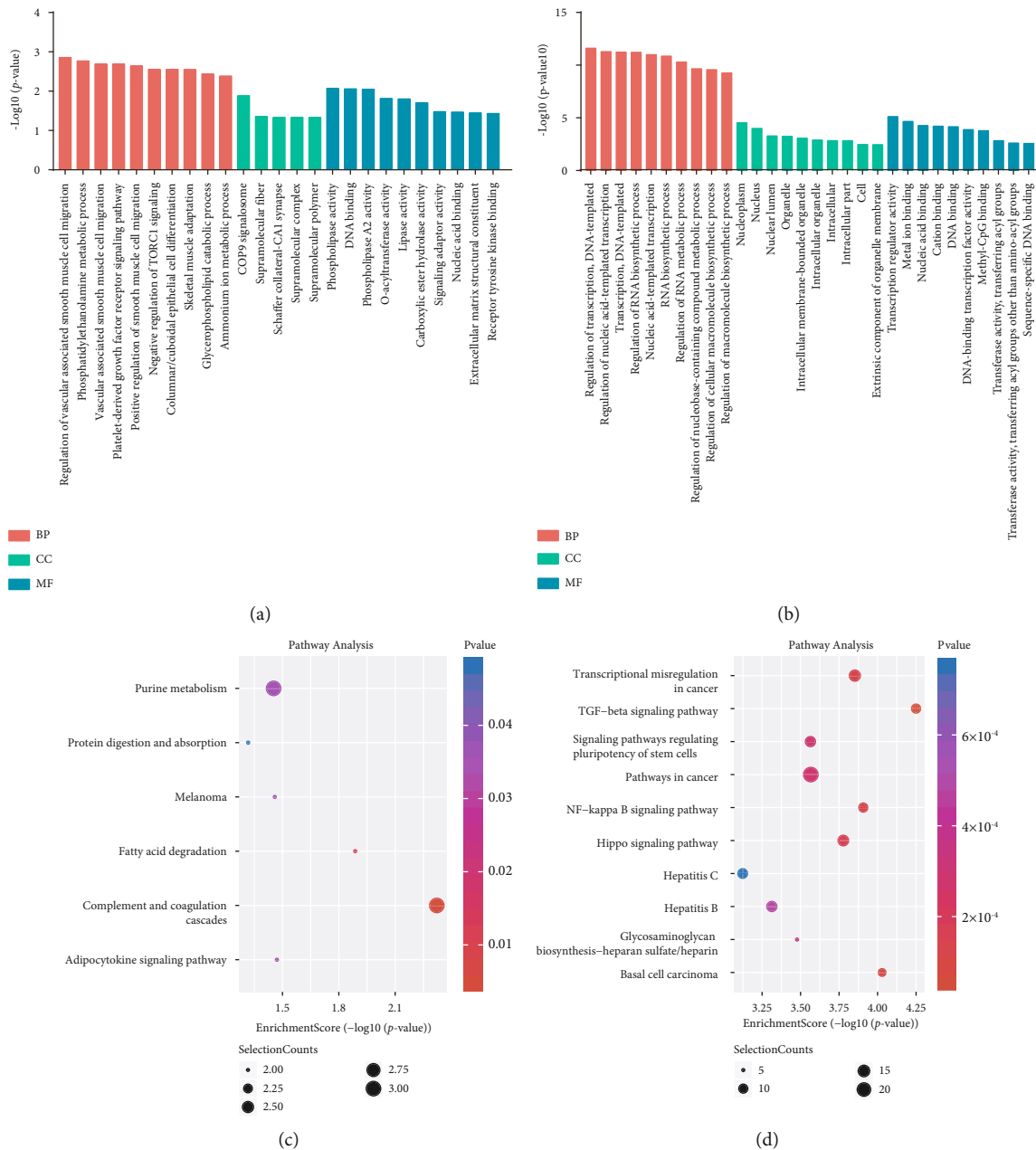


FIGURE 5: Biological functional analysis of differential m<sup>6</sup>A-modified genes. GO analysis of hypermethylated (a) and hypomethylated genes (b) in the *S. aureus* group. KEGG analysis of hypermethylated genes (c) and hypomethylated genes (d) in the *S. aureus* group.

In bovine, studies have shown that *S. aureus* induces an inflammatory response and finally leads to the secretion of cell factors, such as TNF- $\alpha$ , IL-6, and IL-1 [42, 43]. Oxidative stress is a state of imbalance between oxidation and antioxidation, that increases the production of ROS [44]. In mastitis, the release of ROS is key to the inflammatory response [45]. On the one hand, ROS plays an important role in inflammation, apoptosis, and cell growth [46, 47]. On the other hand, ROS can cause oxidation of proteins and DNA, inducing damage to nearby tissues. In this study, we used inactivated *S. aureus* to stimulate MAC-T cells, and we found that the expression levels of the inflammatory factors and ROS increased significantly (Figure 1), consistent with the results of other related studies [47, 48].

m<sup>6</sup>A modification is considered a reversible dynamic modification. In addition, the methylase system determined its biological function [13]. Studies have shown that most diseases are accompanied by changes in methylases [21, 23]. Wu et al. reported the mRNA expression levels of m<sup>6</sup>A related enzymes in bovine mammary epithelial cells treated with aflatoxins B1 and M1 [49]. In this study, the mRNA levels of methyltransferase (METLL3, METLL14, and WTAP) and a demethylase (ALKBH5) were upregulated (Figure 2), which suggests that m<sup>6</sup>A modification may be related to the inflammatory response and oxidative stress induced by *S. aureus* in the MAC-T cells.

With analysis the MeRIP-seq results, we speculated that *S. aureus* may have induced the m<sup>6</sup>A modification of some

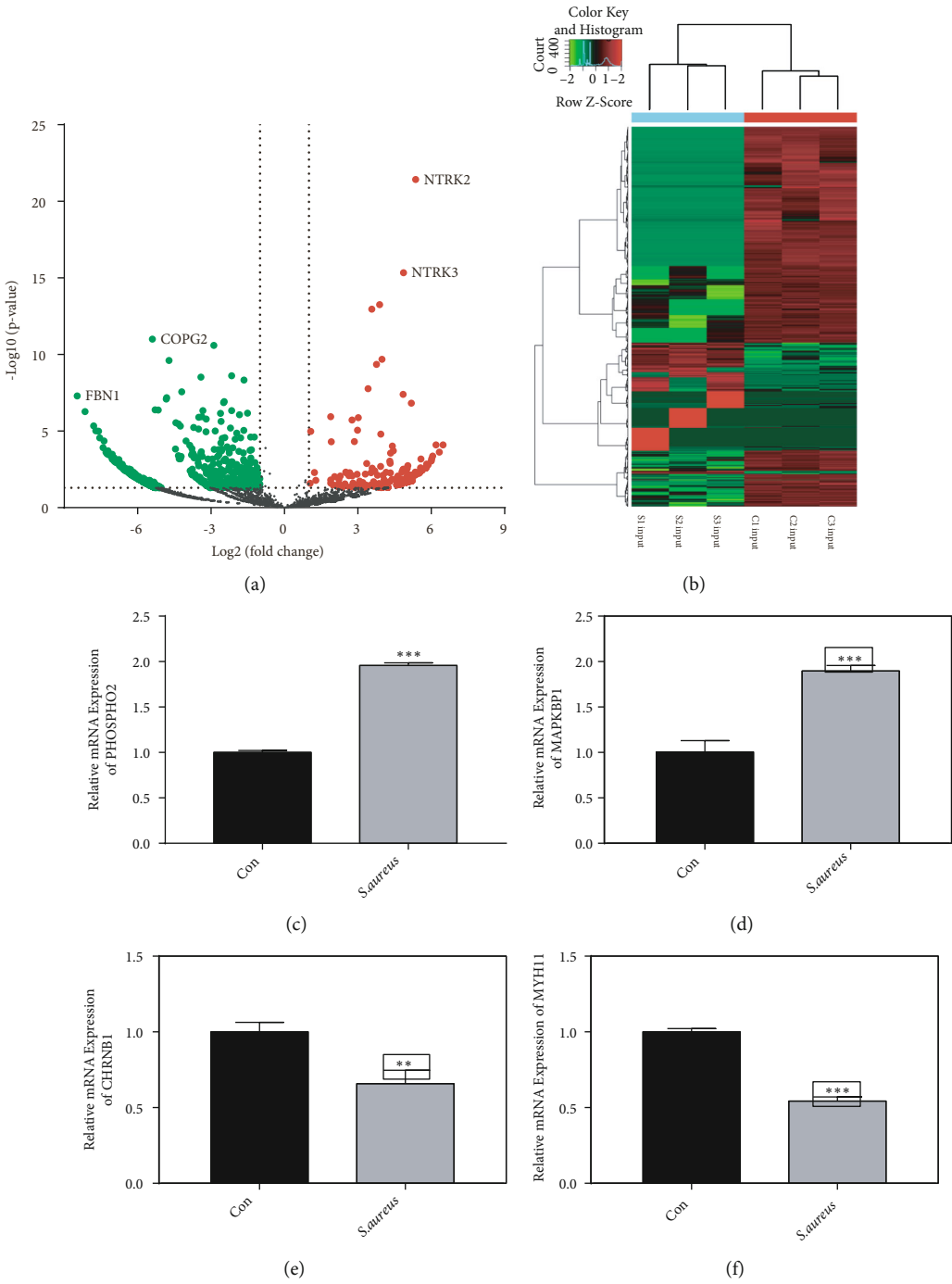


FIGURE 6: Continued.

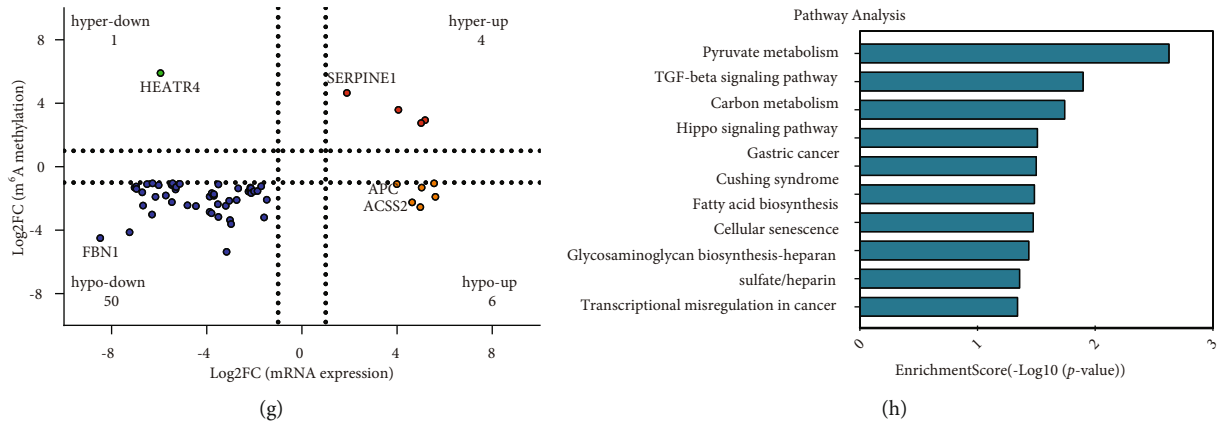


FIGURE 6: Joint analysis of differential mRNA expression and m<sup>6</sup>A modification. (a) Volcano map showing the differential mRNA expressions between the control and *S. aureus* groups ( $p < 0.05$ , fold change  $> 2$ ). (b) Heat map demonstrating the differential mRNA expressions between the three control input samples and three *S. aureus* input samples. (c)–(f) mRNA expressions of PHOSPHO2, MAPKBP1, CHRN1, and MYH11 detected by RT-qPCR. (g) Quadrant diagram showing the genes with differential m<sup>6</sup>A modification ( $p < 0.00001$ , fold change  $> 2$ ) and differential mRNA expression ( $p < 0.05$ , fold change  $> 2$ ). (h) KEGG analysis of the biological functions of 62 genes with differential m<sup>6</sup>A modification and mRNA expression.

TABLE 4: The top 20 differential mRNA expression in *S. aureus* vs. con.

gene_id	LogFC	Log10 (p value)	Regulation
ADGRE3	6.49	-4.09	Up
STARD7	6.33	-3.63	Up
TRIP11	6.20	-4.10	Up
NTRK1	6.06	-3.36	Up
KRT80	6.02	-3.19	Up
LOC527796	6.01	-3.05	Up
RAB4B	5.88	-2.80	Up
MAPKBP1	5.85	-2.77	Up
PHOSPHO2	5.81	-2.84	Up
LOC100849008	5.81	-2.72	Up
FBN1	-8.47	-7.29	Down
MYH11	-8.15	-6.27	Down
ACP2	-7.80	-5.34	Down
PRR29	-7.71	-5.01	Down
LOC112444598	-7.59	-4.99	Down
CHRN1	-7.55	-4.56	Down
PSIP1	-7.41	-3.92	Down
DXO	-7.37	-4.36	Down
DSG1	-7.29	-3.61	Down
GLS	-7.25	-3.58	Down

RNA molecules in MAC-T cells. Therefore, the m<sup>6</sup>A modification map of *S. aureus*-induced MAC-T cells was described using the MeRIP-seq technique. We found 1,006 differential methylation sites in 844 genes, some of which are closely related to the occurrence and development of mastitis. PDGFRA (Figure 3(b)), a hypermethylated molecule, reportedly induced constitutive phosphorylation of Akt, ERK1/2, and STAT3 [50]. Among the hypomethylated molecules, TNF (Figure 3(b)), a cytokine, and NF $\kappa$ B1 and NF $\kappa$ B2

(Table S1), which are important transcription factors, are essential for inflammation and innate immunity [51, 52]. TGF- $\beta$ 2 (Table S1) is a member of the TGF factor superfamily that plays an important role in regulating the initiation, maintenance, and resolution of immune responses and epithelial-mesenchymal transition [53, 54]. TRAF1 (Figure 3(b)) plays an important role in mediating cell survival, differentiation, proliferation, and death [54], and inhibition of TRAF1 can effectively inhibit inflammation, oxidative stress, and apoptosis [55]. We confirmed the m<sup>6</sup>A hypermethylation of PDGFRA and hypomethylation of TNF and TRAF1 through MeRIP-qPCR (Figure 3(c)). However, whether these molecules function through m<sup>6</sup>A modification requires further verification.

Abnormal lipid metabolism and oxidative stress are important factors that lead to the development of inflammatory diseases. Similar metabolic abnormalities have been reported in the early stages of mastitis [56, 57]. Researchers believed that lipids and their metabolites could be used as predictive diagnostic markers, preventive tools, and early treatment interventions for mastitis [57, 58]. In this study, GO analysis of differential m<sup>6</sup>A methylated genes revealed that the BP functions were mainly enriched in the phosphatidylethanolamine metabolic process, glycerophospholipid catabolic process (Figure 5(a)), and so on. The KEGG analysis revealed that the differential m<sup>6</sup>A methylated genes were mainly involved in the fatty acid degradation signaling pathway (Figure 5(c)). Thus, we speculated that m<sup>6</sup>A modification may affect the occurrence of *S. aureus*-induced mastitis through lipid metabolism and oxidative stress. In addition, previous studies have confirmed that bovine mammary epithelial cells transmit inflammatory signals mainly through the TGF, NF- $\kappa$ B, and TNF signaling pathway and other signaling pathways [59, 60]. The KEGG pathway analysis revealed that the differential m<sup>6</sup>A methylated genes were also enriched in the TGF and NF- $\kappa$ B signaling pathways (Figure 5(d)) in the current study. This suggests that m<sup>6</sup>A

TABLE 5: 15 transcripts of differential m<sup>6</sup>A modification and mRNA expression in *S. aureus* vs. con.

Gene name	Change	Chromosome	Peak start	Peak end	Peak_length	m <sup>6</sup> A modification change Peak region	Fold change	Log10 (p value)	mRNA expression change LogFC	Log10 (p value)
ALK	Hyperup	NC_037338.1	70660375	70661760	1385	CDS	7.70	-5.10	5.19	-6.82
ERO1A	Hyper-u	NC_037337.1	11498514	11498840	326	5'UTR	5.13	-5.13	5.02	-2.55
RYBP	Hyperup	NC_037349.1	29277201	29277420	219	3'UTR	5.21	-5.21	4.06	-1.41
SERPINE1	Hyperup	NC_037352.1	35605621	35605860	239	5'UTR	5.22	-5.22	1.90	-1.81
HEATR4	Hyperdown	NC_037337.1	84967915	84968140	225	5'UTR	5.15	-5.15	-5.94	-1.89
FBN1	Hypodown	NC_037337.1	61917881	61918380	499	CDS	-22.53	-7.75	-8.47	-7.29
CD70	Hypodown	NC_037334.1	17908292	17908687	395	CDS	-17.43	-5.40	-7.24	-3.51
LHFPL4	Hypodown	NC_037349.1	17088303	17088792	489	CDS	-2.46	-5.03	-7.03	-3.19
KMT2E	Hypodown	NC_037331.1	46268266	46268531	265	CDS	-2.37	-6.93	-6.96	-3.26
PRPF38A	Hypodown	NC_037330.1	93935321	93935880	559	3'UTR	-2.63	-6.14	-6.95	-3.02
EXT1	Hypoup	NC_037341.1	46477327	46477877	550	CDS	-2.05	-6.07	5.56	-2.60
RPGR	Hypoup	NC_037357.1	104982661	104983554	893	CDS	-2.47	7.23	5.04	-1.69
ARSI	Hypoup	NC_037334.1	61646441	61648420	1979	3'UTR	-5.82	-5.60	4.99	-1.67
ACSS2	Hypoup	NC_037340.1	64232901	64233260	359	3'UTR	-4.76	-5.39	4.64	-1.50
APC	Hypoup	NC_037334.1	43874981	43877340	2359	CDS	-4.16	-5.01	3.99	-9.68

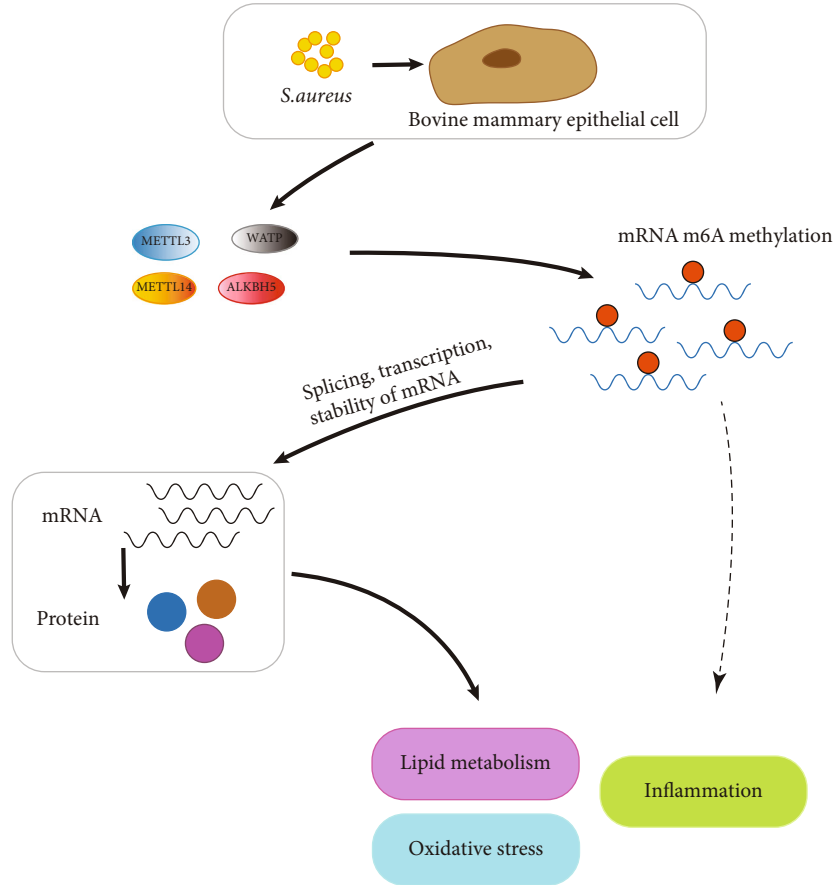


FIGURE 7: Schematic diagram of the potential mechanism of m<sup>6</sup>A modification in MAC-T cells treated by *S. aureus*.

modification may be associated with mastitis. m<sup>6</sup>A modification is well known that affects mRNA splicing, translation, and stability [37–39]. In the GO analysis, we also found that the differential m<sup>6</sup>A modification was mainly related to biological progress items such as RNA biosynthetic process and transcription. Meanwhile, we conducted a joint analysis of differential m<sup>6</sup>A molecules and mRNA. We found 62 genes whose m<sup>6</sup>A modification and mRNA expression levels had changed significantly ( $p < 0.05$ , Figure 6(c)), and the changes in mRNA expression levels might have been caused by the change in the m<sup>6</sup>A modification. Biological analysis of these 62 genes revealed that they were related to pyruvate metabolism, fatty acid biosynthesis, TGF-beta signaling pathway, and so on (Figure 6(d)).

The heat-inactivated *S. aureus* mastitis model retained the main infectious components while avoiding bacterial overgrowth and excessive cell death. There are many ways to inactivate *S. aureus*, such as ultraviolet irradiation (UV) and chemical treatment. However, it has been suggested that gram-positive bacteria are more resistant to ultraviolet light than gram-negative bacteria [61, 62]. The inactivation of *S. aureus* using chemical treatment, such as formaldehyde, is not completely effective [63]. In addition, residual chemical agents may have some effect on mammalian cells during subsequent infection experi-

ments. The heat inactivation method can not only effectively inactivate *S. aureus* but is also simple and easy to perform. Therefore, the establishment of a mastitis model with heat-inactivated *S. aureus* has been recognized and applied by many researchers [30, 64, 65].

Through the above analysis, we speculate that, in MAC-T cells treated with *S. aureus*, m<sup>6</sup>A modification will affect the transcription and translation of mRNA, thus affecting the physiological and pathological processes of inflammation, oxidative stress, and lipid metabolism (Figure 7). However, the mechanism by which m<sup>6</sup>A regulates mastitis in bovine is still unclear. This study thus provides a clue to the mechanism of m<sup>6</sup>A modification in *S. aureus*-induced mastitis and should be explored further in future studies.

## 5. Conclusions

The results of this study clearly show the changes in the m<sup>6</sup>A modification spectrum in *S. aureus*-induced mastitis. We found that the different m<sup>6</sup>A-modified molecules were involved in lipid metabolism, oxidative stress, inflammatory reactions, and other mastitis-related biological processes. This study broadens the research direction for dairy cow mastitis and lays the foundation for further research that the function of m<sup>6</sup>A modification in mastitis.

## Data Availability

The data obtained in this study are available from the corresponding author upon request.

## Conflicts of Interest

There is no conflict of interest.

## Acknowledgments

We thank the technical support and the platform of Huazhong Agricultural University. We thank our coworkers' advice and help. This research was funded by the National Natural Science Foundation of China (Nos. 31972758; 31101874).

## Supplementary Materials

Table S1: differentially methylated RNA sites for *S. aureus* and con. Table S2: differential mRNA expression for *S. aureus* and Con. (*Supplementary Materials*)

## References

- [1] A. Ashraf and M. Imran, "Causes, types, etiological agents, prevalence, diagnosis, treatment, prevention, effects on human health and future aspects of bovine mastitis," *Animal Health Research Reviews*, vol. 21, no. 1, pp. 36–49, 2020.
- [2] H. Chu and S. K. Mazmanian, "Innate immune recognition of the microbiota promotes host-microbial symbiosis," *Nature Immunology*, vol. 14, no. 7, pp. 668–675, 2013.
- [3] Y. Wu, Y. Sun, X. Dong et al., "The synergism of PGN, LTA and LPS in inducing transcriptome changes, inflammatory responses and a decrease in lactation as well as the associated epigenetic mechanisms in bovine mammary epithelial cells," *Toxins*, vol. 12, no. 6, p. 387, 2020.
- [4] C. Lin, Y. Zhu, Z. Hao et al., "Genome-wide analysis of LncRNA in bovine mammary epithelial cell injuries induced by *Escherichia coli* and *Staphylococcus aureus*," *International Journal of Molecular Sciences*, vol. 22, no. 18, p. 9719, 2021.
- [5] T. Matsunaga, S. I. Kamata, N. Kakiuchi, and K. Uchida, "Characteristics of *Staphylococcus aureus* isolated from peracute, acute and chronic bovine mastitis," *The Journal of Veterinary Medical Science*, vol. 55, no. 2, pp. 297–300, 1993.
- [6] T. Tollersrud, K. Kenny, D. A. Caugant, and A. Lund, "Characterisation of isolates of *Staphylococcus aureus* from acute, chronic and subclinical mastitis in cows in Norway," *APMIS*, vol. 108, no. 9, pp. 565–572, 2000.
- [7] L. Sutra and B. Poutrel, "Virulence factors involved in the pathogenesis of bovine intramammary infections due to *Staphylococcus aureus*," *Journal of Medical Microbiology*, vol. 40, no. 2, pp. 79–89, 1994.
- [8] J. I. Jun and L. F. Lau, "CCN1 is an opsonin for bacterial clearance and a direct activator of toll-like receptor signaling," *Nature Communications*, vol. 11, no. 1, p. 1242, 2020.
- [9] B. Liu, Y. Che, M. Zhang et al., "IFN- $\gamma$  activates the TLR4-CCl5 signaling through reducing arginine level, leading to enhanced susceptibility of bovine mammary epithelial cells to *Staphylococcus aureus*," *Inflammation*, vol. 43, no. 6, pp. 2209–2221, 2020.
- [10] J. L. Lai, Y. H. Liu, C. Liu et al., "Indirubin inhibits LPS-induced inflammation via TLR4 abrogation mediated by the NF- $\kappa$ B and MAPK signaling pathways," *Inflammation*, vol. 40, no. 1, pp. 1–12, 2017.
- [11] Y. Bi, Y. Ding, J. Wu, Z. Miao, J. Wang, and F. Wang, "*Staphylococcus aureus* induces mammary gland fibrosis through activating the TLR/NF- $\kappa$ B and TLR/AP-1 signaling pathways in mice," *Microbial Pathogenesis*, vol. 148, article 104427, 2020.
- [12] N. Pumipuntu, S. Kulpeanprasit, S. Santajit et al., "Screening method for *Staphylococcus aureus* identification in subclinical bovine mastitis from dairy farms," *Veterinary World*, vol. 10, no. 7, pp. 721–726, 2017.
- [13] Z. Bi, Y. Liu, Y. Zhao et al., "A dynamic reversible RNA N<sup>6</sup>-methyladenosine modification: current status and perspectives," *Journal of Cellular Physiology*, vol. 234, no. 6, pp. 7948–7956, 2019.
- [14] H. C. Duan, Y. Wang, and G. Jia, "Dynamic and reversible RNA N<sup>6</sup>-methyladenosine methylation," *Wiley Interdiscip Rev RNA*, vol. 10, no. 1, article e1507, 2019.
- [15] C. Gu, X. Shi, C. Dai et al., "RNA m(6)a modification in cancers: molecular mechanisms and potential clinical applications," *The Innovation*, vol. 1, no. 3, article 100066, 2020.
- [16] P. Wang, K. A. Doxtader, and Y. Nam, "Structural basis for cooperative function of Mettl3 and Mettl14 methyltransferases," *Molecular Cell*, vol. 63, no. 2, pp. 306–317, 2016.
- [17] X. Wang, J. Huang, T. Zou, and P. Yin, "Human m6A writers: two subunits, 2 roles," *RNA Biology*, vol. 14, no. 3, pp. 300–304, 2017.
- [18] H. Shi, J. Wei, and C. He, "Where, when, and how: context-dependent functions of RNA methylation writers, readers, and erasers," *Molecular Cell*, vol. 74, no. 4, pp. 640–650, 2019.
- [19] H. Huang, H. Weng, and J. Chen, "m<sup>6</sup>A modification in coding and non-coding RNAs: roles and therapeutic implications in cancer," *Cancer Cell*, vol. 37, no. 3, pp. 270–288, 2020.
- [20] D. Dominissini, S. Moshitch-Moshkovitz, S. Schwartz et al., "Topology of the human and mouse m<sup>6</sup>A RNA methylomes revealed by m6A-seq," *Nature*, vol. 485, no. 7397, pp. 201–206, 2012.
- [21] H. Zhang, X. Shi, T. Huang et al., "Dynamic landscape and evolution of m<sup>6</sup>A methylation in human," *Nucleic Acids Research*, vol. 48, no. 11, pp. 6251–6264, 2020.
- [22] Y. Qin, L. Li, E. Luo et al., "Role of m<sup>6</sup>A RNA methylation in cardiovascular disease (review)," *International Journal of Molecular Medicine*, vol. 46, no. 6, pp. 1958–1972, 2020.
- [23] J. Wang, J. Wang, Q. Gu et al., "The biological function of m<sup>6</sup>A demethylase ALKBH5 and its role in human disease," *Cancer Cell International*, vol. 20, p. 347, 2020.
- [24] C. Zhang, J. Fu, and Y. Zhou, "A review in research progress concerning m<sup>6</sup>A methylation and immunoregulation," *Frontiers in Immunology*, vol. 10, p. 922, 2019.
- [25] Z. Feng, Q. Li, R. Meng, B. Yi, and Q. Xu, "METTL3 regulates alternative splicing of MyD88 upon the lipopolysaccharide-induced inflammatory response in human dental pulp cells," *Journal of Cellular and Molecular Medicine*, vol. 22, no. 5, pp. 2558–2568, 2018.
- [26] H. B. Li, J. Tong, S. Zhu et al., "m<sup>6</sup>A mRNA methylation controls T cell homeostasis by targeting the IL-7/STAT5/SOCS pathways," *Nature*, vol. 548, no. 7667, pp. 338–342, 2017.
- [27] G. Lichinchi, S. Gao, Y. Saletore et al., "Dynamics of the human and viral m(6)A RNA methylomes during HIV-1



- infection of T cells,” *Nature Microbiology*, vol. 1, article 16011, pp. 1–9, 2016.
- [28] D. Han, J. Liu, C. Chen et al., “Anti-tumour immunity controlled through mRNA m<sup>6</sup>A methylation and YTHDF1 in dendritic cells,” *Nature*, vol. 566, no. 7743, pp. 270–274, 2019.
- [29] J. Chen, C. Wang, W. Fei, X. Fang, and X. Hu, “Epitranscriptomic m<sup>6</sup>A modification in the stem cell field and its effects on cell death and survival,” *American Journal of Cancer Research*, vol. 9, no. 4, pp. 752–764, 2019.
- [30] W. Jin, E. M. Ibeagha-Awemu, G. Liang, F. Beaudoin, X. Zhao, and L. L. Guan, “Transcriptome microRNA profiling of bovine mammary epithelial cells challenged with *Escherichia coli* or *Staphylococcus aureus* bacteria reveals pathogen directed micro-RNA expression profiles,” *BMC Genomics*, vol. 15, p. 181, 2014.
- [31] X. Tang, C. Liu, T. Li et al., “Gambogic acid alleviates inflammation and apoptosis and protects the blood-milk barrier in mastitis induced by LPS,” *International Immunopharmacology*, vol. 86, article 106697, 2020.
- [32] Y. Yang, P. J. Hsu, Y. S. Chen, and Y. G. Yang, “Dynamic transcriptomic m<sup>6</sup>A decoration: writers, erasers, readers and functions in RNA metabolism,” *Cell Research*, vol. 28, no. 6, pp. 616–624, 2018.
- [33] J. E. Harper, S. M. Miceli, R. J. Roberts, and J. L. Manley, “Sequence specificity of the human mRNA N<sup>6</sup>-adenosine methylase in *Vitro*,” *Nucleic Acids Research*, vol. 18, no. 19, pp. 5735–5741, 1990.
- [34] L. S. Rocha, D. M. Silva, M. P. Silva et al., “Comparative genomics of *Staphylococcus aureus* associated with subclinical and clinical bovine mastitis,” *PLoS One*, vol. 14, no. 8, article e0220804, 2019.
- [35] M. Cai, W. Fan, X. Li et al., “The regulation of *Staphylococcus aureus*-induced inflammatory responses in bovine mammary epithelial cells,” *Frontiers in Veterinary Science*, vol. 8, article 683886, 2021.
- [36] Y. Zheng, G. Liu, W. Wang et al., “Lactobacillus casei Zhang counteracts blood-milk barrier disruption and moderates the inflammatory response in *Escherichia coli*-induced mastitis,” *Frontiers in Microbiology*, vol. 12, article 675492, 2021.
- [37] I. A. Roundtree, M. E. Evans, T. Pan, and C. He, “Dynamic RNA modifications in gene expression regulation,” *Cell*, vol. 169, no. 7, pp. 1187–1200, 2017.
- [38] Z. M. Zhu, F. C. Huo, and D. S. Pei, “Function and evolution of RNA N<sup>6</sup>-methyladenosine modification,” *International Journal of Biological Sciences*, vol. 16, no. 11, pp. 1929–1940, 2020.
- [39] S. D. Kasowitz, J. Ma, S. J. Anderson et al., “Nuclear m<sup>6</sup>A reader YTHDC1 regulates alternative polyadenylation and splicing during mouse oocyte development,” *PLoS Genetics*, vol. 14, no. 5, article e1007412, 2018.
- [40] Z. X. Rong, Z. Li, J. J. He et al., “Downregulation of Fat Mass and Obesity Associated (FTO) promotes the progression of intrahepatic cholangiocarcinoma,” *Frontiers in Oncology*, vol. 9, p. 369, 2019.
- [41] Y. G. Chen, R. Chen, S. Ahmad et al., “N<sup>6</sup>-Methyladenosine modification controls circular RNA immunity,” *Molecular Cell*, vol. 76, no. 1, pp. 96–109, 2019.
- [42] S. Von Aulock, S. Morath, L. Hareng et al., “Lipoteichoic acid from *Staphylococcus aureus* is a potent stimulus for neutrophil recruitment,” *Immunobiology*, vol. 208, no. 4, pp. 413–422, 2003.
- [43] S. Knapp, S. Von Aulock, M. Leendertse et al., “Lipoteichoic acid-induced lung inflammation depends on TLR2 and the concerted action of TLR4 and the platelet-activating factor receptor,” *Journal of Immunology*, vol. 180, no. 5, pp. 3478–3484, 2008.
- [44] H. Sies, “Oxidative stress: a concept in redox biology and medicine,” *Redox Biology*, vol. 4, pp. 180–183, 2015.
- [45] C. Castillo, J. Hernandez, A. Bravo, M. Lopez-Alonso, V. Pereira, and J. L. Benedito, “Oxidative status during late pregnancy and early lactation in dairy cows,” *Veterinary Journal*, vol. 169, no. 2, pp. 286–292, 2005.
- [46] M. Liu, C. Zhang, X. Xu et al., “Ferulic acid inhibits LPS-induced apoptosis in bovine mammary epithelial cells by regulating the NF- $\kappa$ B and Nrf2 signalling pathways to restore mitochondrial dynamics and ROS generation,” *Veterinary Research*, vol. 52, no. 1, p. 104, 2021.
- [47] A. A. I. Arbab, X. Lu, I. M. Abdalla et al., “Metformin inhibits lipoteichoic acid-induced oxidative stress and inflammation through AMPK/NRF2/NF- $\kappa$ B signaling pathway in bovine mammary epithelial cells,” *Frontiers in Veterinary Science*, vol. 8, article 661380, 2021.
- [48] R. Li, H. Fang, J. Shen et al., “Curcumin alleviates LPS-induced oxidative stress, inflammation and apoptosis in bovine mammary epithelial cells via the NFE2L2 signaling pathway,” *Toxins*, vol. 13, no. 3, p. 208, 2021.
- [49] K. Wu, S. Jia, J. Zhang et al., “Transcriptomics and flow cytometry reveals the cytotoxicity of aflatoxin B(1) and aflatoxin M(1) in bovine mammary epithelial cells,” *Ecotoxicology and Environmental Safety*, vol. 209, article 111823, 2021.
- [50] C. K. M. Ip, P. K. S. Ng, K. J. Jeong et al., “Neomorphic PDGFRA extracellular domain driver mutations are resistant to PDGFRA targeted therapies,” *Nature Communications*, vol. 9, no. 71, article 4583, 2018.
- [51] D. Wallach, “The cybernetics of TNF: old views and newer ones,” *Seminars in Cell & Developmental Biology*, vol. 50, pp. 105–114, 2016.
- [52] B. Hoesel and J. A. Schmid, “The complexity of NF- $\kappa$ B signaling in inflammation and cancer,” *Molecular Cancer*, vol. 12, p. 86, 2013.
- [53] W. Chen and P. Ten Dijke, “Immunoregulation by members of the TGF $\beta$  superfamily,” *Nature Reviews. Immunology*, vol. 16, no. 12, pp. 723–740, 2016.
- [54] M. Maleszewska, J. R. Moonen, N. Huijkman, B. van de Sluis, G. Krenning, and M. C. Harmsen, “IL-1 $\beta$  and TGF $\beta$ 2 synergistically induce endothelial to mesenchymal transition in an NF $\kappa$ B-dependent manner,” *Immunobiology*, vol. 218, no. 4, pp. 443–454, 2013.
- [55] W. Bin, X. Ming, and C. Wen-Xia, “TRAF1 meditates lipopolysaccharide-induced acute lung injury by up regulating JNK activation,” *Biochemical and Biophysical Research Communications*, vol. 511, no. 1, pp. 49–56, 2019.
- [56] E. Dervishi, G. Zhang, D. Hailemariam, S. M. Dunn, and B. N. Ametaj, “Innate immunity and carbohydrate metabolism alterations precede occurrence of subclinical mastitis in transition dairy cows,” *Journal of Animal Science and Technology*, vol. 57, p. 46, 2015.
- [57] F. Zandkarimi, J. Vanegas, X. Fern, C. S. Maier, and G. Bobe, “Metabotypes with elevated protein and lipid catabolism and inflammation precede clinical mastitis in prepartal transition dairy cows,” *Journal of Dairy Science*, vol. 101, no. 6, pp. 5531–5548, 2018.

- [58] L. M. Sordillo, G. A. Contreras, and S. L. Aitken, "Metabolic factors affecting the inflammatory response of periparturient dairy cows," *Animal Health Research Reviews*, vol. 10, no. 1, pp. 53–63, 2009.
- [59] J. Wu, Y. Ding, J. Wang, and F. Wang, "Staphylococcus aureus induces TGF- $\beta$ 1 and bFGF expression through the activation of AP-1 and NF- $\kappa$ B transcription factors in bovine mammary epithelial cells," *Microbial Pathogenesis*, vol. 117, pp. 276–284, 2018.
- [60] I. Ali, M. Yang, Y. Wang et al., "Sodium propionate protect the blood-milk barrier integrity, relieve lipopolysaccharide-induced inflammatory injury and cells apoptosis," *Life Sciences*, vol. 270, article 119138, 2021.
- [61] H. P. Farrell, M. Garvey, M. Cormican, J. G. Laffey, and N. J. Rowan, "Investigation of critical inter-related factors affecting the efficacy of pulsed light for inactivating clinically relevant bacterial pathogens," *Journal of Applied Microbiology*, vol. 108, no. 5, pp. 1494–1508, 2010.
- [62] E. Gayán, D. García-Gonzalo, I. Alvarez, and S. Condón, "Resistance of *Staphylococcus aureus* to UV-C light and combined UV-heat treatments at mild temperatures," *International Journal of Food Microbiology*, vol. 172, pp. 30–39, 2014.
- [63] P. Nikolic, P. Mudgil, and J. Whitehall, "The *in vitro* antibacterial effect of permethrin and formaldehyde on *Staphylococcus aureus*," *Microbiology*, vol. 9, no. 8, article e1054, 2020.
- [64] F. B. Gilbert, P. Cunha, K. Jensen et al., "Differential response of bovine mammary epithelial cells to *Staphylococcus aureus* or *Escherichia coli* agonists of the innate immune system," *Veterinary Research*, vol. 44, no. 1, pp. 1–23, 2013.
- [65] E. M. Ibeagha-Awemu, A. E. Ibeagha, S. Messier, and X. Zhao, "Proteomics, genomics, and pathway analyses of *Escherichia coli* and *Staphylococcus aureus* infected milk whey reveal molecular pathways and networks involved in mastitis," *Journal of Proteome Research*, vol. 9, no. 9, pp. 4604–4619, 2010.

## Research Article

# Sodium Butyrate Ameliorates Oxidative Stress-Induced Intestinal Epithelium Barrier Injury and Mitochondrial Damage through AMPK-Mitophagy Pathway

Xin Li <sup>1,2,3,4</sup> Chunchun Wang,<sup>1,2,3,4</sup> Jiang Zhu,<sup>1,2,3,4</sup> Qian Lin,<sup>1,2,3,4</sup> Minjie Yu,<sup>1,2,3,4</sup> Jiashu Wen,<sup>1,2,3,4</sup> Jie Feng,<sup>1,2,3,4</sup> and Caihong Hu <sup>1,2,3,4</sup>

<sup>1</sup>College of Animal Science, Zhejiang University, Hangzhou 310058, China

<sup>2</sup>Key Laboratory of Molecular Animal Nutrition (Zhejiang University), Ministry of Education, China

<sup>3</sup>Key Laboratory of Animal Nutrition and Feed Science (Eastern of China), Ministry of Agriculture and Rural Affairs, China

<sup>4</sup>Key Laboratory of Animal Feed and Nutrition of Zhejiang Province, China

Correspondence should be addressed to Caihong Hu; [chhu@zju.edu.cn](mailto:chhu@zju.edu.cn)

Received 9 November 2021; Revised 3 January 2022; Accepted 12 January 2022; Published 29 January 2022

Academic Editor: Hao Wu

Copyright © 2022 Xin Li et al. This is an open access article distributed under the Creative Commons Attribution License, which permits unrestricted use, distribution, and reproduction in any medium, provided the original work is properly cited.

Sodium butyrate has gained increasing attention for its vast beneficial effects. However, whether sodium butyrate could alleviate oxidative stress-induced intestinal dysfunction and mitochondrial damage of piglets and its underlying mechanism remains unclear. The present study used a hydrogen peroxide- ( $H_2O_2$ -) induced oxidative stress model to study whether sodium butyrate could alleviate oxidative stress, intestinal epithelium injury, and mitochondrial dysfunction of porcine intestinal epithelial cells (IPEC-J2) in AMPK-mitophagy-dependent pathway. The results indicated that sodium butyrate alleviated the  $H_2O_2$ -induced oxidative stress, decreased the level of reactive oxygen species (ROS), increased mitochondrial membrane potential (MMP), mitochondrial DNA (mtDNA), and mRNA expression of genes related to mitochondrial function, and inhibited the release of mitochondrial cytochrome c (Cyt c). Sodium butyrate reduced the protein expression of recombinant NLR family, pyrin domain-containing protein 3 (NLRP3) and fluorescein isothiocyanate dextran 4 kDa (FD4) permeability and increased transepithelial resistance (TER) and the protein expression of tight junction. Sodium butyrate increased the expression of light-chain-associated protein B (LC3B) and Beclin-1, reduced the expression of P62, and enhanced mitophagy. However, the use of AMPK inhibitor or mitophagy inhibitor weakened the protective effect of sodium butyrate on mitochondrial function and intestinal epithelium barrier function and suppressed the induction effect of sodium butyrate on mitophagy. In addition, we also found that after interference with AMPK $\alpha$ , the protective effect of sodium butyrate on IPEC-J2 cells treated with  $H_2O_2$  was suppressed, indicating that AMPK $\alpha$  is necessary for sodium butyrate to exert its protective effect. In summary, these results revealed that sodium butyrate induced mitophagy by activating AMPK, thereby alleviating oxidative stress, intestinal epithelium barrier injury, and mitochondrial dysfunction induced by  $H_2O_2$ .

## 1. Introduction

The intestinal epithelium barrier is known as the important barrier to prevent the invasion of toxins or antigens [1]. Studies have found that oxidative stress is involved in the intestinal barrier impairment of piglets, which mainly refers to the imbalance of reactive oxygen species (ROS) and antioxidant system [2, 3]. Under oxidative stress, the overproduction of ROS can cause lipid peroxidation, protein, and

DNA damage [4]. Multiple studies have shown that dietary sodium butyrate can protect the intestinal barrier of piglets by providing energy for intestinal epithelial cells, anti-inflammation, histone deacetylation, immune regulation [5–7], etc. The *in vivo* rat experiments and *in vitro* intestinal epithelial cell experiments have demonstrated that the protective effects of intestinal barrier function by sodium butyrate are related to its antioxidant capacity [8–10]. Since mitochondria are the main resource of ROS, the antioxidant

effect of sodium butyrate may result from the targeting on mitochondria.

The gut needs a lot of energy to maintain homeostasis, which is mainly supplied by intracellular mitochondria [9, 10]. However, under oxidative stress, mitochondria are not only the main resource of ROS but also an important attack target of it [11]. Impaired mitochondria induced by oxidative stress can produce more than ten times more ROS than the normal mitochondria, which further aggravated mitochondrial damage [12]. In order to block this vicious cycle, the body will selectively remove damaged mitochondria via lysosome degradation, a process called mitophagy [13]. A recent study reported that sodium butyrate can induce mitophagy in Chinese hamster ovary cells [14]. We speculate that the antioxidant effect of sodium butyrate is related to decreasing mitochondrial ROS production and mitophagy.

Adenosine monophosphate-activated protein kinase (AMPK) is a key energy sensor, as well as an important oxidative stress sensor, which exerts an important role in mitochondrial function and mitophagy [15, 16]. AMPK $\alpha$  is the catalytic core of AMPK, and Toyama et al. found that AMPK is activated in cells under energy-deficient situation, as indicated by that AMPK promoted the further recruitment of multiple proteins related to mitochondrial division by phosphorylating the downstream protein mitochondrial fission factor (MFF), thereby causing mitochondrial division [17, 18], which links the energy receptor AMPK with mitochondrial division. It is well known that sodium butyrate is an important energy substance for intestinal epithelial cells and has the functions of alleviating oxidative stress and protecting the intestinal barrier [9, 19]. Mollica et al. have reported that feeding sodium butyrate to insulin-resistant obese mice can increase liver AMPK activity, reduce ROS production, and improve liver mitochondrial function [20]. However, whether sodium butyrate can alleviate oxidative stress and improve mitochondrial function through AMPK remains unclear. Further research is needed to study the mechanism through which sodium butyrate alleviates oxidative stress and improves intestinal barrier function.

Therefore, this experiment utilized an IPEC-J2 cell oxidative stress model by H<sub>2</sub>O<sub>2</sub> to study the effects of sodium butyrate on intestinal barrier injury, mitochondrial function, mitophagy, and the underlying molecular mechanisms.

## 2. Material and Methods

**2.1. Chemicals.** The IPEC-J2 cell was a courtesy from Prof. Yin Yulong, Institute of Subtropical Agriculture, Chinese Academy of Sciences. H<sub>2</sub>O<sub>2</sub> (Sinopharm Group, China), DMEM-F12 medium (Shanghai Yuanpei Biotechnology, China), and fluorescein isothiocyanate dextran 4kDa (FD4) were obtained from Sigma-Aldrich (St. Louis, Missouri, USA). Trypsin (Beyotime Biotechnology, China), phosphate-buffered saline (PBS) (Bozhan Biotechnology, China), penicillin-streptomycin (Solabao Biotechnology, China), fetal bovine serum (Gemini, Australia), CCK-8 kit (Beyotime Biotechnology, China), MitoSpy™ Red CMXRos (Biologend, USA), immunofluorescence fixative (Sevier Biotechnology, China), Triton-X 100 (Sigma-Aldrich, St. Louis,

MO, USA), Glycine (Sinopharm Group, China), DAPI (Beyotime Biotechnology, China), Goat Anti-Mouse IgG Dylight 594 (Earthox, USA), Goat Anti-Mouse IgG Dylight 488 (Earthox, USA), mitochondrial division inhibitor (Mdivi-1) (Selleck, USA), AMPK inhibitor (Compound C, CC) (Selleck, USA), Lipofectamine RNAiMAX, and Lipofectamine 2000 were obtained from Invitrogen (Invitrogen, USA).

**2.2. Experimental Design and Cell Culture.** IPEC-J2 cells were cultured in DMEM-F12 complete medium (10% fetal bovine serum and 1% antibiotics (penicillin and streptomycin)). The culture conditions are 37°C, 5% CO<sub>2</sub>, and 95% humidity in a carbon dioxide incubator, and the medium is changed every 2 days. The IPEC-J2 cell oxidative stress model is constructed by 600  $\mu$ mol/L H<sub>2</sub>O<sub>2</sub> for 8 hours. This study is divided into three experiments. Experiment 1: control group (control), sodium butyrate group (NaB), oxidative stress group (H<sub>2</sub>O<sub>2</sub>), and sodium butyrate+oxidative stress group (NaB+H<sub>2</sub>O<sub>2</sub>); 600  $\mu$ mol/L H<sub>2</sub>O<sub>2</sub> was treated with cells in the H<sub>2</sub>O<sub>2</sub> group and NaB+H<sub>2</sub>O<sub>2</sub> group for 8 hours. The cells in the control group and NaB group were added with the same amount of PBS. Experiment 2: control group (control), oxidative stress group (H<sub>2</sub>O<sub>2</sub>), sodium butyrate+oxidative stress group (NaB+H<sub>2</sub>O<sub>2</sub>), sodium butyrate+oxidative stress+mitophagy inhibitor group (NaB+H<sub>2</sub>O<sub>2</sub>+Mdivi-1), and sodium butyrate+oxidative stress+AMPK signal pathway inhibitor group (NaB+H<sub>2</sub>O<sub>2</sub>+Compound C); 1 hour before adding H<sub>2</sub>O<sub>2</sub> or PBS, mitophagy inhibitor (Mdivi-1, 1  $\mu$ mol/L) or AMPK signaling pathway inhibitor (Compound C, 10  $\mu$ mol/L) was added into cells. Experiment 3: the experiment is divided into six groups: control group (control+siAMPK $\alpha$ ), oxidative stress group (H<sub>2</sub>O<sub>2</sub>), oxidative stress+interference AMPK $\alpha$  (H<sub>2</sub>O<sub>2</sub>+siAMPK $\alpha$ ), sodium butyrate+oxidative stress group (NaB+H<sub>2</sub>O<sub>2</sub>), and sodium butyrate+oxidative stress+interference AMPK $\alpha$  group (NaB+H<sub>2</sub>O<sub>2</sub>+siAMPK $\alpha$ ). The cells in control, H<sub>2</sub>O<sub>2</sub>, and NaB+H<sub>2</sub>O<sub>2</sub> groups were transfected with siControl. And the cells in control+siAMPK $\alpha$ , H<sub>2</sub>O<sub>2</sub>+siAMPK $\alpha$ , and NaB+H<sub>2</sub>O<sub>2</sub>+siAMPK $\alpha$  groups were transfected with siAMPK $\alpha$ .

**2.3. Cell Viability Experiment.** IPEC-J2 cells in logarithmic phase were seeded in a 96-well plate, 10  $\mu$ l of CCK-8 solution was added to each well, incubated at 37°C for 4h, and the absorbance at 450 nm was measured with a microplate reader (FLx800, Bio-Tek Instruments Inc., Winooski, USA). The cell viability is normalized based on the absorbance of cells in the control group.

**2.4. Transepithelial Electrical Resistance (TER) and FD4 Flux of IPEC-J2 Cells in the Transwell System.** According to the previous study, transwell (Corning, NT, USA) is premoistened with DMEM-F12 medium in the incubator for more than 30 minutes before use [21]. After trypsinization of the cells, stop the reaction with fresh medium, centrifuge at 1500 rpm for 5 min, discard the solution and add a certain volume of fresh medium, adjust the cell concentration to 1  $\times$  10<sup>6</sup> cells/ml, add 150  $\mu$ l cells to the upper chamber suspension, add 1.5 ml of fresh medium to the lower chamber,

and place it in a carbon dioxide incubator for culture. Change the fluid every 2 days. According to the previous study, TER was measured by the Millicell-ERS resistance system (Millipore; Bedford, MA) at three different points in each transwell, and the average of the three measured values was actual TER [22]. The TER value measured without inoculation of the cell culture is the blank TER. The cell monolayer TER = (measured TER – Blank TER) × transwell effective membrane area and expressed in ( $\Omega\cdot\text{cm}^2$ ). FD4 (final concentration 1 mg/ml) was added to the upper chamber of transwell, and 50  $\mu\text{l}$  (supplement with the same volume of fresh medium after sampling) was sampled in the lower chamber at 24 hours and 48 hours, to determine the concentration of FD4 and calculate the permeability of the intestinal epithelium barrier FD4 by a fluorescence microplate reader (FLx800, Bio-Tek Instruments Inc., Winooski, USA).

**2.5. Determination of Cellular Antioxidant Capacity and IL-1 $\beta$ .** After cell treatment, add cell lysate, lyse on ice for 10 min, centrifuge at 4°C for 10 min (12000 rpm/min), and take the supernatant for testing. According to the ELISA kit instructions (Nanjing Jiancheng Bioengineering Institute, Jiangsu, China), the activity of superoxide dismutase (SOD) and GSH (glutathione reductase) antioxidant enzymes, the MDA (malondialdehyde) content, and IL-1 $\beta$  content were measured for each sample.

**2.6. Determination of Cellular ROS Level.** Flow cytometry was conducted to determine the cellular ROS level by a ROS-sensitive fluorescence indicator 2',7'-dichlorofluorescein diacetate (DCFH-DA; Sigma-Aldrich) [23]. In brief, the cells in the 2 ml centrifuge were incubated with 1 ml serum-free diluted DCFH-DA (1 : 1000) at 37°C for 30 min in the dark. After washed twice with PBS and resuspended, flow cytometry (BD, USA) was used to detect the cellular ROS. The data was calculated by FlowJo software 10.4 (V 7.6.1).

**2.7. Measurement of Mitochondrial Membrane Potential (MMP).** The mitochondrial membrane potential was measured by mitochondrial membrane potential assay kit (Beyotime Biotechnology, China) according to the previous study [24]. JC-1 monomers (green) can form aggregates (red fluorescence) in the mitochondria with high  $\Delta\Psi\text{m}$ , which cannot form aggregates in the mitochondria with low  $\Delta\Psi\text{m}$ . Briefly, the cells were incubated with JC-1 working solution 37°C for 25 minutes. After washed for three times with PBS, flow cytometry (BD, USA) or a confocal laser microscope (FV1000, Olympus, Japan) was used to detect mitochondrial membrane potential (MMP).

**2.8. mRNA Expression Level Analysis by Quantitative Real-Time PCR (RT-qPCR).** The total RNA extraction was conducted by Trizol according to the manufacturer's instruction (Takara, Japan). After detecting RNA concentration and purity, it is used for cDNA synthesis (Vazyme, Nanjing, China) and then for RT-qPCR according to the manufacturer's instructions (qPCR, master mix, Vazyme, Nanjing, China) as previously described [25]. The primer sequences

are shown in supplementary Table 1. Glyceraldehyde-3-phosphate dehydrogenase (GAPDH) was used as an internal reference gene to calculate the relative expression of each gene, and the data was normalized using the  $2^{-\Delta\Delta\text{Ct}}$  method.

**2.9. Western Blot Experiment.** The western blot experiment was conducted according to the previous study [26]. Total protein extraction and quantification were performed through the RIPA lysis buffer and BCA protein Assay Kit (Beyotime Biotechnology, Shanghai, China). Proteins from the jejunum mucosa were run and isolated through SDS-PAGE. Then, proteins were transferred to a polyvinylidene difluoride membrane. After blocking with 5% defat milk powder at room temperature for one hour, blots were incubated with specific primary antibodies overnight and then with horseradish peroxidase- (HRP-) conjugated secondary antibodies. BeyoECL Moon kit (Beyotime Biotechnology, China) was used to visualize the protein blot. The primary antibodies including  $\beta$ -actin, PINK1, Parkin, Claudin-1, Occludin, ZO-1, LC3B, Beclin-1, and P62 were purchased from Santa Cruz Biotechnology. Cytochrome c, NLRP3, Caspase-1, IL-1 $\beta$ , HRP-conjugated anti-rabbit IgG, and HRP-conjugated anti-mouse IgG antibodies were purchased from HUABIO (Hangzhou, China).

**2.10. Ultrastructure of IPEC-J2 Cell Mitochondria.** Briefly, the IPEC-J2 cells were fixed in 2.5% glutaraldehyde at 4°C overnight and then postfixed with 1% OsO<sub>4</sub>. After dehydration (gradient concentration of ethanol), infiltration (Spurr resin), embedding, ultrathin sectioning (LEICA EM UC7), and staining (uranyl acetate and alkaline lead citrate for 5 to 10 minutes, respectively), the samples were observed by transmission electron microscope (Hitachi Model H-7650, Tokyo, Japan).

**2.11. Mitochondria Mark by MitoSpy™ Red CMXRos.** MitoSpy™ Mitochondrial Localization Probe (Biolegend, USA) is a cell-permeable fluorescent chemical reagent used to label mitochondria in living cells. According to the manufacturer's instruction, we centrifuge the lyophilized reagent in the centrifuge tube to ensure that the reagent is at the bottom of the vial, add 94  $\mu\text{l}$  DMSO to each tube, and reconstitute MitoSpy™ Red CMXRos to a concentration of 1 mmol/L with DMSO. The stock solution is diluted in serum-free medium to make MitoSpy™ Red CMXRos working solution. After the cell treatment is over, wash once with warm 1X PBS. Add the diluted MitoSpy™ Red CMXRos solution to living cells and place them in an incubator at 37°C for 20-30 min. Wash the cells twice with warm 1X PBS or medium. Fix the cells with immunofluorescence fixative (4% paraformaldehyde) for 10-20 minutes at room temperature. Wash the cells twice with 1X PBS for subsequent experiments.

**2.12. Immunofluorescence Analysis.** The IPEC-J2 cells were seeded in a laser confocal culture dish. After the indicated treatment, the cells were washed twice with precooled PBS, and go through the steps of fixation, permeabilization (Tritox X-100, Beyotime Biotechnology, Shanghai, China), blocking, primary antibody incubation (Claudin-1, LC3B,

and PINK1), secondary antibody incubation (Dylight-conjugated, Earthox, USA), nuclear staining (DAPI), and sealing. The samples were observed and photographed under a confocal laser microscope (FV1000, Olympus, Japan).

**2.13. siRNA and Cell Transfection.** IPEC-J2 cells were seeded into 6-well plates to grow about 80% confluent. The next day, individual targeted siRNA and plasmid were mixed with Lipofectamine RNAiMAX or Lipofectamine 2000 (Invitrogen, USA). The siRNA sequence is as follows: siAMPK $\alpha$  (5'-GCT GCACCAGAAGTAATTTTT-3') and siControl (5'-UUCUCCGAACGUGUCACG UTT-3'). The RNAiMAX/siRNA mixture was added to IPEC-J2 cells in antibiotic-free medium and cultured for 4-6 h. Medium containing siRNA was refreshed with the general medium. Sodium butyrate and H<sub>2</sub>O<sub>2</sub> were added to the indicated group according to the experimental design. Then, the samples were collected for subsequent experiments.

**2.14. Statistical Analysis.** The experimental data was statistically analyzed using the SPSS 20.0 software. One-way ANOVA was used for test analysis. Turkey method was used for multiple comparisons, and the GraphPad Prism 7.01 software was used for graphing.  $P < 0.05$  indicates significant difference.

### 3. Results

**3.1. Effect of Sodium Butyrate on the Oxidative Stress of IPEC-J2 Cells Treated by H<sub>2</sub>O<sub>2</sub>.** The IPEC-J2 cells were treated with different concentrations of H<sub>2</sub>O<sub>2</sub> (200  $\mu$ mol/L, 400  $\mu$ mol/L, 600  $\mu$ mol/L, 800  $\mu$ mol/L, and 1000  $\mu$ mol/L) for 8 hours, and the cell viability was determined. As shown in Figure 1(a), it was found that H<sub>2</sub>O<sub>2</sub> of 600, 800, and 1000  $\mu$ mol/L significantly reduced cell viability ( $P < 0.05$ ). Cells were treated with 0.25, 0.5, 1, 2, 4, 8, and 16  $\mu$ mol/L sodium butyrate for 24 hours, and it was found that 0.25-2 mmol/L sodium butyrate had no significant effect on cell viability, and more than 4 mmol/L would significantly inhibit cell growth (Figure 1(b)). In addition, the cells were treated with 0.25, 0.5, 1, 2, and 4 mmol/L sodium butyrate, and it was found that 1 mmol/L sodium butyrate could effectively inhibit the decrease in cell viability induced by H<sub>2</sub>O<sub>2</sub> ( $P < 0.05$ ) (Figure 1(c)). Therefore, the follow-up experiments used 600  $\mu$ mol/L H<sub>2</sub>O<sub>2</sub>-induced oxidative stress model and 1 mmol/L sodium butyrate pretreatment. As shown in Figures 1(d)-1(f), compared with the control group, H<sub>2</sub>O<sub>2</sub> treatment significantly reduced the SOD and GSH activities of IPEC-J2 cells ( $P < 0.05$ ) and increased the MDA level ( $P < 0.05$ ); meanwhile, compared with the H<sub>2</sub>O<sub>2</sub> group, sodium butyrate significantly inhibited the decreased activity of SOD and GSH induced by H<sub>2</sub>O<sub>2</sub>, alleviated the increase of MDA level ( $P < 0.05$ ). Similarly, flow cytometry data showed that, in comparison with the control group, sodium butyrate pretreatment significantly inhibited the increase in ROS levels induced by H<sub>2</sub>O<sub>2</sub> ( $P < 0.05$ ) (Figure 1(g)).

**3.2. Effect of Sodium Butyrate on the Mitochondrial Function of IPEC-J2 Cells Treated with H<sub>2</sub>O<sub>2</sub>.** Flow cytometry data showed that compared with the control group, H<sub>2</sub>O<sub>2</sub> significantly increased the proportion of depolarized cells ( $P < 0.05$ ), while sodium butyrate pretreatment reversed the increase in the proportion of depolarized cells induced by H<sub>2</sub>O<sub>2</sub> ( $P < 0.05$ ) (Figure 2(a)). In addition, under laser confocal microscope, we found that compared with the control group, H<sub>2</sub>O<sub>2</sub> reduced the ratio of JC-1 aggregates to monomer ( $P < 0.05$ ), indicating that the mitochondrial membrane potential was reduced, and the sodium butyrate treatment alleviated the decrease of cell mitochondrial membrane potential induced by H<sub>2</sub>O<sub>2</sub> ( $P < 0.05$ ) (Figure 2(b)). By detecting the amount of mitochondrial DNA (mtDNA) (Figure 2(c)) and the mRNA expression level of mitochondrial function-related genes (Figure 2(d)), it was found that compared with the control group, H<sub>2</sub>O<sub>2</sub> treatment significantly reduced the amount of mtDNA and the mRNA expression of mitochondrial function-related gene mitochondrial transcription factor A (TFAM), nuclear respiratory factor-1 (NRF-1), and peroxisomal proliferator-activated receptor-g coactivator-1 $\alpha$  (PGC-1 $\alpha$ ) ( $P < 0.05$ ); sodium butyrate significantly alleviated the reduction of mtDNA and mRNA level of mitochondrial function-related genes induced by H<sub>2</sub>O<sub>2</sub> ( $P < 0.05$ ). Similarly, under the transmission electron microscope, it was observed (Figure 2(e)) that the cells in the H<sub>2</sub>O<sub>2</sub> group showed obvious mitochondrial swelling, mitochondrial crista breakage, and mitochondrial vacuolization; sodium butyrate significantly improved the ultrastructure of mitochondria. As shown in Figure 2(f), compared with the control group, H<sub>2</sub>O<sub>2</sub> increased the level of cytochrome c (Cyt c) in the cytoplasm ( $P < 0.05$ ) and decreased the level of Cyt c in the mitochondria ( $P < 0.05$ ), suggesting that H<sub>2</sub>O<sub>2</sub> increased the permeability of the inner and outer mitochondrial membranes and resulted in the release of mitochondrial Cyt c into the cytoplasm, indicating that the mitochondrial function is damaged; compared with the H<sub>2</sub>O<sub>2</sub> group, sodium butyrate alleviated the release of mitochondrial Cyt c caused by H<sub>2</sub>O<sub>2</sub> ( $P < 0.05$ ), indicating that sodium butyrate treatment can help improve mitochondrial function under oxidative stress.

**3.3. Effect of Sodium Butyrate on Inflammasome and Inflammatory Factors of IPEC-J2 Cells Treated with H<sub>2</sub>O<sub>2</sub>.** As shown in Figures 3(a)-3(c), compared with the control group, H<sub>2</sub>O<sub>2</sub> significantly increased the mRNA level and protein level of NLRP3, Caspase-1, and IL-1 $\beta$  in IPEC-J2 cells ( $P < 0.05$ ) and increased the content of IL-1 $\beta$  ( $P < 0.05$ ); compared with the H<sub>2</sub>O<sub>2</sub> group, sodium butyrate significantly reduced the mRNA level and protein expression of NLRP3, Caspase-1, and IL-1 $\beta$  ( $P < 0.05$ ) and reduced the content of IL-1 $\beta$  ( $P < 0.05$ ).

**3.4. Effect of Sodium Butyrate on the Intestinal Epithelium Barrier Function of IPEC-J2 Cells Treated with H<sub>2</sub>O<sub>2</sub>.** As shown in Figure 4(a), compared with the control group, H<sub>2</sub>O<sub>2</sub> significantly reduced TER ( $P < 0.05$ ) and increased the flux of FD4 ( $P < 0.05$ ). Compared with the H<sub>2</sub>O<sub>2</sub>

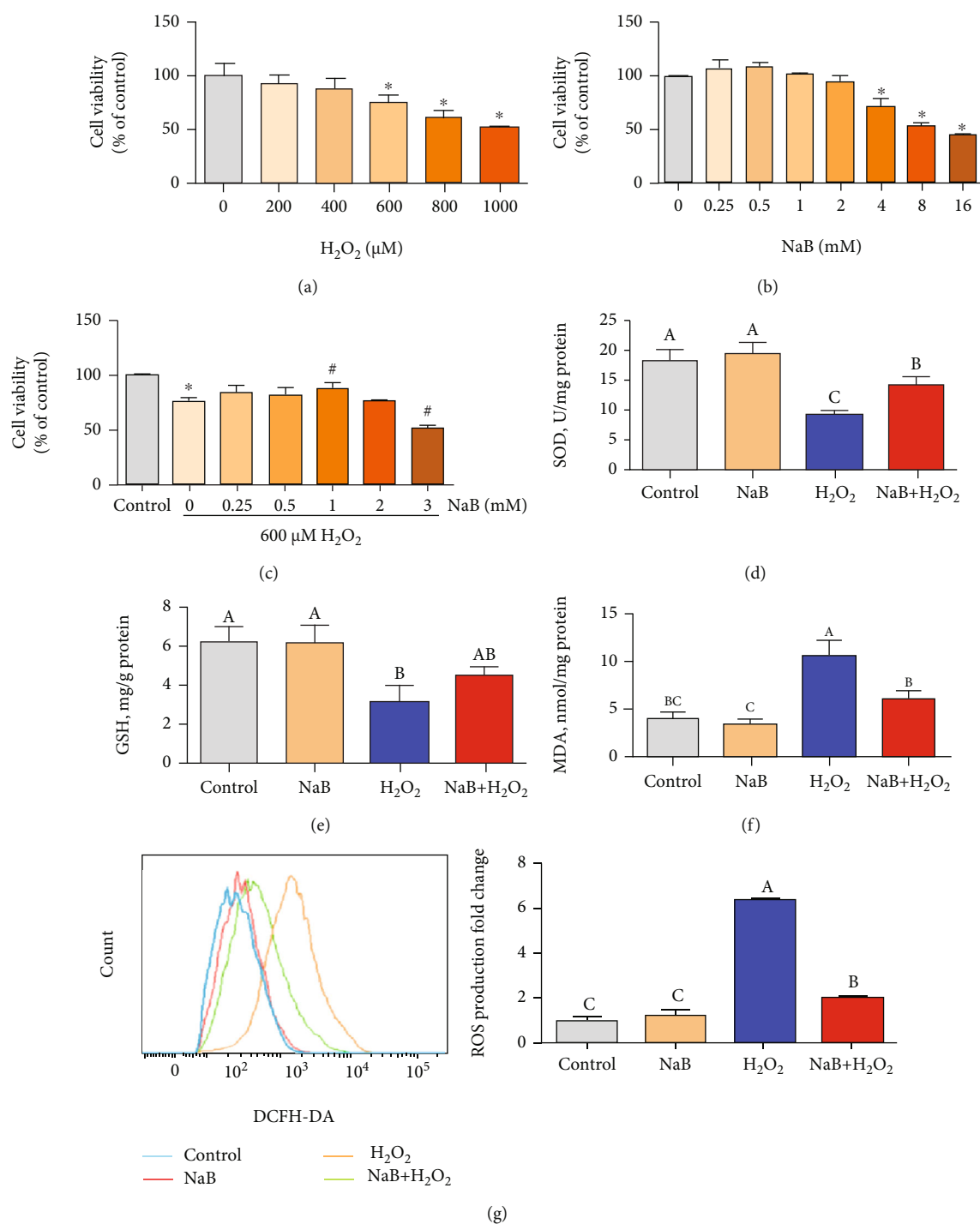
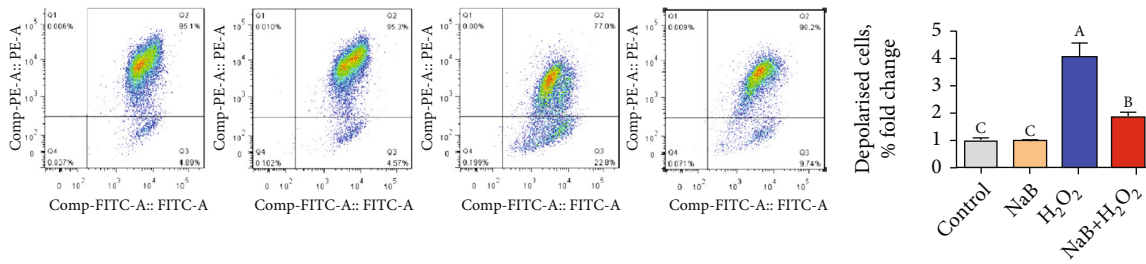


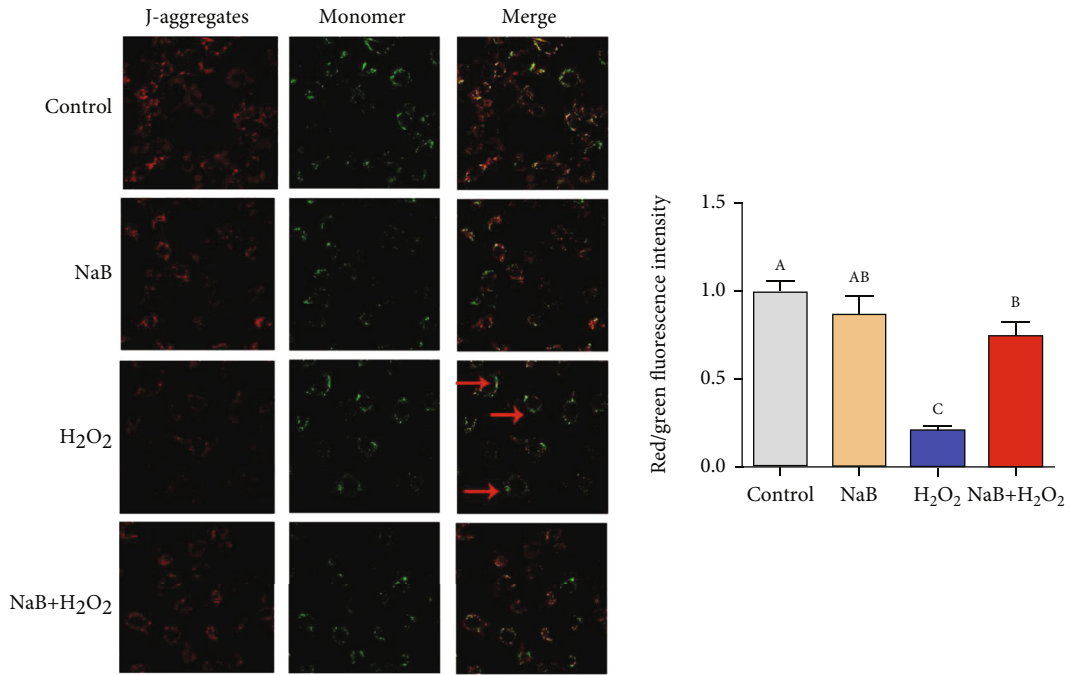
FIGURE 1: Effects of sodium butyrate (NaB) on the oxidative stress of porcine intestinal epithelial cells (IPEC-J2) treated by hydrogen peroxide (H<sub>2</sub>O<sub>2</sub>). (a–c) The effect of different concentrations of H<sub>2</sub>O<sub>2</sub> and NaB on cell viability. (d–f) Cell superoxide dismutase (SOD), glutathione reductase (GSH) activity, and malondialdehyde (MDA) level. (g) Flow cytometry to quantify the reactive oxygen species (ROS) level of IPEC-J2 cells. Different superscript letters within the same row mean significant difference ( $P < 0.05$ ). \* and # mean significant differences ( $P < 0.05$ ) with the control group.

group, sodium butyrate pretreatment significantly alleviated the H<sub>2</sub>O<sub>2</sub>-induced decrease in TER and the increase in FD4 flux ( $P < 0.05$ ). In comparison with the control group, H<sub>2</sub>O<sub>2</sub> significantly reduced the expression of Claudin-1, Occludin, and ZO-1 of IPEC-J2 cells ( $P < 0.05$ );

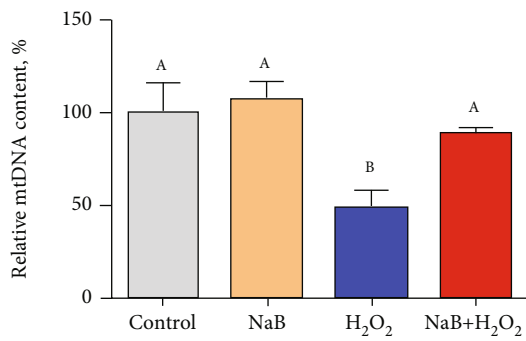
compared with the H<sub>2</sub>O<sub>2</sub> group, sodium butyrate pretreatment significantly increased the protein expression of Claudin-1, Occludin, and ZO-1 in IPEC-J2 cells ( $P < 0.05$ ) (Figure 4(b)). As shown in Figure 4(c), the Claudin-1 protein of IPEC-J2 cells in the control group is mainly



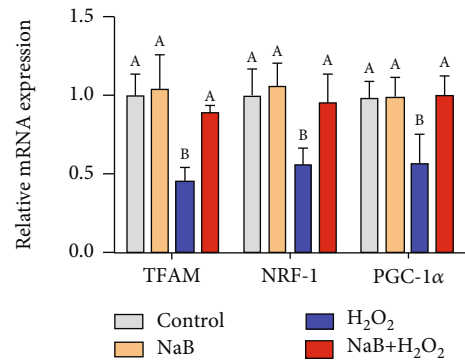
(a)



(b)



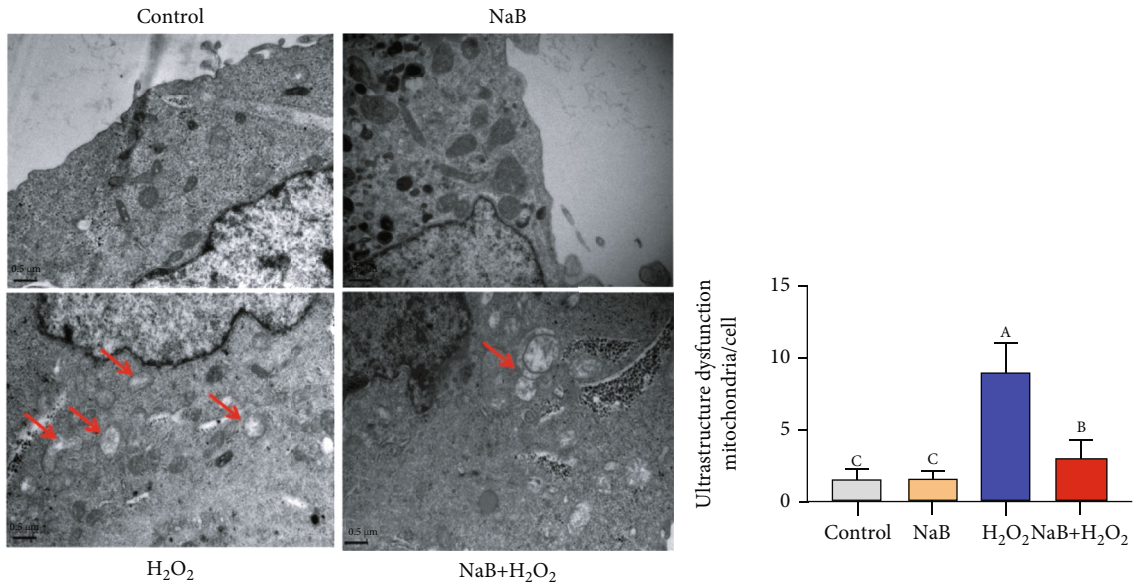
(c)



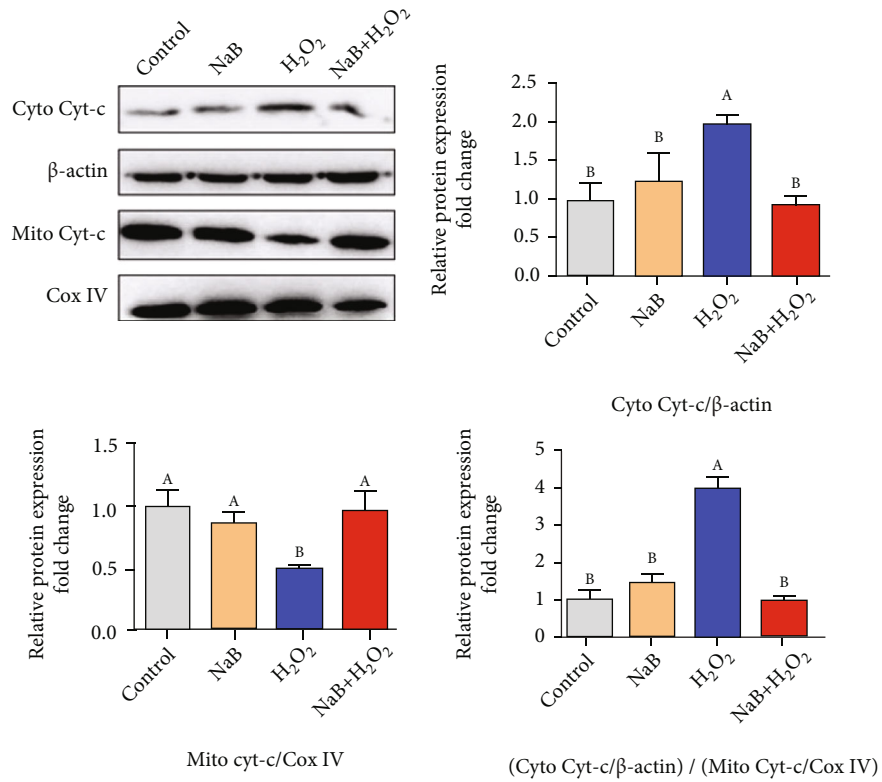
(d)

FIGURE 2: Continued.





(e)



(f)

FIGURE 2: Effects of sodium butyrate (NaB) on the mitochondrial function of porcine intestinal epithelial cells (IPEC-J2) treated with H<sub>2</sub>O<sub>2</sub>. (a) Flow cytometry to detect changes in cell mitochondrial membrane potential. (b) The ratio of red to green of mitochondria JC-1 under a laser confocal microscope and quantification results. (c, d) Mitochondrial DNA (mtDNA) content and mitochondrial transcription factor A (TFAM), nuclear respiratory factor-1 (NRF-1), and peroxisomal proliferator-activated receptor-g coactivator-1 $\alpha$  (PGC-1 $\alpha$ ) gene expression. (e) Ultrastructure of mitochondria under a transmission electron microscope (TEM). (f) Protein expression and quantification of cytochrome c. Different superscript letters within the same row mean significant difference ( $P < 0.05$ ).

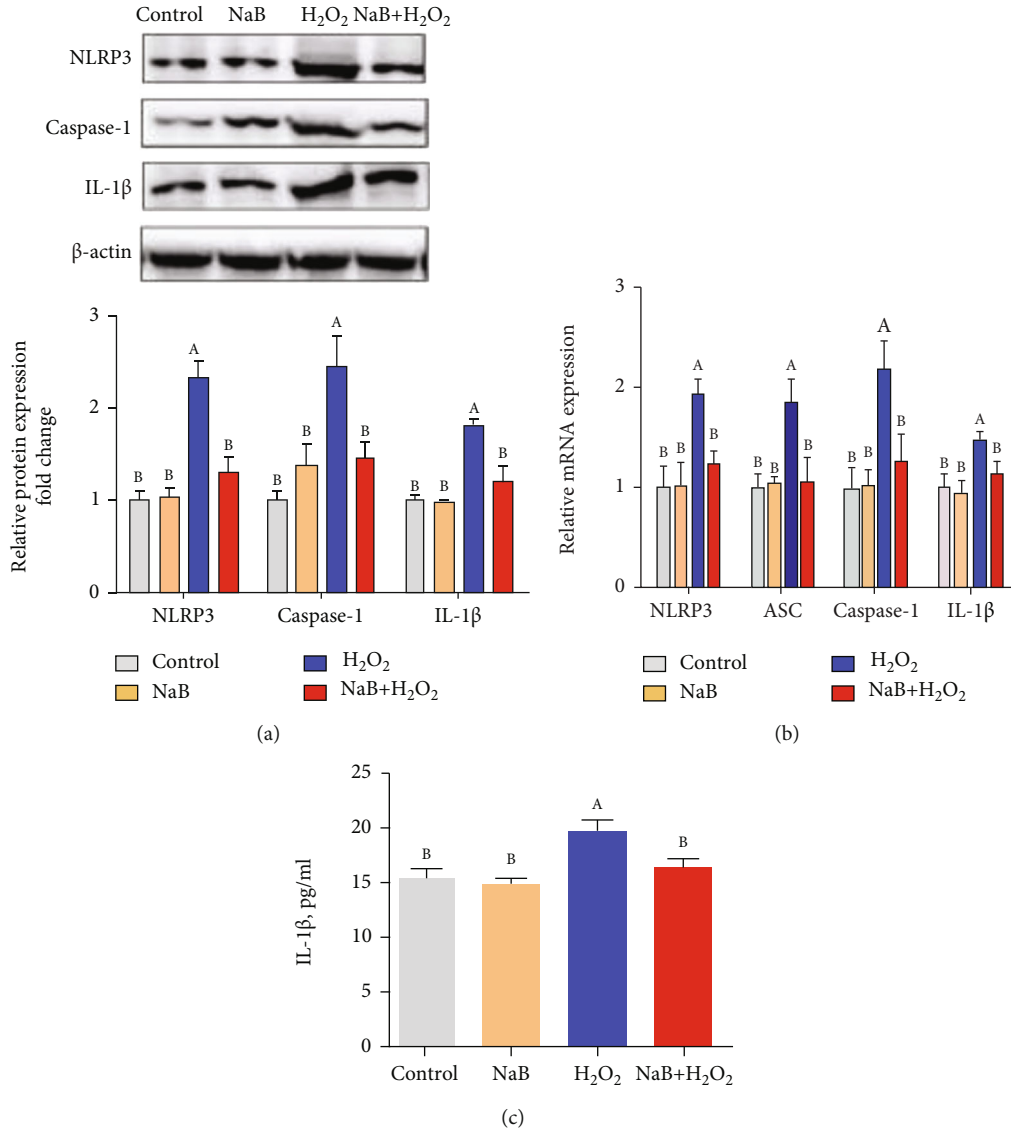


FIGURE 3: Effects of sodium butyrate (NaB) on H<sub>2</sub>O<sub>2</sub> treatment of porcine intestinal epithelial cell (IPEC-J2) inflammasome and inflammatory factors. (a) Protein expression and quantification of recombinant NLR family, pyrin domain-containing protein 3 (NLRP3), Caspase-1, and IL-1β. (b) Relative gene expression of NLRP3, Caspase-1, ASC, and IL-1β. (c) The content of IL-1β in IPEC-J2 cells. Different superscript letters within the same row mean significant difference ( $P < 0.05$ ).

distributed near the cell membrane and forms a continuous ring around the cell membrane; but compared with the control group, the H<sub>2</sub>O<sub>2</sub> treatment destroyed the normal distribution and expression of Claudin-1 ( $P < 0.05$ ). The sodium butyrate pretreatment prevented the disorder of Claudin-1 distribution at the cell boundary and the decrease of protein expression caused by H<sub>2</sub>O<sub>2</sub> ( $P < 0.05$ ).

**3.5. Effect of Sodium Butyrate on Mitophagy of IPEC-J2 Cells Treated with H<sub>2</sub>O<sub>2</sub>.** As shown in Figures 5(a)–5(d), compared with the control group, H<sub>2</sub>O<sub>2</sub> significantly increased the mRNA expression of LC3B, Beclin-1, ATG 5, PINK1, and Parkin of IPEC-J2 cells and reduced the mRNA level of P62 ( $P < 0.05$ ). Compared with the H<sub>2</sub>O<sub>2</sub> group, sodium butyrate pretreatment further increased its mRNA level ( $P < 0.05$ ) and reduced the mRNA expression of P62

( $P < 0.05$ ). Similarly, compared with the H<sub>2</sub>O<sub>2</sub> group, sodium butyrate pretreatment further increased the protein expression of PINK1, Parkin, LC3B, and Beclin-1 ( $P < 0.05$ ) and decreased the expression of P62 ( $P < 0.05$ ). According to the immunofluorescence results (Figure 5(e)), we found that compared with the control group, H<sub>2</sub>O<sub>2</sub> significantly increased the fluorescence intensity of LC3B of IPEC-J2 cells ( $P < 0.05$ ); compared with the H<sub>2</sub>O<sub>2</sub> group, sodium butyrate pretreatment further increased LC3B fluorescence intensity ( $P < 0.05$ ). As shown in Figure 5(f), the results of confocal microscopy showed that under oxidative stress, sodium butyrate promotes the colocalization of LC3B and mitochondria and also increases the colocalization of PINK1, Parkin, and LC3B (Figures 5(g) and 5(h)). Similarly, according to the transmission electron microscope (TEM) results, we also observed the increase of mitophagy vesicles under

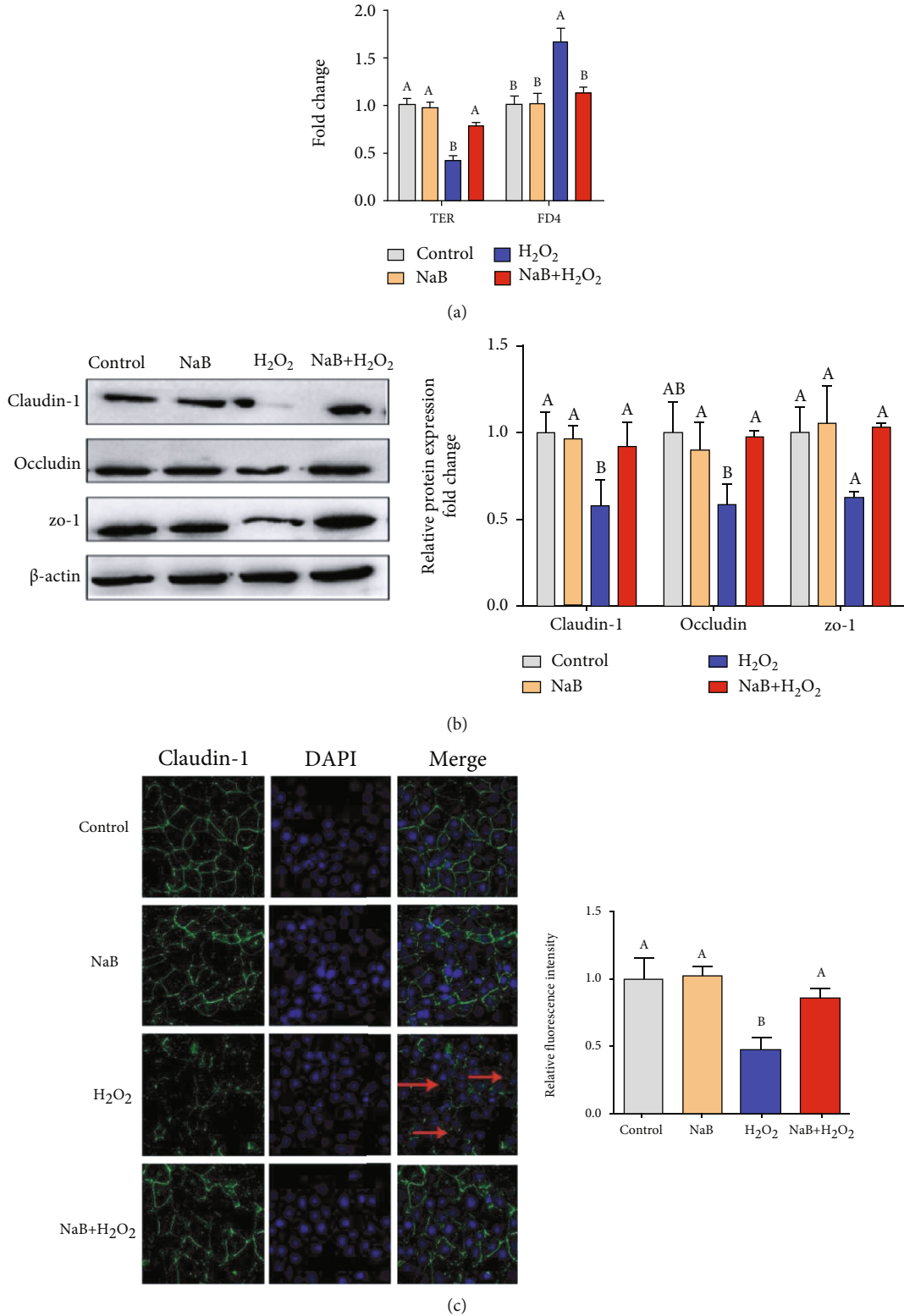


FIGURE 4: Effects of sodium butyrate (NaB) on the barrier function of porcine intestinal epithelial cells (IPEC-J2) treated with hydrogen peroxide (H<sub>2</sub>O<sub>2</sub>). (a) Intestinal epithelial transepithelial resistance (TER) and fluorescein isothiocyanate dextran 4 kDa (FD4) permeability. (b) Protein expression and quantification of Claudin-1, Occludin, and ZO-1. (c) The distribution and quantification of Claudin-1 protein under a confocal microscope. Different superscript letters within the same row mean significant difference ( $P < 0.05$ ).

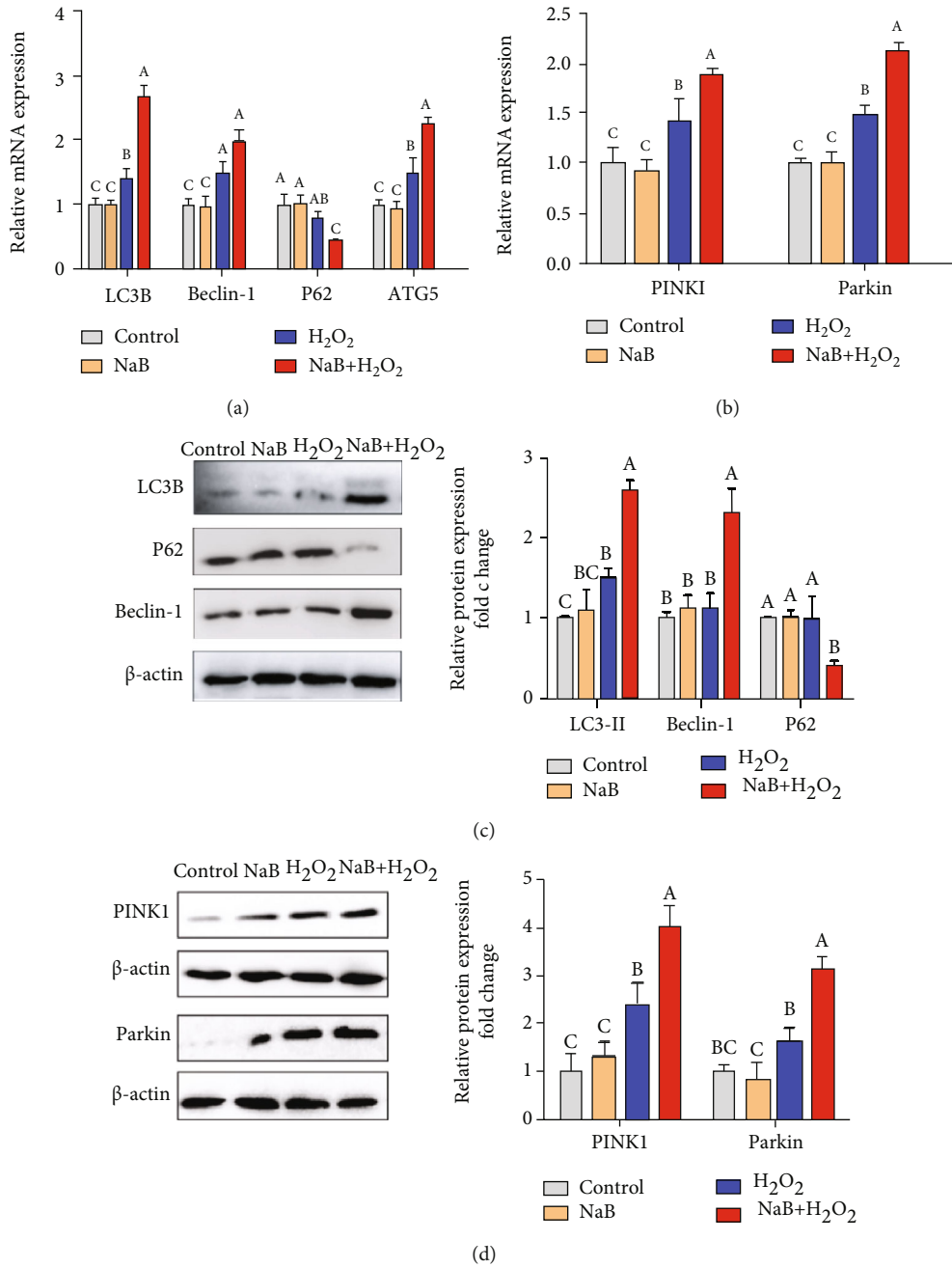
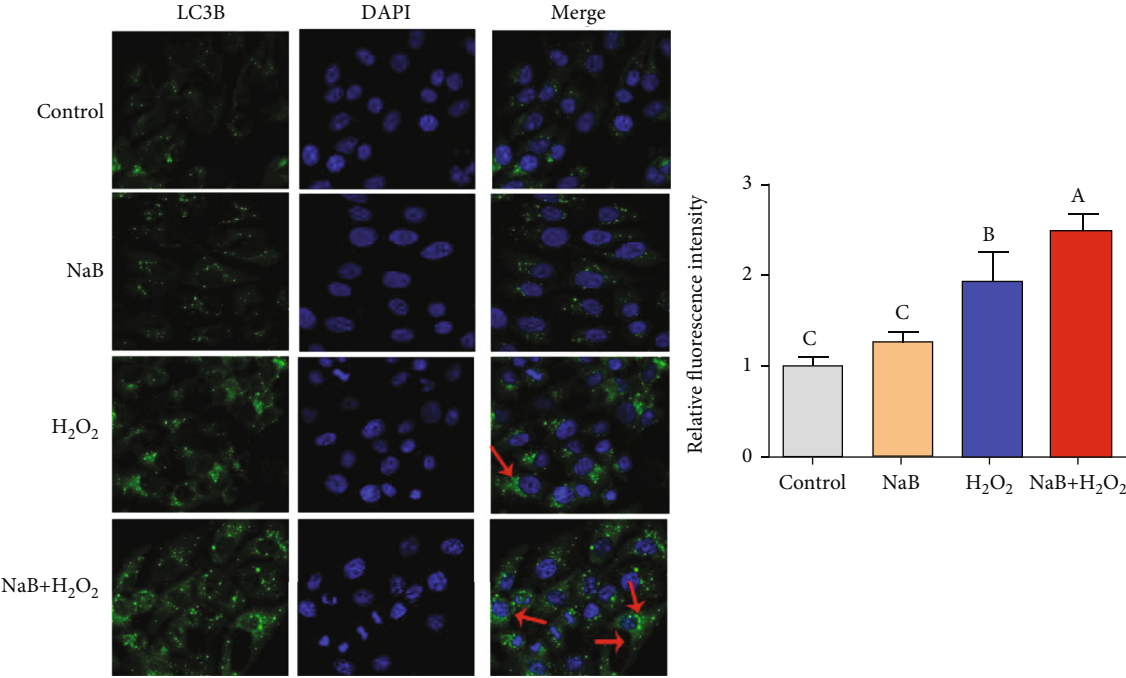
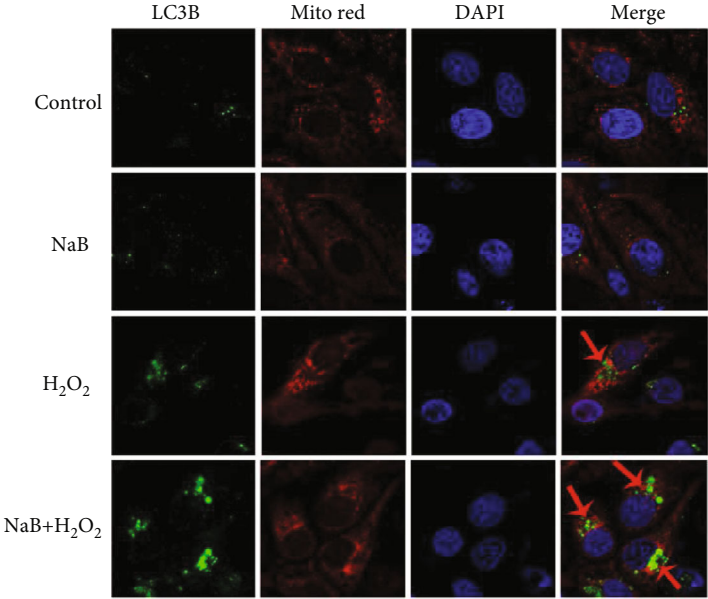


FIGURE 5: Continued.

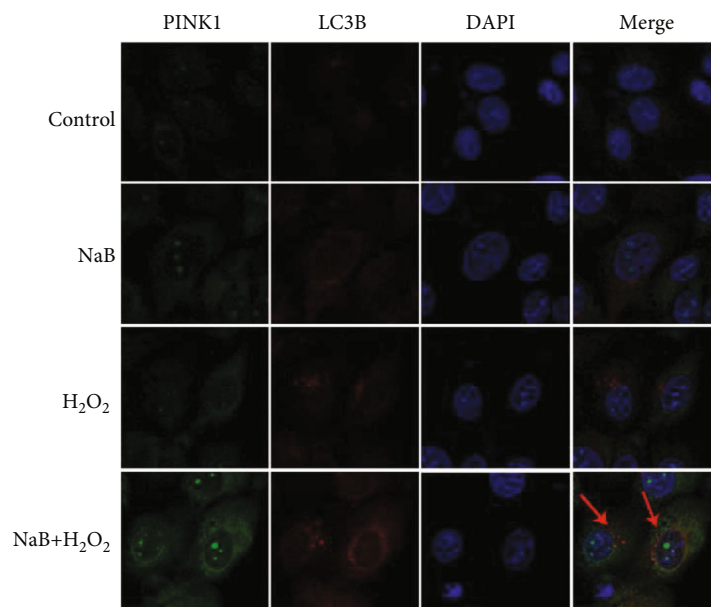


(e)

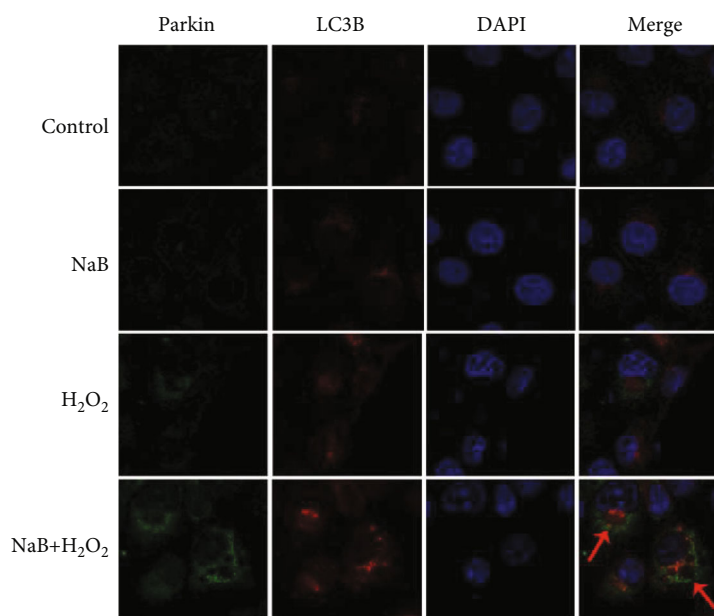


(f)

FIGURE 5: Continued.



(g)



(h)

FIGURE 5: Continued.

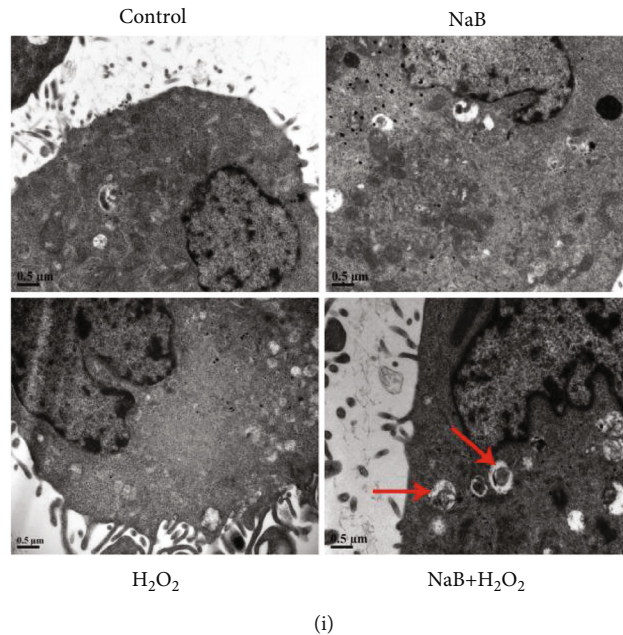


FIGURE 5: Effects of sodium butyrate (NaB) on mitophagy of porcine intestinal epithelial cells (IPEC-J2) treated with H<sub>2</sub>O<sub>2</sub>. (a, b) mRNA expression level of autophagy-related genes. (c, d) Western blot of autophagy-related protein expression and quantification. (e) The protein expression and quantification of light-chain-associated protein B (LC3B) under a laser confocal microscope. (f) Colocalization of mitochondrial Mito Red and autophagy protein LC3B under a laser confocal microscope. (g) Colocalization of mitophagy proteins PINK1 and LC3B under a laser confocal microscope. (h) Colocalization of mitophagy proteins Parkin and LC3B under a laser confocal microscope. (i) Mitophagy vesicles under transmission electron microscope. Different superscript letters within the same row mean significant difference ( $P < 0.05$ ).

the cotreatment of sodium butyrate and H<sub>2</sub>O<sub>2</sub> (Figure 5(i)). These results indicate that sodium butyrate promotes mitophagy in H<sub>2</sub>O<sub>2</sub>-treated IPEC-J2 cells.

**3.6. The Effect of Sodium Butyrate on Oxidative Stress, Intestinal Epithelium Barrier, and Mitophagy of IPEC-J2 Cells after Inhibition of Mitophagy or AMPK $\alpha$ .** As shown in Figures 6(a)–6(c), in comparison with the H<sub>2</sub>O<sub>2</sub> group, sodium butyrate increased the SOD activity ( $P < 0.05$ ) and decreased the MDA level ( $P < 0.05$ ). Compared with the NaB+H<sub>2</sub>O<sub>2</sub> group, Mdivi-1 or Compound C treatment increased the MDA level ( $P < 0.05$ ) and inhibited the SOD activity ( $P < 0.05$ ). These results indicate that inhibition of mitophagy and AMPK $\alpha$  weakens the antioxidant effect of sodium butyrate. As shown in Figure 6(d), compared with the NaB+H<sub>2</sub>O<sub>2</sub> group, Mdivi-1 and Compound C treatments significantly increased ( $P < 0.05$ ) the percentage of depolarized cells (reflecting the decrease in mitochondrial membrane potential). Compared with the NaB+H<sub>2</sub>O<sub>2</sub> group, Mdivi-1 and Compound C treatments significantly increased the ROS levels of IPEC-J2 cells ( $P < 0.05$ ) (Figure 6(e)). These results indicate that inhibition of mitophagy or AMPK $\alpha$  weakens the protective effects of sodium butyrate on mitochondria under oxidative stress. As shown in Figures 6(f) and 6(g), compared with the NaB+H<sub>2</sub>O<sub>2</sub> group, Mdivi-1 or Compound C treatment significantly reduced the TER ( $P < 0.05$ ) and increased FD4 ( $P < 0.05$ ). Mdivi-1 or Compound C treatment also reduced the expression of tight junction proteins Claudin-1, Occlu-

din, and ZO-1 ( $P < 0.05$ ). The data indicated that inhibition of mitophagy or AMPK $\alpha$  weakened the protective effects of sodium butyrate on intestinal epithelium barrier function under oxidative stress.

**3.7. The Effect of Sodium Butyrate on the Mitophagy of IPEC-J2 Cells after Inhibiting Mitophagy or AMPK $\alpha$ .** As shown in Figures 7(a) and 7(b), compared with the NaB+H<sub>2</sub>O<sub>2</sub> group, Mdivi-1 or Compound C treatment significantly reduced Beclin-1 levels ( $P < 0.05$ ) and increased P62 levels ( $P < 0.05$ ). Similarly, compared with the NaB+H<sub>2</sub>O<sub>2</sub> group, Mdivi-1 or Compound C treatment also reduced the expression levels of mitophagy proteins PINK1 and Parkin ( $P < 0.05$ ). Immunofluorescence result showed that inhibition of mitophagy or AMPK $\alpha$  reduced the colocalization of LC3B and mitochondria and reduced the colocalization of PINK1 and LC3B (Figures 7(c) and 7(d)). These results indicate that inhibition of mitophagy and AMPK $\alpha$  suppresses the induction of mitophagy by sodium butyrate.

**3.8. The Effect of Sodium Butyrate on Mitophagy, Oxidative Stress, and Intestinal Epithelium Barrier of IPEC-J2 Cells after Interference with AMPK $\alpha$ .** As shown in Figure 8(a), interference with AMPK $\alpha$  reduced ( $P < 0.05$ ) the protein expression of PINK1 and Parkin and increased the protein expression level of P62 ( $P < 0.05$ ) when compared with the H<sub>2</sub>O<sub>2</sub> group and the NaB+H<sub>2</sub>O<sub>2</sub> group. The results indicated that interference with AMPK $\alpha$  blocked sodium butyrate-induced enhancement of mitophagy. As shown in

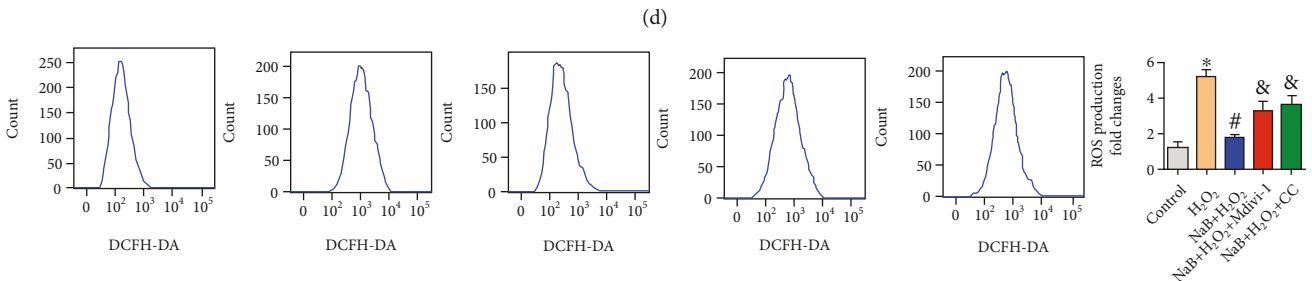
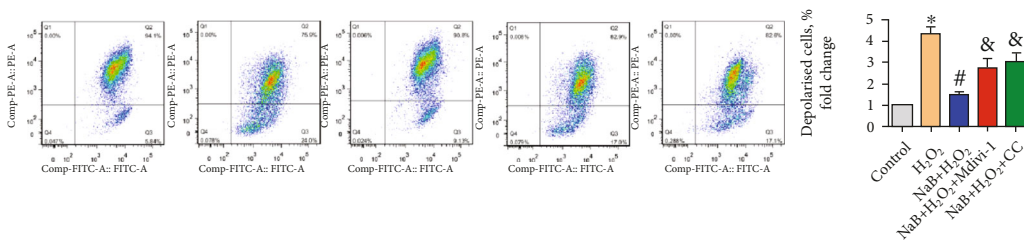
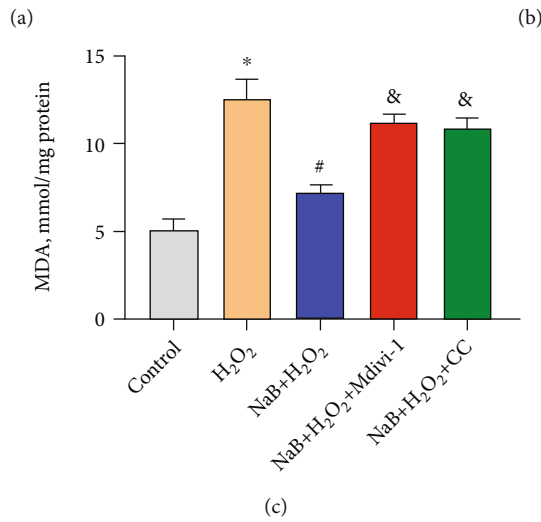
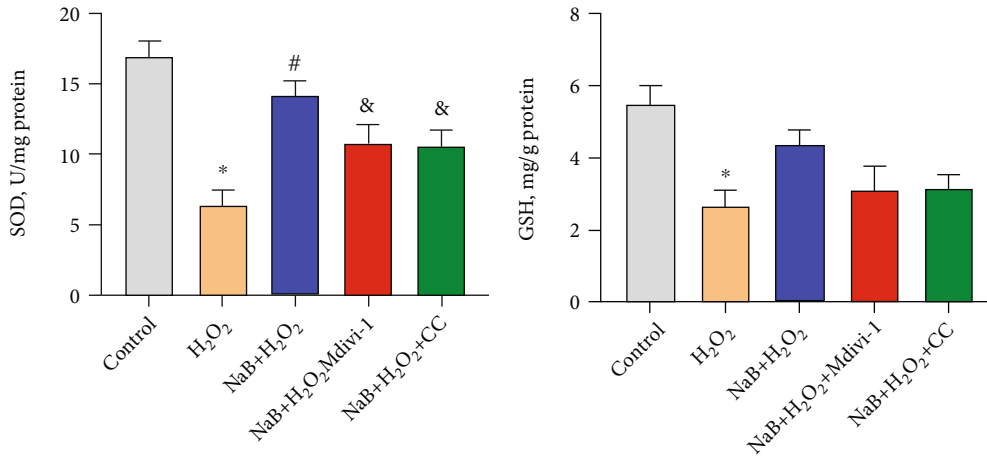


FIGURE 6: Continued.



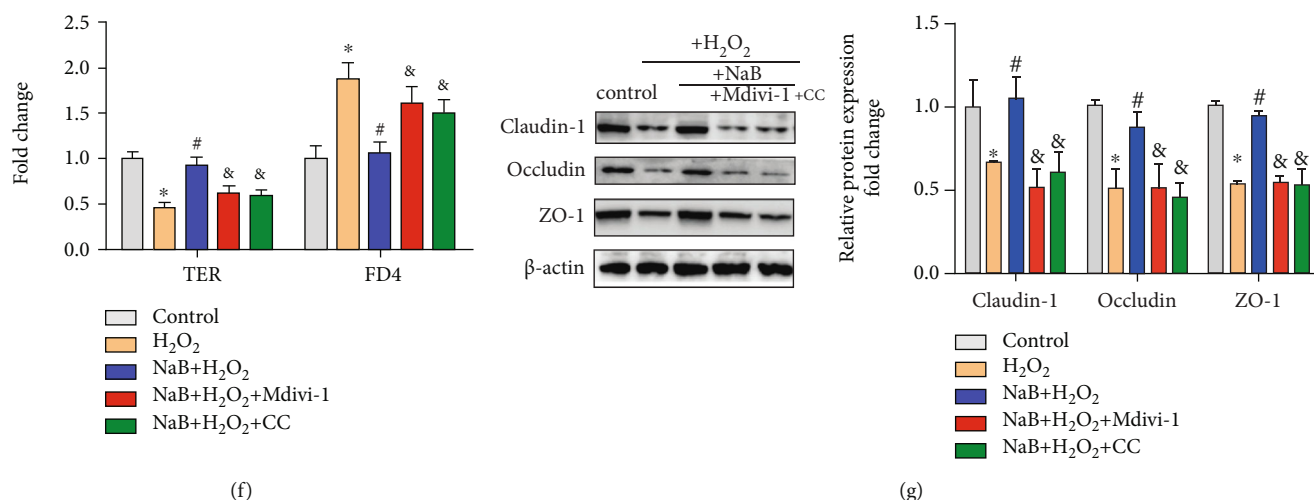


FIGURE 6: Effects of sodium butyrate (NaB) on oxidative stress, intestinal epithelium barrier, and mitophagy of porcine intestinal epithelial cells (IPEC-J2) after inhibiting mitophagy or AMPK. (a–c) Superoxide dismutase (SOD), glutathione reductase (GSH) activity, and malondialdehyde (MDA) content of IPEC-J2 treated with Mdivi-1 or Compound C (CC). (d) Cellular mitochondrial membrane potential quantification by flow cytometry. (e) Cellular reactive oxygen species (ROS) level quantification by flow cytometry. (f) Intestinal epithelial transepithelial resistance (TER) and fluorescein isothiocyanate dextran 4kDa (FD4) permeability. (g) Protein expression and quantification of tight junction Claudin-1, Occludin, and ZO-1. \* indicates a significant difference compared with the control group ( $P < 0.05$ ); # indicates a significant difference compared with the H<sub>2</sub>O<sub>2</sub> group ( $P < 0.05$ ); & indicates a significant difference compared with the NaB+H<sub>2</sub>O<sub>2</sub> group ( $P < 0.05$ ).

Figures 8(b)–8(f), the results showed that interference with AMPK $\alpha$  significantly reduced the activity of SOD and increased the level of MDA ( $P < 0.05$ ) when compared with the NaB+H<sub>2</sub>O<sub>2</sub> group. The interference with AMPK $\alpha$  increased the production of ROS ( $P < 0.05$ ) and decreased the mitochondrial membrane potential ( $P < 0.05$ ) when compared with the H<sub>2</sub>O<sub>2</sub> group and the NaB+H<sub>2</sub>O<sub>2</sub> group, indicating that the role of sodium butyrate on alleviating cellular oxidative stress and mitochondrial dysfunction was counteracted. From the results, it could be concluded that AMPK $\alpha$ -mediated mitophagy is necessary for sodium butyrate's protective effects on cellular redox status and mitochondrial function. As shown in Figures 8(g) and 8(h), interference with AMPK $\alpha$  significantly increased the protein expression of NLRP3 and Caspase-1 when compared with H<sub>2</sub>O<sub>2</sub> and NaB+H<sub>2</sub>O<sub>2</sub> groups ( $P < 0.05$ ), indicating that interference with AMPK $\alpha$  significantly reduced the inhibition of NLRP3 activation by sodium butyrate. At the same time, interference with AMPK $\alpha$  resulted in a decrease in TER ( $P > 0.05$ ) and an increase in FD4 ( $P > 0.05$ ), indicating that interference with AMPK $\alpha$  weakened the protective effect of sodium butyrate on the intestinal epithelium barrier. From the results, it could be concluded that AMPK $\alpha$  is necessary for sodium butyrate to inhibit intestinal inflammation and protect intestinal epithelium barrier of IPEC-J2 cells under oxidative stress.

#### 4. Discussion

Ma et al. reported that sodium butyrate could alleviate the intestinal epithelium barrier damage of IPEC-J2 cells and regulate cellular antioxidant level [8]. So far, no data was found on the effect of sodium butyrate on oxidative stress-

induced intestine damage in IPEC-J2 cells. The present study demonstrated that sodium butyrate protected IPEC-J2 cells from H<sub>2</sub>O<sub>2</sub>-induced oxidative stress, as indicated by the increased SOD and GSH activities and the decreased MDA and ROS level in IPEC-J2 cells. Similarly, Russo et al. found that butyrate could effectively inhibit the decrease of glutathione transferase (GST) activity and the increase of ROS level induced by LPS in Caco-2 cells [27]. Excessive production of ROS would affect the electronic respiration chain of mitochondria, open mitochondrial permeability transition pores, and lead to depolarization of mitochondrial membranes [28]. We found that sodium butyrate alleviated H<sub>2</sub>O<sub>2</sub>-induced decrease in mitochondrial membrane potential (MMP), as indicated by the decreased proportion of depolarized cells and the increased ratio of red (JC-1 polymer)/green (JC-1 polymer) fluorescence intensity when compared with the H<sub>2</sub>O<sub>2</sub> group. Consistent with our research, Li et al. reported that sodium butyrate inhibited LPS-induced MMP loss of bovine mammary epithelial cells [29]. Increased ROS production in mitochondria and decreased MMP in mitochondria can lead to mitochondrial DNA damage, which could be related to abnormal mitochondrial biogenesis [28]. We found that sodium butyrate alleviated mitochondrial dysfunction by increasing mtDNA and mRNA expression levels of mitochondrial function-related genes TFAM, NRF-1, and PGC-1 $\alpha$ . Similarly, a previous study found that sodium butyrate alleviated the oxidative damage of HepG2 cells, as indicated by increasing mtDNA copy number and the mRNA expression of PGC-1 $\alpha$  and TFAM [30]. Changes in mitochondrial function will be accompanied by changes in mitochondrial ultrastructure. Our research showed that H<sub>2</sub>O<sub>2</sub> caused obvious mitochondrial swelling, respiratory ridge breakage, and mitochondrial

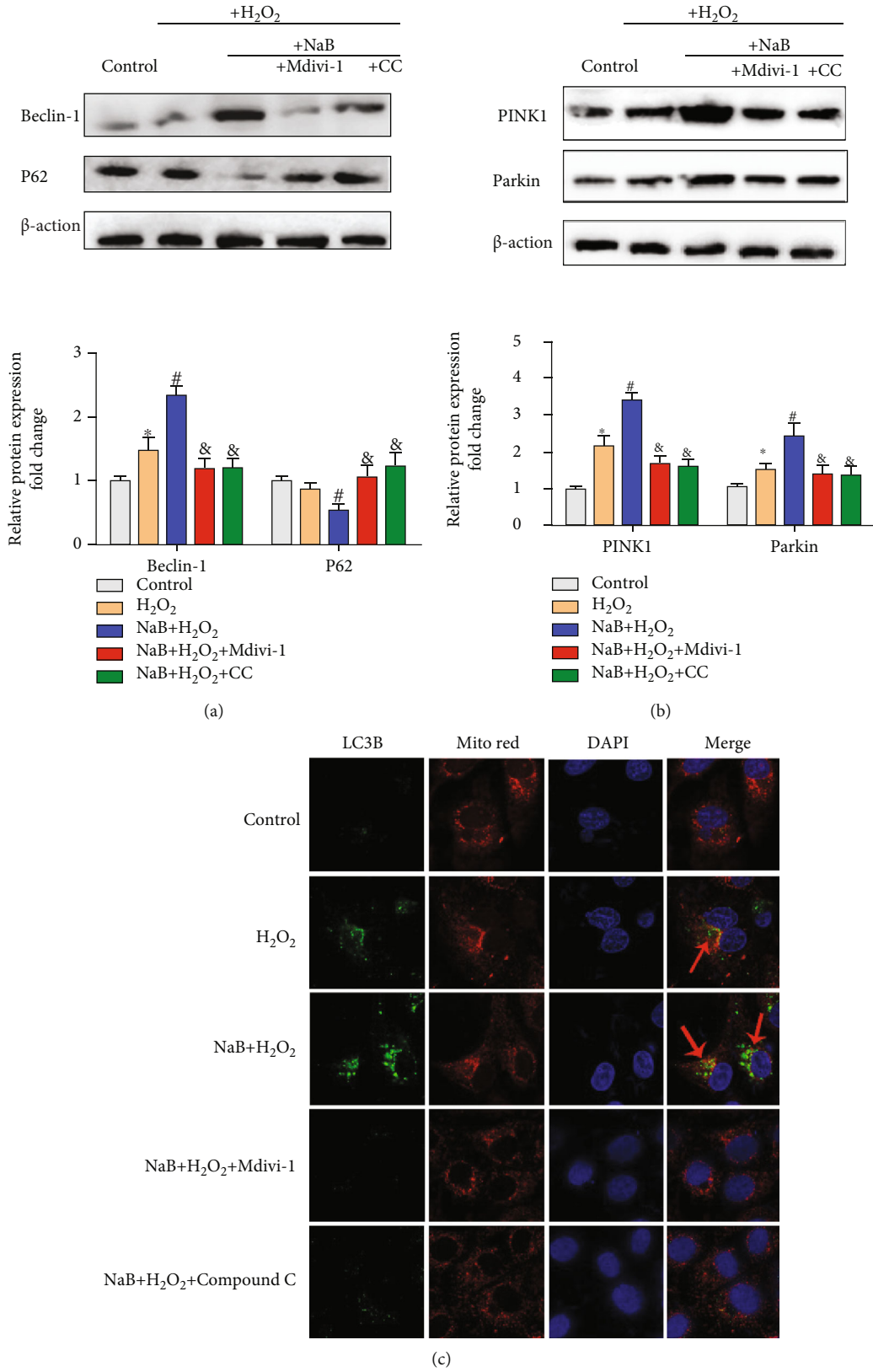


FIGURE 7: Continued.

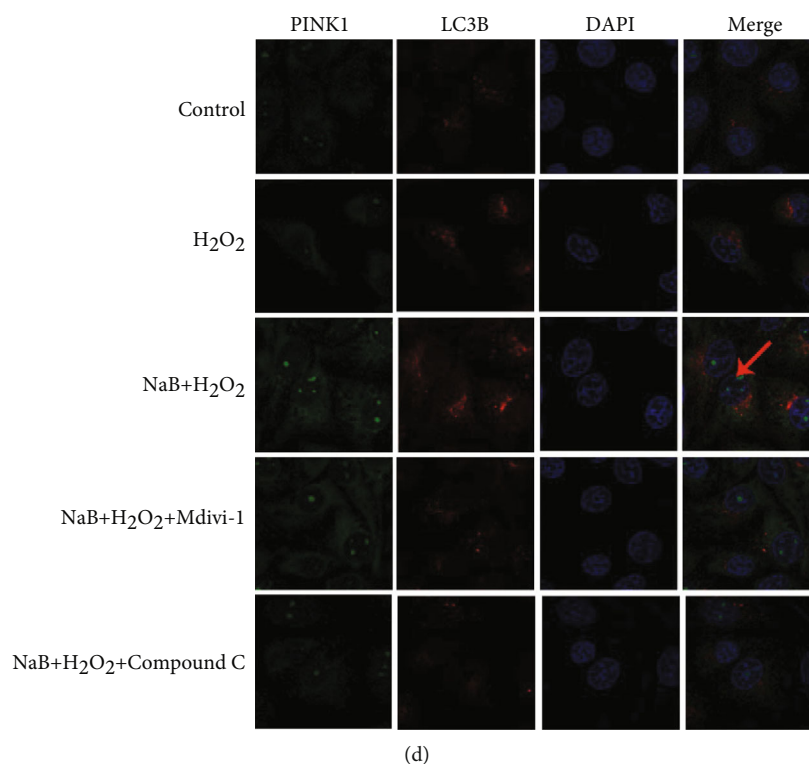


FIGURE 7: Effects of sodium butyrate (NaB) on mitophagy of porcine intestinal epithelial cells (IPEC-J2) after inhibition of mitophagy or AMPK. (a, b) Protein expression and quantification of autophagy protein. (c) Colocalization of mitochondria and light-chain-associated protein B (LC3B) under a laser confocal microscope. (d) Colocalization of mitophagy proteins PINK1 and LC3B under a laser confocal microscope. \* indicates a significant difference compared with the control group ( $P < 0.05$ ); # indicates a significant difference compared with the H<sub>2</sub>O<sub>2</sub> group ( $P < 0.05$ ); & indicates a significant difference compared with the NaB+H<sub>2</sub>O<sub>2</sub> group ( $P < 0.05$ ).

vacuolation while sodium butyrate pretreatment significantly improved the ultrastructure of mitochondria. The changes in the ultrastructure of mitochondria are not only the structural basis of mitochondrial oxidative damage but also lead to the release of Cyt c from mitochondria into the cytoplasm. We found that H<sub>2</sub>O<sub>2</sub> increased Cyt c level in the cytoplasm and decreased Cyt c level in mitochondria, suggesting that H<sub>2</sub>O<sub>2</sub> increased the permeability of the inner and outer mitochondrial membranes, causing the release of mitochondrial Cyt c into the cytoplasm. Meanwhile, sodium butyrate alleviated the release of mitochondrial Cyt c induced by H<sub>2</sub>O<sub>2</sub>, indicating that sodium butyrate treatment could help improve mitochondrial function under oxidative stress. The above results revealed that sodium butyrate could effectively alleviate H<sub>2</sub>O<sub>2</sub>-induced redox status imbalance and mitochondrial impairment.

The intestinal barrier is an important line of defense for the body to prevent harmful substances from invading the body, and maintaining its integrity is vital to the health of the body [31, 32]. We found that sodium butyrate significantly alleviated H<sub>2</sub>O<sub>2</sub>-intestinal epithelium barrier injury of IPEC-J2 cells, as indicated by increasing intestinal epithelium TER and decreasing FD4 permeability. Similarly, Valenzano et al. and Wang et al. found that treatment of Caco-2 cells with a certain concentration of butyric acid could effectively improve the intestinal epithelium barrier [33, 34]. Sodium butyrate also significantly inhibited the

decrease of Claudin-1, Occludin, and ZO-1 in IPEC-J2 cells induced by H<sub>2</sub>O<sub>2</sub>. Consistent with our research, Yan and Ajuwon found that sodium butyrate increased the protein level of Claudin-3 and Claudin-4, thereby alleviating the damage of LPS to the integrity of IPEC-J2 monolayer cells [35]. The integrity of intestinal epithelial cells is not only related to the expression level of tight junction protein but also affected by its distribution area. In our study, we found that after H<sub>2</sub>O<sub>2</sub> treatment, the normal distribution and expression of Claudin-1 were destroyed and sodium butyrate prevented the disorder of Claudin-1 distribution and the decrease of Claudin-1 expression caused by H<sub>2</sub>O<sub>2</sub>. Similarly, studies found that when Caco-2 cells were adversely stimulated, the Occludin and ZO-1 proteins originally expressed on the cell membrane would be transferred to the cytoplasm, thereby increasing cell permeability; however, butyric acid promoted tight junction protein redistribute and increased the expression level of tight junction [9, 36]. These results indicated that sodium butyrate could effectively alleviate the intestinal epithelium barrier damage and the disorder of tight junction protein expression and distribution induced by H<sub>2</sub>O<sub>2</sub> in IPEC-J2 cells.

Oxidative stress could cause intestinal inflammation, as proved by that excessive ROS production in the intestines of patients with ulcerative colitis and Crohn disease weakened antioxidant capacity and aggravated oxidative damage [27]. According to our results, H<sub>2</sub>O<sub>2</sub> increased the mRNA

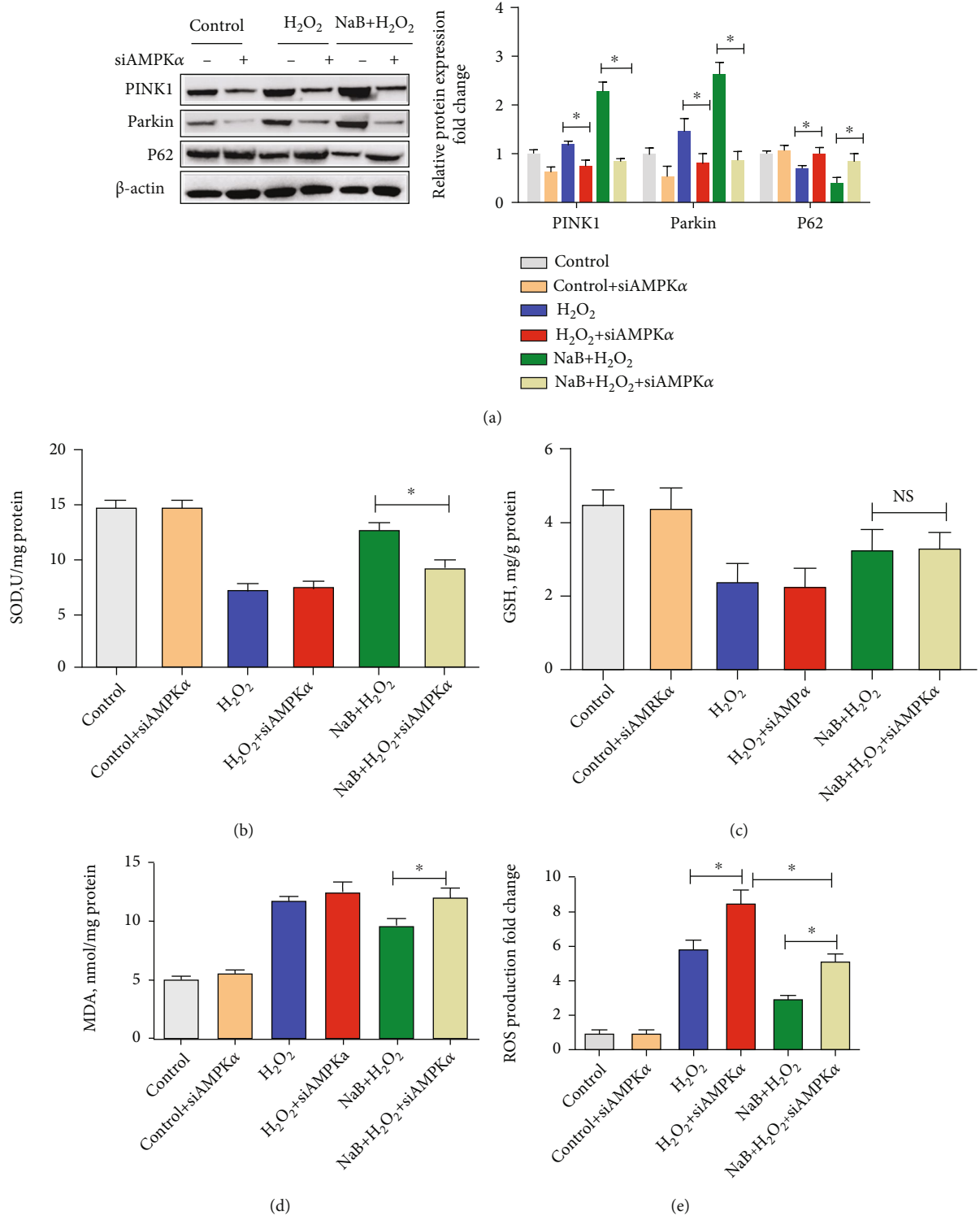


FIGURE 8: Continued.

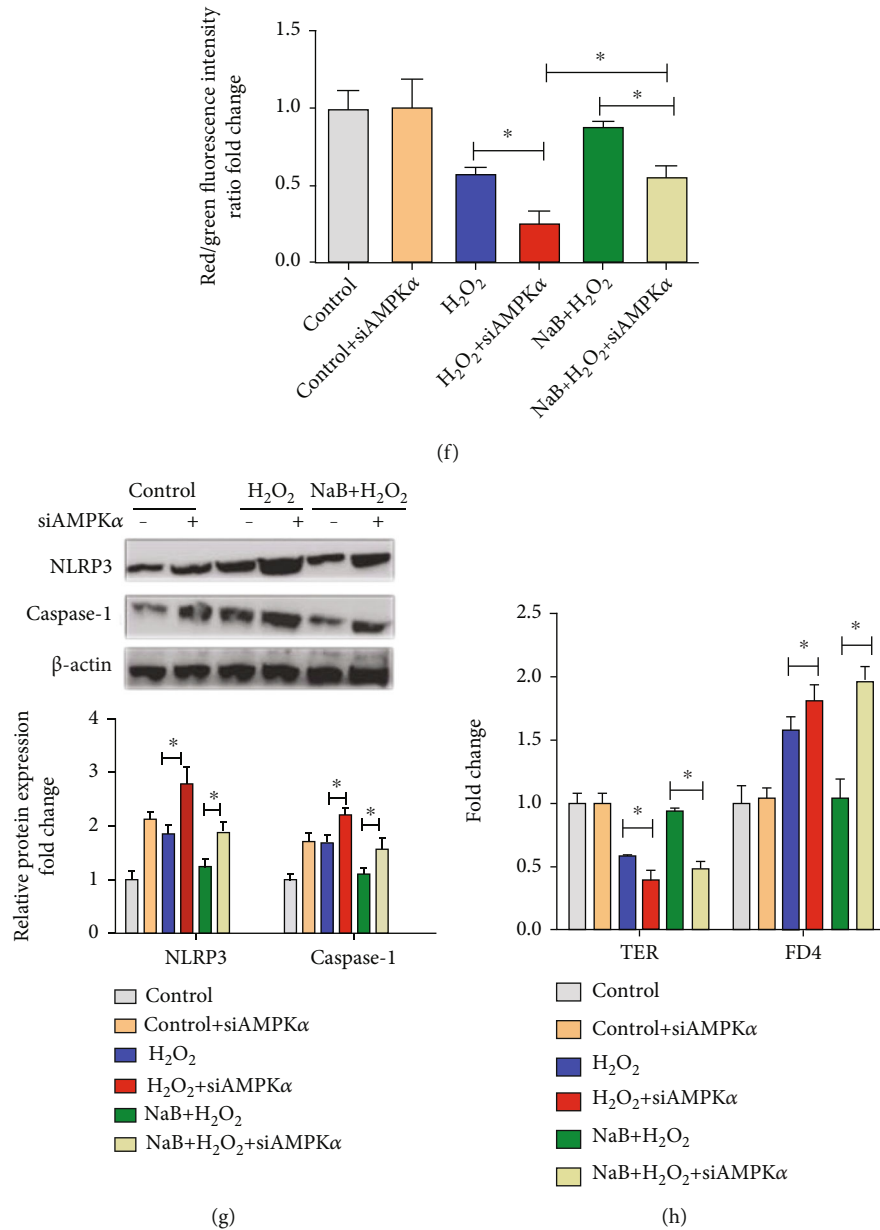


FIGURE 8: Effects of sodium butyrate (NaB) on mitophagy, oxidative stress, and intestinal epithelium barrier after interference with AMPK $\alpha$ . (a) Expression and quantification of mitophagy proteins PINK1, Parkin, and P62. (b–d) Superoxide dismutase (SOD), glutathione reductase (GSH) activity, and malondialdehyde (MDA) content of porcine intestinal epithelial cells (IPEC-J2). (e) Cellular reactive oxygen species (ROS) level of IPEC-J2. (f) Cellular mitochondrial membrane potential of IPEC-J2. (g) Protein expression and quantification of recombinant NLR family, pyrin domain-containing protein 3 (NLRP3) and Caspase-1. (h) Intestinal epithelial transepithelial resistance (TER) and fluorescein isothiocyanate dextran 4 kDa (FD4) permeability. \* indicates a significant difference compared with the control group ( $P < 0.05$ ).

and protein expression of NLRP3, Caspase-1, and IL-1 $\beta$  in IPEC-J2 cells and increased the content of IL-1 $\beta$ , while sodium butyrate pretreatment alleviated this phenomenon. Similarly, NLRP3 inflammasome and IL-1 $\beta$  were activated by H<sub>2</sub>O<sub>2</sub> in rat livers [37]. Jiang et al. also found that in bovine macrophages, sodium butyrate could reduce the inflammatory response caused by LPS by inhibiting the NF- $\kappa$ B and NLRP3 signaling pathways [38]. According to the results, we assumed that sodium butyrate could effec-

tively inhibit the activation of NLRP3 and relieve intestinal inflammation induced by H<sub>2</sub>O<sub>2</sub>.

Mitophagy is a self-protection mechanism to remove dysfunctional mitochondria [39]. However, there were no reports about the effect of sodium butyrate on mitophagy of IPEC-J2 cells. We found that sodium butyrate enhanced mitophagy of IPEC-J2 cells, as indicated by increasing mRNA and protein level of mitophagy protein and promoting the colocalization of LC3B and mitochondria as

well as the colocalization of PINK1, Parkin, and LC3B; meanwhile, we also found that sodium butyrate increased mitophagy vesicles under TEM. Similarly, Zhou et al. found that butyric acid can regulate intestinal epithelial cell autophagy through the HIF-1 $\alpha$  pathway to alleviate colitis [40]. Wang et al. found that sodium butyrate activated the PINK1-Parkin pathway and induced mitophagy [41]. J. S. Lee and G. M. Lee also found that sodium butyrate could induce mitophagy in Chinese hamster ovary (CHO) cells, and mitophagy protein Parkin was recruited to mitochondria, suggesting that sodium butyrate induced mitophagy to remove damaged mitochondria [14]. According to the results above, it was reasonable to assume that sodium butyrate could regulate PINK1 and Parkin and trigger mitophagy to obliterate the damaged mitochondria caused by H<sub>2</sub>O<sub>2</sub>, which could prevent the intestine from metabolism disorders.

In the present experiment, we found that sodium butyrate protected IPEC-J2 cells from H<sub>2</sub>O<sub>2</sub>-induced oxidative damage, intestinal epithelium barrier damage, and mitochondrial impairment and enhanced mitophagy, but its specific molecular mechanism remained to be further studied. AMPK is a key energy sensor that can regulate cell energy metabolism [15]. Mollica et al. have reported that feeding sodium butyrate to insulin-resistant obese mice can increase liver AMPK activity, reduce ROS production, and improve liver mitochondrial function [20]. However, whether sodium butyrate could alleviate oxidative stress of IPEC-J2 cells through AMPK-dependent mitophagy remained to be further explored. Therefore, in the following experiments, we used AMPK inhibitor and mitophagy inhibitor to explore the specific role of AMPK signaling pathway and mitophagy in the protective effects of sodium butyrate on intestinal epithelium barrier. We found that sodium butyrate inhibited the decrease of SOD activity and the increase of MDA level induced by H<sub>2</sub>O<sub>2</sub>. However, the use of mitophagy inhibitor Mdivi-1 or AMPK inhibitor Compound C increased cellular MDA levels and reduced SOD activity. These results indicated that inhibition of mitophagy and AMPK could reduce the antioxidant effect of sodium butyrate. Similarly, Guo et al. found that butyric acid activated the AMPK signaling pathway through GPR109A in bovine mammary epithelial cells (BMECs) and then exerted an antioxidant effect [37]. We found that the ROS level and the percentage of depolarized cells significantly increased after using the mitophagy inhibitor Mdivi-1 or the AMPK inhibitor Compound C. Similarly, Zhao et al. reported that high concentrations of insulin in HepG2 cells could significantly reduce mitochondrial DNA and decrease the mitochondrial membrane potential, while sodium butyrate significantly increased the mitochondrial membrane potential and mitochondrial DNA, which was involved in the GPR43- $\beta$ -AMPK signaling pathway [42]. We also previously reported that tributyrin activated the AMPK-mTOR signaling pathway and improved intestinal mitochondrial function in weaned piglets [25]. These results indicated that inhibition of mitophagy or AMPK $\alpha$  inhibited the protective effects of sodium butyrate on improving mitochondria under oxidative stress of IPEC-J2 cells. In addition, we found that the use of

mitophagy inhibitor Mdivi-1 and AMPK inhibitor Compound C impaired intestinal epithelium barrier function, as indicated by the decreased TER and expression level of tight junction and the increased FD4 permeability of IPEC-J2 cells. Similarly, Elamin et al. reported that sodium butyrate alleviated the barrier dysfunction of Caco-2 cells induced by ethanol *in vitro*, of which the protective effects were suppressed by AMPK inhibitors or siRNA. Miao et al. found that in the Caco-2 cells, sodium butyrate activated AMPK, thereby promoting the reorganization of tight junctions [43]. Therefore, it was reasonable to assume that mitophagy and AMPK were necessary for sodium butyrate to improve the intestinal epithelium barrier under H<sub>2</sub>O<sub>2</sub>-induced oxidative stress. Moreover, we also found that the use of mitophagy inhibitor Mdivi-1 or AMPK inhibitor Compound C inhibited mitophagy, as indicated by decreasing expression level of mitophagy protein and the colocalization of PINK1 and LC3B, suggesting that inhibition of mitophagy or AMPK could suppress the mitophagy induced by sodium butyrate. In accordance with our results, Evans et al. found that butyrate induced autophagy-dependent cell apoptosis of human gingival epithelial cell Ca9-22 to alleviate periodontal disease, as indicated by activating AMPK and inducing the production of LC3B, which was attenuated by AMPK inhibition; in addition, interference with LC3B gene could also significantly inhibit butyrate-induced cell death [44]. Hence, AMPK-mediated mitophagy is necessary for sodium butyrate's protective effects against oxidative stress.

In order to further confirm the role of AMPK in sodium butyrate-induced mitophagy of IPEC-J2 cells, we then used siRNA technology to knock down AMPK $\alpha$ , which was known as the dominating AMPK catalytic subunit. We found that interference with AMPK $\alpha$  reduced the expression level of PINK1 and Parkin and increased the level of P62 when compared with the H<sub>2</sub>O<sub>2</sub> group and the NaB+H<sub>2</sub>O<sub>2</sub> group. Similarly, Luo et al. found that sodium butyrate increased the mRNA and protein expression level of LC3B and activated phosphorylated AMPK, which was suppressed by treatment with siRNA AMPK in colorectal cancer cells [45]. These results indicated that AMPK $\alpha$  can mediate the mitophagy induced by sodium butyrate. Next, we found that interference with AMPK $\alpha$  significantly increased the level of MDA and ROS production and decreased MMP, indicating that the protective effects of sodium butyrate on alleviating cellular oxidative stress and mitochondrial dysfunction were weakened. In addition, interference with AMPK $\alpha$  significantly increased the protein expression of NLRP3 and Caspase-1 in IPEC-J2 cells, indicating that interference with AMPK $\alpha$  weakened the inhibition effect of sodium butyrate on NLRP3 inflammation factors. At the same time, interference with AMPK $\alpha$  impaired intestinal epithelium barrier function, as indicated by decreasing TER and increasing FD4 permeability of IPEC-J2 cells, suggesting that interference AMPK $\alpha$  weakened the protective effects of sodium butyrate on the intestinal epithelium barrier. Our results suggested that sodium butyrate could promote mitophagy via AMPK activation, protect mitochondria, and exert a protective effect on intestinal epithelium barrier of IPEC-J2 cells under oxidative stress.

## 5. Conclusion

In conclusion, our work revealed that sodium butyrate ameliorated oxidative stress and inflammation and enhanced intestinal epithelium barrier function and mitochondrial function through AMPK-mitophagy pathway in IPEC-J2 cells.

## Abbreviations

AMPK:	Adenosine 5'-monophosphate- (AMP-) activated protein kinase
CC:	Compound C
Cyt c:	Cytochrome c
FD4:	Fluorescein isothiocyanate dextran 4kDa
GSH:	Glutathione reductase
H <sub>2</sub> O <sub>2</sub> :	Hydrogen peroxide
IPEC-J2:	Porcine intestinal epithelial cells
IL-1 $\beta$ :	Interleukin-1 $\beta$
SOD:	Superoxide dismutase
LC3B:	Light-chain-associated protein B
mtDNA:	Mitochondrial DNA
MDA:	Malondialdehyde
Mdivi-1:	Mitochondrial division inhibitor 1
NRF-1:	Nuclear respiratory factor-1
NaB:	Sodium butyrate
NLRP3:	Recombinant NLR family, pyrin domain-containing protein 3
PINK1:	PTEN-induced putative kinase 1
PGC-1 $\alpha$ :	Peroxisomal proliferator-activated receptor-coactivator-1 $\alpha$
ROS:	Reactive oxygen species
TFAM:	Mitochondrial transcription factor A
TER:	Transepithelial resistance
ZO-1:	Zonula occludens-1.

## Data Availability

The data used to support the findings of this study are available from the corresponding author upon logical request.

## Ethical Approval

All experiments were carried out in accordance with the Chinese Guidelines for Animal Welfare and Experimental Protocol and were approved by the Animal Care and Use Committee of Zhejiang University.

## Conflicts of Interest

The authors declare that there is no conflict of interest.

## Authors' Contributions

Caihong Hu designed the whole scheme of the experiments; Xin Li, Chunchun Wang, Jiang Zhu, Qian Lin, Minjie Yu, and Jiashu Wen conducted the experiments; Xin Li and Chunchun Wang analyzed data and prepared the initial manuscript; Jie Feng reviewed the manuscript; Caihong Hu had primary responsibility for final content. All authors read

and approved the final manuscript. Chunchun Wang is co-first author.

## Acknowledgments

This research was supported by Zhejiang Provincial Natural Science Foundation of China under Grant No. LZ20C170003, National Natural Science Foundation of China (32172740 and 31872387), and Zhejiang Provincial Key R&D Program of China (2021C02008).

## Supplementary Materials

Table 1: primer sequence for different genes of quantitative real-time (RT-qPCR) analysis. (*Supplementary Materials*)

## References

- [1] S. Cao, H. Xiao, X. Li et al., "AMPK-PINK1/Parkin mediated mitophagy is necessary for alleviating oxidative stress-induced intestinal epithelial barrier damage and mitochondrial energy metabolism Dysfunction in IPEC-J2," *Antioxidants*, vol. 10, no. 12, p. 2010, 2021.
- [2] J. Yin, J. Duan, Z. Cui, W. Ren, T. Li, and Y. Yin, "Hydrogen peroxide-induced oxidative stress activates NF- $\kappa$ B and Nrf2/Keap1 signals and triggers autophagy in piglets," *RSC Advances*, vol. 5, no. 20, pp. 15479–15486, 2015.
- [3] S. Cao, H. Wu, C. Wang et al., "Diquat-induced oxidative stress increases intestinal permeability, impairs mitochondrial function, and triggers mitophagy in piglets1," *Journal of Animal Science*, vol. 96, no. 5, pp. 1795–1805, 2018.
- [4] M. Carocho and I. C. F. R. Ferreira, "A review on antioxidants, prooxidants and related controversy: natural and synthetic compounds, screening and analysis methodologies and future perspectives," *Food and Chemical Toxicology*, vol. 51, pp. 15–25, 2013.
- [5] C. Huang, P. Song, P. Fan, C. Hou, P. Thacker, and X. Ma, "Dietary sodium butyrate decreases postweaning diarrhea by modulating intestinal permeability and changing the bacterial communities in weaned piglets," *The Journal of Nutrition*, vol. 145, no. 12, pp. 2774–2780, 2015.
- [6] D. S. Nielsen, B. B. Jensen, P. K. Theil, T. S. Nielsen, K. E. Knudsen, and S. Purup, "Effect of butyrate and fermentation products on epithelial integrity in a mucus-secreting human colon cell line," *Journal of Functional Foods*, vol. 40, pp. 9–17, 2018.
- [7] E. Grilli, B. Tugnoli, C. J. Foerster, and A. Piva, "Butyrate modulates inflammatory cytokines and tight junctions components along the gut of weaned pigs," *Journal of Animal Science*, vol. 94, supplement 3, pp. 433–436, 2016.
- [8] X. Ma, P. Fan, L. S. Li, S. Y. Qiao, G. L. Zhang, and D. F. Li, "Butyrate promotes the recovering of intestinal wound healing through its positive effect on the tight junctions1," *Journal of Animal Science*, vol. 90, supplement 4, pp. 266–268, 2012.
- [9] E. E. Elamin, A. A. Masclee, J. Dekker, H. J. Pieters, and D. M. Jonkers, "Short-chain fatty acids activate AMP-activated protein kinase and ameliorate ethanol-induced intestinal barrier dysfunction in Caco-2 cell monolayers," *The Journal of Nutrition*, vol. 143, no. 12, pp. 1872–1881, 2013.
- [10] R. Zhang, B. Liu, X. Fan et al., "Aldehyde dehydrogenase 2 protects against post-cardiac arrest myocardial dysfunction

- through a novel mechanism of suppressing mitochondrial reactive oxygen species production,” *Frontiers in Pharmacology*, vol. 11, 2020.
- [11] S. Cao, C. Wang, J. Yan, X. Li, J. Wen, and C. Hu, “Curcumin ameliorates oxidative stress-induced intestinal barrier injury and mitochondrial damage by promoting Parkin dependent mitophagy through AMPK-TFEB signal pathway,” *Free Radical Biology & Medicine*, vol. 147, pp. 8–22, 2020.
  - [12] M. Hytti, E. Korhonen, J. M. Hyttinen et al., “Antimycin A-induced mitochondrial damage causes human RPE cell death despite activation of autophagy,” *Oxidative Medicine and Cellular Longevity*, vol. 2019, Article ID 1583656, 12 pages, 2019.
  - [13] K. Wang and D. J. Klionsky, “Mitochondria removal by autophagy,” *Autophagy*, vol. 7, no. 3, pp. 297–300, 2011.
  - [14] J. Seong Lee and G. M. Lee, “Effect of sodium butyrate on autophagy and apoptosis in Chinese hamster ovary cells,” *Biotechnology Progress*, vol. 28, no. 2, pp. 349–357, 2012.
  - [15] D. G. Hardie, F. A. Ross, and S. A. Hawley, “AMPK: a nutrient and energy sensor that maintains energy homeostasis,” *Nature Reviews Molecular Cell Biology*, vol. 13, no. 4, pp. 251–262, 2012.
  - [16] R. C. Laker, J. C. Drake, R. J. Wilson et al., “Ampk phosphorylation of Ulk1 is required for targeting of mitochondria to lysosomes in exercise-induced mitophagy,” *Nature Communications*, vol. 8, no. 1, p. 548, 2017.
  - [17] E. Q. Toyama, S. Herzig, J. Courchet et al., “AMP-activated protein kinase mediates mitochondrial fission in response to energy stress,” *Science*, vol. 351, no. 6270, pp. 275–281, 2016.
  - [18] S. Herzig and R. J. Shaw, “AMPK: guardian of metabolism and mitochondrial homeostasis,” *Nature Reviews Molecular Cell Biology*, vol. 19, no. 2, pp. 121–135, 2018.
  - [19] D. R. Donohoe, N. Garge, X. Zhang et al., “The microbiome and butyrate regulate energy metabolism and autophagy in the mammalian colon,” *Cell Metabolism*, vol. 13, no. 5, pp. 517–526, 2011.
  - [20] M. P. Mollica, G. M. Raso, G. Cavaliere et al., “Butyrate regulates liver mitochondrial function, efficiency, and dynamics in insulin-resistant obese mice,” *Diabetes*, vol. 66, no. 5, pp. 1405–1418, 2017.
  - [21] J. R. Turner, B. K. Rill, S. L. Carlson et al., “Physiological regulation of epithelial tight junctions is associated with myosin light-chain phosphorylation,” *American Journal of Physiology-Cell Physiology*, vol. 273, no. 4, pp. C1378–C1385, 1997.
  - [22] M. Chalubinski, K. Wojdan, P. Gorzelak, M. Borowiec, and M. Broncel, “The effect of oxidized cholesterol on barrier functions and IL-10 mRNA expression in human intestinal epithelium co-cultured with dendritic cells in the transwell system,” *Food and Chemical Toxicology*, vol. 69, pp. 289–293, 2014.
  - [23] H. J. Shin, J. M. Han, Y. S. Choi, and H. J. Jung, “Pterostilbene suppresses both cancer cells and cancer stem-like cells in cervical cancer with superior bioavailability to resveratrol,” *Molecules*, vol. 25, no. 1, p. 228, 2020.
  - [24] M. Z. Saleem, M. Alshwmi, H. Zhang et al., “Inhibition of JNK-mediated autophagy promotes proscillaridin A-induced apoptosis via ROS generation, intracellular Ca<sup>2+</sup> oscillation and inhibiting STAT3 signaling in breast cancer cells,” *Frontiers in Pharmacology*, vol. 11, pp. 01055–01055, 2020.
  - [25] C. Wang, S. Cao, Z. Shen et al., “Effects of dietary tributyrin on intestinal mucosa development, mitochondrial function and AMPK-mTOR pathway in weaned pigs,” *Journal of Animal Science and Biotechnology*, vol. 10, no. 1, 2019.
  - [26] C. Xue, Y. Li, H. Lv et al., “Oleanolic acid targets the gut–liver axis to alleviate metabolic disorders and hepatic steatosis,” *Journal of Agricultural and Food Chemistry*, vol. 69, no. 28, pp. 7884–7897, 2021.
  - [27] I. Russo, A. Luciani, P. De Cicco, E. Troncone, and C. Ciacci, “Butyrate attenuates lipopolysaccharide-induced inflammation in intestinal cells and Crohn’s mucosa through modulation of antioxidant defense machinery,” *PLoS One*, vol. 7, no. 3, article e32841, 2012.
  - [28] H. P. Indo, M. Davidson, H. C. Yen et al., “Evidence of ROS generation by mitochondria in cells with impaired electron transport chain and mitochondrial DNA damage,” *Mitochondrion*, vol. 7, no. 1–2, pp. 106–118, 2007.
  - [29] L. Li, H. H. Wang, X. T. Nie, W. R. Jiang, and Y. S. Zhang, “Sodium butyrate ameliorates lipopolysaccharide-induced cow mammary epithelial cells from oxidative stress damage and apoptosis,” *Journal of Cellular Biochemistry*, vol. 120, no. 2, pp. 2370–2381, 2019.
  - [30] X. Xing, Z. Jiang, X. Tang et al., “Sodium butyrate protects against oxidative stress in HepG2 cells through modulating Nrf2 pathway and mitochondrial function,” *Journal of Physiology and Biochemistry*, vol. 73, no. 3, pp. 405–414, 2016.
  - [31] D. Y. Liu, W. J. Lou, D. Y. Zhang, and S. Y. Sun, “ROS plays a role in the neonatal rat intestinal barrier damages induced by hyperoxia,” *BioMed Research International*, vol. 2020, Article ID 8819195, 12 pages, 2020.
  - [32] X. Li, J. Wen, L. Jiao et al., “Dietary copper/zinc-loaded montmorillonite improved growth performance and intestinal barrier and changed gut microbiota in weaned piglets,” *Journal of Animal Physiology and Animal Nutrition*, vol. 105, no. 4, pp. 678–686, 2021.
  - [33] M. C. Valenzano, K. Digulio, J. Mercado et al., “Remodeling of tight junctions and enhancement of barrier integrity of the CACO-2 intestinal epithelial cell layer by micronutrients,” *PLoS One*, vol. 10, no. 7, article e0133926, 2015.
  - [34] H. B. Wang, P. Y. Wang, X. Wang, Y. L. Wan, and Y. C. Liu, “Butyrate enhances intestinal epithelial barrier function via up-regulation of tight junction protein claudin-1 transcription,” *Digestive Diseases and Sciences*, vol. 57, no. 12, pp. 3126–3135, 2012.
  - [35] H. Yan and K. M. Ajuwon, “Butyrate modifies intestinal barrier function in IPEC-J2 cells through a selective upregulation of tight junction proteins and activation of the Akt signaling pathway,” *PLoS One*, vol. 12, no. 6, article e0179586, 2017.
  - [36] L. Peng, Z. R. Li, R. S. Green, I. R. Holzman, and J. Lin, “Butyrate enhances the intestinal barrier by facilitating tight junction assembly via activation of AMP-activated protein kinase in Caco-2 cell monolayers,” *The Journal of Nutrition*, vol. 139, no. 9, pp. 1619–1625, 2009.
  - [37] W. Guo, J. Liu, J. Sun et al., “Butyrate alleviates oxidative stress by regulating NRF2 nuclear accumulation and H3K9/14 acetylation via GPR109A in bovine mammary epithelial cells and mammary glands,” *Free Radical Biology and Medicine*, vol. 152, pp. 728–742, 2020.
  - [38] L. Jiang, J. Wang, Z. Liu et al., “Sodium butyrate alleviates lipopolysaccharide-induced inflammatory responses by down-regulation of NF- $\kappa$ B, NLRP3 signaling pathway, and activating histone acetylation in bovine macrophages,” *Frontiers in Veterinary Science*, vol. 7, 2020.
  - [39] S. Saita, M. Shirane, and K. I. Nakayama, “Selective escape of proteins from the mitochondria during mitophagy,” *Nature Communications*, vol. 4, no. 1, p. 1410, 2013.



- [40] C. Zhou, L. Li, T. Li et al., "SCFAs induce autophagy in intestinal epithelial cells and relieve colitis by stabilizing HIF-1 $\alpha$ ," *Journal of Molecular Medicine*, vol. 98, no. 8, pp. 1189–1202, 2020.
- [41] F. Wang, H. Wu, M. Fan et al., "Sodium butyrate inhibits migration and induces AMPK-mTOR pathway-dependent autophagy and ROS-mediated apoptosis via the miR-139-5p/Bmi-1 axis in human bladder cancer cells," *The FASEB Journal*, vol. 34, no. 3, pp. 4266–4282, 2020.
- [42] T. Zhao, J. Gu, H. Zhang et al., "Sodium butyrate-modulated mitochondrial function in high-insulin induced HepG2 cell dysfunction," *Oxidative Medicine and Cellular Longevity*, vol. 2020, Article ID 579674, 16 pages, 2020.
- [43] W. Miao, X. Wu, K. Wang et al., "Sodium butyrate promotes reassembly of tight junctions in Caco-2 monolayers involving inhibition of MLCK/MLC2 pathway and phosphorylation of PKC $\beta$ 2," *International Journal of Molecular Sciences*, vol. 17, no. 10, p. 1696, 2016.
- [44] M. Evans, T. Murofushi, H. Tsuda et al., "Combined effects of starvation and butyrate on autophagy-dependent gingival epithelial cell death," *Journal of Periodontal Research*, vol. 52, no. 3, pp. 522–531, 2017.
- [45] S. Luo, Z. Li, L. Mao, S. Chen, and S. Sun, "Sodium butyrate induces autophagy in colorectal cancer cells through LKB1/AMPK signaling," *Journal of Physiology and Biochemistry*, vol. 75, no. 1, pp. 53–63, 2019.

## Research Article

# Differentially Expressed Hepatic Genes Revealed by Transcriptomics in Pigs with Different Liver Lipid Contents

Wentao Lyu <sup>1,2</sup>, Yun Xiang,<sup>3</sup> Xingxin Wang,<sup>2</sup> Jingshang Li,<sup>1</sup> Caimei Yang,<sup>2</sup> Hua Yang <sup>1</sup>, and Yingping Xiao <sup>1</sup>

<sup>1</sup>State Key Laboratory for Managing Biotic and Chemical Threats to the Quality and Safety of Agro-Products, Institute of Agro-Product Safety and Nutrition, Zhejiang Academy of Agricultural Sciences, Hangzhou 310021, China

<sup>2</sup>College of Animal Sciences & Technology, Zhejiang A & F University, Hangzhou 311300, China

<sup>3</sup>Institute of Animal Husbandry and Veterinary Medicine, Jinhua Academy of Agricultural Sciences, Jinhua 321000, China

Correspondence should be addressed to Yingping Xiao; [xiaoy@zaas.ac.cn](mailto:xiaoy@zaas.ac.cn)

Received 18 September 2021; Revised 24 December 2021; Accepted 11 January 2022; Published 28 January 2022

Academic Editor: Ana Lloret

Copyright © 2022 Wentao Lyu et al. This is an open access article distributed under the Creative Commons Attribution License, which permits unrestricted use, distribution, and reproduction in any medium, provided the original work is properly cited.

The liver is the center for uptake, synthesis, packaging, and secretion of lipids and lipoproteins. The research on lipid metabolism in pigs is limited. The objective of the present study is to identify the genes related to lipid metabolism and oxidative stress in pigs by using transcriptomic analysis. Liver segments were collected from 60 Jinhua pigs for the determination of liver lipid content. The 7 pigs with the highest and lowest liver lipid content were set as group H and group L, respectively. Liver segments and serum samples were collected from each pig of the H and L groups for RNA sequencing and the determination of triglycerides (TG) content and high-density lipoprotein cholesterol (HDL) content, respectively. The HDL content in the serum of pigs in the H group was significantly higher than the L group ( $P < 0.05$ ). From transcriptomic sequencing, 6162 differentially expressed genes (DEGs) were identified, among which 2962 were upregulated and 3200 downregulated genes with the increase in the liver content of Jinhua pigs. After GO enrichment and KEGG analyses, lipid modification, cellular lipid metabolic process, cholesterol biosynthetic process, fatty acid metabolic process, oxidoreduction coenzyme metabolic process, oxidoreductase activity, acting on CH-OH group of donors, response to oxidative stress, nonalcoholic fatty liver disease (NAFLD), sphingolipid metabolism, and oxidative phosphorylation pathways were involved in lipid metabolism and oxidative stress in Jinhua pigs. For further validation, we selected 10 DEGs including 7 upregulated genes (*APOE*, *APOA1*, *APOC3*, *LCAT*, *CYP2E1*, *GPX1*, and *ROMO1*) and 4 downregulated genes (*PPARA*, *PPARGCIA*, and *TXNIP*) for RT-qPCR verification. To validate these results in other pig species, we analyzed these 10 DEGs in the liver of Duroc×Landrace×Yorkshire pigs. Similar expression patterns of these 10 DEGs were observed. These data would provide an insight to understand the gene functions regulating lipid metabolism and oxidative stress and would potentially provide theoretical basis for the development of strategies to modulate lipid metabolism and even control human diabetes and obesity by gene regulations.

## 1. Introduction

The liver is an essential metabolic organ and the central link for the carbohydrate, lipid, and protein metabolism [1]. The liver plays a unique role in controlling the glucose metabolism by maintaining the glucose concentration within the normal range. This is achieved through a strictly regulated enzyme and kinase system. These enzymes and kinases regulate the decomposition or synthesis of glucose in liver cells. The liver is the main processor of protein and amino acid

metabolism, because it is responsible for most of the proteins secreted in the blood (whether based on the quality or range of unique proteins), the processing of amino acids for energy, and disposal of nitrogenous waste from protein degradation in the form of the urea metabolism. Moreover, the liver can also secrete bile for the digestion and decomposition of lipids and the absorption of fat-soluble vitamins [2]. The liver not only oxidizes lipids but also encapsulates the excess lipids, secretes them in other tissues, and stores them, such as adipose tissue. For lipid metabolism, the liver

is the center for uptake, synthesis, packaging, and secretion of lipids and lipoproteins [3]. Hepatocytes are able to extract fatty acids from chylomicron remnants by lipoprotein lipase and oxidize fatty acids to provide energy for themselves and other organs [4]. For carbohydrate metabolism, the liver is capable to store, synthesize, metabolize, and release glucose [3]. Hepatic Krebs cycle allows the liver to maintain a high rate of biodegradation of carbohydrates and lipids to provide energy for the body [5, 6]. For protein and amino acid metabolisms, the liver could also synthesize, secrete, utilize, and metabolize proteins or amino acids [3]. Additionally, the liver could synthesize and secrete various lipoproteins after assembling fatty acids and glycerol into triglycerides. Therefore, the liver is a key connection between the lipid metabolism and glucose and protein metabolisms. Especially for pigs, the liver is one of the most important organs in regulating appetite and body weight as well as several metabolic processes [7].

Oxidative stress is caused by a sharp increase in free radicals in the body or a decline in the ability to scavenge free radicals, thereby disrupting the antioxidant-oxidation balance [8]. There are reports that oxidative stress is related to many diseases and is closely related to the health of the body [9, 10]. The free radicals that play a major role in oxidative stress are reactive oxygen species (ROS) and reactive nitrogen free radicals (RNS) [11]. Under physiological conditions, adipokines can induce the production of ROS and then produce oxidative stress, which in turn leads to the further deposition of lipid [12]. Therefore, understanding the relationship between lipid deposition and oxidative stress can reduce oxidative stress and promote body health by regulating lipid metabolism.

Transcriptome sequencing, also known as RNA sequencing (RNA-seq), is a technique to quantitatively describe the differences in gene types and expression levels at a global level [13]. RNA-seq is a powerful tool that can identify genes related to lipid metabolism and oxidative stress in the liver. Genes related to lipid metabolism were identified by using transcriptome analysis of liver samples in chickens and pigs [14, 15] to understand the effect of liver metabolism on lipid-related phenotypes. Regardless of whether it is for pigs or for humans, excessive lipid deposits will lead to obesity, which will cause a series of inflammatory reactions and eventually lead to a series of diseases, such as insulin resistance and diabetes [16].

As one of the most important economic animals, pigs are raised all over the world. Different breeds of pigs have significantly different genetic composition, which affects different physiological characteristics. The Jinhua pig, named after the city of Jinhua in East China's Zhejiang Province, is a traditional, slow-growing pig breed with a high body lipid content, early sexual maturity, and low fertility [17]. In the production of pigs, lipid deposition not only affects the growth efficiency of pigs but also affects the quality of pork. Excessive lipid deposition will reduce the lean meat rate of pigs, reduce the economic benefits of the pig industry, and also affect the flavor and quality of pork. Therefore, an in-depth understanding of the mechanism of pig lipid deposition can provide scientific targets for the rational regulation

of pig lipid deposition. It has been approved that pigs are very similar to humans in terms of eating style, pancreatic shape and development level, gastrointestinal tract structure, metabolic level, and blood glucose level [18–20]. For phenotypic similarities of pigs to humans, it includes cardiovascular anatomy and function, metabolism, lipoprotein profile, size, tendency to obesity, and omnivorous habits. However, the current research on lipid metabolism and oxidative stress of Jinhua pigs is limited. Therefore, in this paper, liver samples were collected from 14 Jinhua pigs for transcriptome analysis to identify differential expressed genes related to lipid metabolism and oxidative stress. In this study, all pigs were from the same breeding line and fed under the same conditions, so we supposed all of the pigs in the experiment had similar average daily intake, allowing us to focus on differentially expressed genes that regulate lipid metabolism without being affected by the internal environment. It would provide a theoretical basis for the in-depth study of genes regulating lipid metabolism and oxidative in pigs and even for humans to develop strategies to modulate lipid metabolism and regulate related diseases caused by obesity.

## 2. Materials and Methods

*2.1. Ethics Statement.* All animal procedures were approved by the Institutional Animal Care and Use Committee of the Zhejiang Academy of Agricultural Sciences (ZAASDLSY2019-1910), and all methods were performed in accordance with the relevant guidelines and regulations.

*2.2. Animals and Sampling of Animal Trial 1 for the Test.* A total of sixty Jinhua castrated boars at 30 days old were raised in a commercial farm in Jinhua City, Zhejiang Province, China. All of the Jinhua pigs in this study were from the same breeding line, pedigreed Jinhua pigs, which is a Chinese local breed. Pigs were raised in pens with ad libitum access to diets and water. The diet was a commercial corn-soybean-based diet formulated with trace minerals and vitamins to meet the requirements of the National Research Council (NRC, 2012). After fasting for 12 h, all pigs were slaughtered at the age of 270 days. The average thickness of the backfat was measured on the first rib, last rib, and last lumbar vertebrae in the midline using a sliding caliper [18]. The liver segments were collected and stored at  $-80^{\circ}\text{C}$  until RNA isolation and subsequent analysis.

*2.3. Animals and Sampling of Animal Trial 2 for the Validation.* In order to verify the results from animal trial 1, a total of 82 Duroc $\times$ Landrace $\times$ Yorkshire (DLY) pigs at 30 days old were fed with commercial corn-soybean-based diet under standardized environment. The commercial corn-soybean-based diet was formulated with to meet the requirements of the National Research Council (NRC, 2012). At the age of 180 days, all of pigs were sacrificed to measure backfat thickness and collect segments of liver for the determination of lipid content and lipid-related gene expression.

*2.4. Determination of Liver Lipid Content.* We used the Soxhlet [21] extraction method to determine the lipid content of the liver. We use an organic solvent to extract the

lipid in the sample with Soxhlet extractor, make it dissolve in the organic solvent, and then evaporate the solvent, weigh the residual, and measure the lipid content in the sample. The liver lipid content was expressed as percentage of wet weight.

**2.5. Histological Staining.** Histological staining was performed as previously described with minor modifications [17]. Briefly, liver segments of Jinhua pigs were fixed in 4% paraformaldehyde for 1 h at room temperature, cryoprotected in 20% sucrose at 4°C overnight, and embedded in OCT. A series of 12 mm cryosections were prepared and stained with hematoxylin, eosin, and/or Oil Red O (Sigma-Aldrich, St. Louis, MO, United States). The liver sections were photographed by a light microscope (Nikon Corp., Tokyo, Japan).

**2.6. Detection of Serum Biochemical Index.** We determined serum biochemical parameters, including triglycerides (TG) and high-density lipoprotein cholesterol (HDL), using conventional enzymatic determination kits (Nanjing Jiancheng Institute of Bioengineering, Nanjing, Jiangsu, China) and an automatic biochemical analyzer (Hitachi, Tokyo, Japan).

**2.7. RNA Extraction.** Total RNA from liver samples was extracted using TRIzol reagent (Invitrogen, Carlsbad, CA, USA) strictly according to the manufacturer's instructions. A NanoPhotometer® spectrophotometer (IMPLEN, MD, CA, USA) was used to detect RNA purity (OD260/280 and OD260/230 ratios), and an Agilent 2100 Bioanalyzer (Agilent Technologies, Santa Clara, CA, USA) was used to accurately detect RNA integrity.

**2.8. Library Preparation and Transcriptome Sequencing.** A total amount of 1 µg of RNA per sample was used as the input material for RNA sample preparation. Sequencing libraries were generated using the NEBNext® Ultra™ RNA Library Prep Kit for Illumina® (NEB, Ipswich, CA, USA) following the manufacturer's recommendations, and index codes were added to attribute sequences to each sample. To preferentially select cDNA fragments that were 250~300 bp in length, the library fragments were purified with the AMPure XP system (Beckman Coulter, Beverly, USA). Finally, PCR products were purified (AMPure XP system) (Beckman Coulter life sciences division, Indianapolis, Indiana, USA), and library quality was assessed on the Agilent Bioanalyzer 2100 system.

For RNA-seq, a 2 × 150 bp paired-end sequencing was performed in the present study. Clustering of the indexed samples was performed on a cBot Cluster Generation System using TruSeq PE Cluster Kit v3-cBot-HS (Illumina) according to the manufacturer's instructions. After cluster generation, the library preparations were sequenced on an Illumina NovaSeq 6000 platform, and paired-end reads were generated. The raw transcriptome read data are available in the SRA database under accession number PRJNA721126.

**2.9. Data Processing.** Raw reads of fastq format were firstly processed through in-house Perl scripts to remove adapter sequences [22], ploy-N sequences, and low-quality reads. Quality parameters of Q20, GC content, and sequence dupli-

cation level were used for further data filtration. All the downstream analyses were based on the clean reads. The reference genome and gene model annotation files were downloaded from genome website directly (<https://www.ncbi.nlm.nih.gov/genome/?term=Sus+scrofa>). Hisat2 v2.0.5 was used to build the index of the reference genome and align the paired-end clean reads to the reference genome [23].

**2.10. Differential Expression Analysis.** Read counts were generated for each gene using featureCounts v1.5.0-p3 [24]. The expression level for each gene was normalized to quantify fragments per kilobase of transcript sequence per million base-pairs sequenced (FPKM) [25, 26]. The differential expression analysis of two groups was performed using the DESeq2 R package (v1.16.1) [27]. Gene-based expression matrix (with default normalization) was used to compare boars from the H and L groups. DESeq2 provides statistical routines for determining differential expression in digital gene expression data using a model based on the negative binomial distribution. The resulting *P* values were adjusted using the Benjamini and Hochberg approach for controlling the false discovery rate [28]. Genes with an adjusted *P*adj < 0.05 and |log 2fold change| > 1 found by DESeq2 were assigned as differentially expressed.

The clusterProfiler R package was used to implement Gene Ontology (GO, <http://www.geneontology.org/>) enrichment analysis of the differentially expressed genes (DEGs) and test the statistical enrichment of DEGs in Kyoto Encyclopedia of Genes and Genomes (KEGG, <http://www.genome.jp/kegg/>) pathways [29]. GO terms and KEGG pathways with corrected *P* value less than 0.05 were considered significantly enriched. GO terms and KEGG pathways were annotated with InterProScan (<http://www.ebi.ac.uk/Tools/pfa/iprscan/>) [30] and KOBAS (3.0.3) [31], respectively.

**2.11. Validation of Differentially Expressed Genes by RT-qPCR.** To demonstrate the repeatability and precision of the RNA-seq gene expression data derived from the liver tissue libraries, a CFX384 multiple real-time fluorescence quantitative PCR instrument was used for analysis. The real-time quantitative PCR (RT-qPCR) system (20 µL) was as follows: power SYBR® Green Master Mix, 10 µL; upstream and downstream primers (10 µmol/L), 0.5 µL; sterilized distilled water, 8 µL; and cDNA template, 1 µL. The reaction conditions were as follows: 95°C for 1 min, followed by 40 cycles of 95°C for 15 sec and 63°C for 25 sec (for collecting fluorescence data). Finally, the melting curve was drawn at 55-95°C. The reaction for each sample was repeated three times, and the relative expression level of each gene was statistically analyzed as 2<sup>-Ct</sup> (Ct internal reference gene-Ct target gene). The primers used for quantification in the study were designed using Primer-BLAST on the NCBI website (<https://www.ncbi.nlm.nih.gov/tools/primer-blast/>). The gene information for real-time PCR is shown in Table 1, with GAPDH serving as the internal reference gene [32].

**2.12. Statistical Analysis.** Data are expressed as the mean ± standard error of mean (SEM). All statistical analyses were

TABLE 1: Primers for RT-qPCR.

Gene name	Primer sequences (5' to 3')	TM (°C)	Product size (bp)
GAPDH	F: CCAGGGCTGCTTTTAACTCTG R: GTGGGTGGAATCATACTGGAACAT	60	104
APOE	F: GGTGCAGTCCCTGTCTGA R: CTCTATCAGCTCCGTCAGTTC	60	79
APOC3	F: GACACCTCCCTTCTGGACAAA R: GACTCCTTACGCTGGTTAG	60	86
APOA1	F: GAAGGATTTTGCCACCGTGTATG R: GGAGTTTCAGGTTGAGGTGTTTTTC	60	107
LCAT	F: CGGCTGGAGCCCAGTTATATG R: CCCAGCAAGCTTCAGGTAGTA	60	144
PPARA	F: GTTGCAAGGGCTTCTTTTCGG R: CCGAGAGGCACTTGTGGAAA	60	129
PPARGC1A	F: GCTTGACGAGCGTCATTCAG R: GGTCTTCACCAACCAGAGCA	60	100
CYP2E1	F: CACAAGGACAAAGGGGTCATTT R: TGCTCATTGCCCTGTTTCCC	60	110
GPX1	F: TCCAGTGTGTCGCAATGACA R: TCGATGGTCAGAAAGCGACG	60	102
ROMO1	F: GCGTGAAGATGGGCTTTGTG R: TCTGCATCATGGTTTTCCCGA	60	135
TXNIP	F: CATGTTCCCGCATTGTGGTG R: ACCGATGACAACTTCTGCGT	60	100

performed in SPSS version 23. All figures are generated in GraphPad Prism V8.0 and OriginLab 2018. The difference in liver lipid content and backfat thickness between two groups was analyzed by unpaired two-tailed Student's *t*-test and considered significant when the *P* value was no more than 0.05.

### 3. Results

**3.1. Lipid-Related Phenotypes of Jinhua Pigs.** To study the relationship between backfat thickness and liver lipid, we conducted a correlation analysis of backfat thickness. The average backfat thickness and average liver lipid content were  $3.347 \pm 0.5567$  cm and  $5.976 \pm 0.664\%$ , respectively (Figure 1). The linear regression revealed a positive correlation between backfat thickness and liver lipid content ( $R = 0.6407$ ,  $P < 0.001$ ).

For further investigation, we sorted these 60 Jinhua pigs from high to low according to the liver lipid content and set the highest 7 pigs and the lowest 7 pigs as group H and group L, respectively. The mean value of liver content in the H group was 7.19% while that in the L group was 5.08%, showing a significant difference ( $P < 0.0001$ , Figure 2(a)). As expected, the backfat thickness in group H was significantly higher than that in group L ( $P = 0.0003$ , Figure 2(b)).

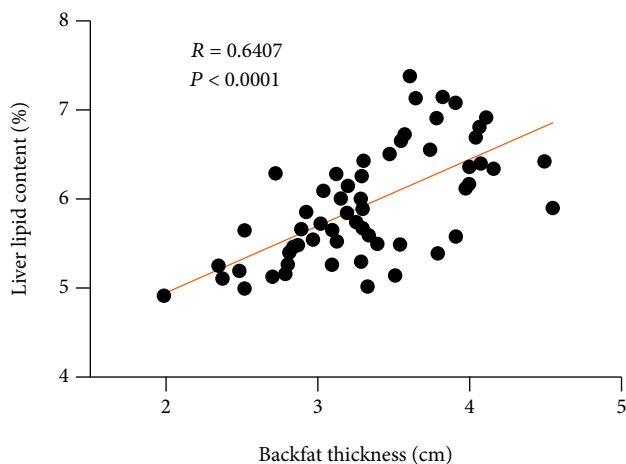


FIGURE 1: The linear regression analysis between the backfat thickness and liver lipid content. The round black dots indicate the 60 Jinhua pigs.

To convince the liver lipid content, we performed the H.E. staining of liver segments. As shown in Figures 2(c) and 2(d), it was clear that liver lipid content in group H is higher than that in group L.

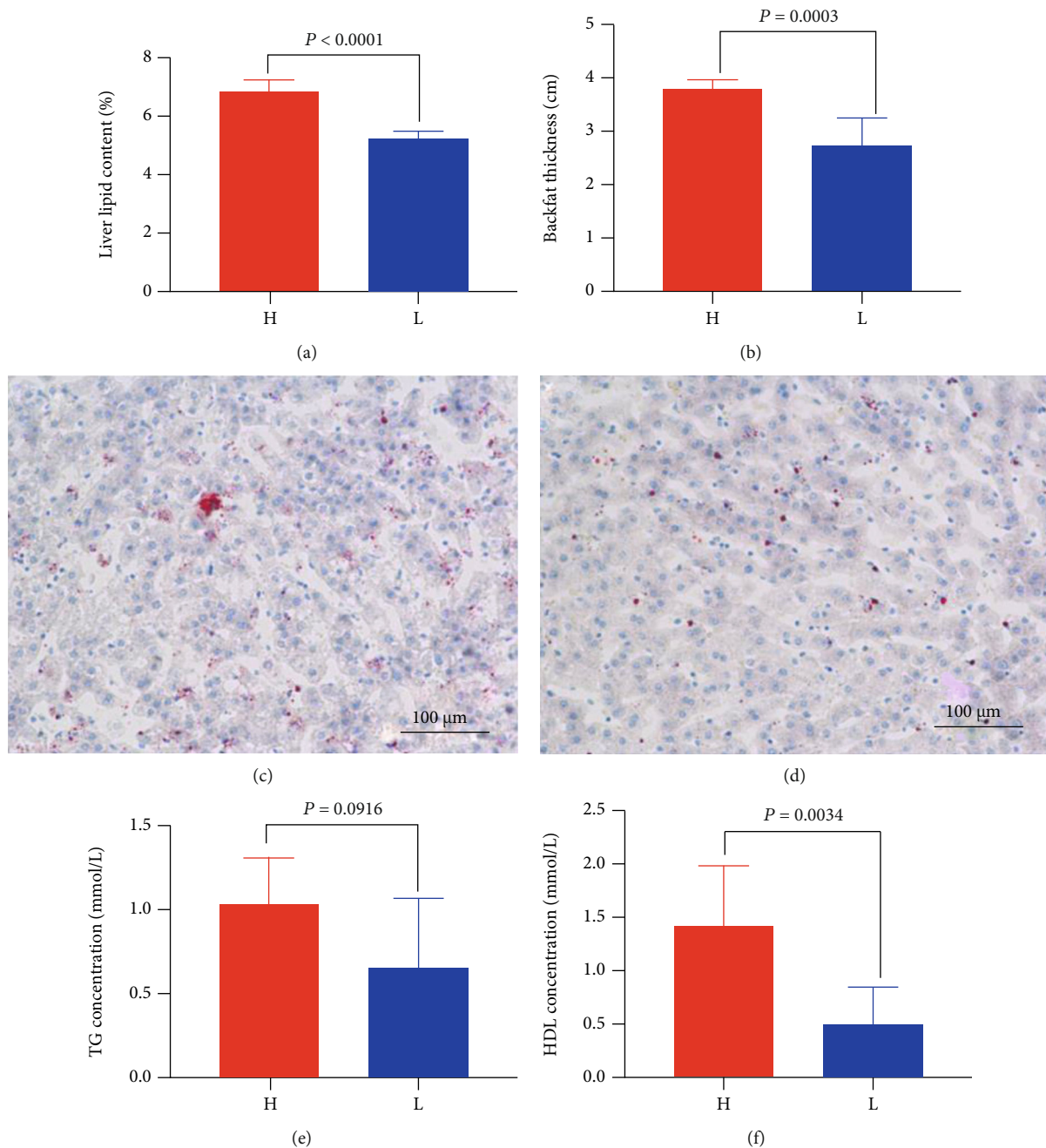


FIGURE 2: Lipid-related phenotypes of Jinhua pigs in group H and group L. (a) The liver lipid content of different groups ( $n = 7$ ). (b) The thickness of backfat in different groups ( $n = 7$ ). (c) Liver sections were enlarged to  $100 \mu\text{m}$  in group H. (d) Liver sections were enlarged to  $100 \mu\text{m}$  in group L. (e) Serum TG concentration in different groups ( $n = 7$ ). (f) Serum HDL concentration in different groups ( $n = 7$ ). H: the high liver lipid content group; L: the low liver lipid content group. Red dots in (c) and (d) indicate lipid droplets. Data were expressed as mean  $\pm$  SEM with statistical analysis by unpaired two-tailed Student's *t*-test.

The average concentration of TG in the serum of group H was 1.033 mmol/L, the average concentration of group L was 0.649 mmol/L, and there was no difference, but group H was higher than group L ( $P = 0.0916$ , Figure 2(e)). The average concentration of HDL in the serum of group H was 1.591 mmol/L, the average concentration of group L was 0.5515 mmol/L, group H was higher than group L, and the difference was significant ( $P = 0.0034$ , Figure 2(f)).

**3.2. Summary of RNA-seq Data.** The average number of original reads for 14 samples was 46996754. After quality control of the original reads with Q20, sequence duplication level, and GC content, there was an average of 45809803 clean reads per sample, accounting for 97.48% of the original reads. The average Q30 value, which is the percentage of bases for which the recognition accuracy exceeds 99.9%, was 95.12%. The samples were of good quality, and the

TABLE 2: Summary of sequence quality and alignment information from the liver transcriptome analysis of Jinhua pigs.

Sample	Read numbers	Clean reads	Clean ratio (%)	Clean bases	Q30 (%)	Total mapped	Mapped ratio (%)
H1	46615168	45213222	96.99	6.85GB	95.29	43613957	96.46
H2	47224788	46062522	97.54	6.76GB	95.22	44406844	96.41
H3	46528606	45425370	97.63	6.72GB	95.36	43487077	95.73
H4	45712164	44501604	97.35	6.77GB	95.24	42959852	96.54
H5	46089942	45064114	97.77	6.88GB	95.33	43422246	96.36
H6	49504486	48370168	97.71	6.79GB	94.72	46645521	96.43
H7	47692912	46119656	96.70	7.24GB	95.43	44351571	96.17
L1	46532476	45643802	98.09	6.78GB	95.31	44141776	96.71
L2	46016438	45069046	97.94	6.91GB	95.45	43475540	96.46
L3	46299018	45354188	97.96	6.83GB	94.81	43944203	96.89
L4	46875078	45157476	96.34	6.68GB	95.03	43471601	96.27
L5	46972136	45833438	97.58	6.76GB	94.99	44268232	96.59
L6	46450896	45277662	97.47	7.26GB	95.16	43693079	96.50
L7	49440452	48244974	97.58	6.92GB	94.37	46387276	96.15

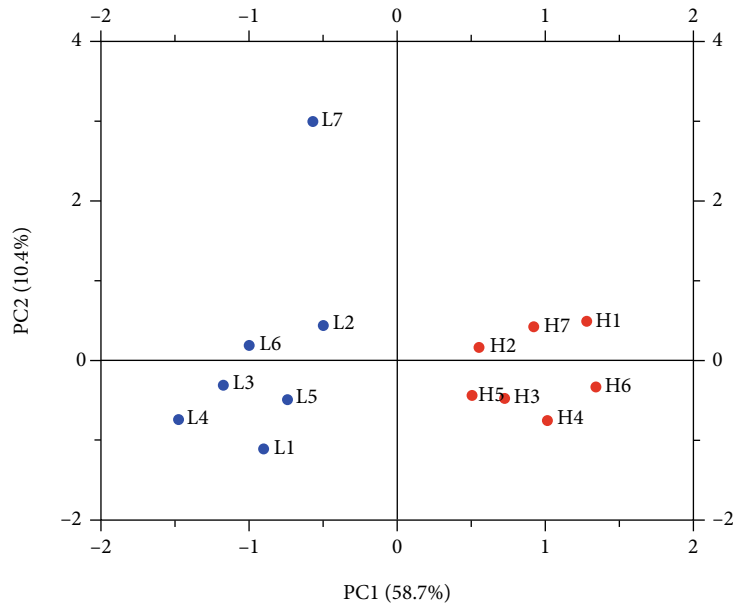


FIGURE 3: Differences between transcriptome replicates of the H and L groups' ducks based on the principal component analysis. Note: the abscissa is the first principal component, and the ordinate is the second principal component.

average number of clean bases was 6.87 GB, averaging over 6 GB. The percentage of reads aligned to the unique location of the reference genome was 95.73% to 96.89% among the clean reads, and the average mapping rate of clean reads mapped to reference genes was 96.41% (Table 2). In summary, the sequencing data was qualified for the subsequent data analysis. To assess intergroup differences and intragroup sample duplication, we performed PCA analysis on readcount of all samples, and the results showed intragroup aggregation and intergroup isolation (Figure 3).

**3.3. Differentially Expressed Genes Analysis.** Group H compared with group L, with  $P_{adj} < 0.05$  and  $|\log_2 - 2\text{fold change}| > 0$  as the threshold, a total of 6162 DEGs were identified.

Among them, we identified 2962 upregulated genes and 3200 downregulated genes when comparing group H to group L (Figure 4). The DEG expression patterns of each sample were clustered on the basis of the  $\log_2$  (fold change) values of their expression ratios, which exhibited good repeatability of samples in two groups (Figure 5).

**3.4. GO Annotation and Enrichment Analysis of Differentially Expressed Genes.** To further elucidate the functional roles of the 6162 DEGs, GO term enrichment analysis was performed to search for significantly overrepresented categories. A total of 178 terms (Table S1) were significantly enriched in the three categories ( $P < 0.05$ ), including biological process, cellular component, and

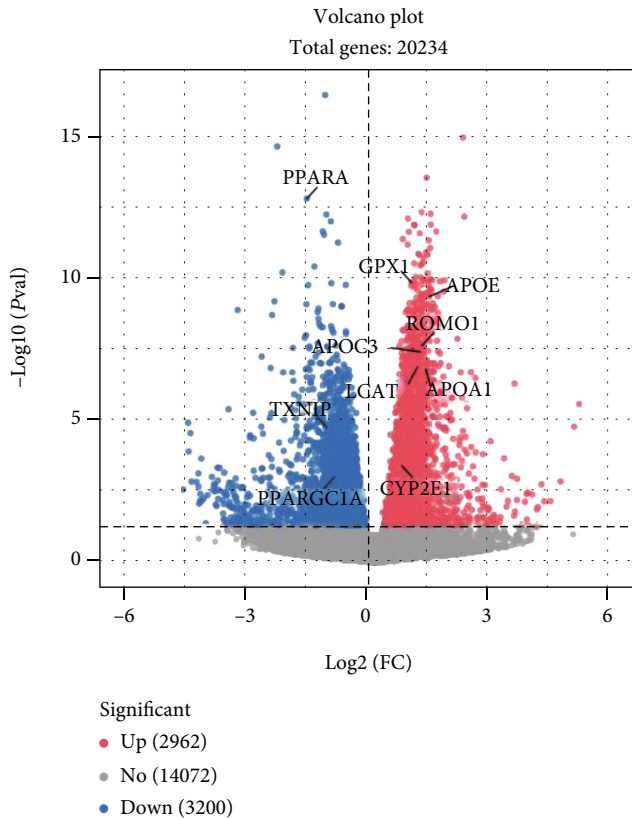


FIGURE 4: Volcano plot of the total expression of genes in both the H and L groups. A total of 21234 genes were expressed in both the H and L groups, and there were 6162 differentially expressed genes (DEGs). The  $x$ -axis represents the  $\log_2$  fold change values for gene expression, and the  $y$ -axis represents the  $-\log_{10}$  significance of the difference in the expression ( $P_{adj} < 0.05$ ). Red dots indicate 2962 upregulated DEGs, blue dots indicate 3200 downregulated DEGs, and gray dots indicate 14072 nondifferentially expressed genes.

molecular function. The top 20 terms (the 20 with the lowest  $P$  value) which include 10 terms for biological process, 8 terms for cell component, and 2 terms for molecular function were further analyzed to determine the associated regulatory functions (Figure 6). Four terms (Table 3) were related to lipid metabolism, namely, lipid modification (GO:0030258), cellular lipid metabolic process (GO:0044255), cholesterol biosynthetic process (GO:0006695), and fatty acid metabolic process (GO:0006641). And three terms (Table 4) were related to oxidative stress, oxidoreduction coenzyme metabolic process (GO:0006733), oxidoreductase activity, acting on CH-OH group of donors (GO:0016614), and response to oxidative stress (GO:0006979). In addition, there were some genes involved in lipid metabolism and oxidative stress in these terms, such as *APOE*, *APOA1*, *APOC3*, *LCAT*, *CYP2E1*, *PPARGC1A*, *GPX1*, *ROMO1*, and *TXNIP*.

**3.5. KEGG Pathway Analysis of DEGs.** To identify the pathways those DEGs involved, we integrated the 6162 DEGs into the KEGG pathway database, and a total of 33 pathways ( $P < 0.05$ ) were significantly enriched (Figure 7, Table S2). There were 2 pathways involved in lipid metabolism

(Table 5), including nonalcoholic fatty liver disease (NAFLD) (ssc04932) and sphingolipid metabolism (ssc00600). And oxidative phosphorylation (ssc00190) was related to oxidative stress (Table 5). There were 10 significantly enriched genes shown in Table 6 which were related to lipid metabolism and oxidative stress. Among them, 4 genes, *APOE*, *PPARGC1A*, *CYP2E1*, and *TXNIP*, were highly enriched both in GO terms and significantly expressed in KEGG pathways; 5 genes, *APOA1*, *APOC3*, *LCAT*, *GPX1*, and *ROMO1*, were only enriched in GO terms; and *PPARA* was only enriched in KEGG pathways.

**3.6. DEG Expression in the Liver of Jinhua Pigs.** To validate the RNA-seq results, 10 DEGs, including 7 upregulated genes (*APOE*, *APOA1*, *APOC3*, *LCAT*, *CYP2E1*, *GPX1*, and *ROMO1*) and 3 downregulated genes (*PPARA*, *PPARGC1A*, and *TXNIP*), were selected for RT-qPCR analysis in the liver of Jinhua pigs. As expected, all the selected DEGs showed a concordant expression pattern between the RNA-seq and qPCR results (Figure 8).

**3.7. Validation of the Lipid-Related Phenotypes and Gene Expression in DLY Pigs.** In order to validate the results from trial 1, we determined the liver lipid content of 82 DLY pigs, and we set the 7 pigs with the highest liver lipid content as the validation high (VH) group and the 7 pigs with the lowest liver lipid content as the validation low (VL) group. The mean of liver lipid content in the VH group was 6.24% while that in VL group was 4.26%, showing a significant difference ( $P < 0.0001$ , Figure 9(a)). As expected, the backfat thickness in the VH group was significantly higher than that in the VL group ( $P < 0.0001$ , Figure 9(b)).

In order to verify the reproducibility of the above results on the other breeds of pigs, RT-qPCR verification of 10 lipid-related genes, namely, *APOE*, *APOA1*, *APOC3*, *LCAT*, *CYP2E1*, *GPX1*, *ROMO1*, *PPARA*, and *PPARGC1A*, were performed on the liver tissues of the DLY pigs in the VH and VL groups. It was found that the expression patterns of these 10 genes were consistent with those in Jinhua pigs (Figure 10) with different liver lipid contents.

## 4. Discussion

As one of the most popular local pig breed in China, Jinhua pigs are famous for the superior meat quality with a higher body lipid content than the commercial pig breeds such as Landrace, Yorkshire, and Duroc [33]. The liver plays an important role in lipid metabolism, which is capable to secrete bile and bile acid salt emulsifying lipids to promote the digestion and absorption of lipids [4]. However, the data on lipid metabolism in Jinhua pigs is limited. In this study, transcriptome analysis was performed in the 14 liver samples to investigate the possible regulation of lipid deposition in Jinhua pigs. Similarly, Wang et al. [34] used RNA-seq technology to study the lipid metabolism mechanism in the liver of Yorkshire pigs and Anqing six-end-white pigs. Several genes responsible for lipid metabolism have been identified including *PPARA*, *PCK1*, *CYP7A1*, *PLIN1*, *ACSL3*, and *RetSat*. Xing et al. [35] conducted RNA-seq analysis on



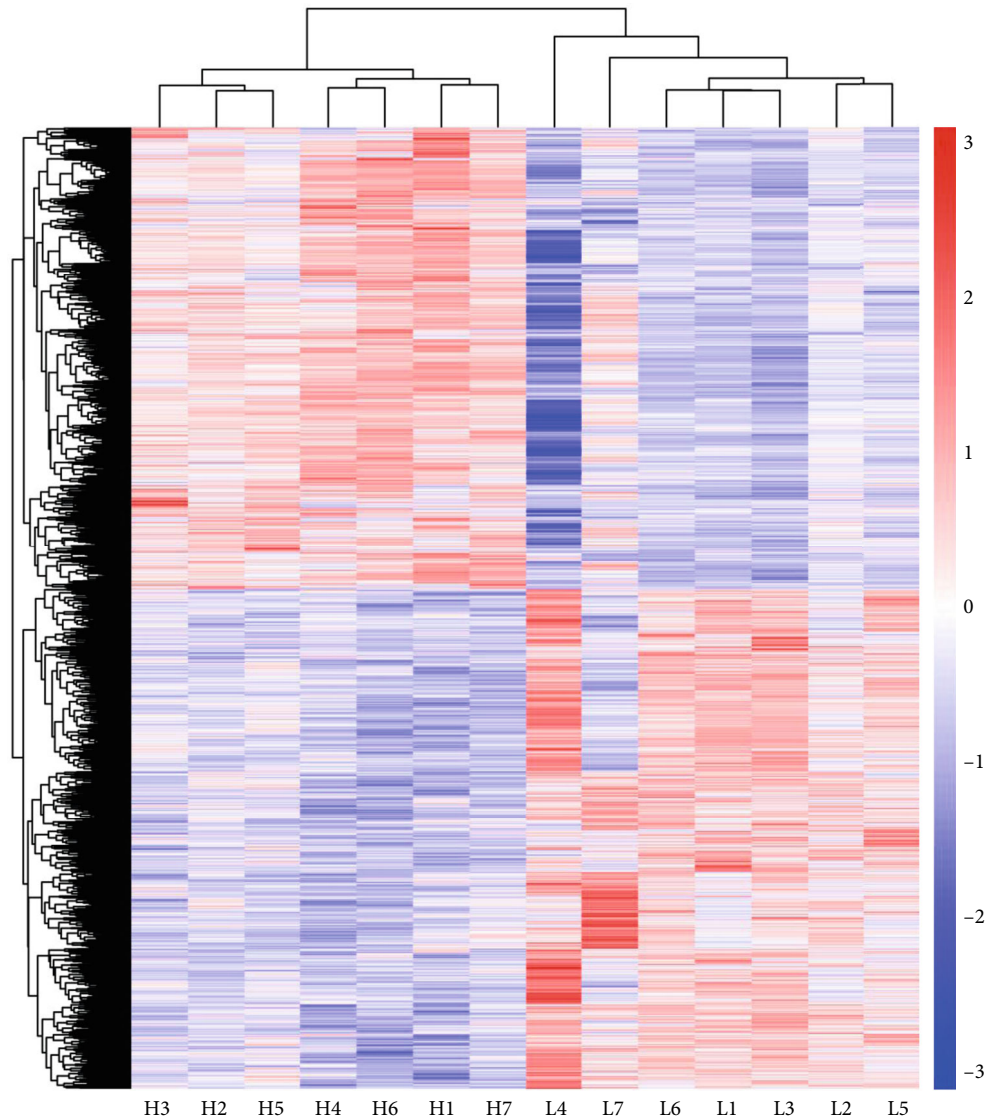


FIGURE 5: Liver tissue expression profiles of 6162 differentially expressed genes (DEGs) in the H vs. L groups. Hierarchical clustering analysis of z-scored FPKM was performed for each DEG between Jinhua pigs in the H and L groups. Colour scale represents FPKM normalized log<sub>10</sub> transformed counts. Horizontal bars represent genes. The vertical column represents samples. Red colour indicates upregulated genes, while blue colour indicates downregulated genes.

the livers of Songliao black pigs with high and low backfat thickness and identified genes involved in lipid regulation which played an important role in liver lipid and fatty acid metabolism, such as *FABP1*, *LCN2*, *PLIN2*, *CYP1A1*, *CYP1A2*, *CYP2A6*, and *CYP26A1*. Obesity is caused by excessive accumulation of lipid and is considered to be the main potential factor for the onset of many diseases (diabetes, cardiovascular, liver diseases, etc.), and these symptoms are all related to oxidative stress [12]. And oxidative stress is one of the factors restricting the pig industry, which has a certain impact on the production performance and health of pigs [8]. We used a larger pig population with 60 individuals and analyzed 14 liver samples, making our results more typical. In order to verify the repeatability of Jinhua pig lipid-related phenotypes and gene expression in other pig species, we conducted RT-qPCR to verify the

expression levels of related genes in DLY white pigs, and the results showed that the expression patterns of related genes in DLY pigs were consistent with those in Jinhua pigs. This shows that our study is universal.

Apolipoproteins is a part of plasma lipoprotein, which is mainly divided into five categories: apolipoproteins A, B, C, D, and E. The basic function of apolipoproteins is to carry lipids and stabilize the structure of lipoproteins. Some apolipoproteins also have functions such as activating lipoprotein metabolism enzymes and recognizing receptors. It plays an important role in lipid transportation and metabolism. Additionally, apolipoproteins are the main component of very low-density lipoprotein (VLDL), chylomicrons (CM), and HDL [36]. Apolipoprotein A1 (*APOA1*), apolipoprotein C3 (*APOC3*), and apolipoprotein E (*APOE*) were positively regulated lipid deposition in the liver of Jinhua pigs. Studies

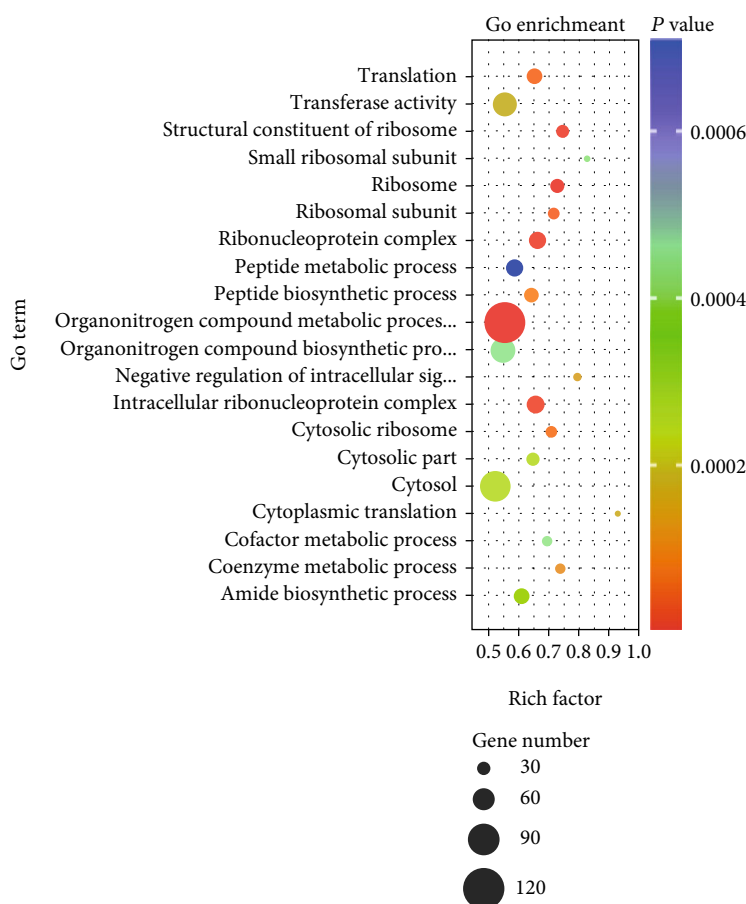


FIGURE 6: GO term enrichment analysis of differentially expressed genes (DEGs). The 20 top terms were obtained by GO enrichment, including 10 terms for biological process, 8 term for cell component, and 2 terms for molecular function. The size of the dots indicates the number of expressed genes in the pathways, and the colour of the dots represents the  $P$  value of the significant pathway.

TABLE 3: The significantly enriched terms associated with lipid metabolism.

Term ID	Description	$P$ value	Gene number
GO:0030258	Lipid modification	0.003820271	14
GO:0044255	Cellular lipid metabolic process	0.029944475	40
GO:0006695	Cholesterol biosynthetic process	0.033857412	8
GO:0006631	Fatty acid metabolic process	0.036584082	21

TABLE 4: The significantly enriched terms associated with oxidative stress.

Term ID	Description	$P$ value	Gene number
GO:0006733	Oxidoreduction coenzyme metabolic process	0.014110964	13
GO:0016614	Oxidoreductase activity, acting on CH-OH group of donors	0.033328294	18
GO:0006979	Response to oxidative stress	0.038686219	19

have shown that *APOE* could also mobilize cholesterol in cells and tissues. A special class of amphiphilic apolipoproteins, like *APOA1* and *APOE*, could combine with ATP to interact with ATP-binding cassette subfamily A member 1 (*ABCA1*), forming a discoidal complex of phospholipids and apolipoproteins [37–39]. The role of this discoidal complex is to dissolve excess cholesterol existing in the plasma

membrane of the cell or cholesterol shed from the cell to the extracellular matrix [40, 41]. Lecithin cholesterol acyltransferase (*LCAT*) can enhance the ability of this discoidal complex to dissolve cholesterol [42]. *LCAT* is an enzyme secreted by the liver that can esterify cholesterol in the center of HDL. With the actions of *APOA1*, *APOD*, and *APOE*, it would result in the further increase in the volume of HDL

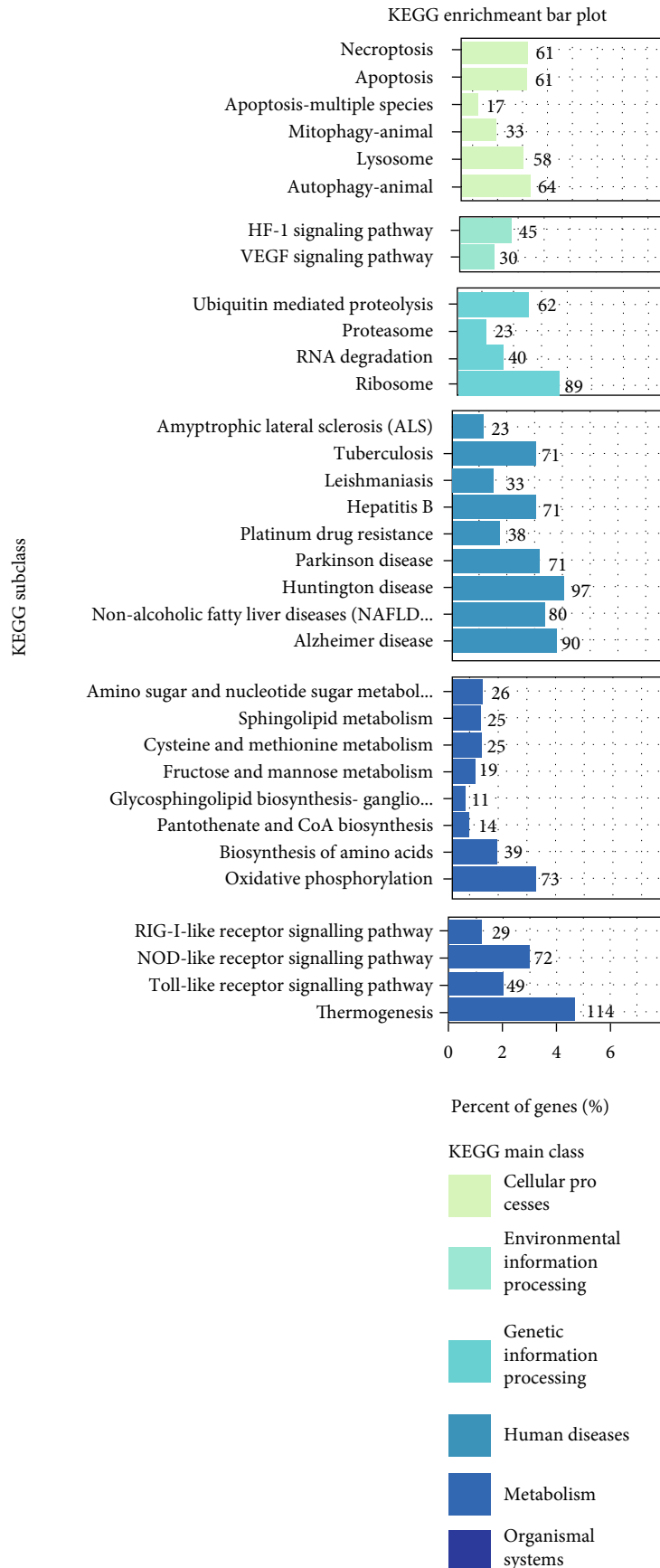


FIGURE 7: KEGG pathway enrichment analysis of differentially expressed genes (DEGs).

TABLE 5: The significantly enriched pathways associated with lipid metabolism and oxidative stress.

Pathway ID	Description	P value	Gene number
ssc04932	Nonalcoholic fatty liver disease (NAFLD)	$1.55503E - 05$	49
ssc00600	Sphingolipid metabolism	0.021170698	25
ssc00190	Oxidative phosphorylation	$2.1411E - 05$	73

TABLE 6: Information of 16 DEGs associated with lipid metabolism and oxidative stress.

Gene name	Gene ID	log2FoldChange	P value	Descriptions
<i>APOE</i>	397576	1.34	$4.58E - 10$	Apolipoprotein E
<i>APOA1</i>	397691	1.26	$1.69E - 07$	Apolipoprotein A1
<i>APOC3</i>	406187	1.12	$4.14E - 08$	Apolipoprotein C3
<i>LCAT</i>	100303723	1.04	$1.41E - 07$	Lecithin-cholesterol acyltransferase
<i>PPARA</i>	397239	-1.67	$1.66E - 13$	Peroxisome proliferator-activated receptor alpha
<i>PPARGCIA</i>	397013	-0.99	0.001012566	PPARG coactivator 1 alpha
<i>CYP2E1</i>	403216	0.66	0.00042474	Cytochrome P450 family 2 subfamily E member 1
<i>GPX1</i>	397403	0.89	$1.49E - 10$	Glutathione peroxidase 1
<i>ROMO1</i>	100154394	1.16	$2.48E - 08$	Reactive oxygen species modulator 1
<i>TXNIP</i>	733688	-1.18	$1.89E - 05$	Thioredoxin interacting protein

Log2FoldChange of readcount by group H (H readcount) vs. group L (L readcount), of which 7 genes upregulated expression ( $\log_2\text{FoldChange} > 0$ ) and 3 genes downregulated expression ( $\log_2\text{FoldChange} < 0$ ).

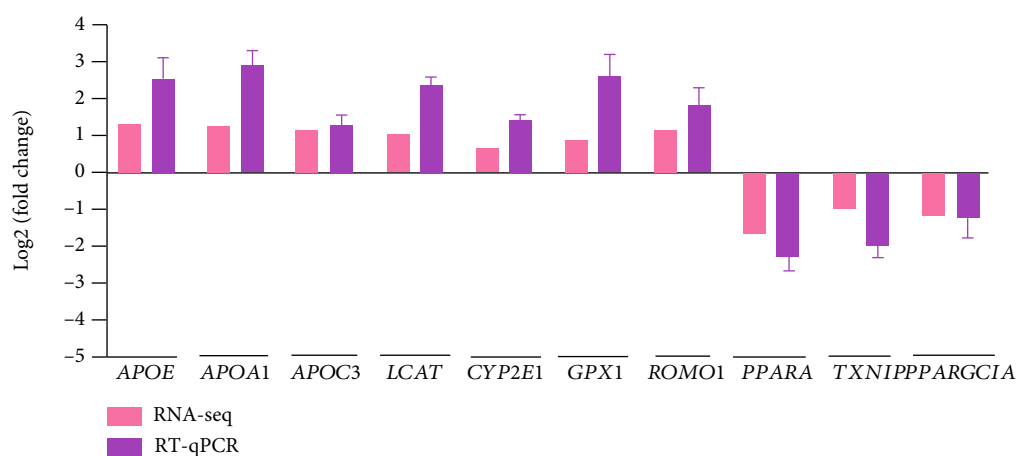


FIGURE 8: Validation of 10 DEGs by RT-qPCR in the liver of Jinhua pigs. The  $\log_2(\text{fold change})$  was calculated when each indicated DEGs in the H group was compared to the L group. For the results of RT-qPCR, the  $2^{-\Delta\Delta Ct}$  method was used to determine the relative expression level of each indicated DEGs in the H group over the L group.

and promote lipid deposition [43]. *APOC3* was related to the regulation of LPL activity. Studies have found that the overexpression of *APOC3* will inhibit the activity of *LPL*, thereby increasing the triglyceride content, leading to lipid deposition [44]. Therefore, it is not surprising to find *APOE*, *APOA1*, *APOC3*, and *LCAT* giving a higher expression in the liver of the pigs in the H group than that in the L group.

Peroxisome proliferator-activated receptor alpha (*PPARA*) and PPARG coactivator 1 alpha (*PPARGCIA*) belong to peroxisome proliferator-activated receptors (PPARs) family. Among them, *PPARA* is mainly expressed in liver cells, cardiomyo-

cytes, and brown adipocytes. *PPARA* participates in the metabolism of sphingolipids in the liver. Sphingolipids are a class of complex lipids with a ceramide structure, which are essential for various biological processes including development and growth [45]. *PPARA* is not only involved in lipid metabolism in the liver but also related to the  $\beta$ -oxidation of mitochondria. Studies have shown that the constitutive mitochondrial  $\beta$ -oxidation activity in the liver of *PPARA* knockout mice is significantly reduced [46]. *PPARGCIA* was first discovered and reported in the screening of mouse brown lipid cDNA library [47]. As a key nuclear transcription coactivator,

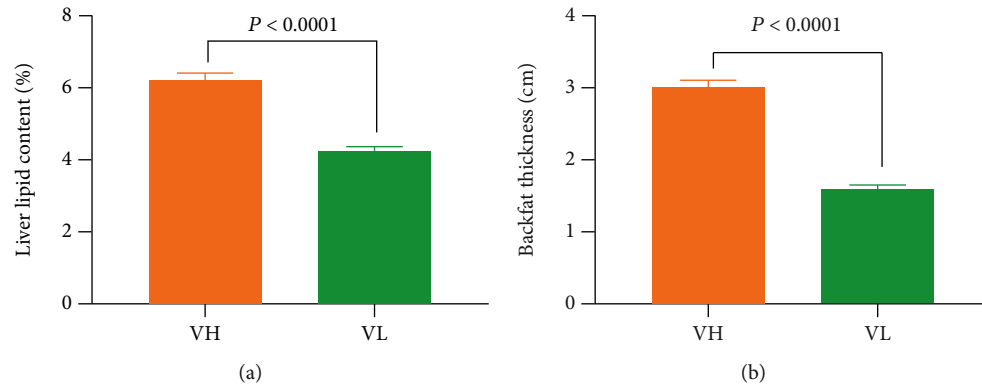


FIGURE 9: The liver lipid content and backfat thickness of DLY pigs in the VH and VL groups. (a) The liver lipid content of different groups ( $n = 7$ ). (b) The thickness of backfat in different groups ( $n = 7$ ). Data was expressed as mean  $\pm$  SEM with statistical analysis by unpaired two-tailed Student's  $t$ -test. VH: validation high group including pigs with high liver lipid content; VL: validation low group including pigs with low liver lipid content.

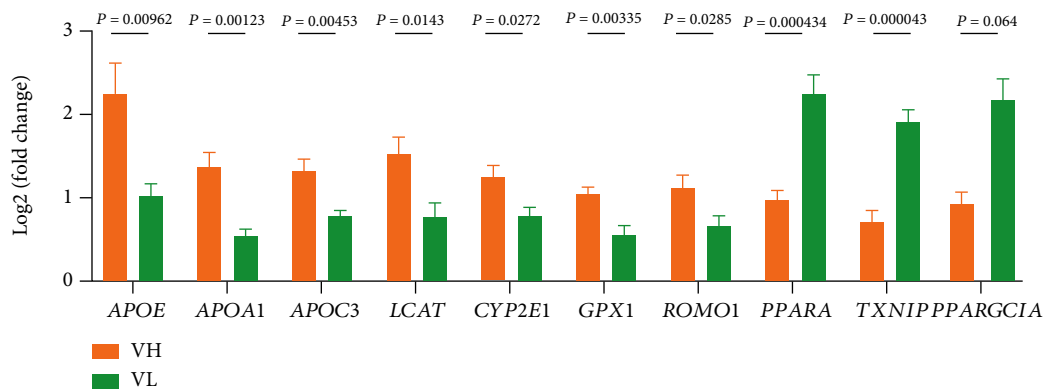


FIGURE 10: Validation of 10 related genes by RT-qPCR in the liver of DLY pigs. For the results of RT-qPCR, the  $2^{-\Delta\Delta Ct}$  method was used to determine the relative expression level of 10 related genes in the VH group over the VL group. VH: validation high group including pigs with high liver lipid content; VL: validation low group including pigs with low liver lipid content.

*PPARGCIA* can bind to many different transcription factors, participate in a series of orderly metabolic processes, and play an important role in regulating mitochondrial biosynthesis, sugar metabolism, fatty acid oxidation, and muscle fiber type conversion [48–50]. *PPARGCIA* also plays a key role in regulating the redox environment of cells by upregulating the functions of antioxidant genes and their derivatives [51] and interacts with PPARs to increase fatty acid oxidation (FAO) [52]. Studies have shown that lysosomes can inhibit the expression of *PPARA* by inhibiting the expression of *PPARGCIA*, thereby causing lipid accumulation in the liver [53]. In this experiment, the expression levels of *PPARA* and *PPARGCIA* were both downregulated, and the lysosomal pathway was enriched and expressed in the KEGG pathway, so this can regulate lipid metabolism in the liver through the above process.

Among the members of the cytochrome P-450 family, the cytochrome P450 family 2 subfamily E member 1 (*CYP2E1*) has been extensively studied because it is metabolically activated by a variety of xenobiotics and carcinogens (including nitrosamines, benzene, vinyl chloride, and halogenated solvents). It is a key enzyme and has a significant

contribution to the metabolism of ethanol to acetaldehyde [54]. In the liver, *CYP2E1* is mainly expressed in the endoplasmic reticulum of hepatocytes in the lobular center, which has high NADPH oxidase activity, that can lead to the production of ROS and significantly promote the induction of oxidative stress in many pathological conditions [55]. *CYP2E1* is related to oxidative stress. In this experiment, *CYP2E1* was upregulated in the H group. One of the most important proteins in the inner mitochondrial membrane is ROS modulator 1 (*ROMO1*), which interferes with the production of ROS, and as the rate of this protein increases, oxidative stress increases, which ultimately leads to some diseases [56]. Studies have shown that the increase in Romo1 expression enhances cellular ROS levels and oxidative DNA damage [57], which consistent with our experimental results. The thioredoxin-interacting protein (*TXNIP*) is a multifunctional adaptor protein for different signaling pathways. *TXNIP* is a multifunctional adaptor protein for different signaling pathways [58]. The main role of *TXNIP* is to negatively regulate the function of thioredoxin (TRX) by inhibiting its reducing ability and promoting cellular oxidative stress [59]. Studies have shown that high levels of

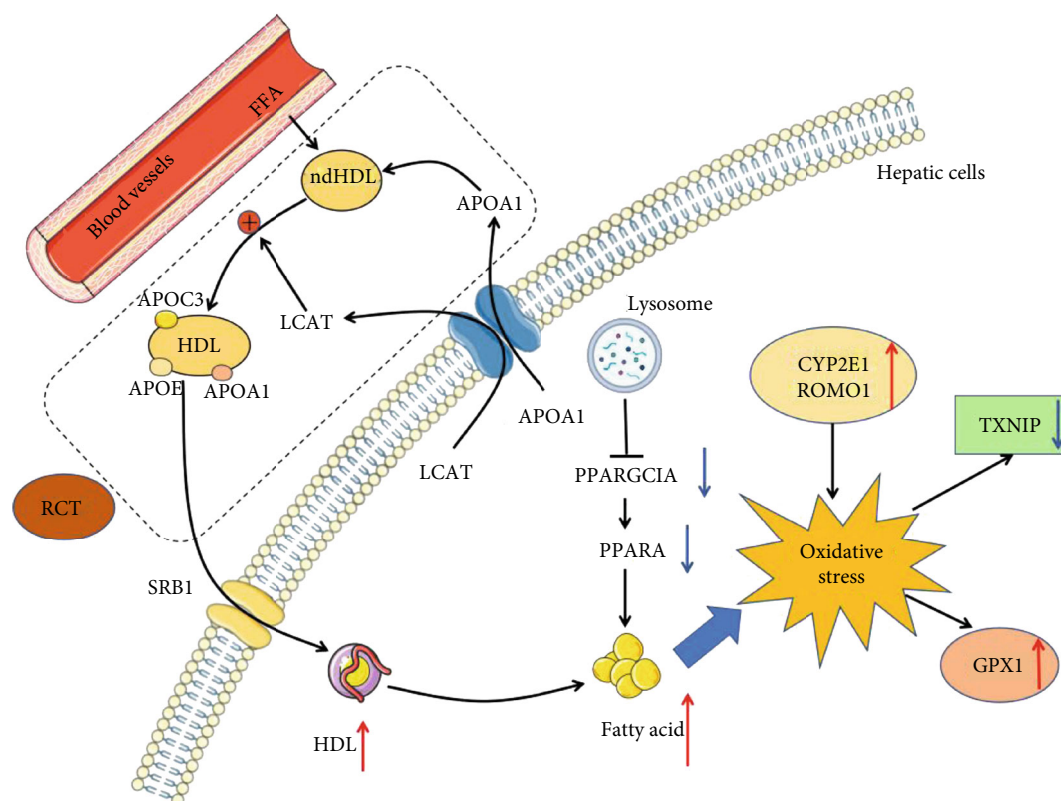


FIGURE 11: Overview of liver lipid metabolism and oxidative stress. RCT: reverse cholesterol transport.

*TXNIP* inhibit the redox activity of cytoplasmic TRX1 and increase the level of ROS. On the contrary, ROS can negatively regulate the expression of *TXNIP*. *GPX1* is an important antioxidant enzyme involved in preventing the harmful accumulation of hydrogen peroxide in cells [60]. It is present in all cells and has been found to be more effective than catalase in removing intracellular peroxides under many physiological conditions [61]. *GPX1* can also reduce lipid hydroperoxides and other soluble hydroperoxides [62] and can reduce 1-linoleoyl lysophosphatidylcholine hydroperoxide, but not tri- or diacylglycerol hydroperoxides [63]. *GPX1* cannot be replaced by any other selenoproteins in protecting against systemic oxidative stress, and *GPX1* has the main antioxidant function in the body [64]. Studies have shown that overexpression of *GPX1* can protect mice under oxidative stress, but it can still cause obesity and diabetes [65].

The accumulation of lipid in the liver is mainly due to a problem in the balance between lipid acquisition and processing [66]. Based on the results above, we summarized the pathways of the lipid metabolism in the liver of Jinhua pigs (Figure 11). *APOA1* is produced and secreted from the liver and released into the plasma to combine with free fatty acids (FFA) to form a ndHDL. Once ndHDL is produced, it will cause cholesterol efflux, and then, ndHDL will absorb the efflux cholesterol; then, it will be esterified by *LCAT* to produce HDL, which carries with *APOA1*, *APOC3*, and *APOE*. It is then transported back to the liver by scavenger receptor B1 (*SRB1*), leading to lipid deposition in the liver. On the other hand, lysosomes could inhibit the expres-

sion of *PPARGC1A*, thereby reducing the expression of *PPARA* as well as resulting in lipid deposition in the liver. Excessive lipid deposition as well as overexpression of *CYP2E1* and *ROMO1* would promote oxidative stress, further inducing the expression of the antioxidant enzyme *GPX1* with high ROS levels suppressing the expression of *TXNIP*.

## 5. Conclusions

In this study, we analyzed the DEGs in pigs with different liver lipid contents. Through GO enrichment analysis and KEGG analysis, it is found that 10 DEGs, namely, *APOE*, *APOA1*, *APOC3*, *LCAT*, *PPARA*, *PPARGC1A*, *CYP2E1*, *GPX1*, *ROMO1*, and *TXNIP*, displayed a crucial regulatory role in lipid metabolism and oxidative stress in the liver of pigs. This study provided insights into the molecular mechanism for regulating lipid metabolism and oxidative stress in pigs even humans.

## Abbreviations

ABCA1:	ATP-binding cassette subfamily A member 1
APOA1:	Apolipoprotein A1
APOC3:	Apolipoprotein C3
APOE:	Apolipoprotein E
CM:	Chylomicrons
CYP1A1:	Cytochrome P450 family 1 subfamily A member 1
CYP2A6:	Cytochrome P450 family 2 subfamily A member 6

CYP7A1:	Cytochrome P450 family 7 subfamily A member 1
CYP26A1:	Cytochrome P450 family 26 subfamily A member 1
CYP2E1:	Cytochrome P450 family 2 subfamily E member 1
DEGs:	Differentially expressed genes
FABP1:	Fatty acid-binding protein 1
FAO:	Fatty acids oxidation
FFA:	Free fatty acids
FPKM:	Fragments per kilobase of transcript sequence per million base-pairs sequenced
GAPDH:	Glyceraldehyde-3-phosphate dehydrogenase
GO:	Gene Ontology
GPX1:	Glutathione peroxidase 1
HDL:	High-density lipoproteins
KEGG:	The Kyoto Encyclopedia of Genes and Genomes
LCAT:	Lecithin-cholesterol acyltransferase
LCN2:	Lipocalin-2
LDL:	Low-density lipoproteins
LPL:	Lipoprotein lipase
ndHDL:	Nascent discoidal HDL
PCK1:	Phosphoenolpyruvate carboxykinase 1
PPARA:	Peroxisome proliferator-activated receptor alpha
PPARGC1A:	PPARG coactivator 1 alpha
PPARs:	Peroxisome proliferator-activated receptors
RCT:	Reverse cholesterol transport
RetSat:	Retinol saturase
ROMO1:	ROS modulator 1
ROS:	Reactive oxygen species
RNA-seq:	RNA sequencing
SCOA:	Succinyl-CoA : 3-ketoacid CoA-transferase
SEM:	Standard error of mean
SRBI:	Scavenger receptor class B type I
TG:	Triglycerides
TRX:	Thioredoxin
TXNIP:	Thioredoxin-interacting protein
VLDL:	Very low-density lipoproteins.

## Data Availability

All data obtained in this study had been deposited to the National Center for Biotechnology Information (NCBI) with the accession number PRJNA721126 (<https://www.ncbi.nlm.nih.gov/bioproject/PRJNA721126>).

## Conflicts of Interest

The authors declare that there is no conflict of interest regarding the publication of this paper.

## Authors' Contributions

X.X.W. conceived the study and drafted the manuscript. W.T.L. and Y.X. performed the experiments. J.S.L. analyzed the data. X.X.W. and C.M.Y. contributed to the formal analysis. H.Y. and Y.P.X. edited the manuscript. W.T.L., Y.X.,

and X.X.W. contributed equally to this work. Wentao Lyu, Yun Xiang, and Xingxin Wang share the first authorship.

## Acknowledgments

This research was supported by the National Natural Science Foundation of China (31972999).

## Supplementary Materials

*Supplementary 1.* Table S1: all enrichment terms in GO analysis.

*Supplementary 2.* Table S2: all enrichment pathways in KEGG analysis.

## References

- [1] T. Andus, J. Bauer, and W. Gerok, "Effects of cytokines on the liver," *Hepatology*, vol. 13, no. 2, pp. 364–375, 1991.
- [2] G. A. Kullak-Ublick and P. J. Meier, "Mechanisms of cholestasis," *Clinics in Liver Disease*, vol. 4, no. 2, pp. 357–385, 2000.
- [3] E. Trefts, M. Gannon, and D. H. Wasserman, "The liver," *Current Biology*, vol. 27, no. 21, pp. 1147–1151, 2000.
- [4] R. Munoz, J. Estany, M. Tor, and O. Doran, "Hepatic lipogenic enzyme expression in pigs is affected by selection for decreased backfat thickness at constant intramuscular fat content," *Meat Science*, vol. 93, no. 3, pp. 746–751, 2013.
- [5] A. Canbay, L. Bechmann, and G. Gerken, "Lipid metabolism in the liver," *Zeitschrift für Gastroenterologie*, vol. 45, no. 1, pp. 35–41, 2007.
- [6] J. G. Jones, "Hepatic glucose and lipid metabolism," *Diabetologia*, vol. 59, no. 6, pp. 1098–1103, 2016.
- [7] B. C. Fam, C. N. Joannides, and S. Andrikopoulos, "The liver: key in regulating appetite and body weight," *Adipocytes*, vol. 1, no. 4, pp. 259–264, 2012.
- [8] Y. Hao, M. Xing, and X. Gu, "Research progress on oxidative stress and its nutritional regulation strategies in pigs," *Animals*, vol. 11, no. 5, p. 1384, 2021.
- [9] Z. Chen and C. Zhong, "Oxidative stress in Alzheimer's disease," *Neuroscience Bulletin*, vol. 30, no. 2, pp. 271–281, 2014.
- [10] K. Daenen, A. Andries, D. Mekahli, A. Van Schepdael, F. Jouret, and B. Bammens, "Oxidative stress in chronic kidney disease," *Pediatric Nephrology*, vol. 34, no. 6, pp. 975–991, 2019.
- [11] D. M. Miller, G. R. Buettner, and S. D. Aust, "Transition metals as catalysts of "autoxidation" reactions," *Free Radical Biology and Medicine*, vol. 8, no. 1, pp. 95–108, 1990.
- [12] A. Fernández-Sánchez, E. Madrigal-Santillán, M. Bautista et al., "Inflammation, oxidative stress, and obesity," *International Journal of Molecular Sciences*, vol. 12, no. 5, pp. 3117–3132, 2011.
- [13] A. K. Gupta and U. D. Gupta, "Next Generation Sequencing and Its Applications," in *Animal Biotechnology*, pp. 345–367, 2014.
- [14] H. Li, T. Wang, C. Xu et al., "Transcriptome profile of liver at different physiological stages reveals potential mode for lipid metabolism in laying hens," *BMC Genomics*, vol. 16, p. 763, 2015.
- [15] Z. Wang, Q. Li, Y. Chamba et al., "Identification of genes related to growth and lipid deposition from transcriptome

- profiles of pig muscle tissue,” *PLoS One*, vol. 10, no. 10, article e0141138, 2015.
- [16] M. F. Gregor and G. S. Hotamisligil, “Inflammatory mechanisms in obesity,” *Annual Review of Immunology*, vol. 29, no. 1, pp. 415–445, 2011.
- [17] H. Yang, Y. Xiao, J. Wang et al., “Core gut microbiota in Jinhua pigs and its correlation with strain, farm and weaning age,” *Journal of Microbiology*, vol. 56, no. 5, pp. 346–355, 2018.
- [18] Y. Xiao, F. Kong, Y. Xiang et al., “Comparative biogeography of the gut microbiome between Jinhua and Landrace pigs,” *Scientific Reports*, vol. 8, no. 1, p. 5985, 2018.
- [19] D. H. Baker, “Animal models in nutrition research,” *Journal of Nutrition*, vol. 138, no. 2, pp. 391–396, 2008.
- [20] D. A. Bellinger, E. P. Merricks, and T. C. Nichols, “Swine models of type 2 diabetes mellitus: insulin resistance, glucose tolerance, and cardiovascular complications,” *ILAR Journal*, vol. 47, no. 3, pp. 243–258, 2006.
- [21] B. W. B. Holman, K. L. Bailes, R. G. Meyer, and D. L. Hopkins, “Effect of modified Soxhlet (Soxtec) and Folch extraction method selection on the total lipid determination of aged beef,” *Journal of Food Science and Technology*, vol. 56, no. 8, pp. 3957–3961, 2019.
- [22] B. Clift, D. Haussler, R. McConnell, T. D. Schneider, and G. D. Stormo, “Sequence landscapes,” *Nucleic Acids Research*, vol. 14, no. 1, pp. 141–158, 1986.
- [23] A. Mortazavi, B. A. Williams, K. McCue, L. Schaeffer, and B. Wold, “Mapping and quantifying mammalian transcriptomes by RNA-Seq,” *Nature Methods*, vol. 5, no. 7, pp. 621–628, 2008.
- [24] Y. Liao, G. K. Smyth, and W. Shi, “featureCounts: an efficient general purpose program for assigning sequence reads to genomic features,” *Bioinformatics*, vol. 30, no. 7, pp. 923–930, 2014.
- [25] D. K. Das, T. Ali, K. Krampis, and O. O. Ogunwobi, “Fibronectin and androgen receptor expression data in prostate cancer obtained from a RNA-sequencing bioinformatics analysis,” *Data in Brief*, vol. 11, pp. 131–135, 2017.
- [26] H. Nishiwaki, M. Ito, S. Negishi, S. Sobue, M. Ichihara, and K. Ohno, “Molecular hydrogen upregulates heat shock response and collagen biosynthesis, and downregulates cell cycles: meta-analyses of gene expression profiles,” *Free Radical Research*, vol. 52, no. 4, pp. 434–445, 2018.
- [27] H. Varet, L. Brillet-Guéguen, J. Y. Coppée, and M. A. Dillies, “SARTools: a DESeq2- and EdgeR-based R pipeline for comprehensive differential analysis of RNA-Seq data,” *PLoS One*, vol. 11, no. 6, article e0157022, 2016.
- [28] J. A. Ferreira and A. H. Zwinderman, “On the Benjamini-Hochberg method,” *Annals of Statistics*, vol. 34, no. 4, 2006.
- [29] G. Yu, L. G. Wang, Y. Han, and Q. Y. He, “clusterProfiler: an R package for comparing biological themes among gene clusters,” *OMICS*, vol. 16, no. 5, pp. 284–287, 2012.
- [30] E. M. Zdobnov and R. Apweiler, “InterProScan—an integration platform for the signature-recognition methods in InterPro,” *Bioinformatics*, vol. 17, no. 9, pp. 847–848, 2001.
- [31] S. Chen, L. Zhang, Y. Su, and X. Zhang, “Screening potential biomarkers for colorectal cancer based on circular RNA chips,” *Oncology Reports*, vol. 39, no. 6, pp. 2499–2512, 2018.
- [32] K. J. Livak and T. D. Schmittgen, “Analysis of Relative Gene Expression Data Using Real-Time Quantitative PCR and the  $2^{-\Delta\Delta C_T}$  Method,” *Methods*, vol. 25, no. 4, pp. 402–408, 2001.
- [33] Z. Miao, L. Wang, Z. R. Xu, J. F. Huang, and Y. R. Wang, “Developmental changes of carcass composition, meat quality and organs in the Jinhua pig and Landrace,” *Animal*, vol. 3, no. 3, pp. 468–473, 2009.
- [34] Y. Wang, W. Zhang, X. Wu et al., “Transcriptomic comparison of liver tissue between Anqing six-end-white pigs and Yorkshire pigs based on RNA sequencing,” *Genome*, vol. 63, no. 4, pp. 203–214, 2020.
- [35] K. Xing, F. Zhu, L. Zhai et al., “The liver transcriptome of two full-sibling Songliao black pigs with extreme differences in backfat thickness,” *Journal of Animal Science and Biotechnology*, vol. 5, no. 1, p. 32, 2014.
- [36] T. Alonzi, C. Mancone, L. Amicone, and M. Tripodi, “Elucidation of lipoprotein particles structure by proteomic analysis,” *Expert Review of Proteomics*, vol. 5, no. 1, pp. 91–104, 2008.
- [37] S. Yokoyama, “Assembly of high-density lipoprotein,” *Arteriosclerosis, Thrombosis, and Vascular Biology*, vol. 26, no. 1, pp. 20–27, 2006.
- [38] R. L. Hamilton, M. C. Williams, C. J. Fielding, and R. J. Havel, “Discoidal bilayer structure of nascent high density lipoproteins from perfused rat liver,” *Journal of Clinical Investigation*, vol. 58, no. 3, pp. 667–680, 1976.
- [39] P. H. Green, A. R. Tall, and R. M. Glickman, “Rat intestine secretes discoid high density lipoprotein,” *Journal of Clinical Investigation*, vol. 61, no. 2, pp. 528–534, 1978.
- [40] S. Wang and J. D. Smith, “ABCA1 and nascent HDL biogenesis,” *BioFactors*, vol. 40, no. 6, pp. 547–554, 2014.
- [41] X. Jin, E. K. Dimitriadis, Y. Liu et al., “Macrophages shed excess cholesterol in unique extracellular structures containing cholesterol microdomains,” *Arteriosclerosis, Thrombosis, and Vascular Biology*, vol. 38, no. 7, pp. 1504–1518, 2018.
- [42] H. Czarnecka and S. Yokoyama, “Regulation of cellular cholesterol efflux by lecithin:cholesterol acyltransferase reaction through nonspecific lipid exchange,” *Journal of Biological Chemistry*, vol. 271, no. 4, pp. 2023–2028, 1996.
- [43] R. Flores, X. Jin, J. Chang et al., “LCAT, ApoD, and ApoA1 expression and review of cholesterol deposition in the cornea,” *Biomolecules*, vol. 9, no. 12, p. 785, 2019.
- [44] S. Kersten, “Physiological regulation of lipoprotein lipase,” *Biochimica et Biophysica Acta*, vol. 1841, no. 7, pp. 919–933, 2014.
- [45] Y. Wang, T. Nakajima, F. J. Gonzalez, and N. Tanaka, “PPARs as metabolic regulators in the liver: lessons from liver-specific PPAR-null mice,” *International Journal of Molecular Sciences*, vol. 21, no. 6, p. 2061, 2020.
- [46] T. Aoyama, J. M. Peters, N. Iritani et al., “Altered constitutive expression of fatty acid-metabolizing enzymes in mice lacking the peroxisome proliferator-activated receptor alpha (PPARalpha),” *Journal of Biological Chemistry*, vol. 273, no. 10, pp. 5678–5684, 1998.
- [47] P. Puigserver, Z. Wu, C. W. Park, R. Graves, M. Wright, and B. M. Spiegelman, “A cold-inducible coactivator of nuclear receptors linked to adaptive thermogenesis,” *Cell*, vol. 92, no. 6, pp. 829–839, 1998.
- [48] T. Y. Huang, D. Zheng, J. A. Houmard, J. J. Brault, R. C. Hickner, and R. N. Cortright, “Overexpression of PGC-1 $\alpha$  increases peroxisomal activity and mitochondrial fatty acid oxidation in human primary myotubes,” *American Journal of Physiology Endocrinology and Metabolism*, vol. 312, no. 4, pp. E253–e263, 2017.
- [49] E. Mormeneo, C. Jimenez-Mallebrera, X. Palomer et al., “PGC-1 $\alpha$  induces mitochondrial and myokine transcriptional programs



- and lipid droplet and glycogen accumulation in cultured human skeletal muscle cells,” *PLoS One*, vol. 7, no. 1, article e29985, 2012.
- [50] N. Nikolić, M. Rhedin, A. C. Rustan, L. Storlien, G. H. Thoresen, and M. Strömstedt, “Overexpression of PGC-1 $\alpha$  increases fatty acid oxidative capacity of human skeletal muscle cells,” *Biochemistry Research International*, vol. 2012, Article ID 714074, 2012.
- [51] J. St-Pierre, S. Drori, M. Uldry et al., “Suppression of reactive oxygen species and neurodegeneration by the PGC-1 transcriptional coactivators,” *Cell*, vol. 127, no. 2, pp. 397–408, 2006.
- [52] D. M. Muoio and T. R. Koves, “Skeletal muscle adaptation to fatty acid depends on coordinated actions of the PPARs and PGC1 $\alpha$ : implications for metabolic disease,” *Applied Physiology, Nutrition, and Metabolism*, vol. 32, no. 5, pp. 874–883, 2007.
- [53] H. W. Tan, B. Anjum, H. M. Shen, S. Ghosh, P. M. Yen, and R. A. Sinha, “Lysosomal inhibition attenuates peroxisomal gene transcription via suppression of PPARA and PPARGC1A levels,” *Autophagy*, vol. 15, no. 8, pp. 1455–1459, 2019.
- [54] S. Sutti, C. Rigamonti, M. Vidali, and E. Albano, “CYP2E1 autoantibodies in liver diseases,” *Redox Biology*, vol. 3, pp. 72–78, 2014.
- [55] Y. Lu and A. I. Cederbaum, “CYP2E1 and oxidative liver injury by alcohol,” *Free Radical Biology and Medicine*, vol. 44, no. 5, pp. 723–738, 2008.
- [56] M. A. Amini, S. S. Talebi, and J. Karimi, “Reactive oxygen species modulator 1 (ROMO1), a new potential target for cancer diagnosis and treatment,” *Chonnam Medical Journal*, vol. 55, no. 3, pp. 136–143, 2019.
- [57] J. S. Chung, S. Park, S. H. Park et al., “Overexpression of Romo1 promotes production of reactive oxygen species and invasiveness of hepatic tumor cells,” *Gastroenterology*, vol. 143, no. 4, pp. 1084–1094.e7, 2012.
- [58] P. Patwari, W. A. Chutkow, K. Cummings et al., “Thioredoxin-independent regulation of metabolism by the alpha-arrestin proteins,” *Journal of Biological Chemistry*, vol. 284, no. 37, pp. 24996–25003, 2009.
- [59] E. Junn, S. H. Han, J. Y. Im et al., “Vitamin D3 up-regulated protein 1 mediates oxidative stress via suppressing the thioredoxin function,” *Journal of Immunology*, vol. 164, no. 12, pp. 6287–6295, 2000.
- [60] E. Lubos, J. Loscalzo, and D. E. Handy, “Glutathione peroxidase-1 in health and disease: from molecular mechanisms to therapeutic opportunities,” *Antioxidants & Redox Signaling*, vol. 15, no. 7, pp. 1957–1997, 2011.
- [61] F. Antunes, D. Han, and E. Cadenas, “Relative contributions of heart mitochondria glutathione peroxidase and catalase to H<sub>2</sub>O<sub>2</sub> detoxification in in vivo conditions,” *Free Radical Biology and Medicine*, vol. 33, no. 9, pp. 1260–1267, 2002.
- [62] J. I. Ramos Martínez, R. Díaz García, and A. M. Galarza, “The kinetic mechanism of glutathione peroxidase from human platelets,” *Thrombosis Research*, vol. 27, no. 2, pp. 197–203, 1982.
- [63] H. S. Marinho, F. Antunes, and R. E. Pinto, “Role of glutathione peroxidase and phospholipid hydroperoxide glutathione peroxidase in the reduction of lysophospholipid hydroperoxides,” *Free Radical Biology and Medicine*, vol. 22, no. 5, pp. 871–883, 1997.
- [64] R. Brigelius-Flohé and M. Maiorino, “Glutathione peroxidases,” *Biochimica et Biophysica Acta*, vol. 1830, no. 5, pp. 3289–3303, 2013.
- [65] M. C. JP, C. A. Roneker, W. Mu et al., “Development of insulin resistance and obesity in mice overexpressing cellular glutathione peroxidase,” *Proceedings of the National Academy of Sciences of the United States of America*, vol. 101, no. 24, pp. 8852–8857, 2004.
- [66] D. H. Ipsen, J. Lykkesfeldt, and P. Tveden-Nyborg, “Molecular mechanisms of hepatic lipid accumulation in non-alcoholic fatty liver disease,” *Cellular and Molecular Life Sciences*, vol. 75, no. 18, pp. 3313–3327, 2018.

## Research Article

# Exploring the Possible Link between the Gut Microbiome and Fat Deposition in Pigs

Guangmin Zhao <sup>1,2</sup>, Yun Xiang,<sup>3</sup> Xiaoli Wang,<sup>1</sup> Bing Dai,<sup>2</sup> Xiaojun Zhang,<sup>3</sup> Lingyan Ma,<sup>1</sup> Hua Yang <sup>1</sup> and Wentao Lyu <sup>1</sup>

<sup>1</sup>State Key Laboratory for Managing Biotic and Chemical Threats to the Quality and Safety of Agro-Products, Institute of Agro-Product Safety and Nutrition, Zhejiang Academy of Agricultural Sciences, Hangzhou 310021, China

<sup>2</sup>College of Animal Science, Zhejiang A&F University, Hangzhou 311300, China

<sup>3</sup>Institute of Animal Husbandry and Veterinary Medicine, Jinhua Academy of Agricultural Sciences, Jinhua 321011, China

Correspondence should be addressed to Wentao Lyu; [lvwt@zaas.ac.cn](mailto:lvwt@zaas.ac.cn)

Received 4 September 2021; Accepted 18 December 2021; Published 22 January 2022

Academic Editor: Zhihao Jia

Copyright © 2022 Guangmin Zhao et al. This is an open access article distributed under the Creative Commons Attribution License, which permits unrestricted use, distribution, and reproduction in any medium, provided the original work is properly cited.

Excessive lipid accumulation and high oxidative stress have become a serious health and economic problem in the pig industry. Fatness characteristics are crucial in pig production since they are closely related to meat quality. The gut microbiome is well acknowledged as a key element in fat deposition. But the link between gut microbiota and fat accumulation in pigs remains elusive. To examine whether there is a link between pigs' gut microbiome, lipogenic properties, and oxidative stress, we selected 5 high-fat pigs and 5 low-fat pigs from 60 250-day-old Jinhua pigs in the present study and collected the colon content, serum sample, and liver and abdominal fat segments from each pig for metagenomic analysis, the oxidative stress assay, and RT-qPCR analysis, respectively. The backfat thickness and fat content of the longissimus dorsi muscle were considerably higher in the high-fat pigs than in the low-fat pigs ( $P < 0.05$ ). An obvious difference in GSH-Px and MDA in the serum between the high- and low-fat pigs was observed. After RT-qPCR analysis, we found the gene expression of *ACCI* and *SREBPI* in the liver and *FAS*, *PPAR $\gamma$* , and *LPL* in the abdominal fat were significantly higher in high-fat pigs than in low-fat pigs ( $P < 0.05$ ). Additionally, metagenomic sequencing revealed that high-fat pigs had a higher abundance of Archaeal species with methanogenesis functions, leading to more-efficient fat deposition, while low-fat pigs had higher abundances of butyrate-producing bacteria species that improved the formation of SCFAs, especially butyrate, thus alleviating fat deposition in pigs. Furthermore, a total of 17 CAZyme families were identified to give significant enrichments in different fat phenotypes of pigs. This study would provide a detailed understanding of how the gut microbiome influences fat deposition in pigs, as well as a hint for improving growth performance and fatness traits by manipulating the gut microbiome.

## 1. Introduction

The gut microbiota is a complex and dynamic ecosystem composed of trillions of microorganisms living in the digestive tract and acting as a regulator and barrier for other metabolic organs [1]. It has been linked to the onset of metabolic disorders such as obesity and oxidative stress. A chronic inflammatory process such as oxidative stress and metabolic disorders may result from the alteration in the structure of gut microbiota [2].

Fatness traits are not only a characteristic of obesity and oxidation injury but also very important in pig production since they are linked to fattening features and meat quality. The accumulation of excessive fat in animals and humans has become an increasing threat to the animal production industry as well as human health, which would lead to obesity and could further set off many other health problems such as cardiovascular disease, arthritis, and dementia. Furthermore, lipid accumulation and impaired lipid metabolism are associated with pathophysiological phenotypes in pigs,

which has turned into a severe economic and health problem in pig production [3].

Chronic inflammation in adipose tissue due to excessive fat accumulation would promote proinflammatory status and oxidative stress [4]. The substantial rise in the generation of free radicals in humans and animals that disrupts the antioxidation-oxidation equilibrium is referred to as oxidative stress [5]. A variety of illnesses have been reported to be pathologically caused by oxidative stress, which has been shown to be correlated with fat accumulation [4]. In pigs, a significant number of free radicals are produced because of oxidative damage, which leads to several diseases [6]. More importantly, the development of the pig industry would be hampered by oxidative stress due to oxidative stress directly limiting the growth performance and health of pigs [5]. Therefore, studying the oxidative stress in pigs is of great significance to pig production, as well as other animals and human health.

Similar to humans, the pig gut microbiota is also a huge, sophisticated, and dynamic microbial population with a variety of vital biological functions [7], including energy harvest, methane synthesis, and the synthesis of short-chain fatty acids (SCFAs) [8]. Pig fatness phenotypes are closely associated with the composition and diversity of the microbial community in the gastrointestinal gut tract. The composition of fatty acids in the adipose tissues and liver could be altered by the activities of the gut microbiota [9]. The Jinhua pig in Zhejiang Province, China, is characterized by its slow growth speed and high intramuscular fat content, which is considered an excellent model for studying fat deposition [10]. In the previous study, we compared the bacterial community structure of obese Jinhua pigs and lean Landrace pigs and illustrated a clear causal connection between gut microbiota and fat deposition by fecal microbiota transplantation [11].

Most of the related studies focused on the differences in the structure of the intestinal microflora and fat deposition among different pig species. However, the relationship between fat-related phenotypes and the gut microbiome in pigs is still unclear. Therefore, in this study, fatness characteristics, fat-related gene expression in abdominal fat and liver, and oxidative stress in serum were measured in high- and low-fat pigs, respectively. Furthermore, the composition, diversity, and potential functions of the gut microbiota between the two groups were studied using a high-throughput metagenomic sequencing technique, further analyzing the association between the gut microbiome and fat deposition. This study will provide basic data for improving fatness traits in pig production by manipulating the gut microbiome.

## 2. Materials and Methods

**2.1. Animal Experiments and Sample Collection.** A total of 60 newly born Jinhua pigs were fed in 6 pens, 10 pigs per pen, in a commercial pig facility with a standard corn-soybean-based diet and water *ad libitum* as described previously [12]. Within two months before slaughter, each pig was healthy and had not been treated with antibiotics. At 250 days of age, pigs were killed to acquire blood samples, liver

segments, and abdominal adipose tissue. Carcass traits, namely, body weight, loin muscle area, backfat thickness, and fat content in longissimus dorsi muscle, were analyzed by a principal component analysis (PCA). These statistics were utilized to determine which pigs were the most extreme for the selection of the most extreme pigs [13, 14]. Five high-fat (H) and five low-fat (L) pigs were chosen to collect luminal samples from the same colon location. Briefly, the gastrointestinal tract was peeled from the enterocolia. The luminal samples were collected from the middle section of each pig's colon. Within 30 min after slaughter, all of the luminal samples were taken and divided into two parts: one was for the measurement of SCFAs, and the other one was placed in a  $-80^{\circ}\text{C}$  refrigerator until DNA extraction after being dipped in liquid nitrogen.

All the procedures for animal experiments were approved by the Zhejiang Academy of Agricultural Sciences Institutional Animal Care strictly according to the relevant rules and regulations (Ethical code: ZAAS-2017-009).

**2.2. Luminal DNA Extraction, Metagenomic Sequencing.** According to the manufacturer's recommendations, the QIAamp Fast DNA Stool Mini Kit (Qiagen, Germany) was used to extract the luminal DNA from each colon content sample. A NanoDrop 1000 spectrophotometer (NanoDrop Technologies, Wilmington, DE, USA) was used to measure the amount and quality of DNA, and sterile water was used to dilute the DNA concentration to a final concentration of 1 ng/L. The Illumina TruSeq™ DNA Sample Prep Kit was used to generate libraries, which were sequenced on an Illumina HiSeq 2500 platform by a commercial sequencing company, Novogene (Beijing, China).

**2.3. De Novo Assembly of Short Reads.** We used Trimmomatic [15] for the quality control of raw datasets to remove the 3'- and 5'-end of reads, eliminate poor quality bases ( $<20$ ), and trim containing 10% N of reads, and small segments ( $<75$  bp). The BWA [16] was performed to align the reads with the pig genome to filter out the host DNA from the reads. Megahit [17] (<https://github.com/voutcn/megahit>) was used to de novo assemble the filtered reads for each sample. Contigs were continuous sequences that had clear linkages between each other.

**2.4. Gene Prediction and Functional Annotation.** The ORFs (open reading frames) from each sample's contigs were predicted using METAPRODIGAL (<http://prodigal.ornl.gov/>). We used cd-hit [18] software (<http://www.bioinformatics.org/cd-hit/>) to exclude the redundant genes (parameters for 95% identity; 90% coverage) from all the predicted ORFs. And then, Salmon [19] (<https://github.com/COMBINE-lab/salmon>) was used to determine gene abundances by mapping the original sequences to anticipated genes. Finally, with BLASTP [20] (BLAST Version 2.2.28+, <http://blast.ncbi.nlm.nih.gov/Blast.cgi>), the taxonomy of the colon microbiota was evaluated against the NR database. The relative abundances of taxa at the domain, phylum, genus, and species levels were determined using taxonomic profiles. The NMDS was conducted at the gene level based on the

Bray-Curtis dissimilarity matrices. The KEGG database (<http://www.genome.jp/kegg/>) was used to annotate the contigs with a BLAST  $E$  value of  $1e-5$ . Hmmscan (<http://hmmer.janelia.org/search/hmmscan>) was used to annotate the CAZy functions.

**2.5. Real-Time Quantitative PCR (RT-qPCR).** Gene expression was measured in the liver and abdominal adipose tissue. According to the manufacturer's instructions, the RNeasy Plus Mini Kit (Qiagen) was used to isolate the total RNA from each sample of abdominal fat and liver segments. The first-strand cDNA was generated using the SuperScript II Reverse Transcription Kit (Invitrogen). The gene expression was evaluated by RT-qPCR on the ABI Prism 7700 Sequence Detector (Applied Biosystems) with gene-specific primers (see Supplementary Tables S1). The following were the reaction conditions: 95°C for 5 min, followed by 40 cycles of 15 s at 94°C, 30 s at 63°C, and 1 min at 72°C and fluorescence collection as previously described [11]. The relative gene expression level was determined by the  $2^{-\Delta\Delta Ct}$  method [21] using the geometric mean of glyceraldehyde 3-phosphate dehydrogenase (GAPDH) mRNA as the housekeeping gene for the data normalization.

**2.6. Colonic Butyrate-Producing Functional Gene Analysis.** The qPCR was performed in triplicate for the DNA extracted from each sample to assess the gene copy number of the butyrate-producing functional genes, namely, butyrate kinase and butyryl CoA: acetate CoA transferase, in pig intestinal contents on an ABI Prism 7700 Sequence Detector (Applied Biosystems) [22, 23] using gene-specific primers (see Supplementary Tables S2) and SYBR Green PCR Master Mix (Takara, Tokyo, Japan). The thermal cycling system was 95°C for 2 min, 35 cycles of 15 s at 95°C, 45 s at 58°C, and 1 min at 72°C. The specificity of the reaction for each gene was verified by a melting curve analysis. Standard curves from known quantities of plasmid DNA were used to determine the copy number of each gene. The data from qPCR experiments was represented as gene copies per gram of luminal content.

**2.7. Oxidative Stress Determination.** Serum antioxidant levels were determined after homogenization with saline (1:9  $w/v$ ) followed by centrifugation at  $11,000 \times g$  for 15 minutes at 4°C. As recommended by the manufacturer's instructions, we used Nanjing Jiancheng Bio (Nanjing, China) diagnostic kits to detect indicators including malondialdehyde (MDA), superoxide dismutase (SOD), and glutathione peroxidase (GSH-Px).

**2.8. SCFA Measurement.** As mentioned in our previous study [24], the gas chromatographic (GC) was used to determine the levels of SCFAs in each luminal content sample. Shortly, the 100 mg luminal content sample was weighed into a 1.5 mL centrifuge tube and suspended in 9 volumes of Milli-Q water. Following a 10 min centrifugation at 10,000 rpm, 1,000  $\mu\text{L}$  of the supernatant was supplemented with 0.2 mL of crotonic acid (internal standard). Finally, following the membrane filtering (0.22  $\mu\text{m}$ ), the mixture was put into the GC-2010 plus (Shimadzu, Kyoto, Japan) with

an FID detector operating at 180°C. The chromatographic conditions were as follows: column 110°C, vaporization chamber 180°C. The carrier gas was nitrogen at 0.06 MPa while the auxiliary gas was hydrogen and air with the pressure of 0.05 MPa and 0.05 MPa, respectively.

**2.9. Statistical Analysis.** All statistical analyses were conducted using the unpaired two-tailed Students'  $t$ -test with a  $P$  value  $< 0.05$  as the level of statistical significance. Data were presented as mean  $\pm$  standard deviation (SD).

### 3. Results

**3.1. Fatness Phenotypes between the High- and Low-Fat Pigs.** To determine whether there is a significant difference in the fatness phenotypes between the two groups, pigs were raised under standard management and sacrificed at 250 days old to determine body weight, loin muscle area, backfat thickness, and fat content of longissimus dorsi muscle. The high-fat pigs showed significantly higher backfat thickness and fat content of longissimus dorsi muscle than the low-fat pigs ( $P < 0.05$ , see Figures 1(b) and 1(d)). However, the two groups had no significant differences in body weight and loin muscle area (see Figures 1(a) and 1(c)).

**3.2. Expression of Lipid Metabolism Genes.** To further test the gene expression of lipid metabolism in the liver and abdominal fat tissue, we collected liver and abdominal fat segments from each of the high- and low-fat pigs, followed by RNA isolation and RT-qPCR analysis. In the liver, the two key lipogenic genes, *ACC1* (acetyl-CoA carboxylase-1) and *FAS* (fatty acid synthase), showed higher levels in the high-fat pigs than in the low-fat pigs, with *ACC1* being significantly higher ( $P < 0.05$ , see Figure 2(a)). Additionally, *SREBP1* (Sterol Regulatory Element Binding Protein-1) was also significantly higher in the liver of high-fat pigs ( $P < 0.05$ ), while the gene expression of *MLXIPL* (MLx-interacting protein-like) showed no significant difference (see Figure 2(a)).

In the abdominal fat tissue, a significant increase in the gene expression of lipogenesis genes, *FAS* and *LPL* (lipoprotein lipase), and the adipogenesis gene *PPAR $\gamma$*  (peroxisome proliferator-activated receptor- $\gamma$ ) in the high-fat pigs was observed ( $P < 0.05$ ). The *ACC1* and *FABP4* (fatty acid-binding proteins 4) showed higher levels in the high-fat pigs than the low-fat pigs with no significant difference ( $P > 0.05$ , see Figure 2(b)).

**3.3. Oxidative Stress Levels in Pigs with Different Fat Deposition.** To evaluate whether oxidative stress functions in the lipid metabolism, the key markers of oxidative stress, including MDA, GSH-Px, and SOD, were further analyzed. The low-fat pigs had decreased MDA content and increased GSH-Px activity compared to the high-fat pigs (see Figure 3,  $P < 0.05$ ).

**3.4. Profiling of the Colon Metagenome in Pigs.** Next, the composition and diversity of the colonic microbiota between the two groups were investigated by metagenomic sequencing. For the construction of libraries, we pooled 10 samples

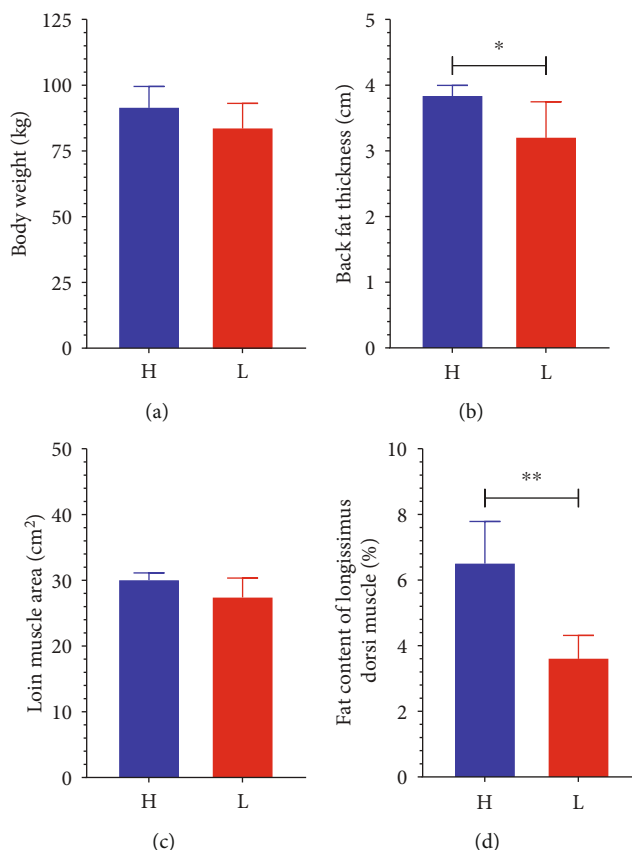


FIGURE 1: Fatness phenotypes in the high- and low-fat pigs. Newly born piglets were fed commercial feed for 250 days before being sacrificed. The body weight (a), backfat thickness (b), loin muscle area (c), and fat content of longissimus dorsi muscle (d) were determined. Data are expressed as mean  $\pm$  SD ( $n = 5$ ) and analyzed by the unpaired two-tailed Students'  $t$ -test. H: the high-fat pigs; L: the low-fat pigs. \* $P < 0.05$  and \*\* $P < 0.01$ .

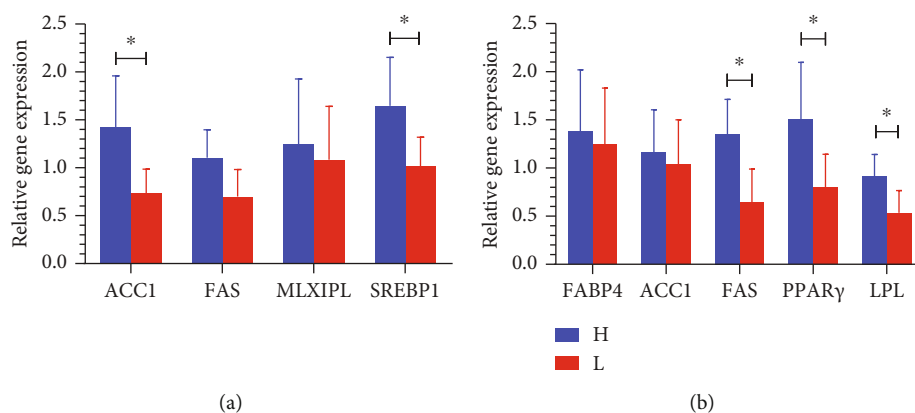


FIGURE 2: Relative gene expression levels of lipid metabolism genes in the liver (a) and abdominal fat (b) of Jinhua pigs. The tissue segments of liver and abdominal fat were collected from the high- and low-fat pigs at 250 days old for RNA isolation. The relative expression level of each indicated gene was determined by RT-qPCR using the  $2^{-\Delta\Delta C_t}$  method. Data normalization employs GAPDH as a housekeeping gene. Data are expressed as mean  $\pm$  SD ( $n = 5$ ) and analyzed by the unpaired two-tailed Students'  $t$ -test. H: the high-fat pigs; L: the low-fat pigs. \* $P < 0.05$ .

of luminal DNA from Jinhua pigs. Each DNA pool included an average of 12.84 Gb of raw data (9.94–19.00 Gb). Clean data ranged from 9.33 Gb to 17.90 Gb after removing low-quality reads and host contamination. All short sequence

data was assembled by Megahit [25] (<https://github.com/voutcn/megahit>). Ten DNA pool samples had a total number of contigs ranging from 243,029 to 710,018 with a length greater than 500 bp. METAProdigal [26] (<http://prodigal>

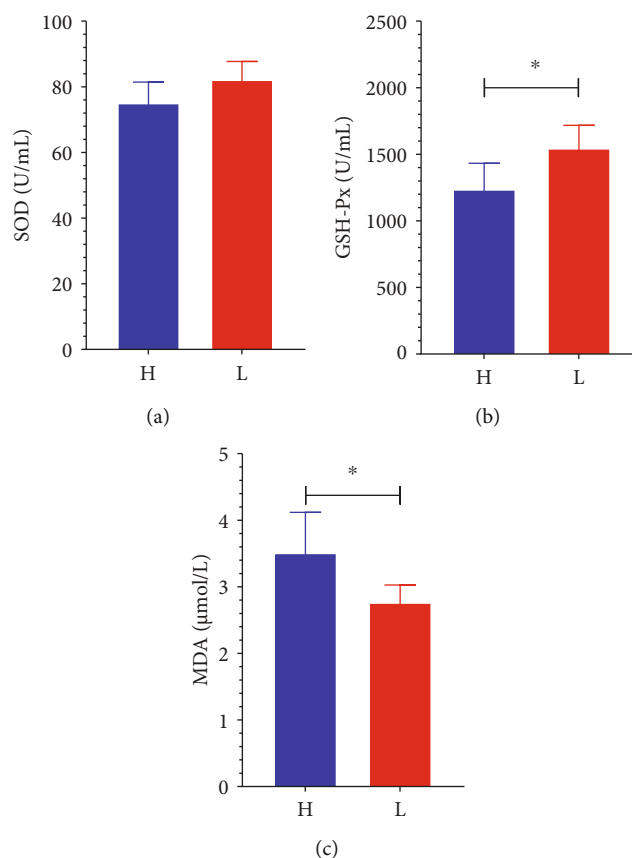


FIGURE 3: Oxidative stress levels in the high- and low-fat pigs. The serum samples were collected from the high- and low-fat pigs at 250 days old for the determination of SOD activity (a), GSH-Px activity (b), and MDA content (c) by different assays. Data are expressed as mean  $\pm$  SD ( $n = 5$ ) and analyzed by the unpaired two-tailed Student's  $t$ -test. H: the high-fat pigs; L: the low-fat pigs. \* $P < 0.05$ .

.ornl.gov/) predicted the open reading frame (ORF) of each contig. A total of 5,617,408 ORFs that were longer than 60 bp were obtained in the pool of ten samples (see Table 1).

**3.5. Comparison of Microbial Domains between High- and Low-Fat Pigs.** Nonmetric multidimensional scaling (NMDS) revealed a robust separation between high- and low-fat pigs (see Figure 4(a)). The microbial structure in the colons of the two groups was compared. The relative abundance of Archaea in the high-fat group was obviously higher than that of low-fat pigs ( $P < 0.05$ ) while eukaryota and viruses were not significantly different ( $P > 0.05$ , see Figure 4(b)). We then compared the relative abundance of Archaea bacterial genera between the colon microbiomes of the two groups with distinct fatness. Two genera (see Figure 4(c)) and seven species (see Figure 4(d)) were identified to give a significant difference in the relative abundances between the two groups ( $P < 0.05$ ), which all belong to the methanogen genus.

**3.6. Significant Difference in Bacterial Community Compositions of Pigs with Distinct Fatness Phenotypes.** As shown in Supplementary Figure S1, the low-fat pigs exhibited a higher  $\alpha$  diversity of gut microbiota than the high-fat pigs. Further studies were performed on the microbial community structures between the two groups

with distinct fatness phenotypes in the colon. *Bacteroidetes* were found in significantly higher abundance in the colons of low-fat pigs than in high-fat pigs ( $P < 0.05$ , Supplementary Figure 2). At the genus level, 13 genera were significantly different between the two groups. *Prevotella* and *Bacteroides* were significantly more abundant in the colons of low-fat pigs ( $P < 0.05$ ). *Prevotella* relative abundance was 2.979% and 5.659% between the two groups, respectively, while *Bacteroides* relative abundance was 1.300% and 1.935%, respectively. Additionally, the relative abundance of *Prevotella* and *Bacteroides* was above 1.0%, whereas most other genera were below 1.0% in the colon. It is worth noting that *Acidaminococcus* was significantly enriched in the low-fat pigs ( $P < 0.05$ , see Figure 5(a)).

At the species level, we discovered 33 bacterial species giving different enrichments between the two groups. Among these species, 12 species were enriched in the high-fat pigs, while the other 21 species were more abundant in the low-fat pigs (see Figure 5(b)). Furthermore, we observed that ten of the 12 species with higher abundances in the high-fat pigs are *Firmicutes* and *Tenericutes*. The bacteria abundant in low-fat pigs have been correlated with fiber fermentation and butyrate production, namely, *Ruminococcus* sp. AF12-5 [27], *Faecalibacterium* sp. OF04-11AC [28], and *Oscillibacter* sp. CAG:155 [29].

TABLE 1: Data summary of metagenomics.

Sample	Raw bases (Mbp)	Clean bases (Mbp)	Contigs	Contigs bases (bp)	N50 (bp)	ORFs	Average length (bp)
H1	11,300	10,500	277327	345242102	1,337	581,709	619.16
H2	9,940	9,330	243029	303872492	1,315	520,091	603.23
H3	10,300	9,570	249525	280357289	1,151	448,785	619.48
H4	12,400	11,500	298036	321492268	1,026	444,650	574.05
H5	15,000	13,800	710018	626251331	824	526,644	610.65
L1	12,500	11,700	304407	394804127	1,379	797,874	629.86
L2	10,500	9,980	285676	351527843	1,283	586,934	636.42
L3	19,000	17,900	399192	555397511	1,523	458,592	539.68
L4	14,200	13,500	275692	415245171	1,805	492,082	504.58
L5	13,300	12,100	351437	358387739	942	760,047	372.78

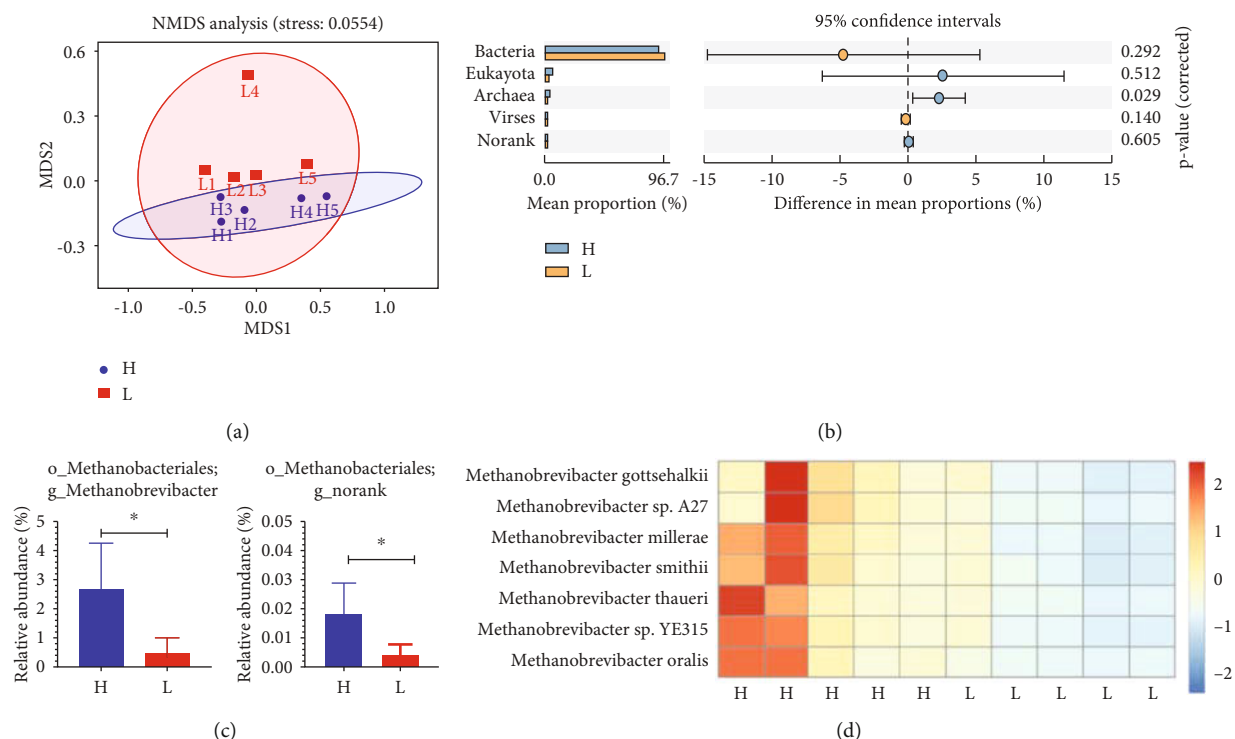


FIGURE 4: Microbial profiles of the high- and low-fat pigs. The colon content samples were collected at 250 days old for DNA isolation and metagenome sequencing. (a) NMDS analysis of colon content samples was performed with the abundance of genes. (b) The relative abundance of microbial domains between the two groups. (c) The relative abundance of Archaea at genus level between the two groups. \* $P < 0.05$ . (d) The relative abundance of Archaea at species level between the two groups. The heatmap was generated with  $z$ -score calculated from the relative abundance of each Archaea species. Data are expressed as mean  $\pm$  SD ( $n = 5$ ) and analyzed by the unpaired two-tailed Student's  $t$ -test. H: the high-fat pigs; L: the low-fat pigs.

**3.7. Gut Microbiome Functional Capacity in Pigs with Different Fatness Phenotypes.** The functional capacity of the gut microbiome between the two groups was further analyzed using KEGG annotation. At Level 2 of KEGG function analysis, "Glycan biosynthesis and metabolism" was the most significantly different metabolic function between the two groups (see Figure 6(a)). At Level 3, "Methane metabolism," "Other glycan degradation," and "RNA polymerase" were found to be the significant markers in the pigs with a distinct fatness phenotype. More importantly, the relative

abundance in the function pathway profile of "Other glycan degradation" was higher in the low-fat pigs than in the high-fat pigs (see Figure 6(b)).

To further study the colonic microbiota's functional capacity, we analyzed the enzymes that break down glycans (CAZymes: Carbohydrate-Active Enzymes) [30]. There were significant differences in the enrichments of 17 CAZyme families between the two groups of pigs ( $P < 0.05$ , see Figure 6(c)). We found 2 enriched CAZyme genes, which function to degrade carbohydrates such as cellulose,

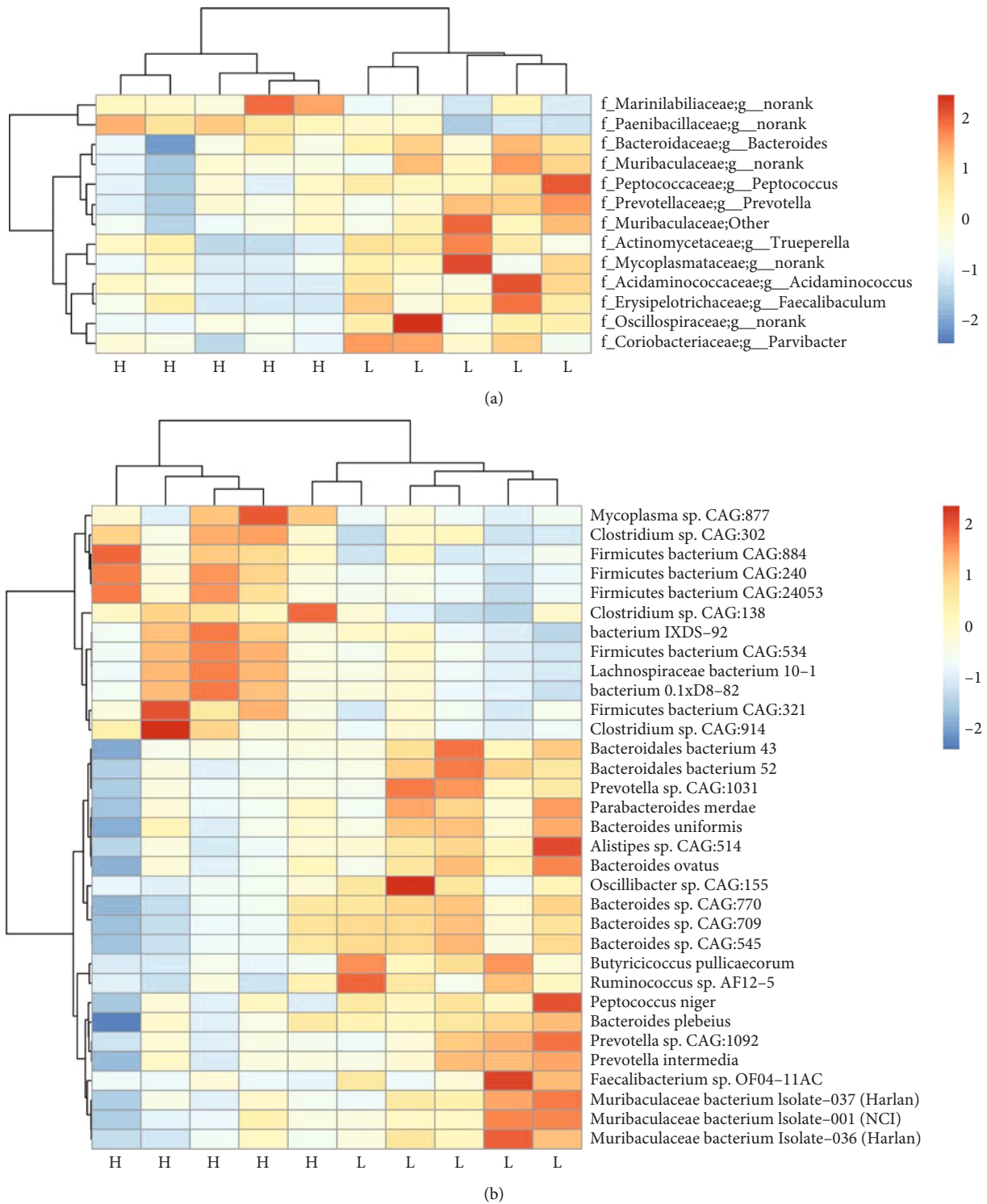


FIGURE 5: The relative abundance of microbiota in the colon of the high- and low-fat pigs. The colon content samples were collected from 5 high-fat and 5 low-fat pigs at 250 days old for DNA isolation and metagenome sequencing. The genus (a) and species (b) levels of bacteria in the colons of high- and low-fat pigs were compared. Heatmaps were generated with z-score calculated from the relative abundance of each bacteria genus (a) or species (b). The top 13 genera and 33 species are shown. H: the high-fat pigs; L: the low-fat pigs.

hemicellulose, and starch, while 6 were enriched in the low-fat pigs (GH28, GH76, GH81, GH106, CE6, and AA6). GTs had the function of carbohydrate synthesis. In the present study, the high-fat pigs had 5 enriched GTs, namely, GT7,

GT66, GT76, GT81, and GT84, while the low-fat pigs had 3 enriched GTs, namely, GT20, GT23, and GT90. In addition, the carbohydrate-binding modules (CBMs) are noncatalytic CAZymes with the function of the breakdown of



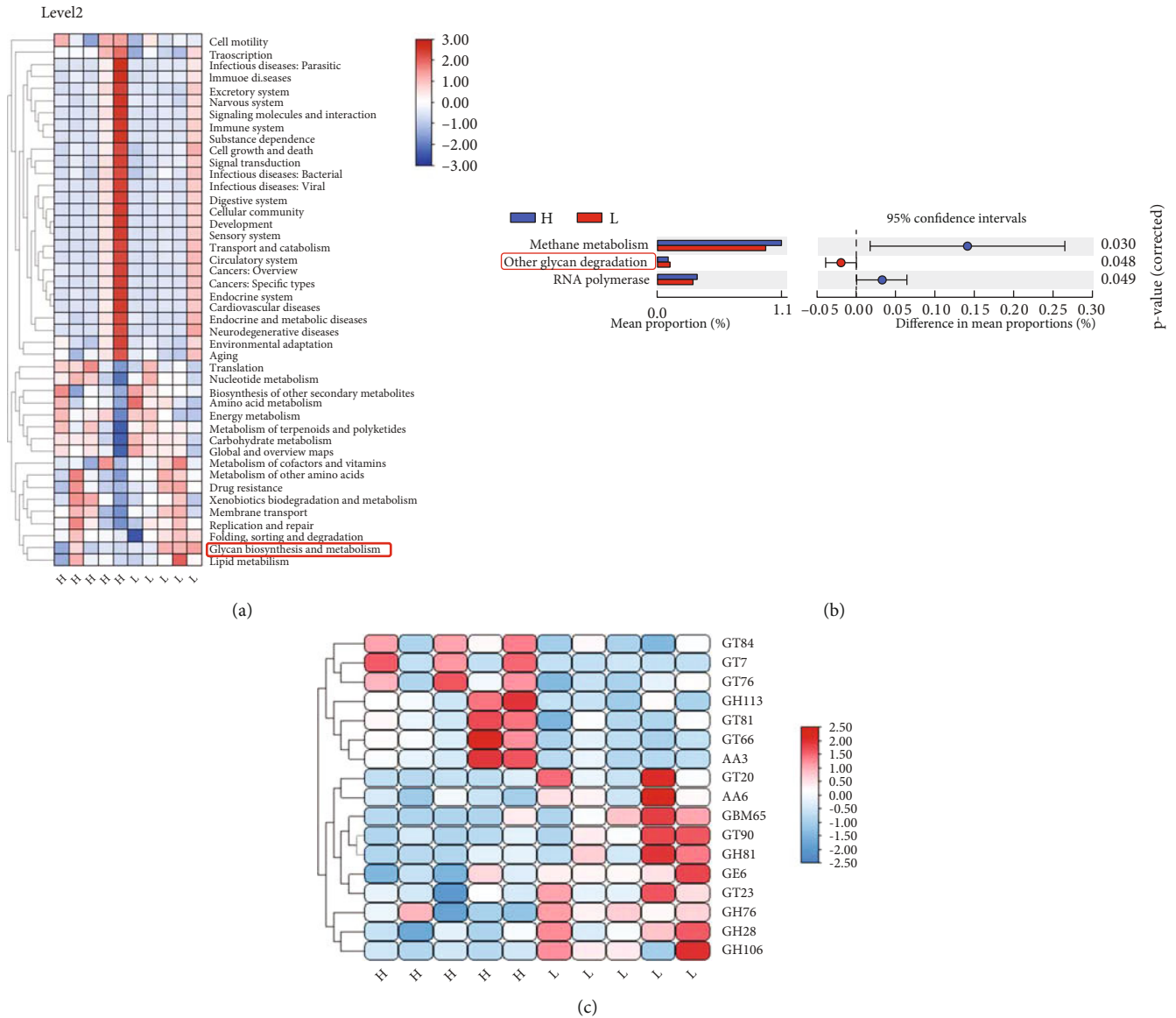


FIGURE 6: Enrichment of CAZymes and KEGG functions in the colon. The colon content samples were collected from 5 high-fat and 5 low-fat pigs at 250 days old for DNA isolation and metagenome sequencing. (a) The relative abundance of each KEGG pathway (Level 2) in the high- and low-fat pigs after an enrichment analysis. (b) The relative abundance of each KEGG subsystem (Level 3) in the high- and low-fat pigs after an enrichment analysis. (c) The relative abundance of each CAZyme functional term after an enrichment analysis. Heatmaps were generated with  $z$ -scores calculated from the relative abundance of each KEGG or CAZyme function. H: the high-fat pigs; L: the low-fat pigs; GH: Glycoside Hydrolase; GT: Glycosyl Transferase; PL: Polysaccharide Lyase; CE: carbohydrate esterases; CBM: carbohydrate-binding module; AA: Auxiliary Activities.

complex carbohydrates. The low-fat pigs had 1 enriched CBMs in the colon, CBM65.

**3.8. Changes in Colonic SCFA Levels in the Pigs with Different Fatness Phenotypes.** To examine whether pigs with different fatness phenotypes would alter the SCFA content in the colon, we quantified the absolute concentrations of the total SCFAs, namely, propionate, acetate, and butyrate. In comparison to the high-fat pigs, the low-fat pigs' colons had much higher levels of acetate, propionate, and butyrate (see Figure 7(a)). Furthermore, the colon of low-fat pigs had a relatively higher abundance of butyryl-CoA acetate-

CoA transferase (see Figure 7(b)), which functions to modulate the butyrate production in the colonic microbiome.

To reveal the potential linkage between gut microbiota and SCFAs, we correlated between differential gut microbiota and SCFA levels. At the species level, *Bacteroides plebeius*, *Bacteroides uniformis*, *Bacteroides ovatus*, *Peptococcus niger*, *Bacteroides* sp. CAG:770, 709, 545, and *Bacteroidales bacterium* 43, which belong to the Bacteroidetes phyla, were positively correlated with intestinal contents SCFA levels, especially with propionate and butyrate. Species *Firmicutes bacterium* CAG:884, 240, 24053 and *Clostridium* sp. CAG:302 (which belongs to phylum Firmicutes)

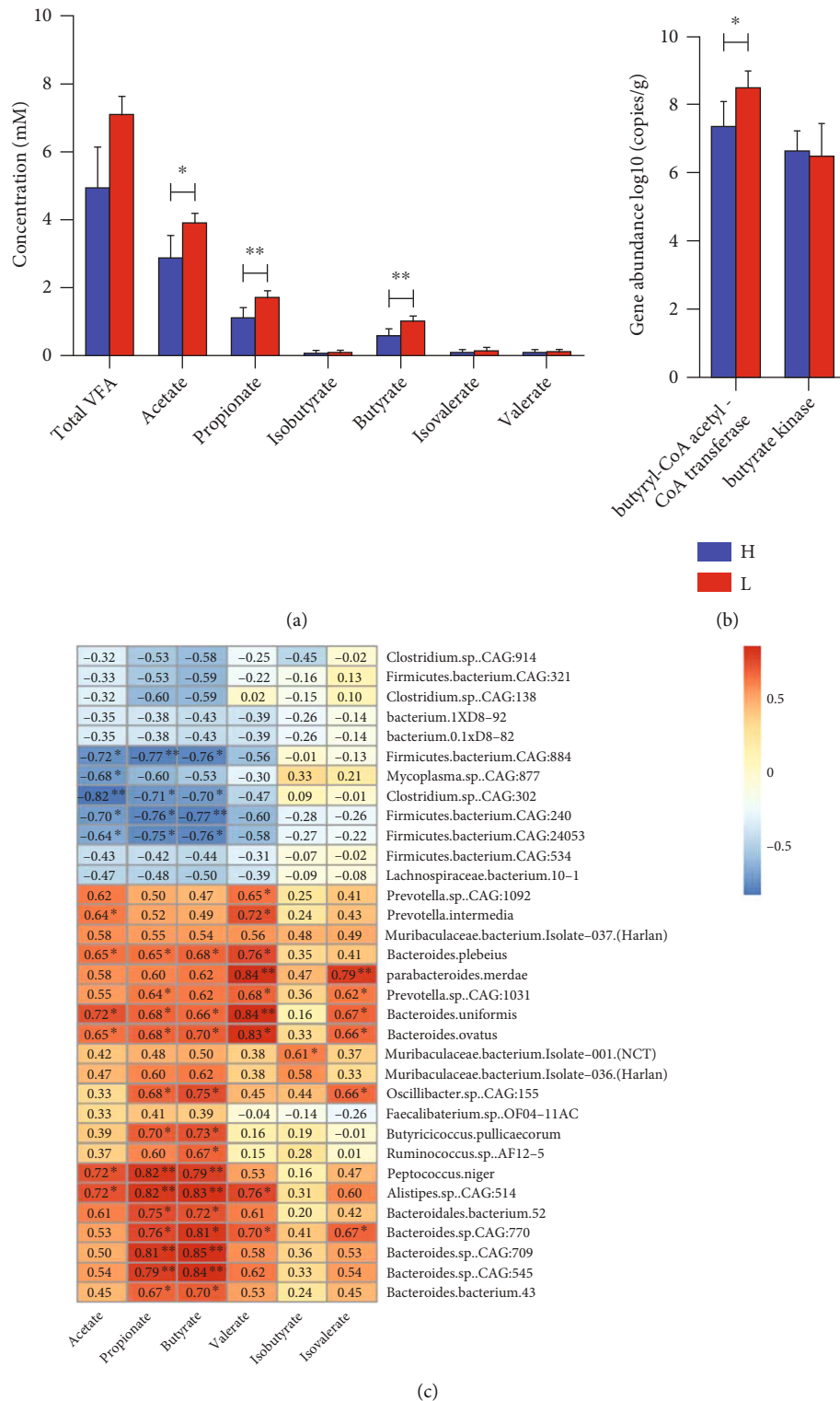


FIGURE 7: The association between colonic SCFA levels and colonic microbiome in the high- and low-fat pigs. The colon content samples were collected from 5 high-fat and 5 low-fat pigs at 250 days old for the determination of SCFA content, DNA isolation, and metagenome sequencing. (a) Concentrations of SCFAs in the colons of the two groups were examined by GC. Data are expressed as mean  $\pm$  SD ( $n = 5$ ) and analyzed by the unpaired two-tailed Student's  $t$ -test. (b) The gene abundance of the butyrate-producing genes in the colon of the high- and low-fat groups. Data was expressed as log10 gene copies of total DNA/g colon content. (c) The Spearman correlation between the 33 differentially abundant species and SCFAs in the colon of Jinhua pigs. The X-axis shows SCFAs, whereas the Y-axis shows bacteria species. The chart's various colors and numbers reflect the correlation coefficient between the SCFA and bacteria species indicated. H: the high-fat pigs; L: the low-fat pigs. \* $P < 0.05$  and \*\* $P < 0.01$ .

were negatively correlated with acetate, propionate, and butyrate levels. These results revealed the changed composition and function of the gut microbiota might well have contributed to the SCFA production in the colon (see Figure 7(c)).

#### 4. Discussion

The gut microbiota is considered essential in the utilization of nutrients and energy and the maintenance of healthy status in farm animals. Thus, the gut microbiota is regarded as an important component affecting the growth performance and development of pigs. Nowadays, numerous studies investigating the structure of the gut microbial community in pigs by metagenomics have been proposed to reveal the association between gut bacterial species and porcine fatness in different breeds [31]. We explored the interaction among the gut microbiota, lipogenic features, and oxidative stress in pigs with two different fat phenotypes. Furthermore, we tried to implicate the possible relationship between the gut microbiome and fat deposition in pigs using metagenomic analysis.

The liver and adipose tissue are the main parts of the body that deposit, metabolize, and transport fat. *ACC1*, *FAS*, *SREBP-1*, and *ChREBP* are the key genes in de novo fat synthesis [32]. The gene expression of *ACC1* and *SREBP-1* was significantly higher in the liver of the high-fat pigs than in the low-fat pigs, indicating that high-fat pigs might have a stronger ability to synthesize fat than low-fat pigs. The abdomen and intestines are the main sites of fat accumulation. The “master regulator” of adipogenesis is *PPAR $\gamma$* , required for fat cell production [33]. The upregulation of *PPAR $\gamma$* , *LPL*, and *FAS* in the high-fat pigs indicated enhanced lipid synthesis in the abdomen. Collectively, the imbalance in lipid metabolism might contribute to the abnormal fat accumulation in pigs.

On the other hand, the development of the pig industry would be hampered by oxidative stress due to oxidative stress directly limiting the growth performance and health of pigs. MDA is a biomarker for free radical species-related damage [34]. In the present study, MDA levels in serum were obviously higher in high-fat pigs than in low-fat pigs. Increased oxidative stress associated with fat consumption may alter the bacterial composition and the expression of lipogenic genes. GSH-Px is a critical enzyme that catalyzes hydrogen peroxide decomposition, which would protect the structure and function of the cell membrane [35]. GSH-Px levels were significantly lower in high-fat pigs. These findings show that high-fat pigs are more susceptible to oxidative stress than low-fat pigs, and hence more susceptible to obesity.

Consistent with our earlier investigation of 16S rRNA gene sequencing in pigs [23], the bacterial community of the two groups showed taxonomic discrepancies. It implies that bacteria contribute more to host fatness than other microbial kingdoms. Bacteria, not other microbial kingdoms, are responsible for the majority of the breakdown and fermentation of feed biopolymers [36]. Interestingly, the majority of the species with significantly increased abun-

dances in the low-fat pigs were from the *Bacteroides* genus, which is one of the most frequent core genera in the pig colony. *Bacteroides* was able to utilize the fermentation of dietary fibers to produce acetate, propionate, and butyrate [24]. *Prevotella* and *Bacteroides* were found to be significantly less abundant in the colons of high-fat pigs than in low-fat pigs. The more *Bacteroides-Prevotella-Porphyrromonas* there are in developing pigs, the better their ability to ferment polysaccharides to SCFAs [37]. Furthermore, *Bacteroides-Prevotella* was negatively correlated with inflammation and fat mass development in diet-induced obese mice [38]. Taken together, these results suggest that enhanced SCFA production in the low-fat pigs might be linked with the higher abundance of *Prevotella* and *Bacteroidetes*, which further alleviate host lipid accumulation.

Accordingly, our findings indicated that colonic SCFA levels were significantly higher in pigs with low-fat in comparison to pigs with high-fat traits. Butyrate could directly activate AMP kinase to prevent mice from having excess fat deposition in the liver [39]. The mice transplanted from lean cotwin’s fecal microbiota showed lower fat storage in adipose tissue compared to the mice transplanted from obese cotwin’s fecal microbiota [40]. Importantly, we found correlations between SCFAs and differential gut microbiota in pigs. The phylum *Firmicutes* and its subordinate species were related to reduced SCFAs, whereas the phylum *Bacteroidetes* and its subordinate species were related to increased SCFAs. All SCFAs showed synchronous correlations with the differential gut microbiota, suggesting that the differential gut microbiota and the SCFAs they produced might work synchronously in fat deposition.

Based on the metagenomics, KEGG analysis revealed the gut microbiome functional changes in the two groups. The metagenomes of the high-fat pigs had a significantly higher enrichment of methane metabolism and RNA polymerase. Methane metabolism, in particular, has been reported to produce methane from hydrogen with carbon dioxide, acetate, and various methyl metabolites [41]. Bacterial NADH dehydrogenases could be suppressed by the improvement of H<sub>2</sub>, resulting in a decrease in ATP output [42]. Methane is able to slow down the gut transport rate, which allows nutrients to stay in contact with the gut for longer, giving more time for nutrients and energy to be absorbed. This might explain why the high-fat pigs gained more weight than the low-fat pigs.

Since glycan degradation was found to be significantly enriched in the functional microbiome of low-fat pigs, we further determined that CAZymes shifted between the two groups in the present study. The results showed that GH, CE, PL, AA, and CBM, which exert a function of carbohydrate degradation, were enriched in low-fat pigs, implying that low-fat pigs might have a better ability to deconstruct complex substrates. For example, the colon of the low-fat pigs showed a higher relative abundance of GH28, GH76, GH81, and GH106, which are polygalacturonosidase [43],  $\alpha$ -1,6-mannanase [44],  $\beta$ -1,3-glucanase [45], and  $\alpha$ -L-rhamnosidase [46], respectively.

In contrast to the low-fat pigs, the higher abundance of GTs in the high-fat pigs showed that the colon microbiomes

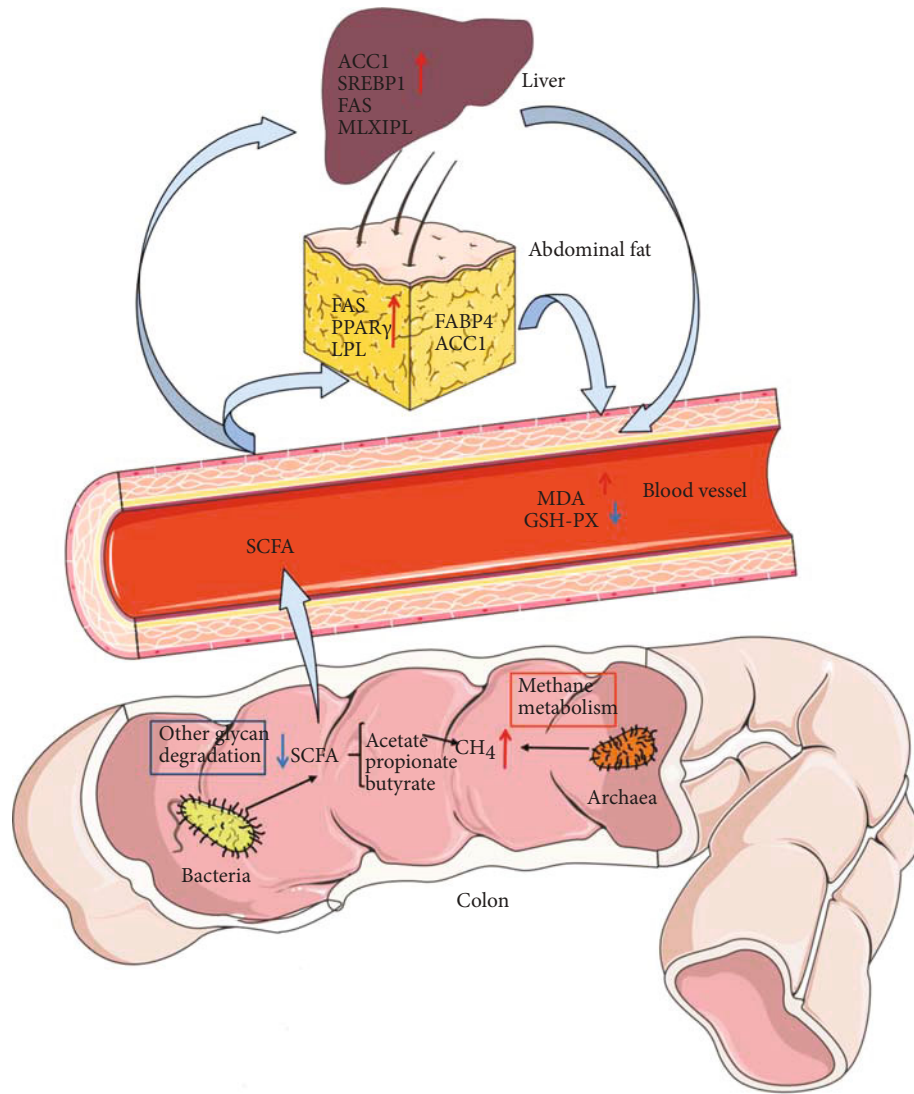


FIGURE 8: Relationship between intestinal microbiome and fat deposition.

of high-fat pigs might have a better capability to utilize hydrolytic products to produce SCFAs, thus providing more energy to high-fat pigs. Generally speaking, feed-efficient animals generate more SCFAs and less methane [36]. The higher level of SCFAs and lower abundance of methanogenic functions in the colon of low-fat pigs suggest that low-fat pigs may be more feed-efficient than high-fat pigs. To confirm our assumptions, further research on feed efficiency and methane emissions is required in the future.

Notably, the higher relative abundance in genus *Methanobrevibacter* and various species, namely, *M. millerae*, *M. gottschalkii*, *M. sp. YE315*, *M. thaueri*, *M. smithii*, *M. sp. A27*, and *M. oralis*, was observed in the colons of high-fat animals, which suggests that more methane might be produced, resulting in more efficient fat deposition in the high-fat pigs [47]. The metagenome gave us a chance to study the gut microbiome at different kingdom levels, such as eukaryote and virus, except for bacteria and Archaea. The interactions between bacteria and eukaryotes or viruses might also change the status of host fat deposition, because our main concern

was not with eukaryotes or viruses in the present study. Additional research in the future is needed.

In summary, we found that there were abundant methanogenic Archaea and relatively lower SCFA-producing bacteria in the colons of high-fat pigs compared to low-fat pigs. The increased methane produced by the Archaea and the decrease of SCFAs would promote fat deposition in the liver and abdomen, which is manifested by the high expression of adipogenic genes in the liver (*ACC1* and *SREBP1*) and abdominal fat (*FAS*, *PPAR $\gamma$* , and *LPL*), furthering the oxidative stress injury (see Figure 8).

## 5. Conclusions

In summary, the high oxidative stress and lipid metabolism dysbiosis in the high-fat pigs could contribute to the fat deposition in Jinhua pigs. Host fat deposition is influenced by both the methanogenesis functions of Archaea and the short-chain fatty acids produced by bacteria. In addition, we discovered 17 CAZyme families and 3 KEGG pathways

(Level 3) with distinct enrichments in the high-fat and low-fat pigs. The present study would give a deep insight into how gut microbiomes influence fat deposition in pigs and provide a hint for improving growth performance and fatness traits by manipulating gut microbiomes.

### Data Availability

The colon metagenome sequences were deposited into NCBI Sequence Read Archive (SRA) under the accession number PRJNA760651 (<http://www.ncbi.nlm.nih.gov/bioproject/760651>).

### Conflicts of Interest

The authors declare that there is no conflict of interest regarding the publication of this paper.

### Authors' Contributions

GMZ conceived of the study and drafted the manuscript. GMZ, XJZ, and YX performed the experiments. LYM analyzed the data. XLW and BD contributed to the formal analysis. GMZ and WTL edited the manuscript. GMZ and YX contributed equally to this work.

### Acknowledgments

This work was supported by the Natural Science Foundation of China (31972999) and the State Key Laboratory for Managing Biotic and Chemical Threats to the Quality and Safety of Agro-products (2010DS700124-ZZ1905).

### Supplementary Materials

Figure S1:  $\alpha$  diversity (Shannon index) of the gene, genus, KEGG orthologs (KO), and eggNOG (OG) functions. Figure S2: comparison of abundance of Bacteroidetes in high-fat and low-fat pigs. Supplementary Table S1-S2: sequences of the primers used in this study. (*Supplementary Materials*)

### References

- [1] S. Jin, J. Dong, L. Wang, P. Gao, and X. Diao, "Effects of weaning on immunity and nutrition in piglets," *Journal of Northeast Agricultural University (English Edition)*, vol. 24, no. 3, pp. 84–89, 2017.
- [2] S. Just, S. Mondot, J. Ecker et al., "The gut microbiota drives the impact of bile acids and fat source in diet on mouse metabolism," *Microbiome*, vol. 6, no. 1, p. 134, 2018.
- [3] C. K. Wung, "Advances in understanding of the role of lipid metabolism in aging," *Cells*, vol. 10, no. 4, p. 880, 2021.
- [4] L. Marseglia, S. Manti, G. D'Angelo et al., "Oxidative stress in obesity: a critical component in human diseases," *International journal of molecular sciences*, vol. 16, no. 1, pp. 378–400, 2015.
- [5] Y. Hao, M. Xing, and X. Gu, "Research progress on oxidative stress and its nutritional regulation strategies in pigs," *Animals: an open access journal from MDPI*, vol. 11, no. 5, p. 1384, 2021.
- [6] C. P. Rubio, E. Mainau, J. J. Cerón et al., "Biomarkers of oxidative stress in saliva in pigs: analytical validation and changes in lactation," *BMC veterinary research*, vol. 15, no. 1, p. 144, 2019.
- [7] S. Greenblum, P. J. Turnbaugh, and E. Borenstein, "Metagenomic systems biology of the human gut microbiome reveals topological shifts associated with obesity and inflammatory bowel disease," *Proceedings of the National Academy of Sciences of the United States of America*, vol. 109, no. 2, pp. 594–599, 2012.
- [8] Gresse, C. Durand, and D. B.-D. Forano, "Microbiota composition and functional profiling throughout the gastrointestinal tract of commercial weaning piglets," *Microorganisms*, vol. 7, no. 9, p. 343, 2019.
- [9] R. Wall, R. P. Ross, F. Shanahan et al., "Metabolic activity of the enteric microbiota influences the fatty acid composition of murine and porcine liver and adipose tissues," *The American journal of clinical nutrition*, vol. 89, no. 5, pp. 1393–1401, 2009.
- [10] T. Wu, Z. Zhang, Z. Yuan et al., "Distinctive genes determine different intramuscular fat and muscle fiber ratios of the longissimus dorsi muscles in Jinhua and Landrace pigs," *PLOS ONE*, vol. 8, no. 1, 2013.
- [11] H. Yang, Y. Xiang, K. Robinson et al., "Gut microbiota is a major contributor to adiposity in pigs," *Frontiers in Microbiology*, vol. 9, article 3045, 2018.
- [12] X. Liu, W. Lyu, L. Liu et al., "Comparison of digestive enzyme activities and expression of small intestinal transporter genes in Jinhua and Landrace pigs," *Frontiers in Physiology*, vol. 12, article 669238, 2021.
- [13] D. Pérez-Montarelo, O. Madsen, E. Alves et al., "Identification of genes regulating growth and fatness traits in pig through hypothalamic transcriptome analysis," *Physiological genomics*, vol. 46, no. 6, pp. 195–206, 2014.
- [14] T. F. Cardoso, R. Quintanilla, A. Castelló, R. González-Prendes, M. Amills, and Á. Cánovas, "Differential expression of mRNA isoforms in the skeletal muscle of pigs with distinct growth and fatness profiles," *BMC genomics*, vol. 19, no. 1, p. 145, 2018.
- [15] A. M. Bolger, M. Lohse, and B. Usadel, "Trimmomatic: a flexible trimmer for Illumina sequence data," *Bioinformatics (Oxford, England)*, vol. 30, no. 15, pp. 2114–2120, 2014.
- [16] H. Li, "Aligning sequence reads, clone sequences and assembly contigs with BWA-MEM," 2013, <https://arxiv.org/abs/1303.3997>.
- [17] R. Li, Y. Li, K. Kristiansen, and J. Wang, "SOAP: short oligonucleotide alignment program," *Bioinformatics*, vol. 24, no. 5, pp. 713–714, 2008.
- [18] W. Li and A. Godzik, "Cd-hit: a fast program for clustering and comparing large sets of protein or nucleotide sequences," *Bioinformatics*, vol. 22, no. 13, pp. 1658–1659, 2006.
- [19] R. Patro, G. Duggal, M. I. Love, R. A. Irizarry, and C. Kingsford, "Salmon provides fast and bias-aware quantification of transcript expression," *Nature Methods: Techniques for life scientists and chemists*, vol. 14, no. 4, pp. 417–419, 2017.
- [20] G. M. Boratyn, J. Thierry-Mieg, D. Thierry-Mieg, B. Busby, and T. L. Madden, "Magic-BLAST, an accurate RNA-seq aligner for long and short reads," *BMC bioinformatics*, vol. 20, no. 1, p. 405, 2019.
- [21] Y. Xiao, C. Wu, K. Li, G. Gui, G. Zhang, and H. Yang, "Association of growth rate with hormone levels and myogenic gene

- expression profile in broilers,” *Journal of Animal Science and Biotechnology*, vol. 8, no. 1, p. 43, 2017.
- [22] J. Quan, G. Cai, M. Yang et al., “Exploring the fecal microbial composition and metagenomic functional capacities associated with feed efficiency in commercial DLY pigs,” *Frontiers in microbiology*, vol. 10, 2019.
- [23] Y. Xiao, F. Kong, Y. Xiang et al., “Comparative biogeography of the gut microbiome between Jinhua and Landrace pigs,” *Scientific reports*, vol. 8, no. 1, 2018.
- [24] H. Yang, Y. Xiao, J. Wang et al., “Core gut microbiota in Jinhua pigs and its correlation with strain, farm and weaning age,” *Journal of Microbiology*, vol. 56, no. 5, pp. 346–355, 2018.
- [25] D. Li, C. M. Liu, R. Luo, K. Sadakane, and T. W. Lam, “MEGA-HIT: an ultra-fast single-node solution for large and complex metagenomics assembly via succinct de Bruijn graph,” *Bioinformatics (Oxford, England)*, vol. 31, no. 10, pp. 1674–1676, 2015.
- [26] D. Hyatt, P. F. LoCasio, L. J. Hauser, and E. C. Uberbacher, “Gene and translation initiation site prediction in metagenomic sequences,” *Bioinformatics*, vol. 28, no. 17, pp. 2223–2230, 2012.
- [27] A. Regassa and C. M. Nyachoti, “Application of resistant starch in swine and poultry diets with particular reference to gut health and function,” *Animal nutrition (Zhongguo xu mu shou yi xue hui)*, vol. 4, no. 3, pp. 305–310, 2018.
- [28] W. Li, X. Wu, X. Hu et al., “Structural changes of gut microbiota in Parkinson’s disease and its correlation with clinical features,” *Science China Life Sciences*, vol. 60, no. 11, pp. 1223–1233, 2017.
- [29] J. Wang, C. Qin, T. He et al., “Alfalfa-containing diets alter luminal microbiota structure and short chain fatty acid sensing in the caecal mucosa of pigs,” *Journal of animal science and biotechnology*, vol. 9, no. 1, p. 11, 2018.
- [30] V. Lombard, H. Golaconda Ramulu, E. Drula, P. M. Coutinho, and B. Henrissat, “The carbohydrate-active enzymes database (CAZy) in 2013,” *Nucleic Acids Research*, vol. 42, no. D1, pp. D490–D495, 2014.
- [31] H. Yang, X. Huang, S. Fang, W. Xin, L. Huang, and C. Chen, “Uncovering the composition of microbial community structure and metagenomics among three gut locations in pigs with distinct fatness,” *Scientific Reports*, vol. 6, no. 1, article 27427, 2016.
- [32] D. Cai, J. Wang, Y. Jia et al., “Gestational dietary betaine supplementation suppresses hepatic expression of lipogenic genes in neonatal piglets through epigenetic and glucocorticoid receptor-dependent mechanisms,” *Biochimica et Biophysica Acta*, vol. 186, no. 1, pp. 41–50, 2016.
- [33] T. Song, Y. Yang, S. Jiang, and J. Peng, “Novel insights into adipogenesis from the perspective of transcriptional and RNA N6-methyladenosine-mediated post-transcriptional regulation,” *Advanced science (Weinheim, Baden-Wuerttemberg, Germany)*, vol. 7, no. 21, p. 2001563, 2020.
- [34] L. Liu, Y. Liu, J. Cui et al., “Oxidative stress induces gastric submucosal arteriolar dysfunction in the elderly,” *World Journal of Gastroenterology*, vol. 19, no. 48, pp. 9439–9446, 2013.
- [35] R. Zhu, Y. Wang, L. Zhang, and Q. Guo, “Oxidative stress and liver disease,” *Hepatology Research*, vol. 42, no. 8, pp. 741–749, 2012.
- [36] M.-Y. Xue, H.-Z. Sun, X.-H. Wu, J. X. Liu, and L. L. Guan, “Multi-omics reveals that the rumen microbiome and its metabolome together with the host metabolome contribute to individualized dairy cow performance,” *Microbiome*, vol. 8, no. 1, p. 64, 2020.
- [37] E. Ivarsson, S. Roos, H. Y. Liu, and J. E. Lindberg, “Fermentable non-starch polysaccharides increases the abundance of *Bacteroides-Prevotella-Porphyromonas* in ileal microbial community of growing pigs,” *animal*, vol. 8, no. 11, pp. 1777–1787, 2014.
- [38] A. M. Neyrinck, S. Possemiers, C. Druart et al., “Prebiotic effects of wheat arabinoxylan related to the increase in bifidobacteria, Roseburia and Bacteroides/Prevotella in diet-induced obese mice,” *PLoS ONE*, vol. 6, no. 6, article e20944, 2011.
- [39] H.-Y. Liu, T. B. Walden, D. Cai et al., “Dietary fiber in bilberry ameliorates pre-obesity events in rats by regulating lipid depot, cecal short-chain fatty acid formation and microbiota composition,” *Nutrients*, vol. 11, no. 6, p. 1350, 2019.
- [40] V. K. Ridaura, J. J. Faith, F. E. Rey et al., “Gut microbiota from twins discordant for obesity modulate metabolism in mice,” *Science (New York, N.Y.)*, vol. 341, no. 6150, article 1241214, 2013.
- [41] Y.-h. Luo, Y. Su, A.-D. G. Wright, L. L. Zhang, H. Smidt, and W. Y. Zhu, “Lean breed Landrace pigs harbor fecal methanogens at higher diversity and density than obese breed Erhualian pigs,” *Archaea*, vol. 2012, Article ID 605289, 9 pages, 2012.
- [42] M. Pimentel, H. C. Lin, P. Enayati et al., “Methane, a gas produced by enteric bacteria, slows intestinal transit and augments small intestinal contractile activity,” *American journal of physiology. Gastrointestinal and liver physiology*, vol. 290, no. 6, pp. G1089–G1095, 2006.
- [43] D. W. Abbott and A. B. Boraston, “The structural basis for exopolysaccharuronase activity in a family 28 glycoside hydrolase,” *Journal of Molecular Biology*, vol. 368, no. 5, pp. 1215–1222, 2007.
- [44] A. J. Thompson, G. Speciale, J. Iglesias-Fernández et al., “Evidence for a boat conformation at the transition state of GH76  $\alpha$ -1, 6-mannanases-key enzymes in bacterial and fungal mannoprotein metabolism,” *Angewandte Chemie International Edition*, vol. 54, no. 18, pp. 5378–5382, 2015.
- [45] B. Pluvinage, A. Fillo, P. Massel, and A. B. Boraston, “Structural analysis of a family 81 glycoside hydrolase implicates its recognition of  $\beta$ -1, 3-glucan quaternary structure,” *Structure (London, England)*, vol. 25, no. 9, pp. 1348–1359.e3, 2017.
- [46] D. Ndeh, A. Rogowski, A. Cartmell et al., “Complex pectin metabolism by gut bacteria reveals novel catalytic functions,” *Nature*, vol. 544, no. 7648, pp. 65–70, 2017.
- [47] R. J. Basseri, B. Basseri, M. Pimentel et al., “Intestinal methane production in obese individuals is associated with a higher body mass index,” *Gastroenterology & hepatology*, vol. 8, no. 1, pp. 22–28, 2012.

## *Retraction*

# **Retracted: Rocaglamide Prolonged Allograft Survival by Inhibiting Differentiation of Th1/Th17 Cells in Cardiac Transplantation**

### **Oxidative Medicine and Cellular Longevity**

Received 8 January 2024; Accepted 8 January 2024; Published 9 January 2024

Copyright © 2024 Oxidative Medicine and Cellular Longevity. This is an open access article distributed under the Creative Commons Attribution License, which permits unrestricted use, distribution, and reproduction in any medium, provided the original work is properly cited.

This article has been retracted by Hindawi following an investigation undertaken by the publisher [1]. This investigation has uncovered evidence of one or more of the following indicators of systematic manipulation of the publication process:

- (1) Discrepancies in scope
- (2) Discrepancies in the description of the research reported
- (3) Discrepancies between the availability of data and the research described
- (4) Inappropriate citations
- (5) Incoherent, meaningless and/or irrelevant content included in the article
- (6) Manipulated or compromised peer review

The presence of these indicators undermines our confidence in the integrity of the article's content and we cannot, therefore, vouch for its reliability. Please note that this notice is intended solely to alert readers that the content of this article is unreliable. We have not investigated whether authors were aware of or involved in the systematic manipulation of the publication process.

Wiley and Hindawi regrets that the usual quality checks did not identify these issues before publication and have since put additional measures in place to safeguard research integrity.

We wish to credit our own Research Integrity and Research Publishing teams and anonymous and named external researchers and research integrity experts for contributing to this investigation.

The corresponding author, as the representative of all authors, has been given the opportunity to register their agreement or disagreement to this retraction. We have kept a record of any response received.

### **References**

- [1] C. Dai, X. Zhou, L. Wang et al., "Rocaglamide Prolonged Allograft Survival by Inhibiting Differentiation of Th1/Th17 Cells in Cardiac Transplantation," *Oxidative Medicine and Cellular Longevity*, vol. 2022, Article ID 2048095, 15 pages, 2022.

Research Article

# Rocaglamide Prolonged Allograft Survival by Inhibiting Differentiation of Th1/Th17 Cells in Cardiac Transplantation

Chen Dai<sup>1</sup>, Xi Zhou<sup>1</sup>, Lu Wang<sup>1</sup>, Rumeng Tan<sup>1</sup>, Wei Wang<sup>2</sup>, Bo Yang<sup>1</sup>, Yucong Zhang<sup>3</sup>, Huibo Shi<sup>1</sup>, Dong Chen<sup>1</sup>, Lai Wei<sup>1</sup>, and Zhishui Chen<sup>1</sup>

<sup>1</sup>Institute of Organ Transplantation, Tongji Hospital, Tongji Medical College, Huazhong University of Science and Technology; Key Laboratory of Organ Transplantation, Ministry of Education; NHC Key Laboratory of Organ Transplantation; Key Laboratory of Organ Transplantation, Chinese Academy of Medical Sciences, Wuhan, China 430030

<sup>2</sup>Department of Immunology, School of Basic Medicine, Tongji Medical College, Huazhong University of Science and Technology, Wuhan, China 430030

<sup>3</sup>Department of Geriatrics, Tongji Hospital, Tongji Medical College, Huazhong University of Science and Technology, Wuhan, China 430030

Correspondence should be addressed to Chen Dai; [cdai26@tjh.tjmu.edu.cn](mailto:cdai26@tjh.tjmu.edu.cn) and Zhishui Chen; [zschen@tjh.tjmu.edu.cn](mailto:zschen@tjh.tjmu.edu.cn)

Received 19 August 2021; Accepted 13 October 2021; Published 17 January 2022

Academic Editor: Yingping Xiao

Copyright © 2022 Chen Dai et al. This is an open access article distributed under the Creative Commons Attribution License, which permits unrestricted use, distribution, and reproduction in any medium, provided the original work is properly cited.

**Background.** Aglaia (Meliaceae) species are used for treating autoimmune disorders and allergic diseases in Asian countries. Rocaglamide, an extract obtained from Aglaia species, exhibits suppressive effect by regulating the T cell subset balance and cytokine network in cancer. However, whether it can be used in organ transplantation is unknown. In this study, we investigated the antirejection effect and mechanism of action of rocaglamide in a mouse cardiac allograft model. **Methods.** Survival studies were performed by administering mice with phosphate-buffered saline (PBS) ( $n=6$ ) and rocaglamide ( $n=8$ ). Heart grafts were monitored until they stopped beating. After grafting, the mice were sacrificed on day 7 for histological, mixed lymphocyte reaction (MLR), enzyme-linked immunosorbent assay (ELISA), and flow cytometric analyses. **Results.** Rocaglamide administration significantly prolonged the median survival of the grafts from 7 to 25 days compared with PBS treatment ( $P < 0.001$ ). On posttransplantation day 7, the rocaglamide-treated group showed a significant decrease in the percentage of Th1 cells ( $7.9 \pm 0.9\%$  vs.  $1.58 \pm 0.5\%$ ,  $P < 0.001$ ) in the lymph nodes and spleen ( $8.0 \pm 2.5\%$  vs.  $2.4 \pm 1.3\%$ ,  $P < 0.05$ ). Rocaglamide treatment also significantly inhibited the production of Th17 cells ( $6.4 \pm 1.0\%$  vs.  $1.8 \pm 0.4\%$ ,  $P < 0.01$ ) in the lymph nodes and spleen ( $5.9 \pm 0.3\%$  vs.  $2.9 \pm 0.8\%$ ,  $P < 0.01$ ). Furthermore, the prolonged survival of the grafts was associated with a significant decrease in IFN- $\gamma$  and IL-17 levels. Our results also showed that NF-AT activation was inhibited by rocaglamide, which also induced p38 and Jun N-terminal kinase (JNK) phosphorylation in Jurkat T cells. Furthermore, by using inhibitors that suppressed p38 and JNK phosphorylation, rocaglamide-mediated reduction in NF-AT protein levels was prevented. **Conclusion.** We identified a new immunoregulatory property of rocaglamide, wherein it was found to regulate oxidative stress response and reduce inflammatory cell infiltration and organ injury, which have been associated with the inhibition of NF-AT activation in T cells.



## 1. Introduction

Organ transplantation is an effective therapy for patients with end-stage organ disease [1]. The oxidative stress caused by the infiltration of inflammatory cells in cardiac allografts results in the production of cytokines and proinflammatory adhesion molecules, which are the main alloantigen-independent factors leading to allograft vasculopathy and organ injury [2]. Previous studies have focused on developing the optimum function of allografts by using immunosuppressive drugs, which are important for investigating the precise cell-mediated immune response and finding a way to downregulate the specific immunoreaction. Eventually, these drugs can reduce the secretion and chemotaxis of inflammatory factors and reduce oxidative stress damage and protect the allograft.

The differentiation of CD4+ T cells is induced by helper T cells, including Th1, Th17, Th2, and regulatory T cells (Tregs). Th1 cells play a key role in triggering immunoreaction, promoting inflammatory infiltration, and exacerbating oxidative stress, and several studies have shown that these types of cells increase the risk of allograft injury and allograft rejection [3, 4].

Naïve CD4+ T cells are usually activated and induced to differentiate into Th1 and Th17 cells, especially in an inflammatory environment. Interleukin-2 (IL-2) and interferon- $\gamma$  (IFN- $\gamma$ ) secreted by Th1 cells can upregulate the production of cytotoxic T lymphocytes, elicit an immune response, and stimulate the activation of natural killer cells. Several studies have shown that Th17 cells are involved in triggering various immune processes such as Th1 cell-mediated inflammation, disordered oxidative stress, and tissue damage after organ transplantation [5]. Interleukin-17 (IL-17) secreted by Th17 cells can induce the production of many cytokines, thus increasing the count of neutrophilic granulocytes and promoting the migration of macrophages to the allograft site. Furthermore, allografts exhibit upregulated levels of IFN- $\gamma$  and IL-17 in the serum in case of acute rejection, which is dangerous and causes inflammatory diseases compared with those with a functional and effective allograft in a transplant model [6]. Acute rejection is observed within 7 days after transplantation in the transplantation models, characterized by binding of different cellular immunoreaction and inflammatory factors, as well as natural antibodies and the oxidation-related epitope malondialdehyde. This rejection results in vascular endothelial damage, vasculitis, thrombosis, tissue destruction, and edema [7–9]. Memory T cells are also an obstacle for transplantation because 40–50% of T cells circulating in the peripheral blood have memory phenotypes [10].

Rocaglamide has attracted attention as a new anticancer drug because it can block the nuclear factor- $\kappa$ B (NF- $\kappa$ B) pathway [11, 12] and can also be used to treat allergic inflammatory and skin diseases [13]. Recently, rocaglamide derivatives have been demonstrated the negatively regulated effects of T cells [12, 14]. Some studies have shown that these derivatives play a crucial role in inhibiting the phorbol myristate acetate- (PMA-) induced expression of NF- $\kappa$ B target genes and sensitizing leukemic T cells to apoptosis induced

by tumor necrosis factor- $\alpha$  (TNF- $\alpha$ ) [12]. Interestingly, rocaglamide suppresses the expression of tumor-related cytokines in the peripheral blood [12, 15]. Several inducible transcription factors, including NF- $\kappa$ B and nuclear factor-AT (NF-AT), can regulate the expression of IL-4, IFN- $\gamma$ , and TNF- $\alpha$  [16, 17]. Ca<sup>2+</sup>-dependent phosphatase calcineurin is activated after the activation of T cells, and thus, these reactions promote the dephosphorylation of NF-AT and their transfer to the nucleus [18]. In the nucleus, a representative productive immunoreaction is induced by the NF-AT protein that synergizes with activator protein 1 (AP1) and other transcription factors. Interestingly, the impairment of NFAT1 and NFAT2 in T cells is related to the severe reduction in the levels of many cytokines such as IFN- $\gamma$ , interleukin-4 (IL-4), interleukin-10 (IL-10), colony-stimulating factor, and TNF. A previous study has shown that the TH1/TH2 lineage selection is decided by the NF-AT protein in cooperation with signal transducer and activator of transcription factors, such as STAT4 downstream of IFN- $\gamma$  for TH1 cells and STAT6 downstream of IL-4 for TH2 cells [19]. Accordingly, the dephosphorylation and transfer of the NF-AT protein lead to the activation and differentiation of T cells, promoting secretion, chemotaxis, and adhesion of corresponding inflammatory factors and exacerbating the injury of oxidative stress and dysfunction of the allograft.

Therefore, we hypothesized that rocaglamide could be used for cell-mediated acute rejection for preventing helper T cell differentiation and T cell-mediated cytokine secretion. To confirm this hypothesis, we developed the mouse allo-cardiac transplantation model, where the donor's heart was transplanted to the abdominal vessels of the recipient. We then studied the effect of rocaglamide treatment on the immune response elicited by the infiltration of inflammatory cells and the induction of oxidative stress.

We found that rocaglamide is a potent immunosuppressive agent that can inhibit T cell proliferation and reduce the infiltration of inflammatory cells. We also found that it can downregulate the Th1 response and decrease the number of Th1 and Th17 cells in the spleen and lymph nodes. Furthermore, rocaglamide inhibited the activity of NF-AT; however, there was no inhibitory effect on the NF- $\kappa$ B activity when rocaglamide was used at a concentration of 100 nM. On the other hand, the reduction in IFN- $\gamma$  and IL-17 levels could be detected in the peripheral blood.

## 2. Materials and Methods

**2.1. Animals.** Female C57BL/6 (B6, H-2b) and BALB/c (H-2d) mice (age: 8–12 weeks) were purchased from Vital River Laboratory Animal Technology Co., Ltd., Beijing, China. All animals were bred in a specific pathogen-free facility of the Key Lab of Organ Transplantation Institute with (22°C, 50% air humidity, and air change). Unlimited access to food and water was provided. Mice (weighing: 22–28 g) were used as donor and recipient, respectively. All procedures were approved by the guidelines of the Institutional Animal Care and Use Committee (IACUC).

**2.2. Heart Transplantation Model.** The hearts from BALB/c were transplanted into the abdominal vessels of C57BL/6 recipients using the microsurgical technique of Luan et al. [20]. Graft survival was monitored daily by palpation. Rejection was defined as the complete loss of a palpable heartbeat [21].

**2.3. Drug Treatment.** Rocaglamide (>98% pure) was procured from ChromaBio (Chengdu, China). The recipients were treated with rocaglamide for 2 weeks (2.5  $\mu\text{g/g}$  in 50  $\mu\text{l}$  phosphate-buffered saline (PBS); intraperitoneal injection (ip);  $n = 8$ ), and the others received PBS alone as control [22].

**2.4. Cells and Cell Culture.** RPMI-1640 medium supplemented with 10% fetal bovine serum (FBS) was used to maintain the Jurkat T leukemia cells (acquired from Clontech) under a 5%  $\text{CO}_2$  atmosphere at 37°C [23].

**2.5. Histological Analysis.** The grafts were resected from the recipient mice on day 7 after transplantation and analyzed by light microscopy. The specimens were fixed with 10% phosphate-buffered formalin, embedded in paraffin, and sliced into 5  $\mu\text{m}$  thick sections. After staining with hematoxylin and eosin (H&E), the samples were analyzed in a blinded manner. According to the International Society of Heart and Lung Transplantation (ISHLT) standard, classification was performed based on the degree of infiltration and the distribution location of inflammatory cells in the grafts [21, 24].

**2.6. Mixed Lymphocyte Reactions (MLR).** T lymphocytes isolated from the recipient's spleens using nylon wool columns (Wako, Osaka, Japan) were used as responder cells, while donor mouse spleen cells were used as stimulator cells. The responder cells ( $5 \times 10^5$  cells) were cocultured with the stimulator cells ( $5 \times 10^4$  cells), which were then treated with mitomycin (40  $\mu\text{g/ml}$ , Amresco, Solon, OH, USA) in 200  $\mu\text{l}$  of RPMI 1640 supplemented with 10% FBS and 1% penicillin and 1% streptomycin. Then, the cells were cultured at 37°C under a humidified atmosphere with 5%  $\text{CO}_2$  for 3 days. The proliferation of the T cells was detected by using the BrdU enzyme-linked immunosorbent assay (ELISA) Kit (MultiSciences, Hangzhou, China). The optical density (OD) values were quantified by an ELISA reader (Model 680, Bio-Rad, Hercules, California, USA).

**2.7. ELISA.** Peripheral blood was gathered via cardiac puncture. The expression of IFN- $\gamma$ , IL-6, and IL-17 were determined by using a commercial ELISA kit (MultiSciences, Hangzhou, China) in the culture supernatants and peripheral blood samples.

**2.8. Flow Cytometry.** The recipients were sacrificed on day 7 for the test experiments. T lymphocytes from the lymph nodes of the recipient mice ( $1 \times 10^6$  cells/100  $\mu\text{l}$ ) were stained using fluorochrome-labeled antibodies in accordance with the manufacturer's instructions. Antibodies used for flow cytometric analysis were IFN- $\gamma$ , IL-17, and CD4 (all from eBioscience). The objective cells harvested per tube ranged from approximately 15000 to 20000, of which 2000 cells were analyzed inside the lymphocyte gate. The stained cells were performed using the Becton-Dickinson FACSCalibur™ System; BD Bio-

sciences, Franklin Lakes, NJ, USA, and analyzed using the FlowJo software (Tree Star Inc., Ashland, OR).

**2.9. Western Blotting.** Jurkat T cells were stimulated with PMA and ionomycin for 2 h with or without rocaglamides, which were added an hour before stimulation. Nuclear proteins were separated and immunoblotted with the antibody against NFATc1. The widely used p38 kinase and Jun N-terminal kinase (JNK) inhibitors, SB203580 and SP600125, were purchased from Selleck. Western blotting was performed, as described previously [12, 25]. Anti-NF-ATc1 mAb (7A6; Alexis Biochemicals) was used for detection purposes.

**2.10. Quantitative Real-Time PCR (qRT-PCR).** According to the instruction of manufacturer, RNA was extracted from the grafts of recipient mice using TRIzol Reagent (Invitrogen, Carlsbad, CA). The primer sequences used are as follows: IFN- $\gamma$  (forward 5'-CGGCACAGTCATTGAAAGCCTA-3', reverse 5'-GTTGCTCATGGCCTGATTGTC-3'), IL-10 (forward 5'-GACCAGCTGGACAACATACTGCTAA-3', reverse 5'-GATAAGGCTTGGCAACCCAAGTAA-3'), and transforming growth factor beta (TGF- $\beta$ ) (forward 5'-TGACGTCACTGGAGTTGTACGG-3', reverse 5'-GGTTCATGTCA TGGATGGTGC-3'). Each gene expression was normalized with GAPDH mRNA content: R- $\beta$ -actin (forward 5'-CATC CGTAAAGACCTCTATGCCAAC-3', reverse 5'-ATGGAG CCACCGATCCACA-3') and ROR- $\gamma\text{t}$  (forward 5'-GCTCCC GGCCTGGTCTGCTC-3', reverse 5'-AGGTGGCGGGG TGGTTTCTGA-3').

**2.11. Statistical Analyses.** Specimens were analyzed in duplicate or triplicate, and the data were presented as the mean  $\pm$  standard deviation from one representative experiment of at least three experiments. The mean survival time of each group was determined using the Kaplan-Meier method and log-rank test. Data of statistical significance were analyzed using a *t*-test.  $P < 0.05$  was considered to be a statistically significant;  $P < 0.01$  and  $P < 0.001$  indicated highly significant differences. All analyses were performed using the GraphPad Prism 5.0 software (GraphPad Software, Inc., San Diego, CA).

### 3. Results

**3.1. Administration of Rocaglamide Further Prolongs Graft Survival.** First, we performed heterotopic cardiac transplantation. Recipients were treated with rocaglamide (2.5  $\mu\text{g/g}$  in 50  $\mu\text{l}$  PBS; ip;  $n = 8$ ), and the control group was treated with PBS (50  $\mu\text{l}$  PBS; ip;  $n = 6$ ). The median survival of grafts (time for rejection) in the rocaglamide-treated group was 25 days compared to that in the control group (7 days;  $P < 0.001$ ). We then determined the effect of rocaglamide on allograft survival. Grafts harvested from B6 recipients of the rocaglamide-treated group showed significantly reduced inflammatory cell infiltration and relatively normal myocardial area on day 7 than that in the control group, in which we found considerable inflammatory cell infiltration and morphological damage (Figures 1(a) and 1(b)).

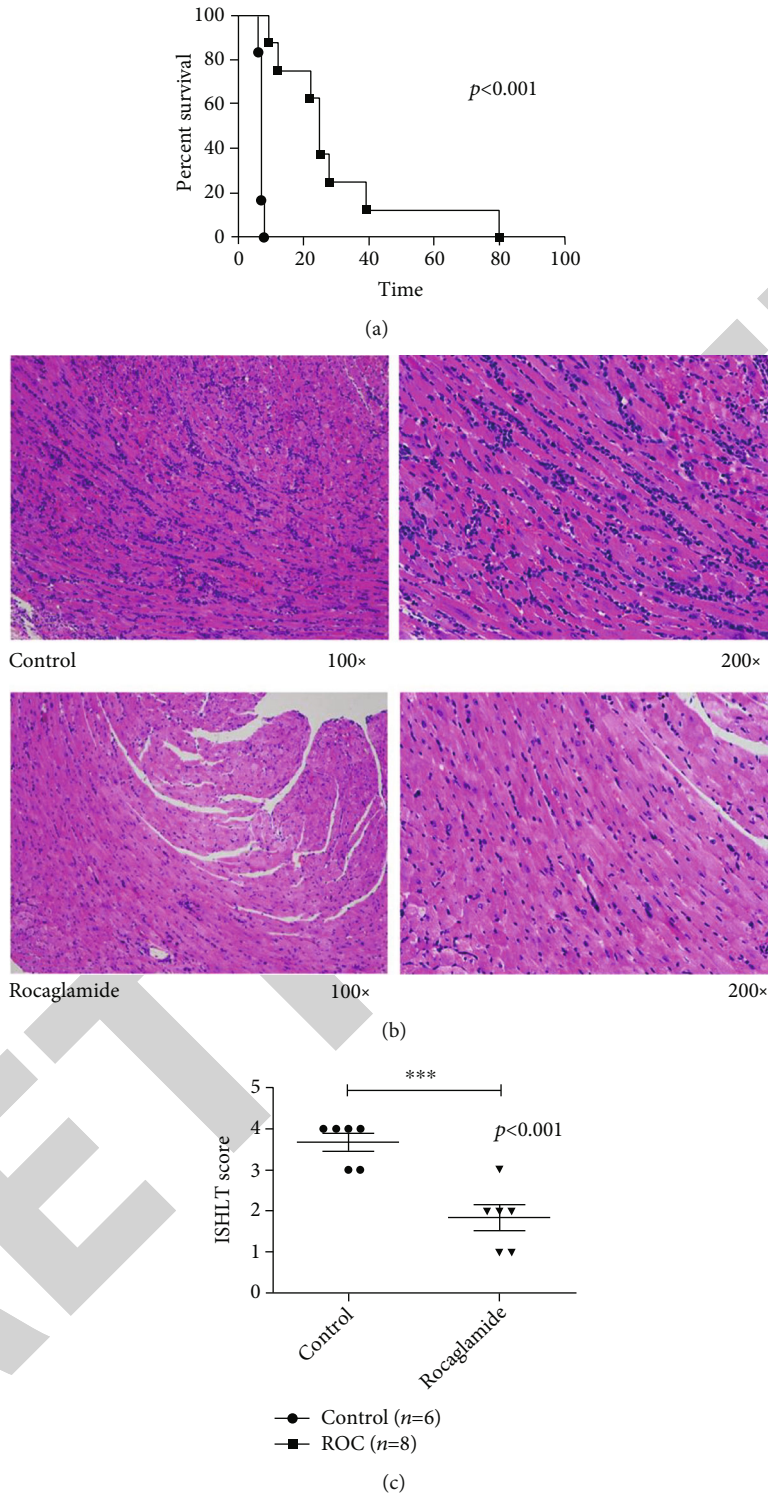


FIGURE 1: Administration of rocaglamide further prolongs graft survival. (a, b) Survival of the graft in cardiac transplantation (Kaplan-Meier plot). Recipients were treated with rocaglamide, and the heart grafts survived for 25 days (median survival). Rocaglamide treatment revealed significantly reduced inflammatory cell infiltration and protected the myocardial architecture. Photographs shown in this figure are representative of 3 animals in each group (a, b: 100x, 200x). (c) The International Society of Heart and Lung Transplantation (ISHLT) scores of the hearts, with each spot representing the score from each slice. The horizontal line represents the mean for each group ( $n = 6$  in each group;  $*P < 0.05$ ,  $**P < 0.01$ , and  $***P < 0.001$ ).

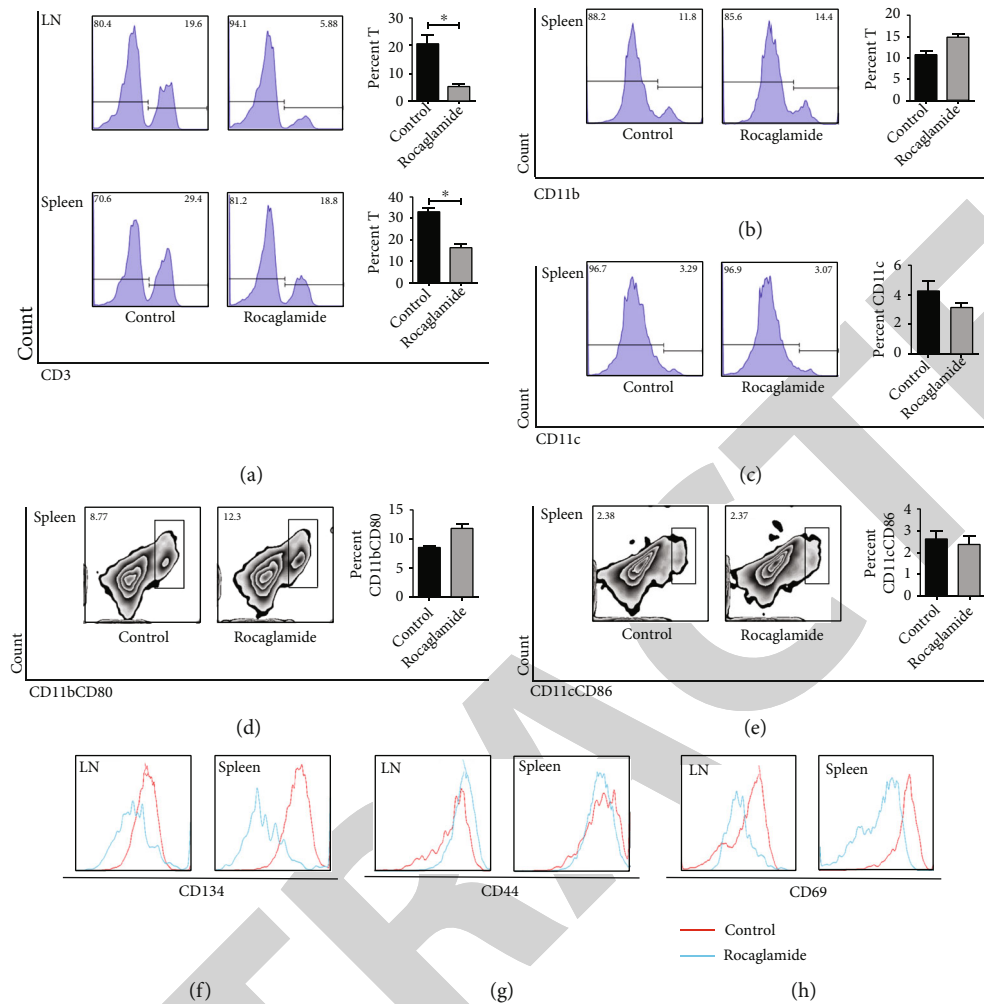


FIGURE 2: Administration of rocglamide inhibits the T cell activation in allograft recipients. (a) Freshly isolated lymphocytes and splenocytes were stained for CD3 and assayed for the incidence of CD3+ cells in the transplantation recipients. Data are presented for a representative experiment of at least three experiments ( $n = 3$ ; \* $P < 0.05$ , \*\* $P < 0.01$ , and \*\*\* $P < 0.001$ ). (b, c) Analyzing the proportion of CD11b+ and CD11c+ antigen-presenting cells in the spleen. (d, e) Proportion of CD11b+ CD80+ cells and CD11c+ CD86+ cells in the spleen. (f, g, and h). Freshly isolated lymphocytes and splenocytes were stained for CD134 (OX40), CD69, and CD44 expression and assayed for the evidence of T cell activation in the transplantation recipients (blue represents the fluorescence intensity of the treatment group, and the red represents the control group).

We analyzed the ISHLT scores of the hearts (Figure 1(c)). Allografts from the control group showed pathological changes such as edema and congestion in myocardial tissues (scores ranged from 3 to 4). However, the rocglamide-treated group showed normal histological characteristics, with scores ranging between 1 and 2. These findings revealed that rocglamide inhibited the infiltration of inflammatory cells, such as neutrophilic granulocytes, and also prevented their migration.

**3.2. Administration of Rocglamide Inhibits the T Cell Activation in Allograft Recipients.** Freshly isolated lymphocytes and splenocytes were stained for determining CD3, CD134 (OX40), CD69, and CD44 expression and assayed for detecting T cell activation in the transplantation recipients. As shown in Figure 2(a), compared with the number of CD3+

cells in the control group (5.88%), that in the rocglamide-treated recipients (19.6%) was suppressed significantly in the lymph nodes and spleen (29.4% vs. 18.8%;  $P < 0.05$ ). To understand how rocglamide treatment affected T cell activation, the levels of CD134, CD69, and CD44 were determined. We found that the levels of CD134 and CD69, considered as indicators of T cell activation, decreased in the lymph nodes and spleen of the treatment group than in the control group (Figures 2(f) and 2(g)). However, there was no significant difference in the level of CD44 (Figure 2(h)). Therefore, these findings indicate that during immune activation, rocglamide could have suppressed the proliferation of T lymphocytes by inhibiting the levels of CD134 and CD69.

We also found that in the case of CD11b+ and CD11c+ antigen-presenting cells in the spleen, rocglamide caused a slight increase in the number of CD11b+ cells (Figure 2(b)),

but this increase was not statistically significant, and rocgamide treatment had no difference in the number of CD11c+ cells (Figure 2(c)). Furthermore, a slight increase in the number of CD11b+ CD80+ cells was observed more in the spleen of the treatment group than that of the control group (8.77% vs. 12.3%, Figure 2(d)); however, there was no difference in the number of CD11c+ CD86+ cells (Figure 2(e)). These effects may have been caused by the inhibition of T cell activation by rocgamide, resulting in the ineffective proliferation of antigen-presenting cells.

**3.3. Rocglamide Administration Decreases the Number of Th1 Cells, Cytokine Expression by Th1 T Cells, and Accumulation of IFN- $\gamma$  in Allograft Recipients.** To evaluate the effect of rocgamide treatment on the number of Th1 cells, which differentiate from CD4+ T cells in an inflammatory environment, lymphocytes and splenocytes were isolated and stained with fluorochrome-conjugated-specific antibodies and analyzed by flow cytometry. We found that the number of CD4+ IFN- $\gamma$ + (Th1) cells in the rocgamide-treated group was markedly suppressed. The percentage of Th1 cells in lymph nodes of the treatment group decreased to 1.33% compared with that in the control group (7.67%;  $P < 0.001$ ; Figure 3(a)). Furthermore, the same decrease in CD4+ IFN- $\gamma$ + (Th1) cells was detected in the spleen (10.7% vs. 2.17%;  $P < 0.05$ ; Figure 3(b)).

IFN- $\gamma$  activates macrophages and causes their aggregation around Th1 cells, eventually leading to the formation of mature macrophages that are potent killers. These mature macrophages in turn activate more naïve CD4+ cells to differentiate into Th1 cells, thereby forming a positive feedback loop.

As Th1 cells and type-1 cytokines such as IFN- $\gamma$  play a key role in allo-reaction, to further support our hypothesis, we determined the expression of IFN- $\gamma$  in the culture supernatants of splenocytes via culturing and analyzing the cells by ELISA. We found markedly reduced IFN- $\gamma$  levels in the culture supernatants of splenocytes in the rocgamide-treated group compared with the control group ( $P < 0.001$ ; Figure 3(c)). Particularly, we observed a significant decrease in the serum IFN- $\gamma$  levels in the treatment group ( $P < 0.01$ ; Figure 3(c)), thus indicating that rocgamide protects the grafts by suppressing the CD4+ IFN- $\gamma$ + (Th1) cells and preventing the secretion of IFN- $\gamma$  in the peripheral blood.

In addition, we observed lesser lymphocytic infiltration and changes in the number of myocardial cells previously. Hence, we determined the expression of graft rejection-related genes by using mRNA extracted from cardiac allografts and performing qRT-PCR. As shown in Figure 3(d), the levels of IFN- $\gamma$  were suppressed in the treatment group ( $P < 0.05$ ). Meanwhile, immunohistochemical staining for IFN- $\gamma$  was performed in the grafts. IFN- $\gamma$ + cells showed that the extent of IFN- $\gamma$  infiltration in the treatment group was lower than that in the control group (Figure 3(e)), thus indicating that rocgamide decreased the accumulation and aggregation of IFN- $\gamma$ .

**3.4. Rocglamide-Treated Prolong Allograft Survival Is Associated with Suppressing Th17 Cells, Cytokine Expression of Th17 T Cells, and IL-17 Infiltration.** T helper 17 cells (Th17) secreting interleukin-17 (IL-17) are a subset of proin-

flammatory T helper cells [26]. Guglani and Khader reported that solid graft rejection was related to the number of Th17 cells in multiple transplant models [27]. To further confirm our hypothesis, we examined the number of Th17 cells in the allografts by flow cytometry. The rocgamide-treated group showed a significant decrease in Th17 cells (1.89%) in the lymph nodes compared with the control group (6.88%;  $P < 0.01$ , Figure 4(a)). Moreover, the number of CD4+ IL-17+ (Th17) cells was reduced to 3.87% in the spleen compared with that in the control group (6.21%;  $P < 0.01$ , Figure 4(b)).

Th17 cells differentiate because naïve T cells are induced by TGF- $\beta$ , IL-6, and IL-21 [28]. A previous study suggested that the Th17 subset is the cause of IL-17-dependent graft rejection [1]. Consistent with the findings of Deng et al. and Mandy et al. [1, 29], we found that IL-17 produced by Th17 cells may play a key role in allograft rejection and its secretion was prevented by rocgamide. To further confirm this finding, we used an ELISA kit to determine the IL-17 levels in culture supernatants. The rocgamide-treated group exhibited a decrease in IL-17 levels compared with the control group ( $P < 0.05$ , Figure 4(c)). We observed no statistical significance in serum IL-17 levels between the two groups, but the treatment group showed a slight decrease in IL-17 levels (Figure 4(c)). Recently, retinoid acid-related orphan receptor gamma t (ROR- $\gamma$ t) has been shown to play an important role in the differentiation of Th17 cells, including the secretion of IL-17 [30, 31]. To determine the role of ROR- $\gamma$ t, we determined the gene expression of ROR- $\gamma$ t in the grafts. Although there was no statistical difference, ROR- $\gamma$ t gene expression was downregulated in the rocgamide-treated group (Figure 4(d)), which may be associated with the decrease in Th17 cells and IL-17 levels.

Furthermore, to evaluate the contribution of Th17 cells within the acute rejection infiltrates, we performed immunohistochemical analysis, which showed that the extent of IL-17 infiltration was markedly reduced in the rocgamide-treated group (Figure 4(e)).

**3.5. Rocglamide Decreases the Memory T Cells but No Effect on Tregs.** Memory T cells, including CD4+ and CD8+ subsets, play a crucial role in accelerated rejection [32]. Moreover, several studies have suggested that memory T cells also play a key role in accelerated rejection [33, 34]. To determine whether rocgamide administration affected the production of effector memory T cells (CD40highCD62low), we analyzed the T lymphocytes obtained from the spleen of recipient mice by flow cytometry.

Interestingly, we found that the CD4+ memory T cells (CD40highCD62low) in the rocgamide group were suppressed compared with the control group (17.0% vs. 24.2%,  $P < 0.05$ , Figure 5(a)). In addition, as several studies indicated that the CD4+ Foxp3+ T cells (Tregs) regulate immune response and induce tolerance, we determined the expression of Tregs but no statistically significant difference was observed (Figure 5(b)).

**3.6. Rocglamide Treatment Changes Cytokine Expression of Allograft Recipients.** In our previous study, we demonstrated that rocgamide suppresses the expression of IFN- $\gamma$  and IL-

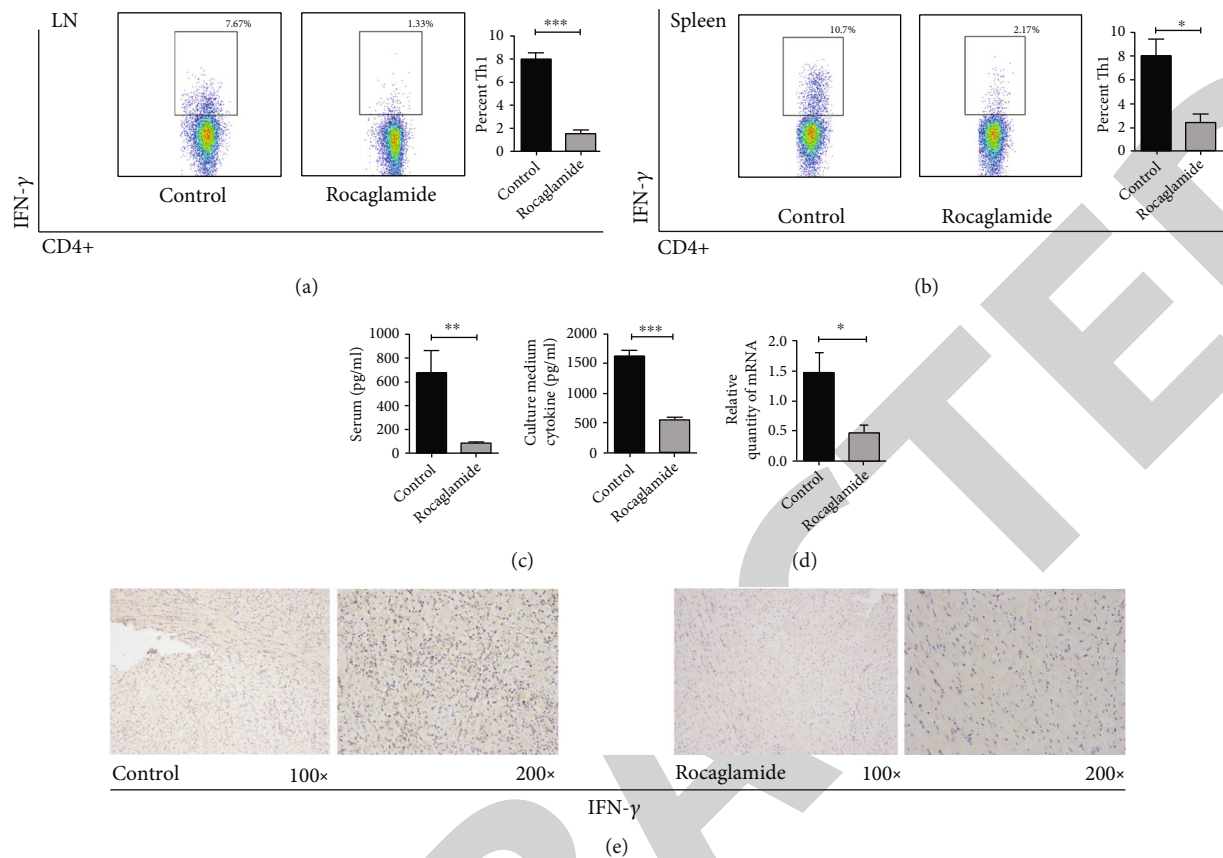


FIGURE 3: Rocaglamide administration decreases Th1 cells, cytokine expression of Th1 T cells, and accumulation of IFN- $\gamma$  in allograft recipients. (a) Analyzing the proportion of CD4+ IFN- $\gamma$ + cells (Th1) in the lymph nodes using fluoro-chrome-conjugated-specific antibodies detected by flow cytometry. Data are presented for a representative experiment of at least three experiments ( $n = 3$ ; \* $P < 0.05$ , \*\* $P < 0.01$ , and \*\*\* $P < 0.001$ ). (b) Proportion of CD4+ IFN- $\gamma$ + cells (Th1) in splenic lymphocytes. (c) Expression of IFN- $\gamma$  in the peripheral blood and culture supernatants detected by ELISA kits. (d) mRNA extracted from cardiac grafts and analyzed by qRT-PCR. The rocaglamide-treated group showed decreased IFN- $\gamma$  in allografts when compared with the control group (\* $P < 0.05$ ). (e) Rocaglamide decreases the accumulation and aggregation of IFN- $\gamma$  in cardiac grafts. Immunohistochemical staining was performed, and the data showed the infiltration of IFN- $\gamma$  was diminished in the rocaglamide-treated group.

17. Interleukin-6 (IL-6) is also a key factor involved in the differentiation of Th17 formation, and hence, we detected its levels in the culture supernatants of splenocytes and serum samples by ELISA. The IL-6 levels in the culture supernatants of the treatment group were significantly lower compared with that in the control group ( $P < 0.001$ , Figure 6(a)). Moreover, their levels were decreased in the serum ( $P < 0.001$ , Figure 6(a)). Interleukin-4 (IL-4) is associated with Th2 responses. However, we found no statistical difference in the IL-4 levels between the two groups (Figure 6(b)). We also did not observe statistically significant differences in the interleukin-10 (IL-10) levels in the serum and culture supernatants (Figure 6(c)). Transforming growth factor-beta (TGF- $\beta$ ) is produced by regulatory T cells (Tregs) and suppresses immune responses. Moreover, TGF- $\beta$  contributes to the formation of Th17 cells [35]. We found no significant differences between the two groups but found a decrease in TGF- $\beta$  levels in the rocaglamide-treated group, both in the culture supernatants and serum (Figure 6(d)), indicating that low expression of TGF- $\beta$  is good for suppressing Th17 cells but has no positive effect on the formation of Tregs.

These findings may indicate that rocaglamide suppresses the differentiation of naïve CD4+ cells into Th1 cells and Th17 cells and inhibits the secretion of cytokines such as IFN- $\gamma$ , IL-6, and IL-17.

**3.7. Rocaglamide Affects the Immune Response Ability of T Cells to the Same Identical Gene Tissues.** Next, we determined the effect of rocaglamide on the spleen of recipients. After posttransplantation day 7, splenic T cells were isolated for MLR assays, and spleen cells from BALB/c mice (no proliferation ability was noticed after treatment with mitomycin C) were used as the antigen. Our results showed that the proliferation of T lymphocytes in the treatment group was significantly inhibited compared with that in the control group ( $P < 0.001$ ) (Figure 6(e)).

**3.8. Rocaglamide Suppresses the Nuclear Expression of NF-AT but Not of NF- $\kappa$ B.** The inducible transcription factors NF-AT and NF- $\kappa$ B, which are ubiquitous, affect the activation of many inflammatory cytokine genes. Furthermore, according to the previous data, rocaglamide treatment

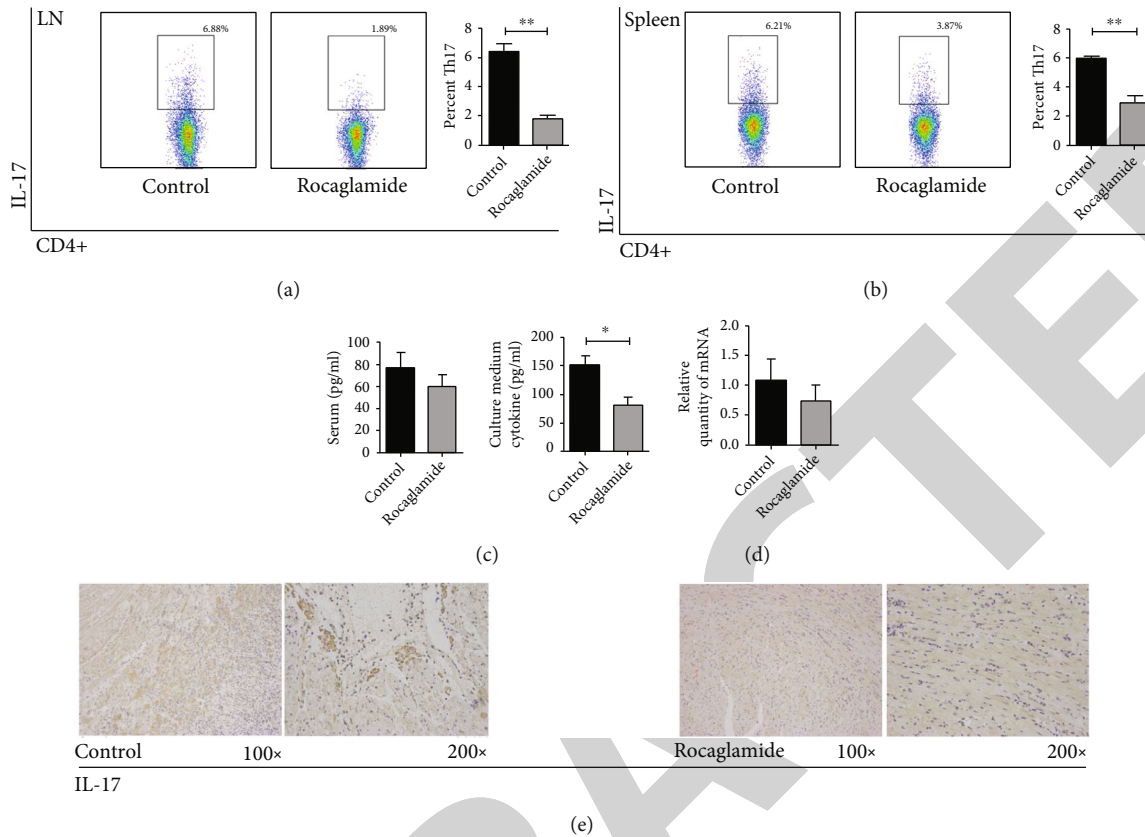


FIGURE 4: Rocaglamide-treated prolonged allograft survival is associated with suppressing Th17 cells, cytokine expression of Th17 T cells, and IL-17 infiltration. (a) Flow cytometric analysis rocaglamide-treated prolonged allograft survival is associated with suppressing Th17 cells in lymph nodes ( $n = 3$ ,  $*P < 0.05$ ,  $**P < 0.01$ , and  $***P < 0.001$ ). (b) Th17 cells in splenic lymphocytes were also suppressed. (c) Expressions of IL-17 in the peripheral blood and culture supernatants were tested by ELISA kits ( $n = 3$ ,  $*P < 0.05$ ,  $**P < 0.01$ , and  $***P < 0.001$ ). (d) mRNA was extracted from cardiac grafts and analyzed by qRT-PCR. The rocaglamide-treated group showed decreased ROR- $\gamma$ t in allografts when compared with the control group. (e) Rocaglamide decreases the accumulation and aggregation of IL-17 (b: 100x, 200x) in cardiac grafts. Immunohistochemical staining was performed, and the data showed that the infiltration of IL-17 was diminished in the rocaglamide-treated group.

inhibited the proliferation of Th1 and Th17 cells. We hypothesized that rocaglamide might inhibit NF-ATc1, AP-1, and NF- $\kappa$ B expression, which might reversely regulate mTOR expression and negatively regulate the immune response. To determine whether rocaglamide affects the nuclear expression levels of NF-AT and the NF- $\kappa$ B subunit p65 in activated T cells, we extracted nuclear proteins from Jurkat T cells that were stimulated by PMA/ionomycin for 2 h with or without rocaglamide. The nuclear levels of NF-AT caused dose-dependent downregulation of T cell activation (Figure 6(f)). However, at this concentration, rocaglamide had no inhibitory effect on NF- $\kappa$ B activity (Figure 6(g)).

**3.9. Rocaglamide Inhibits NF-AT via Activation of the MAPKs, JNK, and p38.** There are two different ways to activate the NF-AT family of proteins: one is activation via the calcium/calmodulin-dependent phosphatase calcineurin, which phosphorylates and promotes nuclear translocation of NF-AT. However, a recent study [36] suggested that rocaglamide has no direct inhibitory effect on calcineurin activity. Previous

studies indicated that the cellular MAPKs, JNK, and p38 can also regulate the nuclear expression of NF-AT. Therefore, to determine the mechanism of the rocaglamide-mediated inhibition of NF-AT activity, we determined the effect of rocaglamide on p38 and pJNK expression. Jurkat T cells were treated with PMA/ionomycin for 2 h with or without rocaglamide. We found that rocaglamide promoted the phosphorylation of p38 without stimulation and enhanced the phosphorylation of pJNK and p38 in the stimulatory environment (Figure 6(h); Figures 7(a) and 7(b)).

To demonstrate whether the activation of MAPKs by rocaglamide induced the reduction in NF-AT activity, Jurkat T cells were treated under the same conditions described previously. The p38 kinase and JNK inhibitors "SB203580" and "SP600125" were, respectively, used depending on the different groups. Group A was administered with normal treatment, group B was treated with the p38 kinase inhibitor (SB 203580), and group C was treated with the JNK inhibitor (SP600125). Data analysis showed that these inhibitors significantly inhibited the rocaglamide-enhanced phosphorylation of p38 (Figures 8(a) and 8(b), the first row). The phosphorylation of

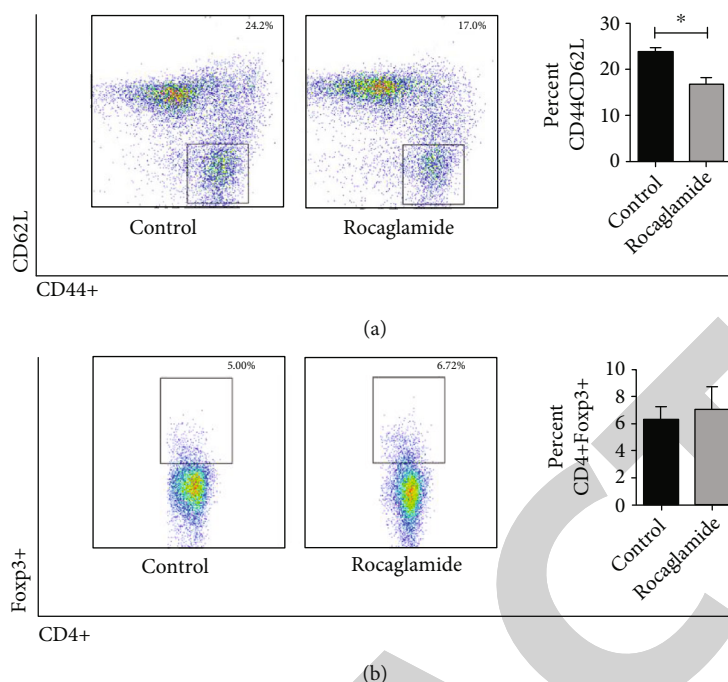


FIGURE 5: Rocaglamide decreases the memory of T cells, but no effect was noted on Treg. (a) Flow cytometric analysis of memory T cells (CD40<sup>high</sup>CD62<sup>low</sup>) considers the proportion of lymphocytes ( $n = 3$ ; \* $P < 0.05$ , \*\* $P < 0.01$ , and \*\*\* $P < 0.001$ ). (b) Flow cytometric analysis of CD4<sup>+</sup> Foxp3<sup>+</sup> regulatory T cells (Tregs).

pJNK was also inhibited by these inhibitors (Figures 8(a) and 8(c), the second row; Figure 7(b)); however, rocaglamide did not promote the phosphorylation of ERK, and there were no significant differences in ERK activities in these three groups (Figures 8(a), 8(b), and 8(c), the third row). The inhibitors inhibited p38 and JNK phosphorylation and prevented the rocaglamide-induced decrease in NF-AT levels (Figures 8(a), 8(b), and 8(c), the fourth row). At the same time, as a control, we examined the nuclear levels of the NF- $\kappa$ B subunit p65 and found no differences in the same experiments (Figures 8(a), 8(b) and 8(c), the fifth row). Therefore, the inhibition of p38 and JNK phosphorylation prevented a rocaglamide-mediated decrease in NF-AT nuclear export. These results demonstrated that rocaglamide-mediated inhibition of NF-AT activity is correlated with the upregulation of JNK/p38.

#### 4. Discussion

The production, differentiation, and activation of T cells play a key role in the immune responses that mediate acute rejection by secreting different types of cytokines. Oxidative stress responses along with the inflammatory cell infiltration of allografts result in the production of cytokines and proinflammatory adhesion molecules, which are the main factors causing vasculopathy and organ injury [37]. First, IFN- $\gamma$  is secreted by Th1 cells at the start of immunoreaction and oxidative stress damage. Second, IFN- $\gamma$  is not only an important activator of macrophages and inducer of class II major histocompatibility complex molecule expression but also an inducer of more undifferentiated naïve CD4<sup>+</sup> cells

(Th0 cells) that differentiate into Th1 cells [38, 39]. Therefore, a positive feedback loop is formed. Some studies have demonstrated that rocaglamide blocks inducible NF- $\kappa$ B DNA-binding activity and I $\kappa$ Ba degradation, which in turn downregulates NF- $\kappa$ B gene expression in T lymphocytes [12].

To the best of our knowledge, this is the first study to report that during transplantation, rocaglamide prolongs allograft survival by reducing the number of CD4<sup>+</sup> IFN- $\gamma$ <sup>+</sup> (Th1) cells by not only decreasing the number of Th1 cells in the lymph nodes but also in the spleen. Th1-type cytokines such as IFN- $\gamma$  and TNF- $\alpha$  stimulate cell-mediated immunoreaction, which causes cytokine production and inflammatory cell aggregation, resulting in more oxidative stress damage and vasculopathy. Thus, the expression of these cytokines is harmful to grafts and causes their rejection. Some recent studies showed that rocaglamide suppresses the secretion of IFN- $\gamma$  and IL-4 in vitro [11, 40]. Interestingly, we first demonstrated that rocaglamide has a suppressive effect on the expression of IFN- $\gamma$  in culture supernatants, peripheral blood samples, and allografts. By analyzing the MLR, we assumed that rocaglamide suppressed the proliferation of T lymphocytes, and eventually, low levels of IFN- $\gamma$  led to lower levels of cytotoxic mediators, lower activation of T cells, and lower differentiation of naïve CD4<sup>+</sup> T cells into the Th1 cells. This sequence of events thus formed another positive feedback loop.

Moreover, Becker et al. reported that rocaglamide promotes mitochondria-mediated apoptosis in leukemia cells [11], which is associated with CD95/CD95L-mediated



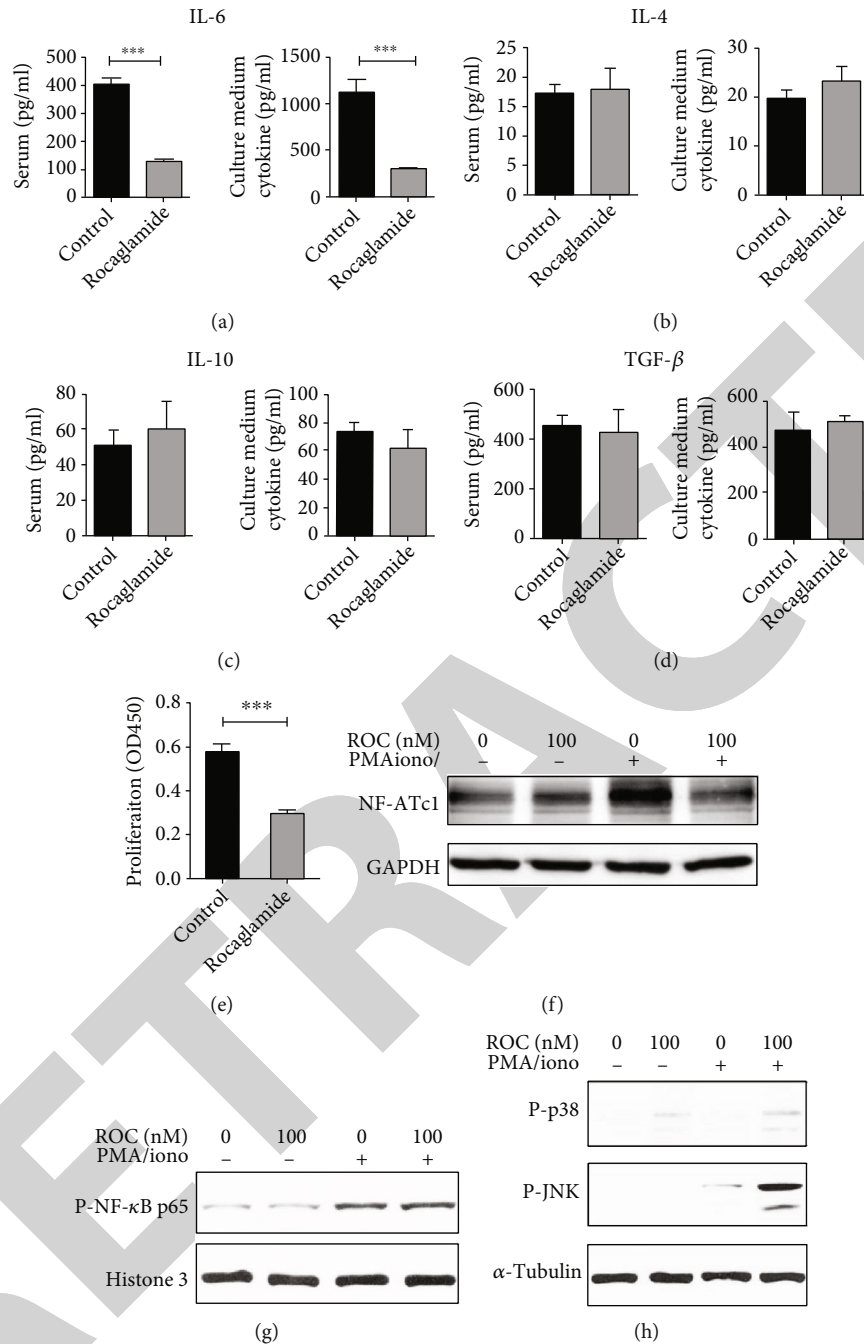


**FIGURE 6:** Rocaglamide treatment changes the cytokine expression of allograft recipients, affects the immune response ability of T cells to the same identical gene tissues, and suppresses the nuclear expression of NF-AT, but not that of NF-κB. (a–d) The levels of IL-6 (a), IL-4 (b), IL-10 (c), and TGF-β (d) in the serum and supernatants curve from MLR were detected by using commercially available ELISA kits. Each reaction was conducted in triplicate (\* $P < 0.05$ , \*\* $P < 0.01$ , and \*\*\* $P < 0.001$ ). (e) To investigate the effectiveness of rocaglamide on the proliferation of T cells, both in the spleen and lymph nodes, and we performed mixed lymphocyte reaction assays. Data from three separate wells were dedicated to each responder-stimulator, and each experiment was repeated thrice ( $n = 3$ ; \* $P < 0.05$ , \*\* $P < 0.01$ , and \*\*\* $P < 0.001$ ). (f) T cell activation induced by the nuclear expression of NF-AT was downregulated. Jurkat T cells were stimulated with PMA and ionomycin for 2h with or without rocaglamides (added 1h before stimulation). Nuclear proteins were extracted and immunoblotted with mAb against NFATc1. (g) The nuclear proteins were immunoblotted with Abs to p65. (h) Rocaglamides activate MAPKs, p38, and JNK. Jurkat T cells were stimulated with PMA and ionomycin for 2h in the absence or presence of various concentrations of rocaglamides (added 1h before stimulation). Total cell lysates were immunoblotted with Abs against phosphorylated p38 (p-p38) and phosphorylated JNK.

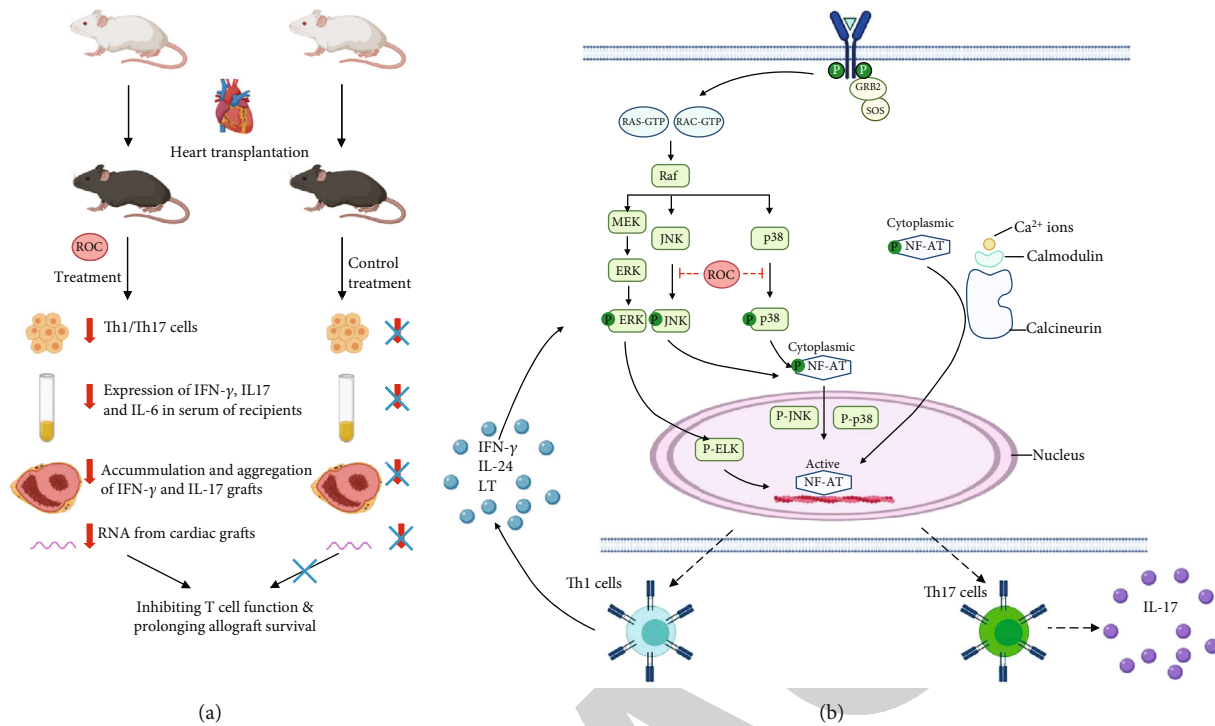


FIGURE 7: Rocaglamide inhibits Th1/Th17 cell differentiation and prolonged graft survival through NF-AT pathway downregulation. (a) Recipients were treated with PBS ( $n = 6$ ) and rocaglamide ( $n = 8$ ) for survival studies. Heart grafts were monitored until they stopped beating. Grafts were performed, and recipients were sacrificed on day 7 for histological, MLR, ELISA, PCR, and flow cytometric analysis. RNA was extracted from the grafts of recipient mice. (b) Rocaglamides inhibit NF-AT via the activation of MAPKs, and rocaglamide can enhance the phosphorylation of pJNK and p38 in the simulation environment. Rocaglamide suppresses the nuclear expression of NF-AT in activated T cells. Rocaglamide suppresses the activation of T cells and reduces naive CD4<sup>+</sup> T cell differentiation into Th1/Th17 cells. Moreover, it decreases the secretion of IFN- $\gamma$  and IL-17; thus, in turn, low-level expression of IFN- $\gamma$  leads to lower cytotoxic mediators, lower activation of T cells, and lower differentiation of naive CD4<sup>+</sup> T cells into the Th1 cells. A feedback loop then begins. However, the inhibition of p38 and JNK phosphorylation prevented rocaglamide-mediated decrease of NF-AT nuclear export.

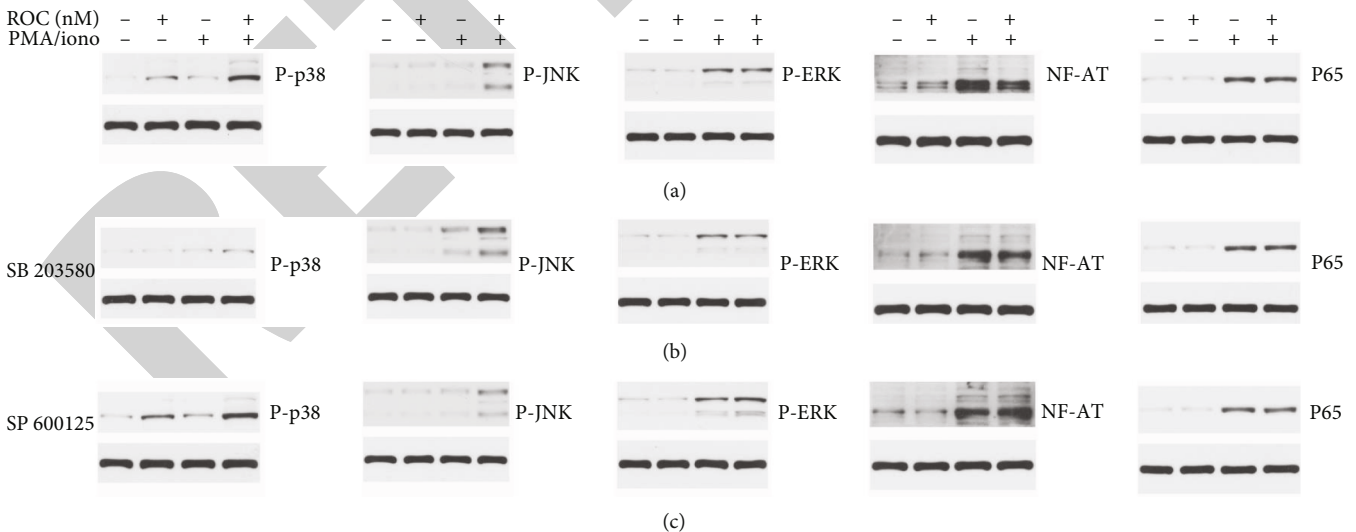


FIGURE 8: Rocaglamide inhibits NF-AT via activation of the MAPKs, JNK, and p38. Jurkat T cells were treated with same condition described previously, and p38 kinase and JNK inhibitors (SB 203580 and SP 600125) were used, respectively, depending on the different group. Group A was normal treated, group B was treated with p38 kinase inhibitor (SB 203580), and group C was treated with JNK inhibitors (SP600125).

apoptosis in T cells. And CD95L is a known NF-AT target gene [41]. A previous study also showed that mTOR directly affects NF-AT-P, and mTOR signaling plays a key regulatory role in the differentiation and activation of Th1 cells [42]. According to our data, rocaglamide downregulated the expression of NF-ATc1, which is correlated with the inhibition of Th1 cell differentiation.

Baumann et al. and Goriely also reported that rocaglamide could inhibit IL-4 production in Jurkat T cells [12, 36]. However, we found no statistical significance of IL-4 levels between the two groups. Another study suggested that the Th17 subset is crucial for rejection and myocardial injury [27]. Th17 cells generate proinflammatory cytokines such as IL-17A, IL-21, and IL-22 [43]. Sica et al. also demonstrated that decreased Th17 cells promote graft survival by reducing the production of interleukin-17 (IL-17) [44]. Several inducible transcription factors such as AP-1 (Fos/Jun) and NF-AT regulate the secretion of IL-4, IFN- $\gamma$ , and TNF- $\alpha$  [45, 46]. We also first reported that rocaglamide could inhibit the differentiation of CD4+ cells into Th17 cells in our cardiac transplantation model. Furthermore, a reduction in IL-17 levels was observed in culture supernatants, serum samples, and allografts. Meanwhile, as shown previously [31], we found that the expression of IL-6, which is associated with proliferation of Th17 cells, was decreased significantly.

Allograft rejection is promoted, and allograft tolerance is prevented via memory T cells in hosts' immune repertoire [34]. Consistent with the findings of previous studies, Pepper et al. reported that the inhibition of CD27/70 reduced the generation of memory T cells [47]. Naïve CD4+ T cells sustainably proliferate and differentiate into different types of helper T cell lineages, including Th1, Th2, and Th17, when exposed to an antigen. Th1 memory cells are produced in vivo after exposure to infection and are differentiated from T-bet and IFN- $\gamma$ -expressing Th1 effector cells [48]. Th1 memory cells showed minimal (or possibly delayed) reexpression of CD62L and CCR7, indicating that these cells are Th1 effector memory cells [47]. Pepper et al. also found that 60% of T-bet+ CXCR5- Th1 memory cells produced IFN- $\gamma$  and IL-2 [47]. A few recent studies showed that IFN- $\gamma$ , IL-17, and IL-4 affect the differentiation and functions of helper T cells of different lineages to some extent. However, the mechanisms by which helper T cells and cytokines promote memory T cells are still unclear. Interestingly, consistent with previous results describing the inhibition of Th1 cells and the expression of IFN- $\gamma$  and IL-17, we found that rocaglamide suppressed the production of effector memory T cells (CD40<sup>high</sup>CD62<sup>low</sup>) in the lymph nodes.

Regulatory T cells are usually required for the prolongation and tolerance of a transplant; however, we found that rocaglamide did not affect CD4+ Foxp3+ T cells. Growth factor-beta (TGF- $\beta$ ) and IL-10, which inhibit helper T cells, also showed no statistical significance.

In summary, our present findings showed that rocaglamide therapy led to a significant prolongation of allograft survival, which was associated with significantly reduced Th1 cells and IFN- $\gamma$ , low levels of IFN- $\gamma$  that led to lower cytotoxic mediators, lower activation of T cells, and lower differentiation of naïve CD4+ T cells into Th1 cells. Furthermore, this is the first

study to report that rocaglamide suppressed the differentiation of naïve CD4+ T cells into Th17 cells, thereby also inducing the marked decrease in IL-17 levels, which might be associated with the inhibition of IL-6. We also found that the phosphorylation of JNK and p38, which are key regulators of NF-AT and indispensable for activating the transcription of cytokine genes, was enhanced by rocaglamide treatment. However, the inhibitory role was nullified when the p38 kinase (SB203580) and JNK inhibitors (SP600125) were used. Over-activation of p38 and JNK may lead to rocaglamide-mediated inhibition of NF-AT activity.

These results indicated that the suppression of Th1 cell proliferation, activation, and differentiation, which might be associated with the expression of NF-AT, was inhibited. Although the mechanisms of the effect of rocaglamide on antigen-presenting cells in oxidative stress injury and transplantation immunity need to be determined, our findings may facilitate the development of a new therapy for IFN- $\gamma$ - and IL-17-mediated rejection and inflammation.

## 5. Conclusion

We found that rocaglamide could be potentially used for preventing cell-mediated acute rejection and alleviating oxidative stress because it prevents T helper cell differentiation and T cell-mediated cytokine secretion. We also found that the suppressive effect of rocaglamide on T helper cell proliferation, activation, and differentiation could be associated with the inhibition of NF-AT expression.

Our results clearly demonstrate a novel immunoregulatory property of rocaglamide, wherein it regulates oxidative stress response and reduces inflammatory cell infiltration and organ injury. Our findings could be useful for surgeons performing organ transplantation and immunologists studying transplantation immunity and inflammatory factors.

## Data Availability

Previously reported data were used to support this study and are at available relevant places within the text as references. The new data used to support the findings of this study may be released upon application to the Institute of Organ Transplantation, Tongji Hospital, Tongji Medical College, Huazhong University of Science and Technology; Key Laboratory of Organ Transplantation, Ministry of Education; NHC Key Laboratory of Organ Transplantation; Key Laboratory of Organ Transplantation, Chinese Academy of Medical Sciences, Wuhan, China. 430030, Zhishui Chen, Wuhan, China. Tel. +86 27 83665203 can be contacted at the corresponding author upon request.

## Disclosure

An abstract of a part of this study was submitted as a poster to the American Transplant Congress, but we did not report it because of new research advances and results, and this is the first time all the results have been submitted to this journal (<https://atcmeetingabstracts.com/abstract/inhibition-of->

th1-and-th17-cell-differentiation-and-prolonged-graft-survival-through-nfat-pathway-downregulation/).

## Conflicts of Interest

The authors declare that there is no conflict of interest regarding the publication of this paper.

## Acknowledgments

Thanks are due to Pro. Markmann who provided help during the research and preparation of the manuscript. This work is supported by the National Natural Science Foundation of China (NSFC) (grant number 81900368).

## Supplementary Materials

*Supplementary 1.* Supplemental Figure 1: rocaglamide decreased the expression of AP-1. Rocaglamides activate MAPKs, p38, and JNK. Jurkat T cells were stimulated with PMA and ionomycin for 2 h in the absence or the presence of various concentrations of rocaglamides (added 1 h before stimulation). Total cell lysates were immunoblotted with Abs against c-Jun.

*Supplementary 2.* Supplemental Figure 2: rocaglamide had no effect on apoptosis in the activated condition flow cytometric analysis rocaglamide-treated cells. We measured apoptosis levels with and without rocaglamide in activated conditions. As shown in the figure below, we found that rocaglamide had no effect on apoptosis in the activated condition. This phenomenon has been discussed in our article.

*Supplementary 3.* Supplemental Figure 3: rocaglamide had no effect on B cells in the recipients. A. Analyzing the proportion of CD19+ using fluorochrome-conjugated-specific antibodies detected by flow cytometry. Data are given one representative experiment of at least three experiments ( $n = 3$ ;  $*P < 0.05$ ,  $**P < 0.01$ , and  $***P < 0.001$ ). B. Serum alloantibody measurement, IgG, and IgM antibodies were analyzed by ELISA. We found that rocaglamide therapy could not reduce the number of CD19+ B cells (A). We found that there was slightly decrease tendency on IgG of recipients treated with rocaglamide, but there was no statistical significance; meanwhile, there were no differences on IgM also (B).

## References

- [1] G. Deng, R. Deng, J. Yao et al., "Trichinella spiralis infection changes immune response in mice performed abdominal heterotopic cardiac transplantation and prolongs cardiac allograft survival time," *Parasitology Research*, vol. 115, no. 1, pp. 407–414, 2016.
- [2] P. Nickerson, W. Steurer, J. Steiger, X. Zheng, A. W. Steele, and T. B. Strom, "Cytokines and the Th1/Th2 paradigm in transplantation," *Current Opinion in Immunology*, vol. 6, no. 5, pp. 757–764, 1994.
- [3] F. A. M. Abo-Aziza, S. H. M. Hendawy, A. H. E. Namaky, and H. M. Ashry, "Th1/Th2 balance and humoral immune response to potential antigens as early diagnostic method of equine Strongylus nematode infection," *Veterinary World*, vol. 10, no. 6, pp. 679–687, 2017.
- [4] K. Nistala and L. R. Wedderburn, "Th17 and regulatory T cells: rebalancing pro- and anti-inflammatory forces in autoimmune arthritis," *Rheumatology*, vol. 48, no. 6, pp. 602–606, 2009.
- [5] W. Kang, Y. Li, Y. Zhuang, K. Zhao, D. Huang, and Y. Sun, "Dynamic analysis of Th1/Th2 cytokine concentration during antiretroviral therapy of HIV-1/HCV co-infected patients," *BMC Infectious Diseases*, vol. 12, no. 1, p. ???, 2012.
- [6] R. Vuillefroy de Silly, F. Coulon, N. Poirier et al., "Transplant tolerance is associated with reduced expression of cystathionine- $\gamma$ -lyase that controls IL-12 production by dendritic cells and TH-1 immune responses," *Blood*, vol. 119, no. 11, pp. 2633–2643, 2012.
- [7] E. Forcade, K. Paz, R. Flynn et al., "An activated Th17-prone T cell subset involved in chronic graft-versus-host disease sensitive to pharmacological inhibition," *JCI Insight*, vol. 2, no. 12, 2017.
- [8] R. D. McFarland, D. C. Douek, R. A. Koup, and L. J. Picker, "Identification of a human recent thymic emigrant phenotype," *Proceedings of the National Academy of Sciences of the United States of America*, vol. 97, no. 8, pp. 4215–4220, 2000.
- [9] J. Y. Zhu, M. Giaisi, R. Köhler et al., "Rocaglamide sensitizes leukemic T cells to activation-induced cell death by differential regulation of CD95L and c-FLIP expression," *Cell Death and Differentiation*, vol. 16, no. 9, pp. 1289–1299, 2009.
- [10] A. Li, L. Yang, X. Geng et al., "Rocaglamide-A potentiates osteoblast differentiation by inhibiting NF- $\kappa$ B signaling," *Molecules and Cells*, vol. 38, no. 11, pp. 941–949, 2015.
- [11] M. S. Becker, P. Schmezer, R. Breuer et al., "The traditional Chinese medical compound rocaglamide protects nonmalignant primary cells from DNA damage-induced toxicity by inhibition of p53 expression," *Cell Death & Disease*, vol. 5, no. 1, article e1000, 2014.
- [12] B. Baumann, F. Bohnenstengel, D. Siegmund et al., "Rocaglamide Derivatives Are Potent Inhibitors of NF- $\kappa$ B Activation in T-cells," *The Journal of Biological Chemistry*, vol. 277, no. 47, pp. 44791–44800, 2002.
- [13] M. Bleumink, R. Kohler, M. Giaisi, P. Proksch, P. H. Krammer, and M. Li-Weber, "Rocaglamide breaks TRAIL resistance in HTLV-1-associated adult T-cell leukemia/lymphoma by translational suppression of c-FLIP expression," *Cell Death and Differentiation*, vol. 18, no. 2, pp. 362–370, 2011.
- [14] L. Pan, J. L. Woodard, D. M. Lucas, J. R. Fuchs, and A. D. Kinghorn, "Rocaglamide, silvestrol and structurally related bioactive compounds from Aglaia species," *Natural Product Reports*, vol. 31, no. 7, pp. 924–939, 2014.
- [15] F. Macián, C. García-Rodríguez, and A. Rao, "Gene expression elicited by NFAT in the presence or absence of cooperative recruitment of Fos and Jun," *The EMBO Journal*, vol. 19, no. 17, pp. 4783–4795, 2000.
- [16] O. Kaminuma, C. Elly, Y. Tanaka et al., "Vav-induced activation of the human IFN- $\gamma$  gene promoter is mediated by upregulation of AP-1 activity," *FEBS Letters*, vol. 514, no. 2-3, pp. 153–158, 2002.
- [17] G. R. Crabtree and E. N. Olson, "NFAT signaling: choreographing the social lives of cells," *Cell*, vol. 109, no. 2, pp. s67–s79, 2002.
- [18] T. Hasegawa, S. H. Visovatti, M. C. Hyman, T. Hayasaki, and D. J. Pinsky, "Heterotopic vascularized murine cardiac

- transplantation to study graft arteriopathy," *Nature Protocols*, vol. 2, no. 3, pp. 471–480, 2007.
- [19] C. Dai, F. N. Lu, N. Jin et al., "Recombinant IL-33 prolongs leflunomide-mediated graft survival by reducing IFN- $\gamma$  and expanding CD4<sup>+</sup>Foxp3<sup>+</sup> T cells in concordant heart transplantation," *Laboratory Investigation*, vol. 96, no. 8, pp. 820–829, 2016.
- [20] Z. Luan, Y. He, F. He, and Z. Chen, "Rocaglamide overcomes tumor necrosis factor-related apoptosis-inducing ligand resistance in hepatocellular carcinoma cells by attenuating the inhibition of caspase-8 through cellular FLICE-like-inhibitory protein downregulation," *Molecular Medicine Reports*, vol. 11, no. 1, pp. 203–211, 2015.
- [21] F. Hajighasemi and A. Mirshafiey, "In vitro effects of propranolol on T helper type 1 cytokine profile in human leukemic T cells," *Int J Hematol Oncol Stem Cell Research*, vol. 10, no. 2, pp. 99–105, 2016.
- [22] Q. Wang, Y. Liu, and X. K. Li, "Simplified technique for heterotopic vascularized cervical heart transplantation in mice," *Microsurgery*, vol. 25, no. 1, pp. 76–79, 2005.
- [23] M. Li-Weber, M. Giasi, and P. H. Krammer, "Involvement of Jun and Rel Proteins in Up-regulation of Interleukin-4 Gene Activity by the T Cell Accessory Molecule CD28," *The Journal of Biological Chemistry*, vol. 273, no. 49, pp. 32460–32466, 1998.
- [24] J. Zhu and W. E. Paul, "CD4 T cells: fates, functions, and faults," *Blood*, vol. 112, no. 5, pp. 1557–1569, 2008.
- [25] D. J. Hartigan-O'Connor, L. A. Hirao, J. M. McCune, and S. Dandekar, "Th17 cells and regulatory T cells in elite control over HIV and SIV," *Current Opinion in HIV and AIDS*, vol. 6, no. 3, pp. 221–227, 2011.
- [26] S. Heidt, D. S. Segundo, R. Chadha, and K. J. Wood, "The impact of Th17 cells on transplant rejection and the induction of tolerance," *Current Opinion in Organ Transplantation*, vol. 15, no. 4, pp. 456–461, 2010.
- [27] L. Guglani and S. A. Khader, "Th17 cytokines in mucosal immunity and inflammation," *Current Opinion in HIV and AIDS*, vol. 5, no. 2, pp. 120–127, 2010.
- [28] H. Oishi, T. Martinu, M. Sato et al., "Halofuginone treatment reduces interleukin-17A and ameliorates features of chronic lung allograft dysfunction in a mouse orthotopic lung transplant model," *The Journal of Heart and Lung Transplantation: the Official Publication of the International Society for Heart Transplantation*, vol. 35, no. 4, pp. 518–527, 2016.
- [29] M. J. McGeachy, K. S. Bak-Jensen, Y. Chen et al., "TGF- $\beta$  and IL-6 drive the production of IL-17 and IL-10 by T cells and restrain TH-17 cell-mediated pathology," *Nature Immunology*, vol. 8, no. 12, pp. 1297–1390, 2007.
- [30] D. M. Talia, D. Deliyanti, A. Agrotis, and J. L. Wilkinson-Berka, "Inhibition of the nuclear receptor ROR $\gamma$  and interleukin-17A suppresses neovascular retinopathy: involvement of immunocompetent microglia," *Arteriosclerosis, Thrombosis, and Vascular Biology*, vol. 36, no. 6, pp. 1186–1196, 2016.
- [31] M. D. Pescovitz, "B cells: a rational target in alloantibody-mediated solid organ transplantation rejection," *Clinical Transplantation*, vol. 20, no. 1, pp. 48–54, 2006.
- [32] T. Haudebourg, N. Poirier, and B. Vanhove, "Depleting T-cell subpopulations in organ transplantation," *Transplant International*, vol. 22, no. 5, pp. 509–518, 2009.
- [33] M. V. Florentin-Martial Mbitikon-Kobo, M.-C. Michallet, M. Tomkowiak et al., "Characterization of a CD44/CD122int memory CD8 T cell subset generated under sterile inflammatory conditions," *Journal of Immunology*, vol. 182, no. 6, pp. 3846–3854, 2009.
- [34] S. Todd, R. J. D. Davidson, J. Andersson, and E. M. Shevach, "Cutting Edge: IL-2 is essential for TGF- $\beta$ -Mediated induction of Foxp3<sup>+</sup>T regulatory cells," *Journal of Immunology*, vol. 178, no. 7, pp. 4022–4026, 2007.
- [35] P. Proksch, M. Giasi, M. K. Treiber et al., "Rocaglamide derivatives are immunosuppressive phytochemicals that target NF-AT activity in T cells," *The Journal of Immunology*, vol. 174, no. 11, pp. 7075–7084, 2005.
- [36] S. Goriely and M. Goldman, "The interleukin-12 family: new players in transplantation immunity," *American Journal of Transplantation*, vol. 7, no. 2, pp. 278–284, 2007.
- [37] N. D. Verma, R. Boyd, C. Robinson, K. M. Plain, G. T. Tran, and B. M. Hall, "Interleukin-12p70 prolongs allograft survival by induction of interferon gamma and nitric oxide production," *Transplantation*, vol. 82, no. 10, pp. 1324–1333, 2006.
- [38] B. A. Johnson 3rd, B. Baban, and A. L. Mellor, "Targeting the immunoregulatory indoleamine 2,3 dioxygenase pathway in immunotherapy," *Immunotherapy*, vol. 1, no. 4, pp. 645–661, 2009.
- [39] T. A. Zaichuk, E. H. Shroff, R. Emmanuel, S. Filleur, T. Nelius, and O. V. Volpert, "Nuclear factor of activated T cells balances angiogenesis activation and inhibition," *The Journal of Experimental Medicine*, vol. 199, no. 11, pp. 1513–1522, 2004.
- [40] C. Rommel, S. C. Bodine, B. A. Clarke et al., "Mediation of IGF-1-induced skeletal myotube hypertrophy by PI(3)K/Akt/mTOR and PI(3)K/Akt/GSK3 pathways," *Nature Cell Biology*, vol. 3, no. 11, pp. 1009–1013, 2001.
- [41] J. S. Serody and G. R. Hill, "The IL-17 differentiation pathway and its role in transplant outcome," *Biology of Blood and Marrow Transplantation: journal of the American Society for Blood and Marrow Transplantation*, vol. 18, no. 1, pp. S56–S61, 2012.
- [42] W. He, Z. Fang, F. Wang et al., "Galectin-9 significantly prolongs the survival of fully mismatched cardiac allografts in mice," *Transplantation*, vol. 88, no. 6, pp. 782–790, 2009.
- [43] E. Y. Tsai, J. Yie, D. Thanos, and A. E. Goldfeld, "Cell-type-specific regulation of the human tumor necrosis factor alpha gene in B cells and T cells by NFATp and ATF-2/JUN," *Molecular and Cellular Biology*, vol. 16, no. 10, pp. 5232–5244, 1996.
- [44] A. Sica, L. Dorman, V. Viggiano et al., "Interaction of NF- $\kappa$ B and NFAT with the Interferon- $\gamma$  Promoter," *The Journal of Biological Chemistry*, vol. 272, no. 48, pp. 30412–30420, 1997.
- [45] K. Yamaura, O. Boenisch, T. Watanabe et al., "Differential requirement of CD27 costimulatory signaling for Naïve versus alloantigen-primed effector/memory CD8<sup>+</sup>T cells," *American Journal of Transplantation : Official Journal of the American Society of Transplantation and the American Society of Transplant Surgeons*, vol. 10, no. 5, pp. 1210–1220, 2010.
- [46] L. E. Harrington, K. M. Janowski, J. R. Oliver, A. J. Zajac, and C. T. Weaver, "Memory CD4 T cells emerge from effector T-cell progenitors," *Nature*, vol. 452, no. 7185, pp. 356–360, 2008.

## *Retraction*

# **Retracted: Novel lncRNA AL033381.2 Promotes Hepatocellular Carcinoma Progression by Upregulating PRKRA Expression**

### **Oxidative Medicine and Cellular Longevity**

Received 26 September 2023; Accepted 26 September 2023; Published 27 September 2023

Copyright © 2023 Oxidative Medicine and Cellular Longevity. This is an open access article distributed under the Creative Commons Attribution License, which permits unrestricted use, distribution, and reproduction in any medium, provided the original work is properly cited.

This article has been retracted by Hindawi following an investigation undertaken by the publisher [1]. This investigation has uncovered evidence of one or more of the following indicators of systematic manipulation of the publication process:

- (1) Discrepancies in scope
- (2) Discrepancies in the description of the research reported
- (3) Discrepancies between the availability of data and the research described
- (4) Inappropriate citations
- (5) Incoherent, meaningless and/or irrelevant content included in the article
- (6) Peer-review manipulation

The presence of these indicators undermines our confidence in the integrity of the article's content and we cannot, therefore, vouch for its reliability. Please note that this notice is intended solely to alert readers that the content of this article is unreliable. We have not investigated whether authors were aware of or involved in the systematic manipulation of the publication process.

Wiley and Hindawi regrets that the usual quality checks did not identify these issues before publication and have since put additional measures in place to safeguard research integrity.

We wish to credit our own Research Integrity and Research Publishing teams and anonymous and named external researchers and research integrity experts for contributing to this investigation.

The corresponding author, as the representative of all authors, has been given the opportunity to register their agreement or disagreement to this retraction. We have kept a record of any response received.

### **References**

- [1] F. Wang, L. Zhu, Q. Xue et al., "Novel lncRNA AL033381.2 Promotes Hepatocellular Carcinoma Progression by Upregulating PRKRA Expression," *Oxidative Medicine and Cellular Longevity*, vol. 2022, Article ID 1125932, 24 pages, 2022.

## Research Article

# Novel lncRNA AL033381.2 Promotes Hepatocellular Carcinoma Progression by Upregulating PRKRA Expression

Feiran Wang <sup>1,2</sup>, Lirong Zhu <sup>2</sup>, Qiang Xue <sup>3</sup>, Chong Tang <sup>4</sup>, Weidong Tang <sup>2</sup>,  
Nannan Zhang <sup>1</sup>, Chen Dai <sup>5</sup>, and Zhong Chen <sup>2</sup>

<sup>1</sup>Medical College of Nantong University, Nantong, Jiangsu 226000, China

<sup>2</sup>Department of General Surgery, Affiliated Hospital of Nantong University, Nantong, Jiangsu 226000, China

<sup>3</sup>Department of Radiotherapy, Affiliated Hospital of Nantong University, Nantong, Jiangsu 226000, China

<sup>4</sup>Department of General Surgery, Affiliated Hospital 2 of Nantong University, Nantong, Jiangsu 226000, China

<sup>5</sup>Institute of Organ Transplantation, Tongji Hospital, Tongji Medical College, Huazhong University of Science and Technology; Key Laboratory of Organ Transplantation, Ministry of Education, NHC Key Laboratory of Organ Transplantation, Key Laboratory of Organ Transplantation, Chinese Academy of Medical Sciences, Wuhan, Hubei 430030, China

Correspondence should be addressed to Chen Dai; [cdai26@tjh.tjmu.edu.cn](mailto:cdai26@tjh.tjmu.edu.cn) and Zhong Chen; [chenzgs@163.com](mailto:chenzgs@163.com)

Received 22 October 2021; Revised 22 November 2021; Accepted 3 December 2021; Published 6 January 2022

Academic Editor: Hao Wu

Copyright © 2022 Feiran Wang et al. This is an open access article distributed under the Creative Commons Attribution License, which permits unrestricted use, distribution, and reproduction in any medium, provided the original work is properly cited.

Hepatocellular carcinoma (HCC) is a common malignant tumor that is characterized by aggressiveness and poor prognosis. Accumulating evidence indicates that oxidative stress plays a crucial role in carcinogenesis, whereas the potential mechanism between oxidative stress and carcinogenic effects remains elusive. In recent years, long noncoding RNAs (lncRNAs) in cancers have attracted extensive attention and have been shown to be involved in oxidative stress response and carcinogenesis. Nevertheless, the roles of lncRNA AL033381.2 in regulating the development and progression of HCC still remain unclear. The purpose of our study was to evaluate the potential effects and molecular mechanisms of AL033381.2 that may be involved in oxidative stress response in HCC. Using bioinformatics analyses based on the TCGA database, we screened and identified a novel lncRNA AL033381.2 in HCC, which may be involved in oxidative stress responses. qRT-PCR analysis revealed that AL033381.2 is upregulated in HCC tissues. Through *in vitro* and *in vivo* experiments, we found that AL033381.2 dramatically facilitates the growth and metastasis of HCC. Mechanistically, RNA pull-down experiments, mass spectrometry, PathArray™, and RIP were used to determine that AL033381.2 binds to PRKRA and may be involved in AL033381.2-mediated oncogenic functions in HCC cells. Moreover, rescue experiments demonstrated that PRKRA overexpression rescues the abilities of HCC cell proliferation, migration, and invasion that were affected by AL033381.2 knockdown. Furthermore, we produced a nanoparticle-based siRNA delivery system and tested its therapeutic effects *in vivo*. The results showed that the *in vivo* growth rate of the tumors treated with the nanoparticle/AL033381.2 siRNA complexes was dramatically lower than those treated with the nanoparticle/scramble siRNA complexes. Taken together, our results suggest that the novel lncRNA AL033381.2 may be involved in oxidative stress response by targeting oxidative stress-related genes in HCC. AL033381.2 plays vital oncogenic roles in HCC progression and may be a novel therapeutic marker for HCC diagnosis and treatment.

## 1. Introduction

Hepatocellular carcinoma (HCC) is one of the major causes of cancer mortality around the world, and the occurrence of HCC continues to increase in China [1, 2]. As most HCC patients are commonly diagnosed at the advanced stage, and effective therapies and molecular targeted drugs are

lacking, the prognosis of HCC patients remains poor [3, 4]. In recent years, a growing body of research has focused on targeted therapy for HCC [5]. The pathogenesis of HCC is a multistep process that is related to the gradual accumulation of genetic changes that accurately locate various cellular and molecular events, such as oxidative stress, endoplasmic reticulum stress, and abnormal cell cycles [6]. Oxidative

stress is considered to play a crucial role in the initiation and promotion of carcinogenesis, and it can accelerate the progression of HCC through endogenous or exogenous injury and excessive production of reactive oxygen species (ROS) and active nitrogen (RNS), as well as reduced antioxidant defense [7]. More specifically, oxidative stress injury can affect the expression of cell survival genes, and its products promote the growth and differentiation of normal cells and eventually lead to the reduction of cell apoptosis and the formation of tumor cells [8]. Therefore, the level of oxidative stress can be a promising predictor of HCC diagnosis and treatment. Hence, it is crucial to clarify the mechanism of HCC progression and identify the valuable therapeutic targets for HCC.

Increasing evidence has demonstrated that several lncRNAs that are nonprotein-coding RNAs with a length of more than 200 nucleotides can be induced by oxidative stress, and thus, they are considered to be potential therapeutic targets in various cancers [9, 10]. In recent years, extensive evidence has revealed that lncRNA expression profiles are dysregulated in multiple malignancies and play a vital role in facilitating cancer progression through various molecular mechanisms [11]. lncRNAs are associated with regulating gene expression, chromatin remodeling, transcription control, splicing regulation, mRNA stabilization, microRNA processing, and protein stability maintenance [12]. Therefore, lncRNAs play vital roles in tumor growth, invasion, and metastasis [13]. Nevertheless, numerous lncRNAs have yet to be functionally characterized. Hence, a comprehensive understanding of the roles of lncRNAs in the occurrence and development of HCC will help to enrich our knowledge of the molecular mechanisms of HCC progression and also provide new insights into the development of therapeutic for HCC.

We identified oxidative stress-responsive lncRNA AL033381.2, which is a newly discovered lncRNA involved in tumor progression. In our study, we first report that AL033381.2 is notably elevated in HCC tissues, thereby implying that AL033381.2 plays a tumor-promoting role in HCC progression. Additionally, AL033381.2 enhances the abilities of HCC cell proliferation, migration, and invasion by regulating PRKRA. Moreover, we investigated the potential of AL033381.2 siRNA as a possible therapeutic target in HCC using a PLGA-based nanoparticle delivery system and tested its therapeutic effect *in vivo*. Our findings suggest that AL033381.2 can be potentially utilized as a diagnostic molecular biomarker and novel therapeutic target for HCC patients.

## 2. Materials and Methods

**2.1. RNA-Sequencing Data Download and Analysis.** For liver hepatocellular carcinoma (LIHC), the TCGA database [14] contains 374 samples with available data, including 50 samples with paired tissue (cancer and normal) RNA-sequencing (RNA-seq) data. A total of 317 patients were sampled with RNA-seq data and pathological data. Statistically significant differentially expressed lncRNAs (DELncRNAs) were screened out by R language analysis. The cut-

off value was  $|\log_2 \text{FC (fold change)}| > 1$  and FDR (false discovery rate)  $< 0.05$ .

**2.2. Cell Culture and Clinical Specimens.** Hep3B, Huh-7, HepG2, and SK-HEP-1 cell lines were obtained by the Cell Bank of the Chinese Academy of Sciences, which were authenticated by STR profiling. Cells were maintained in DMEM supplement with 10% FBS (Gibco) and cultured at 37°C under 5% CO<sub>2</sub>.

Besides, matched pairs of fresh HCC tissues and adjacent normal tissue samples ( $n = 30$ ) from HCC patients were collected from January 2020 to January 2021 for Western blot analysis, with informed consent. Our study was approved by the Institutional Research Ethics Committee of the Affiliated Hospital of Nantong University.

**2.3. Cell Transfection.** The recombinant lentivirus of lncRNA AL033381.2 knockdown (shAL033381.2), negative control (shCtrl), and lentiviruses expressing PRKRA (LV-PRKRA) were synthesized by GeneChem (Shanghai). Hep3B and Huh-7 cells were infected with lentivirus at a MOI of 10 using Eni.S+polybrene. The target sequences of shAL033381.2 are as follows: 5'-GGAAAGAATAGTAGACATAATAGC-3' (forward) and 5'-GAGCCGACACGGTTAGGATCC-3' (reverse).

**2.4. Fluorescence In Situ Hybridization (FISH).** The subcellular localization of AL033381.2 in cells was tested by the FISH kit (RiboBio) following manufacturer's instruction, which was employed as previously described [15]. The AL033381.2 probe for FISH is 5'-CACGACTCTGGCAAGGTGAT-3'. The fluorescence was detected and photographed under a laser confocal microscope.

**2.5. Immunohistochemistry (IHC).** The IHC staining assay was implemented as previously described [16]. Caspase-3 was detected with primary antibody (Abcam, ab184787) at 1:2400 dilution; E-cadherin was detected with primary antibody (Proteintech, 20874-1-AP) at 1:1800 dilution; Ki67 was detected with primary antibody (Abcam, ab15580) at 1:9600 dilution; MMP2 was detected with primary antibody (Proteintech, 10373-2-AP) at 1:100 dilution; MMP-9 was detected with primary antibody (CST, #13667) at 1:50 dilution; N-Cadherin was detected with primary antibody (Abcam, ab18203) at 1:600 dilution; PCNA was detected with primary antibody (CST, #2586) at 1:200 dilution; and PRKRA was detected with primary antibody (Affinity Biosciences, DF7334) at 1:500 dilution.

**2.6. Quantitative Real-Time PCR.** Total RNA was extracted by TRIzol (Invitrogen), which was then subjected to reverse transcriptase reaction with M-MLV reverse transcriptase (Takara). qPCR was carried out by SYBR Master Mixture (TaKaRa) and conducted using the LightCycler 480 II Detection System (Roche). The relative RNA levels were calculated by the  $2^{-\Delta\Delta C_t}$  method, and GAPDH was applied for internal control. Primer sequences are listed: AL033381.2, 5'-CTGTAAGAAGTAAGGTCGGG-3' (forward) and 5'-GCGTCCTCCTCCATAAGAT-3' (reverse).



**2.7. Western Blot Analysis.** Western blot was conducted according to the previous protocol [17]. The primary antibodies were diluted to 1:500 for MMP9 (CST, #13667); diluted to 1:1000 for PRKRA (Affinity Biosciences, DF7334), P-eIF2 $\alpha$  (CST, #3398), PKR (Abcam, ab32052), UBE2I (Abcam, ab75854), P-p53 (Abcam, ab33889), and MMP2 (CST, #40994); diluted to 1:2000 for N-cadherin (Proteintech, 22018-1-AP); and diluted to 1:5000 for eIF2 $\alpha$  (CST, #5324), E-Cadherin (Proteintech, 20874-1-AP), and  $\beta$ -actin (Santa Cruz, sc-69879). Then, secondary antibodies were diluted to 1:10000 for Rabbit IgG (CST, #7074) and Mouse IgG (CST, #7076). The protein bands were visualized using the ECL detection kit (ECL, Thermo).

**2.8. Cell Proliferation Assay.** For cell counting assay, lentivirus-infected (shCtrl and shAL033381.2) cells were seeded at 96-well plates and cultured with 3000 cells/well. The plate was then tested by Celigo Image Cytometer (Nexcelom) for five days, and the proliferation curve was then created. For MTT assay, lentivirus-infected (shCtrl and shAL033381.2) cells were seeded into 96-well plates at  $2 \times 10^3$  cells/well and incubated for 5 days at 37°C. Subsequently, 20  $\mu$ L MTT solution (5 mg/mL) was added to each well and cultured at 37°C for 4 h. Cell viability was detected at the absorbance of 490 nm. For EdU assay, the positive cells in each group were counted and analyzed under the fluorescence microscope after using Cell-Light<sup>TM</sup> EdU Apollo567 kit (Ribo) in vitro according to manufacturer's instruction.

**2.9. Colony Formation Assay.** Cells were plated in 6-well plates with 5% CO<sub>2</sub> at a density of 1000 cells/dish at 37°C. Two weeks later, colonies were fixed with 4% paraformaldehyde for 30 minutes and stained for 10 minutes with crystal violet. All colonies were washed several times with ddH<sub>2</sub>O, dried, and photographed.

**2.10. Transwell Assay.** Cell migration or invasion abilities were conducted by Transwell chambers (Corning, 8  $\mu$ m pore size) uncoated or coated with Matrigel, respectively. Firstly,  $1 \times 10^5$  cells per well suspended in 100  $\mu$ L FBS-free culture medium was seeded to the upper chamber, with a lower chamber filled with 600  $\mu$ L 30% FBS culture medium. After 24 hours, the filters were fixed and stained. In each chamber, the field of view was randomly selected for microscope photograph, and cell number was calculated.

**2.11. Flow Cytometry.** Cells were seeded in six-well plates for cell apoptosis and cell cycle analyses and cultured overnight until reaching 70%-80% confluency. For cell apoptosis, cells were collected and stained with 10  $\mu$ L Annexin V-APC (eBioscience) and incubated in darkness for 15 minutes. For cell cycle, cells were resuspended and stained with PI (Sigma, 50 ng/mL) and RNase (Thermo Fisher Scientific, 10 ng/mL) for 20 minutes in darkness. Finally, cells were analyzed with Flow Cytometer (BD, C6 PLUS). Data analysis was performed by using the Novo Express software.

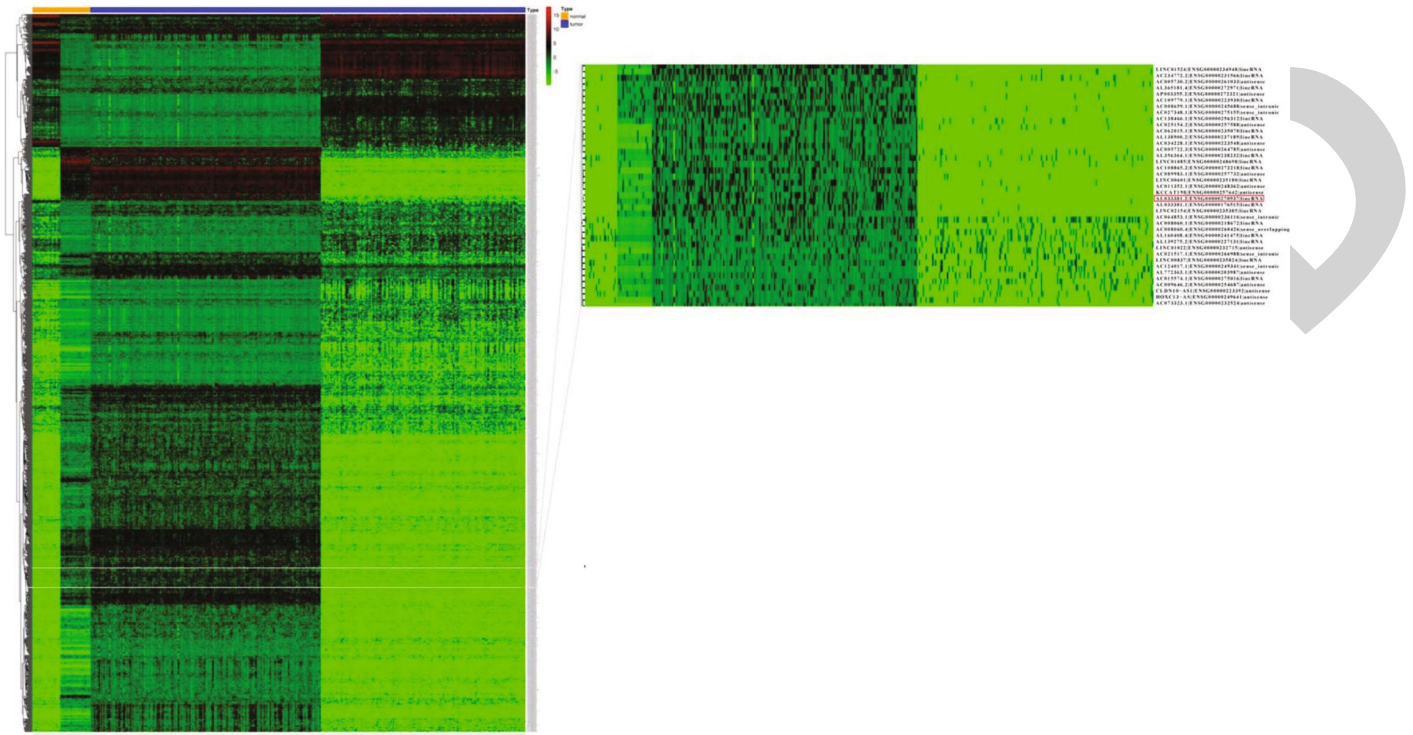
**2.12. Tumor Xenograft Experiment.** Huh-7 cells ( $1 \times 10^7$ ) were injected subcutaneously into the right flank of BALB/

c nude mice (4-week-old). Tumor sizes and mice weights were detected every three days. Tumor volume (mm<sup>3</sup>) was determined: tumor volume = width<sup>2</sup>  $\times$  length/2. Forty-five days after cell injection, the mice were euthanized, and the tumor tissues were weighed. Ethical approval for the animal experiments was obtained from the Animal Ethics Committee of Affiliated Hospital of Nantong University.

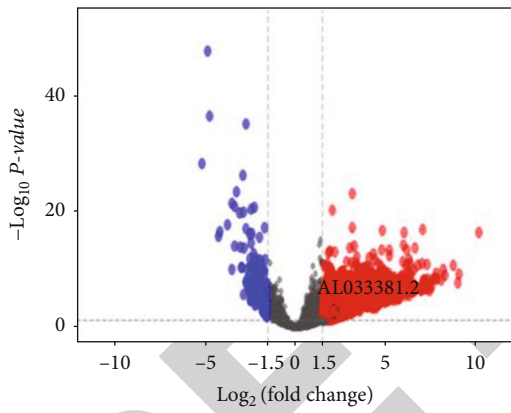
**2.13. RNA Immunoprecipitation Assay (RIP).** RIP experiments were employed using the Magna RIP RNA-Binding Protein Immunoprecipitation Kit following manufacturer's protocol. Antibodies against snRNP70 and normal IgG were, respectively, used as positive and negative controls. qRT-PCR was utilized to determine the RNA enrichment of AL033381.2, which was normalized to the amount of the enriched U1 RNA. Then, the qRT-PCR products were collected for agarose gel electrophoresis, and the existence of AL033381.2 and PRKRA was directly observed.

**2.14. RNA Pull-down Assay and Mass Spectrometry Analysis.** AL033381.2 was transcribed using T7 RNA polymerase in vitro, followed by purification with an RNeasy Plus mini kit. Purified RNAs were labeled with Biotin RNA labeling Mix. Proteins extracted from cells were mixed with biotinylated AL033381.2 or antisense RNA probe that was synthesized by GeneChem and incubated with streptavidin agarose beads. The related proteins were separated by gel electrophoresis and then visualized by silver staining. LncRNA-binding proteins were eluted and subjected to mass spectrometry. LC-MS/MS data were analyzed for protein identification and quantification using PEAKS Studio 8.5. Finally, the eluted proteins were analyzed by Western blotting.

**2.15. Preparation and Characterization of Nanoparticle/siRNA Complexes.** As previously described [18], PLGA nanoparticles were produced by oil-in-water solvent evaporation technology with minor modifications. First, a 10% polymer solution was formed by dissolving 100 mg PLGA in 1 mL dichloromethane. Three milliliters of 7% polyvinyl alcohol aqueous solution was then added to the polymer solution and emulsified by sonication for 120 s. Subsequently, the emulsion was added into 50 mL of a 1% polyvinyl alcohol aqueous solution. These mixtures were sonicated for 180 s and stirred for 24 h to vaporize the dichloromethane. After that, the nanoparticle suspension was washed, centrifuged at 13,000 rpm for 5 min, and resuspended in ddH<sub>2</sub>O. Approximately 100  $\mu$ L of the nanoparticle aqueous solution was mixed with 2  $\mu$ L of polyethyleneimine polymer aqueous solution to form polyethyleneimine-modified nanoparticles. Then, we performed a gel retardation assay to test the best proportion of nanoparticles and siRNA. Subsequently, the polyethyleneimine-modified nanoparticle suspension was added to the siRNA solution of polymer nitrogen and RNA phosphate, gently mixed, and cultured for 15 min to yield nanoparticle/siRNA complexes. Finally, the ultrastructure of the nanoparticle/siRNA complexes was examined by scanning electron microscopy. The average hydrodynamic diameter of nanoparticle/siRNA complexes was measured by dynamic light scattering. Finally, Zetaplus



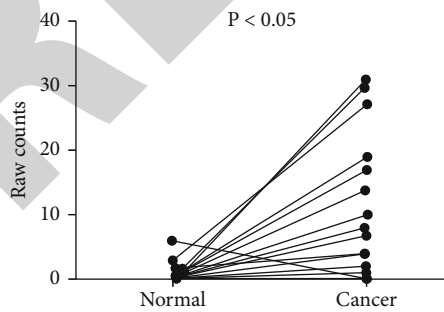
(a)



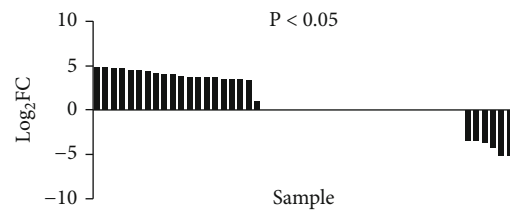
(b)

GeneName	Ensembl ID	LogFC	P Value	FDR
AL033381.2	ENSG00000270937.1	2.1434	1.1674E-03	6.7547E-03

(c)



(d)



(e)

FIGURE 1: Continued.

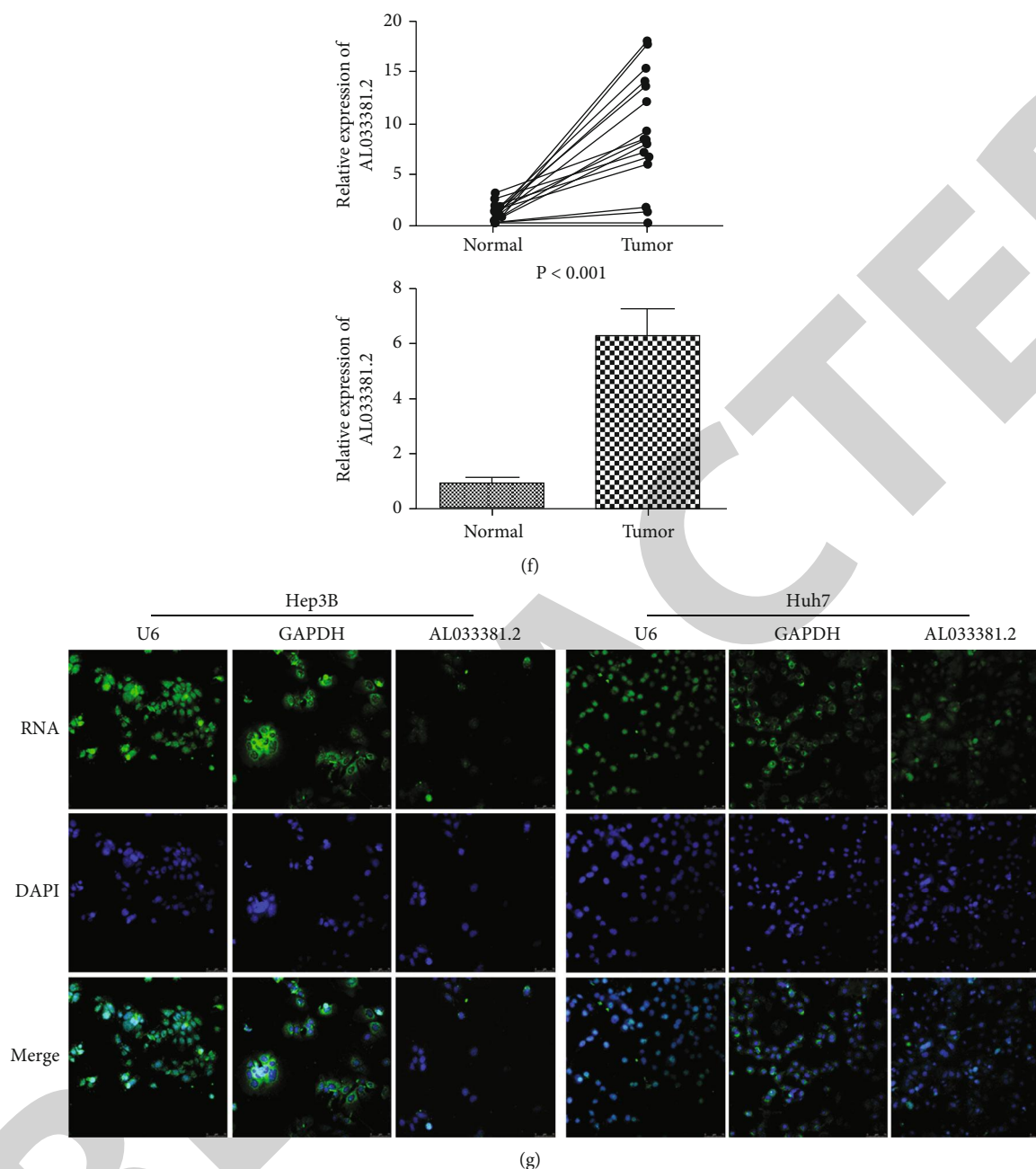


FIGURE 1: LncRNA-AL033381.2 expression is upregulated in HCC tissues. (a, b) Heatmaps and volcano plots of the differential expressed lncRNAs between LIHC tissues ( $n = 374$ ) and normal controls ( $n = 50$ ) in TCGA, including the increased levels of AL033381.2. (c) The differential expression of AL033381.2 in the original data of each TCGA RNA-seq sample can be represented by a line graph. The vertical axis is the original data of the expression level of each sample, and the horizontal axis is the cancer tissue and normal tissue of the sample, with one broken line for each sample. (d) The differential expression of AL033381.2 in cancer ( $n = 50$ ) and normal tissue samples ( $n = 50$ ) can be demonstrated by  $\log_2FC$ ,  $P$  value, and FDR in the TCGA database. (e) Differential gene expression can also be shown in a histogram. The vertical axis is the  $\log_2FC$ , and the horizontal axis is different samples, and the  $\log_2FC$  of each sample is represented by a column diagram. (f) The relative expression of AL033381.2 between HCC samples and corresponding normal tissues was compared by qRT-PCR analysis ( $n = 30$ ). (g) The subcellular location of AL033381.2 in Hep3B and Huh7 cells was determined by FISH analysis after transfection. Nuclei were stained with DAPI. U6 or GAPDH was used as nuclear and cytosolic markers, respectively.

was used to detect the zeta potential of the complexes at 25°C with a 90° scattering angle.

**2.16. In Vivo Tumor Inhibition of AL033381.2 siRNA-Loaded Nanoparticles.** Huh7 cells were inoculated into the armpit of

18–22 g nude mice to establish a tumor xenograft model. The animals were weighed and randomly divided into two groups, namely, nanoparticle/scramble siRNA complexes and nanoparticle/AL033381.2 siRNA complexes, when the tumor volume of the animals reached about 50 mm<sup>3</sup>.

TABLE 1: Analysis of the significant difference of AL033381.2 expression level in clinicopathologic characteristics.

Clinical parameters	AL033381.2 expression		Total	P value
	Low expression	High expression		
Pathological grade				
G1/2	149	83	232	0.119
G3/4	75	59	134	
Total	224	142	366	
T stage				
T1	121	60	181	0.032
T2	53	41	94	
T3/4	51	42	93	
Total	225	143	368	
TNM				
Stage I	115	56	171	0.011
Stage II	51	35	86	
Stage III/IV	46	44	90	
Total	212	135	347	

Statistical analyses were performed by the Mann-Whitney *U* test. \**P* value < 0.05 was considered statistically significant.

TABLE 2: Correlation analysis of clinicopathologic characteristics with AL033381.2 expression.

	AL033381.2 expression	T stage	Pathological grade
AL033381.2 expression			
Correlation coefficient	1.000	0.095	0.117
Significance (double tail)		0.070	0.029
T stage			
Correlation coefficient	0.095	1.000	0.981
Significance (double tail)	0.070		0.000
Pathological grade			
Correlation coefficient	0.117	0.981	1.000
Significance (double tail)	0.029	0.000	.

Statistical analyses were performed by Spearman's test. \**P* value < 0.05 was considered statistically significant.

Subsequently, the tumor sizes were observed with a Vernier caliper every other day and calculated as  $\text{Volume} = \text{Width}^2 \times \text{Length} / 2$ . The mice were euthanized 16 days later, and tumors were dissected and weighed. The animal ethical statement was previously described.

**2.17. Statistical Analysis.** All statistical analysis was conducted using SPSS 25.0. All data are presented as means  $\pm$  standard deviation from at least 3 independent experiments. Then, Student's *t*-test (two-tailed), chi-squared tests, and one-way ANOVA were performed to compare the significance of differences between groups. Statistically significance was chosen as *P* < 0.05.

### 3. Results

**3.1. LncRNA AL033381.2 Is Upregulated in HCC Tissues.** To investigate novel lncRNAs that play a key role in HCC, we analyzed the DElncRNAs between tumor and normal tissues in the TCGA database and identified AL033381.2 as one of the highly upregulated candidates in HCC that has

not been reported and studied to date (Figures 1(a) and 1(b)). Then, bioinformatics analysis of TCGA data revealed that AL033381.2 expression is highly upregulated in liver cancer tissues relative to paired adjacent normal tissues (Figures 1(c)–1(e), *P* < 0.05). To further assess the roles of AL033381.2 in HCC, we evaluated the expression level of AL033381.2 in a cohort of 30 HCC tissue samples and matched adjacent normal samples by qRT-PCR analysis. Our results showed that the AL033381.2 expression level is upregulated in HCC tissues compared to paired adjacent normal tissues (Figure 1(f), *P* < 0.001). Moreover, as shown in Supplementary Figure S1, qRT-PCR analysis showed that AL033381.2 is expressed in Hep3B, Huh-7, HepG2, and SK-HEP-1 cell lines.

To investigate the mechanism by which AL033381.2 acts as an oncogenic lncRNA by driving tumorigenesis in HCC, we analyzed the subcellular distribution by FISH. The results indicated that AL033381.2 exhibited a predominantly cytoplasmic localization in Hep3B and Huh-7 cells (Figure 1(g)), which suggests that AL033381.2 might exert regulatory functions in the cytoplasm.

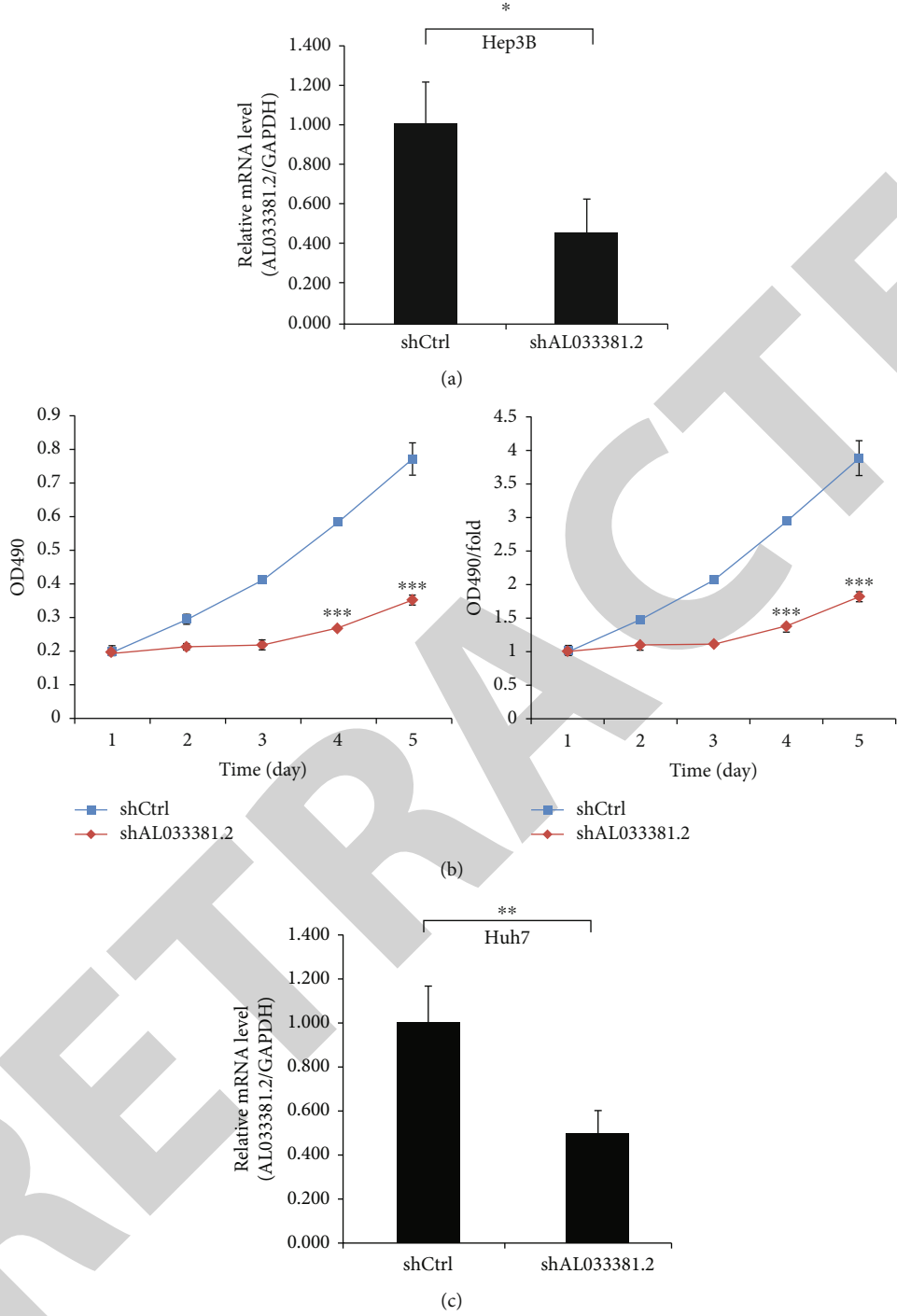
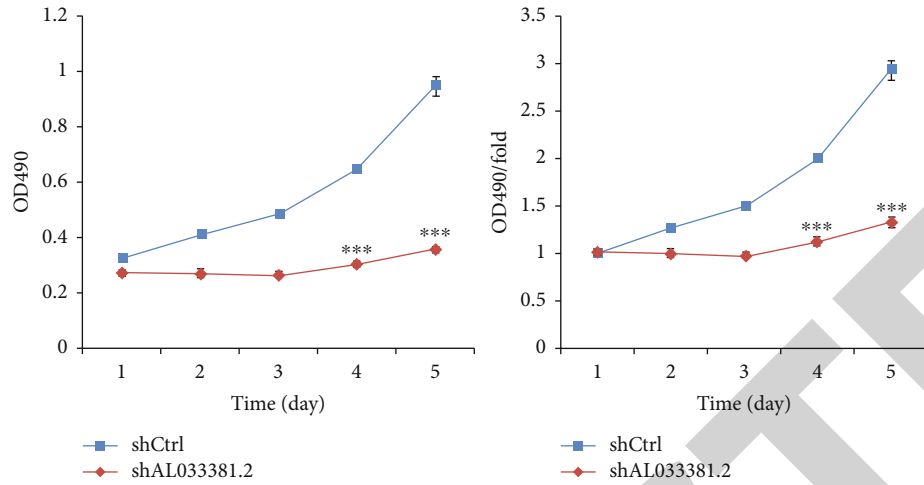
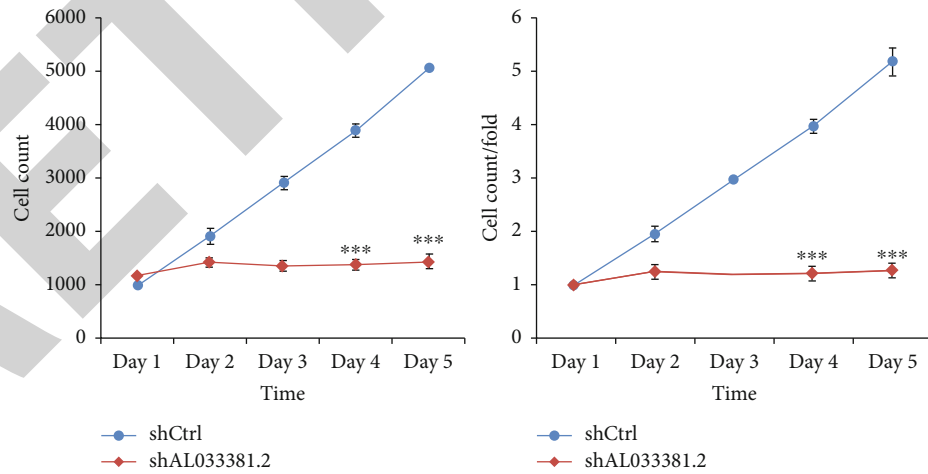
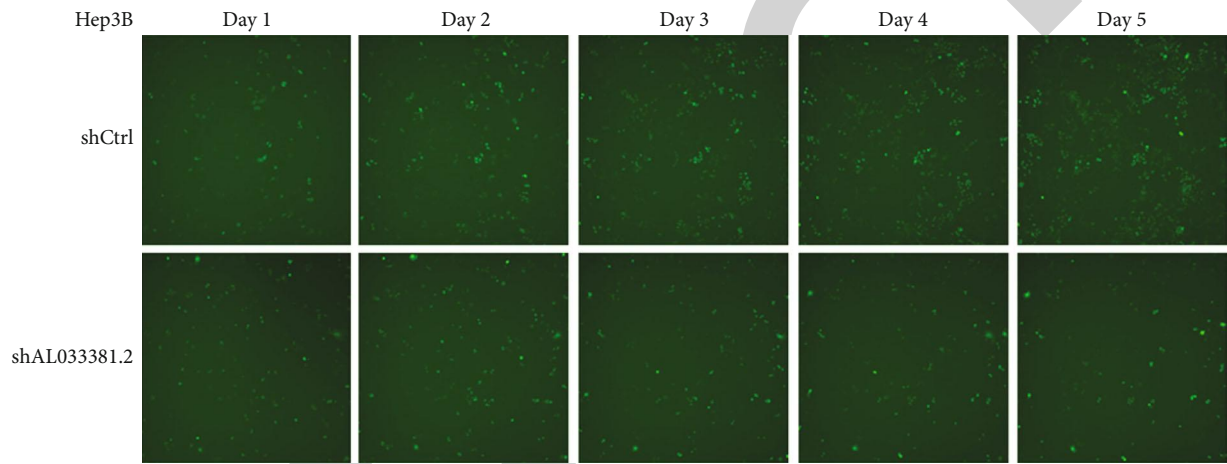


FIGURE 2: Continued.



(d)



(e)

FIGURE 2: Continued.

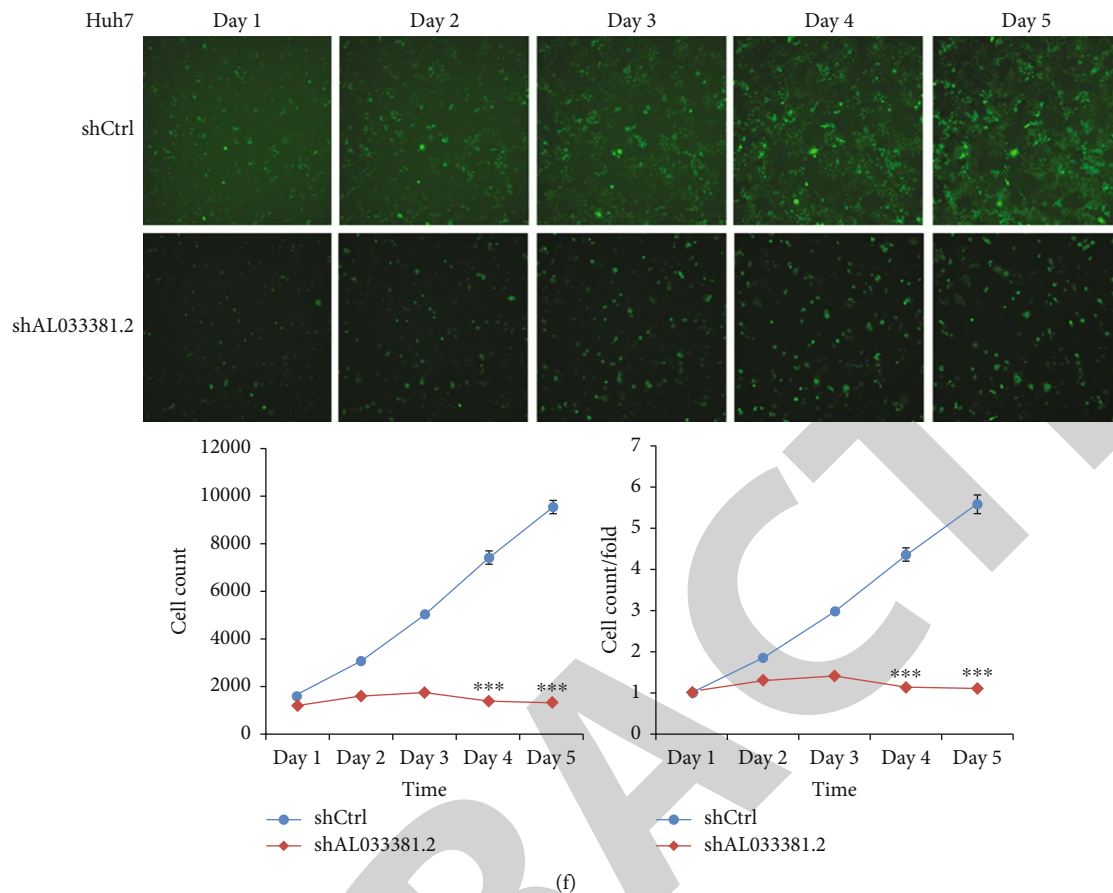
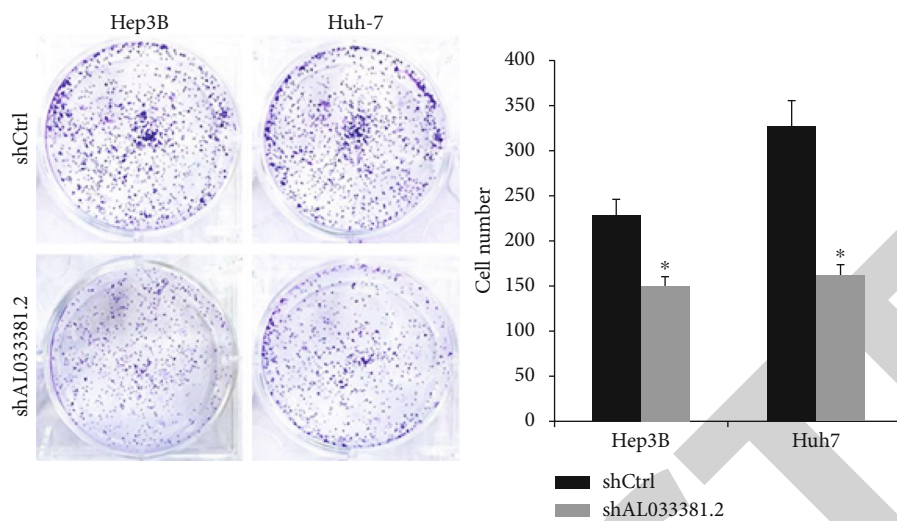


FIGURE 2: Knockdown of AL033381.2 suppressed the proliferation of HCC cells. (a, c) The mRNA expression level of AL033381.2 in Hep3B and Huh-7 cells was determined by qRT-PCR analysis. (b, d) The proliferative rates of Hep3B and Huh-7 cells were assessed by MTT assay. (e, f) After infection of lentivirus shAL033381.2 or shCtrl, celigo cell counting assay was employed to assess the viability of Hep3B and Huh-7 cells. \* $P < 0.05$ ; \*\* $P < 0.01$ ; \*\*\* $P < 0.001$ .

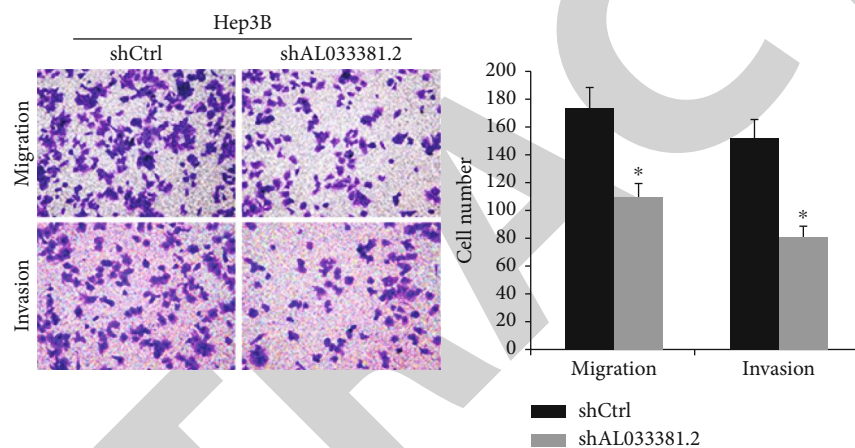
We also performed the Mann-Whitney  $U$  test to analyze the significance of different expression levels of AL033381.2 in various clinical data at different levels. As we can see from the significance index of the test, the expression of AL033381.2 was markedly different in the cancer tissues of patients with different T stages and pathological stages at the significance level of 0.05. It is suggested that the AL033381.2 expression level may be correlated to T stage and pathological stage (Table 1). Moreover, Spearman's test was used to statistically analyze the correlation between the AL033381.2 expression level in cancer tissues and clinical data to preliminarily explore the potential role of these clinical data in the genesis and development of liver cancer. The significance index of the test indicated that the AL033381.2 expression level in tumor tissues was remarkably correlated to the pathological stage of the patients at a significance level of 0.05, suggesting that the expression level of this gene might be used as an indicator for clinical diagnosis of the pathological stage. The AL033381.2 expression was positively associated with the pathological stage level, suggesting that the AL033381.2 expression level gradually increased with the progression of liver cancer (Table 2).

**3.2. Knockdown of AL033381.2 Suppresses Cell Proliferation, Migration, and Invasion and Promotes Apoptosis.** The roles of AL033381.2 in cell proliferation, cell viability, colony formation ability, cell migration, and invasion abilities were analyzed by MTT, Celigo Imaging Cytometry System, colony formation, EdU, and Transwell assays, respectively. First, compared to the shCtrl group, mRNA expression of AL033381.2 in Hep3B and Huh-7 cells was downregulated after transduction with lentivirus shAL033381.2 (Figures 2(a) and 2(c)). MTT assays revealed that the viability of Hep3B and Huh-7 cells was notably reduced in the shAL033381.2 group compared with the shCtrl group (Figures 2(b) and 2(d)). Furthermore, Celigo cell counting assays revealed that cell proliferation was remarkably suppressed in the shAL033381.2 group compared with the shCtrl group in Hep3B and Huh-7 cells (Figures 2(e) and 2(f)).

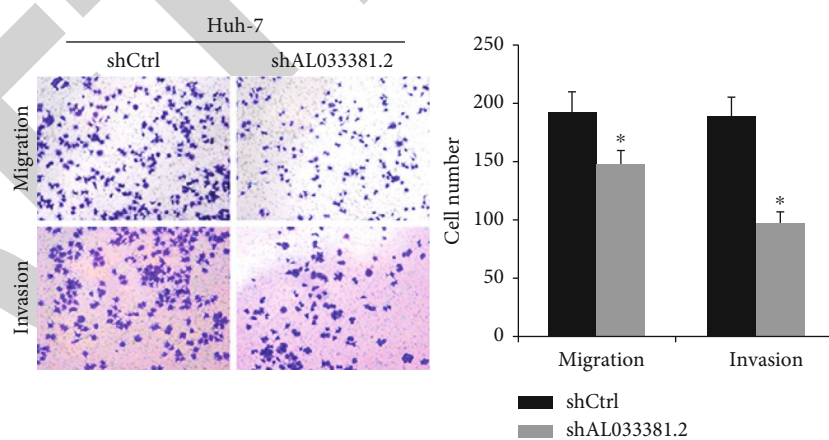
Additionally, colony formation assays showed that fewer colonies were formed by Hep3B and Huh-7 cells in the shAL033381.2 group compared with the shCtrl group (Figure 3(a)). Moreover, we assessed the effects of AL033381.2 on the abilities of HCC cell migration and invasion by Transwell assays. Our results demonstrated that the number of migrating and invasive cells was markedly



(a)



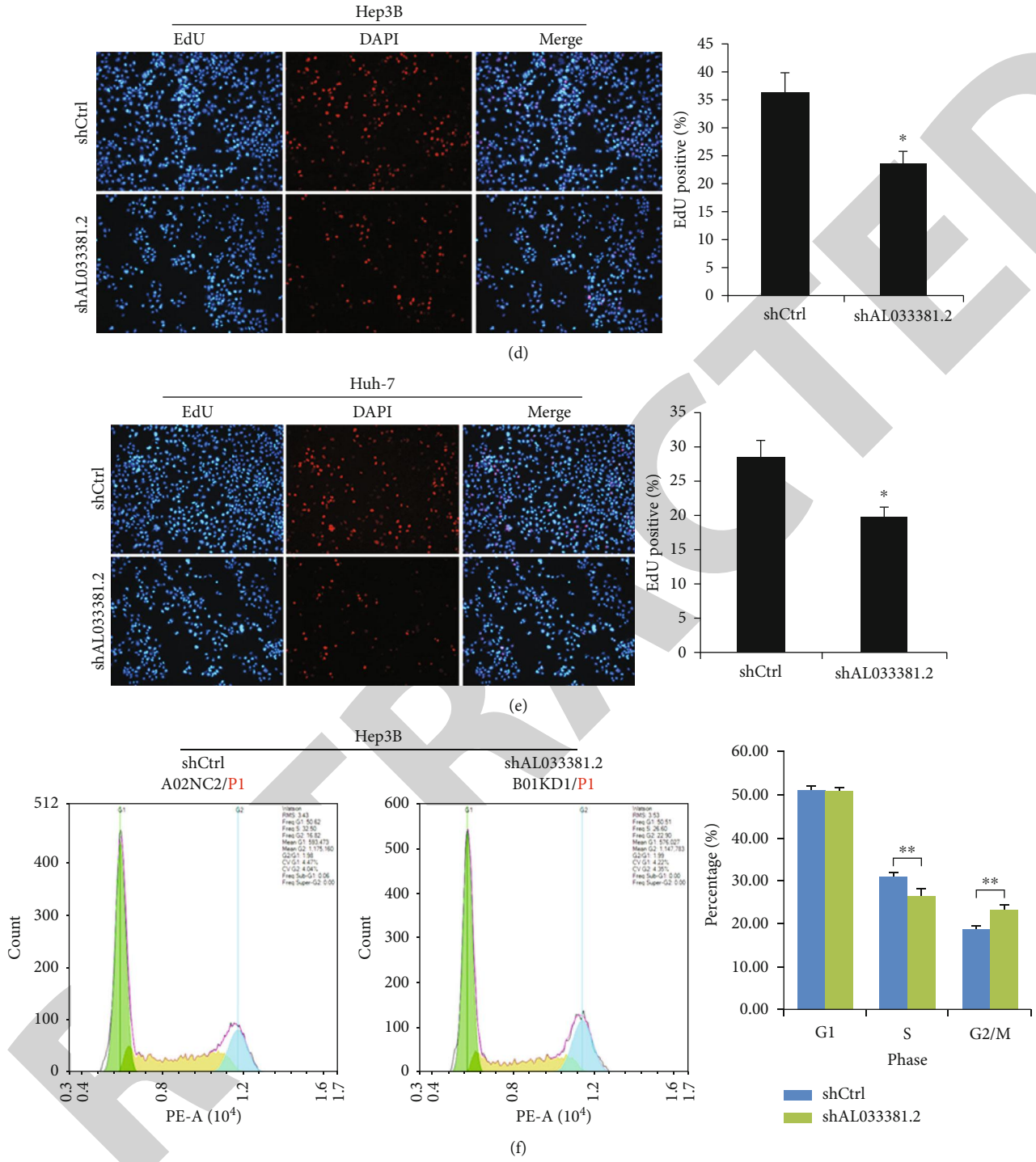
(b)



(c)

FIGURE 3: Continued.





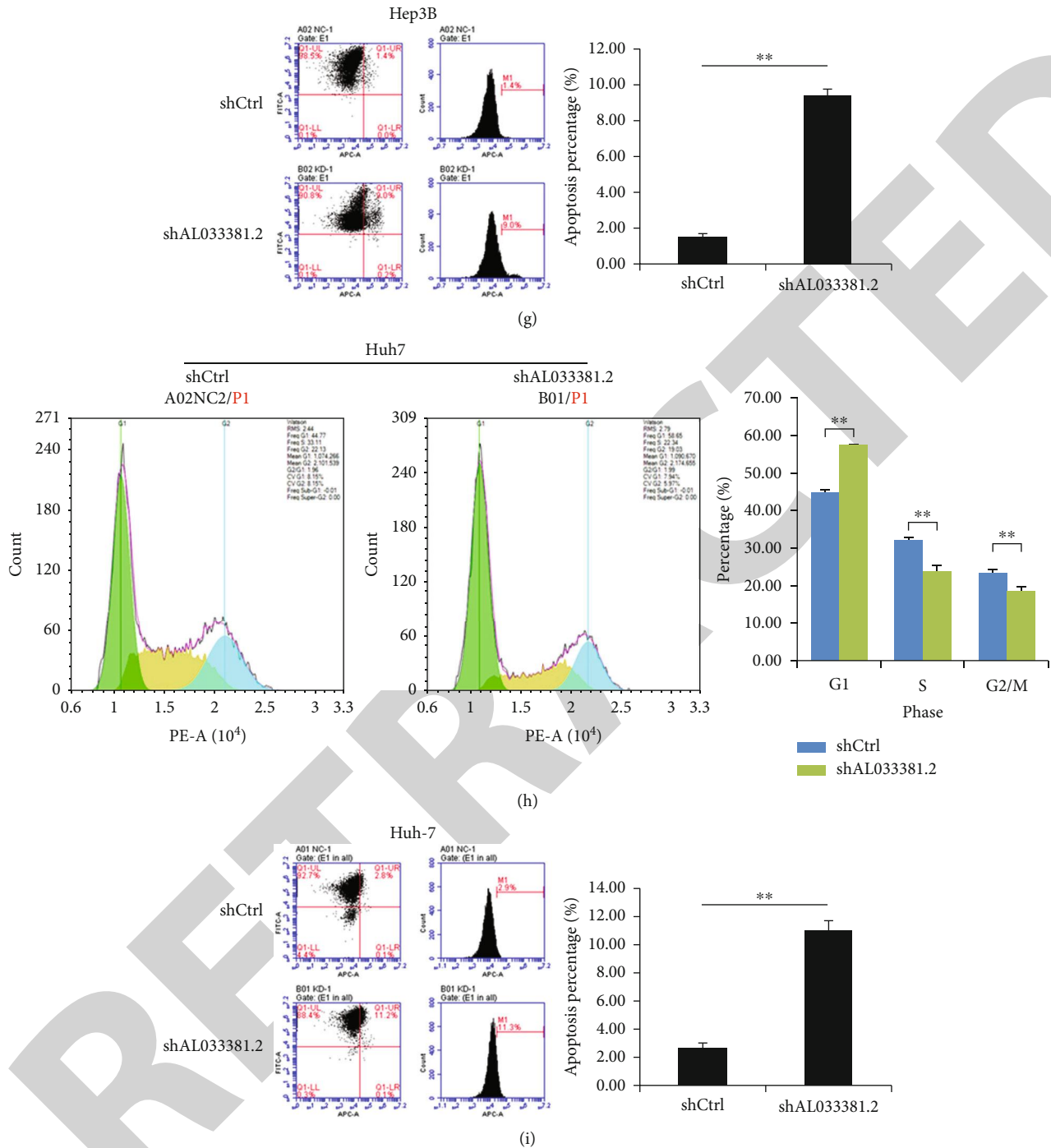


**FIGURE 3:** Knockdown of AL033381.2 suppressed the proliferation, migration, and invasion of HCC cells and induced cell apoptosis and regulates the cell cycle process. (a) Colony formation assay was employed to examine the effects of AL033381.2 knockdown on the proliferation of Hep3B and Huh-7 cells. (b, c) Transwell assay was employed to measure the effects of AL033381.2 knockdown on cell migration and invasion of Hep3B and Huh-7 cells. (d, e) EdU incorporation assay was used to evaluate the abilities of DNA replication on Hep3B and Huh-7 cells after infection of lentivirus shAL033381.2 or shCtrl. (f–i) The apoptosis and cell cycle distribution of Hep3B and Huh-7 cells were analyzed by flow cytometry after shAL033381.2 or shCtrl lentivirus transfection. \* $P < 0.05$ ; \*\* $P < 0.01$ .

reduced upon transfection with lentivirus shAL033381.2 compared to the shCtrl group (Figures 3(b) and 3(c)). Additionally, EdU proliferation assays were performed to assess the effects of AL033381.2 on the DNA replication of HCC cells. We found that cell proliferation was inhibited after

transfection with lentivirus shAL033381.2 in Hep3B and Huh-7 cells (Figures 3(d) and 3(e)).

To further explore the mechanisms of AL033381.2 on cell proliferation, we conducted flow cytometry to detect the distribution of the cell cycle and the apoptosis rate of

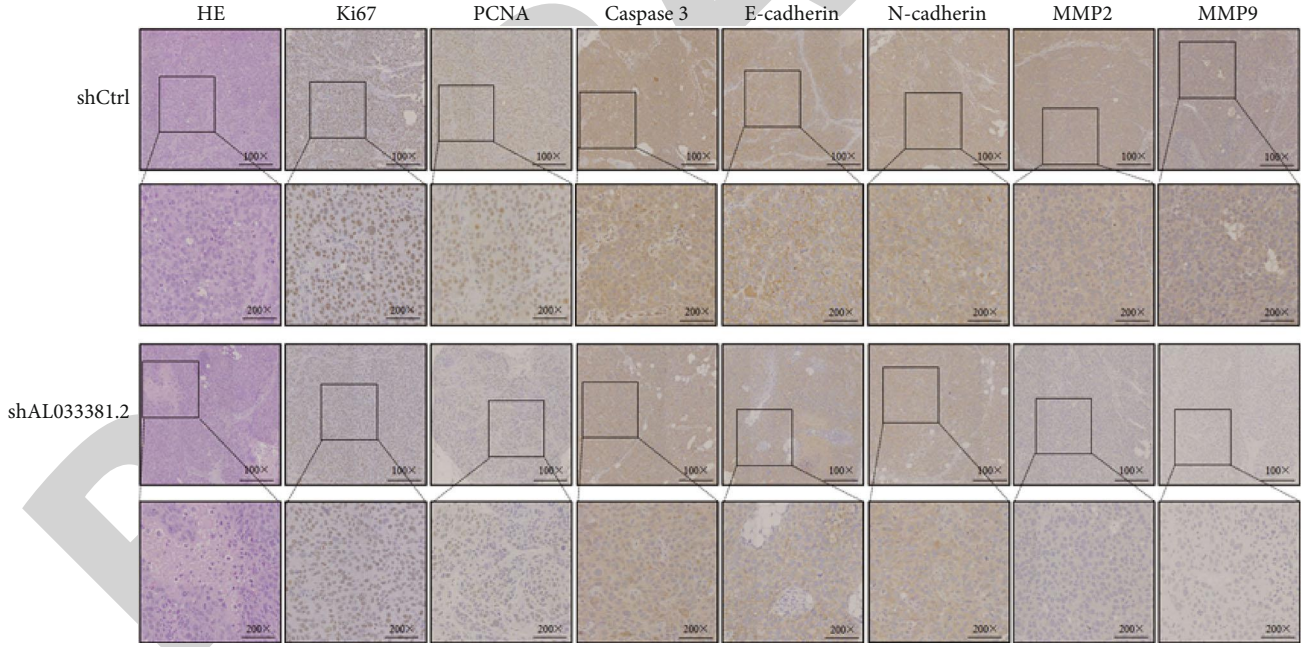
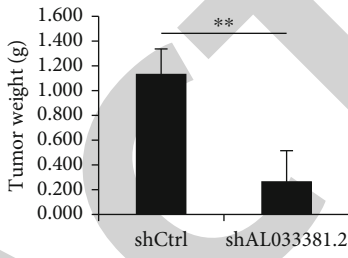
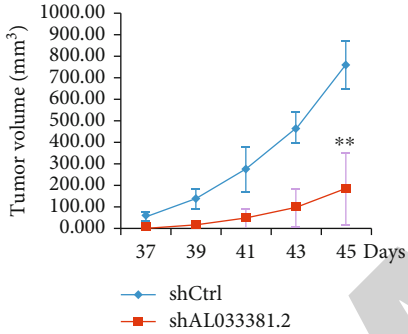


FIGURE 4: Continued.

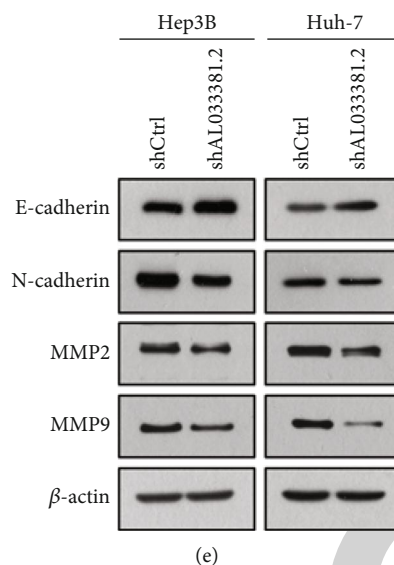


FIGURE 4: Knockdown of AL033381.2 inhibited tumor growth *in vivo*. (a) Typical images of xenograft tumors formed by Huh-7 cells transfected with shCtrl or shAL033381.2 from each group of mice. (b, c) Tumor volume and tumor weight in each group of mice. (d) Typical H&E staining and IHC staining images of Ki-67, PCNA, Caspase 3, E-cadherin, N-cadherin, MMP2, and MMP9 in xenograft tumor tissues from each group of mice.  $**P < 0.01$ . (e) The expression of E-cadherin, N-cadherin, MMP2, and MMP9 at the protein level in transfected cells with shCtrl or shAL033381.2 were examined by Western blot analysis.

HCC cells transfected with lentivirus shAL033381.2. Cell cycle analysis indicated that the cell percentage in the G0/G1 phase was obviously elevated, and the percentage of Hep3B and Huh-7 cells in the S phase markedly decreased after transfection with lentivirus shAL033381.2 (Figures 3(f) and 3(h)). Furthermore, we found that the rate of apoptosis in Hep3B and Huh-7 cells increased after transfection with lentivirus shAL033381.2 (Figures 3(g) and 3(i)). Collectively, these results suggest that AL033381.2 plays a pivotal role in regulating HCC pathogenesis.

**3.3. Knockdown of AL033381.2 Suppresses Tumor Growth *In Vivo*.** To further verify the roles of AL033381.2 in tumor growth of HCC cells *in vivo*, we calculated the weight and volume of tumors using the xenograft model. Our results revealed that the shAL033381.2 group showed dramatically reduced tumor volume and weight compared with those in the shCtrl group (Figures 4(a)–4(c)). IHC staining revealed reduced expression of Ki-67, PCNA, caspase-3, E-cadherin, N-cadherin, MMP2, and MMP9 in the shAL033381.2 group, while H&E staining indicated more extensive focal necrosis in the shAL033381.2 group (Figure 4(d)). In parallel, the elevated expression level of E-cadherin and reduced expression level of N-cadherin, MMP2, and MMP9 at the protein levels in the Hep3B and Huh-7 cells were found to be associated with the shAL033381.2 group (Figure 4(e)). Our above results confirm that AL033381.2 plays a vital role in *in vivo* HCC tumorigenesis.

**3.4. AL033381.2 Binds to the PRKRA Protein.** Bioinformatics analysis was performed to predict the secondary structure of AL033381.2 (Supplementary Figure S2). To further elucidate that the molecular mechanism of AL033381.2 involves tumor promotion, we performed an RNA pull-down assay

using biotin-labeled RNA to identify potential proteins binding to AL033381.2 in Huh-7 cells. The remaining bands specific to AL033381.2 were subjected to LS/MS mass spectrometry (Figures 5(a) and 5(b)). According to the list of differential genes in the results of mass spectrometry (Supplementary Figure S3, S4), the subcellular localization of genes was matched through the IPA database, and the genes identified as cytoplasmic were selected to draw a network diagram together with cell proliferation and apoptosis (Figure 5(c)). The direct interaction between AL033381.2 and its RNA-binding proteins was further confirmed by Western blotting of Huh-7 cell lysate using antibodies against STAU1, PRKRA, PRDX2, RNH1, KRT8, and ETV6 (Supplementary Figure S5). Then, RIP assay followed by qRT-PCR demonstrated that the enrichment of AL033381.2 precipitated by antibodies against PRKRA, PRDX2, RNH1, and ETV6 dramatically increased compared with the control IgG in Huh-7 cells (Figure 5(d)). Consistently, Western blotting followed by RIP assays confirmed the capability of PRKRA, PRDX2, RNH1, and ETV6 to bind to AL033381.2 in Huh-7 cells (Figure 5(e)). Moreover, we employed an additional RNA pull-down assay followed by Western blotting using the PRKRA antibody to determine the interaction of AL033381.2 with PRKRA. The results showed that labeled AL033381.2, but not antisense, indicated the ability to specifically retrieve PRKRA from cell extracts (Figure 5(f)). Furthermore, the RIP assay verified that AL033381.2 was precipitated by the PRKRA antibody (Figure 5(g)). In addition, to explore the effects of AL033381.2 on PRKRA, we assessed the protein expression level of PRKRA in Huh-7 cells transfected with shAL033381.2 or shCtrl lentivirus. Western blotting confirmed that PRKRA protein expression notably decreased with shAL033381.2 transfection (Figure 5(h)). The above findings suggest that AL033381.2 interacts with

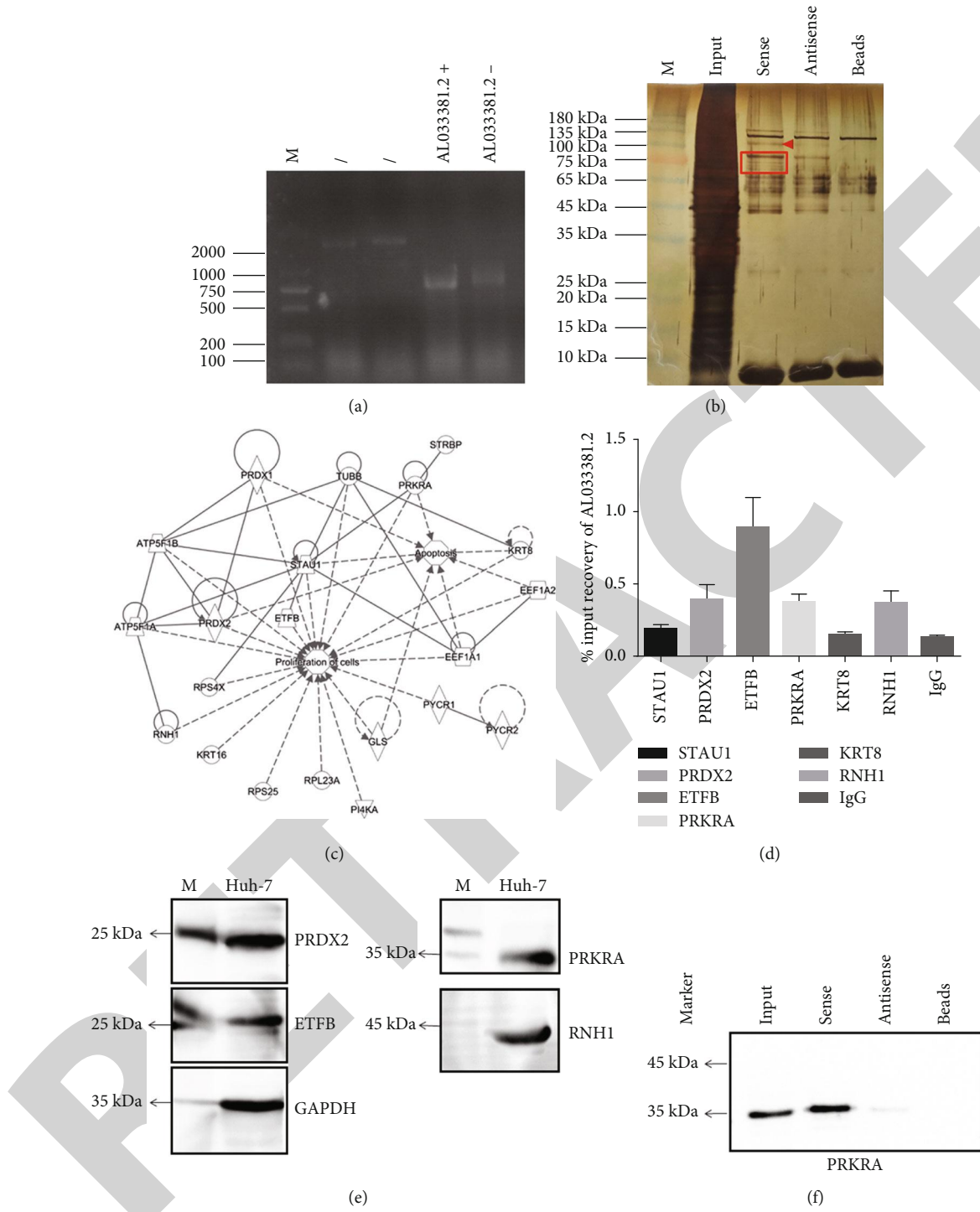


FIGURE 5: Continued.

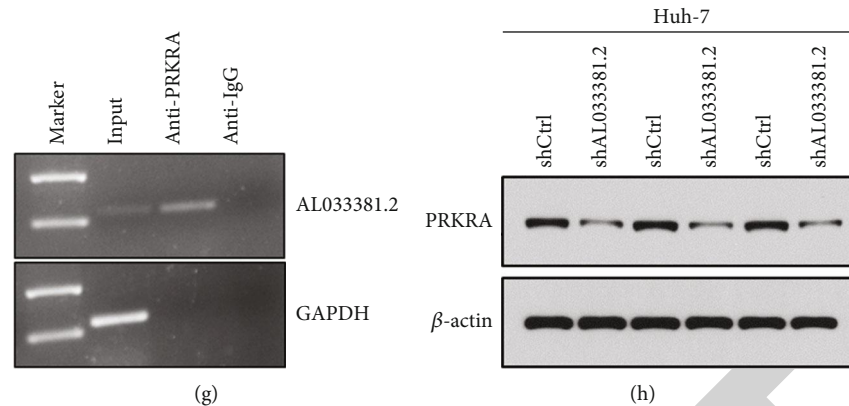


FIGURE 5: AL033381.2 interacts with PRKRA. (a, b) The specific biotin-labeled AL033381.2 probe was added to the cell lysate, and the precipitated proteins were resolved by SDS-PAGE and then stained with silver. The AL033381.2 probe was analyzed by using SDS-PAGE. The antisense of AL033381.2 and the beads serve as the control. The AL033381.2-specific bands (red rectangle) were excised and analyzed using mass spectrometry. (c) IPA analysis identified the genes located in the cytoplasm were associated with cell proliferation and apoptosis. (d) RIP assay showed that STAU1, PRDX2, ETV6, PRKRA, KRT8, and RNH1 interacted with AL033381.2 in Huh-7 cells by RT-qPCR analysis. (e) Western blot results exhibited the capability of PRKRA, PRDX2, RNH1, and ETV6 binding to AL033381.2 in Huh-7 cells. (f) RNA pull-down assay was conducted in Huh-7 cells using biotinylated AL033381.2 or antisense RNA probe transcribed in vitro and measured by western blots. (g) RIP assay was employed in Huh-7 cells using an antibody against PRKRA to determine AL033381.2 RNA enrichment in immunoprecipitated complexes with IgG as a negative control. (h) Western blot analysis was applied to determine the protein level of PRKRA after transfection of the cells with shAL033381.2 or shCtrl.

PRKRA protein, which in turn contributes to the regulation of HCC progression.

**3.5. Restoration of PRKRA Rescues AL033381.2 Knockdown-Mediated Suppression of Cell Proliferation, Migration, and Invasion.** Following the determination that the downstream targets of AL033381.2 are PRKRA, PRDX2, RNH1, and ETV6, we performed *in vitro* experiments to explore whether these genes could mediate the inhibitory effects of AL033381.2 knockdown. According to Celigo cell counting assays, only PRKRA overexpression could partially abrogate the inhibition of the cell proliferation induced by AL033381.2 knockdown compared with the controls (Figure 6). To further investigate whether AL033381.2 functions in a PRKRA-mediated manner in HCC progression, we conducted additional experiments to verify the recovery effects of PRKRA overexpression lentivirus and lentivirus shAL033381.2 coinfecting HCC cells. MTT and colony formation assays demonstrated that PRKRA overexpression partially abrogated the decreased viability and clonogenicity of Hep3B and Huh7 cells caused by AL033381.2 knockdown (Figures 7(a)–7(d)). Furthermore, Transwell assays showed that knockdown of AL033381.2 suppressed the migration and invasion of Hep3B and Huh7 cells, whereas PRKRA overexpression partially abolished these effects (Figures 7(e) and 7(f)). Meanwhile, EdU assays indicated that overexpressing PRKRA rescued the reduction in the proliferation of Hep3B and Huh7 cells caused by AL033381.2 knockdown (Figures 7(g) and 7(h)).

To further confirm whether AL033381.2 is related to the EMT pathway via modulating PRKRA, we transfected HCC cells with lentivirus shAL033381.2 and PRKRA overexpression lentivirus. As presented in Figure 7(i), shAL033381.2 upregulated E-cadherin expression and downregulated N-cadherin, MMP2, and MMP9 expression in Hep3B and

Huh-7 cells, whereas overexpression of PRKRA abolished these effects. Our results consistently indicated that AL033381.2 inhibits HCC progression via activation of PRKRA.

**3.6. In Vivo Antitumor Efficacy of Nanoparticle/siRNA Complexes.** The morphology of the nanoparticle/siRNA complexes was analyzed by SEM, which presented representative images of the empty nanoparticles and nanoparticle/siRNA complexes (Figure 8(a)). As shown in Figure 8(b), the hydrodynamic diameter of complexes demonstrated that the mean diameter of the empty nanoparticles and nanoparticle/siRNA complexes was ~103 nm and 108 nm, respectively. A gel retardation assay showed that nanoparticles containing siRNA exhibited the best retarding effect when the N/P ratio was 6:1 (Figure 8(c)). Then, we performed a slower sustained release profile of siRNA from the nanoparticle/siRNA complexes, and we observed that about 90% of the loaded siRNA were released within 27 days (Supplementary Figure S6). The zeta potential of the empty nanoparticles and nanoparticle/siRNA complexes was about -15.2 mV and 23.1 mV, respectively. Moreover, we performed flow cytometry to test the transfection efficiency of nanoparticle/FAM-siRNA complexes. FAM-siRNA was delivered into the Huh7 cells, with a transfection efficiency of about ~70% (Figures 8(d) and 8(e)), indicating that the nanoparticle/siRNA complexes possess good transfection efficiency in Huh7 cells.

Furthermore, to evaluate the *in vivo* antitumor efficacy of the nanoparticle/AL033381.2 siRNA complexes, we calculated the weight and volume of tumors after different formulations were administrated into nude mice. The mice treated with nanoparticle/AL033381.2 siRNA complex group exhibited lower tumor volume and weight compared with the scrambled group, thus demonstrating that AL033381.2 siRNA-loaded nanoparticles presented better anticancer

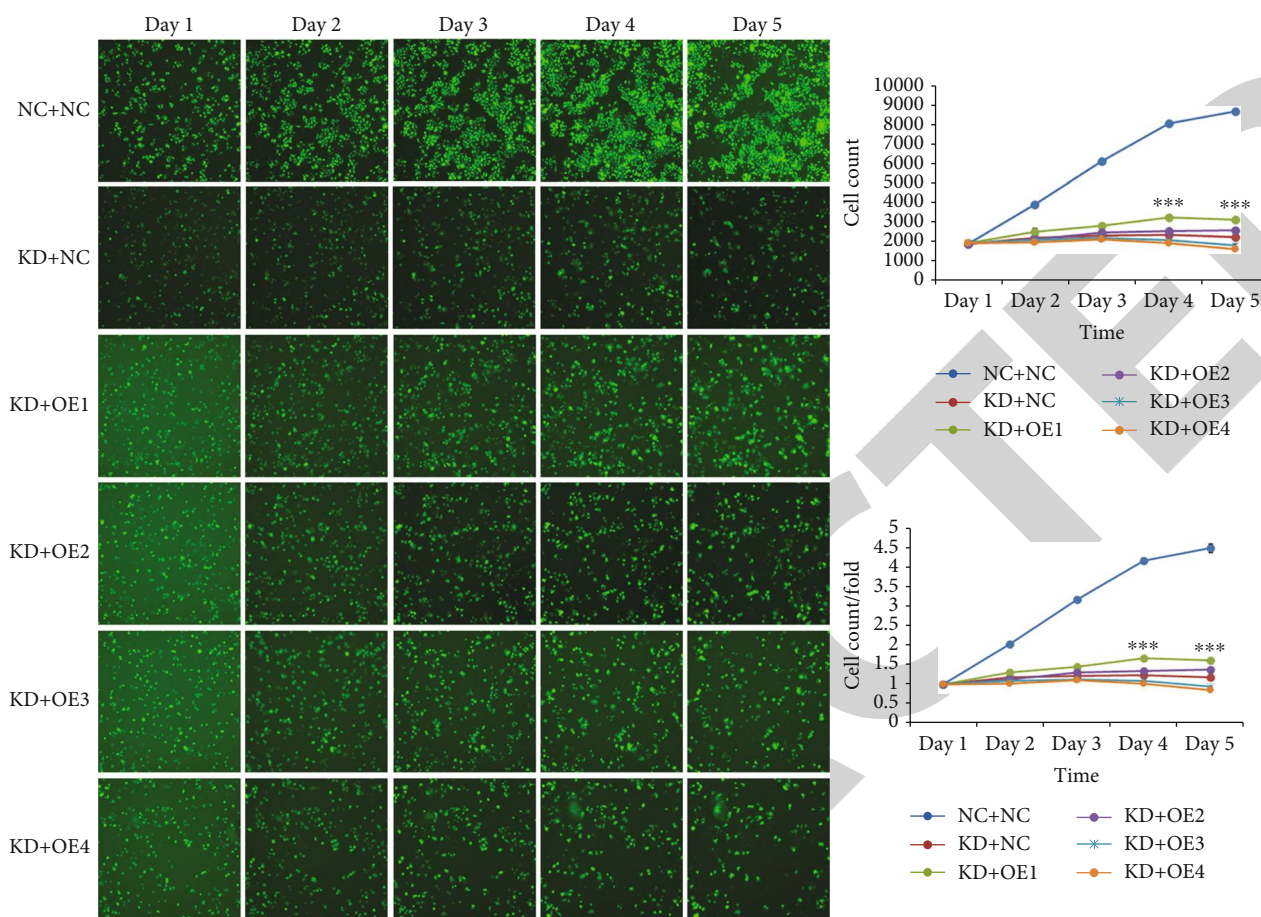


FIGURE 6: Overexpression of PRKRA rescued the cell proliferation caused by AL033381.2 knockdown in HCC cells. Celigo cell counting assay indicated that the proliferation of HCC cells was suppressed significantly in KD+NC group cells compared with NC+NC group cells, and overexpression of PRKRA (KD+OE1) rescued the inhibition of the cell proliferation induced by AL033381.2 knockdown. NC+NC group: normal target cells (Huh-7) and negative control lentivirus-infected cells (shCtrl); KD+NC group: shAL033381.2 lentivirus-infected cells (shAL033381.2) and overexpression of empty vector lentivirus-infected cells; KD+OE1 group: shAL033381.2 lentivirus-infected cells and the downstream gene PRKRA overexpressed lentivirus-infected cells; KD+OE2 group: shAL033381.2 lentivirus-infected cells and the downstream gene PRDX2 overexpressed lentivirus-infected cells; KD+OE3 group: shAL033381.2 lentivirus-infected cells and the downstream gene RNH1 overexpressed lentivirus-infected cells; KD+OE4 group: shAL033381.2 lentivirus-infected cells and the downstream gene ETVF overexpressed lentivirus-infected cells.  $***P < 0.001$ .

efficacy (Figures 8(f)–8(h)). In addition, we assessed the expression of AL033381.2 at the mRNA level from tumor samples of mice treated with several complexes using qRT-PCR, which indicated that AL033381.2 expression in mice treated with the nanoparticle/AL033381.2 siRNA complex group was dramatically lower than those in the scrambled group (Figure 8(i)). The above results demonstrated that AL033381.2 may potentially be utilized as a therapeutic target, and the nanoparticle drug delivery system can be an effective therapeutic alternative.

#### 4. Discussion

Emerging research has revealed that the vital roles of lncRNAs in tumorigenesis and tumor progression in several cancers have attracted increasing attention [19]. The accumulation of lncRNAs has been associated with tumorigenesis, including HCC [20, 21]. For instance, Wen et al. showed

that the lncRNA ANCR accelerates the EMT and migration and invasion of HCC cells by modulating HNRNP1 [22]. Zhang et al. demonstrated that lncRNA UPK1A-AS1 indicates poor prognosis in HCC and interacts with EZH2 to promote cell growth [23]. Most recently, Zhang et al. have shown that LIN28B-AS1 is associated with IGF2BP1 and promotes human HCC cell progression *in vitro* and *in vivo*. [24]. Although accumulating studies have shown the potential oncogenic roles of lncRNAs in a variety of cancers [25, 26], AL033381.2 is still a novel lncRNA molecule, and its role in tumor progression remains unclear.

In this study, we attempted to determine the expression profile and biological effects of AL033381.2 in HCC and elucidate its potential molecular mechanism. Then, we identified the differentially expressed lncRNAs in the TCGA database in both cancer tissues and normal tissues by integrating bioinformatics analysis. Our results indicated that in liver cancer, AL033381.2 is markedly upregulated and

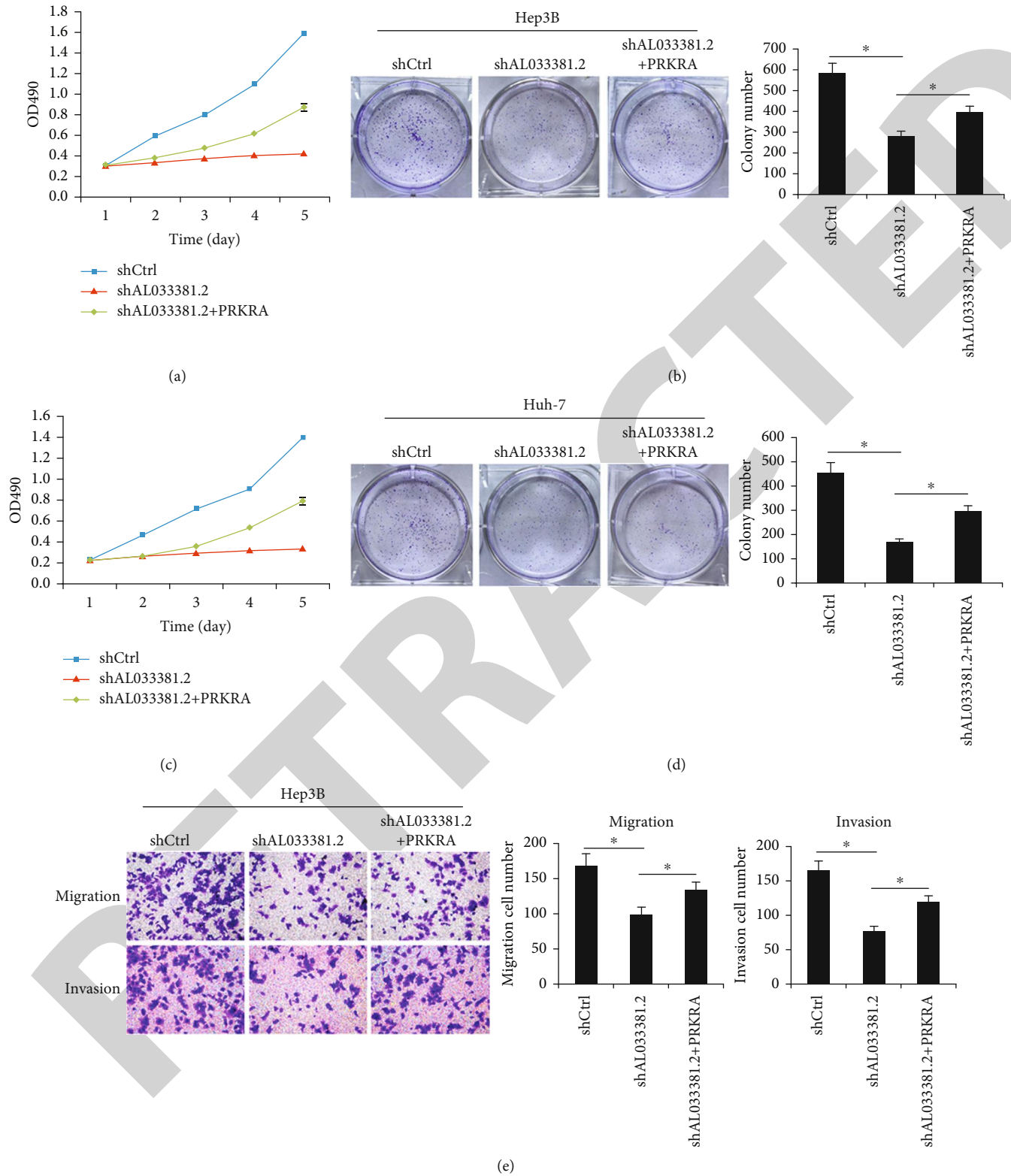
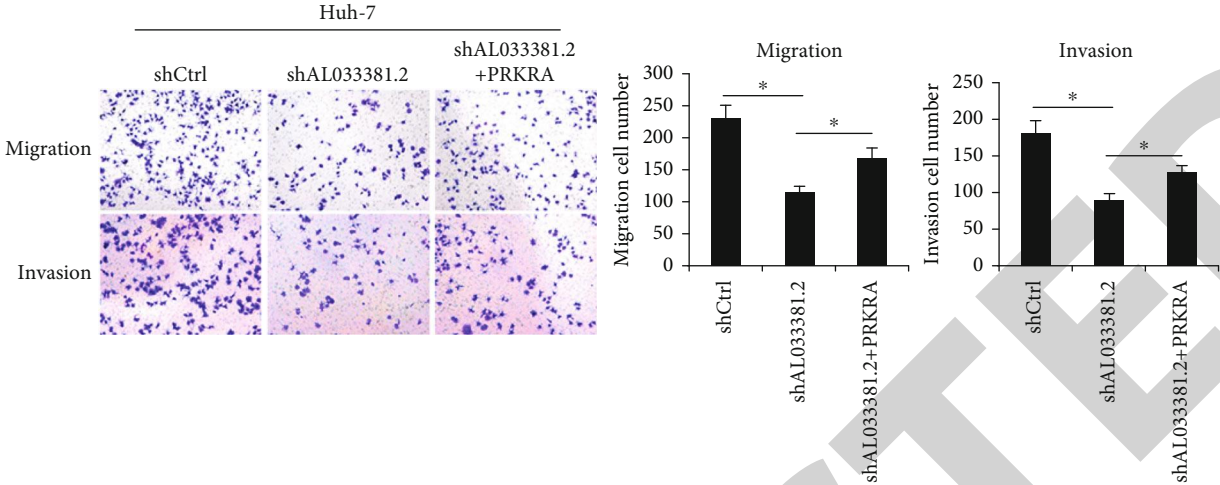
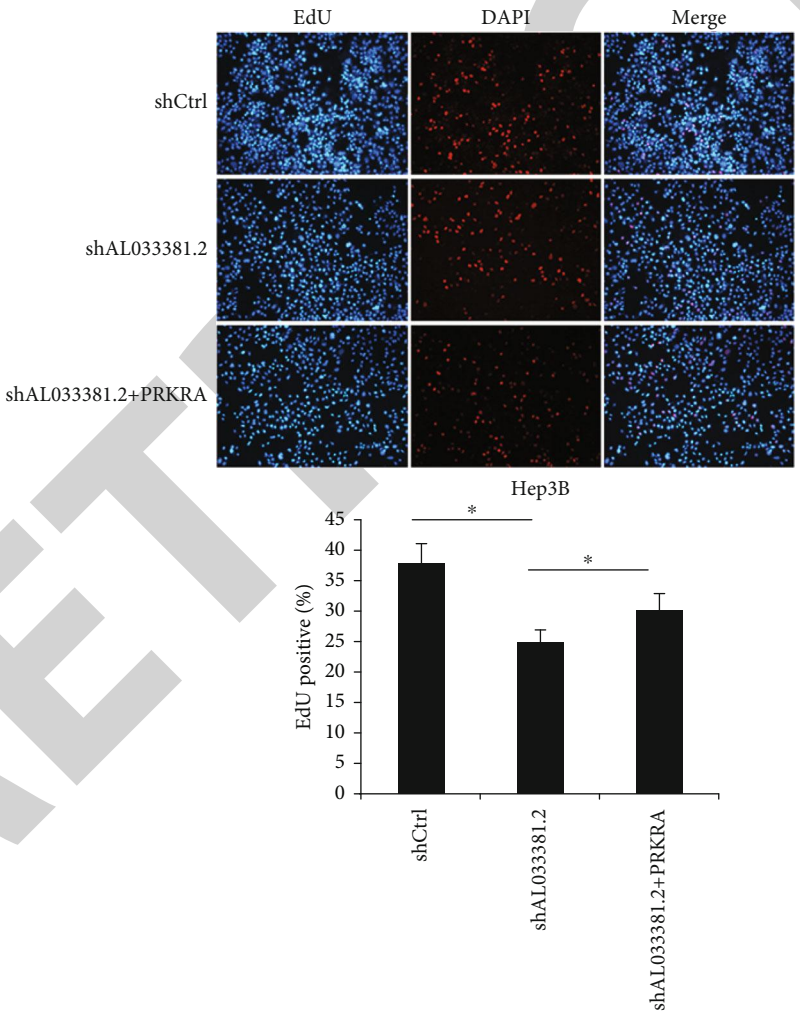


FIGURE 7: Continued.





(f)



(g)

FIGURE 7: Continued.

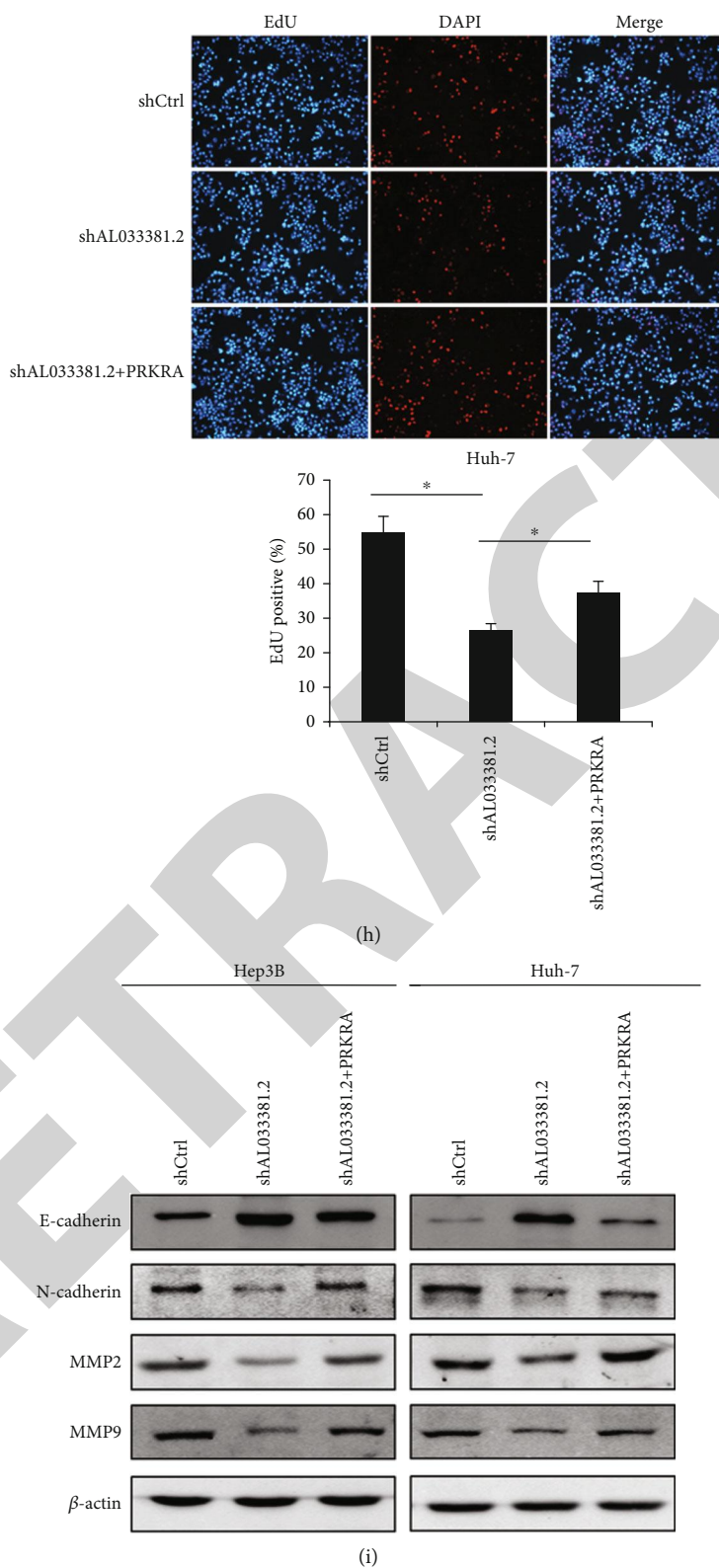
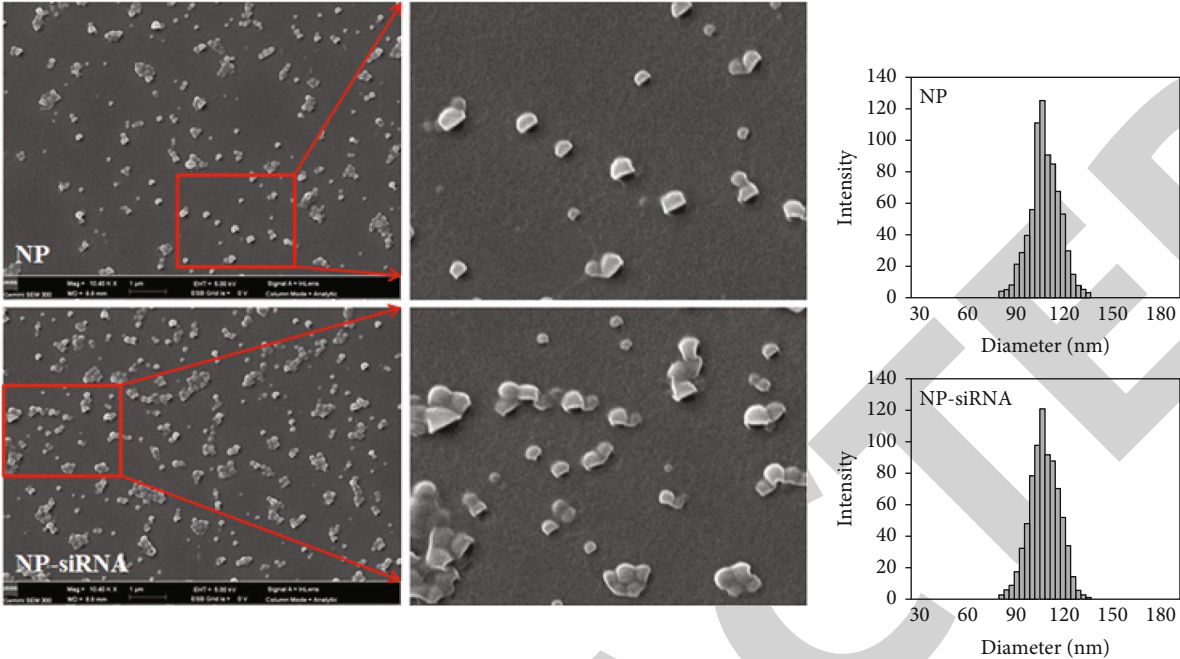


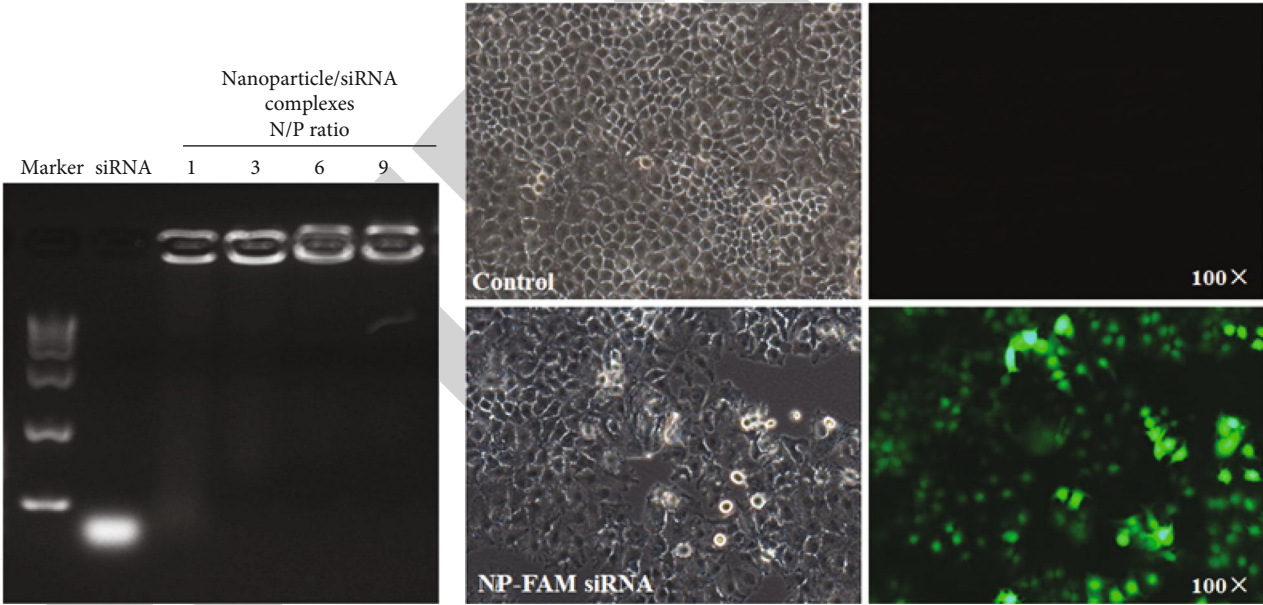
FIGURE 7: Overexpression of PRKRA rescued the inhibitory effects mediated by AL033381.2 knockdown in HCC cells. (a-h) The inhibitory functions of AL033381.2 silencing on cell viability, proliferation, migration, and invasion were measured by MTT (a, c), colony formation assays (b, d), Transwell (e, f), and EdU staining assays (g, h) in Hep3B and Huh-7 cells transfected with the PRKRA overexpressed lentivirus or control vector, respectively. (i) The expressions levels of E-cadherin, N-cadherin, MMP2, and MMP9 were detected by Western blot analysis in Hep3B and Huh-7 cells that were transfected with shCtrl, shAL033381.2, or shAL033381.2+PRKRA groups, respectively. \* $P < 0.05$ .



(a)

(b)

Huh-7



(c)

(d)

FIGURE 8: Continued.

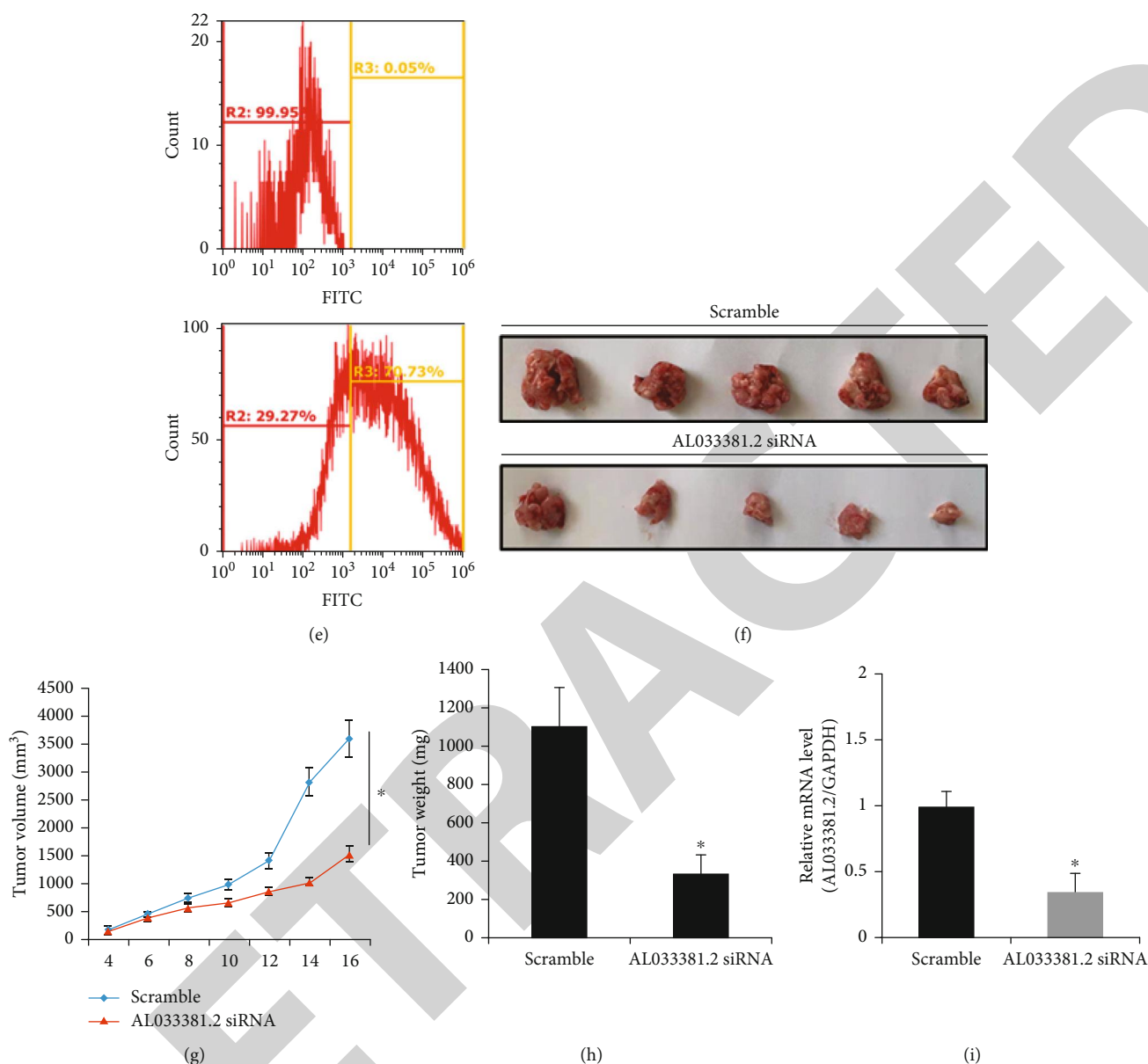


FIGURE 8: Characterization, transfection efficiency, and in vivo antitumor efficacy of nanoparticle/siRNA complexes. (a) Representative scanning electron microscopy images of the empty nanoparticles and nanoparticle/siRNA complexes; magnification 10,400x. (b) Hydrodynamic diameter distribution of the empty nanoparticles and nanoparticle/siRNA complexes. (c) A gel retardation assay of nanoparticle/siRNA complexes at different N/P ratios. (d, e) Representative fluorescent images, matched bright images, and transfection efficiency of Huh7 cells transfected with empty nanoparticles and nanoparticle/siRNA complexes. (f) The representative images of tumor growth in the subcutaneous xenograft model of Huh7 cells in nude mice. (g, h) In vivo antitumor results revealed the effects of tumor volume and weight after the treatment with nanoparticle/scramble siRNA complexes (scramble) and nanoparticle/AL033381.2 siRNA complexes (AL033381.2 siRNA). \* $P < 0.05$ . (i) The relative mRNA expression level of AL033381.2 between the scramble and AL033381.2 siRNA Huh7 cell lines.

closely correlated to some clinicopathological parameters, including T stage, TNM stage, and pathological grade. To further verify the sequencing results, we investigated the expression of AL033381.2 using qPCR in a cohort of 30 HCC tissues and corresponding normal tissues, and we found that AL033381.2 expression was observably increased in HCC tissues compared to matched normal tissues. In addition, numerous studies have revealed that owing to the involvement of lncRNAs in the regulation of tumor-related genes, lncRNAs are involved in several cell processes, includ-

ing cell proliferation, growth, differentiation, and apoptosis [27]. Based on our experimental findings, AL033381.2 consistently acts as an oncogene that promotes the proliferation and metastasis of HCC cells *in vivo* and *in vitro*.

Epithelial-to-mesenchymal transition (EMT) is a biological process wherein epithelial cells lose the requirements for physical contact with adjacent cells and acquire mesenchymal characteristics, including enhanced migratory and invasive behaviors [28]. In particular, lncRNAs positively regulate the EMT process in HCC [29]. Here, we demonstrate

that AL033381.2 promotes EMT progression in HCC cells and thus could be utilized as a new target for molecular targeted therapy of HCC. Consequently, the abnormal expression and crucial functions of AL033381.2 in HCC prompted us to further elucidate its potential regulatory mechanism.

LncRNAs exert their functions in multiple mechanisms, including scaffolding nuclear and cytoplasmic complexes, gene expression modulation, and cotranscriptional regulations [30]. Moreover, the function of lncRNAs is often related to their subcellular location [31]. Cytoplasmic lncRNAs may be involved in regulating protein stability and translational modification [32]. In this study, to further evaluate the molecular mechanisms of AL033381.2 in promoting HCC tumorigenesis, we first performed FISH assays, which indicated that AL033381.2 is predominantly cytoplasmic and possibly exerts its biological function at the posttranscriptional level. Mechanically, RNA pull-down and mass spectrometry analysis finally identified PRKRA as one of several proteins bound to AL033381.2. Moreover, we demonstrated that PRKRA interacts with AL033381.2 using RIP and RNA pull-down assays. PRKRA, which is a known cellular protein activator of PKR kinase [33], participates in microRNA processing and interacts with members of the RNAi pathway such as Dicer and Ago2 [34]. A previous study has shown that PRKRA is upregulated in lung adenocarcinoma [35]. Recent studies have also demonstrated that treatment with siPRKRA plus oxaliplatin imparts a significant antitumor effect on mucinous ovarian cancer cells [33]. Furthermore, in our study, functional analyses indicated that AL033381.2 knockdown markedly suppresses HCC cell proliferation and metastasis and that this effect is partially rescued by simultaneous PRKRA overexpression. Additionally, our studies have shown that AL033381.2 could promote the EMT pathway by regulating PRKRA.

Recent studies have shown that nonviral vectors, nanoparticle gene vectors in particular, have low toxicity and biodegradability [36]. In our study, PLGA nanoparticles were prepared as siRNA transfection vectors. The growth rate of AL033381.2 siRNA-loaded nanoparticle-Huh-7 tumors in nude mice was notably slower than the control group, indicating that nanoparticle/AL033381.2 siRNA complexes significantly inhibit tumorigenesis *in vivo* and thus impart positive therapeutic effects.

## 5. Conclusions

This is the first report that shows that lncRNA AL033381.2 imparts carcinogenic effects on HCC by interacting with PRKRA. Nanoparticle/AL033381.2 siRNA complexes also exhibit favorable therapeutic effects *in vivo* and have the potential to become a novel therapeutic target worthy of further investigation. This study provides a novel investigation of the potential therapeutic target of AL033381.2 and provides a better understanding of the pathogenesis and molecular treatment strategies of HCC. Consequently, further research is needed to elucidate the regulatory mechanisms of the AL033381.2/PRKRA axis and identify particular targets for therapeutic applications to HCC.

## Data Availability

The data that support the findings of this study are available from the corresponding authors upon reasonable request.

## Conflicts of Interest

The authors have no conflicts of interest to declare.

## Authors' Contributions

Feiran Wang and Lirong Zhu contributed equally to this work.

## Acknowledgments

This work was supported by grants from the National Natural Science Foundation of China (no. 81871927 to Zhong Chen and no. 81900368 to Chen Dai) and the Nantong Science and Technology Project (MS12020024 and MB2020058 to Weidong Tang).

## Supplementary Materials

Figure S1: the results of qRT-PCR showed that AL033381.2 was expressed in Hep3B, Huh-7, HepG2, and SK-HEP-1 cells. The relative mRNA expression (AL033381.2/GAPDH) was determined by the  $2^{-\Delta\Delta Ct}$  method. Figure S2: the secondary structure of AL033381.2 (ENST00000603854) is shown as predicted by InCAR (<https://lncar.renlab.org>). Figure S3: to exclude from antisense, mass spectrometry analysis showed the target gene list from AL033381.2 sense. Figure S4: mass spectrometry analysis of PRKRA binding to AL033381.2. Figure S5: Western blot analysis for RNH1, STAU1, ETV6, PRKRA, Peroxiredoxin2 (PRDX2), and Cytokeratin8 (KRT8) protein levels in Huh-7 cell lysates. Figure S6: *in vitro* cumulative release profiles of siRNA from the nanoparticle/siRNA complexes. (*Supplementary Materials*)

## References

- [1] J. L. Raoul and J. Edeline, "Systemic treatment of hepatocellular carcinoma: standard of care in China and elsewhere," *The Lancet Oncology*, vol. 21, no. 4, pp. 479–481, 2020.
- [2] D. Y. Xie, Z. G. Ren, J. Zhou, J. Fan, and Q. Gao, "2019 Chinese clinical guidelines for the management of hepatocellular carcinoma: updates and insights," *Hepatobiliary surgery and nutrition*, vol. 9, no. 4, pp. 452–463, 2020.
- [3] X. F. Xu, H. Xing, J. Han et al., "Risk factors, patterns, and outcomes of late recurrence after liver resection for hepatocellular carcinoma: a multicenter study from China," *JAMA Surgery*, vol. 154, no. 3, pp. 209–217, 2019.
- [4] A. G. Singal and C. C. Murphy, "Hepatocellular carcinoma: a roadmap to reduce incidence and future burden," *Journal of the National Cancer Institute*, vol. 111, no. 6, pp. 527–528, 2019.
- [5] S. Ogasawara, S. P. Choo, J. T. Li, and C. Yoo, "Evolving treatment of advanced hepatocellular carcinoma in the Asia-Pacific region: a review and multidisciplinary expert opinion," *Cancers (Basel)*, vol. 13, no. 11, p. 2626, 2021.

## *Retraction*

# **Retracted: Dietary Quercetin Supplementation Attenuates Diarrhea and Intestinal Damage by Regulating Gut Microbiota in Weanling Piglets**

### **Oxidative Medicine and Cellular Longevity**

Received 8 January 2024; Accepted 8 January 2024; Published 9 January 2024

Copyright © 2024 Oxidative Medicine and Cellular Longevity. This is an open access article distributed under the Creative Commons Attribution License, which permits unrestricted use, distribution, and reproduction in any medium, provided the original work is properly cited.

This article has been retracted by Hindawi following an investigation undertaken by the publisher [1]. This investigation has uncovered evidence of one or more of the following indicators of systematic manipulation of the publication process:

- (1) Discrepancies in scope
- (2) Discrepancies in the description of the research reported
- (3) Discrepancies between the availability of data and the research described
- (4) Inappropriate citations
- (5) Incoherent, meaningless and/or irrelevant content included in the article
- (6) Manipulated or compromised peer review

The presence of these indicators undermines our confidence in the integrity of the article's content and we cannot, therefore, vouch for its reliability. Please note that this notice is intended solely to alert readers that the content of this article is unreliable. We have not investigated whether authors were aware of or involved in the systematic manipulation of the publication process.

Wiley and Hindawi regrets that the usual quality checks did not identify these issues before publication and have since put additional measures in place to safeguard research integrity.

We wish to credit our own Research Integrity and Research Publishing teams and anonymous and named external researchers and research integrity experts for contributing to this investigation.

The corresponding author, as the representative of all authors, has been given the opportunity to register their agreement or disagreement to this retraction. We have kept a record of any response received.

### **References**

- [1] B. Xu, W. Qin, Y. Xu et al., "Dietary Quercetin Supplementation Attenuates Diarrhea and Intestinal Damage by Regulating Gut Microbiota in Weanling Piglets," *Oxidative Medicine and Cellular Longevity*, vol. 2021, Article ID 6221012, 19 pages, 2021.

## Research Article

# Dietary Quercetin Supplementation Attenuates Diarrhea and Intestinal Damage by Regulating Gut Microbiota in Weanling Piglets

Baoyang Xu,<sup>1,2</sup> Wenxia Qin,<sup>1,2</sup> Yunzheng Xu,<sup>1,2</sup> Wenbo Yang,<sup>1,2</sup> Yuwen Chen,<sup>1,2</sup>  
Juncheng Huang,<sup>1,2</sup> Jianan Zhao,<sup>1,2</sup> and Libao Ma <sup>1,2</sup>

<sup>1</sup>College of Animal Sciences and Technology, Huazhong Agricultural University, Wuhan, Hubei 430070, China

<sup>2</sup>Hubei Provincial Engineering Laboratory for Pig Precision Feeding and Feed Safety Technology, Wuhan, 430070 Hubei, China

Correspondence should be addressed to Libao Ma; [malibao@mail.hzau.edu.cn](mailto:malibao@mail.hzau.edu.cn)

Received 13 September 2021; Accepted 26 November 2021; Published 13 December 2021

Academic Editor: Demin Cai

Copyright © 2021 Baoyang Xu et al. This is an open access article distributed under the Creative Commons Attribution License, which permits unrestricted use, distribution, and reproduction in any medium, provided the original work is properly cited.

Antioxidant polyphenols from plants are potential dietary supplementation to alleviate early weaning-induced intestinal disorders in piglets. Recent evidences showed polyphenol quercetin could reshape gut microbiota when it functioned as anti-inflammation or antioxidation agents in rodent models. However, the effect of dietary quercetin supplementation on intestinal disorders and gut microbiota of weanling piglets, along with the role of gut microbiota in this effect, both remain unclear. Here, we determined the quercetin's effect on attenuating diarrhea, intestinal damage, and redox imbalance, as well as the role of gut microbiota by transferring the quercetin-treated fecal microbiota to the recipient piglets. The results showed that dietary quercetin supplementation decreased piglets' fecal scores improved intestinal damage by increasing tight junction protein occludin, villus height, and villus height/crypt depth ratio but decreased crypt depth and intestinal epithelial apoptosis (TUNEL staining). Quercetin also increased antioxidant capacity indices, including total antioxidant capacity, catalase, and glutathione/oxidized glutathione disulfide but decreased oxidative metabolite malondialdehyde in the jejunum tissue. Fecal microbiota transplantation (FMT) from quercetin-treated piglets had comparable effects on improving intestinal damage and antioxidative capacity than dietary quercetin supplementation. Further analysis of gut microbiota using 16S rDNA sequencing showed that dietary quercetin supplementation or FMT shifted the structure and increased the diversity of gut microbiota. Especially, anaerobic trait and carbohydrate metabolism functions of gut microbiota were enriched after dietary quercetin supplementation and FMT, which may owe to the increased antioxidative capacity of intestine. Quercetin increased the relative abundances of Fibrobacteres, *Akkermansia muciniphila*, *Clostridium butyricum*, *Clostridium celatum*, and *Prevotella copri* but decreased the relative abundances of Proteobacteria, *Lactobacillus coleohominis*, and *Ruminococcus bromii*. Besides, quercetin-shifted bacteria and carbohydrate metabolites short chain fatty acids were significantly related to the indices of antioxidant capacity and intestinal integrity. Overall, dietary quercetin supplementation attenuated diarrhea and intestinal damage by enhancing the antioxidant capacity and regulating gut microbial structure and metabolism in piglets.

## 1. Introduction

Early weaning is a critical strategy for improving the efficiency of modern swine breeding system but usually results in physiological, environmental, and social stress for piglets [1]. These stresses occur particularly during the initial post-weaning period, which is frequently characterized by transient anorexia, gut microbiota dysbiosis, severe intestinal

damage, infections, and diarrhea, compromising the anti-disease's ability of young piglets [2, 3]. The disturbed gastrointestinal functionality during the first two weeks triggers oxidative stress, which, characterized by an imbalance between the production of free radicals and the scavenging ability of the antioxidant defense system, has been involved in the initiation and pathogenesis of early weaning-induced intestinal disorders [1, 4, 5]. Therapy for piglets' weaning

stress mainly relies on the use of zinc and copper beyond nutritional requirements and the excessive use of antimicrobials, which raised major concerns for environmental burden and antimicrobial resistance [6]. In the quest for sustainable alternatives, the appropriate nutrients with favorable antioxidant activity could alleviate intestinal damage in weaning piglets.

Antioxidant compounds, specifically polyphenols from plants, can scavenge free radicals and alleviating intestinal disorders associated with oxidative stress [7]. Quercetin as a flavonoid polyphenol molecule is commonly found in vegetables, fruits, and Chinese herbs [8]. Quercetin showed excellent assets among the six antioxidants investigated in vitro for supplementation in pig diet [9]. Only 5–10% ingested quercetin is absorbed in the small intestine, and thus, 90–95% reach the colon [10, 11]. Mammalian gut harbors trillions of microbes, especially in the hindgut caecum and colon, namely gut microbiota, which have intimate, ancient, and/or mutualistic associations with hosts [12, 13]. Combination of quercetin and resveratrol can reduce obesity by restoring the gut microbiota dysbiosis in high-fat diet-fed rats [14]. Besides, dietary quercetin improved the oxidative stress in association with its ability to recover the gut microbiota diversity in mice with dextran sodium sulfate-induced colitis [15]. Compared to the considerable amount of researches in rodent models, there however is a lack of researches focused on quercetin's beneficial effects on pigs [16]. The causality between gut microbiota and quercetin's antioxidative function is also unclear.

We hypothesized dietary quercetin can attenuate intestinal damage and redox imbalance, and gut microbiota is a potential pharmacodynamic target for quercetin in weaning piglets. Fecal microbiota transplantation (FMT) is to establish a donor-like gut microbiome by transferring donor fecal microbiota to a recipient [17]. FMT provides an effective approach to uncover the role of gut microbiota in the pharmacodynamic effect of plant-derived active ingredients [18, 19]. To test our hypothesis, we determined the quercetin's effect on improving intestinal damage, redox imbalance, and gut microbial dysbiosis after supplying weanling piglets with dietary 0.1% quercetin supplementation and meanwhile transferred their fecal microbiota to the FMT recipient piglets.

## 2. Materials and Methods

**2.1. Experimental Design and Animals.** This animal experiment was approved by the Scientific Ethics Committee of Huazhong Agricultural University (approval numbers HZAUSW2018015). We allotted 60 early weaned piglets (Duroc × Landrace × Yorkshire) with age of 21 days into three groups randomly (20 piglets each group): control group fed basal diet and 2 mL saline every other day (Ctrl); quercetin group fed diet supplemented with 0.1% quercetin [20, 21] (content 95.18%, Hengrui Tongda, Chengdu, China) and 2 mL saline every other day (QT); and fecal microbiota transplantation group received 2 mL fecal microbiota suspension from QT group every other day (FQT). These piglets were free to diet and water for 14 days. The basal diet was formulated to meet the pigs' nutrients need

(NRC, 2012, Table S1), and the dose of dietary quercetin supplementation was based on the literature and our prior pretrial [20]. At d14 postweaning, we randomly selected 20 piglets (six from Ctrl and seven from QT and FQT, respectively) for sampling.

**2.2. Fecal Microbiota Transplantation.** The fecal suspension was prepared using our previous protocol with minor optimization [22]. Briefly, fresh feces samples were obtained from piglets of QT group and immediately homogenized in sterile and O<sub>2</sub>-free saline. The fecal microbiota suspension that passed through the sterilized gauze and then a 0.224 mm stainless cell strainer was centrifugated at 3500×g for 10 min to get fecal microbial precipitate. We then resuspended the fecal microbial precipitate in saline and then fed piglets from FQT group by oral administration from day 2 to day 10 post weaning (2 mL each piglet every other day).

**2.3. Piglet Growth Performance and Fecal Scores.** The growth performance of piglets was determined by the average daily gain (ADG) and average daily feed intake (ADFI). Meanwhile, we recorded fecal scores with a scale: 1, normal, solid feces; 2, soft, looser than normal feces, slight diarrhea; 3, moderate diarrhetic feces; and 4, liquid, severe diarrhetic feces for all pigs daily [23].

**2.4. Histomorphology Examination of the Jejunum Tissue.** We sampled 2 cm of jejunum tissue and then fixed it with 4% paraformaldehyde overnight. We evaluated the histomorphology of jejunum tissue examination by examining hematoxylin- and eosin-stained (H&E) jejunum tissue sections (10 μm) using an Olympus BX51 microscope with integrated digital imaging analysis system (Olympus Co., Tokyo, Japan).

**2.5. Apoptosis Assessment of Jejunal Epitheliums.** The terminal deoxynucleotidyl transferase dUTP nick-end labeling (TUNEL) assay was used to mark apoptotic jejunal epitheliums [24]. The average optical density (AOD) was used to determine the apoptotic jejunal epitheliums in the sections. The AOD of TUNEL (green) in the sections was determined by ImageJ [25].

**2.6. Antioxidant Capacity Evaluation of the Jejunum Tissue.** We determined the activities of total antioxidant capacity (T-AOC, BC1315), catalase (CAT, BC0205), malondialdehyde (MDA, BC0025), glutathione (GSH, BC1175)/oxidized glutathione disulfide (GSSG, BC1185), and nitric oxide (NO, BC1475) in jejunum tissue using commercial kits from Solarbio Science & Technology (Beijing, China) according to the manufacturer's instructions, respectively.

**2.7. Tight Junction Protein Determination of the Jejunum Tissue.** We determined the tight junction proteins of the jejunum tissue using western blotting as described before [26]. Briefly, the total protein of jejunum tissue was extracted and then preserved at −80°C for subsequent analysis. We quantified the concentration of total protein using BCA assays (Thermo Scientific, 23250), separated them



using sodium dodecyl sulfate-polyacrylamide gel electrophoresis, and then transferred them to membranes for western blotting. Polyclonal antibodies occludin (Cell Signaling Technology, 91131S, 1:1000) and Claudin-1 (ProteinTech, 13050-1-AP, 1:1000) were used as primary antibodies and incubated with membranes overnight at 4°C. The membranes were then incubated with secondary antibodies. The western blot results were analyzed using the ImageJ software.

**2.8. Microbial DNA Extraction and PCR Amplification.** Microbial community genomic DNA was extracted from fecal samples (stool from the rectum) using the TGuide S96 Magnetic Soil/Stool DNA Kit (TIANGEN, China) according to manufacturer's instructions. The hypervariable region V4 of the bacterial 16S rRNA gene was amplified with primer pairs 515F (5'-GTGYCAGCMGCCGCGGTAA-3') and 806R2 (5'-GGACTACNVTGGGTWTCTAAT-3'). The PCR amplification of 16S rRNA gene was performed as follows: initial denaturation at 95°C for 3 min, followed by 25 cycles of denaturing at 95°C for 30 s, annealing at 50°C for 30 s, extension at 72°C for 40 s, single extension at 72°C for 7 min, and end at 4°C. Purified amplicons were pooled in equimolar and paired end (PE) sequenced (2 × 250) on an NovaSeq 6000 platform (Illumina, San Diego, USA) at Biomarker Technologies Co, Ltd. (Beijing, China).

**2.9. Illumina NovaSeq Sequencing and Processing of Sequencing Data.** According to quality of single nucleotide, raw data was primarily filtered by Trimmomatic [27] (version 0.33). Identification and removal of primer sequences were processed by Cutadapt [28] (version 1.9.1). PE reads obtained from previous steps were assembled by USEARCH [29] (version 10) and followed by chimera removal using UCHIME [30] (version 8.1). USEARCH [29] (version 10.0) was applied to cluster sequences into operational taxonomic units (OTUs) with similarity over 97%. The taxonomy of each OTU representative sequence was analyzed by RDP Classifier against the 16S rRNA database Silva [31] (Release132) and Greengenes [32] (version 13.5).

**2.10. Function Prediction and Metabolites Determination of Gut Microbiota.** We employed PICRUSt2 to predict the functional composition of gut bacterial communities [33]. We determined the gut microbial metabolites SCFAs including acetic acid, propionic acid, butyric acid, valeric acid, isobutyric acid, and isovaleric acid in the stools of the jejunum and colon using gas chromatography with our previous method [26, 34]. Briefly, 1 g of the stool sample was weighed into a 2 mL centrifuge tube with 1 mL of methanol added. After being vortexed for 30 s, the sample was centrifuged for 10 min (12,000 g, 4°C). The supernatant (1 mL) was transferred into centrifuge tubes (2 mL) and mixed with 0.2 mL 25% metaphosphoric acid. After 30 min at 4°C, the tubes were centrifuged for 10 min (12,000 g, 4°C) again. Aliquots of the supernatant (1 mL) were analyzed using a gas chromatography method.

**2.11. Phenotype Prediction of Gut Microbiota.** We employed BugBase to determine the biologically relevant gut microbiome phenotype at organism level [35]. Firstly, BugBase normalizes OTU by predicting 16S copy number. Microbial phenotype is predicted based on given precalculated files. For biological data of each sample, relative abundance of trait is estimated in full range of coverage thresholds (0 to 1, increment: 0.01). Subsequently, for each trait in users' data, the coverage threshold with the highest variance in all samples is selected. With such threshold, BugBase can generate a table with organism-level phenotype predictions, which contains relative abundance of predicted phenotype in each sample. Based on specified metadata, an automated hypothesis test is performed and can be visualized as taxa-contribution plots depicting the relative abundances of trait-possessing taxa.

**2.12. Data Processing and Statistics Analysis.** Experimental data were analyzed by one-way ANOVA and the Duncan multiple comparison test with the GraphPad 8.0 software. The results were presented as the mean ± SEM. Significance was presented as \* $P < 0.05$ , \*\* $P < 0.01$ , and \*\*\* $P < 0.01$ .

### 3. Results

**3.1. Dietary Quercetin Supplementation and FMT Attenuated Diarrhea, Intestinal Barrier Function, and Redox Imbalance in Weanling Piglets.** To determine the effect of dietary quercetin supplementation on piglets' weaning stress and the role of gut microbiota, we fed weaning piglets with diet supplemented with QT and then transferred their fecal microbiota to recipient piglets. The results indicated that quercetin decreased piglets' fecal scores at d7 ( $P < 0.01$ ) and d14 postweaning ( $P < 0.05$ ), as well as FQT at d7 ( $P < 0.05$ ) but not at d14 postweaning (Figure 1(a)). Dietary quercetin supplementation and FMT also both increased ADFI ( $P < 0.05$ , Figure S1(a)) and ADG ( $P < 0.01$ , Figure S1(b)) of piglets at d7-d14 postweaning. QT and FQT increased the expression of tight junction protein occludin in the jejunum tissue ( $P < 0.05$ ) (Figure 1(b)). Besides, QT increased antioxidant indices including T-AOC ( $P < 0.05$ ) (Figure 1(c)), CAT ( $P < 0.01$ ) (Figure 1(d)), and GSH/GSSG ( $P < 0.01$ ) (Figure 1(f)), but decreased oxidative metabolite MDA ( $P < 0.01$ ) (Figure 1(e)) in the jejunum tissue. FQT also increased antioxidant indices including T-AOC ( $P < 0.05$ ) (Figure 1(c)), CAT ( $P < 0.05$ ) (Figure 1(d)), and GSH/GSSG ( $P < 0.05$ ) (Figure 1(f)) but decreased oxidative metabolite MDA ( $P < 0.01$ ) (Figure 1(e)) in the jejunum tissue. QT and FQT had no significant effect on NO in the jejunum tissue (Figure 1(g)). These results suggested that dietary quercetin supplementation and FMT attenuated diarrhea, intestinal barrier function, and redox imbalance in weanling piglets.

**3.2. Dietary Quercetin Supplementation and FMT Improved Intestinal Morphology and Intestinal Epithelial Apoptosis in Weanling Piglets.** Further histomorphological analysis and intestinal epithelial apoptosis analysis showed that QT improved the morphology of jejunum (Figure 2(a)) by

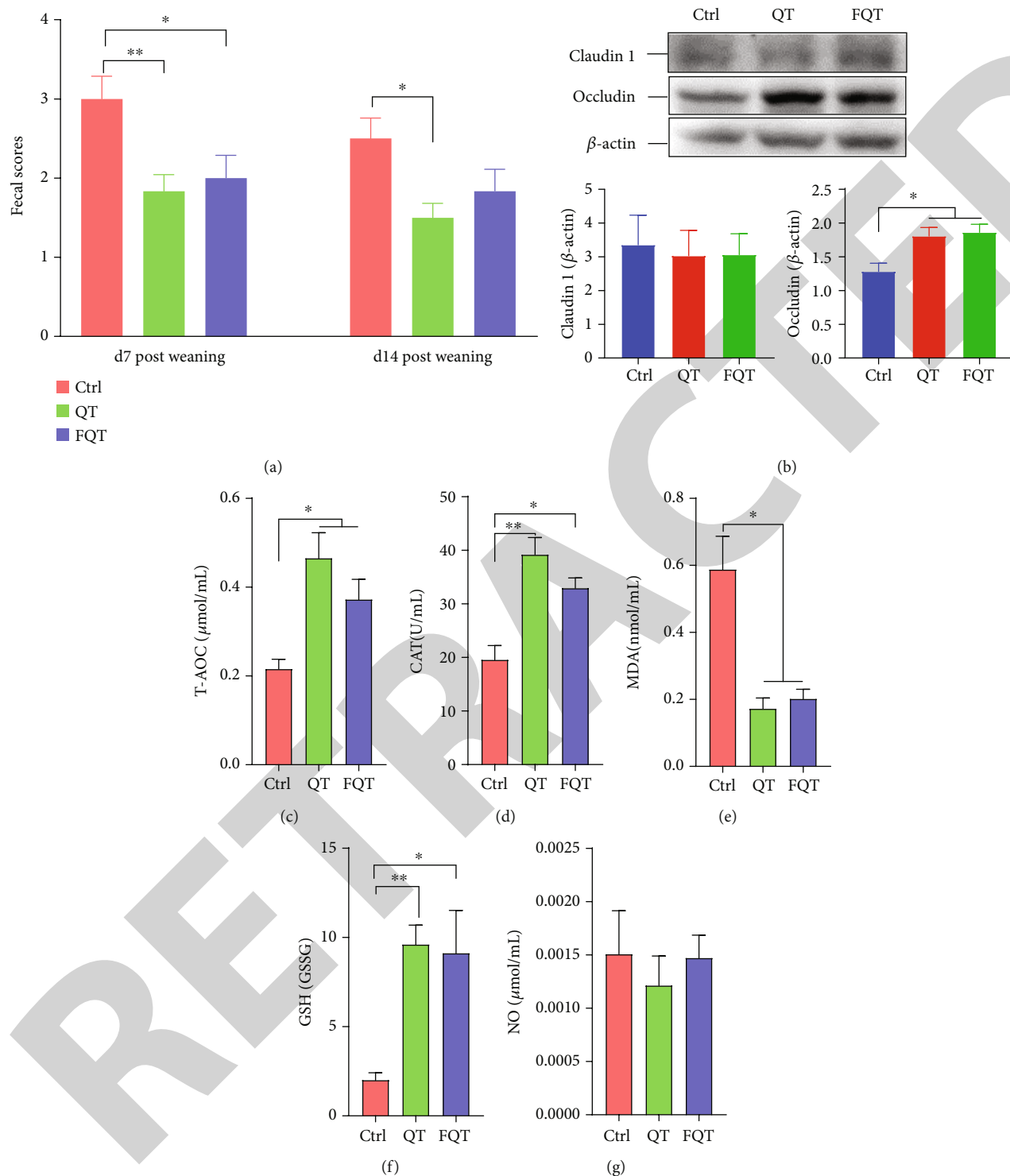


FIGURE 1: The effect of dietary quercetin supplementation and FMT on diarrhea, intestinal damage, and redox imbalance in weanling piglets. (a) Fecal scores of piglets. (b) Western blot of tight junction proteins Claudin-1 and occludin in the jejunum tissue. (c–g) Antioxidant indices including T-AOC, CAT, MDA, GSH/GSSG, and NO in the jejunum tissue. \* $P < 0.05$ , \*\* $P < 0.01$ , and \*\*\* $P < 0.001$ .

increasing villus height ( $P < 0.05$ ) (Figure 2(b)) and villus height/crypt depth ratio ( $P < 0.001$ ) (Figure 2(d)), but decreasing crypt depth ( $P < 0.05$ ) (Figure 2(c)) and the AOD of TUNEL staining ( $P < 0.01$ ) (Figure 2(e)) of the jejunum tissue than those of Ctrl. Compared with Ctrl, FQT also improved the morphology of the jejunum (Figure 2(a)) by

increasing villus height ( $P < 0.05$ ) (Figure 2(b)) and villus height/crypt depth ratio ( $P < 0.01$ ) (Figure 2(d)) but had no significant effect on crypt depth ( $P < 0.05$ ) (Figure 2(c)) and decreasing the AOD of TUNEL staining ( $P < 0.05$ ) (Figure 2(e)) of the jejunum tissue. These results suggested that dietary quercetin supplementation and FMT improved

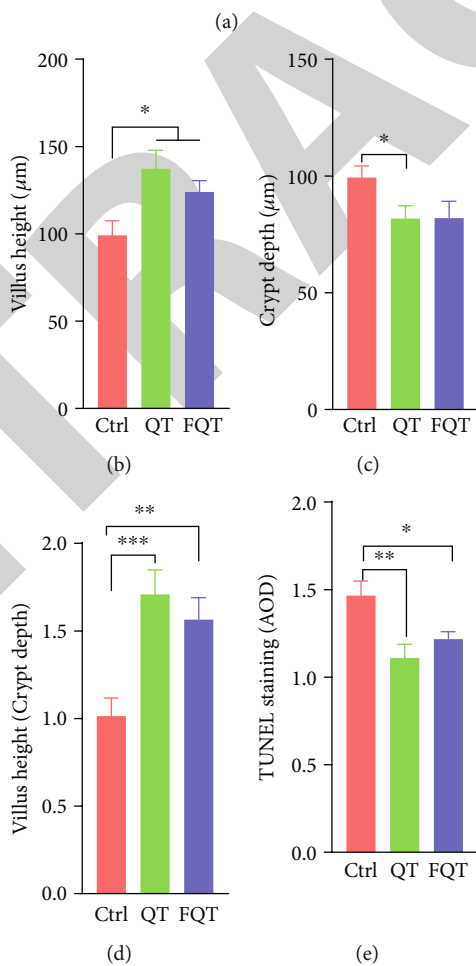
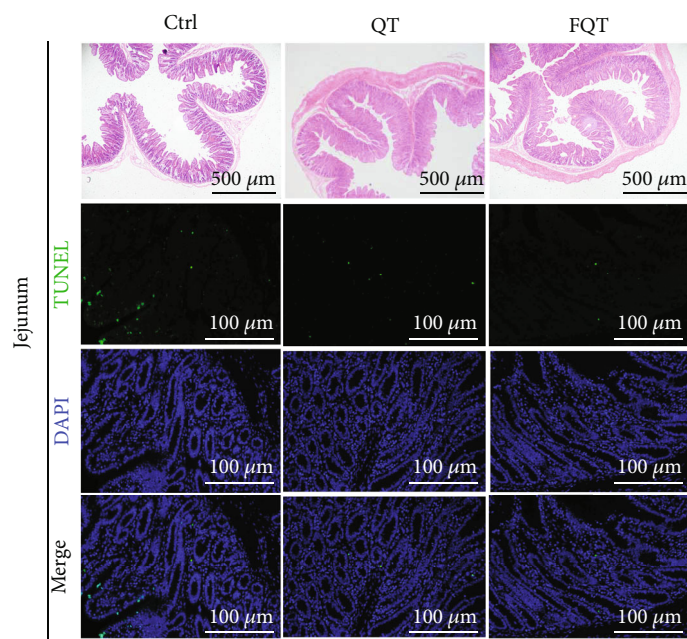


FIGURE 2: The effect of dietary quercetin supplementation and FMT on intestinal morphology and intestinal epithelial apoptosis in weanling piglets. (a) Representative H&E or TUNEL stained jejunum sections. (b) Villus height. (c) Crypt depth. (d) Villus height/crypt depth ratio. (e) AOD of TUNEL staining (green). Scale bar 500 μm (H&E) and 100 μm (TUNEL); \* $P < 0.05$ , \*\* $P < 0.01$ , and \*\*\* $P < 0.001$ .

intestinal morphology and intestinal epithelial apoptosis in weanling piglets.

**3.3. Dietary Quercetin Supplementation and FMT Shifted the Structure and Diversity of Gut Microbiota in Weanling Piglets.** To explore the role of gut microbiota in the improvement of jejunum damage and oxidative stress by dietary quercetin supplementation and FMT in weanling piglets, we profiled the gut microbiota using 16S rDNA amplicon high-throughput sequencing. Rarefaction curve of OTU number gradually becomes flat indicating that sequencing data was adequate to present most species in the sample (Figure 3(a)). The beta diversity among groups presented by PCoA (PC1 and PC2 explained 48.85% of the variation) illustrated that the QT group ( $P < 0.01$ ) and FQT group ( $P < 0.05$ ) formed a distinct cluster markedly away from the Ctrl group, respectively (Figure 3(b)). For single sample, QT increased alpha diversity indices of observed species ( $P < 0.01$ ) (Figure 3(c)), Chao1 ( $P < 0.05$ ) (Figure 3(d)), ACE ( $P < 0.05$ ) (Figure 3(e)), and PD\_whole\_tree ( $P < 0.01$ ) (Figure 3(h)) but had no effect on Shannon (Figure 3(f)), Simpson (Figure 3(g)), and Coverage (Figure 3(i)) than those of Ctrl. Compared with Ctrl, FQT increased ACE ( $P < 0.05$ ) (Figure 3(e)). These results suggested that dietary quercetin supplementation and FMT shifted the structure and diversity of gut microbiota in weanling piglets.

**3.4. Dietary Quercetin Supplementation and FMT Altered the Taxon Abundance of Gut Microbiota in Weanling Piglets.** The linked bar plots illustrated that dietary quercetin supplementation and FMT markedly shifted the relative abundance of bacteria at different taxon levels including phylum (Figure 4(a)), species (Figure 4(b)), family (Figure S2(a)), order (Figure S2(b)), and genus (Figure S2(c)). In detail, QT increased the relative abundances of Fibrobacteres ( $P < 0.05$ ) (Figure 4(c)), *Akkermansia muciniphila* ( $P < 0.01$ ) (Figure 4(e)), *Clostridium butyricum* ( $P < 0.01$ ) (Figure 4(f)), *Clostridium celatum* ( $P < 0.01$ ) (Figure 4(g)), and *Prevotella copri* ( $P < 0.05$ ) (Figure 4(i)) but decreased the relative abundances of Proteobacteria ( $P < 0.01$ ) (Figure 4(d)), *Lactobacillus coleohominis* ( $P < 0.01$ ) (Figure 4(h)), and *Ruminococcus bromii* ( $P < 0.05$ ) (Figure 4(j)) than those of Ctrl. FQT increased the relative abundances of *Akkermansia muciniphila* ( $P < 0.05$ ) (Figure 4(e)) but decreased the relative abundances of Proteobacteria ( $P < 0.05$ ) (Figure 4(d)) than those of Ctrl. These results suggested that dietary quercetin supplementation and FMT altered the taxon abundance of gut microbiota in weanling piglets.

**3.5. Dietary Quercetin Supplementation and FMT Altered the Phenotype of Gut Microbiota in Weanling Piglets.** We determined the biologically relevant gut microbiome phenotype at organism level using BugBase [35]. The results showed that QT and FQT had no effect on the relative abundance of aerobic trait (Figure 5(a)) and facultatively anaerobic trait (Figure 5(c)) but significantly increased the relative abundance of anaerobic trait ( $P < 0.01$  for Ctrl vs. QT and  $P < 0.05$  for Ctrl vs. FQT) (Figure 5(b)). Taxa-contribution plots that depicted the relative abundances of trait-possessing taxa

showed that genera, including *Campylobacter* and *Lactobacillus*, mainly contribute to the aerobic trait (Figure 5(d)); genera including *Blautia*, *Dorea*, *Oscillospira*, *Parabacteroides*, *Phascolarctobacterium*, *Prevotella*, *Roseburia*, *Ruminococcus*, *Treponema*, *Prevotella*, *Ruminococcus*, *Eubacterium bifforme*, *Prevotella copri*, *Faecalibacterium prausnitzii*, and *Prevotella stercorea* mainly contribute to the anaerobic trait (Figure 5(e)); genera (*Catenibacterium*, *Streptococcus*, and *p-75-a5*), phylum 1630-c5, and species *Lactobacillus reuteri* mainly contribute to the facultatively anaerobic trait (Figure 5(f)). These results suggested that dietary quercetin supplementation and FMT significantly increased the anaerobic trait of gut microbiota in weanling piglets.

**3.6. Dietary Quercetin Supplementation and FMT Altered the Function and Metabolites of Gut Microbiota in Weanling Piglets.** We investigated the function alteration of gut microbiota using PICRUSt2 and further analyzed their difference with the software STAMP [36]. Compared with Ctrl, QT increased the functions of membrane transport, carbohydrate metabolism, translation, replication and repair, and nucleotide metabolism but decreased the functions of global and overview maps, amino acid metabolism, metabolism of cofactors and vitamins, and energy metabolism (Figure 6(a)). FQT increased the functions of carbohydrate metabolism, membrane transport, translation, nucleotide metabolism, lipid metabolism, replication and repair, and xenobiotics biodegradation and metabolism but decreased the functions of global and overview maps, metabolism of cofactors and vitamins, amino acid metabolism, energy metabolism, glycan biosynthesis, and metabolism than those of Ctrl (Figure 6(b)). Among these shifted functions of the gut microbiota, carbohydrate metabolism function is responsible for the gut microbial fermentation of carbohydrates under a strictly anaerobic environment to produce SCFAs which benefit the host [37]. Compared with Ctrl, QT increased the SCFAs concentrations of colonic stool and jejunal stool including propionic acid ( $P < 0.01$ ) and butyric acid ( $P < 0.05$ ) (Figures 6(c) and 6(d)). FQT also increased the SCFA concentrations including propionic acid ( $P < 0.05$ ) in colonic stool (Figure 6(c)), as well as propionic acid ( $P < 0.01$ ) and butyric acid ( $P < 0.05$ ) in jejunal stool (Figure 6(d)). These results suggested that dietary quercetin supplementation and FMT altered the function and metabolites of gut microbiota in weanling piglets.

**3.7. The Identified Differential Bacteria were Notably Corrected with the Indices of Antioxidant Capacity and Intestinal Integrity in Weanling Piglets.** We employed Spearman's rank correlation coefficient and significance testing to determine the correlation between the identified differential bacteria and the indices of antioxidant capacity and intestinal integrity. With LDA value  $> 4$ , we identified *Oscillospira* as marker taxon of Ctrl; *Veillonellaceae*, *Phascolarctobacterium*, *Clostridia*, *Clostridiales*, and *Prevotella copri* as marker taxon of QT; and *Erysipelotrichaceae*, *Erysipelotrichi*, and *Erysipelotrichales* as marker taxon of FQT (Figure 7(a)). Cladogram based on LEfSe analysis helps visualize the most importance microbial communities in each group. Cladogram plot indicated that *Oscillospira* was the marker taxon

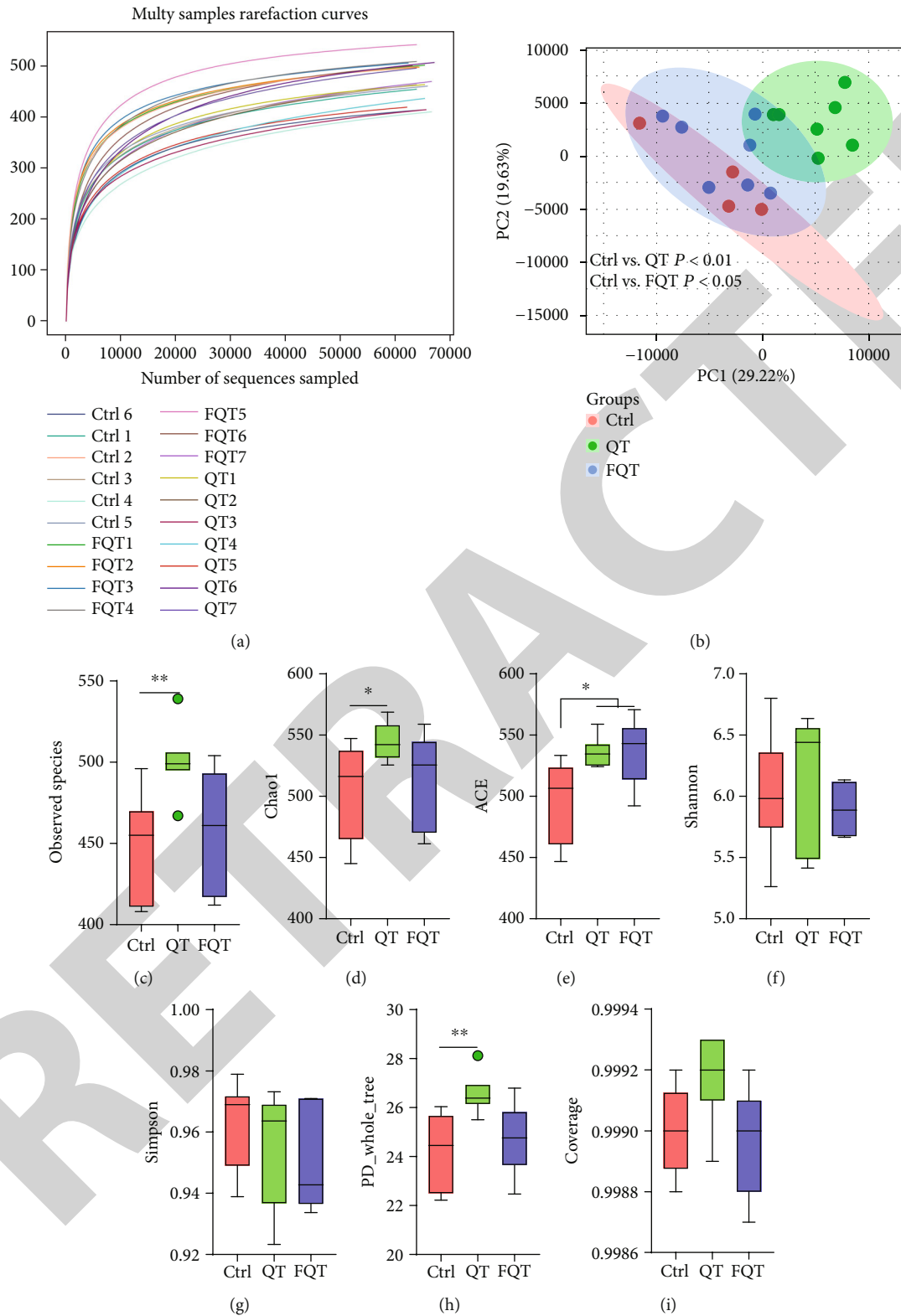


FIGURE 3: The effect of dietary quercetin supplementation and FMT on gut microbiota in weanling piglets. (a) Multisamples' rarefaction curves of OTU numbers that detected from a randomly sampled sequence. (b) The structure shifts (beta diversity) presented by PCoA plot based on unweighted UniFrac. (c-i) The alpha diversity indices of observed species, Chao1, ACE, Shannon, Simpson, PD\_whole\_tree, and Coverage. \* $P < 0.05$ , \*\* $P < 0.01$ , and \*\*\* $P < 0.001$ .

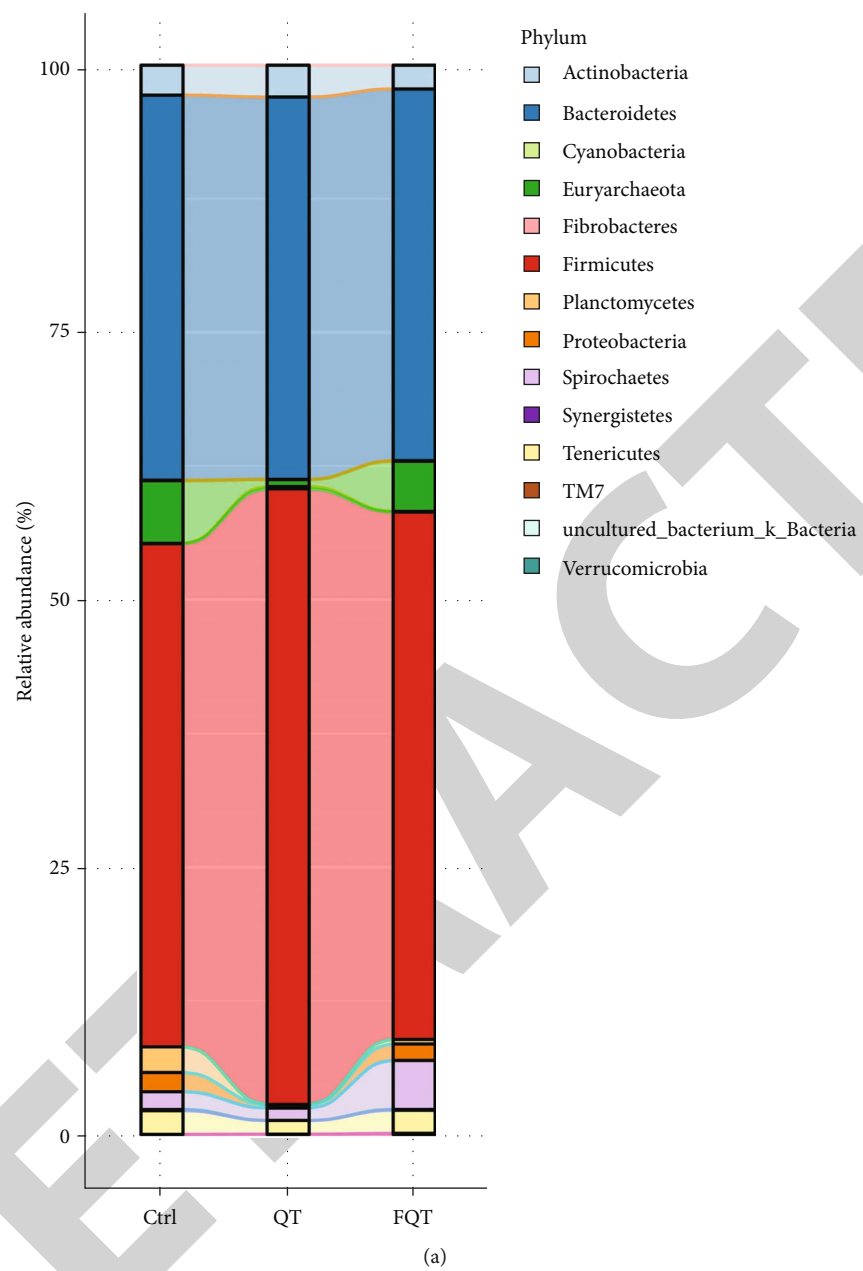
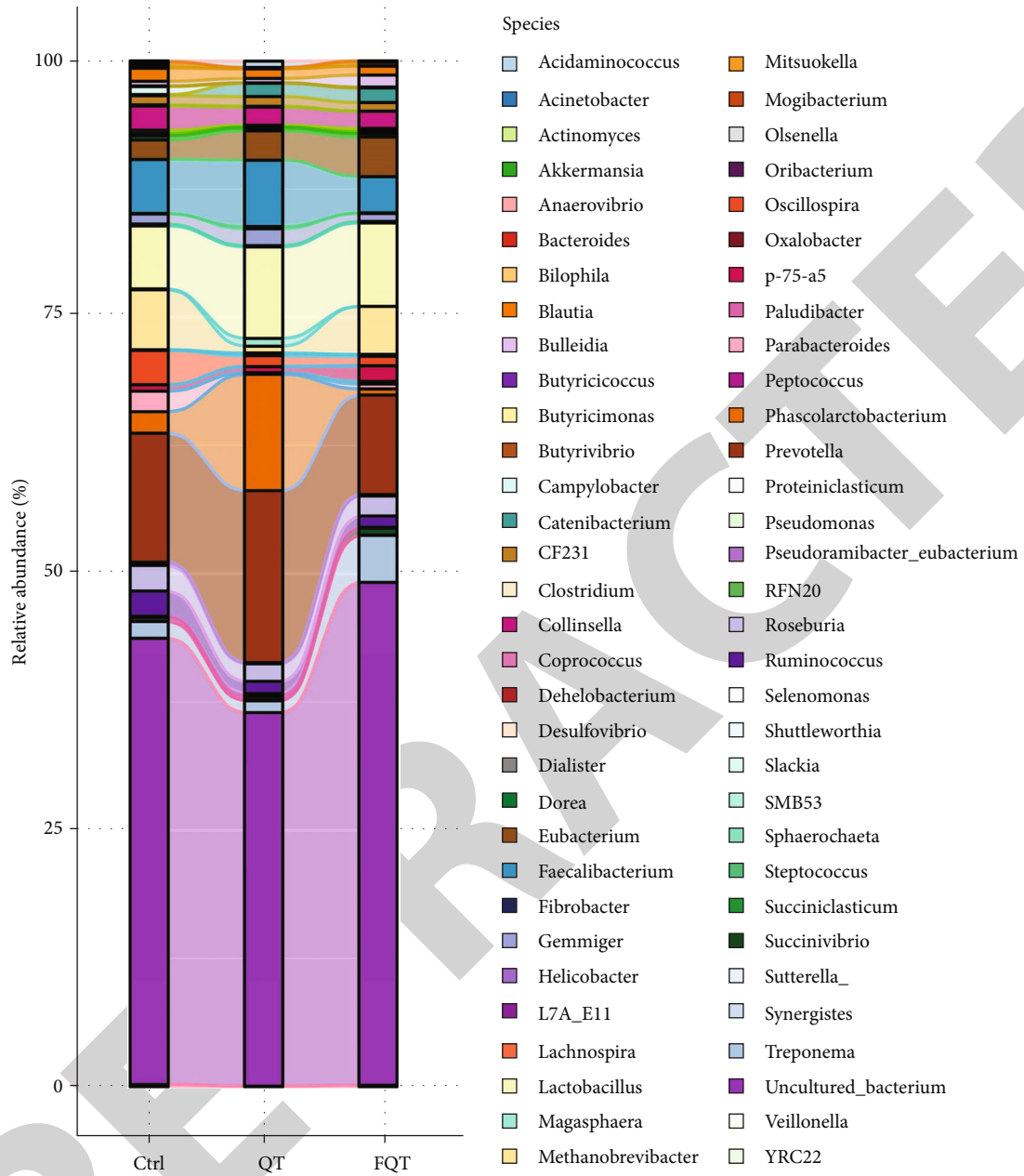
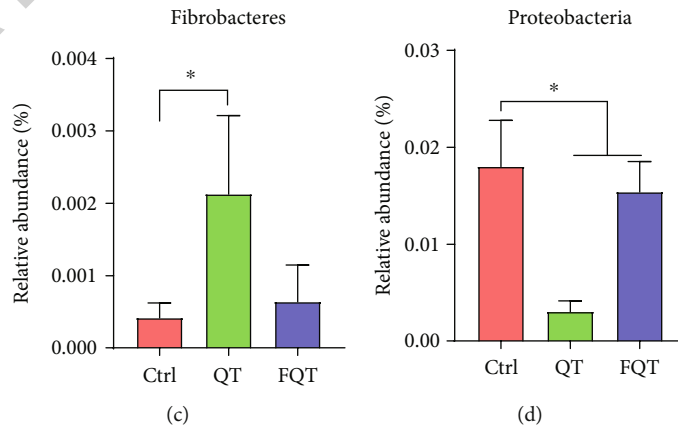


FIGURE 4: Continued.



(b)



(c)

(d)

FIGURE 4: Continued.

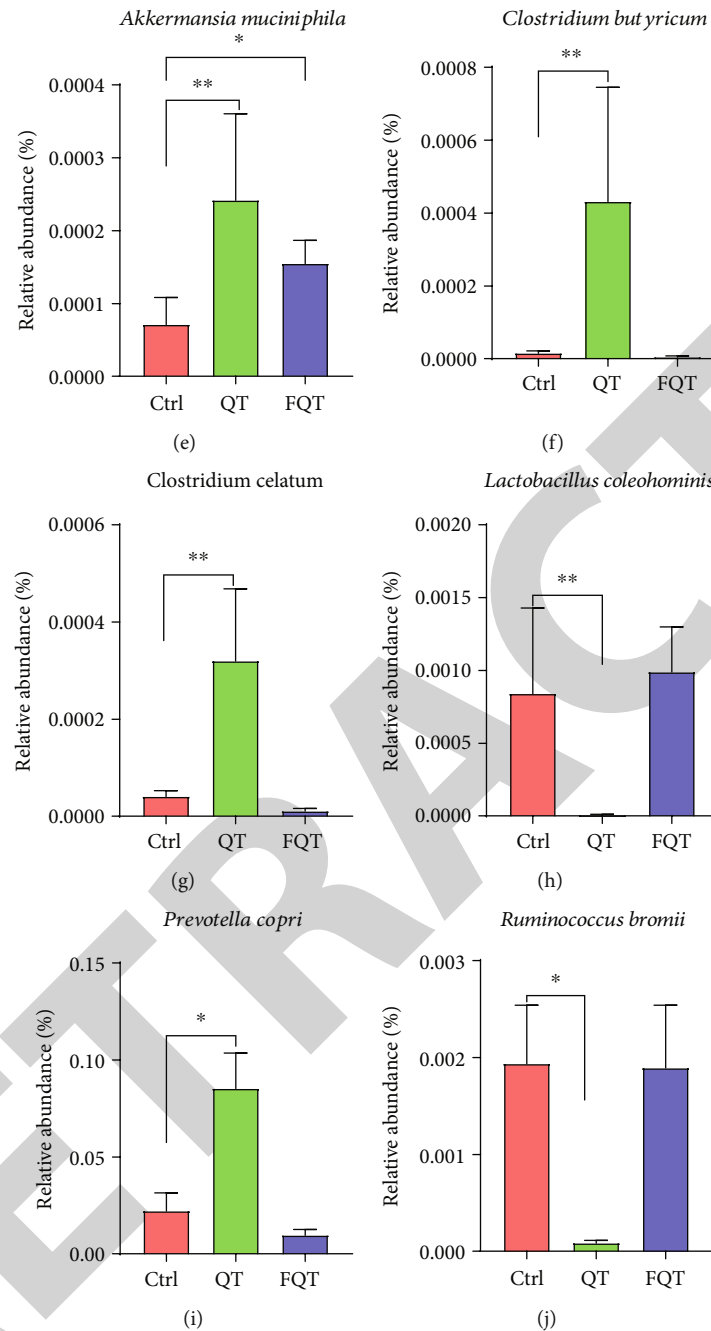


FIGURE 4: The effect of dietary quercetin supplementation and fmt on the taxon abundance of gut microbiota in weaning piglets. The relative abundance of gut microbiota at levels of phylum (a) and species (b), respectively. (c-j) The relative abundance changes of differential bacteria. \* $P < 0.05$ , \*\* $P < 0.01$ , and \*\*\* $P < 0.001$ .

of Ctrl; *Prevotella copri*, *Phascolarctobacterium*, *Veillonellaceae*, and *Clostridiales* were the marker taxon of QT; *Erysipelotrichaceae* and *Erysipelotrichales* were the marker taxon of FQT (Figure 7(b)). For the indices of antioxidant capacity (Figure 7(c)), *Fibrobacteres* ( $P < 0.001$ ), *Erysipelotrichales* ( $P < 0.05$ ), *Erysipelotrichaceae* ( $P < 0.05$ ), *Erysipelotrichi* ( $P < 0.05$ ), jejunal propionic acid ( $P < 0.01$ ), jejunal butyric acid ( $P < 0.01$ ), colonic propionic acid ( $P < 0.05$ ), and colonic butyric acid ( $P < 0.05$ ) were positively associated with T-AOC, but *Oscillospira* ( $P < 0.001$ ) and *Lactobacillus*

*coleohominis* ( $P < 0.001$ ) were negatively associated with T-AOC. *Fibrobacteres* ( $P < 0.05$ ), *Clostridium butyricum* ( $P < 0.05$ ), *Prevotella copri* ( $P < 0.05$ ), jejunal propionic acid ( $P < 0.001$ ), colonic propionic acid ( $P < 0.05$ ), and colonic butyric acid ( $P < 0.05$ ) were positively associated with CAT, but *Oscillospira* ( $P < 0.001$ ) and *Lactobacillus coleohominis* ( $P < 0.001$ ) were negatively associated with CAT. *Oscillospira* ( $P < 0.001$ ), Proteobacteria ( $P < 0.05$ ), and *Lactobacillus coleohominis* ( $P < 0.001$ ) were positively associated with MDA, but jejunal propionic acid ( $P < 0.01$ ) and jejunal



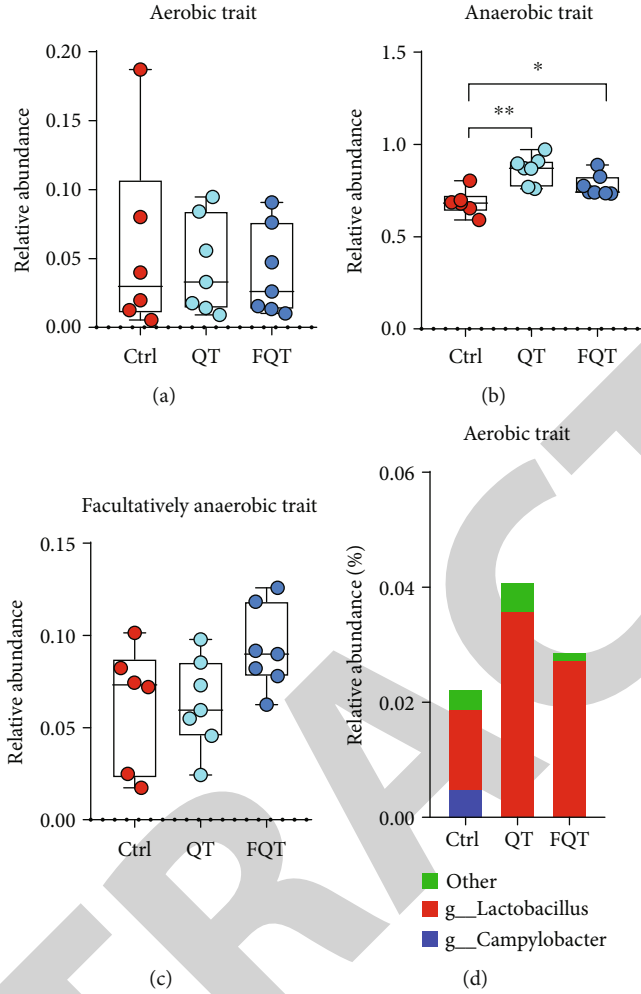


FIGURE 5: Continued.

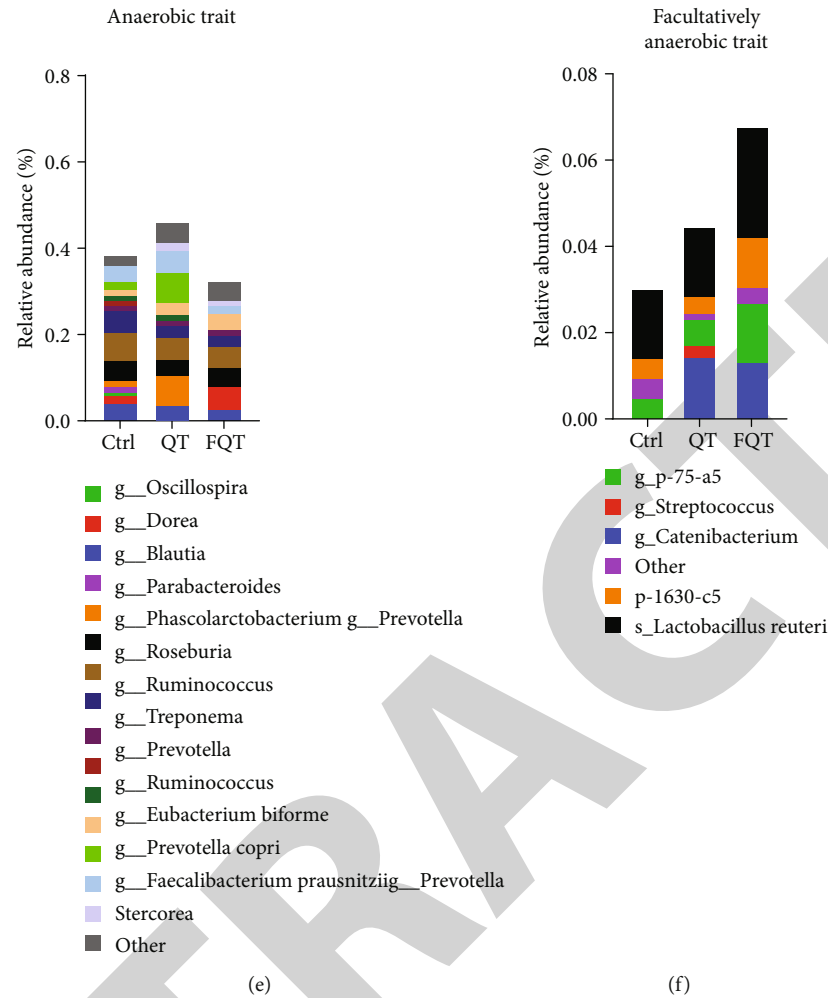
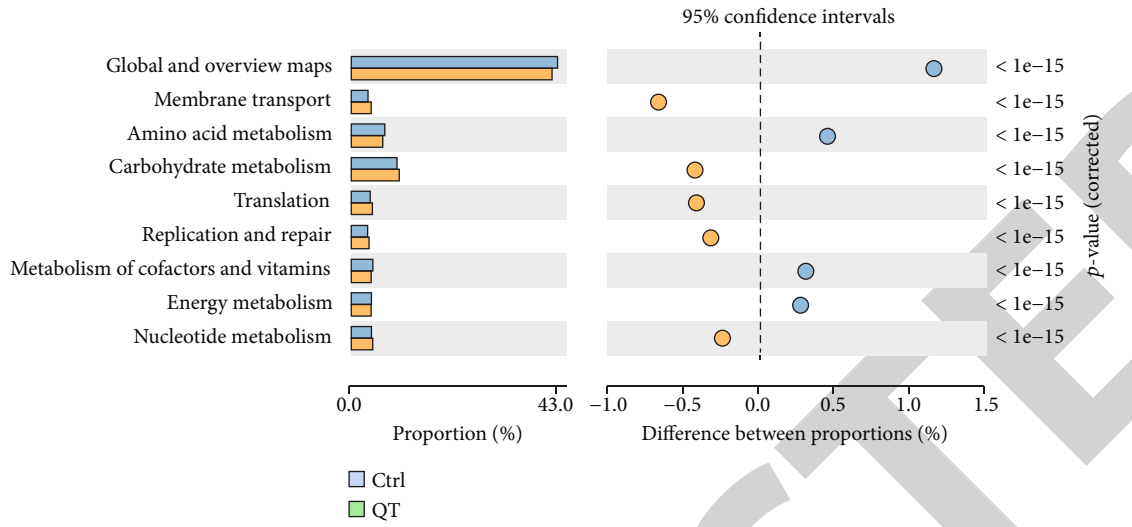


FIGURE 5: The effect of dietary quercetin supplementation and FMT on the phenotype of gut microbiota in weanling piglets. Gut microbial phenotype prediction using BugBase including aerobic (a), anaerobic (b), and facultatively anaerobic (c), respectively. Taxa-contribution plots depicting the relative abundances of trait-possessing taxa at species level including aerobic species (d), anaerobic species (e), and facultatively anaerobic species (f), respectively. \* $P < 0.05$ , \*\* $P < 0.01$ , and \*\*\* $P < 0.001$ . g, genus; s, species; p, phylum.

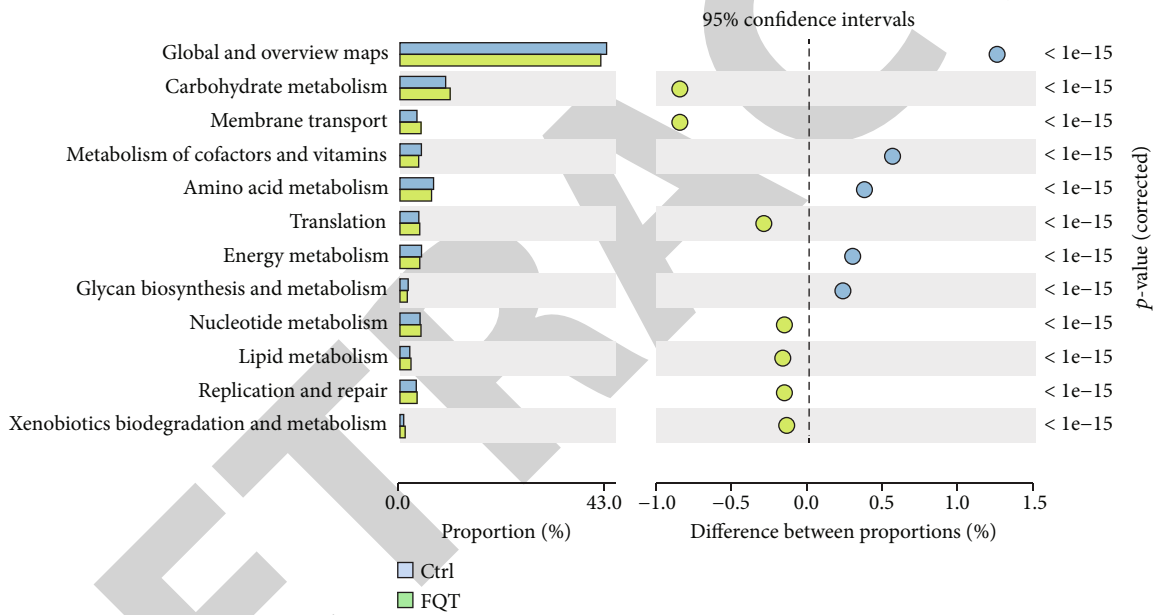
butyric acid ( $P < 0.05$ ) were negatively associated with MDA. *Fibrobacteres* ( $P < 0.05$ ), *Erysipelotrichales* ( $P < 0.05$ ), *Erysipelotrichaceae* ( $P < 0.05$ ), *Erysipelotrichi* ( $P < 0.05$ ), jejunal propionic acid ( $P < 0.01$ ), and colonic propionic acid ( $P < 0.01$ ) were positively associated with GSH/GSSG. For the indices of intestinal integrity, *Fibrobacteres* ( $P < 0.05$ ), jejunal propionic acid ( $P < 0.01$ ), and colonic butyric acid ( $P < 0.05$ ) were positively associated with villus height/villus depth. *Oscillospira* was positively associated with TUNEL\_AOD ( $P < 0.01$ ), but *Clostridium butyricum*, jejunal propionic acid ( $P < 0.01$ ), and colonic propionic acid ( $P < 0.05$ ) were negatively associated with TUNEL\_AOD ( $P < 0.05$ ). *Akkermansia muciniphila* was positively associated with Claudin-1 ( $P < 0.01$ ). Jejunal propionic acid ( $P < 0.01$ ), jejunal butyric acid ( $P < 0.05$ ), and colonic butyric acid ( $P < 0.05$ ) were positively associated with occludin, but *Oscillospira* was negatively associated with occludin ( $P < 0.01$ ). Overall, the identified differential bacteria and increased SCFAs were closely correlated with the indices of antioxidant capacity and intestinal integrity.

#### 4. Discussion

Early weaning stress-induced intestinal damage and further oxidative stress triggered gut microbiota dysbiosis and intestinal function disorder [1]. The gut microbiota dysbiosis emerges as a leading cause of enteric infections and post-weaning diarrhea because of gut microbiota's function on digestion and fermentation of dietary nutrients, maintenance of normal functions of the intestine, regulation of the immune responses, and protection from pathogenic bacteria [1, 38, 39]. Recent studies indicated that dietary antioxidant supplementation can effectively improve redox status, gut microbiota, and intestinal function of piglets in response to early weaning stress [40, 41]. Quercetin, as a flavonoid polyphenol, showed excellent antioxidative capacity tested in vitro for supplementation in pig diet [9]. Studies with rodent models showed that quercetin could reduce obesity and improve the oxidative stress by restoring the gut microbiota dysbiosis [14, 15]. However, there is a lack of research focused on quercetin's beneficial effects on pigs [16]. For



(a)



(b)

FIGURE 6: Continued.

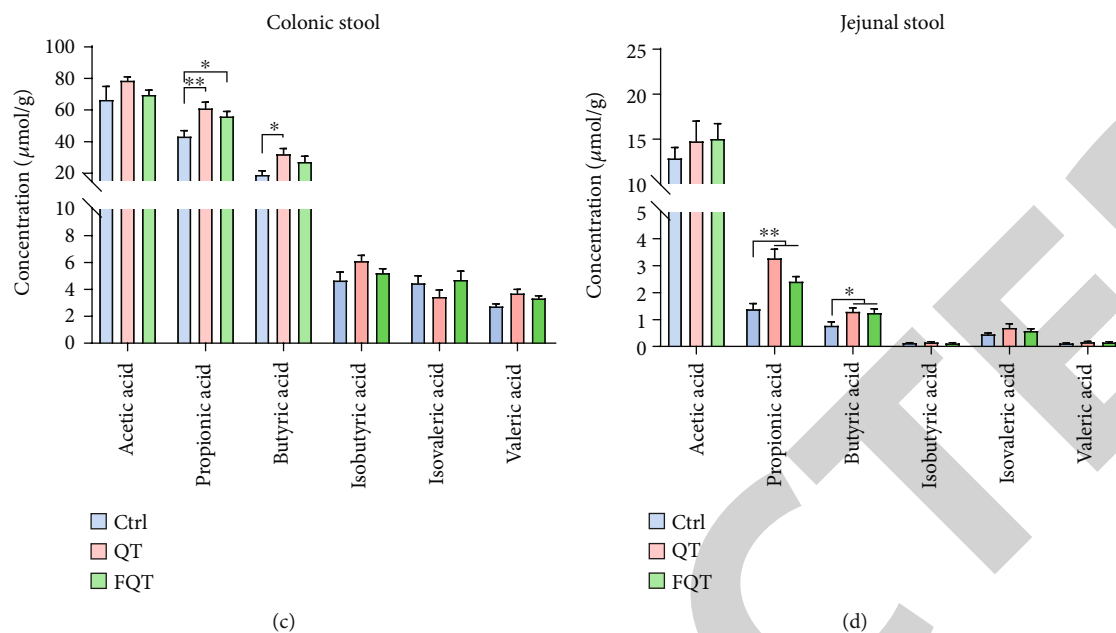
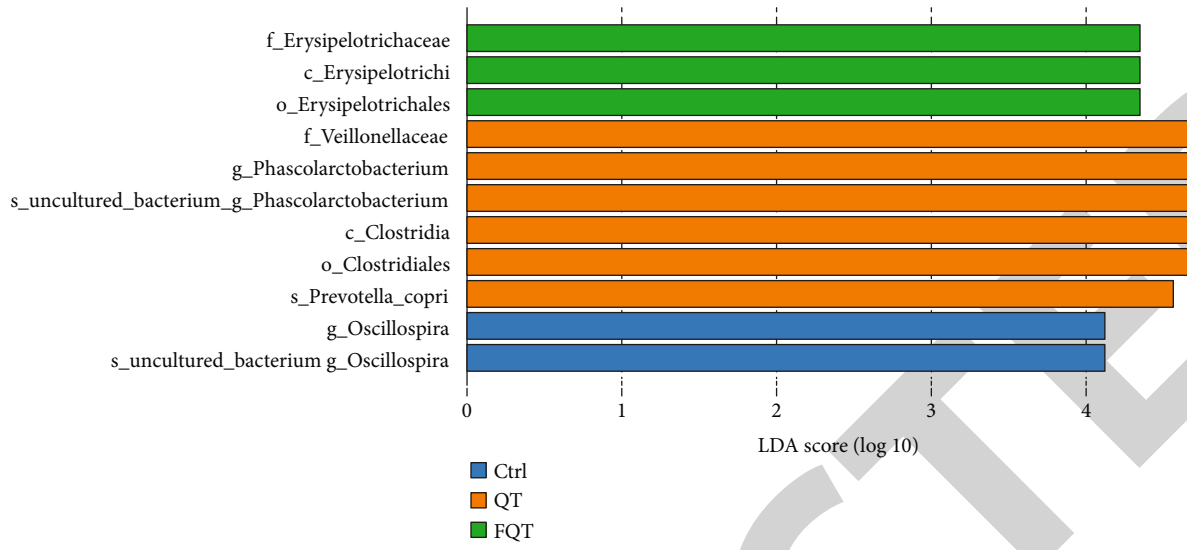


FIGURE 6: The effect of dietary quercetin supplementation and FMT on the function and metabolites of gut microbiota in weanling piglets. The significant difference of functional composition of gut microbiota for Ctrl vs. QT (a) and Ctrl vs. FQT (b). The gut microbial metabolite SCFAs including acetic acid, propionic acid, butyric acid, isobutyric acid, isovaleric acid, and valeric acid in colonic stool and jejunal stool, respectively. \* $P < 0.05$ , \*\* $P < 0.01$ , and \*\*\* $P < 0.001$ .

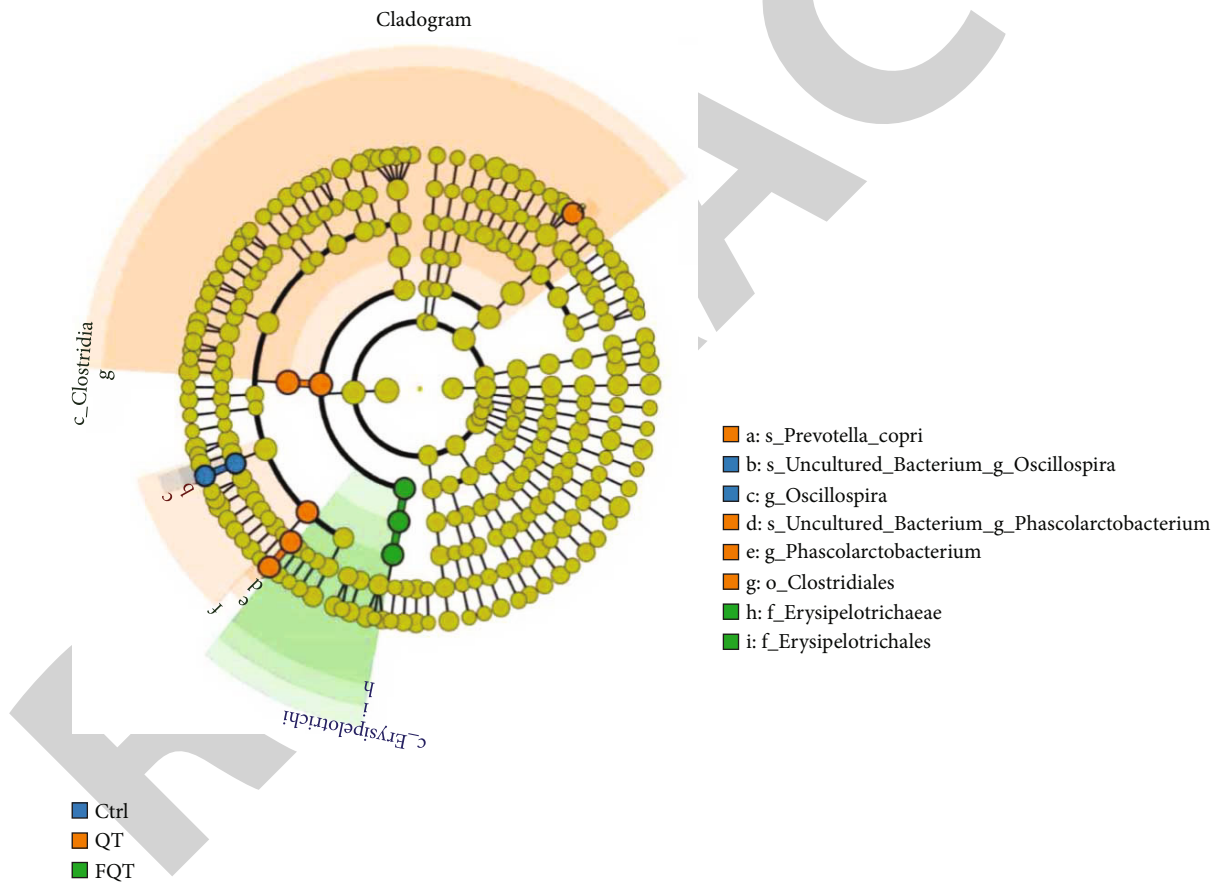
weaning piglets, the weaning stress-induced intestinal inflammation and damage triggered the release of reactive species such as NO and oxygen into the intestinal lumen which result in the apoptosis of intestinal epithelial cell and serve diarrhea [1]. Here, we found that dietary 0.1% quercetin supplementation (1000 mg/kg diet) or FMT from quercetin-treated piglets could improve diarrhea, intestinal barrier function, redox balance, intestinal morphology, and intestinal epithelial apoptosis in weanling piglets. Compared well with our results, the *Psidium guajava* leaf extract with quercetin as active constituent relieved infectious diarrhea induced by enteropathogenic *Escherichia coli* in rats [42]. Weaning transition generally results in small intestine atrophy, reduction in nutrient and electrolyte absorption, and decreased barrier function [1]. We found that dietary quercetin not only improved the barrier function indicated by increased the expression of tight junction protein occludin but also relieved small intestine atrophy by improving villus height, crypt depth, and villus height/crypt depth ratio in the jejunum tissue. These benefits of dietary quercetin were further confirmed by the increased ADG and ADFI. As antioxidant compounds, polyphenols are capable of scavenging free radicals and alleviating intestinal disorders associated with oxidative stress [7]. Given that weaning stress triggers oxidative stress, which is characterized by an imbalance between the production of free radicals and the scavenging ability of the antioxidant defense system, has been involved in the intestinal disorders [1, 4, 5], we further determined the oxidative indices and found that dietary quercetin increased antioxidant capacity of the jejunum indicated by increased T-AOC, CAT, and GSH/GSSG but decreased oxidative metabolite MDA. Similarly, polyphenol extracted from wild *Lonicera caerulea* berry can effectively enhance

antioxidant capacity in vitro and in vivo [43]. Therefore, dietary quercetin could attenuate intestinal damage and redox imbalance in weanling piglets.

Earlier research found that pig cecal microbiota had the capacity to degrade quercetin monoglycosides [44]. Besides, increasing evidences indicated that the gut microbiota contributes to the beneficial effect of polyphenols, especially quercetin [11, 45, 46]. In this study, fecal microbiota from quercetin-treated piglets had a comparable effect on attenuating intestinal damage and redox imbalance, indicating that gut microbiota mediated quercetin's beneficial effect in weanling piglets. These beneficial effects of quercetin-shifted gut microbiota indicated that dietary quercetin could by regulating gut microbiota not just by the direct involvement of antioxidant/anti-inflammatory pathways to play its pharmacological effects. Similarly, Jang et al. demonstrated that cocoa-derived polyphenols can contribute to gut health in association with gut microbiota in pigs [47]. We further discovered the shift of gut microbiota using 16S rDNA high-throughput sequencing and beta diversity presented by PCoA among groups showed that quercetin or FMT from quercetin-treated piglets not only significantly shifted the structure of gut microbiota but also increased their alpha diversity in weanling piglets. This gut microbiota-shift effect had been also found in tea polyphenols, which improved the diversity of gut microbiota dysbiosis induced by antibiotic in mice [48]. Compared with untreated piglets, quercetin increased the SCFA-producing bacteria (*Fibrobacteres*, *Clostridium butyricum*, *Clostridium celatum*, and *Prevotella copri*) [37, 49] and anti-inflammation *Akkermansia muciniphila* [50] but decreased the relative abundances of *Lactobacillus coleohominis*, *Ruminococcus bromii*, and Proteobacteria that is a microbial signature of dysbiosis in gut microbiota



(a)



(b)

FIGURE 7: Continued.

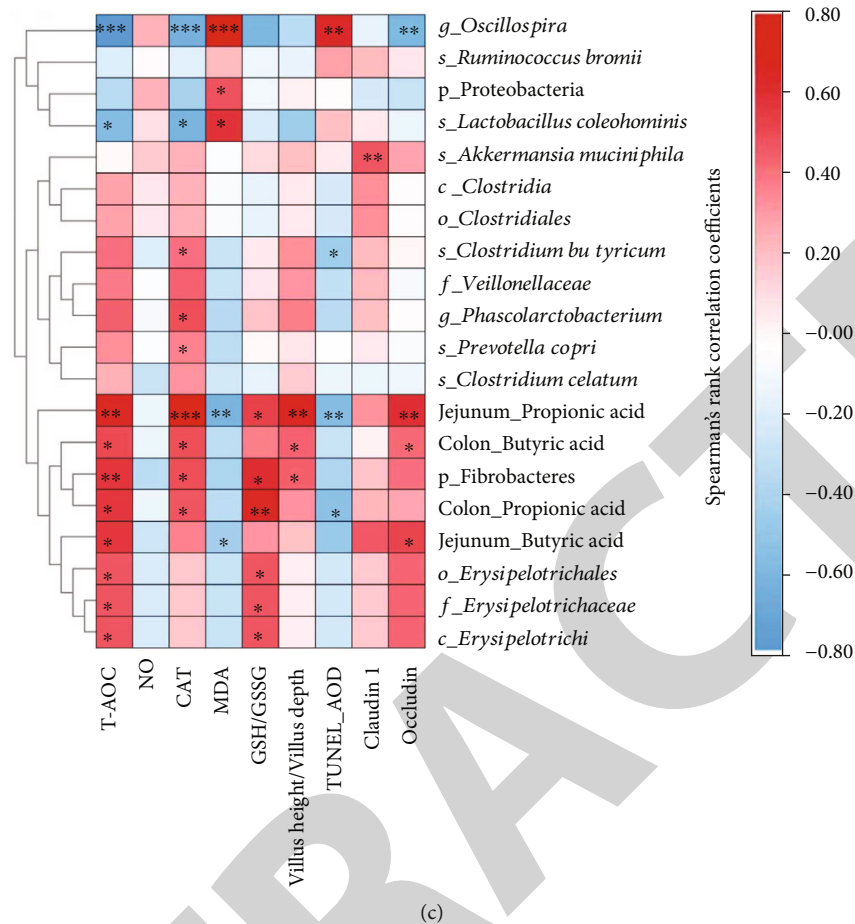


FIGURE 7: The correlation between the identified differential bacteria and the indices of antioxidant capacity and intestinal integrity. (a) LDA value distribution histogram. (b) Cladogram based on LefSe analysis. Circles from inner to outer layers represent taxonomic level from phylum to species. The dots on circles represent a term on corresponding taxonomic level. The size of the dots indicates relative abundance. Species with certain color means the abundance of this species is the highest in corresponding group. (c) Heat map of Spearman's rank correlation coefficient and significant test between the differential bacteria/marker bacteria and the antioxidant indices/intestinal integrity indices, respectively. \* $P < 0.05$ , \*\* $P < 0.01$ , and \*\*\* $P < 0.001$ . p, phylum; c, class; f, family; g, genus; s, species.

[51]. Comparable with quercetin treatment, FMT from quercetin-treated piglets increased the relative abundances of *Akkermansia muciniphila* but decreased the relative abundances of Proteobacteria than those of untreated piglets. These results suggested that dietary quercetin supplementation or FMT from quercetin-treated piglets increased the diversity of gut microbiota and enriched beneficial bacteria but decreased potential pathogenic bacteria in weanling piglets.

Given that reactive oxygen species (ROS) enriched in inflamed intestine is able to trigger gut microbiota dysbiosis [1, 52–54], we employed BugBase, a novel method for analyzing complex microbiome data and providing biologically relevant microbiome phenotype predictions, to determine the effect of quercetin on gut microbiome phenotype [35]. We found that dietary quercetin supplementation or FMT from quercetin-treated piglets significantly increased the relative abundance of anaerobic trait. The gut microbes are extremely oxygen sensitive, and therefore, they have own individual ecological niche along the gut lumen [55, 56]. Nitrate and ROS derived from the intestine confer the aerobic and facultative anaerobic microbes with growth superi-

ority than obligate anaerobic bacteria in the inflamed gut [54, 57]. Therefore, the shift of gut microbiome phenotype was compared well with the enhanced anticapacity by dietary quercetin supplementation or FMT from quercetin-treated piglets. Further analysis of the relative abundances of trait-possessing taxa indicated that genera including *Blautia*, *Dorea*, *Oscillospira*, *Parabacteroides*, *Phascolarctobacterium*, *Dorea*, *Oscillospira*, *Parabacteroides*, *Phascolarctobacterium*, *Prevotella*, *Roseburia*, *Ruminococcus*, *Treponema*, *Prevotella*, *Ruminococcus*, *Eubacterium bifforme*, *Prevotella copri*, *Faecalibacterium prausnitzii*, and *Prevotella stercorea* mainly contribute to the anaerobic trait. The anaerobic environment in hindgut contributes to the fermentation of carbohydrates to produce the SCFAs, which generally benefit host [37, 49]. Therefore, dietary quercetin supplementation or FMT from quercetin-treated piglets increased anaerobic trait and improved the dysbiosis of gut microbiota in weanling piglets.

We further determined the effect of dietary quercetin supplementation or FMT from quercetin-treated piglets on gut microbial function using PICRUST2 and found that they both increased the functions of carbohydrate metabolism,

membrane transport, translation, and nucleotide metabolism but decreased the functions of global and overview maps, metabolism of cofactors and vitamins, amino acid metabolism, and energy metabolism. Among these shifted functions of the gut microbiota, carbohydrate metabolism function is responsible for the gut microbial fermentation of carbohydrates under a strictly anaerobic environment to produce SCFAs which benefit the host [37]. These results were compared well with the increased relative abundance of anaerobic trait, which were further supported by the increased SCFA concentrations in colonic stool and jejunal stool. Propionic acid could improve intestinal barrier function and reduce inflammation and oxidative stress via the signal transducer and activator of transcription 3 signaling pathway in dextran sulfate sodium-induced colitis mice [58]. Besides, stimulation of G-protein-coupled receptor 43 by SCFAs was necessary for the normal resolution of intestinal inflammatory responses [59]. Therefore, the increased SCFAs by dietary quercetin supplementation and FMT may contribute to the improvement of diarrhea and intestinal damage in weanling piglets. This role of SCFAs was further validated by the significantly positive correlation among the increased SCFA concentration and antioxidative indices. Besides, dietary quercetin supplementation or FMT from quercetin-treated piglets shifted bacteria were significantly in correlation with the indices of antioxidant capacity and intestinal integrity. Overall, dietary quercetin supplementation attenuated intestinal damage by improving the antioxidant capacity and regulating gut microbial structure and metabolism in piglets.

## 5. Conclusion

Our results revealed dietary quercetin supplementation attenuated diarrhea and intestinal damage by enhancing the antioxidative capacity and thereby increased gut microbiota's anaerobic trait and carbohydrate metabolism function, which promoted the SCFA production. Further, FMT suggested that gut microbiota mediated the beneficial effect of dietary quercetin supplementation on attenuating diarrhea and intestinal damage in weanling piglets.

## Data Availability

The datasets used and/or analyzed during the current study are available from the corresponding author on reasonable request.

## Conflicts of Interest

The authors declare that there is no conflict of interest regarding the publication of this paper.

## Authors' Contributions

Baoyang Xu and Libao Ma designed the experiment. Wenxia Qin, Yunzheng Xu, Wenbo Yang, Yuwen Chen, Jianan Zhao, and Juncheng Huang performed the experiment and analyzed the experimental data. Baoyang Xu, Wenxia Qin,

and Libao Ma wrote this paper. All authors critically reviewed and approved the manuscript. Baoyang Xu and Wenxia Qin contributed equally to this work.

## Acknowledgments

This work was supported by the National Natural Science Foundation Regional Innovation and Development Joint Fund Project (U20A2055) and School Independent Innovation Fund (2662019PY059).

## Supplementary Materials

*Supplementary 1.* Figure S1: the effect of dietary quercetin supplementation and FMT on the ADFI and ADG of piglets. (a) ADFI at d0-d7 and d7-d14 postweaning of piglets. (b) ADG at d0-d7 and d7-d14 postweaning of piglets. \* $P < 0.05$ , \*\* $P < 0.01$ , and \*\*\* $P < 0.001$ .

*Supplementary 2.* Figure S2: the effect of dietary quercetin supplementation and FMT on the taxon abundance of gut microbiota in weanling piglets. Linked bar plot of the relative abundance of gut microbiota at levels of Family (a), Order (b), and Genus (c), respectively.

*Supplementary 3.* Table S1: ingredients and nutrients composition of the basal diet offered to piglets.

## References

- [1] R. Gresse, F. Chaucheyras-Durand, M. A. Fleury, T. Van de Wiele, E. Forano, and S. Blanquet-Diot, "Gut microbiota dysbiosis in postweaning piglets: understanding the keys to health," *Trends in Microbiology*, vol. 25, no. 10, pp. 851–873, 2017.
- [2] J. M. Campbell, J. D. Crenshaw, and J. Polo, "The biological stress of early weaned piglets," *Journal of Animal Science and Biotechnology*, vol. 4, no. 1, p. 19, 2013.
- [3] J. P. Lallès, P. Bosi, H. Smidt, and C. R. Stokes, "Nutritional management of gut health in pigs around weaning," *The Proceedings of the Nutrition Society*, vol. 66, no. 2, pp. 260–268, 2007.
- [4] J. Yin, M. M. Wu, H. Xiao et al., "Development of an antioxidant system after early weaning in piglets," *Journal of Animal Science*, vol. 92, no. 2, pp. 612–619, 2014.
- [5] L. H. Zhu, K. L. Zhao, X. L. Chen, and J. X. Xu, "Impact of weaning and an antioxidant blend on intestinal barrier function and antioxidant status in pigs," *Journal of Animal Science*, vol. 90, no. 8, pp. 2581–2589, 2012.
- [6] S. Yazdankhah, K. Rudi, and A. Bernhoft, "Zinc and copper in animal feed - development of resistance and co-resistance to antimicrobial agents in bacteria of animal origin," *Microbial Ecology in Health and Disease*, vol. 25, 2014.
- [7] T. Hussain, B. Tan, Y. Yin, F. Blachier, M. C. Tossou, and N. Rahu, "Oxidative stress and inflammation: what polyphenols can do for us?," *Oxidative Medicine and Cellular Longevity*, vol. 2016, Article ID 7432797, 9 pages, 2016.
- [8] M. Harwood, B. Danielewska-Nikiel, J. F. Borzelleca, G. W. Flamm, G. M. Williams, and T. C. Lines, "A critical review of the data related to the safety of quercetin and lack of evidence of in vivo toxicity, including lack of genotoxic/carcinogenic

- properties,” *Food and Chemical Toxicology*, vol. 45, no. 11, pp. 2179–2205, 2007.
- [9] H. Vergauwen, S. Prims, J. Degroote et al., “In vitro investigation of six antioxidants for pig diets,” *Antioxidants*, vol. 5, no. 4, 2016.
- [10] R. Santangelo, A. Silvestrini, and C. Mancuso, “Ginsenosides, catechins, quercetin and gut microbiota: current evidence of challenging interactions,” *Food and Chemical Toxicology*, vol. 123, pp. 42–49, 2019.
- [11] U. Shabbir, M. Rubab, E. B. Daliri, R. Chelliah, A. Javed, and D. H. Oh, “Curcumin, quercetin, catechins and metabolic diseases: the role of gut microbiota,” *Nutrients*, vol. 13, no. 1, p. 206, 2021.
- [12] P. S. Cooke, T. E. Spencer, F. F. Bartol, and K. Hayashi, “Uterine glands: development, function and experimental model systems,” *Molecular Human Reproduction*, vol. 19, no. 9, pp. 547–558, 2013.
- [13] M. C. Wu and P. J. Dziuk, “Ovarian influence on uterine growth in prepubertal gilts,” *Journal of Animal Science*, vol. 66, no. 11, pp. 2893–2898, 1988.
- [14] L. Zhao, Q. Zhang, W. Ma, F. Tian, H. Shen, and M. Zhou, “A combination of quercetin and resveratrol reduces obesity in high-fat diet-fed rats by modulation of gut microbiota,” *Food & Function*, vol. 8, no. 12, pp. 4644–4656, 2017.
- [15] Z. Hong and M. Piao, “Effect of quercetin monoglycosides on oxidative stress and gut microbiota diversity in mice with dextran sodium sulphate-induced colitis,” *BioMed Research International*, vol. 2018, Article ID 8343052, 7 pages, 2018.
- [16] M. Luehring, R. Blank, and S. Wolffram, “Vitamin E-sparing and vitamin E-independent antioxidative effects of the flavonol quercetin in growing pigs,” *Animal Feed Science and Technology*, vol. 169, no. 3, pp. 199–207, 2011.
- [17] A. Khoruts and M. J. Sadowsky, “Understanding the mechanisms of faecal microbiota transplantation,” *Nature Reviews Gastroenterology & Hepatology*, vol. 13, no. 9, pp. 508–516, 2016.
- [18] S. Dong, M. Zhu, K. Wang et al., “Dihydromyricetin improves DSS-induced colitis in mice via modulation of fecal-bacteria-related bile acid metabolism,” *Pharmacological Research*, vol. 171, article 105767, 2021.
- [19] M. Wu, P. Li, Y. An et al., “Phloretin ameliorates dextran sulfate sodium-induced ulcerative colitis in mice by regulating the gut microbiota,” *Pharmacological Research*, vol. 150, article 104489, 2019.
- [20] P. Ader, A. Wessmann, and S. Wolffram, “Bioavailability and metabolism of the flavonol quercetin in the pig,” *Free Radical Biology & Medicine*, vol. 28, no. 7, pp. 1056–1067, 2000.
- [21] J. Degroote, H. Vergauwen, N. Van Noten et al., “The effect of dietary quercetin on the glutathione redox system and small intestinal functionality of weaned piglets,” *Antioxidants*, vol. 8, no. 8, p. 312, 2019.
- [22] B. Xu, W. Qin, Y. Yan et al., “Gut microbiota contributes to the development of endometrial glands in gilts during the ovary-dependent period,” *Journal of Animal Science and Biotechnology*, vol. 12, no. 1, p. 57, 2021.
- [23] G. F. Yi, J. A. Carroll, G. L. Allee et al., “Effect of glutamine and spray-dried plasma on growth performance, small intestinal morphology, and immune responses of *Escherichia coli* K88<sup>+</sup>-challenged weaned pigs,” *Journal of Animal Science*, vol. 83, no. 3, pp. 634–643, 2005.
- [24] Y. Gavrieli, Y. Sherman, and S. A. Ben-Sasson, “Identification of programmed cell death in situ via specific labeling of nuclear DNA fragmentation,” *The Journal of Cell Biology*, vol. 119, no. 3, pp. 493–501, 1992.
- [25] C. A. Schneider, W. S. Rasband, and K. W. Eliceiri, “NIH Image to Image J: 25 years of image analysis,” *Nature Methods*, vol. 9, no. 7, pp. 671–675, 2012.
- [26] B. Xu, Y. Yan, B. Yin et al., “Dietary glycyl-glutamine supplementation ameliorates intestinal integrity, inflammatory response, and oxidative status in association with the gut microbiota in LPS-challenged piglets,” *Food & Function*, vol. 12, no. 8, pp. 3539–3551, 2021.
- [27] A. M. Bolger, M. Lohse, and B. Usadel, “Trimmomatic: a flexible trimmer for Illumina sequence data,” *Bioinformatics*, vol. 30, no. 15, pp. 2114–2120, 2014.
- [28] A. Kechin, U. Boyarskikh, A. Kel, and M. Filipenko, “cutPrimers: a new tool for accurate cutting of primers from reads of targeted next generation sequencing,” *Journal of Computational Biology*, vol. 24, no. 11, pp. 1138–1143, 2017.
- [29] R. C. Edgar, “UPARSE: highly accurate OTU sequences from microbial amplicon reads,” *Nature Methods*, vol. 10, no. 10, pp. 996–998, 2013.
- [30] R. C. Edgar, B. J. Haas, J. C. Clemente, C. Quince, and R. Knight, “UCHIME improves sensitivity and speed of chimera detection,” *Bioinformatics*, vol. 27, no. 16, pp. 2194–2200, 2011.
- [31] C. Quast, E. Pruesse, P. Yilmaz et al., “The SILVA ribosomal RNA gene database project: improved data processing and web-based tools,” *Nucleic Acids Research*, vol. 41, pp. D590–D596, 2013.
- [32] T. Z. DeSantis, P. Hugenholtz, N. Larsen et al., “Greengenes, a chimera-checked 16S rRNA gene database and workbench compatible with ARB,” *Applied and Environmental Microbiology*, vol. 72, no. 7, pp. 5069–5072, 2006.
- [33] G. M. Douglas, V. J. Maffei, J. R. Zaneveld et al., “PICRUSt2 for prediction of metagenome functions,” *Nature Biotechnology*, vol. 38, no. 6, pp. 685–688, 2020.
- [34] Y. Yan, B. Xu, B. Yin et al., “Modulation of gut microbial community and metabolism by dietary glycyl-glutamine supplementation may favor weaning transition in piglets,” *Frontiers in Microbiology*, vol. 10, article 3125, 2019.
- [35] T. Ward, J. Larson, J. Meulemans et al., “BugBase predicts organism-level microbiome phenotypes,” 2017.
- [36] D. H. Parks, G. W. Tyson, P. Hugenholtz, and R. G. Beiko, “STAMP: statistical analysis of taxonomic and functional profiles,” *Bioinformatics*, vol. 30, no. 21, pp. 3123–3124, 2014.
- [37] G. den Besten, K. van Eunen, A. K. Groen, K. Venema, D.-J. Reijngoud, and B. M. Bakker, “The role of short-chain fatty acids in the interplay between diet, gut microbiota, and host energy metabolism,” *Journal of Lipid Research*, vol. 54, no. 9, pp. 2325–2340, 2013.
- [38] C. G. Buffie and E. G. Pamer, “Microbiota-mediated colonization resistance against intestinal pathogens,” *Nature Reviews Immunology*, vol. 13, no. 11, pp. 790–801, 2013.
- [39] N. Kamada, S. U. Seo, G. Y. Chen, and G. Nunez, “Role of the gut microbiota in immunity and inflammatory disease,” *Nature Reviews Immunology*, vol. 13, no. 5, pp. 321–335, 2013.
- [40] J. Xu, C. Xu, X. Chen et al., “Regulation of an antioxidant blend on intestinal redox status and major microbiota in early weaned piglets,” *Nutrition*, vol. 30, no. 5, pp. 584–589, 2014.



## Review Article

# Emerging Pathological Engagement of Ferroptosis in Gut Diseases

Weihua Gao <sup>1,2,3</sup> Ting Zhang <sup>1,3,4</sup> and Hao Wu <sup>1,3,4</sup>

<sup>1</sup>Hubei Hongshan Laboratory, Wuhan, Hubei 430070, China

<sup>2</sup>State Key Laboratory of Agricultural Microbiology, College of Animal Science and Technology, Huazhong Agricultural University, Wuhan 430070, China

<sup>3</sup>Interdisciplinary Sciences Institute, Huazhong Agricultural University, Wuhan, Hubei 430070, China

<sup>4</sup>State Key Laboratory of Agricultural Microbiology, College of Veterinary Medicine, Huazhong Agricultural University, Wuhan 430070, China

Correspondence should be addressed to Hao Wu; [whao.1988@mail.hzau.edu.cn](mailto:whao.1988@mail.hzau.edu.cn)

Weihua Gao and Ting Zhang contributed equally to this work.

Received 18 June 2021; Accepted 6 October 2021; Published 25 October 2021

Academic Editor: Alin Ciobica

Copyright © 2021 Weihua Gao et al. This is an open access article distributed under the Creative Commons Attribution License, which permits unrestricted use, distribution, and reproduction in any medium, provided the original work is properly cited.

Inflammatory bowel disease (IBD), including ulcerative colitis and Crohn's disease, is mainly characterized by chronic and progressive inflammation that damages the gastrointestinal mucosa. Increasing studies have enlightened that dysregulated cell death occurs in the inflamed sites, leading to the disruption of the intestinal barrier and aggravating inflammatory response. Ferroptosis, a newly characterized form of regulated cell death, is driven by the lethal accumulation of lipid peroxides catalyzed by cellular free iron. It has been widely documented that the fundamental features of ferroptosis, including iron deposition, GSH exhaustion, GPX4 inactivation, and lipid peroxidation, are manifested in the injured gastrointestinal tract in IBD patients. Furthermore, manipulation of the critical ferroptotic genes could alter the progression, severity, or even morbidity of the experimental colitis. Herein, we critically summarize the recent advances in the field of ferroptosis, focusing on interpreting the potential engagement of ferroptosis in the pathogenesis of IBD. Moreover, we are attempting to shed light on a perspective insight into the possibility of targeting ferroptosis as novel therapeutic designs for the clinical intervention of these gastrointestinal diseases.

## 1. Introduction

Ferroptosis, a novel nonapoptotic form of regulated cell death driven by the lethal accumulation of iron-catalyzing lipid peroxides, was firstly defined by Dixon and colleagues in 2012 [1]. Since then, ferroptosis has been widely characterized in a wide spectrum of cultured cells and animal models. Distinct from other well-understood forms of regulated cell death, ferroptosis relies on the dedicated executing machinery constituted of the peroxidation of polyunsaturated fatty acid- (PUFA-) containing phospholipids (PLs), the availability of redox-active iron, and the inactivation of the lipid peroxide repair system [2]. Morphologically, ferroptosis is typically manifested by the shrinkage of mitochondria with increased membrane density and reduction

in mitochondrial cristae [1, 3]. However, the hallmarks of apoptotic cell death, including plasma membrane blebbing and chromatin condensation, as well as the morphological character of necroptosis, swelling of cytoplasmic organelles, are rarely observed during ferroptotic cell death [4, 5]. Biochemically, the cytochrome c release, caspase activation, and poly(ADP-ribose) polymerase 1 cleavage (the biochemical hallmarks of apoptosis), as well as the activation of receptor-interacting protein 1, receptor-interacting protein 3, and mixed lineage kinase-like (the biochemical hallmarks of necroptosis), are dispensable for ferroptosis.

Over the years, extensive progress has been achieved in the field of ferroptosis. Specifically, the identification of potent inducers (e.g., Erastin, RSL3, FIN56, and FINO2) and specific inhibitors (e.g., DFO, Fer-1, and Lip-1) and

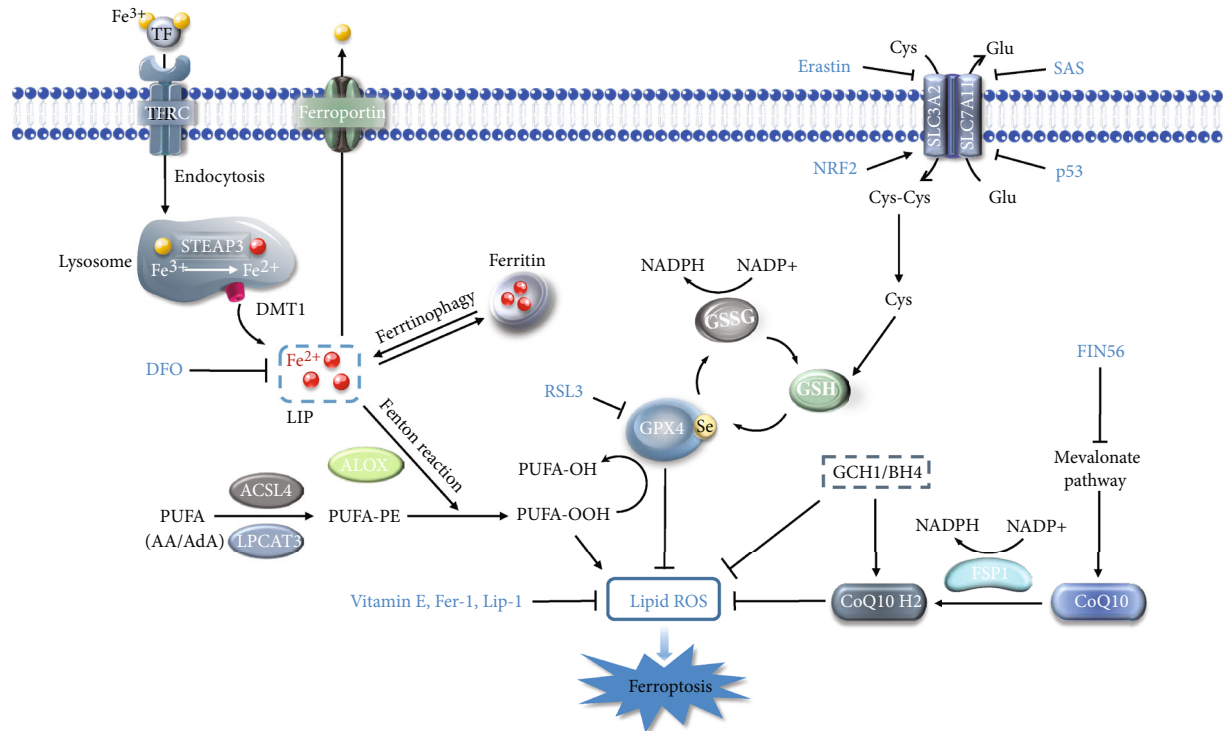


FIGURE 1: Key regulators and major signaling circuits of ferroptosis. Iron homeostasis directly influences ferroptotic sensitivity. Once absorbed by cells, ferric iron ( $\text{Fe}^{3+}$ ) can be reduced into ferrous iron ( $\text{Fe}^{2+}$ ) and chelated by ferritin or existed as labile iron. The build-up of LIP directly facilitates lipid peroxidation of PUFAs (especially AA or AdA) containing PE *via* the Fenton reaction. ACSL4 and LPCAT3 are indispensable for motivating and esterifying the PUFAs into PE for the next peroxidation. LOX families also catalyze the dioxygenation of PUFA-PE, which ultimately lead to the accumulation of lipid peroxides and cell membrane rupture. GPX4 acts as a master regulator of ferroptosis by detoxifying lipid peroxides into lipid alcohol in support of its cofactor GSH. GSH synthesis relies on multiple processes, especially the cysteine supply mediated by system  $\text{X}_C^-$ . Besides, the FSP1-CoQ10-NADPH axis and GCH1-BH4 axis function as lipophilic antioxidant systems parallel to the GPX4-GSH axis. The inducers and inhibitors of ferroptosis are indicated in red.

the characterization of core regulatory components (e.g., SLC7A11, GPX4, FSP1, P53, and NRF2) support the fundamental understanding of the ferroptotic cell death (Figure 1). Moreover, emerging pieces of evidence suggest the pathological implication of dysregulated ferroptosis in the occurrence or progression of various human diseases. Herein, we summarize the recent advances of ferroptosis and dissect the potential engagement of ferroptosis in the pathogenesis of gastrointestinal diseases, attempting to elaborate the possibility of targeting ferroptosis in the therapeutic designs for the clinical intervention of gastrointestinal diseases.

## 2. Ferroptosis

Numerous pioneering studies have enlightened the fundamental characteristics of ferroptosis prior to the concept termed. In 1955, Eagle found that cystine deprivation triggers cell death with a distinct microscopic morphology compared to the deprivation of other amino acids [6, 7]. In the following decades, increasing pieces of evidence emerged that cystine deprivation leads to oxidative cell death in fibroblasts [8], embryonic cortical neurons [9, 10], and hepatocytes [11]. Besides, this cell death could be mitigated by the lipophilic antioxidant vitamin E [8] and the iron chelator deferoxamine (DFO) [12].

In 2003, Dolma and colleagues performed a lethal compound screen of genotype-selective antitumor agents and found that Erastin performs specific lethal cytotoxicity of engineered cells expressing oncogenic RAS. However, this cell death sharply differs from apoptosis. Specifically, neither caspase activation nor nuclear fragmentation was observed [4]. In 2008, two RAS-selective lethal compounds, RSL3 and RSL5, were identified in another compound screen [13]. RSL3 and RSL5 induce similar nonapoptotic cell death. Importantly, RSL3- and Erastin-mediated cell death could be alleviated by DFO and vitamin E but not by the apoptosis inhibitor z-VAD or necroptosis inhibitor necrostatin-1. Therefore, ferroptosis was coined to describe this iron- and lipid peroxidation-dependent cell death [1].

**2.1. Ferroptosis Inducers and Inhibitors.** Potent ferroptosis inducers and specific ferroptosis inhibitors have been identified during the last decade. According to the respective mechanisms of action, ferroptosis inducers are currently classified into four groups:

(1) *Glutathione (GSH) Scavengers.* Erastin depletes GSH by suppressing cystine uptake *via* restraining the cystine/glutamine antiporter system  $\text{X}_C^-$  [13]. Additionally, two metabolically stable derivatives, Piperazine Erastin [14] and

Imidazole Ketone Erastin [15], equip better water solubility and perform better antitumor activity in the xenograft tumor model. Likewise, sulfasalazine [16], sorafenib [17], and artesunate [18] also drive ferroptosis through exhausting GSH.

(2) *Glutathione Peroxidase 4 (GPX4) Inhibitors*. GPX4 is the sole peroxidase for catalyzing lipid peroxides into the corresponding lipid alcohols with the assistance of its cofactor GSH [19]. This class of inducers, including RSL3, Altretamine [20], and DPI17 [14], could directly inhibit GPX4.

(3) *FIN56*. FIN56 initiates ferroptosis via two distinct mechanisms. FIN56 induces GPX4 degradation in an elusive manner. Alternatively, FIN56 activates squalene synthase to deplete coenzyme Q10 (CoQ10) in the mevalonate pathway and thus impair the cellular antioxidant capacity [21].

(4) *FINO2*. FINO2 represents a unique type of organic lipophilic peroxide, which oxidizes cellular labile iron preferentially, leading to extensive oxidation of PUFAs. In addition, indirect inactivation of GPX4 also contributes to the lethal potency of FINO2 [22].

Similarly, the specific ferroptosis inhibitors could antagonize ferroptosis *via* different mechanisms. Firstly, iron chelators could confine labile free iron, leading to the deceleration of lipid peroxidation. Secondly,  $\beta$ -mercaptoethanol subverts Erastin-induced ferroptosis through forming disulfide with cystine and facilitating cystine uptake bypass system  $X_C^-$  [23]. Thirdly, radical-trapping antioxidants, including vitamin E and aromatic amine-based ferrostatin-1 (Fer-1) and lipoxstatin-1 (Lip-1), could halt the cascade of propagating lipid radicals and protect lipids from autoxidation [3, 24]. Fourthly, lipoxygenase (LOX) inhibitors, such as Zileuton (5-LOX inhibitor), Baicalein (12-LOX inhibitor), and NDGA (general LOX inhibitor), could counteract lipid peroxidation catalyzed by LOXs [25, 26]. Moreover, thiazolidinedione, the inhibitor of acyl-CoA synthetase long-chain family member 4 (ACSL4), represses the activation of PUFA esterification and consequently reduces the oxidizable substrates addicted by ferroptosis [27]. The identification of these inducers and inhibitors supported the primary understanding of the principal program of ferroptosis.

**2.2. Iron and Ferroptosis.** The trace element iron is critically important for tremendous biochemical processes, including oxygen transport, DNA synthesis, transcription, damage repair, redox reactions, and mitochondrial electron transport [28]. Iron also acts as a redox-active toxicant when excessive labile iron is available, which catalyzes reactive oxygen species (ROS) generation *via* the Fenton reaction. In general, most circulating iron is bound to the transferrin (TF) in the form of ferric iron ( $Fe^{3+}$ ). TF-Fe is captured by transferrin receptor 1 (TFR1) on the cell membrane and absorbed through endocytosis.  $Fe^{3+}$  is then escaped from the TF, reduced to ferrous iron ( $Fe^{2+}$ ) mediated by the endosome reductase (e.g., six-transmembrane epithelial antigen

of the prostate 3), and subsequently released to the cytosol by divalent metal transporter 1 (DMT1/SLC11A2). Cytosolic iron is persistently sequestered by ferritin or transported into mitochondria for the biosynthesis of the iron-sulfur cluster or heme, two vital iron-containing cofactors for hundreds of proteins. The excessive cellular iron could be exported by ferroportin (FPN) [28].

Iron-dependent lipid peroxidation is one of the most fundamental characteristics of ferroptosis. It is thus expectable that manipulation of cellular iron metabolism or availability could change the ferroptotic sensitivity. Importantly, knockdown of iron regulatory proteins 1 and 2 (IRP1/2), the master cellular iron sensors and regulators, sharply decreases the labile iron pool (LIP) and antagonizes ferroptosis [1, 29]. Similarly, knockdown of TFR1 or ectopic overexpression of FPN impairs effective intracellular iron accumulation and abrogates ferroptosis [30, 31]. In addition, phosphorylation of heat shock protein beta-1 was reported to combat Erastin-induced ferroptosis by hindering TFR1 traffic through sustaining actin filaments and thus antagonizing iron uptake [32]. Recent studies revealed that ferritinophagy, a selective autophagy to degrade ferritin for iron motivation, plays a crucial role in ferroptosis initiation. Nuclear receptor coactivator 4 (NCOA4) acts as the selective cargo receptor responsible for recruiting and delivering ferritin to lysosomes for degradation [33]. Knockdown of autophagy-related genes (e.g., *Atg5* and *Atg7*) or ferritinophagy-specific *Ncoa4* impairs ferritinophagy and reduces the cellular labile iron, leading to ferroptotic insensitivity in various cell lines [34, 35]. Burgeoning pieces of evidence have put forward an indispensable involvement of iron in ferroptosis. At least two potential mechanisms including the Fenton reaction and activation of the enzymatic activity of iron-containing LOXs are implicated in iron facilitating the ferroptotic program [36].

**2.3. Lipid Peroxides and Ferroptosis.** As the cornerstone of cell membranes, lipid composition directly determines the biomembrane properties including fluidity, permeability, and integrity [37]. Increasing studies suggest that lipid peroxidation serves as the ultimate executor for ferroptotic cell death, although the exact mechanism is vague [38]. Lipid peroxidation leads to lipidomic alteration and compromise of the biomembrane properties (increased membrane curvature and permeability, formation of structured lipid pores, and micellization) [39, 40], which initiate exacerbating feedback to destruct biomembrane structure and dynamics. Furthermore, 4-hydroxy-2-nonenals (4-HNEs) and malondialdehydes (MDAs), two major secondary lipid peroxidation products generated by the decomposition of oxidized PUFAs, could bring out abnormal covalent modifications in proteins and nucleic acids, which could also initiate the death program [41, 42].

PUFAs, rather than saturated fatty acids or monounsaturated fatty acids (MUFAs), are preferentially oxidized by reactive radicals [26, 43, 44]. By utilizing redox lipidomic assay, it was reported that only PLs containing PUFAs (especially arachidonoyl (AA) and adrenoyl (AdA)) are the lipid precursors to undergo peroxidation preceding ferroptosis

[45]. Exposure to exogenous PUFAs increases ferroptotic sensitivity. In striking contrast, supplementation of deuterated PUFAs, which are inactive to hydrogen abstraction, or administration of exogenous MUFAs (oleic acid (OA)), which competitively reduce PUFA incorporation into PLs, remodels the lipidomic composition, decelerates the accumulation of lipid peroxides, and thus potently protects cells from ferroptosis [45–47]. Furthermore, pharmacological or genetic suppression of lysophosphatidylcholine acyltransferase 3 (*Lpcat3*) and *Acs14*, which are responsible for PUFA activation and subsequent esterification for membrane insertion, sharply prevents ferroptosis [1, 27, 45, 48, 49].

LOXs are nonheme, iron-containing dioxygenases with diverse isoforms, which oxygenate AA at different carbon positions [43, 50]. Early studies had demonstrated that deficiency or silence of arachidonate-15-lipoxygenase (*Alox15*) (encoding 12/15-LOX) or arachidonate-15-lipoxygenase type B (*Alox15b*) and arachidonate lipoxygenase 3 (*Alox3*) leads to dramatic resistance to GSH depletion-induced cell death [47, 51, 52]. Moreover, supplementation of 5-, 12-, and 15-hydroperoxyeicosatetraenoic acid, the production of LOX catalysis, accelerates the ferroptotic program elicited by GPX4 depletion [5]. Furthermore, inactivation of *Alox15* is not sufficient to rescue the embryonic lethality of *Gpx4*<sup>-/-</sup> mice [5, 50, 53]. One potential assumption is that LOX-mediated lipid peroxidation mainly contributes to the initial build-up of the cellular lipid peroxide pool, while lipid autoxidation dominates the subsequent ferroptotic execution [25]. The alternative assumption is that other enzymes exist to catalyze lipid peroxidation bypass LOXs. Specifically, it was recently reported that NADPH-cytochrome P450 reductase (POR) and NADH-cytochrome b5 reductase (CYB5R1) could mediate the peroxidation of PUFAs of membrane PLs. By transferring electrons from the donor NADPH, POR and CYB5R1 support the generation of hydrogen peroxides, which subsequently react with iron to generate reactive hydroxyl radicals for the PUFA peroxidation [54, 55].

**2.4. Antioxidant Defense Systems and Ferroptosis.** To date, three major antioxidant defense systems have been elaborated to protect cells from ferroptosis including the GPX4-GSH axis, FSP1-CoQ10-NADPH axis, and GCH1-BH4 axis.

The selenoprotein GPX4 is the sole peroxidase that reduces the deleterious lipid peroxides to nontoxic lipid alcohols within biomembranes at the cost of oxidizing two GSH to GSSG [14, 56]. GSH, a thiol-containing tripeptide ( $\gamma$ -glutamate-cysteine-glycine) serving as an indispensable cofactor of GPX4, is recycled by NAD(P)H and glutathione reductase [57]. In this regard, disruption of GSH synthesis could initiate ferroptosis in diverse circumstances. Pharmacological inhibition of system X<sub>C</sub><sup>-</sup>, the antiporter composed of solute carrier family 7 member 11 (SLC7A11) and solute carrier family 3 member 2 (SLC3A2), essential for exchanging intracellular glutamate and extracellular cystine, was reported to trigger ferroptosis in multiple types of cultured cells [1, 58, 59]. Notably, P53 facilitates ferroptosis by transcriptionally downregulating SLC7A11 [60]. CD8<sup>+</sup> T cells enhance ferroptosis of tumor cells through releasing inter-

feron gamma (IFN $\gamma$ ) and repressing the expression of SLC3A2 and SLC7A11 in tumor cells [61]. Moreover, nuclear factor erythroid 2-related factor 2 (NRF2) was reported to combat ferroptotic cell death *via* upregulating SLC7A11 and thus facilitating GSH synthesis [62]. Collaboratively, these studies illuminate the core role of the GPX4-GSH axis in scavenging lipid peroxides and counteracting ferroptosis.

The FSP1-CoQ10-NADPH pathway was recently characterized to compensate and synergize with the canonical GPX4-GSH pathway to detoxify lipid peroxides and defend against ferroptosis. Two independent studies based on genome-wide CRISPR-Cas9 screening for genes against ferroptosis in the absence of GPX4 coincidentally identified that the flavoprotein ferroptosis suppressor protein 1 (FSP1, previously known as AIFM2) restrains ferroptosis by catalyzing the reduction of ubiquinone (namely, CoQ10) to ubiquinol in an NADPH-dependent manner [63, 64]. Intriguingly, CoQ10 is mainly generated from the mevalonate pathway, which has been demonstrated to dominate ferroptotic sensitivity. Specifically, the mevalonate-derived isopentenyl pyrophosphate can modulate the translation of selenocysteine-containing GPX4 by stabilizing the Sec-specific tRNA expression [65].

More recently, a novel mechanistic scheme accounting for cell endogenous protection from ferroptosis converges on the GCH1-BH4 axis. By utilizing whole-genome CRISPR-Cas9 screening, GTP cyclohydrolase-1 (GCH1) was nominated as a key factor to antagonize ferroptosis [66, 67]. The natural antioxidant tetrahydrobiopterin (BH4) generated by GCH1 was found to suppress ferroptosis through selectively protecting membrane PLs with two PUFA tails from oxidative degradation or alternatively promoting CoQ10 biosynthesis, which is crucial for the elimination of lipid peroxides. The proposal of the GCH1-BH4 axis provides further insights into ferroptosis resistance.

### 3. Ferroptosis and Inflammatory Bowel Disease

IBD, including ulcerative colitis (UC) [68] and Crohn's disease (CD) [69], is mainly characterized by severe gastrointestinal tract inflammation and mucosal destruction. UC is primarily disordered in the large intestine, featuring continuous mucosal inflammation beginning in the rectum and then generally extending proximally in gut tracts. Rectal bleeding, diarrhea, and abdominal pain, accompanied with ulcerations and erythema formation, are widely manifested in UC. CD principally occurs in the ileum and colon, and the typical clinical manifestations include abdominal pain, chronic diarrhea, weight loss, and fatigue. Although the exact etiology of IBD is not well understood, a combination of genetic susceptibility, harmful environmental factors, deregulated host immune system, and gut microbiota dysbiosis has been proved to be associated with the pathogenesis of IBD [70]. With the rapidly rising incidence and prevalence, IBD has emerged as a global health challenge, which will bring a considerable rise in healthcare costs [71].

The monolayer intestinal epithelial cells (IECs) covering the intestinal wall play a critical role in nutrient absorption

and physical separation of the hosts from the harmful gut bacteria in the intestinal lumen. IECs are composed of multiple types of epithelial cells that differentiate from intestinal stem cells residing in the crypts, including nutrient-absorptive enterocytes, mucin glycoprotein-producing goblet cells, antimicrobial peptide-secreting Paneth cells, and hormone-secreting enteroendocrine cells [72]. It is well documented that apoptotic cell death has been observed in these different types of epithelial cells at the inflamed sites in patients with UC and CD [73, 74]. Furthermore, induction of epithelial cell apoptosis has also been evident in independent animal colitis models [75–77]. In the meantime, the expression of apoptosis-associated proteins such as the Fas cell surface death receptor, Fas ligand, BCL2 associated X, and tumor protein p53 (P53) is dramatically increased at the inflamed sites [78]. Excessive endoplasmic reticulum (ER) stress, accompanied with the overproduction of proinflammatory tumor necrosis factor alpha (TNF- $\alpha$ ) released from the infiltrated macrophages, promotes epithelial cell apoptosis and further disrupts the integrity of the intestinal barrier [79–81]. Genetic ablation of critical proapoptotic components, including Puma and P53, significantly inhibits IEC apoptosis and relieves dextran sodium sulfate- (DSS-) and 2,4,6-trinitrobenzene sulfonic acid- (TNBS-) induced colitis in mice [82, 83]. Besides, other forms of regulated cell death, including necroptosis, pyroptosis, and autophagic cell death, were all evidenced to be involved in the IEC death and implicated in the colitis pathogenesis [84–87]. The IEC death would result in the collapse of the intestinal barrier, leading to the infiltration of gut bacteria and thus aggravating the inflammation.

Ferroptosis is a newly characterized form of regulated cell death. As mentioned above, iron overload, GSH depletion, GPX4 inactivation, and lipid peroxidation constitute the fundamental features of ferroptosis. Direct and indirect studies have enlightened a tight link between ferroptosis and intestinal diseases.

**3.1. Iron and IBD.** The earlier study suggested that the clinical symptoms of IBD include iron deficiency and anemia due to bleeding and malabsorption, which seriously influence individual health [88]. Oral iron administration has been clinically used to improve the IBD patients with iron deficiency anemia [89]. However, excessive iron administration leads to iron overload in the intestinal tract, resulting in the dysregulated production of ROS and disturbing the gut microbiota, which may exacerbate the illness of IBD [90–92]. Hereditary hemochromatosis is an iron overload disease due to recessive mutations in the hemochromatosis gene (*Hfe*), and it is characterized by increased iron absorption in the proximal intestine [93]. It was reported that some patients with hereditary hemochromatosis exhibit histologic abnormalities accompanied with increased intraepithelial neutrophil infiltration and lamina propria lymphocyte infiltration in the intestinal tract [94]. MDA was elevated in the colon tissue of the *Hfe* knockout mice, the murine model of human hereditary hemochromatosis, suggesting iron overload facilitates oxidative damage in the gut [95]. Importantly, *Hfe* knockout mice are more susceptible to the

development of experimental colitis, as evidenced by more severe rectal bleeding and diarrhea, higher colonic mucosal injury with frequent ulcerations, and a markedly increased loss of villus integrity [96]. Collaboratively, these studies thus highlight a pathological role of iron overload in the development of colitis. It is supposed that iron deposition in the intestine results in severe oxidative stress and facilitates lipid peroxidation through the Fenton reaction, which is probably pathogenic for colitis [97–99]. However, it is still elusive whether iron deposition initiates ferroptosis and is responsible for aggravated IEC death, mucosal damage, and intestinal inflammation. Ablin and colleagues reported that oral administration of iron chelator deferiprone (DFP) protects against experimental colitis and gastric ulceration in rats [100]. However, another study raised an opposite argument that oral iron supplementation in young rats has a beneficial effect on the prevention of TNBS-induced colitis [101].

**3.2. GSH and IBD.** GSH depletion is a critical signature of ferroptosis. It is now well understood that GSH exhaustion and GPX4 inactivation are widely observed in the inflamed mucosa from patients with IBD and in experimental animal models of colitis [102, 103]. The elevated oxidative insult in inflamed sites exhausts the endogenous GSH, while the reduced plasma cysteine and decreased enzymatic activity of mucosal  $\gamma$ -glutamylcysteine synthetase or  $\gamma$ -glutamyl transferase essential for GSH biosynthesis decelerate the de novo synthesis of GSH in patients with CD and UC [104]. Administration of the specific inhibitor of  $\gamma$ -glutamylcysteine synthetase, the rate-limiting enzyme for GSH synthesis, leads to a rapid decline of GSH and a substantial loss of the epithelial cells in the jejunal and colonic mucosa [105]. On the contrary, replenishment of GSH through administration of GSH [106], GSH ester [106], N-acetylcysteine [107], or L-cysteine [108] could restore the intestinal GSH abundance and significantly improve colonic health. GSH could confer the cellular antioxidative capacity by directly scavenging ROS and supporting the enzymatic activity of glutathione S-transferases to defend against oxidative stress, which are protective for the gastrointestinal tract from chronic inflammation [109].

**3.3. GPX4 and IBD.** Antioxidant enzyme GPX4 is responsible for scavenging lipid hydroperoxides and antagonizing ferroptosis [5]. Early studies indicated a genetic association between GPX4 and CD by using a meta-analysis of GWAS [110, 111]. Reduced GPX4 activity accompanied with elevated lipid peroxidation was characterized in the intestinal epithelium in patients with CD. A diet enriched in PUFAs, but not saturated fatty acids, induces focal enteritis in IEC-specific *Gpx4*<sup>+/-</sup> mice. More strikingly, IEC *Gpx4*<sup>+/-</sup> mice are more susceptible to colonic inflammation induced by DSS, as compared to the wild-type littermates, highlighting the notion that GPX4 is crucial for maintaining gut homeostasis by protecting from lipid peroxidation [112]. Furthermore, an increasing number of studies have suggested a tight association between IBD and the secondary metabolites of lipid peroxidation such as MDA and 4-HNE [112, 113]. The content of AA, one of the most oxidizable PUFAs

preferentially for lipid peroxidation, is markedly elevated in PLs of the colonic mucosa in patients with UC [114, 115]. Therefore, the inactivation of GPX4 and the elevation of lipid peroxides indicate the possibility that GPX4 determines gut homeostasis by antagonizing lipid peroxidation. Moreover, a reduced level of serum selenium was evidenced to be associated with the pathogenesis of UC and CD [116, 117]. Selenium deficiency in mice exacerbates intestinal injury [118], while selenium supplementation has been reported to be protective in IBD patients [119–122]. It is still elusive whether selenium supplementation ameliorating intestinal injury depends on the transcriptional activation of GPX4 or not [65, 123]. In addition, selenium supplementation in cultured Caco-2 cells could significantly prevent the transport of lipid hydroperoxides and thus decline cellular lipid peroxidation [124].

**3.4. LOXs and IBD.** LOXs catalyze the production of lipid hydroperoxides and drive ferroptotic cell death [45, 50]. Several LOX isoforms have been identified to be involved in the pathogenesis of IBD. More specifically, the levels of *Alox5* and *Alox15* are upregulated in the colonic mucosa in patients with IBD and in the experimental colitis mouse model, respectively [125, 126]. Systemic deletion of *Alox15* suppresses the production of lipid peroxidation metabolite 12-hydroxyeicosatetraenoic acid, stabilizes the tight junction protein ZO-1 and maintains the intestinal barrier integrity, decreases macrophage infiltration, and reduces the expression of proinflammatory genes, thus alleviating colonic damage in DSS-induced experimental colitis in mice. Conversely, transgenic overexpression of human *Alox15* renders mice more susceptible to DSS-induced colitis [127]. Similarly, deficiency of *Alox15* was reported to protect mice from DNBS-induced mucosal injury. Phosphatidylethanolamine-binding protein 1 (PEBP1) is a master regulatory molecule for 15-LOX by dominating the substrate specificity of 15-LOX to PUFA-phosphatidylethanolamines (PUFA-PE), facilitating the generation of lipid peroxides [128]. It suggested a positive correlation between the PEBP1 expression and the severity of IBD. More importantly, PEBP1 deficiency protects mice from DSS- or TNBS-induced colitis and accelerates mucosal recovery from injury [129]. Similarly, the supplementation of Zileuton, the potent 5-LOX inhibitor, maintains the tight junction proteins to prevent the decrease in the tight junctional permselectivity induced by TNBS [130]. Other 5-LOX-selective inhibitors, including A-64077 and MK-0591, could alleviate the inflammatory status in the colon of UC patients [131–134]. Collectively, these studies suggest a critical role of LOXs and their metabolites in determining gut inflammation and intestinal homeostasis.

**3.5. GCH1/BH4 and IBD.** Folate, also known as folic acid and vitamin B<sub>9</sub>, is regarded as a major endogenous antioxidant to defend against oxidative insults [135]. It is well recognized that folate is commonly deficient in patients with UC due to malabsorption [136, 137]. Administration of folate or its metabolic precursor BH4 was evidenced to relieve colitis-related tissue damage, detrimental inflammation, and malignant tumorigenesis [138, 139]. GCH1-

mediated BH4 biosynthesis is crucial for ferroptosis resistance by remodeling lipidomic composition and suppressing lipid peroxidation [67, 140]. Ionizing radiation decreases BH4 levels and increases superoxide anion accumulation in patients and rats after radiotherapy due to the downregulation of GCH1. BH4 supplementation could prevent intestinal ischemia, improve vascular endothelial function, relieve intestinal villus injury, and thus alleviate radiation enteritis [141]. Collectively, these studies thus indicate an essential role of GCH1-mediated BH4 and folate biosynthesis in maintaining intestinal homeostasis.

**3.6. The Emergence of Ferroptosis in Intestinal Diseases.** As summarized above, the fundamental features of ferroptosis, including iron deposition, accumulation of lipid peroxidation, GSH exhaustion, GPX4 inactivation, and LOX upregulation, have been elucidated to be implicated in the pathogenesis of IBD. Additionally, recent studies have enlightened a direct engagement of ferroptosis in the pathogenesis of IBD. The ER stress signaling is involved in the IEC ferroptosis during chemical colitis, as evidenced by the elevated expression of ER stress-associated G protein-coupled receptor 78, phosphorylated eukaryotic initiation factor 2, activating transcription factor 4, and C/EBP homologous protein. Specifically, selective inhibition of protein kinase RNA-like endoplasmic reticulum kinase, the critical stress sensor of ER stress signaling, sharply reduces IEC ferroptosis and significantly ameliorates experimental colitis. NF- $\kappa$ B activation could protect against IEC cell death during acute intestinal inflammation. Importantly, specific deletion of the nuclear factor kappa B p65 subunit (NF- $\kappa$ Bp65) in IECs leads to upregulated ER stress-mediated ferroptosis and aggravates DSS-induced colitis in mice [142]. More importantly, Fer-1, the specific inhibitor for ferroptosis, could ameliorate DSS-induced colitis [142]. Other well-characterized ferroptosis inhibitors, including Lip-1, iron chelator DFP, and antioxidant butylated hydroxyanisole, could all decelerate ferroptotic hallmarks and alleviate colonic damage [143]. Similarly, curculigoside, a natural ingredient from *Curculigo orchiooides* Gaertn with multiple biological activities, was recently identified to attenuate DSS-induced UC in mice. Mechanistically, curculigoside supports GPX4 expression and thus protects against ferroptotic cell death in a selenium-dependent manner [144]. These research studies collaboratively put forward the notion of the pathological engagement of ferroptosis in colitis.

ACSL4 is responsible for the esterification of AA and AdA into PLs to facilitate the subsequent peroxidation. Genetic and pharmacological inhibition of ACSL4 protects cells from lipid peroxidation and ferroptosis [27, 45, 49]. It was previously reported that ACSL4 is upregulated in the ileum and colon of patients with CD and UC [145] and in DSS-induced experimental colitis in mice [143]. Intestinal ischemia/reperfusion injury is a life-threatening condition associated with a high mortality rate, which commonly occurs in numerous clinical pathologies such as small intestinal volvulus, acute mesenteric ischemia, shock, trauma, and small bowel transplantation [146]. Recently, Li and colleagues reported that ACSL4 is sharply induced in ischemic intestines compared with normal intestines, possibly *via* the

TABLE 1: Promising molecules targeting ferroptosis in IBD.

Effect	Drug	Target	Mechanisms	Model	References
	Curculigoside	GPX4	Increases selenium sensitivity and promotes GPX4 expression	IEC-6 cells, UC mice	[144]
	NAC	GSH	Increases mucosal GSH levels	UC rats	[107]
	SAM	GSH	Serves as a precursor for GSH biosynthesis and antagonizes ROS	UC mice	[176]
	PTCA	GSH	Functions as a cysteine prodrug that stimulates GSH biosynthesis	UC mice	[176]
	DFP	Iron	Chelates excessive free iron and suppresses iron-dependent lipid peroxidation	UC mice	[100, 143, 177]
	DFO	Iron	Chelates excessive free iron and suppresses iron-dependent lipid peroxidation	UC mice	[142, 143, 177]
	Maltol	Iron	Oxyradical scavenger and/or iron chelation	UC rats	[177]
	Fer-1	ROS	Blocks lipid peroxidation and restrains ROS overgeneration	UC mice	[142, 143]
	Lip-1	ROS	Lipophilic antioxidants	UC mice	[143]
	Simvastatin	ROS	Decreases the TNF- $\alpha$ level and reduces oxidative stress	IECs, UC mice, UC rats	[178–180]
Inhibitors	Rosuvastatin	ROS	Decreases the TNF- $\alpha$ level and reduces oxidative stress	UC mice, UC rats	[180, 181]
	Vitamin E	ROS	Protects against lipid peroxidation and scavenges free radicals	UC rats	[98, 99, 182, 183]
	TMG	ROS	Protects against lipid peroxidation and scavenges free radicals	UC rats	[184, 185]
	AA	ROS	Increases the activities of GPX and reduces oxidative stress	UC mice	[186, 187]
	5-ASA	ROS	Scavenges oxygen-derived free radicals	IBD patients	[188, 189]
	CoQ10	ROS	Antioxidant and anti-inflammatory properties	UC rats	[190, 191]
	Melatonin	ROS	Antioxidant and anti-inflammatory properties	UC rats, UC mice	[192, 193]
	LS	ROS	Reduces lipid peroxidation and restores the levels of innate antioxidants	UC mice	[113]
	BH4	ROS	Reduces oxidative stress and rebalances lipid signaling <i>via</i> alkylglycerol monooxygenase	UC mice	[139]
	Zileuton	5-LOX	Functions as a 5-LOX inhibitor to increase PGE2 levels and reduces myeloperoxidase activity	IBD patients, UC rats	[134, 194]
Inducers	Oral iron	Iron	Exacerbates oxidative stress through the Fenton reaction	UC rats	[98, 182]

Abbreviations: AA: acetic acid; AA: ascorbic acid; BH4: tetrahydrobiopterin; CoQ10: coenzyme Q10; DFP: deferiprone; DFO: deferoxamine; DSS: dextran sodium sulfate; Fer-1: ferrostatin-1; Lip-1: liproxstatin-1; LS: *Lagerstroemia speciosa* leaves; NAC: N-acetylcysteine; PTCA: 2(R,S)-n-propylthiazolidine-4(R)-carboxylic acid; SAM: S-adenosylmethionine; TMG: vitamin E derivative, 2-(alpha-D-glucopyranosyl)methyl-2,5,7,8-tetra-methylchroman-6-ol; TNBS: trinitrobenzene sulfonic acid; 5-ASA: 5-aminosalicylic acid.

transcription factor special protein 1. More importantly, the core hallmarks of ferroptosis, including iron deposition, reduction of the GPX4 activity and GSH level, rupture of the outer mitochondrial membrane, and accumulation of lipid peroxidation, are manifested in the intestine after reperfusion. The typical ferroptosis inhibitor Lip-1 could strongly block lipid peroxidation and suppress cell death both *in vitro* and *in vivo*. Similarly, oral administration of rosiglitazone could inhibit ACSL4, suppress lipid peroxidation, and thus alleviate ischemia/reperfusion-related mucosal injury. Moreover, siRNA-mediated ACSL4 silence also protects Caco-2 cells from hypoxia/reoxygenation-induced lipid peroxidation and cell death [147]. Therefore, this study thus shed new light on the pathological engagement of ACSL4-mediated ferroptosis in intestinal ischemia/reperfusion injury.

**3.7. Other Ferroptosis Regulators in Intestinal Diseases.** Iron overload, lipid peroxidation, GSH depletion, and GPX4

inactivation constitute the fundamental features of ferroptosis. Besides, there are other ferroptosis regulators that have been evidenced to be associated with the pathogenesis or progression of intestinal diseases.

P53, one of the most famous tumor suppressors, is mutated in many types of human cancers. Specifically, P53 is mutated in about 55%-60% of human colorectal cancers, and its mutations are associated with a poor prognosis in colorectal cancers [148]. Besides colorectal cancer, a high frequency of P53 mutations was also reported in patients with chronic UC [149]. In response to diverse stimuli, P53 is stabilized to mediate metabolic reprogramming, cell cycle arrest, cellular senescence, and even cell death [150]. Genetic depletion of P53 leads to a significantly reduced cell death of IECs, but the colonic inflammation is not altered in a murine colitis model [83]. Other studies indicated that the knockout of P53 leads to comparable histopathologic changes of chronic colitis. However, a significantly greater incidence

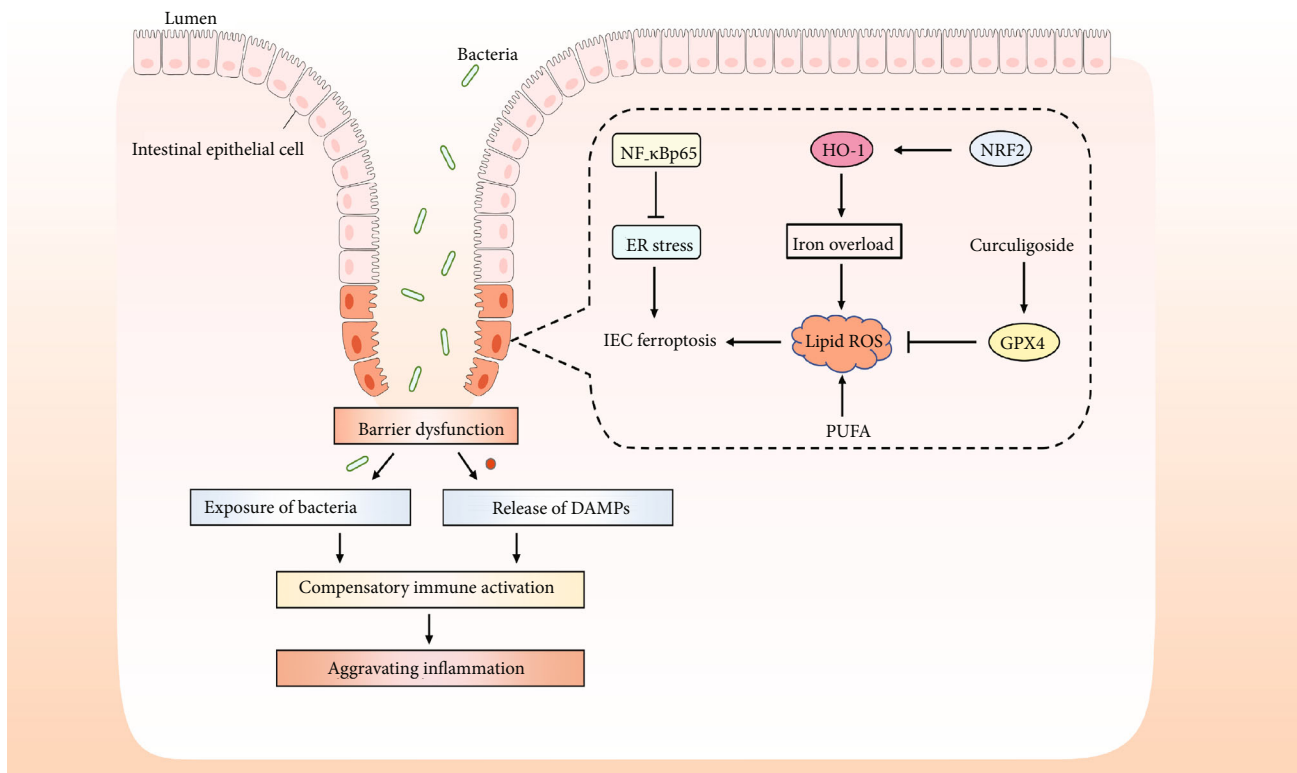


FIGURE 2: Emerging role of ferroptosis in inflammatory bowel disease. Ferroptosis has been directly implicated in the pathogenesis of IBD in recent studies. IEC ferroptosis seems to promote disruptions in epithelial barrier function, thereby allowing luminal antigens and cellular damage-associated molecular patterns (DAMPs) released into the bowel wall. Subsequently, immune cells and cytokine production are activated excessively, which in turn lead to intestinal inflammation and epithelial injury.

and multiplicity of cancers are observed during P53 deficiency [151–153]. Recently, it was reported that P53 suppresses cystine uptake, disturbs GSH biosynthesis, and thus sensitizes cells to ferroptosis. Mechanistically, P53 transcriptionally restrains the expression of cystine/glutamate antiporter subunit SLC7A11 [60, 154, 155]. Alternatively, P53 could facilitate the ferroptotic program by directly activating its target gene spermidine/spermine N1-acetyltransferase 1 and the downstream *Alox15* [156] or through transcriptionally upregulating the mitochondrial glutaminase 2 [30]. However, other studies suggest an opposite notion that P53 may inhibit ferroptotic cell death through dipeptidyl peptidase-4 [157] or cyclin-dependent kinase inhibitor 1A [158]. Whether P53-modulated ferroptotic sensitivity accounts for the pathogenesis or malignancy of colitis or not is still ambiguous.

The transcription factor NRF2, encoded by the *Nfe2l2* gene, plays a central role in the cytoprotective antioxidant system in response to a variety of oxidative, inflammatory, and metabolic stresses. NRF2 dominates the basal and induced expression of a series of antioxidant response element-dependent genes [159]. The increased severity of DSS-induced colitis and the elevated susceptibility of colitis-associated colorectal cancer in NRF2-ablated mice were found to be associated with the decreased expression of antioxidant genes and detoxifying enzymes, as well as the increased expression of proinflammatory cytokines [160, 161]. Among them, heme oxygenase-1 (HO-1) presents pronounced anti-inflammatory and antioxidative

properties in protecting mice from colitis-associated inflammatory injury and oxidative stress [162, 163]. As the main antioxidant axis, NRF2/HO-1 also dominates ferroptotic sensitivity. Ectopic expression or activation of NRF2 counteracts ferroptosis, whereas knockdown of NRF2 elevates the ferroptotic sensitivity in response to diverse ferroptosis inducers [164–166]. It is thus expectable that a variety of compounds that activate NRF2 could alleviate colitis-associated mucosal damage and colonic inflammation [167].

In addition, other ferroptosis regulators, including NADPH oxidases [168–171] and CD44 [172–175], are evidenced to be associated with the pathogenesis of IBD in patients or in colitis models. These proteins, including P53, NRF2, NADPH oxidases, and CD44, are all multifaceted. Thus, the exact involvement of these molecules in mediating ferroptotic regulation in colitis needs further investigation.

#### 4. Conclusive Remarks and Perspective

IBD is increasing worldwide and has become a global disease in both developed regions and developing countries. The increasing medicinal cost and substantial elevation in the risk of colorectal cancer are greatly affecting the life quality of patients and families. Although the exact pathogenesis of IBD is poorly defined, multiple lines of evidence indicate that genetic susceptibility, deleterious environmental factors, and an imbalanced gut microbial ecosystem could impinge on the gut homeostasis and thus facilitate inflammatory



response [195]. Uncontrolled cell death has been widely observed in the diseased mucosa in patients and animal models, which could disturb the tight junction of the intestinal barrier and then aggravate the inflammation by releasing the gut microorganisms.

Ferroptosis is a newly identified form of regulated cell death. Iron overload, GSH exhaustion, GPX4 inactivation, and lipid peroxidation are the major features of ferroptosis. Dysregulated ferroptosis has been evidenced to be implicated in the pathogenesis and progression of many human diseases [196]. Furthermore, targeting induction of ferroptosis provides a potential therapeutic strategy for the clinical intervention of cancers, especially the other traditional therapy-resistant cancers [197, 198]. As mentioned above, the major features of ferroptosis have been extensively observed in the diseased mucosa in patients and animal models. Importantly, genetic or pharmacological manipulation of ferroptosis-related genes could alter the incidence, severity, or progression of the experimental colitis by using the corresponding murine models. More directly, some potent ferroptosis inhibitors, including iron chelators, GSH or GSH derivate GSH ester, selenium, LOX inhibitors, folate, or BH4, could decline lipid peroxidation and alleviate colitis-associated intestinal injury (Table 1). Moreover, Fer-1 and Lip-1, two specific inhibitors of ferroptosis, could relieve colitis in murine models. On the contrary, the ferroptosis sensitizers, including iron,  $\gamma$ -glutamylcysteine synthetase inhibitor BSO, and dietary PUFAs, could accelerate lipid peroxidation and aggravate colitis. Collaboratively, these studies thus highlight the critical importance of dysregulated ferroptosis in the pathogenesis of IBD.

It should not be ignored that abnormalities of both the innate and adaptive immune responses against harmful intestinal microorganisms, antigens, or extrinsic pathogens play important roles in the pathogenesis of IBD. The healthy mucosa contains a delicate balance of innate lymphoid cells, macrophages, neutrophils, and dendritic cells, as well as the adaptive immune response associated with T and B cells. The hyperactivation of the intestinal immune system due to the epithelial cell death and intestinal barrier disruption leads to the subsequently excessive secretion of proinflammatory cytokines and chemokines, which could result in secondary damage to the intestinal mucosa and a vicious cycle [199, 200]. Furthermore, previous studies indicated resistance to cell death of lamina propria lymphocytes in inflamed tissues in UC patients due to the altered expression of cell death-associated proteins [201–203]. Therefore, it is supposed that the IEC ferroptosis leads to intestinal barrier disruption, gut microorganism release, and hyperactivation of intestinal immune response, resulting in aggravation of colitis-associated mucosal injury. Furthermore, the ferroptotic IECs would release some immunogenic molecules, which may further facilitate local inflammation (Figure 2) [204]. However, besides IECs, whether intestinal immune cells undergo ferroptosis in the pathogenesis of intestinal injury or not is elusive. If so, whether this ferroptosis in certain types of intestinal immune cells contributes to the pathogenesis or progression of intestinal diseases or not needs more investigations.

Regarding the beneficial effect of diverse ferroptosis inhibitors in relieving colitis-associated tissue injury (Table 1), it is of great therapeutic potential for selective manipulation of ferroptosis in the prevention and intervention of colitis. Therefore, more extensive investigations are needed to further dissect the exact implication of ferroptosis in the pathogenesis of IBD and other related intestinal diseases. Specifically, to dissect the detailed underlying molecular mechanism for which ferroptosis mediates mucosal damage in inflamed tissues, to explore the specific types of epithelial cells in which dysregulated ferroptosis occurs leading to the hyperactivation of intestinal inflammation, and to identify the more selective and potent ferroptosis inhibitors with lower side effects for pharmacological intervention of IBD will help to obtain the full aerial view of ferroptosis and provide some future translational applications.

## Abbreviations

4-HNEs:	4-Hydroxy-2-nonenals
5-ASA:	5-Aminosalicylic acid
AA:	Arachidonoyl
ACSL4:	Acyl-CoA synthetase long-chain family member 4
AdA:	Adrenoyl
ALOX:	Arachidonate lipoxygenase
BH4:	Tetrahydrobiopterin
CD:	Crohn's disease
CoQ10:	Coenzyme Q10
CYB5R1:	NADH-cytochrome b5 reductase
DAMPs:	Damage-associated molecular patterns
DFO:	Deferoxamine
DFP:	Deferiprone
DMT1:	Divalent metal transporter 1
DSS:	Dextran sodium sulfate
ER:	Endoplasmic reticulum
Fe <sup>2+</sup> :	Ferrous iron
Fe <sup>3+</sup> :	Ferric iron
Fer-1:	Ferrostatin-1
FPN:	Ferroportin
FSP1:	Ferroptosis suppressor protein 1
GCH1:	GTP cyclohydrolase-1
GPX4:	Glutathione peroxidase 4
GSH:	Glutathione
HFE:	Hemochromatosis gene
HO-1:	Heme oxygenase-1
IBD:	Inflammatory bowel disease
IECs:	Intestinal epithelial cells
IFN $\gamma$ :	Interferon gamma
IRP1/2:	Iron regulatory proteins 1 and 2
LIP:	Labile iron pool
Lip-1:	Lipoxstatin-1
LOXs:	Lipoxygenases
LPCAT3:	Lysophosphatidylcholine acyltransferase 3
MDAs:	Malondialdehydes
MUFAs:	Monounsaturated fatty acids
NCOA4:	Nuclear receptor coactivator 4
NF- $\kappa$ B:	Nuclear factor kappa B
NRF2:	Nuclear factor erythroid 2-related factor 2

P53: Tumor protein p53  
 PE: Phosphatidylethanolamines  
 PEBP1: PE-binding protein 1  
 PLs: Phospholipids  
 POR: P450 reductase  
 PUFAs: Polyunsaturated fatty acids  
 ROS: Reactive oxygen species  
 SLC3A2: Solute carrier family 3 member 2  
 SLC7A11: Solute carrier family 7 member 11  
 TF: Transferrin  
 TFR1: Transferrin receptor 1  
 TNBS: 2,4,6-Trinitrobenzene sulfonic acid  
 TNF- $\alpha$ : Tumor necrosis factor alpha  
 UC: Ulcerative colitis.

## Conflicts of Interest

The authors declare that there is no conflict of interest regarding the publication of this paper.

## Authors' Contributions

Weihua Gao and Ting Zhang contributed equally to this work.

## Acknowledgments

Work in the authors' laboratory is supported by the National Natural Science Foundation of China (32070738), the Fundamental Research Funds for the Central Universities (Project No. 2662020DKPY009), and the State Key Laboratory of Medicinal Chemical Biology, Nankai University (2020015).

## References

- [1] S. J. Dixon, K. M. Lemberg, M. R. Lamprecht et al., "Ferroptosis: an iron-dependent form of nonapoptotic cell death," *Cell*, vol. 149, no. 5, pp. 1060–1072, 2012.
- [2] S. J. Dixon and B. R. Stockwell, "The hallmarks of ferroptosis," *Annual Review of Cancer Biology*, vol. 3, no. 1, pp. 35–54, 2019.
- [3] N. Yagoda, M. von Rechenberg, E. Zaganjor et al., "RAS-RAF-MEK-dependent oxidative cell death involving voltage-dependent anion channels," *Nature*, vol. 447, no. 7146, pp. 864–868, 2007.
- [4] S. Dolma, S. L. Lessnick, W. C. Hahn, and B. R. Stockwell, "Identification of genotype-selective antitumor agents using synthetic lethal chemical screening in engineered human tumor cells," *Cancer Cell*, vol. 3, no. 3, pp. 285–296, 2003.
- [5] J. P. Friedmann Angeli, M. Schneider, B. Proneth et al., "Inactivation of the ferroptosis regulator Gpx4 triggers acute renal failure in mice," *Nature Cell Biology*, vol. 16, no. 12, pp. 1180–1191, 2014.
- [6] H. Eagle, "The specific amino acid requirements of a human carcinoma cell (STRAIN HeLa) in tissue culture," *The Journal of Experimental Medicine*, vol. 102, no. 1, pp. 37–48, 1955.
- [7] H. Eagle, "Nutrition needs of mammalian cells in tissue culture," *Science*, vol. 122, no. 3168, pp. 501–504, 1955.
- [8] S. Bannai, H. Tsukeda, and H. Okumura, "Effect of antioxidants on cultured human diploid fibroblasts exposed to cystine-free medium," *Biochemical and Biophysical Research Communications*, vol. 74, no. 4, pp. 1582–1588, 1977.
- [9] R. R. Ratan and J. M. Baraban, "Apoptotic AN in an in vitro model of neuronal oxidative stress," *Clinical and Experimental Pharmacology*, vol. 22, no. 4, pp. 309–310, 1995.
- [10] R. R. Ratan, T. H. Murphy, and J. M. Baraban, "Macromolecular synthesis inhibitors prevent oxidative stress-induced apoptosis in embryonic cortical neurons by shunting cysteine from protein synthesis to glutathione," *Journal of Neuroscience*, vol. 14, no. 7, pp. 4385–4392, 1994.
- [11] J. R. Mitchell, D. J. Jollow, W. Z. Potter, D. C. Davis, J. R. Gillette, and B. B. Brodie, "Acetaminophen-induced hepatic necrosis. I. Role of drug metabolism," *Journal of Pharmacology and Experimental Therapeutics*, vol. 187, no. 1, pp. 185–194, 1973.
- [12] T. H. Murphy, M. Miyamoto, A. Sastre, R. L. Schnaar, and J. T. Coyle, "Glutamate toxicity in a neuronal cell line involves inhibition of cystine transport leading to oxidative stress," *Neuron*, vol. 2, no. 6, pp. 1547–1558, 1989.
- [13] W. S. Yang and B. R. Stockwell, "Synthetic lethal screening identifies compounds activating iron-dependent, nonapoptotic cell death in oncogenic-RAS-harboring cancer cells," *Chemistry & Biology*, vol. 15, no. 3, pp. 234–245, 2008.
- [14] W. S. Yang, R. SriRamaratnam, M. E. Welsch et al., "Regulation of ferroptotic cancer cell death by GPX4," *Cell*, vol. 156, no. 1–2, pp. 317–331, 2014.
- [15] Y. Zhang, H. Tan, J. D. Daniels et al., "Imidazole ketone erastin induces ferroptosis and slows tumor growth in a mouse lymphoma model," *Cell Chemical Biology*, vol. 26, no. 5, pp. 623–633.e629, 2019.
- [16] P. W. Gout, A. R. Buckley, C. R. Simms, and N. Bruchovsky, "Sulfasalazine, a potent suppressor of lymphoma growth by inhibition of the x<sub>c</sub><sup>-</sup> cystine transporter: a new action for an old drug," *Leukemia*, vol. 15, no. 10, pp. 1633–1640, 2001.
- [17] E. Lachaier, C. Louandre, C. Godin et al., "Sorafenib induces ferroptosis in human cancer cell lines originating from different solid tumors," *Anticancer Research*, vol. 34, no. 11, pp. 6417–6422, 2014.
- [18] N. Eling, L. Reuter, J. Hazin, A. Hamacher-Brady, and N. R. Brady, "Identification of artesunate as a specific activator of ferroptosis in pancreatic cancer cells," *Oncoscience*, vol. 2, no. 5, pp. 517–532, 2015.
- [19] J. Fujii, T. Homma, and S. Kobayashi, "Ferroptosis caused by cysteine insufficiency and oxidative insult," *Free Radical Research*, vol. 54, no. 11–12, pp. 969–980, 2020.
- [20] J. H. Woo, Y. Shimoni, W. S. Yang et al., "Elucidating compound mechanism of action by network perturbation analysis," *Cell*, vol. 162, no. 2, pp. 441–451, 2015.
- [21] K. Shimada, R. Skouta, A. Kaplan et al., "Global survey of cell death mechanisms reveals metabolic regulation of ferroptosis," *Nature Chemical Biology*, vol. 12, no. 7, pp. 497–503, 2016.
- [22] M. M. Gaschler, A. A. Andia, H. Liu et al., "FINO<sub>2</sub> initiates ferroptosis through GPX4 inactivation and iron oxidation," *Nature Chemical Biology*, vol. 14, no. 5, pp. 507–515, 2018.
- [23] T. Ishii, S. Bannai, and Y. Sugita, "Mechanism of growth stimulation of L1210 cells by 2-mercaptoethanol in vitro. Role of the mixed disulfide of 2-mercaptoethanol and cysteine," *Journal of Biological Chemistry*, vol. 256, no. 23, pp. 12387–12392, 1981.

- [24] O. Zilka, R. Shah, B. Li et al., "On the mechanism of cytoprotection by ferrostatin-1 and liproxstatin-1 and the role of lipid peroxidation in ferroptotic cell death," *ACS Central Science*, vol. 3, no. 3, pp. 232–243, 2017.
- [25] R. Shah, M. S. Shchepinov, and D. A. Pratt, "Resolving the role of lipoxygenases in the initiation and execution of ferroptosis," *ACS Central Science*, vol. 4, no. 3, pp. 387–396, 2018.
- [26] M. Conrad and D. A. Pratt, "The chemical basis of ferroptosis," *Nature Chemical Biology*, vol. 15, no. 12, pp. 1137–1147, 2019.
- [27] S. Doll, B. Proneth, Y. Y. Tyurina et al., "ACSL4 dictates ferroptosis sensitivity by shaping cellular lipid composition," *Nature Chemical Biology*, vol. 13, no. 1, pp. 91–98, 2017.
- [28] D. J. Lane, A. M. Merlot, M. L. Huang et al., "Cellular iron uptake, trafficking and metabolism: key molecules and mechanisms and their roles in disease," *Biochimica et Biophysica Acta (BBA)-Molecular Cell Research*, vol. 1853, no. 5, pp. 1130–1144, 2015.
- [29] C. P. Anderson, M. Shen, R. S. Eisenstein, and E. A. Leibold, "Mammalian iron metabolism and its control by iron regulatory proteins," *Biochimica Et Biophysica Acta (BBA)-Molecular Cell Research*, vol. 1823, no. 9, pp. 1468–1483, 2012.
- [30] M. Gao, P. Monian, N. Quadri, R. Ramasamy, and X. Jiang, "Glutaminolysis and transferrin regulate ferroptosis," *Molecular Cell*, vol. 59, no. 2, pp. 298–308, 2015.
- [31] S. Ma, E. S. Henson, Y. Chen, and S. B. Gibson, "Ferroptosis is induced following siramesine and lapatinib treatment of breast cancer cells," *Cell Death & Disease*, vol. 7, no. 7, article e2307, 2016.
- [32] X. Sun, Z. Ou, M. Xie et al., "HSPB1 as a novel regulator of ferroptotic cancer cell death," *Oncogene*, vol. 34, no. 45, pp. 5617–5625, 2015.
- [33] J. D. Mancias, X. Wang, S. P. Gygi, J. W. Harper, and A. C. Kimmelman, "Quantitative proteomics identifies NCOA4 as the cargo receptor mediating ferritinophagy," *Nature*, vol. 509, no. 7498, pp. 105–109, 2014.
- [34] W. Hou, Y. Xie, X. Song et al., "Autophagy promotes ferroptosis by degradation of ferritin," *Autophagy*, vol. 12, no. 8, pp. 1425–1428, 2016.
- [35] M. Gao, P. Monian, Q. Pan, W. Zhang, J. Xiang, and X. Jiang, "Ferroptosis is an autophagic cell death process," *Cell Research*, vol. 26, no. 9, pp. 1021–1032, 2016.
- [36] S. Doll and M. Conrad, "Iron and ferroptosis: a still ill-defined liaison," *IUBMB Life*, vol. 69, no. 6, pp. 423–434, 2017.
- [37] T. Harayama and H. Riezman, "Understanding the diversity of membrane lipid composition," *Nature Reviews Molecular Cell Biology*, vol. 19, no. 5, pp. 281–296, 2018.
- [38] H. Bayir, T. S. Anthonymuthu, Y. Y. Tyurina et al., "Achieving life through death: redox biology of lipid peroxidation in ferroptosis," *Cell Chemical Biology*, vol. 27, no. 4, pp. 387–408, 2020.
- [39] E. Agmon, J. Solon, P. Bassereau, and B. R. Stockwell, "Modeling the effects of lipid peroxidation during ferroptosis on membrane properties," *Scientific Reports*, vol. 8, no. 1, p. 5155, 2018.
- [40] A. J. Hulbert, "Metabolism and longevity: is there a role for membrane fatty acids?," *Integrative and Comparative Biology*, vol. 50, no. 5, pp. 808–817, 2010.
- [41] A. Ayala, M. F. Munoz, and S. Arguelles, "Lipid peroxidation: production, metabolism, and signaling mechanisms of malondialdehyde and 4-hydroxy-2-nonenal," *Oxidative Medicine and Cellular Longevity*, vol. 2014, Article ID 360438, 31 pages, 2014.
- [42] G. Barrera, S. Pizzimenti, E. S. Ciamporcerio et al., "Role of 4-hydroxynonenal-protein adducts in human diseases," *Antioxidants & Redox Signaling*, vol. 22, no. 18, pp. 1681–1702, 2015.
- [43] M. M. Gaschler and B. R. Stockwell, "Lipid peroxidation in cell death," *Biochemical and Biophysical Research Communications*, vol. 482, no. 3, pp. 419–425, 2017.
- [44] P. L. Else, "Membrane peroxidation in vertebrates: potential role in metabolism and growth," *European Journal of Lipid Science and Technology*, vol. 119, no. 6, article 1600319, 2017.
- [45] V. E. Kagan, G. Mao, F. Qu et al., "Oxidized arachidonic and adrenic PEs navigate cells to ferroptosis," *Nature Chemical Biology*, vol. 13, no. 1, pp. 81–90, 2017.
- [46] L. Magtanong, P. J. Ko, M. To et al., "Exogenous monounsaturated fatty acids promote a ferroptosis-resistant cell state," *Cell Chemical Biology*, vol. 26, no. 3, pp. 420–432.e9, 2019.
- [47] W. S. Yang, K. J. Kim, M. M. Gaschler, M. Patel, M. S. Shchepinov, and B. R. Stockwell, "Peroxidation of polyunsaturated fatty acids by lipoxygenases drives ferroptosis," *Proceedings of the National Academy of Sciences*, vol. 113, no. 34, pp. E4966–E4975, 2016.
- [48] S. J. Dixon, G. E. Winter, L. S. Musavi et al., "Human haploid cell genetics reveals roles for lipid metabolism genes in non-apoptotic cell death," *ACS Chemical Biology*, vol. 10, no. 7, pp. 1604–1609, 2015.
- [49] H. Yuan, X. Li, X. Zhang, R. Kang, and D. Tang, "Identification of ACSL4 as a biomarker and contributor of ferroptosis," *Biochemical and Biophysical Research Communications*, vol. 478, no. 3, pp. 1338–1343, 2016.
- [50] J. Loscalzo, "Membrane redox state and apoptosis: death by peroxide," *Cell Metabolism*, vol. 8, no. 3, pp. 182–183, 2008.
- [51] A. Seiler, M. Schneider, H. Förster et al., "Glutathione peroxidase 4 senses and translates oxidative stress into 12/15-lipoxygenase dependent- and AIF-mediated cell death," *Cell Metabolism*, vol. 8, no. 3, pp. 237–248, 2008.
- [52] R. Shintoku, Y. Takigawa, K. Yamada et al., "Lipoxygenase-mediated generation of lipid peroxides enhances ferroptosis induced by erastin and RSL3," *Cancer Science*, vol. 108, no. 11, pp. 2187–2194, 2017.
- [53] S. H. Brütsch, C. C. Wang, L. Li et al., "Expression of inactive glutathione peroxidase 4 leads to embryonic lethality, and inactivation of the Alox15 Gene does not rescue such knock-in mice," *Antioxidants & Redox Signaling*, vol. 22, no. 4, pp. 281–293, 2015.
- [54] Y. Zou, H. Li, E. T. Graham et al., "Cytochrome P450 oxidoreductase contributes to phospholipid peroxidation in ferroptosis," *Nature Chemical Biology*, vol. 16, no. 3, pp. 302–309, 2020.
- [55] B. Yan, Y. Ai, Q. Sun et al., "Membrane damage during ferroptosis is caused by oxidation of phospholipids catalyzed by the oxidoreductases POR and CYB5R1," *Molecular Cell*, vol. 81, no. 2, pp. 355–369.e10, 2021.
- [56] R. Brigelius-Flohe and M. Maiorino, "Glutathione peroxidases," *Biochimica et Biophysica Acta (BBA)-General Subjects*, vol. 1830, no. 5, pp. 3289–3303, 2013.
- [57] S. C. Lu, "Regulation of glutathione synthesis," *Current Topics in Cellular Regulation*, vol. 36, pp. 95–116, 2001.

- [58] S. J. Dixon, D. N. Patel, M. Welsch et al., "Pharmacological inhibition of cystine-glutamate exchange induces endoplasmic reticulum stress and ferroptosis," *Elife*, vol. 3, article e02523, 2014.
- [59] J. Y. Cao and S. J. Dixon, "Mechanisms of ferroptosis," *Cellular and Molecular Life Sciences*, vol. 73, no. 11-12, pp. 2195–2209, 2016.
- [60] L. Jiang, N. Kon, T. Li et al., "Ferroptosis as a p53-mediated activity during tumour suppression," *Nature*, vol. 520, no. 7545, pp. 57–62, 2015.
- [61] W. Wang, M. Green, J. E. Choi et al., "CD8<sup>+</sup> T cells regulate tumour ferroptosis during cancer immunotherapy," *Nature*, vol. 569, no. 7755, pp. 270–274, 2019.
- [62] C. J. Harvey, R. K. Thimmulappa, A. Singh et al., "Nrf2-regulated glutathione recycling independent of biosynthesis is critical for cell survival during oxidative stress," *Free Radical Biology and Medicine*, vol. 46, no. 4, pp. 443–453, 2009.
- [63] K. Bersuker, J. M. Hendricks, Z. Li et al., "The CoQ oxidoreductase FSP1 acts parallel to GPX4 to inhibit ferroptosis," *Nature*, vol. 575, no. 7784, pp. 688–692, 2019.
- [64] S. Doll, F. P. Freitas, R. Shah et al., "FSP1 is a glutathione-independent ferroptosis suppressor," *Nature*, vol. 575, no. 7784, pp. 693–698, 2019.
- [65] I. Ingold, C. Berndt, S. Schmitt et al., "Selenium utilization by GPX4 is required to prevent hydroperoxide-induced ferroptosis," *Cell*, vol. 172, no. 3, pp. 409–422.e21, 2018.
- [66] V. A. N. Kraft, C. T. Bezjian, S. Pfeiffer et al., "GTP cyclohydrolase 1/tetrahydrobiopterin counteract ferroptosis through lipid remodeling," *ACS Central Science*, vol. 6, no. 1, pp. 41–53, 2020.
- [67] M. Soula, R. A. Weber, O. Zilka et al., "Metabolic determinants of cancer cell sensitivity to canonical ferroptosis inducers," *Nature Chemical Biology*, vol. 16, no. 12, pp. 1351–1360, 2020.
- [68] I. Ordas, L. Eckmann, M. Talamini, D. C. Baumgart, and W. J. Sandborn, "Ulcerative colitis," *Lancet*, vol. 380, no. 9853, pp. 1606–1619, 2012.
- [69] J. Torres, S. Mehandru, J. F. Colombel, and L. Peyrin-Biroulet, "Crohn's disease," *Lancet*, vol. 389, no. 10080, pp. 1741–1755, 2017.
- [70] F. Imhann, A. Vich Vila, M. J. Bonder et al., "Interplay of host genetics and gut microbiota underlying the onset and clinical presentation of inflammatory bowel disease," *Gut*, vol. 67, no. 1, pp. 108–119, 2018.
- [71] S. C. Ng, H. Y. Shi, N. Hamidi et al., "Worldwide incidence and prevalence of inflammatory bowel disease in the 21st century: a systematic review of population-based studies," *Lancet*, vol. 390, no. 10114, pp. 2769–2778, 2018.
- [72] L. G. van der Flier and H. Clevers, "Stem cells, self-renewal, and differentiation in the intestinal epithelium," *Annual Review of Physiology*, vol. 71, pp. 241–260, 2009.
- [73] M. Iwamoto, T. Koji, K. Makiyama, N. Kobayashi, and P. K. Nakane, "Apoptosis of crypt epithelial cells in ulcerative colitis," *The Journal of Pathology*, vol. 180, no. 2, pp. 152–159, 1996.
- [74] A. Di Sabatino, R. Ciccocioppo, O. Luinetti et al., "Increased enterocyte apoptosis in inflamed areas of Crohn's disease," *Diseases of the Colon & Rectum*, vol. 46, no. 11, pp. 1498–1507, 2003.
- [75] A. Nenci, C. Becker, A. Wullaert et al., "Epithelial NEMO links innate immunity to chronic intestinal inflammation," *Nature*, vol. 446, no. 7135, pp. 557–561, 2007.
- [76] L. Eckmann, T. Nebelsiek, A. A. Fingerle et al., "Opposing functions of IKK $\beta$  during acute and chronic intestinal inflammation," *Proceedings of the National Academy of Sciences*, vol. 105, no. 39, pp. 15058–15063, 2008.
- [77] M. R. Frey, K. L. Edelblum, M. T. Mullane, D. Liang, and D. B. Polk, "The ErbB4 growth factor receptor is required for colon epithelial cell survival in the presence of TNF," *Gastroenterology*, vol. 136, no. 1, pp. 217–226, 2009.
- [78] A. Vetuschi, G. Latella, R. Sferra, R. Caprilli, and E. Gaudio, "Increased proliferation and apoptosis of colonic epithelial cells in dextran sulfate sodium-induced colitis in rats," *Digestive Diseases and Sciences*, vol. 47, no. 7, pp. 1447–1457, 2002.
- [79] S. S. Cao, E. M. Zimmermann, B. M. Chuang et al., "The unfolded protein response and chemical chaperones reduce protein misfolding and colitis in mice," *Gastroenterology*, vol. 144, no. 5, pp. 989–1000.e1006, 2013.
- [80] A. Kaser, A. H. Lee, A. Franke et al., "XBP1 links ER stress to intestinal inflammation and confers genetic risk for human inflammatory bowel disease," *Cell*, vol. 134, no. 5, pp. 743–756, 2008.
- [81] T. Goretsky, R. Dirisina, P. Sinh et al., "p53 mediates TNF-induced epithelial cell apoptosis in IBD," *The American Journal of Pathology*, vol. 181, no. 4, pp. 1306–1315, 2012.
- [82] W. Qiu, B. Wu, X. Wang et al., "PUMA-mediated intestinal epithelial apoptosis contributes to ulcerative colitis in humans and mice," *The Journal of Clinical Investigation*, vol. 121, no. 5, pp. 1722–1732, 2011.
- [83] R. Dirisina, R. B. Katzman, T. Goretsky et al., "p53 and PUMA independently regulate apoptosis of intestinal epithelial cells in patients and mice with colitis," *Gastroenterology*, vol. 141, no. 3, pp. 1036–1045, 2011.
- [84] C. Gunther, E. Martini, N. Wittkopf et al., "Caspase-8 regulates TNF-alpha-induced epithelial necroptosis and terminal ileitis," *Nature*, vol. 477, no. 7364, pp. 335–339, 2011.
- [85] P. S. Welz, A. Wullaert, K. Vlantis et al., "FADD prevents RIP3-mediated epithelial cell necrosis and chronic intestinal inflammation," *Nature*, vol. 477, no. 7364, pp. 330–334, 2011.
- [86] C. Ma, D. Yang, B. Wang et al., "Gasdermin D in macrophages restrains colitis by controlling cGAS-mediated inflammation," *Science Advances*, vol. 6, no. 21, article eaaz6717, 2020.
- [87] R. Schwarzer, H. Jiao, L. Wachsmuth, A. Tresch, and M. Pasparakis, "FADD and caspase-8 regulate gut homeostasis and inflammation by controlling MLKL- and GSDMD-mediated death of intestinal epithelial cells," *Immunity*, vol. 52, no. 6, pp. 978–993.e976, 2020.
- [88] D. N. Seril, J. Liao, K. L. Ho, A. Warsi, C. S. Yang, and G. Y. Yang, "Dietary iron supplementation enhances DSS-induced colitis and associated colorectal carcinoma development in mice," *Digestive Diseases and Sciences*, vol. 47, no. 6, pp. 1266–1278, 2002.
- [89] T. W. Lee, M. R. Kolber, R. N. Fedorak, and S. V. van Zanten, "Iron replacement therapy in inflammatory bowel disease patients with iron deficiency anemia: a systematic review and meta-analysis," *Journal of Crohn's and Colitis*, vol. 6, no. 3, pp. 267–275, 2012.
- [90] T. Werner, S. J. Wagner, I. Martinez et al., "Depletion of luminal iron alters the gut microbiota and prevents Crohn's disease-like ileitis," *Gut*, vol. 60, no. 3, pp. 325–333, 2011.
- [91] M. Constante, G. Fragoso, J. Lupien-Meilleur, A. Calve, and M. M. Santos, "Iron supplements modulate colon microbiota

- composition and potentiate the protective effects of probiotics in dextran sodium sulfate-induced colitis," *Inflammatory Bowel Diseases*, vol. 23, no. 5, pp. 753–766, 2017.
- [92] T. Lee, T. Clavel, K. Smirnov et al., "Oral versus intravenous iron replacement therapy distinctly alters the gut microbiota and metabolome in patients with IBD," *Gut*, vol. 66, no. 5, pp. 863–871, 2017.
- [93] J. N. Feder, A. Gnirke, W. Thomas et al., "A novel MHC class I-like gene is mutated in patients with hereditary haemochromatosis," *Nature Genetics*, vol. 13, no. 4, pp. 399–408, 1996.
- [94] W. X. Zhou, X. R. Wu, A. E. Bennett, and B. Shen, "Endoscopic and histologic abnormalities of gastrointestinal tract in patients with hereditary hemochromatosis," *Journal of Clinical Gastroenterology*, vol. 48, no. 4, pp. 336–342, 2014.
- [95] R. G. Stevens, J. E. Morris, G. A. Cordis, L. E. Anderson, D. W. Rosenberg, and L. B. Sasser, "Oxidative damage in colon and mammary tissue of the HFE-knockout mouse," *Free Radical Biology and Medicine*, vol. 34, no. 9, pp. 1212–1216, 2003.
- [96] S. Sivaprakasam, B. Ristic, N. Mudaliar et al., "Hereditary hemochromatosis promotes colitis and colon cancer and causes bacterial dysbiosis in mice," *Biochemical Journal*, vol. 477, no. 19, pp. 3867–3883, 2020.
- [97] K. Erichsen, A. M. Milde, G. Arslan et al., "Low-dose oral ferrous fumarate aggravated intestinal inflammation in rats with DSS-induced colitis," *Inflammatory Bowel Diseases*, vol. 11, no. 8, pp. 744–748, 2005.
- [98] J. Carrier, E. Aghdassi, I. Platt, J. Cullen, and J. P. Allard, "Effect of oral iron supplementation on oxidative stress and colonic inflammation in rats with induced colitis," *Alimentary Pharmacology & Therapeutics*, vol. 15, no. 12, pp. 1989–1999, 2001.
- [99] J. C. Carrier, E. Aghdassi, K. Jeejeebhoy, and J. P. Allard, "Exacerbation of dextran sulfate sodium-induced colitis by dietary iron supplementation: role of NF- $\kappa$ B," *International Journal of Colorectal Disease*, vol. 21, no. 4, pp. 381–387, 2006.
- [100] J. Ablin, O. Shalev, E. Okon, F. Karmeli, and D. Rachmilewitz, "Deferiprone, an oral iron chelator, ameliorates experimental colitis and gastric ulceration in rats," *Inflammatory Bowel Diseases*, vol. 5, no. 4, pp. 253–261, 1999.
- [101] C. Ettreiki, P. Gadonna-Widehem, I. Mangin, M. Coëffier, C. Delayre-Orthez, and P. M. Anton, "Juvenile ferric iron prevents microbiota dysbiosis and colitis in adult rodents," *World Journal of Gastroenterology: WJG*, vol. 18, no. 21, pp. 2619–2629, 2012.
- [102] G. D. Buffinton and W. F. Doe, "Depleted mucosal antioxidant defences in inflammatory bowel disease," *Free Radical Biology and Medicine*, vol. 19, no. 6, pp. 911–918, 1995.
- [103] E. Goldin, E. Ardite, J. I. Elizalde et al., "Gastric mucosal damage in experimental diabetes in rats: role of endogenous glutathione," *Gastroenterology*, vol. 112, no. 3, pp. 855–863, 1997.
- [104] B. Sido, V. Hack, A. Hochlehnert, H. Lipps, C. Herfarth, and W. Dröge, "Impairment of intestinal glutathione synthesis in patients with inflammatory bowel disease," *Gut*, vol. 42, no. 4, pp. 485–492, 1998.
- [105] J. Martensson, A. Jain, and A. Meister, "Glutathione is required for intestinal function," *Proceedings of the National Academy of Sciences*, vol. 87, no. 5, pp. 1715–1719, 1990.
- [106] C. Loguercio, G. D'Argenio, M. Delle Cave et al., "Glutathione supplementation improves oxidative damage in experimental colitis," *Digestive and Liver Disease*, vol. 35, no. 9, pp. 635–641, 2003.
- [107] E. Ardite, M. Sans, J. Panes, F. J. Romero, J. M. Pique, and J. C. Fernandez-Checa, "Replenishment of glutathione levels improves mucosal function in experimental acute colitis," *Laboratory Investigation*, vol. 80, no. 5, pp. 735–744, 2000.
- [108] C. J. Kim, J. Kovacs-Nolan, C. Yang, T. Archbold, M. Z. Fan, and Y. Mine, "L-cysteine supplementation attenuates local inflammation and restores gut homeostasis in a porcine model of colitis," *Biochimica et Biophysica Acta (BBA)-General Subjects*, vol. 1790, no. 10, pp. 1161–1169, 2009.
- [109] J. H. Kim, J. B. Ahn, D. H. Kim et al., "Glutathione S-transferase theta 1 protects against colitis through goblet cell differentiation via interleukin-22," *FASEB Journal*, vol. 34, no. 2, pp. 3289–3304, 2020.
- [110] L. Jostins, S. Ripke, R. K. Weersma et al., "Host-microbe interactions have shaped the genetic architecture of inflammatory bowel disease," *Nature*, vol. 491, no. 7422, pp. 119–124, 2012.
- [111] B. Khor, A. Gardet, and R. J. Xavier, "Genetics and pathogenesis of inflammatory bowel disease," *Nature*, vol. 474, no. 7351, pp. 307–317, 2011.
- [112] L. Mayr, F. Grabherr, J. Schwarzler et al., "Dietary lipids fuel GPX4-restricted enteritis resembling Crohn's disease," *Nature Communications*, vol. 11, no. 1, p. 1775, 2020.
- [113] G. Chaudhary, U. B. Mahajan, S. N. Goyal, S. Ojha, C. R. Patil, and S. B. Subramanya, "Protective effect of *Lagerstroemia speciosa* against dextran sulfate sodium induced ulcerative colitis in C57BL/6 mice," *American Journal of Translational Research*, vol. 9, no. 4, pp. 1792–1800, 2017.
- [114] P. S. de Silva, A. Olsen, J. Christensen et al., "An association between dietary arachidonic acid, measured in adipose tissue, and ulcerative colitis," *Gastroenterology*, vol. 139, no. 6, pp. 1912–1917, 2010.
- [115] T. Nishida, H. Miwa, A. Shigematsu, M. Yamamoto, M. Iida, and M. Fujishima, "Increased arachidonic acid composition of phospholipids in colonic mucosa from patients with active ulcerative colitis," *Gut*, vol. 28, no. 8, pp. 1002–1007, 1987.
- [116] L. J. Hinks, K. D. Inwards, B. Lloyd, and B. Clayton, "Reduced concentrations of selenium in mild Crohn's disease," *Journal of Clinical Pathology*, vol. 41, no. 2, pp. 198–201, 1988.
- [117] T. Castro Aguilar-Tablada, M. Navarro-Alarcon, J. Quesada Granados, C. Samaniego Sánchez, J. Á. Rufián-Henares, and F. Noguera-Lopez, "Ulcerative colitis and Crohn's disease are associated with decreased serum selenium concentrations and increased cardiovascular risk," *Nutrients*, vol. 8, no. 12, p. 780, 2016.
- [118] C. W. Barrett, K. Singh, A. K. Motley et al., "Dietary selenium deficiency exacerbates DSS-induced epithelial injury and AOM/DSS-induced tumorigenesis," *PLoS One*, vol. 8, no. 7, article e67845, 2013.
- [119] B. Speckmann and H. Steinbrenner, "Selenium and selenoproteins in inflammatory bowel diseases and experimental colitis," *Inflammatory Bowel Diseases*, vol. 20, no. 6, pp. 1110–1119, 2014.
- [120] H. Vargas-Robles, K. F. Castro-Ochoa, A. F. Citalan-Madrid, and M. Schnoor, "Beneficial effects of nutritional supplements on intestinal epithelial barrier functions in experimental colitis models in vivo," *World Journal of Gastroenterology*, vol. 25, no. 30, pp. 4181–4198, 2019.

- [121] R. Reddavid, O. Rotolo, M. G. Caruso et al., "The role of diet in the prevention and treatment of inflammatory bowel diseases," *Acta Bio Medica: Atenei Parmensis*, vol. 89, no. 9-S, pp. 60–75, 2018.
- [122] M. Bitiren, A. Z. Karakilcik, M. Zerir et al., "Protective effects of selenium and vitamin E combination on experimental colitis in blood plasma and colon of rats," *Biological Trace Element Research*, vol. 136, no. 1, pp. 87–95, 2010.
- [123] I. Alim, J. T. Caulfield, Y. Chen et al., "Selenium drives a transcriptional adaptive program to block ferroptosis and treat stroke," *Cell*, vol. 177, no. 5, pp. 1262–1279.e1225, 2019.
- [124] K. Wingler, C. Muller, K. Schmehl, S. Florian, and R. Brigelius-Flohe, "Gastrointestinal glutathione peroxidase prevents transport of lipid hydroperoxides in CaCo-2 cells," *Gastroenterology*, vol. 119, no. 2, pp. 420–430, 2000.
- [125] J. Jupp, K. Hillier, D. H. Elliott et al., "Colonic expression of leukotriene-pathway enzymes in inflammatory bowel diseases," *Inflammatory Bowel Diseases*, vol. 13, no. 5, pp. 537–546, 2007.
- [126] J. C. Masterson, E. N. McNamee, S. A. Fillon et al., "Eosinophil-mediated signalling attenuates inflammatory responses in experimental colitis," *Gut*, vol. 64, no. 8, pp. 1236–1247, 2015.
- [127] S. Kroschwald, C. Y. Chiu, D. Heydeck et al., "Female mice carrying a defective Alox15 gene are protected from experimental colitis via sustained maintenance of the intestinal epithelial barrier function," *Biochimica et Biophysica Acta (BBA)-Molecular and Cell Biology of Lipids*, vol. 1863, no. 8, pp. 866–880, 2018.
- [128] S. E. Wenzel, Y. Y. Tyurina, J. Zhao et al., "PEBP1 wards ferroptosis by enabling lipoxygenase generation of lipid death signals," *Cell*, vol. 171, no. 3, pp. 628–641.e626, 2017.
- [129] W. Lin, C. Ma, F. Su et al., "Raf kinase inhibitor protein mediates intestinal epithelial cell apoptosis and promotes IBDs in humans and mice," *Gut*, vol. 66, no. 4, pp. 597–610, 2017.
- [130] E. Mazzon, L. Sautebin, A. P. Caputi, and S. Cuzzocrea, "5-Lipoxygenase modulates the alteration of paracellular barrier function in mice ileum during experimental colitis," *Shock*, vol. 25, no. 4, pp. 377–383, 2006.
- [131] L. S. Laursen, J. Naesdal, K. Bukhave, K. Lauritsen, and J. Rask-Madsen, "Selective 5-lipoxygenase inhibition in ulcerative colitis," *Lancet*, vol. 335, no. 8691, pp. 683–685, 1990.
- [132] J. Hillingsø, J. Kjeldsen, L. S. Laursen et al., "Blockade of leukotriene production by a single oral dose of MK-0591 in active ulcerative colitis," *Clinical Pharmacology & Therapeutics*, vol. 57, no. 3, pp. 335–341, 1995.
- [133] J. Rask-Madsen, K. Bukhave, L. S. Laursen, and K. Lauritsen, "5-Lipoxygenase inhibitors in the treatment of inflammatory bowel disease," *Advances in Prostaglandin, Thromboxane, and Leukotriene Research*, vol. 22, pp. 113–124, 1994.
- [134] J. Rask-Madsen, K. Bukhave, L. S. Laursen, and K. Lauritsen, "5-Lipoxygenase inhibitors for the treatment of inflammatory bowel disease," *Agents and Actions*, vol. 36, no. 3, pp. C37–C46, 1992.
- [135] R. Joshi, S. Adhikari, B. S. Patro, S. Chattopadhyay, and T. Mukherjee, "Free radical scavenging behavior of folic acid: evidence for possible antioxidant activity," *Free Radical Biology and Medicine*, vol. 30, no. 12, pp. 1390–1399, 2001.
- [136] Y. Pan, Y. Liu, H. Guo et al., "Associations between folate and vitamin B12 levels and inflammatory bowel disease: a meta-analysis," *Nutrients*, vol. 9, no. 4, p. 382, 2017.
- [137] L. Elsborg and L. Larsen, "Folate deficiency in chronic inflammatory bowel diseases," *Scandinavian Journal of Gastroenterology*, vol. 14, no. 8, pp. 1019–1024, 1979.
- [138] B. A. Lashner, P. A. Heidenreich, G. L. Su, S. V. Kane, and S. B. Hanauer, "Effect of folate supplementation on the incidence of dysplasia and cancer in chronic ulcerative colitis. A case-control study," *Gastroenterology*, vol. 97, no. 2, pp. 255–259, 1989.
- [139] K. Zschiebsch, C. Fischer, G. Pickert et al., "Tetrahydrobiopterin attenuates DSS-evoked colitis in mice by rebalancing redox and lipid signalling," *Journal of Crohn's and Colitis*, vol. 10, no. 8, pp. 965–978, 2016.
- [140] X. Wei, X. Yi, X. H. Zhu, and D. S. Jiang, "Posttranslational modifications in ferroptosis," *Oxidative Medicine and Cellular Longevity*, vol. 2020, Article ID 8832043, pp. 1–12, 2020.
- [141] T. Yan, T. Zhang, W. Mu et al., "Ionizing radiation induces BH<sub>4</sub> deficiency by downregulating GTP-cyclohydrolase 1, a novel target for preventing and treating radiation enteritis," *Biochemical Pharmacology*, vol. 180, article 114102, 2020.
- [142] M. Xu, J. Tao, Y. Yang et al., "Ferroptosis involves in intestinal epithelial cell death in ulcerative colitis," *Cell Death & Disease*, vol. 11, no. 2, p. 86, 2020.
- [143] Y. Chen, P. Zhang, W. Chen, and G. Chen, "Ferroptosis mediated DSS-induced ulcerative colitis associated with Nrf2/HO-1 signaling pathway," *Immunology Letters*, vol. 225, pp. 9–15, 2020.
- [144] S. Wang, W. Liu, J. Wang, and X. Bai, "Curculigoside inhibits ferroptosis in ulcerative colitis through the induction of GPX4," *Life Sciences*, vol. 259, article 118356, 2020.
- [145] S. Heimerl, C. Moehle, A. Zahn et al., "Alterations in intestinal fatty acid metabolism in inflammatory bowel disease," *Biochimica et Biophysica Acta (BBA)-Molecular Basis of Disease*, vol. 1762, no. 3, pp. 341–350, 2006.
- [146] I. H. Mallick, W. Yang, M. C. Winslet, and A. M. Seifalian, "Ischemia-reperfusion injury of the intestine and protective strategies against injury," *Digestive Diseases and Sciences*, vol. 49, no. 9, pp. 1359–1377, 2004.
- [147] Y. Li, D. Feng, Z. Wang et al., "Ischemia-induced ACSL4 activation contributes to ferroptosis-mediated tissue injury in intestinal ischemia/reperfusion," *Cell Death & Differentiation*, vol. 26, no. 11, pp. 2284–2299, 2019.
- [148] M. Nakayama and M. Oshima, "Mutant p53 in colon cancer," *Journal of Molecular Cell Biology*, vol. 11, no. 4, pp. 267–276, 2019.
- [149] S. P. Hussain, P. Amstad, K. Raja et al., "Increased p53 mutation load in noncancerous colon tissue from ulcerative colitis: a cancer-prone chronic inflammatory disease," *Cancer Research*, vol. 60, no. 13, pp. 3333–3337, 2000.
- [150] V. J. N. Bykov, S. E. Eriksson, J. Bianchi, and K. G. Wiman, "Targeting mutant p53 for efficient cancer therapy," *Nature Reviews Cancer*, vol. 18, no. 2, pp. 89–102, 2018.
- [151] B. J. Leibowitz, L. Yang, L. Wei et al., "Targeting p53-dependent stem cell loss for intestinal chemoprotection," *Science Translational Medicine*, vol. 10, no. 427, p. 7610, 2018.
- [152] S. Fujii, T. Fujimori, H. Kawamata et al., "Development of colonic neoplasia in p53 deficient mice with experimental colitis induced by dextran sulphate sodium," *Gut*, vol. 53, no. 5, pp. 710–716, 2004.
- [153] W. C. Chang, R. A. Coudry, M. L. Clapper et al., "Loss of p53 enhances the induction of colitis-associated neoplasia by

- dextran sulfate sodium,” *Carcinogenesis*, vol. 28, no. 11, pp. 2375–2381, 2007.
- [154] B. Chu, N. Kon, D. Chen et al., “ALOX12 is required for p53-mediated tumour suppression through a distinct ferroptosis pathway,” *Nature Cell Biology*, vol. 21, no. 5, pp. 579–591, 2019.
- [155] Y. Wang, L. Yang, X. Zhang et al., “Epigenetic regulation of ferroptosis by H2B monoubiquitination and p53,” *EMBO Reports*, vol. 20, no. 7, article e47563, 2019.
- [156] Y. Ou, S. J. Wang, D. Li, B. Chu, and W. Gu, “Activation of SAT1 engages polyamine metabolism with p53-mediated ferroptotic responses,” *Proceedings of the National Academy of Sciences*, vol. 113, no. 44, pp. E6806–E6812, 2016.
- [157] Y. Xie, S. Zhu, X. Song et al., “The tumor suppressor p53 limits ferroptosis by blocking DPP4 activity,” *Cell Reports*, vol. 20, no. 7, pp. 1692–1704, 2017.
- [158] A. Tarangelo, L. Magtanong, K. T. Biegging-Rolett et al., “p53 suppresses metabolic stress-induced ferroptosis in cancer cells,” *Cell Reports*, vol. 22, no. 3, pp. 569–575, 2018.
- [159] Q. Ma, “Role of Nrf2 in oxidative stress and toxicity,” *Annual Review of Pharmacology and Toxicology*, vol. 53, pp. 401–426, 2013.
- [160] T. O. Khor, M. T. Huang, K. H. Kwon, J. Y. Chan, B. S. Reddy, and A. N. Kong, “Nrf2-deficient mice have an increased susceptibility to dextran sulfate sodium-induced colitis,” *Cancer Research*, vol. 66, no. 24, pp. 11580–11584, 2006.
- [161] T. O. Khor, M. T. Huang, A. Prawan et al., “Increased susceptibility of Nrf2 knockout mice to colitis-associated colorectal cancer,” *Cancer Prevention Research*, vol. 1, no. 3, pp. 187–191, 2008.
- [162] J. Li, H. Wang, Z. Zheng et al., “Mkp-1 cross-talks with Nrf2/Ho-1 pathway protecting against intestinal inflammation,” *Free Radical Biology and Medicine*, vol. 124, pp. 541–549, 2018.
- [163] S. Dun, X. Wang, Y. Ma et al., “Nrf2-induced miR-23a-27a-24-2 cluster modulates damage repair of intestinal mucosa by targeting the Bach1/HO-1 axis in inflammatory bowel diseases,” *Free Radical Biology and Medicine*, vol. 163, pp. 1–9, 2020.
- [164] X. Sun, Z. Ou, R. Chen et al., “Activation of the p62-Keap1-NRF2 pathway protects against ferroptosis in hepatocellular carcinoma cells,” *Hepatology*, vol. 63, no. 1, pp. 173–184, 2016.
- [165] J. L. Roh, E. H. Kim, H. Jang, and D. Shin, “Nrf2 inhibition reverses the resistance of cisplatin-resistant head and neck cancer cells to artesunate-induced ferroptosis,” *Redox Biology*, vol. 11, pp. 254–262, 2017.
- [166] M. Dodson, R. Castro-Portuguez, and D. D. Zhang, “NRF2 plays a critical role in mitigating lipid peroxidation and ferroptosis,” *Redox Biology*, vol. 23, article 101107, 2019.
- [167] Y. Yang, X. Cai, J. Yang et al., “Chemoprevention of dietary digitoflavone on colitis-associated colon tumorigenesis through inducing Nrf2 signaling pathway and inhibition of inflammation,” *Molecular Cancer*, vol. 13, no. 1, pp. 1–14, 2014.
- [168] E. Stenke, G. Aviello, A. Singh et al., “NADPH oxidase 4 is protective and not fibrogenic in intestinal inflammation,” *Redox Biology*, vol. 37, article 101752, 2020.
- [169] T. Yu, P. Wan, X. D. Zhu et al., “Inhibition of NADPH oxidase activities ameliorates DSS-induced colitis,” *Biochemical Pharmacology*, vol. 158, pp. 126–133, 2018.
- [170] W. H. Yang, C. C. Ding, T. Sun et al., “The Hippo pathway effector TAZ regulates ferroptosis in renal cell carcinoma,” *Cell Reports*, vol. 28, no. 10, pp. 2501–2508.e2504, 2019.
- [171] W. H. Yang, Z. Huang, J. Wu, C. K. C. Ding, S. K. Murphy, and J. T. Chi, “A TAZ-ANGPTL4-NOX2 axis regulates ferroptotic cell death and chemoresistance in epithelial ovarian cancer,” *Molecular Cancer Research*, vol. 18, no. 1, pp. 79–90, 2020.
- [172] W. M. Rosenberg, D. G. Jackson, J. M. Trowell et al., “Increased expression of CD44v6 and CD44v3 in ulcerative colitis but not colonic Crohn’s disease,” *Lancet*, vol. 345, no. 8959, pp. 1205–1209, 1995.
- [173] B. M. Wittig, B. Johansson, M. Zoller, C. Schwarzler, and U. Gunthert, “Abrogation of experimental colitis correlates with increased apoptosis in mice deficient for CD44 variant exon 7 (CD44v7),” *The Journal of Experimental Medicine*, vol. 191, no. 12, pp. 2053–2064, 2000.
- [174] B. M. Wittig, R. Sabat, P. Holzlohner et al., “Absence of specific alternatively spliced exon of CD44 in macrophages prevents colitis,” *Mucosal Immunology*, vol. 11, no. 3, pp. 846–860, 2018.
- [175] T. Liu, L. Jiang, O. Tavana, and W. Gu, “The deubiquitylase OTUB1 mediates ferroptosis via stabilization of SLC7A11,” *Cancer Research*, vol. 79, no. 8, pp. 1913–1924, 2019.
- [176] H. S. Oz, T. S. Chen, C. J. McClain, and W. J. de Villiers, “Antioxidants as novel therapy in a murine model of colitis,” *The Journal of Nutritional Biochemistry*, vol. 16, no. 5, pp. 297–304, 2005.
- [177] M. Minaian, E. Mostaghel, and P. Mahzouni, “Preventive therapy of experimental colitis with selected iron chelators and anti-oxidants,” *International Journal of Preventive Medicine*, vol. 3, Suppl 1, pp. S162–S169, 2012.
- [178] J. Y. Lee, J. S. Kim, J. M. Kim, N. Kim, H. C. Jung, and I. S. Song, “Simvastatin inhibits NF-kappaB signaling in intestinal epithelial cells and ameliorates acute murine colitis,” *International Immunopharmacology*, vol. 7, no. 2, pp. 241–248, 2007.
- [179] M. Ikeda, F. Takeshima, H. Isomoto et al., “Simvastatin attenuates trinitrobenzene sulfonic acid-induced colitis, but not oxazolone-induced colitis,” *Digestive Diseases and Sciences*, vol. 53, no. 7, pp. 1869–1875, 2008.
- [180] R. A. Maheshwari, R. Balaraman, G. U. Sailor, and D. B. Sen, “Protective effect of simvastatin and rosuvastatin on trinitrobenzene sulfonic acid-induced colitis in rats,” *Indian Journal of Pharmacology*, vol. 47, no. 1, pp. 17–21, 2015.
- [181] Y. Naito, K. Katada, T. Takagi et al., “Rosuvastatin, a new HMG-CoA reductase inhibitor, reduces the colonic inflammatory response in dextran sulfate sodium-induced colitis in mice,” *International Journal of Molecular Medicine*, vol. 17, no. 6, pp. 997–1004, 2006.
- [182] J. Carrier, E. Aghdassi, J. Cullen, and J. P. Allard, “Iron supplementation increases disease activity and vitamin E ameliorates the effect in rats with dextran sulfate sodium-induced colitis,” *The Journal of Nutrition*, vol. 132, no. 10, pp. 3146–3150, 2002.
- [183] T. Yoshikawa, S. Takahashi, and M. Kondo, “Possible role of free radicals in the chronic inflammation of the gut,” *EXS*, vol. 62, pp. 353–358, 1992.
- [184] Y. Isozaki, N. Yoshida, M. Kuroda et al., “Effect of a novel water-soluble vitamin E derivative as a cure for TNBS-induced colitis in rats,” *International Journal of Molecular Medicine*, vol. 17, no. 3, pp. 497–502, 2006.

- [185] N. Yoshida, T. Yoshikawa, T. Yamaguchi et al., "A novel water-soluble vitamin E derivative protects against experimental colitis in rats," *Antioxidants & Redox Signaling*, vol. 1, no. 4, pp. 555–562, 1999.
- [186] H. Yan, H. Wang, X. Zhang, X. Li, and J. Yu, "Ascorbic acid ameliorates oxidative stress and inflammation in dextran sulfate sodium-induced ulcerative colitis in mice," *International Journal of Clinical and Experimental Medicine*, vol. 8, no. 11, pp. 20245–20253, 2015.
- [187] K. Kondo, K. Hiramoto, Y. Yamate, K. Goto, H. Sekijima, and K. Ooi, "Ameliorative effect of high-dose vitamin C administration on dextran sulfate sodium-induced colitis mouse model," *Biological and Pharmaceutical Bulletin*, vol. 42, no. 6, pp. 954–959, 2019.
- [188] I. Ahnfelt-Ronne, O. H. Nielsen, A. Christensen, E. Langholz, V. Binder, and P. Riis, "Clinical evidence supporting the radical scavenger mechanism of 5-aminosalicylic acid," *Gastroenterology*, vol. 98, 5 Part 1, pp. 1162–1169, 1990.
- [189] N. J. Simmonds, A. D. Millar, D. R. Blake, and D. S. Rampton, "Antioxidant effects of aminosalicylates and potential new drugs for inflammatory bowel disease: assessment in cell-free systems and inflamed human colorectal biopsies," *Alimentary Pharmacology & Therapeutics*, vol. 13, no. 3, pp. 363–372, 1999.
- [190] C. Liu, R. M. Russell, D. E. Smith et al., "The effect of dietary glutathione and coenzyme Q10 on the prevention and treatment of inflammatory bowel disease in mice," *International Journal for Vitamin and Nutrition Research*, vol. 74, no. 1, pp. 74–85, 2004.
- [191] E. M. El Morsy, R. Kamel, and M. A. Ahmed, "Attenuating effects of coenzyme Q10 and amlodipine in ulcerative colitis model in rats," *Immunopharmacology and Immunotoxicology*, vol. 37, no. 3, pp. 244–251, 2015.
- [192] G. Tahan, R. Gramignoli, F. Marongiu et al., "Melatonin expresses powerful anti-inflammatory and antioxidant activities resulting in complete improvement of acetic-acid-induced colitis in rats," *Digestive Diseases and Sciences*, vol. 56, no. 3, pp. 715–720, 2011.
- [193] P. P. Trivedi and G. B. Jena, "Melatonin reduces ulcerative colitis-associated local and systemic damage in mice: investigation on possible mechanisms," *Digestive Diseases and Sciences*, vol. 58, no. 12, pp. 3460–3474, 2013.
- [194] V. P. Singh, C. S. Patil, and S. K. Kulkarni, "Effect of 5-lipoxygenase inhibition on events associated with inflammatory bowel disease in rats," *Indian Journal of Experimental Biology*, vol. 42, no. 7, pp. 667–673, 2004.
- [195] Y. C. Pai, L. T. Weng, S. C. Wei et al., "Gut microbial transcytosis induced by tumor necrosis factor-like 1A-dependent activation of a myosin light chain kinase splice variant contributes to IBD," *Journal of Crohn's and Colitis*, vol. 15, no. 2, pp. 258–272, 2020.
- [196] A. Viktorinova and M. Durfinova, "Mini-review: is iron-mediated cell death (ferroptosis) an identical factor contributing to the pathogenesis of some neurodegenerative diseases?," *Neuroscience Letters*, vol. 745, article 135627, 2021.
- [197] C. Ou, W. Na, W. Ge et al., "Biodegradable charge transfer complexes for glutathione depletion induced ferroptosis and NIR-II photoacoustic imaging guided cancer photothermal therapy," *Angewandte Chemie International Edition*, vol. 60, no. 15, pp. 8157–8163, 2021.
- [198] Z. Guan, J. Chen, X. Li, and N. Dong, "Tanshinone IIA induces ferroptosis in gastric cancer cells through p53-mediated SLC7A11 down-regulation," *Bioscience Reports*, vol. 40, no. 8, 2020.
- [199] M. T. Abreu, "Updates in mucosal immunology for inflammatory bowel diseases," *Current Opinion in Gastroenterology*, vol. 34, no. 6, pp. 375–376, 2018.
- [200] R. Caruso, B. C. Lo, and G. Nunez, "Host-microbiota interactions in inflammatory bowel disease," *Nature Reviews Immunology*, vol. 20, no. 7, pp. 411–426, 2020.
- [201] M. Boirivant, M. Marini, G. Di Felice et al., "Lamina propria T cells in Crohn's disease and other gastrointestinal inflammation show defective CD2 pathway-induced apoptosis," *Gastroenterology*, vol. 116, no. 3, pp. 557–565, 1999.
- [202] J. Itoh, C. de La Motte, S. A. Strong, A. D. Levine, and C. Fiocchi, "Decreased Bax expression by mucosal T cells favours resistance to apoptosis in Crohn's disease," *Gut*, vol. 49, no. 1, pp. 35–41, 2001.
- [203] H. S. de Souza, G. A. West, N. Rebert, C. de la Motte, J. Drazba, and C. Fiocchi, "Increased levels of survivin, via association with heat shock protein 90, in mucosal T cells from patients with Crohn's disease," *Gastroenterology*, vol. 143, no. 4, pp. 1017–1026.e1019, 2012.
- [204] L. Shi, Y. Liu, M. Li, and Z. Luo, "Emerging roles of ferroptosis in the tumor immune landscape: from danger signals to anti-tumor immunity," *FEBS Journal*, 2021.



## Research Article

# Exogenous and Endogenous Serine Deficiency Exacerbates Hepatic Lipid Accumulation

Liuqin He,<sup>1,2</sup> Yonghui Liu,<sup>1,2</sup> Di Liu,<sup>3</sup> Yanzhong Feng,<sup>3</sup> Jie Yin<sup>1,2</sup> ,<sup>4</sup> and Xihong Zhou<sup>1,2</sup> 

<sup>1</sup>Hunan Provincial Key Laboratory of Animal Intestinal Function and Regulation, Laboratory of Animal Nutrition and Human Health, College of Life Sciences, Hunan Normal University, Changsha 410081, China

<sup>2</sup>Hunan Provincial Key Laboratory of Animal Nutritional Physiology and Metabolic Process, Institute of Subtropical Agriculture, Chinese Academy of Sciences, Changsha 410125, China

<sup>3</sup>Institute of Animal Husbandry, Heilongjiang Academy of Agricultural Sciences, Harbin 150086, China

<sup>4</sup>College of Animal Science and Technology, Hunan Agricultural University, Changsha 410128, China

Correspondence should be addressed to Jie Yin; [yinjie@hunau.edu.cn](mailto:yinjie@hunau.edu.cn) and Xihong Zhou; [xhzhou@isa.ac.cn](mailto:xhzhou@isa.ac.cn)

Received 9 June 2021; Revised 13 September 2021; Accepted 4 October 2021; Published 19 October 2021

Academic Editor: Demin Cai

Copyright © 2021 Liuqin He et al. This is an open access article distributed under the Creative Commons Attribution License, which permits unrestricted use, distribution, and reproduction in any medium, provided the original work is properly cited.

Serine is involved in the regulation of hepatic lipid metabolism. However, whether exogenous or endogenous serine deficiency affects lipid accumulation in the liver and related mechanisms is unclear. Here, we investigated the effects of serine deficiency on hepatic fat accumulation in mice fed a serine-deficient diet or in mice supplemented with the D-3-phosphoglycerate dehydrogenase (PHGDH) inhibitor NCT-503. Both treatments produced an increase in body weight and liver weight and higher triglyceride content in the liver. Both treatments also exacerbated hepatic inflammatory responses and oxidative stress. Importantly, NCT-503 supplementation significantly inhibited PHGDH activity and decreased the serine content in the liver. Dietary serine deficiency significantly affected the colonic microbiota, characterized by a decreased ratio of *Firmicutes/Bacteroidetes* and decreased proportion of *Bifidobacterium*. Dietary serine deficiency additionally resulted in significantly decreased colonic and serum acetate and butyrate levels. The collective results indicate that NCT-503 supplementation may contribute to overaccumulation of hepatic lipid, by causing hepatic serine deficiency, while dietary serine deficiency may produce similar outcomes by affecting the gut-microbiota-liver axis.

## 1. Introduction

Hepatocytes are the most metabolically active cell type in the body, with diverse physiological and metabolic functions [1]. Decreased or increased metabolism of hepatocytes can result in complicated disorders and development of diseases, including fatty liver disease and cancer [2]. Imbalance in lipid metabolism in the liver is a hallmark of nonalcoholic fatty liver disease [3]. However, the underlying mechanisms leading to hepatic lipid overaccumulation and steatosis remain unclear.

Serine is a metabolically necessary amino acid that is a pivotal link between glycolysis and one-carbon and lipid metabolism, as well as purine and glutathione synthesis. Thus, serine has a critical role in a variety of biological functions. Genome-scale metabolic modeling of hepatocytes has

demonstrated the involvement of serine deficiency in the development of fatty liver disease [1]. Importantly, exogenous serine supplementation can alleviate lipid overaccumulation and oxidative stress in the liver of subjects with high-fat-induced fatty liver disease or alcoholic fatty liver diseases [4, 5]. Interestingly, 3-phosphoglycerate dehydrogenase (PHGDH), the key enzyme involved in the de novo synthesis of serine, is also closely associated with the development of fatty liver diseases [6]. Knockdown of the *PHGDH* gene reduces hepatic serine content, while PHGDH-derived serine helps maintain general lipid homeostasis [7]. The aforementioned findings indicate that both exogenous and endogenous serine have critical roles in the regulation of hepatic lipid metabolism. However, whether exogenous serine deficiency affects hepatic lipid deposition remains unknown. Moreover, the possible effects of directly targeting

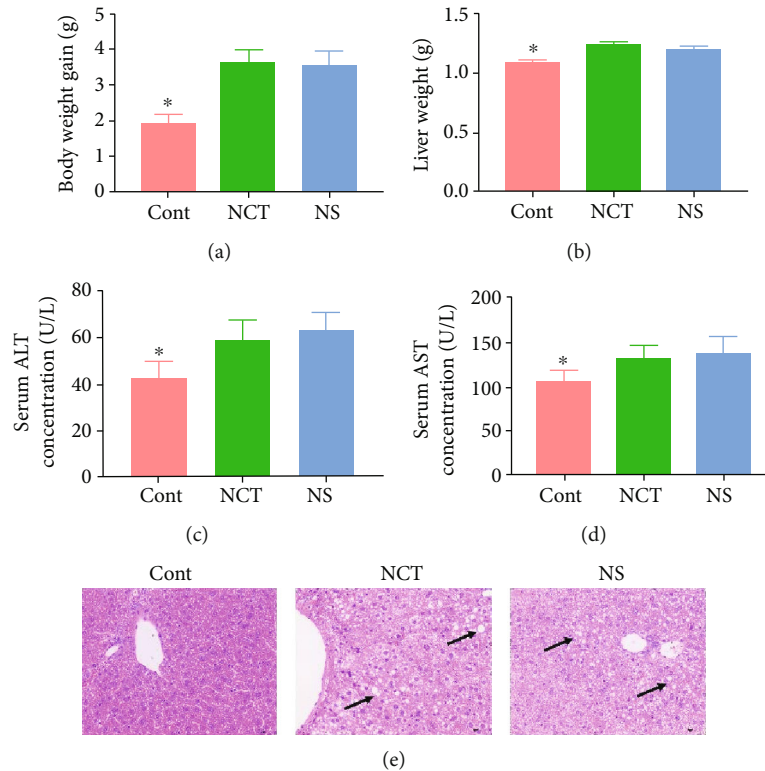


FIGURE 1: Serine deficiency resulted in increased body weight gain and impaired liver morphology: (a) body weight gain, (b) liver weight, ALT (c) and AST (d) concentrations in serum, and (e) HE staining ( $\times 200$ ). Arrows, impaired hepatocytes. CONT: mice were fed on the control diet; NS: mice were fed on the serine- and glycine-deficient diet; NCT: mice were fed on the control diet and supplemented with NCT-503. ALT: alanine aminotransferase; AST: aspartate aminotransferase. Data are presented as means  $\pm$  SEM.  $n = 8$ . \*Mean values were significantly different between CONT and NCT, NS ( $P < 0.05$ ).

the activity of PHGDH enzyme on hepatic lipid accumulation need to be explored.

Importantly, recent studies have focused on the effects of serine deficiency on inflammatory responses and oxidative stress [8, 9]. Whether exogenous or endogenous serine deficiency affects lipid accumulation in the liver and the related mechanisms remain to be elucidated. Subsequently, we conducted the current study to investigate the effects of exogenous serine deficiency by using a serine-deficient diet or endogenous serine deficiency by supplementing an PHGDH inhibitor NCT-503, on hepatic fat accumulation in mice. The results indicated that NCT-503 supplementation may contribute to overaccumulation of hepatic lipid, by causing hepatic serine deficiency, while dietary serine deficiency may produce similar outcomes by affecting the gut-microbiota-liver axis. Our results would enrich the understanding of serine as a modulator of lipid metabolism in liver and suggest the application of serine in lipid metabolism disorder-related diseases.

## 2. Materials and Methods

**2.1. Animal Care and Experimental Design.** Twenty-four C57BL/6J male mice (6-week-old) were purchased from HUNAN Slac Laboratory Animal Central. All animals were housed in pathogen-free colonies at  $22 \pm 2^\circ\text{C}$ , with a relative humidity of  $50 \pm 5\%$  and a lighting cycle of 12 h/d. All ani-

mals had free access to food and water. All mice were randomly assigned into three treatment groups: (i) mice were fed on the control diet (CONT); (ii) mice were fed on the serine- and glycine-deficient diet (NS); and (iii) mice were fed on the control diet and supplemented with NCT-503 (NCT), a specific inhibitor of PHGDH. The experiment lasted six weeks. NCT-503 was supplemented with a daily dosage of 40 mg/kg body weight as previously did [10]. The diets were purchased from Research Diets (New Brunswick, NJ, USA), and diet composition was presented in Supplementary Table 1.

NCT-503 was purchased from Selleck (Shanghai, China).

The experimental protocol was approved by the Protocol Management and Review Committee of Institute of Subtropical Agriculture, and mice were treated according to the animal care guidelines of the Institute of Subtropical Agriculture (Changsha, China). During the experiment, body weight was recorded every week. At the end, the blood samples were obtained from the retroorbital sinus, and the serum was stored. Then, all mice were sacrificed by cervical dislocation, and the abdomen was opened to obtain and weigh the liver. Liver samples were collected and fixed in 4% formaldehyde for 24 h, and they were also collected and immediately frozen in liquid nitrogen. Colonic content was collected for the analysis of gut microbiota and short-chain fatty acids (SCFAs).

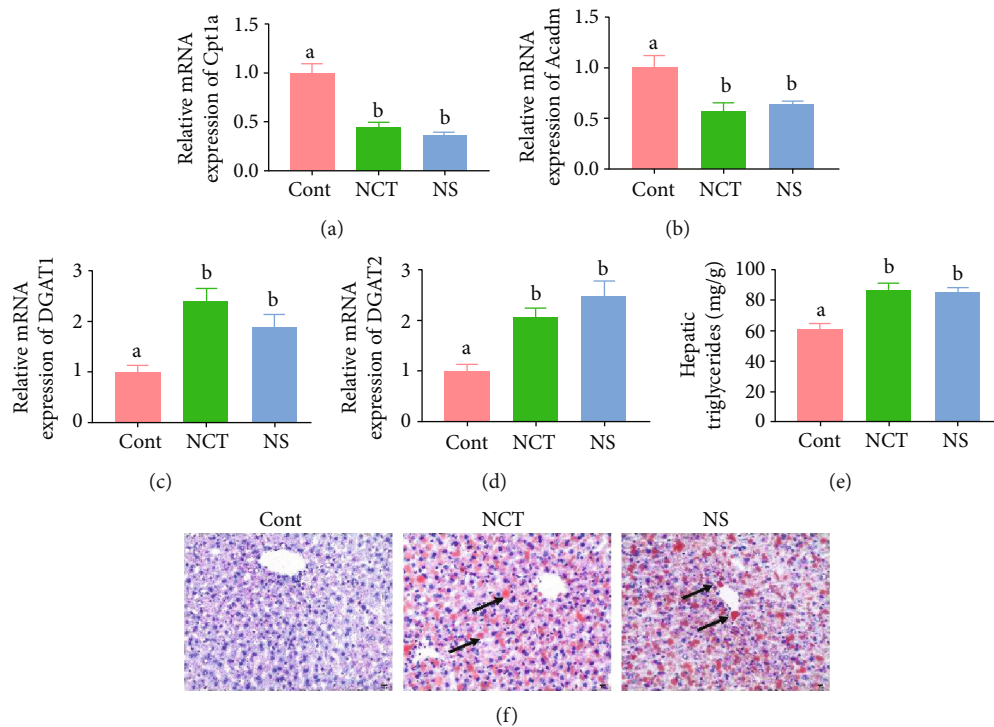


FIGURE 2: Serine deficiency exacerbated hepatic lipid accumulation. Cpt1a: carnitine palmitoyltransferase 1a; Acadm: medium-chain acyl-CoA dehydrogenase; DGAT: diacylglycerol O-acyltransferase. Relative mRNA expression of *Cpt1a* (a), *Acadm* (b), *DGAT1* (c), and *DGAT2* (d). (e) Oil Red O staining ( $\times 200$ ). Arrows, lipid droplet. CONT: mice were fed on the control diet; NS: mice were fed on the serine- and glycine-deficient diet; NCT: mice were fed on the control diet and supplemented with NCT-503. Data are presented as means  $\pm$  SEM.  $n = 8$ . <sup>a,b</sup>Means of the bars with different letters were significantly different among groups ( $P < 0.05$ ).

**2.2. Biochemical Assays.** Biochemical assays for aspartate aminotransferase (AST) and alanine aminotransferase (ALT) level were performed with commercially available kits (Beyotime, Shanghai, China).

**2.3. Hematoxylin-Eosin and Oil Red O Staining.** Hematoxylin-erosin (HE) and Oil Red O staining were performed as previously did [5]. Fresh liver samples immediately fixed in 4% formaldehyde, were paraffin embedded, sectioned into  $8\mu\text{m}$  thickness, and then stained either with HE or Oil Red O.

**2.4. Determination of Hepatic Triglycerides and Glutathione Contents.** Hepatic lipid was extracted using a modified Folch method [11]. Triglycerides were measured using commercially available colorimetric kit (BSBE, Beijing, China). Reduced glutathione (GSH) content was measured using the corresponding commercial colorimetric assay kits (Beyotime, Shanghai, China) according to the manufacturer's instructions.

**2.5. Determination of PHGDH Activity.** PHGDH activity was determined using enzyme-linked immunosorbent assay according to the manufacturer's instructions (MEIMIAN, Suzhou, China). Protein concentration was determined by BCA Protein Assay (Pierce Biotechnology, Rockford, IL, USA).

**2.6. RT-qPCR Analysis.** RT-qPCR analysis was performed as previously did [12]. Total RNA was isolated from liver samples using TRIzol Reagent (Invitrogen), and cDNA was obtained using the PrimeScript RT reagent kit (Takara, Dalian, China). RT-qPCR was performed using SYBR Green mix (Takara). All samples were run in triplicate, and the results were calculated by normalizing the mRNA expression of target genes to  $\beta$ -actin mRNA. The primer sequences [13] are shown in Supplementary Table 2.

**2.7. Determination of Reactive Oxygen Species Content.** Hepatic reactive oxygen species (ROS) content was determined as previously did [14]. As abovementioned,  $10\mu\text{m}$  sections were stained with dihydroethidium (Sigma-Aldrich) for 20 min at  $37^\circ\text{C}$  in a humidified 5%  $\text{CO}_2$  incubator. Representative pictures were captured by fluorescence microscopy, and fluorescence intensity was calculated by Image Browser software (Leica, Wetzlar, Germany).

**2.8. Determination of Serine Concentration.** Serine concentration in serum and liver was measured as previously did [15]. Briefly, grounded liver samples (50 mg) and serum were added with 10% sulfosalicylic acid. After completely vortexed, the supernatant was obtained after centrifuged at  $12\,000\text{g}$  for 10 minutes and filtered through  $0.22\mu\text{m}$  filters for the determination of serine concentration.

**2.9. Gut Microbiota Profiling.** Gut microbiota profiling was assayed as previously described [8]. Briefly, DNA was

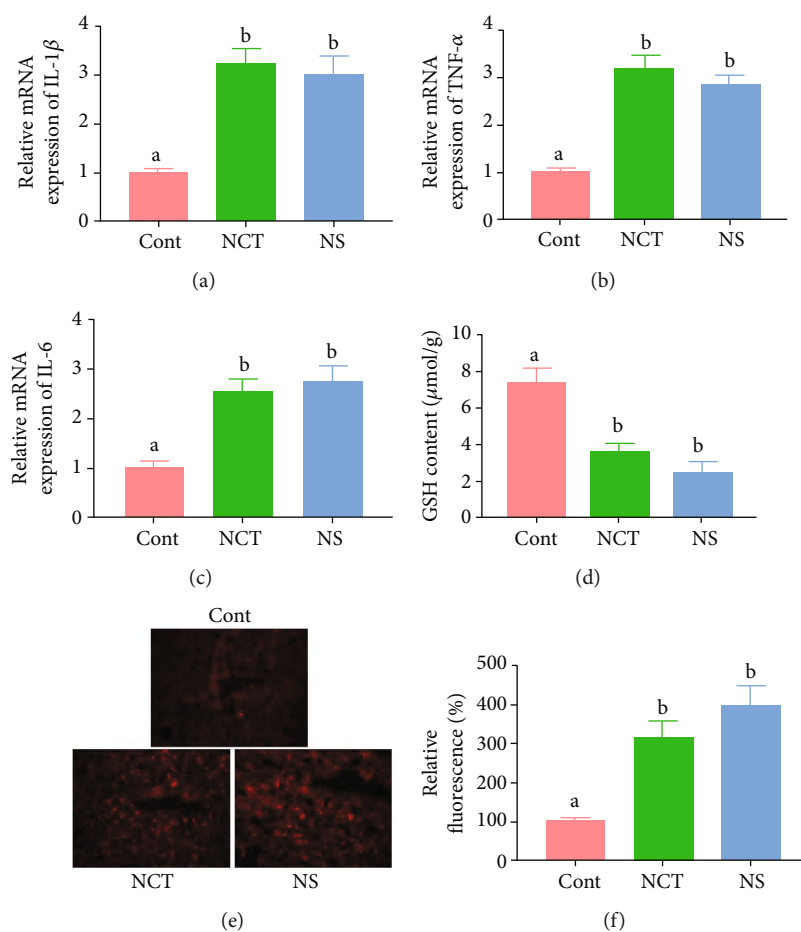


FIGURE 3: Serine deficiency aggravated oxidative and inflammatory status in liver. GSH: glutathione. Relative mRNA expression of  $IL-1\beta$  (a),  $TNF-\alpha$  (b), and  $IL-6$  (c). (d) GSH content in the liver. (e) ROS content (red) in the liver. (f) Relative fluorescence of ROS staining. CONT: mice were fed on the control diet; NS: mice were fed on the serine- and glycine-deficient diet; NCT: mice were fed on the control diet and supplemented with NCT-503. Data are presented as means  $\pm$  SEM.  $n = 8$  for the mRNA expression and GSH content and  $n = 3$  for ROS staining. <sup>a,b</sup>Means of the bars with different letters were significantly different among groups ( $P < 0.05$ ).

extracted from colonic contents and isolated using the QIAamp DNA stool Mini Kit (Qiagen, Shanghai, China). Bacterial 16S rDNA gene sequences (V3–V4 region) were amplified, and PCR was performed using Phusion High-Fidelity PCR Master Mix reagent (New England BioLabs Inc). Amplicons purified using Qiagen Gel Extraction Kit (Qiagen) were sequenced using the Illumina HiSeq2500 platform. Quality filtering and analysis were performed using USEARCH, while adhering to the QIIME quality-controlled process based on 97% sequence similarity (Novogene, Beijing, China).

**2.10. Determination of SCFA Content.** SCFAs were measured as previously did [16]. Briefly, fecal samples were collected and ground in liquid nitrogen. Then, the samples were mixed with pure water (300%, w/v), homogenized and centrifuged to collect fecal homogenate. Serum samples were collected after centrifugation at 1200 g for 15 min at 4°C. Then, the fecal homogenate or serum was mixed with 5 M HCl and extracted with anhydrous diethyl ether. Next, the extracts were derivatized with O-bis(trimethyl-silyl)-trifluor-

oacetamide. Finally, the profiling of SCFAs was analyzed by the gas chromatography/mass spectrometry.

**2.11. Statistical Analysis.** Significance between treatments was analyzed using one-way ANOVA followed by Student–Newman–Keuls post hoc test, using the data statistics software SPSS 18.0. Data are presented as means  $\pm$  SEM. Mean values were considered significantly different when  $P < 0.05$ .

### 3. Results

**3.1. Serine Deficiency Resulted in Increased Body Weight Gain and Impaired Liver Morphology.** As shown in Figure 1, body weight gain and liver weight were significantly lower in the CONT group than those in the NCT and NS group (Figures 1(a) and 1(b)). To investigate the effects of serine deficiency on the liver function, we firstly determined serum concentrations of ALT and AST. The results showed that ALT and AST concentrations were significantly lower in the CONT group than those in the NCT and NS group (Figures 1(c) and 1(d)). Additionally,

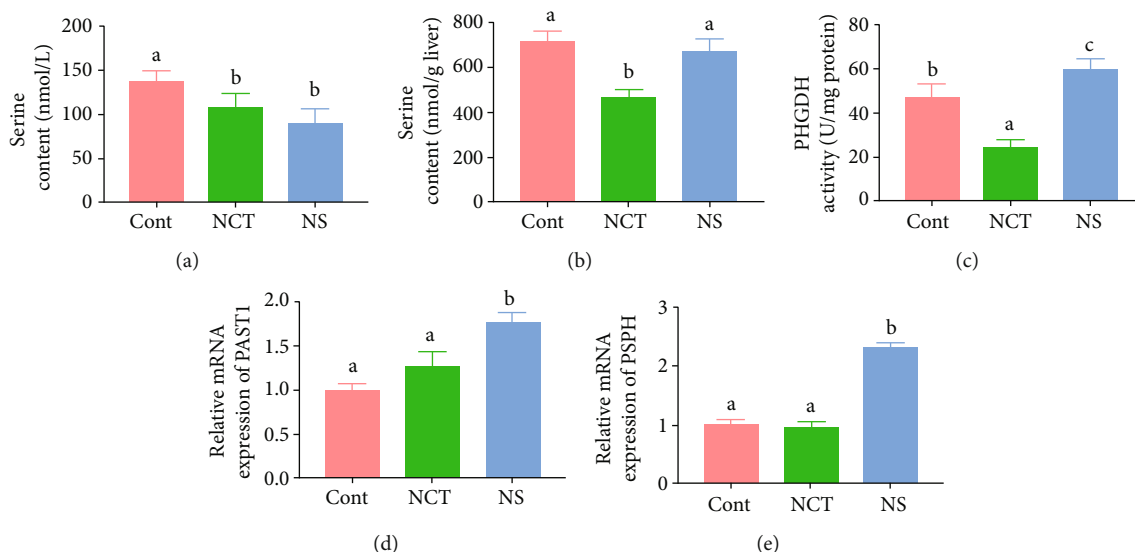


FIGURE 4: Dietary NCT-503 supplementation decreased serine content in liver. PHGDH: phosphoglycerate dehydrogenase; PAST1: phosphoserine aminotransferase; PSPH: phosphoserine phosphatase. Serine content in serum (a) and liver (b). (c) PHGDH activity. Relative mRNA expression of *PAST1* (d) and *PSPH* (e). CONT: mice were fed on the control diet; NS: mice were fed on the serine-and glycine-deficient diet; NCT: mice were fed on the control diet and supplemented with NCT-503. Data are presented as means  $\pm$  SEM.  $n = 8$ . <sup>a,b,c</sup>Means of the bars with different letters were significantly different among groups ( $P < 0.05$ ).

the results of HE staining showed that the liver morphology was impaired in both the NCT and NS group, as indicated by vacuolization and damaged hepatocytes (Figure 1(e)).

**3.2. Serine Deficiency Exacerbated Hepatic Lipid Accumulation.** To investigate whether serine deficiency affects lipid metabolism in the liver, we determined the expression of genes involved in fatty acid oxidation and triglyceride synthesis. The results showed that the mRNA expression of *Cpt1a* and *Acadm* was significantly decreased (Figures 2(a) and 2(b)) while the mRNA expression of *DGAT1* and *DGAT2* was significantly increased (Figures 2(c) and 2(d)) in the liver of mice in the NCT and NS group, when compared with those of the CONT group. Furthermore, hepatic triglyceride content was significantly higher in mice in the NCT and NS group than those in the CONT group (Figure 2(e)). The results of Oil Red O staining further confirmed an increased accumulation of lipid in mice in the NCT and NS group (Figure 2(f)).

**3.3. Serine Deficiency Aggravated Oxidative and Inflammatory Status in the Liver.** To investigate whether serine deficiency affects inflammatory responses, we determined genes expression of inflammatory cytokines in the liver. The results showed that the mRNA expression of *IL-1 $\beta$* , *TNF- $\alpha$* , and *IL-6* was significantly increased in mice in the NCT and NS group, when compared with those of the CONT group (Figures 3(a) and 3(c)). To investigate whether serine deficiency affects oxidative status, we determined the content of GSH and ROS in the liver. The results showed that GSH content was significantly decreased (Figure 3(d)) while ROS level was significantly increased (Figures 3(e) and 3(f)) in mice in the NCT and NS group, when compared with those of the CONT group.

**3.4. Dietary NCT-503 Supplementation Decreased Serine Content in the Liver.** To investigate whether serine deficiency affects serine content in mice, we determined serine content in the serum and liver. The results showed that serine content in the serum and liver was significantly decreased in mice in the NCT and NS group, when compared with those of the CONT group (Figure 4(a)). Notably, serine content in the liver was significantly decreased in mice in the NCT group, while it was not significantly changed in mice in the NS group (Figure 4(b)). Importantly, PHGDH activity (Figure 4(c)) and mRNA expression of *PAST1* and *PSPH* were significantly higher in mice in the NS group (Figures 4(d) and 4(e)), while PHGDH activity was significantly lower in mice in the NCT group (Figure 4(c)), when compared with those of the CONT group.

**3.5. Dietary Serine Deficiency Altered Microbiota Composition in Colonic Content.** To investigate whether serine deficiency altered microbiota composition, we used 16S rDNA gene sequencing for bacterial identification in colonic content. The results showed that no significant change was observed in microbiota composition between mice in the CONT group and NCT group (Figure 5). Although no significant changes were observed in Shannon and Chao1 index (Figures 5(a) and 5(b)),  $\beta$ -diversity was tended to increase (Figure 5(c)) in mice in the NS group, when compared with those of the CONT group. Unweighted principal coordinate analysis indicated no clear difference in beta-diversity among the treatment groups (Figure 5(d)). Notably, the ratio of *Firmicutes* to *Bacteroidetes* (Figures 5(e) and 5(f)) and the relative abundance of *Bifidobacterium* (Figures 5(g) and 5(h)) were decreased in mice in the NS group, when compared with those of the CONT group.

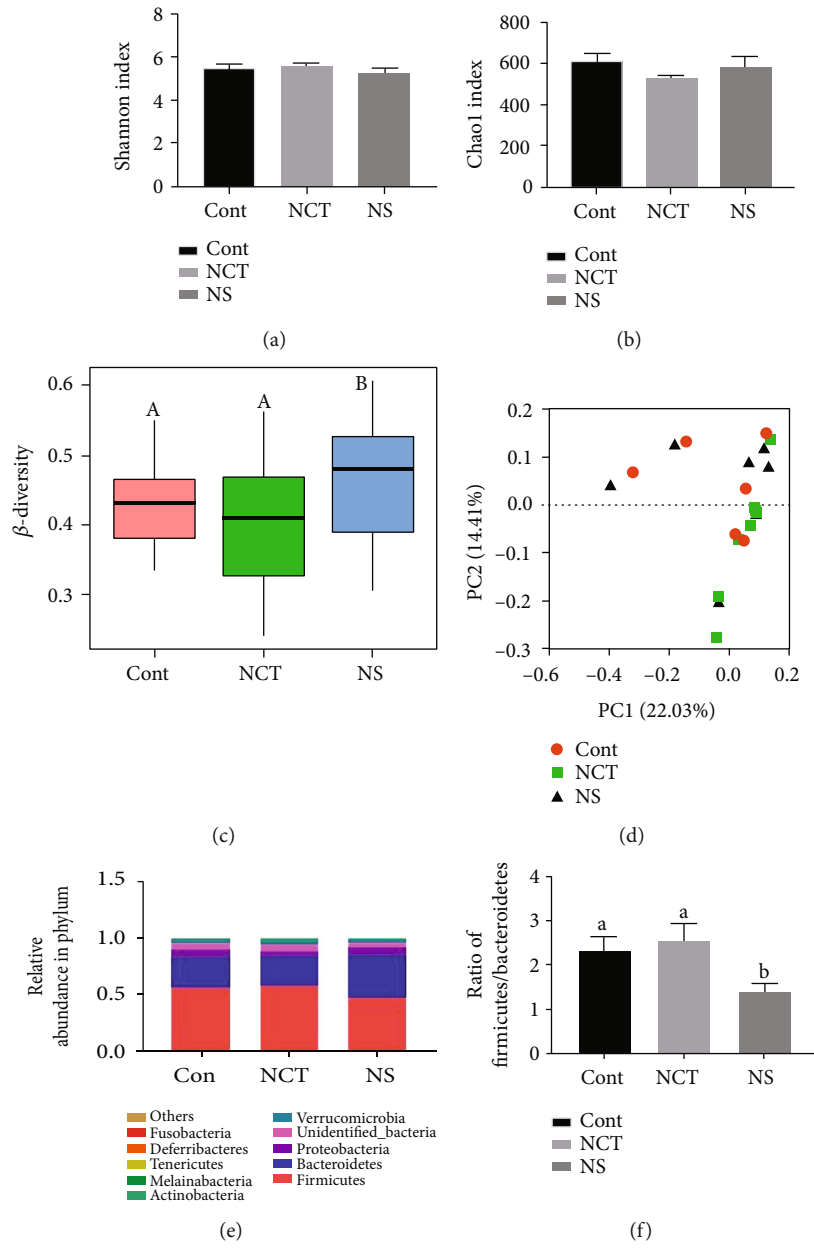


FIGURE 5: Continued.

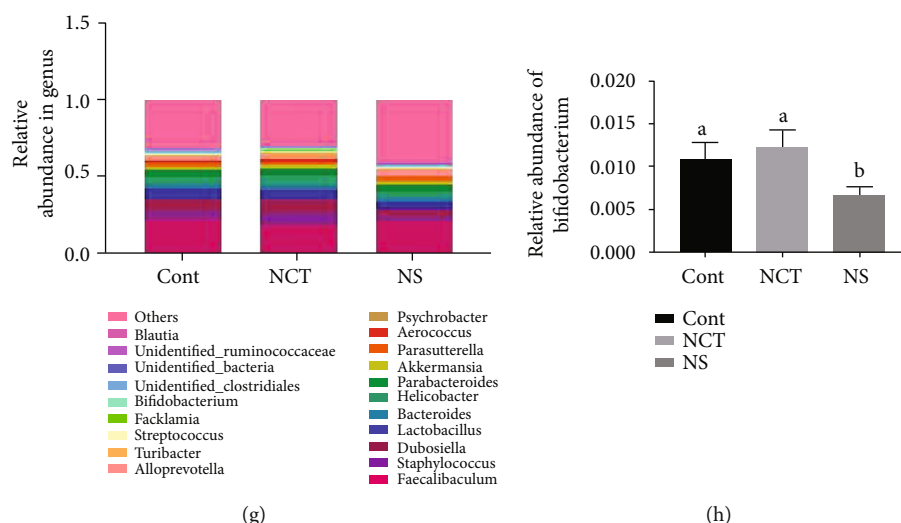


FIGURE 5: Dietary serine deficiency altered microbiota composition in colonic content. (a) Shannon index. (b) Chao1 index. (c)  $\beta$ -Diversity. (d) PCoA plot of the microbiota based on an unweighted UniFrac metric. (e) Relative abundance of predominant bacteria at the phylum level. (f) Ratio of *Firmicutes* to *Bacteroidetes*. (g) Relative abundance of predominant bacteria at the genus level. (h) Relative abundance of *Bifidobacterium*. CONT: mice were fed on the control diet; NS: mice were fed on the serine- and glycine-deficient diet; NCT: mice were fed on the control diet and supplemented with NCT-503. Data are presented as means  $\pm$  SEM.  $n = 6$  for the CONT group and  $n = 7$  for the NCT and NS group. <sup>a,b</sup>Means of the bars with different letters were significantly different among groups ( $P < 0.05$ ). <sup>A,B</sup>Means of the bars with different letters were tended to differ between NS and CONT and NCT ( $0.05 < P < 0.1$ , which was considered as a tendency).

**3.6. Dietary Serine Deficiency Decreased Contents of SCFAs in Colonic Contents and Serum.** To further investigate whether the changes of microbiota composition accompanied by changes of metabolites, we determined the contents of SCFAs. As shown in Figure 6, dietary serine deficiency significantly decreased acetate and butyrate contents in both colonic contents and serum in mice, while it had no effects on propionate content. Additionally, NCT-503 supplementation had no effects on acetate, propionate, and butyrate contents in either colonic contents or serum in mice.

#### 4. Discussion

Both exogenous and endogenous serine are involved in the regulation of lipid metabolism [1, 6]. In the present study, we found that both endogenous serine deficiency via inhibition of de novo serine synthesis and exogenous serine deficiency resulted in increases in body weight and liver weight. Increased liver weight was accompanied by increased lipid accumulation. Inhibition of PHGDH activity resulted in decreased serine content in the liver, which may contribute to aggravated oxidative and inflammatory status, whereas dietary serine deficiency did not affect the serine content in the liver. Notably, dietary serine deficiency decreased the ratio of *Firmicutes* to *Bacteroidetes* in the colonic microbiota. Importantly, dietary serine deficiency also decreased the relative colonic abundance of *Bifidobacterium* and the metabolites of acetate and butyrate. These changes may explain why exogenous serine deficiency results in lipid overaccumulation in the liver. Our results suggest that exogenous and endogenous serine deficiencies disrupt hepatic lipid metabolism by different mechanisms (Figure 7).

Serine can be derived from food and protein turnover and can be synthesized de novo from 3-phosphoglycerate and directly from glycine. Of these mechanisms, de novo biosynthesis is the main mechanism. As expected, dietary serine deficiency and inhibition of PHGDH caused a significant decrease in serum serine content in mice. Notably, only inhibition of PHGDH caused reduction in the liver serine content. Hepatic serine content was not affected by dietary serine deficiency. Surprisingly, we observed increased hepatic PHGDH activity and upregulated expression of *PAST1* and *PSPH*, which encode the enzymes involved in de novo serine biosynthesis. These results indicate that the increase in de novo biosynthesis may compensate for dietary serine deficiency to meet the serine requirement in the liver.

Hepatic serine is closely involved in lipid metabolism [4, 5, 7]. Hepatic serine deficiency contributes to the overaccumulation of lipids in the liver [1, 6]. In the present study, we further confirmed that the inhibition of de novo serine biosynthesis by administration of NCT-503 resulted in hepatic serine deficiency and then lipid accumulation, as indicated by the results of Oil Red O staining and increased hepatic triglyceride content. A previous study had shown that a lack of the *PHGDH* gene expression may inhibit SIRT1 activity and further increase lipid accumulation [6]. However, in the present study, we directly targeted PHGDH activity, which may have produced different responses. Consequently, the underlying mechanisms by which serine deficiency in the liver contributes to lipid accumulation need to be studied further. Disturbances in lipid metabolism are often accompanied by increased inflammatory responses and oxidative stress. We found increased expression of pro-inflammatory cytokines, decreased GSH content, and increased ROS content in the liver of mice treated with

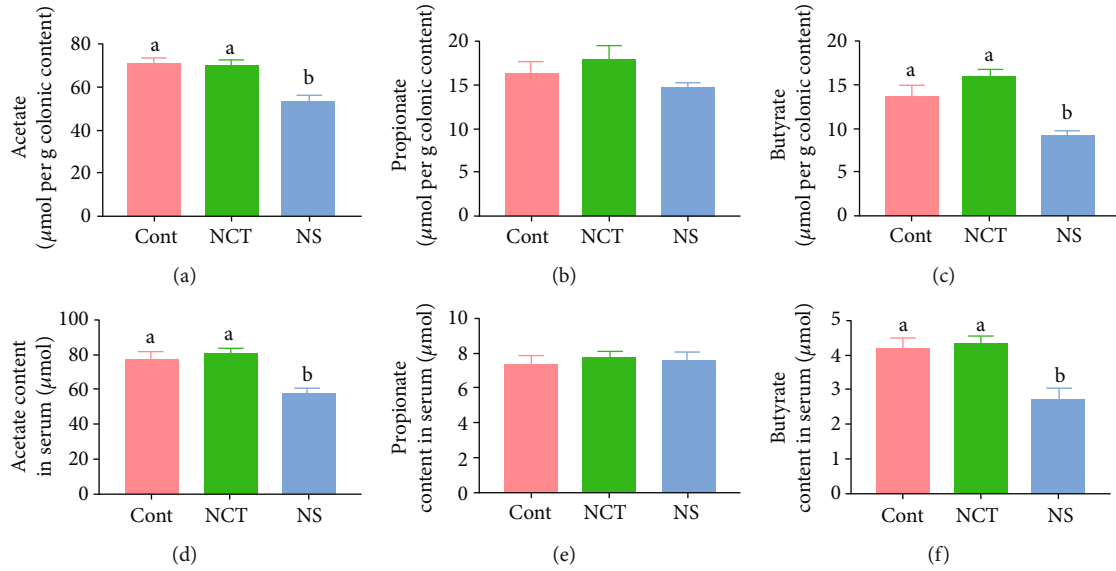


FIGURE 6: Dietary serine deficiency decreased contents of short-chain fatty acids in colonic contents and serum. Acetate (a), propionate (b), and butyrate (c) content in colonic content. Acetate (d), propionate (e), and butyrate (f) content in serum. CONT: mice were fed on the control diet; NS: mice were fed on the serine- and glycine-deficient diet; NCT: mice were fed on the control diet and supplemented with NCT-503. Data are presented as means  $\pm$  SEM.  $n = 8$ . <sup>a,b</sup>Means of the bars with different letters were significantly different among groups ( $P < 0.05$ ).

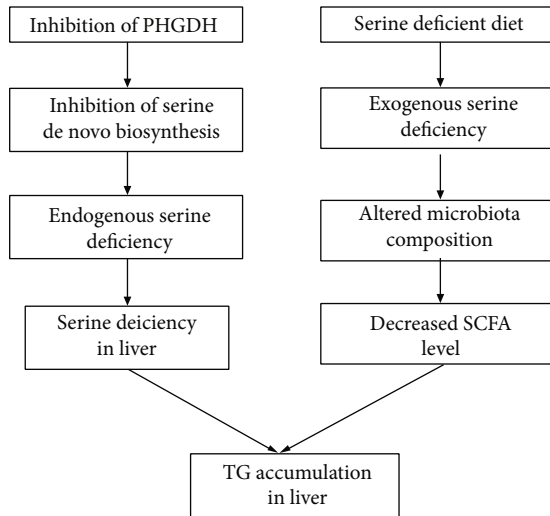


FIGURE 7: The different mechanisms responsible for hepatic lipid accumulation caused by endogenous and exogenous serine deficiency.

NCT-503. These results suggest that inhibition of de novo serine biosynthesis exacerbates the inflammatory and oxidative status in the liver.

Dietary serine deficiency did not cause changes in hepatic serine content. Thus, other factors may be involved in the disturbance of lipid accumulation and oxidative and inflammatory status. Dysbiosis in the gut microbiota contributes to the pathogenesis of fatty liver disease [17]. Changes in the microbiome and their metabolites can result in liver inflammation and fibrosis. We previously described that either dietary serine supplementation or serine defi-

ciency can regulate gut microbiota composition [8, 18]. These observations suggest that dietary serine deficiency may affect hepatic lipid accumulation through the gut-microbiota-liver axis. Importantly, the ratio of *Firmicutes* to *Bacteroidetes* and the relative abundance of *Bifidobacterium* decreased in mice fed a serine deficiency diet. Although the association of *Firmicutes* and *Bacteroidetes* abundance with fatty liver disease remains to be contradictory [19, 20], an important function of the *Bifidobacterium* genus is to produce acetate, which can be converted into butyrate by other bacteria [21, 22]. These results suggest that dietary serine deficiency may affect the gut microbiota and thus cause changes in their metabolites, including short-chain fatty acids. We also observed decreased contents of acetate and butyrate in both the serum and colonic contents. It has been suggested that SCFAs can ameliorate lipogenesis, inflammatory response, and oxidative damage in the liver tissue [23]. We hypothesize that the decreased production of SCFAs affected by dietary serine deficiency may contribute to lipid overaccumulation in the liver. However, whether decreased *Bifidobacterium* genus contributes to the decreased SCFAs and then results in fatty liver needs to be studied.

## 5. Conclusions

In the present study, exogenous and endogenous serine deficiencies exacerbated hepatic lipid accumulation via different mechanisms. Specifically, inhibition of serine de novo biosynthesis resulted in hepatic serine deficiency and further contributed to the fatty liver, while dietary serine deficiency altered the microbiota composition and further resulted in the development of fatty liver via the gut-microbiota-liver axis.



## Data Availability

The data used to support the findings of this study are available from the corresponding author upon request.

## Conflicts of Interest

There is no conflict of interest.

## Authors' Contributions

Liuqin He and Yonghui Liu contributed equally to this work.

## Acknowledgments

This work was financially supported by “Huxiang Young Talents Plan” Project of Hunan Province (2020RC3052), Young Elite Scientists Sponsorship Program by CAST (2019QNR001), Youth Innovation Promotion Association CAS, and China Agriculture Research System of MOF and MARA (CARS-35).

## Supplementary Materials

Supplementary Table 1: components of the control diet, serine, and glycine deficient (SGD) diet used in the experiments. These two diets were purchased from Research Diets (New Brunswick, NJ, USA). Supplementary Table 2: sequences of primers used for RT-qPCR in the experiments. *Cpt1a*: carnitine palmitoyltransferase 1a; *Acadm*: medium-chain acyl-CoA dehydrogenase; *DGAT*: diacylglycerol O-acyltransferase; *PAST1*: phosphoserine aminotransferase; *PSPH*: phosphoserine phosphatase. (*Supplementary Materials*)

## References

- [1] A. Mardinoglu, R. Agren, C. Kampf, A. Asplund, M. Uhlen, and J. Nielsen, “Genome-scale metabolic modelling of hepatocytes reveals serine deficiency in patients with non-alcoholic fatty liver disease,” *Nature Communications*, vol. 5, no. 1, p. 3083, 2014.
- [2] G. Baffy, E. M. Brunt, and S. H. Caldwell, “Hepatocellular carcinoma in non-alcoholic fatty liver disease: an emerging menace,” *Journal of Hepatology*, vol. 56, no. 6, pp. 1384–1391, 2012.
- [3] G. Bedogni, H. S. Kahn, S. Bellentani, and C. Tiribelli, “A simple index of lipid overaccumulation is a good marker of liver steatosis,” *BMC Gastroenterology*, vol. 10, no. 1, p. 98, 2010.
- [4] W. C. Sim, H. Q. Yin, H. S. Choi et al., “L-serine supplementation attenuates alcoholic fatty liver by enhancing homocysteine metabolism in mice and rats,” *The Journal of Nutrition*, vol. 145, no. 2, pp. 260–267, 2015.
- [5] X. Zhou, L. He, S. Zuo et al., “Serine prevented high-fat diet-induced oxidative stress by activating AMPK and epigenetically modulating the expression of glutathione synthesis-related genes,” *Biochimica et Biophysica Acta - Molecular Basis of Disease*, vol. 1864, no. 2, pp. 488–498, 2018.
- [6] W. C. Sim, W. Lee, H. Sim et al., “Downregulation of PHGDH expression and hepatic serine level contribute to the development of fatty liver disease,” *Metabolism*, vol. 102, p. 154000, 2020.
- [7] Y. P. Kang, A. Falzone, M. Liu et al., “PHGDH supports liver ceramide synthesis and sustains lipid homeostasis,” *Cancer & Metabolism*, vol. 8, no. 1, p. 6, 2020.
- [8] F. Wang, H. Zhou, L. Deng, L. Wang, J. Chen, and X. Zhou, “Serine deficiency exacerbates inflammation and oxidative stress via microbiota-gut-brain axis in D-galactose-induced aging mice,” *Mediators of Inflammation*, vol. 2020, Article ID 5821428, 7 pages, 2020.
- [9] L. He, H. Zhang, and X. Zhou, “Weanling offspring of dams maintained on serine-deficient diet are vulnerable to oxidative stress,” *Oxidative Medicine and Cellular Longevity*, vol. 2018, Article ID 8026496, 10 pages, 2018.
- [10] N. Jin, A. Bi, X. Lan et al., “Identification of metabolic vulnerabilities of receptor tyrosine kinases- driven cancer,” *Nature Communications*, vol. 10, no. 1, p. 2701, 2019.
- [11] J. Folch, M. Lees, and G. H. S. Stanley, “A simple method for the isolation and purification of total lipides from animal tissues,” *The Journal of Biological Chemistry*, vol. 226, no. 1, pp. 497–509, 1957.
- [12] X. H. Zhou, Y. H. Liu, L. Y. Zhang, X. F. Kong, and F. N. Li, “Serine-to-glycine ratios in low-protein diets regulate intramuscular fat by affecting lipid metabolism and myofiber type transition in the skeletal muscle of growing-finishing pigs,” *Animal Nutrition*, vol. 7, no. 2, pp. 384–392, 2021.
- [13] K. Wang, X. Jin, Q. Li et al., “Propolis from different geographic origins decreases intestinal inflammation and Bacteroides spp. populations in a model of DSS-induced colitis,” *Mol Nutr Food Res*, vol. 62, article e1800080, no. 17, 2018.
- [14] X. Feng, H. Zhang, M. Shi, Y. Chen, T. Yang, and H. Fan, “Toxic effects of hydrogen sulfide donor NaHS induced liver apoptosis is regulated by complex IV subunits and reactive oxygen species generation in rats,” *Environmental Toxicology*, vol. 35, no. 3, pp. 322–332, 2020.
- [15] L. He, J. Long, X. Zhou, Y. Liu, T. Li, and X. Wu, “Serine is required for the maintenance of redox balance and proliferation in the intestine under oxidative stress,” *The FASEB Journal*, vol. 34, no. 3, pp. 4702–4717, 2020.
- [16] S. Zhang, H. Wang, and M. J. Zhu, “A sensitive GC/MS detection method for analyzing microbial metabolites short chain fatty acids in fecal and serum samples,” *Talanta*, vol. 196, pp. 249–254, 2019.
- [17] C. Leung, L. Rivera, J. B. Furness, and P. W. Angus, “The role of the gut microbiota in NAFLD,” *Nature Reviews. Gastroenterology & Hepatology*, vol. 13, no. 7, pp. 412–425, 2016.
- [18] H. Zhang, R. Hua, B. Zhang, X. Zhang, H. Yang, and X. Zhou, “Serine alleviates dextran sulfate sodium-induced colitis and regulates the gut microbiota in mice,” *Frontiers in Microbiology*, vol. 9, p. 3062, 2018.
- [19] J. Boursier and A. M. Diehl, “Implication of gut microbiota in nonalcoholic fatty liver disease,” *PLoS Pathogens*, vol. 11, no. 1, article e1004559, 2015.
- [20] N. Alkhoury, R. de Vito, A. Alisi et al., “Development and validation of a new histological score for pediatric non- alcoholic fatty liver disease,” *Journal of Hepatology*, vol. 57, no. 6, pp. 1312–1318, 2012.
- [21] L. De Vuyst and F. Leroy, “Cross-feeding between bifidobacteria and butyrate-producing colon bacteria explains bifidobacterial competitiveness, butyrate production, and gas production,” *International Journal of Food Microbiology*, vol. 149, no. 1, pp. 73–80, 2011.

- [22] A. Riviere, M. Selak, D. Lantin, F. Leroy, and L. De Vuyst, "Bifidobacteria and butyrate-producing colon bacteria: importance and strategies for their stimulation in the human gut," *Frontiers in Microbiology*, vol. 7, p. 979, 2016.
- [23] Y. Ji, Y. Yin, Z. Li, and W. Zhang, "Gut microbiota-derived components and metabolites in the progression of non-alcoholic fatty liver disease (NAFLD)," *Nutrients*, vol. 11, no. 8, p. 1712, 2019.

## Research Article

# ***Lactobacillus plantarum* Exhibits Antioxidant and Cytoprotective Activities in Porcine Intestinal Epithelial Cells Exposed to Hydrogen Peroxide**

Jing Wang<sup>1,2</sup>, Wei Zhang<sup>1,2</sup>, Sixin Wang<sup>1,2</sup>, Yamin Wang<sup>1</sup>, Xu Chu<sup>1,3</sup> and Haifeng Ji<sup>1,2</sup>

<sup>1</sup>Institute of Animal Husbandry and Veterinary Medicine, Beijing Academy of Agriculture and Forestry Sciences, 100097 Beijing, China

<sup>2</sup>Sino-US Joint Laboratory of Animal Science, Beijing Academy of Agriculture and Forestry Sciences, 100097 Beijing, China

<sup>3</sup>College of Agriculture, Qinghai University, 810016 Xining, China

Correspondence should be addressed to Jing Wang; wangjing976119@126.com

Received 22 May 2021; Accepted 12 July 2021; Published 31 July 2021

Academic Editor: Tongxing Song

Copyright © 2021 Jing Wang et al. This is an open access article distributed under the Creative Commons Attribution License, which permits unrestricted use, distribution, and reproduction in any medium, provided the original work is properly cited.

Probiotics are widely used for protection against stress-induced intestinal dysfunction. Oxidative stress plays a critical role in gastrointestinal disorders. It is established that probiotics alleviate oxidative stress; however, the mechanism of action has not been elucidated. We developed an *in vitro* intestinal porcine epithelial cells (IPEC-J2) model of oxidative stress to explore the antioxidant effect and potential mode of action of *Lactobacillus plantarum* ZLP001. The IPEC-J2 cells were preincubated with and without *L. plantarum* ZLP001 for 3 h and then exposed to hydrogen peroxide (H<sub>2</sub>O<sub>2</sub>) for 4 h. Pretreatment with *L. plantarum* ZLP001 protected IPEC-J2 cells against H<sub>2</sub>O<sub>2</sub>-induced oxidative damage as indicated by cell viability assays and significantly alleviated apoptosis elicited by H<sub>2</sub>O<sub>2</sub>. *L. plantarum* ZLP001 pretreatment decreased reactive oxygen species production and the cellular malondialdehyde concentration and increased the mitochondrial membrane potential compared with H<sub>2</sub>O<sub>2</sub> treatment alone, suggesting that *L. plantarum* ZLP001 promotes the maintenance of redox homeostasis in the cells. Furthermore, *L. plantarum* ZLP001 regulated the expression and generation of some antioxidant enzymes, thereby activating the antioxidant defense system. Treatment with *L. plantarum* ZLP001 led to nuclear erythroid 2-related factor 2 (Nrf2) enrichment in the nucleus compared with H<sub>2</sub>O<sub>2</sub> treatment alone. Knockdown of Nrf2 significantly weakened the alleviating effect of *L. plantarum* ZLP001 on antioxidant stress in IPEC-J2 cells, suggesting that Nrf2 is involved in the antioxidative effect of *L. plantarum* ZLP001. Collectively, these results indicate that *L. plantarum* ZLP001 is a promising probiotic bacterium that can potentially alleviate oxidative stress.

## 1. Introduction

Oxidative stress is caused by an imbalance between prooxidants and antioxidants and is implicated in extensive human and animal diseases. Oxidative stress is often associated with the accumulation of reactive oxygen species (ROS), which can induce DNA hydroxylation, protein denaturation, and lipid peroxidation [1] and thus compromise the viability of cells, ultimately causing several diseases [2]. The intestine is more vulnerable to oxidative stress owing to its continuous exposure to the luminal environment. Intestinal oxidative stress influences the digestibility and absorption of nutrients

and can cause various intestinal diseases [3, 4]. In particular, during the critical life phases of animals, such as weaning, the underdeveloped intestine combined with depressed intake can lead to the insufficient synthesis of endogenous antioxidants. Therefore, antioxidant supplementation strategies have been considered. Dietary antioxidants, such as vitamins C and E, and metals, such as Zn and Cu, can neutralize oxidative molecules and play an important role in maintaining redox homeostasis in humans and animals [5, 6].

Probiotic bacteria have been shown to exhibit antioxidant activity both *in vitro* and *in vivo* [7–9]. Several probiotic strains and their products present in food exert remarkable

antioxidant activities, and these strains exhibit high viability in anaerobic environments, have a strong oxygen radical-scavenging ability, and produce several antioxidant enzymes [10–12]. Antioxidative properties vary widely among bacterial strains, indicating that they are strain specific [7, 13]. Probiotics have been demonstrated to exert antioxidant activities in various host cells and the human body by modulating the redox status by scavenging free radicals, chelating metal ions, regulating enzymes, and modulating the intestinal microbiota [8, 9]. Further, it has been reported that probiotics exert antioxidant activity mainly through the induction of detoxifying enzymes via the activation of transcription factor nuclear erythroid 2-related factor 2 (Nrf2) [14, 15]. Other regulatory pathways involving Sirt1, MAPK, and PKC, which may trigger the dissociation of Nrf2 or enhance the cell homeostasis, are also involved in the regulation of their antioxidant action [9]. However, several questions regarding the underlying mechanisms of the antioxidative roles of probiotics, such as concentration effects, mitochondrial function, and Nrf2 dissociation pattern, remain unsolved.

In our previous studies, we demonstrated that *L. plantarum* ZLP001 isolated from healthy piglet ileal mucosa [16] exerts a strong antioxidant ability, is highly viable in hydrogen peroxide, has a high oxygen radical-scavenging ability *in vitro*, and alleviates oxidative stress in weaning piglets *in vivo* [17]. However, the antioxidant capacity of *L. plantarum* ZLP001 under oxidative stress or its mechanisms of action is not well understood. Therefore, in this study, we evaluated the effect of *L. plantarum* ZLP001 pretreatment in an *in vitro* model of oxidative stress using porcine intestinal epithelial cells (IPEC-J2) treated with hydrogen peroxide ( $H_2O_2$ ).

## 2. Materials and Methods

**2.1. Bacterial Strain, Cells, and Culture Conditions.** *L. plantarum* ZLP001 was originally isolated in our laboratory, from the ileal mucosa of healthy piglets 4 w after weaning. The strain was identified by the China Center of Industrial Culture Collection (Beijing, China) and is preserved in the China General Microbiological Culture Collection Center (CGMCC No. 7370). *L. plantarum* ZLP001 cells were cultured in improved de Man, Rogosa, and Sharpe liquid medium (10 g peptone, 5 g yeast powder, 20 g glucose, 10 g beef extract, 5 g sodium acetate, 2 g ammonium citrate dibasic, 2 g dipotassium phosphate, 0.58 g magnesium sulfate, 0.19 g manganese sulfate, 1 mL of Tween-80, and water to 1,000 mL; pH 6.5) at 37°C under anaerobic conditions.

The porcine intestinal epithelial cell line (IPEC-J2) was a generous gift from Dr. Glenn Zhang (Oklahoma State University, Stillwater, OK). The IPEC-J2 cells were cultured in DMEM/F12, a 1:1 mixture of Dulbecco's modified Eagle's medium and Ham's F-12 (Gibco™, Thermo Fisher Scientific, Waltham, MA, USA) supplemented with 10% fetal bovine serum (FBS; Gibco™), streptomycin (100 µg/mL), penicillin (100 U/mL), and 1% ITS premix (5 µg/mL insulin, 5 µg/mL transferrin, 5 ng/mL selenium; ScienCell, San Diego, CA) at

37°C in a 5%  $CO_2$  and 95% air atmosphere with 90% humidity.

**2.2. Oxidative Stress Model Establishment.** An *in vitro* oxidative stress model was established by treating IPEC-J2 cells with  $H_2O_2$ . Cell viability was assessed using the methyl thiazolyl tetrazolium (MTT) assay. IPEC-J2 cells were seeded in 6-well tissue culture plates (Costar, Corning Inc., Corning, NY, USA) at  $2.5 \times 10^5$  cells/well and cultured overnight with 2 mL of complete culture medium. After treatment with  $H_2O_2$  at final concentrations of 0, 250, 500, 750, 1000, 1250, 1500, and 1750 µmol/L for 4 h, the cells were incubated with 5 mg/mL of MTT working solution at 37°C for 4 h. The absorbance at 490 nm was measured using a Multiskan FC instrument (Thermo Fisher Scientific, Waltham, MA, USA). The median lethal dose (LD50) of  $H_2O_2$  was calculated by probability unit and the optimal concentration of  $H_2O_2$  was selected to establish the IPEC-J2 cell-based oxidative stress model.

**2.3. Cell Treatments.** IPEC-J2 cells were seeded in 6-well tissue-culture plates at  $2.5 \times 10^5$  cells/well. After overnight culture, the complete culture medium was replaced with culture medium without antibiotics, and the cells were incubated with *L. plantarum* ZLP001 at  $10^5$ ,  $10^6$ ,  $10^7$ ,  $10^8$ , or  $10^9$  CFU/well for 2 h, 3 h, or 4 h. After the bacteria were washed away with PBS, the cells were cultured in a complete culture medium with or without  $H_2O_2$  (optimal  $H_2O_2$  concentration obtained from the above experiment) for 4 h. Cell viability was determined using the MTT assay.

To estimate the antioxidant effect of *L. plantarum* ZLP001 on IPEC-J2 cells, four treatments were designed: a control, a *L. plantarum* ZLP001 treatment (optimal concentration and incubation time based on the above experiment), a  $H_2O_2$  treatment, and a *L. plantarum* ZLP001 pretreatment +  $H_2O_2$  treatment. After overnight culture, IPEC-J2 cells were incubated with *L. plantarum* ZLP001 in a complete culture medium without antibiotics for 3 h. Then, the bacteria were washed away with PBS, and the cells were cultured in a complete culture medium with or without  $H_2O_2$  for 4 h. In addition, IPEC-J2 cells were cultured in a complete culture medium without antibiotics for 3 h and then treated or not treated with  $H_2O_2$  under the conditions described above as oxidative stress control and nontreated control, respectively.

**2.4. Observation of Cell Morphology.** Morphological changes in IPEC-J2 cells after the treatments were observed under an optical microscope (Olympus, Tokyo, Japan) at a magnification of 100x. Images were acquired using the cellSens Entry system (Olympus).

**2.5. Detection of Cell Apoptosis and Necrosis.** Apoptosis and necrosis in treated IPEC-J2 cells were detected using the Apoptosis and Necrosis Assay Kit (C1056) (Beyotime Biotechnology, Haimen, China). After the treatments, the cells were stained with Hoechst 33342 (10 ng/mL) and propidium iodide (PI, 10 ng/mL) at 4°C in the dark for 20 min, according to the manufacturer's instructions. Condensed or fragmented nuclei of apoptotic cells were visualized and photographed under an inverted fluorescence microscope (IX71, Olympus).

Apoptotic cells were also detected by flow cytometry using an Annexin V PE/7-AAD Assay Kit (CA1030) (Solarbio, Beijing, China). Immediately after the treatments, the cells were collected and resuspended in a binding buffer. One hundred microliters of cell suspension were mixed with 5  $\mu$ L of Annexin V/PE and incubated in the dark at room temperature for 5 min. After the addition of 10  $\mu$ L of 20  $\mu$ g/mL 7-AAD and 400  $\mu$ L of PBS, the cells were immediately analyzed by flow cytometry (FACScalibur™, BD Biosciences, San Jose, CA, USA). Experiments were performed in triplicate.

**2.6. Assessment of Intracellular ROS Generation.** Intracellular ROS accumulation was measured using a commercial ROS detection kit (S0033S) (Beyotime Biotechnology, Haimen, China) with the green, fluorescent probe DCFH-DA (2',7'-dichlorofluorescein diacetate). After the treatments, the culture medium was removed, the ROS indicator DCFH-DA (10  $\mu$ M) in fresh FBS-free medium was added, and the cells were incubated at 37°C for 30 min. The cells were visualized and photographed under a fluorescence microscope (IX71, Olympus). To quantify ROS production, the fluorescence intensity was measured using a fluorescence microplate reader (Tecan, Männedorf, Switzerland) at excitation/emission wavelengths of 525/610 nm. ROS levels are expressed as the percentage of treated cells compared to control cells. Experiments were performed in triplicate.

**2.7. Measurement of the Mitochondrial Membrane Potential (MMP).** The Mitochondrial Membrane Potential Assay Kit (Beyotime Biotechnology, Haimen, China) with the membrane-permeable dye, JC-1, was used to detect mitochondrial depolarization in cells. After the treatments, the cells were incubated in JC-1 solution at 37°C for 15 min. The potential-dependent aggregation of JC-1 in the mitochondria (labeled with red fluorescence) and of the monomeric form of JC-1 in the cytosol after mitochondrial membrane depolarization (labeled with green fluorescence) were detected using flow cytometry. The MMP is reflected by the proportion of JC-1 aggregates and monomers. Experiments were performed in triplicate.

**2.8. Determination of Lactate Dehydrogenase (LDH) and Malondialdehyde (MDA).** After the treatments, the cells were gently washed twice with PBS and lysed using RIPA Lysis Buffer (containing PMSF) (Solarbio, Beijing, China) for 10 min. The cells were centrifuged and 10,000  $\times g$  at 4°C for 10 min, and the supernatants were collected. Protein concentrations were determined using a bicinchoninic acid (BCA) protein assay (BCA Protein Assay Kit; Pierce, Madison, WI, USA). Then, the levels of LDH and MDA were determined using a LDH assay kit (A020-2) and MDA assay kit (A003-2) (Jiancheng, Nanjing, China). Experiments were performed in triplicate.

**2.9. Determination of Glutathione and Oxidized Glutathione (GSH and GSSG) Concentrations.** The cell sample collection and protein extraction and concentration evaluation were the same as above for the determination of LDH and MDA. Thereafter, the concentration of GSH and GSSG was deter-

mined using a GSH assay kit (A006-1-1) and GSSG assay kit (A061-2-1) (Jiancheng, Nanjing, China). Experiments were performed in triplicate.

**2.10. Determination of T-AOC, T-SOD, CAT, and GSH-Px Activities.** The total antioxidant capacity (T-AOC, A015-1-2) and the activities of total superoxide dismutase (T-SOD, A001-1-2), catalase (CAT, A007-1-1), and glutathione peroxidase (GSH-Px, A005-1-2) were determined using commercial assay kits (Jiancheng, Nanjing, China). After the treatments, the cells were lysed, and cellular protein concentrations were determined as above. Then, the T-SOD, CAT, and GSH-Px activities are determined according to the instructions of the manufacturer and expressed as U/mg protein. Experiments were performed in triplicate.

**2.11. Establishment of Nrf2-Knockdown IPEC-J2 Cells.** Porcine Nrf2 siRNA 5'-GCCCAUUGAUCUCUCUGAUTT-3' (sense) and 5'-AUCAGAGAGAUCAAUGGGCTT-3' (antisense) were synthesized at GenePharma Co. Ltd. (Shanghai, China). The IPEC-J2 cells were seeded into 6-well plates (2.5  $\times 10^5$  cells/well), cultured overnight, and transfected with siRNAs using Lipofectamine 2000 (Invitrogen, Carlsbad, CA, USA) according to the manufacturer's instructions.

**2.12. Quantitative Reverse-Transcription Polymerase Chain Reaction (RT-qPCR).** Total RNA was extracted from treated cells using RNazol reagent (Molecular Research Center, Cincinnati, OH, USA) according to the manufacturer's instructions. RNA concentrations were determined using a NanoDrop spectrophotometer (Thermo Fisher Scientific, Waltham, MA, USA). The RNA (1  $\mu$ g) was reverse-transcribed into cDNA using an iScript™ cDNA Synthesis Kit (Bio-Rad, Hercules, CA, USA) according to the manufacturer's instructions. The qPCRs were run using iTaq™ Universal SYBR Green Supermix (Bio-Rad) in a QuantStudio 3 Real-Time PCR System (Thermo Fisher Scientific, Waltham, MA, USA). Porcine-specific primers used in this study were referred from other references or designed with Primer 5.0, and the sequences are listed in Supplementary Table S1. Target gene expression was normalized to that of glyceraldehyde-3-phosphate dehydrogenase (GAPDH); relative fold changes in gene expression were calculated using the  $2^{-\Delta\Delta C_t}$  method [18].

**2.13. Western Blot.** IPEC-J2 cells were collected after the treatments, and total proteins were extracted and protein concentrations were determined as above description. Equal amounts of protein (30  $\mu$ g) were loaded per lane and the protein was separated at 110 V for 1 h and then transferred to the PDVF membrane at 4°C and 90 V for 60-100 min. After blocking with 5% skim milk, the blots were incubated with primary antibodies at 4°C overnight. After three washes with Tris-buffered saline, the blots were incubated with an HRP-conjugated secondary antibody. Chemiluminescence detection was performed using Western Blot Luminance Reagent (Santa Cruz Biotechnology, Santa Cruz, CA, USA) according to the manufacturer's instructions. The antibodies used in this study are listed in Supplementary Table S2.

Immunoreactive bands were imaged using the ChemiDoc XRS system (Bio-Rad) and were quantified using ImageJ (National Institutes of Health, Bethesda, MD, USA).

**2.14. Statistical Analysis.** All results are expressed as the mean  $\pm$  standard error of the mean (SEM). Data analyses were performed using Prism version 6 (GraphPad Software, Inc., San Diego, CA, USA). Means were compared using one-way analysis of variance (ANOVA) followed by Duncan's *post hoc* tests in SPSS (version 20.0, SPSS Inc., Chicago, IL, USA). Means of two groups were compared using unpaired Student's two-tailed *t*-test.  $P < 0.05$  was considered a significant difference.

### 3. Results

**3.1. Establishment of an Oxidative Stress Model in IPEC-J2 Cells.** To establish the oxidative stress model in porcine IPEC-J2 cells, we used the MTT method to determine the cell viability of IPEC-J2 after treatment with  $H_2O_2$ . As shown in Figure 1(a),  $H_2O_2$  dose-dependently decreased the viability of IPEC-J2 cells. After 4 h of treatment with  $1,000 \mu M H_2O_2$ , the cell viability of IPEC-J2 was reduced to  $52.8\% \pm 4.7\%$ . Therefore, this concentration of  $1,000 \mu M$  and 4 h treatment time were used to induce oxidative stress in subsequent experiments.

**3.2. *L. plantarum* ZLP001 Attenuated the Cell Damage Caused by  $H_2O_2$ .** As shown in Figure 1(b), a 3-h pretreatment with  $10^6$  or  $10^7$  CFU *L. plantarum* ZLP001 increased IPEC-J2 cell viability by approximately up to 70%-75% after  $H_2O_2$  insult, indicating that *L. plantarum* ZLP001 attenuates  $H_2O_2$ -induced cell damage. Lower and higher concentrations of *L. plantarum* ZLP001 were less effective, while  $10^9$  CFU *L. plantarum* ZLP001 decreased the viability of IPEC-J2 directly and did not protect against  $H_2O_2$ -induced damage. Pretreatment with *L. plantarum* ZLP001 for 3 h more effectively protected cell viability than 2 h or 4 h pretreatment. We selected  $10^6$  CFU *L. plantarum* ZLP001 concentration and 3 h pretreatment time to proceed with further research.

Cell morphology after the different treatments was examined by optical microscopy (Figure 1(c)). Compared with normal cells, the gaps between  $H_2O_2$ -treated IPEC-J2 cells were enlarged, and the cell membrane showed a loose structure. After pretreatment with *L. plantarum* ZLP001, less damage to cell integrity was observed.

LDH is a soluble cytosolic enzyme that is released when the cell membrane is damaged. To confirm the protective effect of *L. plantarum* ZLP001 on IPEC-J2 cells, LDH leakage after  $H_2O_2$  treatment was measured (Figure 1(d)). While  $H_2O_2$ -treated IPEC-J2 cells showed significant LDH release compared to nontreated cells, pretreatment with *L. plantarum* ZLP001 strongly reduced LDH leakage in the culture supernatant.

**3.3. *L. plantarum* ZLP001 Alleviates  $H_2O_2$ -Induced Apoptosis and Necrosis in IPEC-J2 Cells.** Hoechst 33342 and PI staining results showed that  $H_2O_2$  considerably stimulated apoptosis (bright blue) and necrosis (bright red) in IPEC-J2 cells, indicating  $H_2O_2$ -induced oxidative damage. *L. plantarum*

ZLP001 pretreatment significantly ameliorated  $H_2O_2$ -induced apoptosis and necrosis (Figure 2(a)). These findings were confirmed by flow cytometry results (Figures 2(b) and 2(c)).

The expression of the apoptosis-associated proteins, Bcl-2, Bax, and active caspase-3, was evaluated by western blot to further understand the antiapoptotic effect of the *L. plantarum* ZLP001 strain. Expression of the antiapoptotic factor Bcl-2 was enhanced by *L. plantarum* ZLP001 treatment, whereas no obvious increase was observed after  $H_2O_2$  treatment alone (Figures 2(d) and 2(e)). After  $H_2O_2$  treatment, activated caspase-3 expression was significantly increased, and this induction was alleviated by *L. plantarum* ZLP001 pretreatment. No significant effect on Bax expression was observed.

**3.4. *L. plantarum* ZLP001 Regulates the Cellular Redox State in  $H_2O_2$ -Treated IPEC-J2 Cells.** To evaluate the regulatory effect of *L. plantarum* ZLP001 on the  $H_2O_2$ -induced IPEC-J2 cell redox state, we measured intracellular ROS production using a cell-permeable, nonfluorescent probe DCFH-DA (Figures 3(a) and 3(b)). Unsurprisingly, ROS accumulation was significantly increased after exposure to  $H_2O_2$ , indicating that  $H_2O_2$  caused an intracellular burst of ROS in IPEC-J2 cells. However, pretreatment of the cells with *L. plantarum* ZLP001 obviously suppressed the ROS burst induced by  $H_2O_2$  in IPEC-J2 cells.

To further investigate the redox state, the MMP was determined (Figures 3(c) and 3(d)), which can be affected by  $H_2O_2$ -induced ROS release. After  $H_2O_2$  treatment alone, the J-aggregate-to-J-monomer ratio in IPEC-J2 cells was obviously decreased. After *L. plantarum* ZLP001 pretreatment, this ratio was increased, demonstrating the positive effect of *L. plantarum* ZLP001 on the redox state in IPEC-J2 cells.

Next, we detected GSSG and GSH, which serve as important indicators of the cellular redox state (Figure 3(e)). After  $H_2O_2$  treatment, intracellular GSSG levels were significantly increased, while GSH levels were markedly decreased ( $P < 0.05$ ). However, pretreatment with *L. plantarum* ZLP001 showed a tendency to prevent the effects of  $H_2O_2$  on both GSSG ( $P > 0.05$ ) and GSH ( $P < 0.05$ ). The GSSG and GSH levels in *L. plantarum* ZLP001-treated cells were similar to those in control cells ( $P > 0.05$ ).

MDA is the main product of ROS-induced lipid peroxidation. As an excellent indicator of oxidative stress, we also measured the MDA levels in the treated IPEC-J2 cells. As shown in Figure 3(f), MDA levels in  $H_2O_2$ -treated IPEC-J2 cells were markedly increased compared to those in control cells, indicating the occurrence of lipid peroxidation. *L. plantarum* ZLP001 pretreatment significantly inhibited lipid peroxidation in IPEC-J2 cells, as indicated by the lower levels of MDA.

**3.5. *L. plantarum* ZLP001 Upregulates the Antioxidant Defense System in  $H_2O_2$ -Treated IPEC-J2 Cells.** The effect of *L. plantarum* ZLP001 on the antioxidant defense system in the cells was examined to further investigate how *L. plantarum* ZLP001 alleviated oxidative stress in the cells. The T-

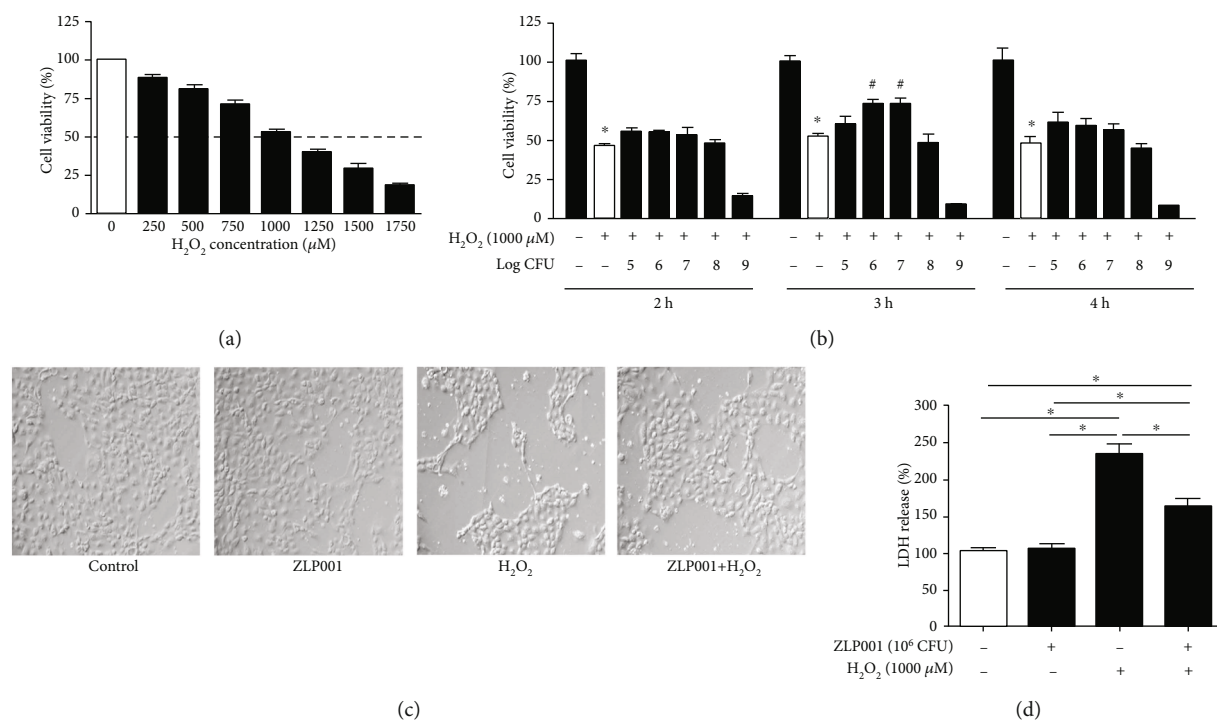


**FIGURE 1:** *Lactobacillus plantarum* ZLP001 protects IPEC-J2 cells against H<sub>2</sub>O<sub>2</sub>-induced oxidative stress damage. (a) H<sub>2</sub>O<sub>2</sub>-induced IPEC-J2 cell viability reduction. IPEC-J2 cells were incubated with the indicated concentrations of H<sub>2</sub>O<sub>2</sub> for 4 h; after which, cell viability was measured by the methyl thiazolyl tetrazolium (MTT) assay. (b) *L. plantarum* ZLP001 protects against H<sub>2</sub>O<sub>2</sub>-induced cell damage. IPEC-J2 cells were incubated with or without *L. plantarum* ZLP001 at the indicated concentrations for 2 h, 3 h, or 4 h; after which, the medium was replaced with fresh medium containing 1,000 μM H<sub>2</sub>O<sub>2</sub>. After incubation for 4 h, cell viability was measured by the MTT assay. (c) Morphological analysis of the protective effect of *L. plantarum* ZLP001 (10<sup>6</sup> CFU, 3 h) against H<sub>2</sub>O<sub>2</sub>-induced IPEC-J2 cell damage by microscopy. (d) Lactate dehydrogenase (LDH) release after the treatments as determined using a LDH assay. All data represent the mean ± standard error of mean (SEM) of three independent experiments. Means were compared by one-way ANOVA followed by Duncan's *post hoc* tests. \**P* < 0.05. The means of the two groups were compared using Student's *t*-test. \**P* < 0.05 vs. nontreated control cells; #*P* < 0.05 vs. H<sub>2</sub>O<sub>2</sub>-treated cells.

AOC activities in *L. plantarum* ZLP001-treated cells showed a numerical increase compared with the normal control group (Figure 4(a)). While the pretreatment of *L. plantarum* ZLP001 can significantly attenuate the decrease of T-AOC activity caused by H<sub>2</sub>O<sub>2</sub>.

As shown in Figure 4(b), the *HO-1*, *GSTA1*, and *TRXR1* mRNA expressions were significantly elevated in cell response to H<sub>2</sub>O<sub>2</sub>, whereas *CAT* expression was significantly decreased, indicating that the cells activated antioxidant mechanisms to protect themselves from oxidative stress. Compared with H<sub>2</sub>O<sub>2</sub> treatment alone, *L. plantarum* ZLP001 pretreatment obviously suppressed *HO-1* and *TRXR1* mRNA expression, whereas it increased *SOD1* and *CAT* expression. *L. plantarum* ZLP001 treatment alone markedly elevated the mRNA expression of *SOD1* and *GPX2*, whereas no significant effects on other antioxidant enzymes were observed compared with control cells.

We further determined the activities of T-SOD, CAT, and GSH-Px using commercial assay kits (Figures 4(c)–4(e)). In line with the gene expression results, these enzyme activities treated or pretreated with *L. plantarum* ZLP001 were significantly regulated compared with control and H<sub>2</sub>O<sub>2</sub> treatment alone. After *L. plantarum* ZLP001 pretreatment, the decline in antioxidant enzymes caused by H<sub>2</sub>O<sub>2</sub>

was alleviated. These results indicate that *L. plantarum* ZLP001 boosts endogenous antioxidant molecules. Collectively, the antioxidant effect of *L. plantarum* ZLP001 can be attributed to the activation of the antioxidant defense system.

**3.6. *L. plantarum* ZLP001 Activates Nrf2 Signaling Pathway in IPEC-J2 Cells.** To further explore the mode of action of *L. plantarum* ZLP001, we evaluated Nrf2 expression in IPEC-J2 cells treated with different concentrations of *L. plantarum* ZLP001 (Figures 5(a) and 5(b)). Immunoblotting results revealed that *L. plantarum* ZLP001 treatment dose-dependently decreased cytosolic Nrf2 and promoted nuclear Nrf2 accumulation, especially at 10<sup>7</sup> CFU, indicating the occurrence of nuclear translocation of Nrf2. Cytosolic Keap1 accumulation was enhanced after *L. plantarum* ZLP001 treatment, especially at 10<sup>6</sup> and 10<sup>7</sup> CFU.

Next, we evaluated the translocation of Nrf2 after H<sub>2</sub>O<sub>2</sub> treatment and pretreatment with *L. plantarum* ZLP001. As shown in Figures 5(c) and 5(d), H<sub>2</sub>O<sub>2</sub> treatment alone had a remarkable effect on Nrf2 translocation from the cytosol to the nucleus. However, after pretreatment with *L. plantarum* ZLP001, the amount of Nrf2 in the cytosol showed a further decrease, while no significant accumulation of Nrf2 was observed in the nucleus compared with H<sub>2</sub>O<sub>2</sub> treatment

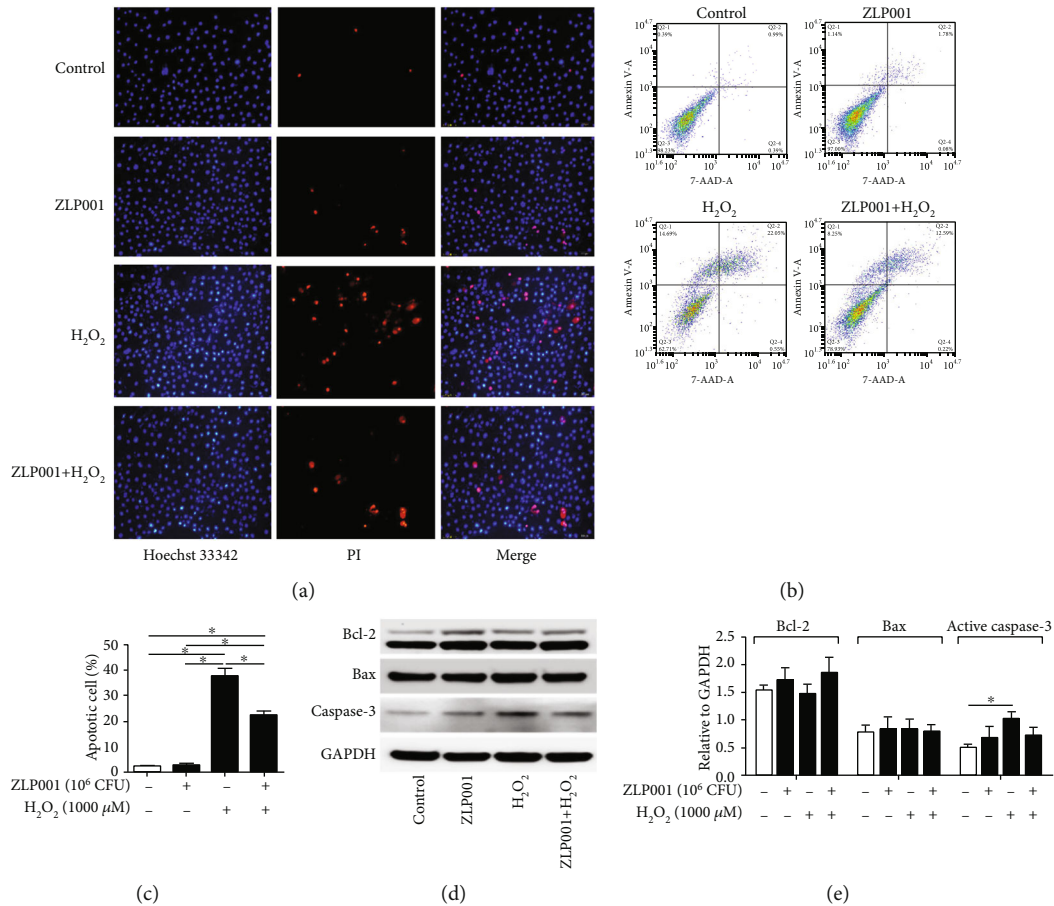


**FIGURE 2:** *Lactobacillus plantarum* ZLP001 inhibits H<sub>2</sub>O<sub>2</sub>-induced apoptosis in IPEC-J2 cells. IPEC-J2 cells were incubated with or without 10<sup>6</sup> CFU *L. plantarum* ZLP001 for 3 h; after which, the medium was replaced with a fresh medium containing 1,000 μM H<sub>2</sub>O<sub>2</sub>, and the cells were further incubated for 4 h. (a) Apoptosis detection based on Hoechst 33342 staining and PI staining. (b) Flow-cytometric analysis of apoptotic cells. (c) Quantification of apoptotic cells based on flow cytometry data. (d) Western blot analysis of Bcl-2, Bax, and active caspase-3 expression. (e) Quantitative analysis of apoptosis-related protein levels. All data represent the mean ± standard error of mean (SEM) of three independent experiments. Means were compared by one-way ANOVA followed by Duncan's *post hoc* test. \**P* < 0.05.

alone. The amount of Keap1 in the cytosol numerically increased after *L. plantarum* ZLP001 treatment alone, and significant differences were observed after H<sub>2</sub>O<sub>2</sub> treatment alone and pretreatment with *L. plantarum* ZLP001.

**3.7. Nrf2 siRNA Abolishes the Antioxidative Effects of *L. plantarum* ZLP001.** To further clarify the role of Nrf2 in the alleviation of oxidative stress by *L. plantarum* ZLP001, we evaluated cell viability and ROS production after Nrf2 knockdown in IPEC-J2 cells. Cells treated with Nrf2 siRNA effectively exhibited lower levels of Nrf2 than negative control siRNA-transfected cells and nontransfected control cells at both the gene and the protein level (Figures 6(a) and 6(b)). Nrf2 siRNA-transfected IPEC-J2 cells showed considerably lower cell viability than negative control cells when challenged with H<sub>2</sub>O<sub>2</sub> (Figure 6(c)). The antioxidant-protective effect of *L. plantarum* ZLP001 was also blocked by Nrf2 siRNA, and the cells showed reduced viability when compared with negative control siRNA-transfected cells. Furthermore, Nrf2 knockdown weakened the effect of *L. plantarum* ZLP001 in preventing ROS generation in response to the H<sub>2</sub>O<sub>2</sub> challenge (Figure 6(d)). These results demonstrate that

Nrf2 siRNA abolishes the antioxidative action of *L. plantarum* ZLP001, suggesting that the Nrf2 pathway is involved in this action.

## 4. Discussion

An imbalance in the intestinal microbiota under stress or pathological conditions can result in the growth of pathogens, which may produce oxygen to generate an aerobic environment, thus rendering the intestine in an oxidative stress state [19, 20]. Intestinal oxidative stress causes damage to the epithelial barrier and affects nutrient digestibility and absorption and can lead to various diseases [3, 21, 22]. Thus, intestinal redox homeostasis is critical for maintaining host health. Although some probiotics have antioxidant capacity, the underlying mechanisms are not completely understood. In this study, we aimed to clarify the antioxidant capacity of *L. plantarum* ZLP001 under oxidative stress and its potential mechanism.

H<sub>2</sub>O<sub>2</sub> is a strong oxidant capable of oxidizing a variety of moieties, which is why it is commonly used to establish an oxidative stress model to study redox-regulated processes in



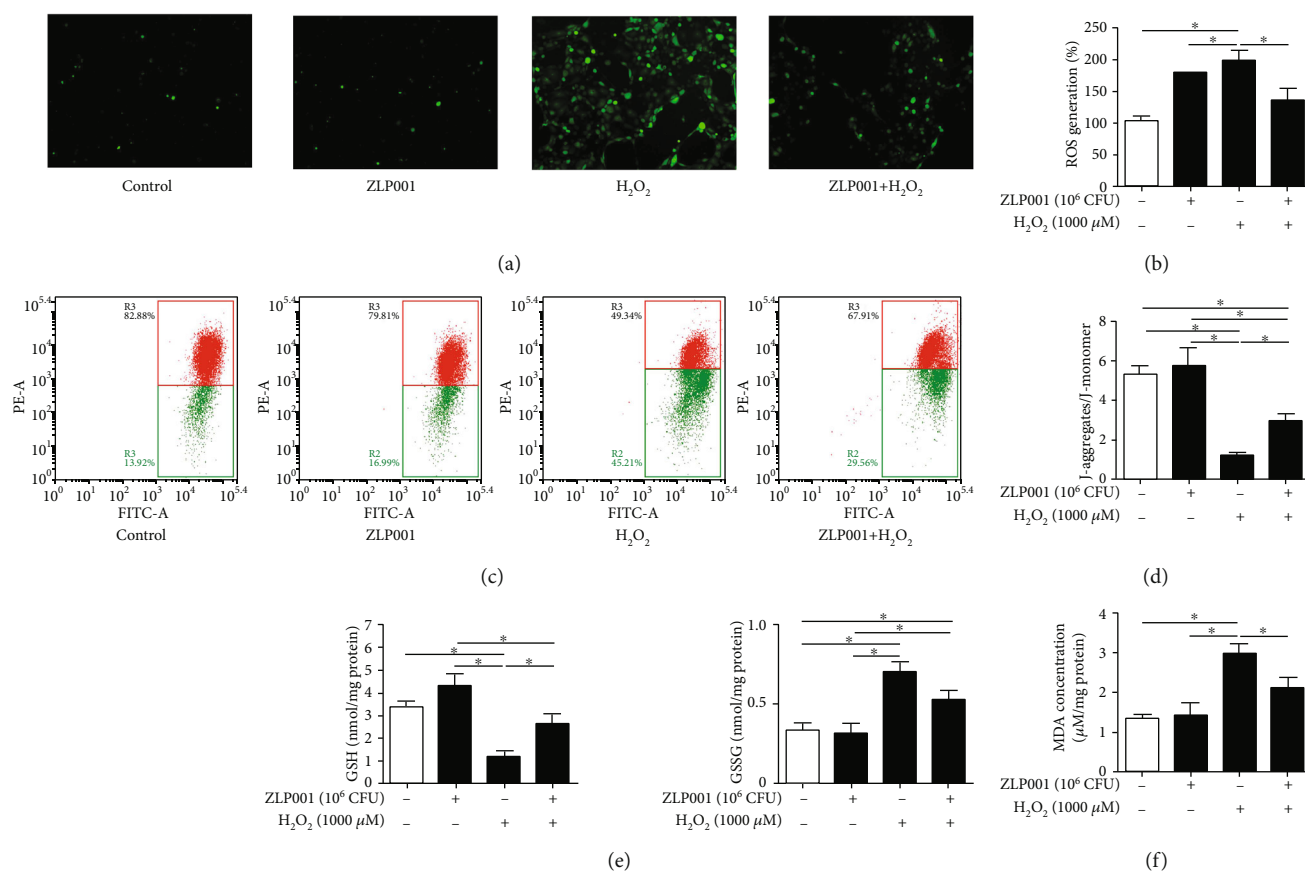


FIGURE 3: *Lactobacillus plantarum* ZLP001 improves the H<sub>2</sub>O<sub>2</sub>-induced redox state in IPEC-J2 cells. IPEC-J2 cells were incubated with or without 10<sup>6</sup> CFU *L. plantarum* ZLP001 for 3 h; after which, the medium was replaced with a fresh medium containing 1,000 μM H<sub>2</sub>O<sub>2</sub>, and the cells were further incubated for 4 h. (a) *L. plantarum* ZLP001 prevents H<sub>2</sub>O<sub>2</sub>-induced ROS accumulation in IPEC-J2 cells as indicated by DCFH-DA staining. (b) Quantification of the ROS levels based on DCFH-DA fluorescence. (c) Effect of *L. plantarum* ZLP001 on the mitochondrial membrane potential (MMP) in H<sub>2</sub>O<sub>2</sub>-induced IPEC-J2 cells as analyzed by flow cytometry. (d) Quantification of the effect on the MMP based on flow-cytometric data. (e) Concentrations of glutathione (GSH) and oxidized glutathione (GSSG) were determined using GSSG and GSH detection assays. (f) Concentrations of malondialdehyde (MDA) were determined using an MDA assay kit. All data represent the mean ± standard error of mean (SEM) of three independent experiments. Means were compared one-way ANOVA followed by Duncan's *post hoc* tests. \**P* < 0.05.

various cell types [23–25]. In the present study, MTT assays and the LD50 results demonstrated that treatment with 1,000 μM H<sub>2</sub>O<sub>2</sub> for 4 h was sufficient to induce oxidative stress in IPEC-2 cells. Pretreatment with *L. plantarum* ZLP001 (10<sup>6</sup> CFU, 3 h) significantly alleviated the decrease of cell viability and release of LDH caused by H<sub>2</sub>O<sub>2</sub>, suggesting that *L. plantarum* ZLP001 has antioxidant capacity and can protect cell integrity. Previous studies have demonstrated that epithelial barrier injury is associated with oxidative stress [22, 26]. Our previous study revealed that *L. plantarum* ZLP001 has a positive effect on intestinal barrier function [27]; therefore, we speculate that the fortifying effect of *L. plantarum* ZLP001 on the intestinal barrier may be partially associated with its antioxidant ability. We used morphological analysis to observe nuclear condensation and DNA fragmentation, which are hallmarks of cell apoptosis [28, 29]. Apoptosis is generally induced when cells are subjected to oxidative stress [30, 31]. H<sub>2</sub>O<sub>2</sub>-treated IPEC-J2 cells showed obvious apoptosis, as demonstrated by the appearance of apoptotic nuclei based on Hoechst staining, compared with

control cells. Pretreatment with *L. plantarum* ZLP001 obviously lowered the population of apoptotic nuclei in H<sub>2</sub>O<sub>2</sub>-induced IPEC-J2 cells. Flow cytometry results confirmed these findings. Probiotics have been previously demonstrated to have antiapoptotic effects and thus improve barrier function [32], suggesting they can indeed improve cell viability. Further, treatment with *L. plantarum* ZLP001 enhanced the expression of Bcl-2, while pretreatment suppressed the increase in activated caspase-3 caused by H<sub>2</sub>O<sub>2</sub>, corroborating the potential antiapoptotic role of *L. plantarum* ZLP001. Similar results were obtained by [14] using the probiotic strain *Bacillus amyloliquefaciens* SC06, although they only detected apoptosis-related gene expression and showed the image results. Taken together, our results indicate that *L. plantarum* ZLP001 has the potential to preserve intestinal integrity and barrier function under oxidative stress.

To confirm the antioxidant effect of *L. plantarum* ZLP001, we determined ROS production, MDA levels, and MMP. ROS are generated essentially for cellular growth and proliferation and have regulatory effects under

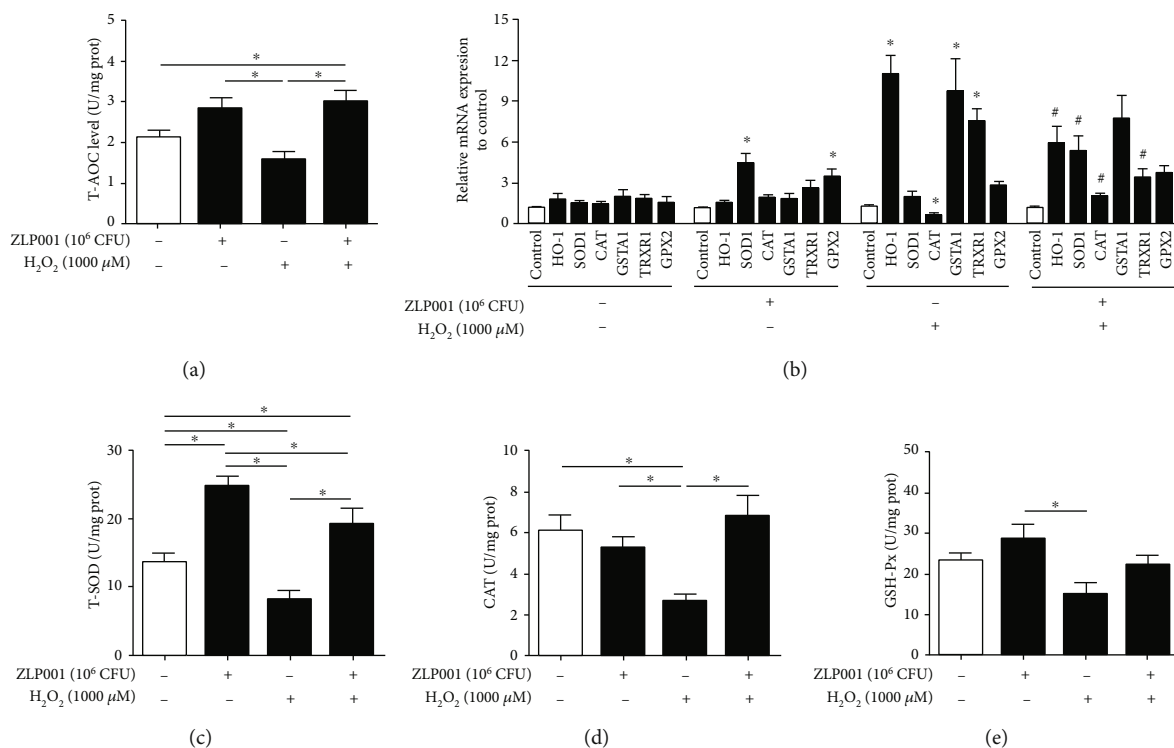


FIGURE 4: Effect of *Lactobacillus plantarum* ZLP001 on antioxidant enzyme expression and activity in IPEC-J2 cells. IPEC-J2 cells were incubated with 10<sup>6</sup> CFU *L. plantarum* ZLP001 for 3 h; after which, the medium was replaced with a fresh medium containing 1,000 μM H<sub>2</sub>O<sub>2</sub>, and the cells were further incubated for 4 h. (a) T-SOD activity in lysed cells was determined using a commercial assay kit. (b) The mRNA levels of *HO-1*, *SOD-1*, *CAT*, *GSTA1*, *TRXR1*, and *GPX2* as determined by RT-qPCR. (c–e) T-SOD, CAT, GSH-Px activities in lysed cells were determined using commercial assay kits. All data represent the mean ± standard error of mean (SEM) of three independent experiments. Differences between groups were analyzed by one-way ANOVA followed by Duncan's *post hoc* tests. \**P* < 0.05. Differences between two groups were determined by Student's *t*-test. \**P* < 0.05 vs. nontreated control cells; #*P* < 0.05 vs. H<sub>2</sub>O<sub>2</sub>-treated cells.

physiological conditions [33–35]. Under normal conditions, intracellular ROS levels are maintained at a sustainable level. However, ROS overproduction, which occurs when ROS levels exceed the endogenous cellular capacity to remove them, will lead to oxidative damage of intracellular macromolecules, thus inducing a series of oxidative stress reactions [36]. H<sub>2</sub>O<sub>2</sub> induced an intracellular ROS burst in IPEC-J2 cells as revealed by DCFH-DA staining. Pretreatment with *L. plantarum* ZLP001 remarkably reduced ROS accumulation induced by H<sub>2</sub>O<sub>2</sub>. The conversion of GSH to GSSG corroborated that *L. plantarum* ZLP001 could alleviate the oxidative stress caused by H<sub>2</sub>O<sub>2</sub>. GSH actively participates in scavenging ROS, but the conversion of GSH to GSSG after oxidation leads to the protein glutathionylation [37]. Levels of MDA, a product of lipid peroxidation, exhibited similar trends as the ROS levels in the present study. H<sub>2</sub>O<sub>2</sub> treatment stimulated MDA secretion, whereas *L. plantarum* ZLP001 pretreatment inhibited the production of MDA induced by H<sub>2</sub>O<sub>2</sub>. As the largest contributors to intracellular oxidant production in most cell types, mitochondria are the site of major oxidative processes [38] and play a critical role in the oxidative stress-induced cell death [39]. We measured the MMP to evaluate the redox state of mitochondria. H<sub>2</sub>O<sub>2</sub> decreased the MMP, whereas *L. plantarum* ZLP001 pretreatment enhanced the MMP. Mitochondrial dysfunction as

indicated by a decrease in the MMP is considered a characteristic feature of early apoptosis [40]. The decrease in the MMP after H<sub>2</sub>O<sub>2</sub> treatment in the present study suggested that apoptosis would be induced in the IPEC-J2 cells. Pretreatment with *L. plantarum* ZLP001 enhanced the MMP and markedly suppressed IPEC-J2 apoptosis. Thus, *L. plantarum* ZLP001 can effectively modulate the antioxidant status in IPEC-J2 cells. The limitation of our study is that the active molecules of this strain were not deeply studied. Studies have demonstrated that antioxidant molecules produced by probiotic strains, like exopolysaccharides and ferulic acid, may be the key factors that probiotics play their antioxidant activity [41, 42]. Further isolation, purification, and structural elucidation may also need to evaluate the main active ingredients of *L. plantarum* ZLP001.

Enhancing the host antioxidant defense system leads to ROS scavenging in the body, thus alleviating oxidative stress. The protective effect of probiotics involves both nonenzymatic and enzymatic redox mechanisms [43]. To further investigate the antioxidant mechanisms of *L. plantarum* ZLP001, we evaluated T-AOC and mRNA expression and activities of some antioxidant-associated enzymes in IPEC-J2 lysates. T-AOC normally reflects the capacity of the nonenzymatic antioxidant defense system [44] and is often used as a biomarker to investigate oxidative status [45]. The elevation

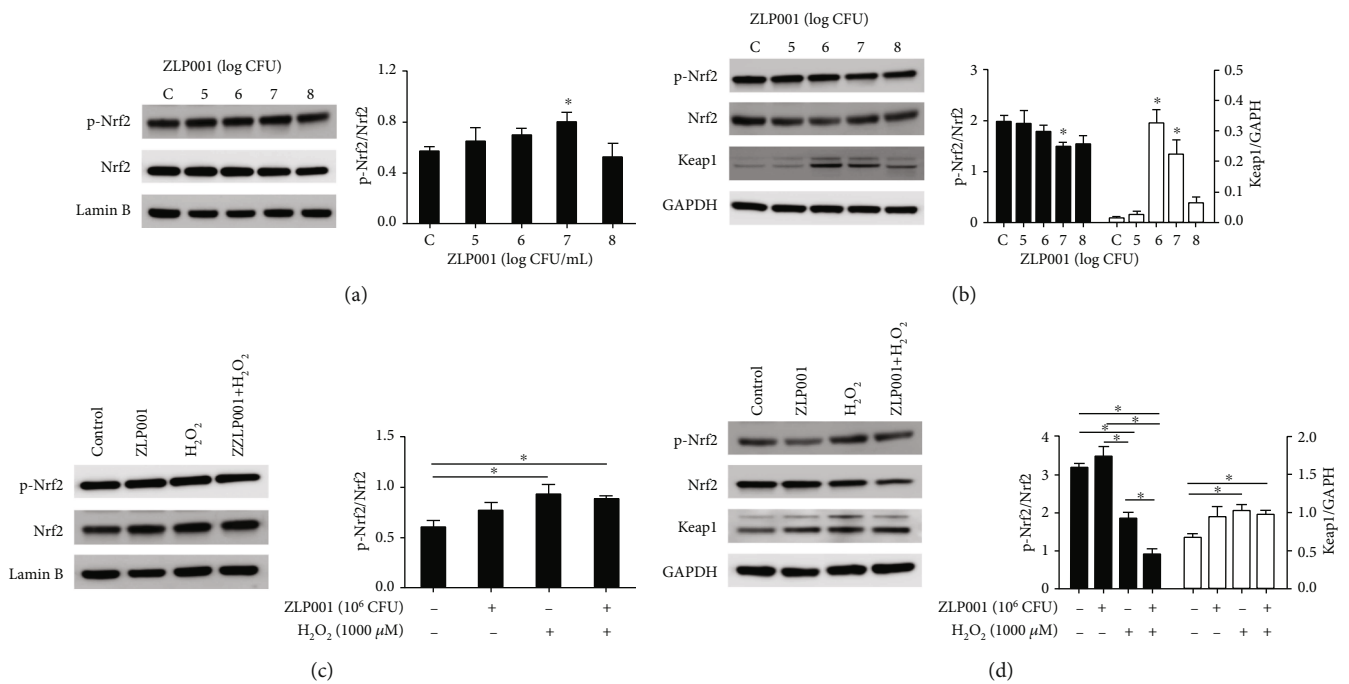


FIGURE 5: Effects of *Lactobacillus plantarum* ZLP001 on the Nrf2/Keap1 pathways in IPEC-J2 cells. (a) Protein levels of Nrf2 and p-Nrf2 as detected by western blot in nucleus (treated with different concentrations of *L. plantarum* ZLP001). (b) Protein levels of Nrf2, p-Nrf2, and Keap1 as detected by western blot in cytoplasm (treated with different concentrations of *L. plantarum* ZLP001). IPEC-J2 cells were incubated with indicated concentrations of *L. plantarum* ZLP001 for 3 h. After isolation of the nuclei from the cells, the nuclear Nrf2 and cytosolic Nrf2 and Keap1 were determined by immunoblotting. (c) Protein levels of Nrf2 and p-Nrf2 as detected by western blot in nucleus (treated with *L. plantarum* ZLP001 followed by H<sub>2</sub>O<sub>2</sub>). (d) Protein levels of Nrf2, p-Nrf2, and Keap1 as detected by western blot in cytoplasm (treated with *L. plantarum* ZLP001 followed by H<sub>2</sub>O<sub>2</sub>). IPEC-J2 cells were incubated with or without 10<sup>6</sup> CFU *L. plantarum* ZLP001 for 3 h; after which, the medium was replaced with a fresh medium containing 1,000 μM H<sub>2</sub>O<sub>2</sub>, and the cells were further incubated for 4 h. After isolation of the nuclei from the cells, the nuclear Nrf2 and cytosolic Nrf2 and Keap1 were determined by immunoblotting. All data represent the mean ± standard error of mean (SEM) of three independent experiments. Differences between the two groups were determined by Student's *t*-test. \**P* < 0.05 vs. nontreated control cells. Differences between groups were analyzed by one-way ANOVA followed by Duncan's *post hoc* tests. \**P* < 0.05.

in T-AOC after pretreatment with *L. plantarum* ZLP001 demonstrated that *L. plantarum* ZLP001 suppresses oxidative stress at least in part via the nonenzymatic antioxidant defense system. HO-1, a phase II enzyme, is transcriptionally regulated by various stimuli [46]. HO-1 is extremely sensitive to H<sub>2</sub>O<sub>2</sub> induction and can be used as a sensitive target to screen antioxidants [14]. In the present study, we observed induction of *HO-1* gene expression by H<sub>2</sub>O<sub>2</sub>, which was suppressed by *L. plantarum* ZLP001 pretreatment. Antioxidant enzymes, such as SOD and CAT, can detoxify ROS to safe molecules, thus protecting cells against ROS damage [47, 48]. Increased expression of *SOD1* after *L. plantarum* ZLP001 treatment alone and increased *CAT* expression after *L. plantarum* ZLP001 pretreatment compared with H<sub>2</sub>O<sub>2</sub> treatment was observed in the present study. Therefore, we also determined the expression levels of some other antioxidant-associated genes. *L. plantarum* ZLP001 treatment alone increased *GPX2* expression to elevate the antioxidant capacity. Similar results have been obtained in *Labeo rohita* fed probiotic and symbiotic diets [49]. The increase in *GSTA1* expression after H<sub>2</sub>O<sub>2</sub> exposure may suggest a self-protective response to mitigate H<sub>2</sub>O<sub>2</sub> toxicity [50]. Thioredoxin system activation was also observed after

H<sub>2</sub>O<sub>2</sub> treatment, and *L. plantarum* ZLP001 pretreatment decreased *TRXR1* expression, which is consistent with findings for several *Bacillus* strains research [14].

To confirm that *L. plantarum* ZLP001 enhanced the antioxidant system in IPEC-J2 cells, we measured antioxidase activity in IPEC-J2 cell lysates. In line with the gene expression results, *L. plantarum* ZLP001 increased T-SOD activity, and *L. plantarum* ZLP001 pretreatment alleviated the suppression of these enzyme activities by H<sub>2</sub>O<sub>2</sub>. The regulatory effects of probiotic strains on host antioxidative enzymes have been widely verified *in vitro* (in various cell models) and *in vivo* (in serum and in diverse tissues) [43, 50–52]. Our findings suggest that *L. plantarum* ZLP001 can dramatically improve the antioxidant status in IPEC-J2 cells by promoting cellular antioxidant defense systems against species generating ROS, thus rendering cells more resistant to the H<sub>2</sub>O<sub>2</sub> challenge.

As the key endogenous pathway regulating the antioxidant system, activation of the Nrf2/Keap1-antioxidant response element (ARE) axis increases the transcription of antioxidant response elements, thus protecting cells and tissues against ROS damage [53–55]. The altered phase II gene expression and antioxidase activities imply that *L. plantarum*

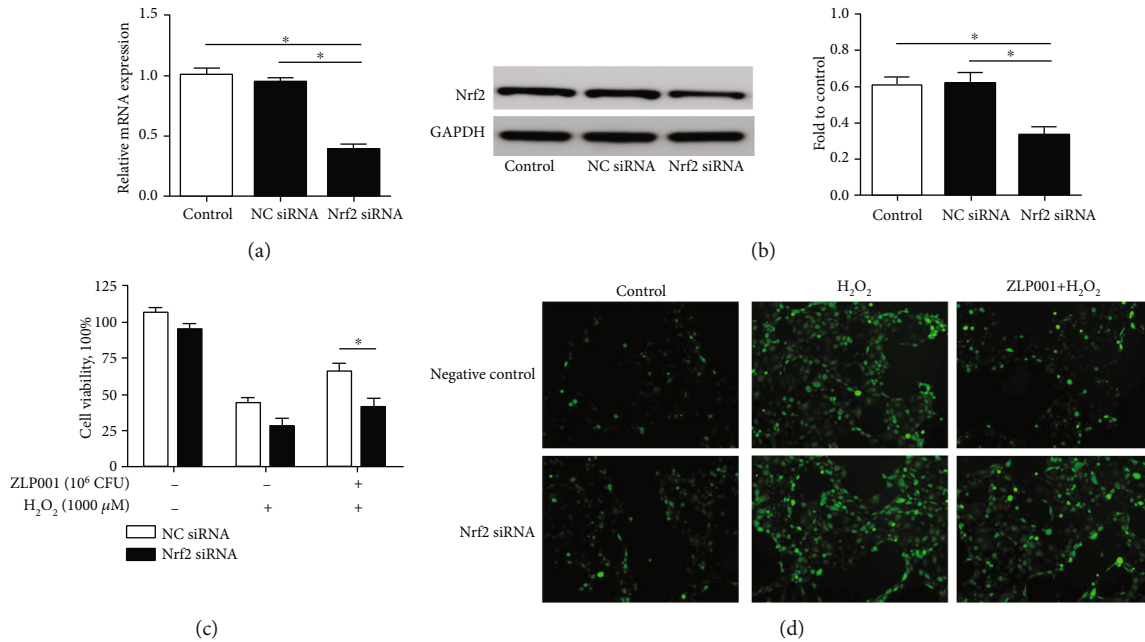


FIGURE 6: Effect of *Lactobacillus plantarum* ZLP001 on  $H_2O_2$ -induced oxidant stress in Nrf2-knockdown IPEC-J2 cells. IPEC-J2 cells were transfected with Nrf2 siRNA or negative control siRNA, and the efficiency of Nrf2 silencing was evaluated by RT-qPCR and western blot. (a) The mRNA level of Nrf2. (b) Western blot analysis of Nrf2 protein levels. Nrf2-knockdown and control cells were incubated with or without  $10^6$  CFU *L. plantarum* ZLP001 for 3 h; after which, the medium was replaced with a fresh medium containing 1,000  $\mu$ M  $H_2O_2$ , and the cells were further incubated for 4 h. (c) Cell viability was measured using the methyl thiazolyl tetrazolium assay. The results were normalized to negative control siRNA-transfected cells without  $H_2O_2$  and *L. plantarum* ZLP001 treatment. (d) ROS production was assessed by DCFH-DA staining and fluorescence microscopy. All data represent the mean  $\pm$  standard error of mean (SEM) of three independent experiments. Differences between groups were analyzed by one-way ANOVA followed by Duncan's *post hoc* tests. \* $P < 0.05$ . Differences between the two groups were determined using Student's *t* test. \* $P < 0.05$  vs. negative control siRNA-treated cells.

ZLP001 may affect the Nrf2/Keap1 pathway. Therefore, we investigated whether the Nrf2/Keap1-ARE pathway was involved in the antioxidant function of *L. plantarum* ZLP001. The expression of Nrf2/Keap1 pathway-related proteins in IPEC-J2 cells was enhanced by *L. plantarum* ZLP001, although differences were only significant at  $10^7$  CFU. Previous studies have also revealed that probiotic administration in high fat diet-fed mice can induce Nrf2 expression compared with the control, and probiotic treatment alone *in vitro* was able to induce Nrf2 phosphorylation in IPEC-1 cells [14, 56]. However, as different probiotic strains induce variable levels of Nrf2 expression [57], we plan to conduct a comparative study of multiple strains and to investigate other potential pathways. Nrf2 is normally activated when cells are exposed to oxidants and electrophiles, thus protecting the cells against oxidative stress [54].  $H_2O_2$  stress increased Nrf2 phosphorylation in the present study, which concurs with Wang et al. [14]. After pretreatment with *L. plantarum* ZLP001, we observed enhanced dissociation of Nrf2 in the cytosol, but it did not accumulate in the nucleus compared to  $H_2O_2$  treatment alone. Kobayashi and Yamamoto [58] reported that a phase II-activated defense system makes cells more resistant to subsequent even greater challenges. Thus, it is possible that *L. plantarum* ZLP001 may have activated Nrf2 before our detection time point, which made the IPEC-J2 cells more resistant to the subsequent challenge with  $H_2O_2$  without a need for the continued accumulation of

Nrf2. We further evaluated the cell viability, ROS production, and mRNA expression levels of antioxidative enzymes after Nrf2 knockdown in IPEC-J2 cells. The protective effect of *L. plantarum* ZLP001 on  $H_2O_2$ -induced IPEC-J2 cell damage was abolished under Nrf2 deficiency. These results confirm that the Nrf2-ARE signaling pathway is involved in the protective effect of *L. plantarum* ZLP001 and regulates the expression and activity of antioxidative enzymes to strengthen the defense against  $H_2O_2$ -induced oxidative stress in IPEC-J2 cells. Similarly, previous studies in different cells and hosts have reported that probiotic strains attenuate oxidative stress by upregulating Nrf2 expression, and by increasing the expression of antioxidative and cytoprotective genes [14, 15, 59]. However, Nrf2 activation by *L. plantarum* ZLP001 was not as significant as we expected and was not consistent with the antioxidant activity. As we have mentioned, other signaling pathways may also be involved in antioxidant regulation of *L. plantarum* ZLP001. Probiotics can attenuate hepatic oxidative stress via activating SIRT1 signaling [60] and ameliorate  $H_2O_2$ -induced epithelial barrier disruption through a PKC- and MAPK-dependent mechanism [61]. Whether these pathways were contributed to the antioxidant activity of *L. plantarum* ZLP001 is unknown. Thus, more robust, in-depth studies are required to unravel the precise antioxidant mechanism of *L. plantarum* ZLP001.

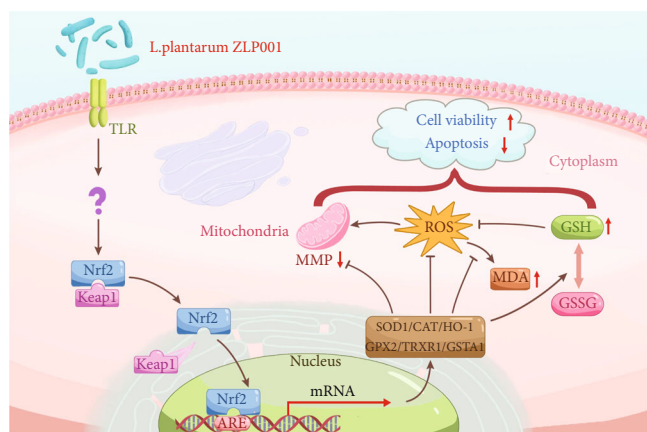


FIGURE 7: Suggested antioxidant protection mechanism of *Lactobacillus plantarum* ZLP001. *L. plantarum* ZLP001 may activate the Keap1-Nrf2 complex; after which, dissociated Nrf2 translocates to the nucleus and activates the transcription of cytoprotective genes, regulating the cellular redox state and activating the antioxidant defense system, thus alleviating cell apoptosis and necrosis caused by  $H_2O_2$ -induced oxidative stress.

## 5. Conclusions

We demonstrated that *L. plantarum* ZLP001 can alleviate oxidative damage induced by  $H_2O_2$  in porcine epithelial cells. Pretreatment with *L. plantarum* ZLP001 alleviated  $H_2O_2$ -induced cell oxidative damage by regulating the redox state of cells and enhancing the antioxidant defense system, and Nrf2/Keap1-ARE signaling is involved in its protective mechanisms (Figure 7). Our results improve our understanding of the underlying mechanism of *L. plantarum* ZLP001 in protecting against oxidative stress, and it can be developed into a therapeutic or protective treatment for animals under oxidative stress. However, whether Nrf2 signaling is activated at an earlier time point as we speculated and which signaling triggered the dissociation of Nrf2 from its constitutive inhibitor, Keap1, or other potential pathways contribute to its antioxidation remain to be investigated more extensively.

## Data Availability

The data generated during the present study are available from the corresponding authors upon request.

## Conflicts of Interest

The authors declare no conflict of interest.

## Authors' Contributions

JW conceived the study and drafted the manuscript. JW, WZ, and XCH performed the experiments. WZ analyzed the data. SW and YW contributed to the formal analysis. JW and HJ edited the manuscript. JW and WZ contributed equally to this work.

## Acknowledgments

The authors would like to thank Dr. Ri Qi for helpful suggestions and Dr. Tao Feng for strong support. This study was supported by the Beijing Natural Science Foundation (grant number 6202004), the National Natural Science Foundation of China (grant number 31972576), and the Special Program on Science and Technology Innovation Capacity Building of BAAFS (grant number KJCX201914).

## Supplementary Materials

Supplementary Table S1: sequences of the primers used in this study. Supplementary Table S2: antibodies used in this study. (*Supplementary Materials*)

## References

- [1] M. Schieber and N. S. Chandel, "ROS function in redox signaling and oxidative stress," *Current Biology*, vol. 24, no. 10, pp. R453–R462, 2014.
- [2] J. Lykkesfeldt and O. Svendsen, "Oxidants and antioxidants in disease: oxidative stress in farm animals," *Veterinary Journal*, vol. 173, no. 3, pp. 502–511, 2007.
- [3] J. X. Zhang, L. Y. Guo, L. Feng et al., "Soybean  $\beta$ -conglycinin induces inflammation and oxidation and causes dysfunction of intestinal digestion and absorption in fish," *PLoS One*, vol. 8, no. 3, article e58115, 2013.
- [4] A. Bhattacharyya, R. Chattopadhyay, S. Mitra, and S. E. Crowe, "Oxidative stress: an essential factor in the pathogenesis of gastrointestinal mucosal diseases," *Physiological Reviews*, vol. 94, no. 2, pp. 329–354, 2014.
- [5] A. Salami, A. Guinguina, J. O. Agboola, A. A. Omede, E. M. Agbonlahor, and U. Tayyab, "Review: *In vivo* and *postmortem* effects of feed antioxidants in livestock: a review of the implications on authorization of antioxidant feed additives," *Animal*, vol. 10, no. 8, pp. 1375–1390, 2016.
- [6] S. Janciauskiene, "The beneficial effects of antioxidants in health and diseases," *Chronic Obstructive Pulmonary Diseases*, vol. 7, no. 3, pp. 182–202, 2020.
- [7] V. Mishra, C. Shah, N. Mokashe, R. Chavan, H. Yadav, and J. Prajapati, "Probiotics as potential antioxidants: a systematic review," *Journal of Agricultural and Food Chemistry*, vol. 63, no. 14, pp. 3615–3626, 2015.
- [8] Y. Wang, Y. Wu, Y. Wang et al., "Antioxidant properties of probiotic bacteria," *Nutrients*, vol. 9, no. 5, p. 521, 2017.
- [9] T. Feng and J. Wang, "Oxidative stress tolerance and antioxidant capacity of lactic acid bacteria as probiotic: a systematic review," *Gut Microbes*, vol. 12, no. 1, article 1801944, 2020.
- [10] M. Y. Lin and C. L. Yen, "Antioxidative ability of lactic acid bacteria," *Journal of Agricultural and Food Chemistry*, vol. 47, no. 4, pp. 1460–1466, 1999.
- [11] T. Virtanen, A. Pihlanto, S. Akkanen, and H. Korhonen, "Development of antioxidant activity in milk whey during fermentation with lactic acid bacteria," *Journal of Applied Microbiology*, vol. 102, no. 1, pp. 106–115, 2007.
- [12] G. Mu, Y. Gao, Y. Tuo et al., "Assessing and comparing antioxidant activities of lactobacilli strains by using different chemical and cellular antioxidant methods," *Journal of Dairy Science*, vol. 101, no. 12, pp. 10792–10806, 2018.

- [13] A. Amaretti, M. di Nunzio, A. Pompei, S. Raimondi, M. Rossi, and A. Bordoni, "Antioxidant properties of potentially probiotic bacteria: *in vitro* and *in vivo* activities," *Applied Microbiology and Biotechnology*, vol. 97, no. 2, pp. 809–817, 2013.
- [14] Y. Wang, Y. Wu, Y. Wang et al., "*Bacillus amyloliquefaciens* SC06 alleviates the oxidative stress of IPEC-1 via modulating Nrf2/Keap1 signaling pathway and decreasing ROS production," *Applied Microbiology and Biotechnology*, vol. 101, no. 7, pp. 3015–3026, 2017.
- [15] X. Lin, Y. Xia, G. Wang et al., "*Lactobacillus plantarum* AR501 alleviates the oxidative stress of d-galactose-induced aging mice liver by upregulation of Nrf2-mediated antioxidant enzyme expression," *Journal of Food Science*, vol. 83, no. 7, pp. 1990–1998, 2018.
- [16] J. Wang, H. F. Ji, D. Y. Zhang et al., "Assessment of probiotic properties of *Lactobacillus plantarum* ZLP001 isolated from gastrointestinal tract of weaning pigs," *African Journal of Biotechnology*, vol. 10, no. 54, pp. 11303–11308, 2011.
- [17] J. Wang, H. Ji, S. Wang et al., "*Lactobacillus plantarum* ZLP001: *in vitro* assessment of antioxidant capacity and effect on growth performance and antioxidant status in weaning piglets," *Asian-Australasian Journal of Animal Sciences*, vol. 25, no. 8, pp. 1153–1158, 2012.
- [18] K. J. Livak and T. D. Schmittgen, "Analysis of relative gene expression data using real-time quantitative PCR and the  $2^{-\Delta\Delta C_T}$  method," *Methods*, vol. 25, no. 4, pp. 402–408, 2001.
- [19] L. Y. Hu, D. W. Chen, P. Zheng et al., "The bidirectional interactions between resveratrol and gut microbiota: an insight into oxidative stress and inflammatory bowel disease therapy," *Biomed Research International*, vol. 2019, Article ID 5403761, 9 pages, 2019.
- [20] B. Mishra and R. Jha, "Oxidative stress in the poultry gut: potential challenges and interventions," *Frontiers in Veterinary Science*, vol. 6, p. 60, 2019.
- [21] A. Thomson, D. Hemphill, and K. N. Jeejeebhoy, "Oxidative stress and antioxidants in intestinal disease," *Journal of Digestive Diseases*, vol. 16, no. 3, pp. 152–158, 1998.
- [22] Z. Sun, K. Olanders, Å. Lason et al., "Effective treatment of gut barrier dysfunction using an antioxidant, a PAF inhibitor, and monoclonal antibodies against the adhesion molecule PECAM-1," *Journal of Surgical Research*, vol. 105, no. 2, pp. 220–233, 2002.
- [23] Y. Zou, J. Wang, J. Peng, and H. Wei, "Oregano essential oil induces SOD1 and GSH expression through Nrf2 activation and alleviates hydrogen peroxide-induced oxidative damage in IPEC-J2 cells," *Oxidative Medicine and Cellular Longevity*, vol. 2016, Article ID 5987183, 13 pages, 2016.
- [24] X. Chi, X. Ma, Z. Li et al., "Protective effect of epigallocatechin-3-gallate in hydrogen peroxide-induced oxidative damage in chicken lymphocytes," *Oxidative Medicine and Cellular Longevity*, vol. 2020, Article ID 7386239, 15 pages, 2020.
- [25] J. J. Yang, X. B. Song, Y. Feng et al., "Natural ingredients-derived antioxidants attenuate H<sub>2</sub>O<sub>2</sub>-induced oxidative stress and have chondroprotective effects on human osteoarthritic chondrocytes via Keap1/Nrf2 pathway," *Free Radical Biology and Medicine*, vol. 152, pp. 854–864, 2020.
- [26] I. E. Blasig, C. Bellmann, J. Cording et al., "Occludin protein family: oxidative stress and reducing conditions," *Antioxidants & Redox Signaling*, vol. 15, no. 5, pp. 1195–1219, 2011.
- [27] J. Wang, H. F. Ji, S. X. Wang et al., "Probiotic *Lactobacillus plantarum* promotes intestinal barrier function by strengthening the epithelium and modulating gut microbiota," *Frontiers in Microbiology*, vol. 9, p. 1953, 2018.
- [28] Y. Higuchi, "Chromosomal DNA fragmentation in apoptosis and necrosis induced by oxidative stress," *Biochemical Pharmacology*, vol. 66, no. 8, pp. 1527–1535, 2003.
- [29] E. A. Prokhorova, A. V. Zamaraev, G. S. Kopeina, B. Zhivotovsky, and I. N. Lavrik, "Role of the nucleus in apoptosis: signaling and execution," *Cellular and Molecular Life Sciences*, vol. 72, no. 23, pp. 4593–4612, 2015.
- [30] K. Sinha, J. Das, P. B. Pal, and P. C. Sil, "Oxidative stress: the mitochondria-dependent and mitochondria-independent pathways of apoptosis," *Archives of Toxicology*, vol. 87, no. 7, pp. 1157–1180, 2013.
- [31] A. Hanikoglu, H. Ozben, F. Hanikoglu, and T. Ozben, "Hybrid compounds & oxidative stress induced apoptosis in cancer therapy," *Current Medicinal Chemistry*, vol. 27, no. 13, pp. 2118–2132, 2020.
- [32] Y. Y. Yu, J. Lu, K. Oliphant, N. Gupta, K. Claud, and L. Lu, "Maternal administration of probiotics promotes gut development in mouse offsprings," *PLoS One*, vol. 15, no. 8, article e0237182, 2020.
- [33] C. R. Reczek and N. S. Chandel, "ROS-dependent signal transduction," *Current Opinion in Cell Biology*, vol. 33, pp. 8–13, 2015.
- [34] G. S. Shadel and T. L. Horvath, "Mitochondrial ROS signaling in organismal homeostasis," *Cell*, vol. 163, no. 3, pp. 560–569, 2015.
- [35] S. Banerjee, S. Ghosh, A. Mandal, N. Ghosh, and P. C. Sil, "ROS-associated immune response and metabolism: a mechanistic approach with implication of various diseases," *Archives of Toxicology*, vol. 94, no. 7, pp. 2293–2317, 2020.
- [36] G. Pizzino, N. Irrera, M. Cucinotta et al., "Oxidative stress: harms and benefits for human health," *Oxidative Medicine and Cellular Longevity*, vol. 2017, Article ID 8416763, 13 pages, 2017.
- [37] L. Flohé, "The fairytale of the GSSG/GSH redox potential," *Biochimica et Biophysica Acta*, vol. 1830, no. 5, pp. 3139–3142, 2013.
- [38] K. M. Holmström and T. Finkel, "Cellular mechanisms and physiological consequences of redox-dependent signalling," *Nature Reviews Molecular Cell Biology*, vol. 15, no. 6, pp. 411–421, 2014.
- [39] S. Orrenius, V. Gogvadze, and B. Zhivotovsky, "Mitochondrial oxidative stress: implications for cell death," *Annual Review of Pharmacology and Toxicology*, vol. 47, no. 1, pp. 143–183, 2007.
- [40] J. D. Ly, D. R. Grubb, and A. Lawen, "The mitochondrial membrane potential ( $\Delta\psi(m)$ ) in apoptosis: an update," *Apoptosis*, vol. 8, no. 2, pp. 115–128, 2003.
- [41] W. Li, J. Ji, X. Chen, M. Jiang, X. Rui, and M. Dong, "Structural elucidation and antioxidant activities of exopolysaccharides from *Lactobacillus helveticus* MB2-1," *Carbohydrate Polymers*, vol. 102, pp. 351–359, 2014.
- [42] C. Tomaro-Duchesneau, S. Saha, M. Malhotra et al., "Effect of orally administered *L. fermentum* NCIMB 5221 on markers of metabolic syndrome: an *in vivo* analysis using ZDF rats," *Applied Microbiology and Biotechnology*, vol. 98, no. 1, pp. 115–126, 2014.
- [43] A. Finamore, R. Ambra, F. Nobili, I. Garaguso, A. Raguzzini, and M. Serafini, "Redox role of *Lactobacillus casei* Shirota against the cellular damage induced by 2,2'-Azobis (2-

- amidinopropane) dihydrochloride-induced oxidative and inflammatory stress in enterocytes-like epithelial cells,” *Frontiers in Immunology*, vol. 9, article 1131, 2018.
- [44] G. Bartosz, “Non-enzymatic antioxidant capacity assays: limitations of use in biomedicine,” *Free Radical Research*, vol. 44, no. 7, pp. 711–720, 2010.
- [45] I. Peluso and A. Raguzzini, “Salivary and urinary total antioxidant capacity as biomarkers of oxidative stress in humans,” *Pathology Research International*, vol. 2016, Article ID 5480267, 14 pages, 2016.
- [46] S. W. Ryter and A. M. K. Choi, “Heme oxygenase-1: molecular mechanisms of gene expression in oxygen-related stress,” *Antioxidant & Redox Signaling*, vol. 4, no. 4, pp. 625–632, 2002.
- [47] H. Yang and T. H. Lee, “Antioxidant enzymes as redox-based biomarkers: a brief review,” *BMB Reports*, vol. 48, no. 4, pp. 200–208, 2015.
- [48] X. G. Lei, J. H. Zhu, W. H. Cheng et al., “Paradoxical roles of antioxidant enzymes: basic mechanisms and health implications,” *Physiological Reviews*, vol. 96, no. 1, pp. 307–364, 2016.
- [49] G. Devi, R. Harikrishnan, B. A. Paray, M. K. al-Sadoon, S. H. Hoseinifar, and C. Balasundaram, “Effect of symbiotic supplemented diet on innate-adaptive immune response, cytokine gene regulation and antioxidant property in *Labeo rohita* against *Aeromonas hydrophila*,” *Fish & Shellfish Immunology*, vol. 89, pp. 687–700, 2019.
- [50] F. Chen, H. Wang, J. Chen et al., “*Lactobacillus delbrueckii* ameliorates intestinal integrity and antioxidant ability in weaned piglets after a Lipopolysaccharide challenge,” *Oxidative Medicine and Cellular Longevity*, vol. 2020, Article ID 6028606, 10 pages, 2020.
- [51] S. Noureen, A. Riaz, M. Arshad, and N. Arshad, “*In vitro* selection and *in vivo* confirmation of the antioxidant ability of *Lactobacillus brevis* MG000874,” *Journal of Applied Microbiology*, vol. 126, no. 4, pp. 1221–1232, 2019.
- [52] Y. Zhang, R. du, L. Wang, and H. Zhang, “The antioxidative effects of probiotic *Lactobacillus casei* Zhang on the hyperlipidemic rats,” *European Food Research and Technology*, vol. 231, no. 1, pp. 151–158, 2010.
- [53] V. O. Tkachev, E. B. Menshchikova, and N. K. Zenkov, “Mechanism of the Nrf2/Keap1/ARE signaling system,” *Biochemistry*, vol. 76, no. 4, pp. 407–422, 2011.
- [54] Q. Ma, “Role of Nrf2 in oxidative stress and toxicity,” *Annual Review of Pharmacology and Toxicology*, vol. 53, no. 1, pp. 401–426, 2013.
- [55] T. Suzuki and M. Yamamoto, “Molecular basis of the Keap1-Nrf2 system,” *Free Radical Biology and Medicine*, vol. 88, Part B, pp. 93–100, 2015.
- [56] D. Gao, Z. Gao, and G. Zhu, “Antioxidant effects of *Lactobacillus plantarum* via activation of transcription factor Nrf2,” *Food & Function*, vol. 4, no. 6, pp. 982–989, 2013.
- [57] R. Chauhan, A. Sudhakaran Vasanthakumari, H. Panwar et al., “Amelioration of colitis in mouse model by exploring antioxidative potentials of an indigenous probiotic strain of *Lactobacillus fermentum* Lf1,” *Biomed Research International*, vol. 2014, Article ID 206732, 12 pages, 2014.
- [58] M. Kobayashi and M. Yamamoto, “Molecular mechanisms activating the Nrf2-Keap1 pathway of antioxidant gene regulation,” *Antioxidants & Redox Signaling*, vol. 7, no. 3-4, pp. 385–394, 2005.
- [59] E. Kobatake, H. Nakagawa, T. Seki, and T. Miyazaki, “Protective effects and functional mechanisms of *Lactobacillus gasseri* SBT2055 against oxidative stress,” *PLoS One*, vol. 12, no. 5, article e0177106, 2017.
- [60] Y. Liu, Q. Liu, J. Hesketh et al., “Protective effects of selenium-glutathione-enriched probiotics on CCl<sub>4</sub>-induced liver fibrosis,” *The Journal of Nutritional Biochemistry*, vol. 58, pp. 138–149, 2018.
- [61] A. Seth, F. Yan, D. B. Polk, and R. K. Rao, “Probiotics ameliorate the hydrogen peroxide-induced epithelial barrier disruption by a PKC- and MAP kinase-dependent mechanism,” *American Journal of Physiology-Gastrointestinal and Liver Physiology*, vol. 294, no. 4, pp. G1060–G1069, 2008.